


Spring 1996

The Progressive Failure Analysis of Cut Slope in Anisotropic Strain Softening Soils

Jong Woon Choi
Old Dominion University

Follow this and additional works at: https://digitalcommons.odu.edu/cee_etds

 Part of the [Civil Engineering Commons](#), and the [Mechanical Engineering Commons](#)

Recommended Citation

Choi, Jong W.. "The Progressive Failure Analysis of Cut Slope in Anisotropic Strain Softening Soils" (1996). Doctor of Philosophy (PhD), dissertation, Civil/Environmental Engineering, Old Dominion University, DOI: 10.25777/hxrx-1q88
https://digitalcommons.odu.edu/cee_etds/41

This Dissertation is brought to you for free and open access by the Civil & Environmental Engineering at ODU Digital Commons. It has been accepted for inclusion in Civil & Environmental Engineering Theses & Dissertations by an authorized administrator of ODU Digital Commons. For more information, please contact digitalcommons@odu.edu.

**THE PROGRESSIVE FAILURE ANALYSIS OF CUT SLOPE
IN ANISOTROPIC STRAIN SOFTENING SOILS**

By

Jong Woon Choi

A Dissertation Submitted to the Faculty
of Old Dominion University
in Partial Fulfillment of the Requirement of the Degree of

Doctor of Philosophy
in
Civil and Environmental Engineering

OLD DOMINION UNIVERSITY

May, 1996

Approved by:

Prof. Isao Ishibashi (Chair)

Prof. A. Osman Akan

Prof. Duc T. Nguyen

Prof. Yozo Mikata

ABSTRACT

THE PROGRESSIVE FAILURE ANALYSIS OF CUT SLOPE IN ANISOTROPIC STRAIN SOFTENING SOILS

Jong Woon Choi

Old Dominion University, 1995

Advisor: Prof. Isao Ishibashi

The failure phenomena in earth structures such as slopes and embankments on clay foundations are a consequence of the formation of failure surfaces. It has been repeatedly confirmed that the ratio of the actually mobilized strength along the failure surface to the undrained strength determined in the laboratory decreases significantly with increasing stiffness of the soil. The discrepancy may be due mainly to the progressive failure with anisotropic stress-strain-strength relations (Bishop, 1971), while other explanations can be invoked such as the rate of shear, the effects of the sample size and disturbance. Unfortunately, there has been no specific case study from which the effect of progressive failure can be clearly deduced among other factors, and therefore the significance of progressive failure in slope stability has been uncertain.

A finite difference computer code, FLAC (Itasca Consulting Group, 1993), with the isotropic Mohr-Coulomb plasticity model, is used to analyze the undrained progressive failure of a strain softening soil during a slope excavation process. The focus of the study is on the short-term stability of slopes. In the first series of analyses, which are aimed at the evaluation of anisotropic strength effect on slope stability, the isotropic Mohr-Coulomb plasticity model is slightly modified to implement the anisotropic nature of undrained strength. In order to implement the anisotropic nature of undrained strength of clay, the major principal stress direction of individual element is computed after each computational time step, and undrained strength of the element is reassigned based on the predetermined relations between them. This approach enables the explicit treatment of anisotropic nature of the undrained strength.

In the second series of analyses, which are aimed at the evaluation of progressive failure effect on slope stability, the stress-strain-strength relations determined based on existing laboratory data from the literature are closely curve-fitted as a function of the plastic shear strain. In order to define the stress-strain-strength relations for the entire elements with varying i angles, the typical laboratory soil testings are considered as variations of a testing method in which i angles at the incipient failure differ. In addition, the resulting stress-strain-strength relations are assumed to systematically vary in their patterns. Consequently, for a given i angle distribution in the slope, individual element has its own unique stress-strain-strength relations such that the relative pattern of

stress-strain relations for varying stress paths are explicitly implemented to evaluate the progressive failure effect.

Since the first series of analyses are focused on the anisotropic nature of undrained strength alone, while the second ones are concerned about the anisotropic stress-strain-strength relations, the difference in their results is attributed to the effect of progressive failure. It was explicitly shown that the anisotropic stress-strain-strength relations are always accompanied by the sequential mobilization of peak strengths of the elements along the failure surface. Consequently, it was confirmed that the summation of the peak strengths mobilized along the failure surface is significantly less than that of the isotropic compression strengths. However, the strength reduction due to the anisotropic stress-strain relations (progressive failure) was found to be not as critical as that caused by the anisotropic undrained strength. In addition, several anisotropic strength variations along with varying degree of strain softening are parametrically implemented. It was found that the effect of strength anisotropy is more critical than that of strain softening. Based on this research, the strain compatibility technique in the slope stability analysis proposed by Koutsoftas and Ladd (1985) is critically reassessed.

**This dissertation is dedicated to
my parents.**

ACKNOWLEDGEMENTS

The author wishes to take this opportunity to acknowledge his sincerest gratitude to Professor Isao Ishibashi for continuous guidance and enlightenment throughout the Ph.D. program. Particularly, he is appreciative of his time, effort and patience in the discussions which often extended to a few hours.

The author also expresses his gratitude to professors Akan, Nguyen, and Mikata for guidance through the course work and for serving on the advisory committee.

During the Ph.D. program, the author worked on a two-year slope analysis project which was sponsored by the Army Corps of Engineers, Norfolk District. During the project, he expanded his horizon and gained valuable practical experience in geotechnical engineering. He would like to thank Mr. David Pezza, P.E., chief of geotechnical engineering division, for his help during the project.

The author is greatly appreciative of his parents for their support and encouragement during the study. He also would like to thank his in-laws in Korea for bearing with his family's absence during the study. The author is greatly indebted to his lovely wife, Yeon-Soo Choi, for her invaluable assistance and never-ending endurance during the study.

TABLE OF CONTENTS

ABSTRACT	i
TITLE PAGE	iv
DEDICATION	v
ACKNOWLEDGEMENTS	vi
TABLE OF CONTENTS	vii
LIST OF TABLES	xi
LIST OF FIGURES	xiii
LIST OF SYMBOLS	xxvi
1. INTRODUCTION	1
2. OBJECTIVE AND SCOPE OF THE STUDY	4
3. LITERATURE SURVEY	5
3.1 Introduction	5
3.2 Framework of the Slope Stability Analysis	6
3.2.1 Prerequisite for the Slope Stability Analysis	6
3.2.2 Factor of Safety	10
3.2.3 Drainage and Loading Conditions	11
3.3 Slope Stability Analysis Methods	15
3.3.1 Introduction	15
3.3.2 Classical Plastic Equilibrium Methods	16
3.3.3 Limit Equilibrium Analysis	19
3.3.3.1 Introduction	19
3.3.3.2 Principle of Limit Equilibrium Analysis	20
3.3.4 Limit Analysis	24
3.3.5 Finite Element Analysis	26
3.3.5.1 Linear Elastic Models	26

3.3.5.2 Multilinear Elastic Models	27
3.3.5.3 Hyperbolic Elastic Models	28
3.3.5.4 Plasticity Models	29
3.3.5.4.1 Perfect Plasticity Models	29
3.3.5.4.1.1 Yield Criteria	31
3.3.5.4.1.2 Flow Rule	34
3.3.5.4.2 Strain Hardening Models	35
3.3.5.4.2.1 Plasticity Hardening Models	35
3.3.5.4.2.2 Cap Hardening Models	38
3.3.5.4.3 Strain Softening Models	40
3.4. Pseudo-Progressive Failure Analyses	46
3.4.1 Introduction	46
3.4.2 Progressive Failure Analyses Using LEA Methods	47
3.4.2.1 Residual Method	47
3.4.2.2 Conlon's Approach	48
3.4.2.3 Bishop's Approach	50
3.4.2.4 Chandler and Skempton's Approach	53
3.4.2.5 Lo and Lee's Method	54
3.4.2.6 Ladd and Koutsoftas's Approach	55
3.4.2.7 Mesri and Abdel-Ghaffar's Method	59
3.5 Stress-Strain-Strength Relations of Soils	62
3.5.1 Introduction	62
3.5.2 Plastic Yielding Behavior of Soils	63
3.5.2.1 Strain Hardening Behavior	65
3.5.2.2 Strain Softening Behavior	67
3.5.3 Failure Modes	69
3.5.4 Undrained Shear Strength Anisotropy	72
3.5.4.1 Normalized Shear Strength Behavior of Clays	72
3.5.4.2 Sources of Anisotropy	74
3.5.4.3 Observation of Undrained Strength Anisotropy	77

3.5.5	General Stress-Strain Behavior of Soils	84
3.5.5.1	Data Collection of Stress-Strain Relations	84
3.5.5.1.1	Normally Consolidated Clays	84
3.5.5.1.2	Overconsolidated Clays	98
3.5.5.2	Generalization of Stress-Strain Curves	104
3.5.5.2.1	Correlation of Stress-Strain Curves	104
3.5.5.2.2	Consolidation Pressure Effects on the Stress-Strain Relations	108
4.	MODE OF LOADING AND STRESS-STRAIN MODELLING	113
4.1	Analysis of Loading Mode	113
4.2	Stress-Strain Modelling	130
4.2.1	Stress-Strain Model in the Anisotropic Analysis	131
4.2.1.1	Anisotropy of the Undrained Strength	131
4.2.1.2	Determination of i angle	138
4.2.1.3	Elastic Properties Determination	139
4.2.2	Stress-Strain Modelling in the Strain Hardening and Softening Analysis	146
4.2.2.1	Basic Approaches	146
4.2.2.2	Stress-Strain Modelling in the Active Region	154
4.2.2.3	Stress-Strain Modelling in the Passive Region	163
4.3	Analysis Procedure	166
4.3.1	Anisotropic Strength Analyses	166
4.3.2	Anisotropic Strength with Strain Softening Analyses	169
5.	EXPLICIT FINITE DIFFERENCE METHOD (FLAC)	173
5.1	FLAC (Fast Lagrangian Analysis of Continua) Formulation	173
5.2	Mohr-Coulomb Plasticity Model	178
5.2.1	Yield Criteria	178
5.2.2	Flow Rule	179
5.2.3	Strain Softening/Hardening Implementation	181

6. SLOPE STABILITY ANALYSIS USING FLAC	183
6.1 Classification of Analyses Based on Material Types	183
6.2 Normally Consolidated Clays	186
6.2.1 Homogeneous Strength Profile	186
6.2.1.1 Isotropic Strength Case (A analysis)	188
6.2.1.2 Anisotropic Strength Case (B analysis)	190
6.2.1.3 Anisotropic Strength with Strain Hardening and Softening Cases (C and D analyses)	207
6.2.2 Linearly Increasing Strength Profile	226
6.2.2.1 Isotropic Strength Case (A analysis)	228
6.2.2.2 Anisotropic Strength Cases (B analysis)	243
6.2.2.3 Anisotropic Strength with Strain Hardening and Softening Cases (C and D analyses)	266
6.3 Overconsolidated Clay	308
6.3.1 Introduction	308
6.3.2 Isotropic Strength Case (A analysis)	312
6.3.3 Anisotropic Strength Cases (B analysis)	318
6.3.4 Anisotropic Strength with Strain Hardening and Softening Cases (C and D analyses)	343
7. SUMMARY AND CONCLUSIONS	370
7.1 Summary	370
7.1.1 Homogeneous Strength Cases	370
7.1.2 Linearly Increasing Strength Cases	371
7.1.3 Overconsolidated Clay Cases	372
7.2 Conclusions	375
BIBLIOGRAPHY	378
APPENDIX	391
VITA	393

LIST OF TABLES

Table 3.1	Summary of the stress-strain-strength relations of various clays	99
Table 3.2	Summary of the parameters of the stress-strain-strength relations	106
Table 6.1	Analysis classification based on the stress-strain relation	183
Table 6.2	Analysis classification based on the strength anisotropy variation	185
Table 6.3	Analysis classification based on the degree of strain softening	185
Table 6.4	Summary of FLAC analyses	186
Table 6.5	Summary of excavation heights with number of layer excavation	188
Table 6.6	Summary of the available strength ratio at failure	203
Table 6.7	Summary of the peak mobilized strength ratios	218
Table 6.8	Summary of the peak strength ratios using the strain compatibility technique	225
Table 6.9	Summary of excavation heights (meters) with the number of layer excavation	228
Table 6.10	Slope information	228
Table 6.11	Summary of factors of safety from A and B series analyses	253

Table 6.12	Summary of the available strength ratios from B(30) and B (60) analyses	266
Table 6.13a	Summary of the peak mobilized strength ratios (30 degree slope)	294
Table 6.13b	Summary of the peak mobilized strength ratios (60 degree slope)	294
Table 6.14	Summary of the peaks of summations of undrained strength using the strain compatibility technique	303
Table 6.15	Summary of excavation heights (meters) with the number of layer excavation	312
Table 6.16a	Summary of the peak mobilized strength ratios (C analysis)	357
Table 6.16b	Summary of the peak mobilized strength ratios (D and E analyses)	357
Table 6.17	Summary of the peak strength ratios using the strain compatibility technique	366
Table 6.18	Summary of the peak mobilized strength ratios from the entire cases	375

LIST OF FIGURES

Fig. 3.1	Yield criteria for soils: (a) Mohr-Coulomb criterion; (b) Extended Tresca criterion; and (c) Extended von Mises criterion.	33
Fig. 3.2	The numerical procedure of iterative process of the stress release and transfer (Lo and Lee, 1973).	43
Fig. 3.3	A simplified strain softening model using the elasto-plastic theory (Kalteziotis and Kyrou, 1985).	43
Fig. 3.4	The definition of brittleness index of soil	51
Fig. 3.5	Possible local residual factor distributions	51
Fig. 3.6	Relations between the correct factor of safety and the residual factor	56
Fig. 3.7	Anisotropic stress-strain relations of AGS clay	57
Fig. 3.8	Relations between the correction factor (η) and the plasticity index (I_p)	60
Fig. 3.9	Relations between mobilized cohesion intercept (c'_{mob}) and measured cohesion intercept (c')	60
Fig. 3.10	Idealized stress-strain models	64
Fig. 3.11	Approximation of stress-strain relations by elasto-plastic model	66
Fig. 3.12	Undrained strength ratios with varying OCR for several clays (Ladd and Foott, 1974)	75

Fig. 3.13	Undrained strength anisotropy from K_0 -consolidated undrained (CK_0U) tests on normally consolidated clays and silts (Ladd, 1986)	79
Fig. 3.14	Undrained strength variation with the major principal stress direction (i angle)	81
Fig. 3.15	OCR vs. undrained strength ratio and shear strain at failure from K_0 -consolidated undrained (CK_0U) tests: (a) (AGS plastic marine clay); and (b) (James Bay sensitive marine clay)	82
Fig. 3.16	Comparison of stress-strain relations: (a) plane strain, K_0 triaxial, and isotropic triaxial compression tests; (b) triaxial and plane strain tests (Vaid and Campanella, 1974)	86
Fig. 3.17	Effect of anisotropic consolidation stress on the stress-strain relations (Ladd, 1964)	89
Fig. 3.18	Effect of anisotropic consolidation stress on the stress-strain relations (Ladd, 1977)	90
Fig. 3.19	Analogy of stress-strain behavior of compression and extension tests to the earth pressure-displacement pattern of active and passive modes	92
Fig. 3.20	Stress-strain relations of AGS clay (Ladd, 1986)	94
Fig. 3.21	Stress-strain relations of San Francisco Bay mud (Duncan and Dunlop, 1969)	95
Fig. 3.22	Stress-strain relations of Mangle clay (Bjerrum and Landva, 1966)	96
Fig. 3.23	Stress-strain relations of intact overconsolidated clay with varying ratios of laboratory σ'_{vc} to in situ σ'_p (Lefebvre et al., 1983)	101
Fig. 3.24	Variation of stress-strain relations with varying δ values of overconsolidated clay prepared with directional shear cell (Ladd et al., 1985)	103

Fig. 3.25	Variation of strain at peak stress depending on the consolidation stress (Peck, 1967)	109
Fig. 3.26	Contour of equal strain for normally consolidated clays: (a) Amuay clay; (b) Remolded blue clay; and (c) Lagunillas clay (Lambe, 1964)	111
Fig. 4.1	Finite difference mesh	114
Fig. 4.2	Nodal displacements with increasing excavation heights	116
Fig. 4.3	History of maximum unbalance force	117
Fig. 4.4a	Variation of normal stresses in the horizontal with excavation	118
Fig. 4.4b	Variation of normal stresses in the vertical with excavation	119
Fig. 4.5a	Variation of shear stress components with excavation	120
Fig. 4.5b	Variation of normalized shear stresses with excavation	121
Fig. 4.6	Loading conditions in the laboratory soil testings	123
Fig. 4.7	Variation in the normalized shear stresses with excavation ...	125
Fig. 4.8a	Variation of i angles with excavation ($K_o=0.85$)	127
Fig. 4.8b	Variation of i angles with excavation ($K_o=1.00$)	128
Fig. 4.8c	The variation of i angles with excavation ($K_o=1.15$)	129
Fig. 4.9	Isotropic elasto-plastic model	132
Fig. 4.10	Pseudo-anisotropic elasto-plastic model	133
Fig. 4.11	The Mohr circle stress presentation of an element	135
Fig. 4.12	Relations between the plastic shear strains and i angles	137
Fig. 4.13	Distribution of i angles along the normalized failure surface distance at the state of incipient failure	140

Fig. 4.14	Distribution of i angles in the slope at the state of incipient failure	141
Fig. 4.15	Relations between the vertical consolidation stress and the shear strain at the peak stress	143
Fig. 4.16	Relations between the vertical consolidation stress and the elastic shear moduli	145
Fig. 4.17	Regions for the stress-strain relations interpretation	148
Fig. 4.18a	Variation of shear stress components of the toe elements with excavation	150
Fig. 4.18b	Comparison of i angle variations between the toe elements and the extension test	151
Fig. 4.19	Pattern of i angle variations depending on the magnitudes of the shear stress components	153
Fig. 4.20	i angles at failure in direct simple shear test using the pure shear assumption	155
Fig. 4.21	Stress-strain modelling (a) Active region and (b) Passive region	157
Fig. 4.22	Strain softening pattern depending on the constant strain parameters, ϵ_c	159
Fig. 4.23a	Examples of stress-strain relations: Active region	161
Fig. 4.23b	Examples of stress-strain relations: Passive region	162
Fig. 4.24	Pattern of strain hardening depending on the constant strain parameters, ϵ_c	165
Fig. 4.25	Flow chart for the pseudo-anisotropic strength analysis	167
Fig. 4.26	Flow chart for the anisotropic strain hardening and softening analysis	170
Fig. 5.1	Composition of the finite difference element in FLAC	174

Fig. 6.1	Finite difference mesh	187
Fig. 6.2	Maximum shear stress ratio (τ_{\max}/S_u) distribution, A analysis .	189
Fig. 6.2	Maximum shear stress ratio (τ_{\max}/S_u) distribution, A analysis .	190
Fig. 6.3	Maximum shear strain distribution, A analysis	192
Fig. 6.3	Maximum shear strain distribution, A analysis	193
Fig. 6.4	Variation of factors of safety at the Modified Bishop's surface, A analysis	195
Fig. 6.5	Distribution of local factors of safety along the Modified Bishop's surface (5th layer excavation), A analysis ..	197
Fig. 6.6	Distribution of i angles along the normalized failure surface distance (5th layer excavation), B-1 analysis ...	198
Fig. 6.7	Distribution of i angles in the slope (5th layer excavation), B-1 analysis	199
Fig. 6.8	Nodal displacements with increasing excavation heights, A and B series analyses	201
Fig. 6.9	Variation of the available strength ratio, B series analyses	202
Fig. 6.10	Maximum shear stress ratio (τ_{\max}/S_u) distribution, B-1 analysis	204
Fig. 6.10	Maximum shear stress ratio (τ_{\max}/S_u) distribution, B-1 analysis	205
Fig. 6.11	History of maximum unbalance force, B-1 analysis	206
Fig. 6.12a	Nodal displacements with increasing excavation heights, A, B-1 and C series analyses	208
Fig. 6.12b	Nodal displacements with increasing excavation heights, A, B-1 and D series analyses	209
Fig. 6.13	Distribution of maximum shear strain (6th layer excavation), D-4-b analyses	210

Fig. 6.14a	Sequence of the peak strength mobilization with time steps, D-1-c analysis	212
Fig. 6.14b	Sequence of the peak strength mobilization with time steps, D-1-c analysis	213
Fig. 6.15a	Variation of the mobilized strength ratio with time steps, C-1-a analysis	215
Fig. 6.15b	Variation of the mobilized strength ratio with time steps, C-1-c analysis	216
Fig. 6.15c	Variation of the mobilized strength ratio with time steps, D-1-c analysis	217
Fig. 6.16	Distribution of plastic shear strain along the normalized failure surface distance, C-1-c analysis	221
Fig. 6.17	Examples of strength and plastic shear strain relations, C-1-b analysis	222
Fig. 6.18a	Variation of strength ratios (strain compatibility concept), C-1 analyses	223
Fig. 6.18b	Variation of strength ratios (strain compatibility concept), D-1 analyses	224
Fig. 6.19	Finite difference meshes: (a) 30 degree slope; and (b) 60 degree slope	227
Fig. 6.20	The position of critical surface based on the slope inclination and the strength increment ratio	230
Fig. 6.21	Maximum shear strain distribution, A analysis	232
Fig. 6.21	Maximum shear strain distribution, A analysis	233
Fig. 6.21	Maximum shear strain distribution, A analysis	234
Fig. 6.22	Maximum shear strain distribution, A analysis	235
Fig. 6.22	Maximum shear strain distribution, A analysis	236
Fig. 6.22	Maximum shear strain distribution, A analysis	237

Fig. 6.23a	Variation of factors of safety at the Modified Bishop's surface, A (30) analysis	238
Fig. 6.23b	Variation of factors of safety at the Modified Bishop's surface, A (60) analysis	239
Fig. 6.24a	Distribution of local factors of safety along the Modified Bishop's surface (16th layer excavation), A (30) analysis	241
Fig. 6.24b	Distribution of local factors of safety along the Modified Bishop's surface (16th layer excavation), A (60) analysis	242
Fig. 6.25a	Distribution of i angles along the normalized failure surface distance (15th layer excavation), B-1 (30) analysis	244
Fig. 6.25b	Distribution of i angles along the normalized failure surface distance (15th layer excavation), B-1 (60) analysis	245
Fig. 6.26	Distribution of i angles in the slope: (a) B-1 (30) analysis; and (b) B-1 (60) analysis	246
Fig. 6.27a	Nodal displacements with increasing excavation heights, A and B (30) series analyses	248
Fig. 6.27b	Nodal displacements with increasing excavation heights, A and B (60) series analyses	249
Fig. 6.28	Maximum shear stress ratio (τ_{\max}/S_u) distribution, B-3 (30) analysis	250
Fig. 6.28	Maximum shear stress ratio (τ_{\max}/S_u) distribution, B-3 (30) analysis	251
Fig. 6.28	Maximum shear stress ratio (τ_{\max}/S_u) distribution, B-3 (30) analysis	252
Fig. 6.29	Maximum shear stress ratio (τ_{\max}/S_u) distribution, B-4 (60) analysis	254

Fig. 6.29	Maximum shear stress ratio (τ_{\max}/S_u) distribution, B-4 (60) analysis	255
Fig. 6.30a	Variation of local factors of safety distribution (16th layer excavations), B (30) analyses	257
Fig. 6.30b	Variation of local factors of safety distribution (16th layer excavations), B (60) analyses	258
Fig. 6.31a	Failure sequence of the elements along the failure surface, B-3 (30) analyses	259
Fig. 6.31b	Failure sequence of the elements along the failure surface, B-4 (60) analyses	260
Fig. 6.32	Maximum shear strain distribution: (a) B-3 (30) analysis (b) B-4 (60) analysis	262
Fig. 6.33	Comparison of failure surface locations: (a) B (30) analyses; and (b) B (60) analyses	263
Fig. 6.34a	Variation of the available strength ratio, B (30) analyses	264
Fig. 6.34b	Variation of the available strength ratio, B (60) analyses	265
Fig. 6.35	Variation of normalized shear stress of the elements along the failure surface, B-1 (60)	267
Fig. 6.36a	Nodal displacements with increasing excavation heights, A, B-1 and C-1 (30) series analyses	268
Fig. 6.36b	Nodal displacements with increasing excavation heights, A, B-1 and C-1 (60) series analyses	269
Fig. 6.37a	Nodal displacements with increasing excavation heights, A, B-1 and C-3 (30) series analyses	271
Fig. 6.37b	Nodal displacements with increasing excavation heights, A, B-1 and C-4 (60) series analyses	272
Fig. 6.38a	Nodal displacements with increasing excavation heights, A, B-1 and D-3 (30) series analyses	274

Fig. 6.38b	Nodal displacements with increasing excavation heights, A, B-1 and D-4 (60) series analyses	275
Fig. 6.39	Maximum shear strain distribution, C-3-b (30) analysis	276
Fig. 6.39	Maximum shear strain distribution, C-3-b (30) analysis	277
Fig. 6.39	Maximum shear strain distribution, C-3-b (30) analysis	278
Fig. 6.40	Maximum shear strain distribution, C-4-b (60) analysis	279
Fig. 6.40	Maximum shear strain distribution, C-4-b (60) analysis	280
Fig. 6.41a	Sequence of the peak strength mobilization with time steps, C-3-b (30) analysis	282
Fig. 6.41b	Sequence of the peak strength mobilization with time steps, C-3-b (30) analysis	283
Fig. 6.42a	Variation in the distribution of the peak strength mobilization ratios along the failure surface (16th layer excavation), C-3-b (30) analysis	284
Fig. 6.42b	Variation in the distribution of the peak strength mobilization ratios along the failure surface, (16th layer excavation) C-3-c (30) analysis	285
Fig. 6.43a	Failure sequence of the elements along the failure surface, C-3-b (30) analysis	286
Fig. 6.43b	Failure sequence of the elements along the failure surface, D-3-b (30) analysis	287
Fig. 6.44a	Failure sequence of the elements along the failure surface, C-4-b (60) analysis	289
Fig. 6.44b	Failure sequence of the elements along the failure surface, D-4-b (60) analysis	290
Fig. 6.45a	Variation of the mobilized strength ratio with time steps, C-3-c (30) analysis	292
Fig. 6.45b	Variation of the mobilized strength ratio with time steps, C-4-c (60) analysis	293

Fig. 6.46a	Distribution of plastic shear strain along the normalized failure surface distance, C-3-c (30) analysis	297
Fig. 6.46b	Distribution of plastic shear strain along the normalized failure surface distance, C-4-c (60) analysis	298
Fig. 6.47	Examples of strength and plastic shear strain relations, C-3-b (30) analysis	299
Fig. 6.48a	Variation of strength ratios (strain compatibility concept), C-3 (30) analyses	301
Fig. 6.48b	Variation of strength ratios (strain compatibility concept), C-4 (60) analyses	302
Fig. 6.49a	History of maximum unbalance force, C-3-c (30) analysis	304
Fig. 6.49b	History of nodal velocity in the horizontal direction, C-3-c (30) analysis	305
Fig. 6.50	The comparison of failure surfaces: (a) C-3 and D-3 (30) analyses; and (b) C-4 and D-4 (60) analyses	307
Fig. 6.51	Variation of OCR with depth	310
Fig. 6.52	Undrained strength profile	311
Fig. 6.53	Finite difference mesh	313
Fig. 6.54	Maximum shear strain distribution, A analysis	314
Fig. 6.54	Maximum shear strain distribution, A analysis	315
Fig. 6.54	Maximum shear strain distribution, A analysis	316
Fig. 6.54	Maximum shear strain distribution, A analysis	317
Fig. 6.55	Maximum shear stress ratio (τ_{\max}/S_u) distribution, A analysis	319
Fig. 6.55	Maximum shear stress ratio (τ_{\max}/S_u) distribution, A analysis	320

Fig. 6.55	Maximum shear stress ratio (τ_{\max}/S_u) distribution, A analysis	321
Fig. 6.55	Maximum shear stress ratio (τ_{\max}/S_u) distribution, A analysis	322
Fig. 6.56a	Variation of factors of safety at the Modified Bishop's surface, A analysis	323
Fig. 6.56b	Distribution of local factors of safety along the Modified Bishop's surface (7th layer excavation), A analysis ..	324
Fig. 6.57a	Distribution of i angles along the normalized failure surface distance (7th layer excavation), B-1 analysis ...	327
Fig. 6.57b	Distribution of i angles in the slope (7th layer excavation), B-1 analysis	328
Fig. 6.58	Maximum shear strain distribution, B-1 analysis	329
Fig. 6.58	Maximum shear strain distribution, B-1 analysis	330
Fig. 6.58	Maximum shear strain distribution, B-1 analysis	331
Fig. 6.58	Maximum shear strain distribution, B-1 analysis	332
Fig. 6.59	Maximum shear stress ratio (τ_{\max}/S_u) distribution, B-1 analysis	335
Fig. 6.59	Maximum shear stress ratio (τ_{\max}/S_u) distribution, B-1 analysis	336
Fig. 6.59	Maximum shear stress ratio (τ_{\max}/S_u) distribution, B-1 analysis	337
Fig. 6.59	Maximum shear stress ratio (τ_{\max}/S_u) distribution, B-1 analysis	338
Fig. 6.60a	Failure sequence of the elements along the failure surface, B-1 analysis	339

Fig. 6.60b	Locations of the elements along the failure surface, B-1 analysis	340
Fig. 6.61a	Variation of factors of safety at the failure surface, B-1 analysis	341
Fig. 6.61b	Distribution of local factors of safety along the failure surface (7th layer excavation), B-1 analysis	342
Fig. 6.62	Maximum shear strain distribution: (a) C-1-c analysis; (b) D-1-c analysis; and (c) E-1-c analysis	344
Fig. 6.62	Maximum shear strain distribution: (a) C-1-c analysis; (b) D-1-c analysis; and (c) E-1-c analysis	345
Fig. 6.63	Comparison of failure surfaces, C, D and E analyses	347
Fig. 6.64a	Nodal displacements with increasing excavation heights, A, B-1 and C-1 series analyses	348
Fig. 6.64b	Nodal displacements with increasing excavation heights, A, B-1 and D-1 series analyses	349
Fig. 6.64c	Nodal displacements with increasing excavation heights, A, B-1 and E-1 series analyses	350
Fig. 6.65a	Sequence of the peak strength mobilization with time steps, C-1-c analysis	352
Fig. 6.65b	Sequence of the peak strength mobilization with time steps, C-1-c analysis	353
Fig. 6.65c	Variation of the mobilized strength ratio with time steps, E-1-c analysis	354
Fig. 6.66a	Failure sequence of the elements along the failure surface, C-1-c analysis	355
Fig. 6.66b	Locations of the elements along the failure surface, C-1-c analysis	356
Fig. 6.67a	Variation of the mobilized strength ratio with time steps, C-1-c analysis	358

Fig. 6.67b	Variation of the mobilized strength ratio with time steps, D-1-c analysis	359
Fig. 6.67c	Variation of the mobilized strength ratio with time steps, E-1-c analysis	360
Fig. 6.68a	Plastic shear strain distribution along the failure surface, C-1-c analysis	362
Fig. 6.68b	Plastic shear strain distribution along the failure surface, D-1-c analysis	363
Fig. 6.68c	Plastic shear strain distribution along the failure surface, E-1-c analysis	364
Fig. 6.69	Mobilized strengths for the toe and the crest elements at the peak mobilized strength ratio, E-1-c analysis	365
Fig. 6.70a	Variation of strength ratios (strain compatibility concept), C-1 analyses	367
Fig. 6.70b	Variation of strength ratios (strain compatibility concept), D-1 analyses	368
Fig. 6.70c	Variation of strength ratios (strain compatibility concept), E-1 analyses	369
Fig. 6.71	Distributions of i angles along the failure surfaces	374

LIST OF SYMBOLS

I_B	Brittleness Index
c'	cohesion intercept of a soil determined from the drained test
c_p	cohesion corresponding to the peak in the stress-strain relation
c_r	cohesion at the residual state
D	proportion of the slope surface in which the residual strength operates
e	void ratio
f	loading function beyond the initial yielding
F	factor of safety
F_c	corrected factor of safety
f_y	Hoeg's yield criterion
G	shear modulus of the material
H	slope of the relation between the axial stress and the axial plastic strain in the uniaxial loading test
H'	hardening modulus
H_{ex}	excavation height
i	angle between the major principal stress direction and the vertical axis

I_l	Liquid Index
I_p	Plasticity Index
J_2	the second invariant of the deviatoric stress tensor
K	coefficient of strength anisotropy ($S_{u(h)}/S_{u(v)}$)
k	yield stress of a material in the pure shear state
K_o	coefficient of earth pressure at rest
L	length of the whole slip surface
LL	Liquid Limit
OCR	Overconsolidated Ratio
PSC	plane strain compression test
PSE	plane strain extension test
Q	plastic potential function
q	maximum shear stress (y axis) in the p - q diagram
R	radius of the Mohr circle
R_l	local residual factor
S_u	undrained shear strength
$S_{u(c)}$	undrained strength in the compression test
$S_{u(e)}$	undrained strength in the extension test
$S_{u(h)}$	undrained strength with the major principal stress applied in the horizontal direction

$S_{u(i)}$	undrained strength with the major principal stress applied at i angle from the vertical axis
S_{uo}	undrained strength of ground surface soil
$S_{u(v)}$	undrained strength with the major principal stress applied in the vertical direction
TC	triaxial compression test
TE	triaxial extension test
δD	depth increment
$d\epsilon'_{ij}$	increments of the plastic shear strain components
δS_u	undrained strength increment
ϵ_c	constant strain parameter
$\bar{\epsilon}_p$	plastic shear strain
γ_c	maximum shear strain at the peak shear stress in the plane strain compression test
γ_e	maximum shear strain at the peak shear stress in the plane strain extension test
γ_f	maximum shear strain at failure (at the peak shear stress)
γ_{max}	maximum shear strain
μ	Poisson's ratio
c'_{mob}	mobilized cohesion intercept
ϕ'	internal friction angle of a soil determined from the drained test

ϕ'_{mob}	mobilized internal friction angle
ϕ'_r	internal friction angle at the residual state
λ	positive scalar factor of proportionality
σ'	effective normal stress on the plane of consideration
σ'_c	average (mean) principal stress
σ_h	normal stress in the horizontal direction
σ_{ij}	stress tensor components
σ_x	normal stress in x direction
σ_y	normal stress in y direction
σ_v	normal stress in the vertical direction
σ'_{vo}	effective vertical overburden pressure
τ	shear stress on the potential failure surface
τ_{ave}	average shear resistance along the entire failure surface
τ_c	shear resistance of the active portion of the failure surface
γ_d	measured shear strain in the direct simple shear test
τ_e	shear resistance of the passive portion of the failure surface
τ_f	available shear strength of a soil at failure
τ_h	applied shear stress on the horizontal plane of the specimen in the direct simple shear test
τ_{max}	maximum shear stress

- τ_r shear stress at the residual state in the stress-strain relations
- τ_{xy} shear stress component in x - y plane
- η ratio of the peak strength to the mobilized strength during failure

1. INTRODUCTION

Failure of earth structures such as earth slopes, earth embankments and dams has inflicted heavy loss of life and property worldwide. In spite of the progress made, the understanding of the mechanism of slope failure and its analysis have generally been insufficient to prevent such accidents. Slope failures typically involve the formation of a failure surface followed by relative sliding between the two masses of soil along the surface. Traditionally, the slope stability analysis is preceded by the determination of the soil strengths by subsequently replacing the soil's stress-strain relation by a perfectly rigid plastic material. This replacement involves the assumption that the strengths are independent of strain. Therefore, the slope should not fail until the shear stress at every point along a potential failure surface reaches the maximum shear strength (limit equilibrium analysis).

In contrast, most soils are inherently anisotropic in the stress-strain-strength characteristics. It has been repeatedly confirmed even for normally consolidated clays that the undrained strength decreases as the major principal stress direction deviates from the vertical ($i=0^\circ$) toward the horizontal ($i=90^\circ$). The i angle is defined herein as the angle between the vertical and the major principal stress direction. In addition, the stress-strain relationship patterns are completely

different for different i angles at failure. For a given soil, for example, the compression mode ($i=0^\circ$) generates brittle behavior (strain softening) with the peak stress occurring at a small strain, while the extension mode ($i=90^\circ$ degree) results in a much more resilient pattern where the peak occurs at a large strain, which is about 10 times greater than that of the compression mode. The stress path that a soil in a slope experiences depends on the location of the particular soil element. For example, soil around the crest of the potential failure surface is under the loading condition similar to the plane strain compression mode, whereas a soil near the toe is loaded in the plane strain extension mode. The stress path in the intermediate portion can best be simulated by the direct simple shear mode (Ladd, 1986).

Because of the anisotropy and strain softening in the stress-strain relations, the strength of the soil, in reality, is not necessarily fully mobilized along the failure surface simultaneously. Instead, the failure of a body of clay starts at a point where the shear strength is fully mobilized and spreads over the rest of the surface. Once the failure occurs, the strength drops to the residual values in an orderly manner. The failure of this type is termed "the progressive failure". As a result, the summation of mobilized strengths during failure is much smaller than the summation of those peak strengths. Consequently, it invalidates the results of computations based on the conventional assumption of simultaneous failure with their peak strengths as in the limit equilibrium analysis.

It is now clear that the progressive failure analysis is required for a valid assessment of geotechnical engineering problems, which in turn requires a suitable material model implemented in a computer-based numerical analysis such as finite element analysis or finite difference analysis. Therefore, the recent research in soil mechanics is directed toward better understanding of the mechanical behavior of soil and the development of more advanced constitutive models within the framework of continuum mechanics. Ideally, the constitutive model should be able to describe the relative pattern of stress-strain relations of varying stress paths in which both the strain hardening and softening behavior at large strains are fully addressed. The development of such an ideal constitutive model, however, seems to be far away from the practical application upon considering the current state. As a result, there has been no specific case study from which the effect of progressive failure can be clearly deduced.

2. OBJECTIVE AND SCOPE OF THE STUDY

The objective of this study is to evaluate (a) the strength anisotropy effect and (b) the progressive failure effect on slope stability. First, the strength anisotropy effect will be evaluated in the analyses in which parametric anisotropic strengths are explicitly implemented. Second, the progressive failure effect will be evaluated in the analyses in which the laboratory-determined constitutive behavior will be closely curve-fitted for varying stress paths. The strain hardening for passive mode elements and the strain softening for active mode elements will be explicitly addressed. Particularly, the strain softening effect will be parametrically evaluated.

The scope of the study will be confined to the cut slopes of normally consolidated and lightly overconsolidated clays without any surface loading. The focus of the study is on the short-term stability of slopes. The delayed failure due to strain energy release with time and weathering process in highly overconsolidated clays is not included. To focus on the fundamental phenomena, the slope is assumed to be free of stratigraphic variations, boundary constraints on potential slip surfaces, and of other defects (fissures, slickensides, etc.) that may be encountered in practice.

3. LITERATURE SURVEY

3.1 Introduction

Partly for simplicity in practice and partly because of the historical development of mechanics of deformable solids, the problems of soil mechanics are often divided into two distinct groups: the elasticity problems and the stability problems. They are then treated in two separate and unrelated ways. The elasticity problems deal with stress or deformation of the soil when no failure of the soil is involved. Stresses at points in a soil mass under a footing, or behind a retaining wall, deformations around tunnels or excavations, and all settlement problems belong to this category. Solutions to these problems are often obtained by using the theory of linear elasticity. When the stress intensity first reaches a certain critical value, which is called the yield value, the soil leaves the elastic range and enters the plastic range, which indicates continuous deformation at a constant state of stress. In order to maintain plastic flow, the stress intensity must be at the yield value but can never exceed this value. As soon as the stress intensity drops below this value, any change of strain is of a purely elastic nature.

The stability problems on the other hand deal with the conditions of ultimate failure of a mass of soil. The problems of active and passive earth pressure, bearing capacity, and stability of slopes are most often considered in this

category. The most important feature of such problems is the determination of the loads which will cause failure of the soil mass. Solutions to these problems are often obtained using the theory of perfect plasticity.

Intermediate between the elasticity problems and stability problems mentioned above are the ones known as progressive failure problems. These problems are accompanied by the elastic-plastic transition from the initial linear elastic state to the ultimate failure state of the soil by plastic flow. In reality most slopes fail progressively and the analysis based on the progressive failure concept is of greater generality than any other types of analyses. Consequently, there have been a number of attempts to model the problems of this nature in the context of plasticity theory ever since Terzaghi and Peck (1948) pointed out the significance of the phenomena.

3.2 Framework of the Slope Stability Analysis

3.2.1 Prerequisites for the Slope Stability Analysis

The mathematics of slope stability analyses are well understood and good numerical precision can be expected. However, the final solution requires much more than this. The overall accuracy of a solution depends largely on competence and judgement in defining the problem properly and in selecting the soil and pore water pressure parameters which are representative of the field conditions (Fredlund, 1984). Informed judgement is often more important than mathematical competence, and more difficult to acquire. There may be two

separate sets of considerations required to be taken, which are independent of any particular method of slope stability analysis. They are: (a) the importance of site investigation aimed at understanding the nature of potential failure which might develop, (b) the importance of appropriate modeling of the problems and of interpretation of the analytical results.

Before any analysis is undertaken it is necessary to have a clear sense of the geological profile and its geotechnical properties. This requires good quality site investigation. Field investigations in relatively small slopes include only a sufficient number of holes to establish the stratigraphy, plus enough samples to determine the required strength parameters. For sophisticated stability analyses of larger-scale slopes, detailed stress-strain relations of soils should be included in the geotechnical investigation to obtain the extent and pattern of the deformations in slopes. Particular care must be taken to evaluate macro-structural features such as sand lenses, desiccation cracking and fissures resulting from overconsolidation, frost action, etc., particularly at shallow depths (Thomson and Kjartanson, 1985; Crooks et al., 1986). These may have considerable impact on the strength parameters which should be used, and they may also influence the distribution and magnitude of pore water pressures in the slope.

When large pre-existing slide masses are encountered, then extensive site investigation is needed to determine the extent of the slide mass and the position of the slide surface. Geophysical (resistivity) methods have proved very useful in slides in riverbank shales and clay tills in Saskatchewan (Christiansen, 1983;

Yoshida and Krahn, 1985). In those cases, careful searches should be made for narrow bands of sheared material where the shear strength has reduced from peak to residual values. Even with continuous sampling these are usually very difficult to spot using normal drilling procedures (Graham, 1986).

In the application of a slope stability method to an actual problem, correct solutions can only be obtained if the potential failure mechanism is properly understood and correctly utilized in the model. For example, slopes of the wedge-type potential failures cannot be successfully analyzed with methods in which failures occur in circular modes. In limit equilibrium methods differences in final answers caused by the inappropriately assumed failure mechanism may be as large as 60 percent (Graham, 1968). This may also be the case for numerical methods such as finite element analysis. In such continuum mechanics computer codes, the failure mechanism retrieved in the numerical models depends on inputs such as boundary conditions, discontinuity of material properties, site-specific geological conditions, which in turn require thorough site investigation and informed judgement. Therefore, when the finite element analysis gives a factor of safety associated with a seemingly erroneous failure mechanism, the result can be immediately questioned for its reliability based on engineering judgement.

Generally, it is believed in the limit equilibrium analysis that the choice of the assumed shape of the potential failure surfaces has more significant impact on the accuracy of the answer than has the choice of the particular limit equilibrium analysis method. Given identical specifications of geometry, soil properties, and

pore water pressures, a series of good modern limit equilibrium analyses rarely produce differences greater than about five percent in the calculated factors safety (Fredlund and Krahn, 1977). All methods of slope stability no matter how correct fundamentally and how correctly they are implemented can produce erroneous results. In such cases good engineering judgement is required in modelling the problem and interpretation of analytical results. For example, error in the final solution can be created by inappropriate definition of the type of problem solved. A common error of this type is the use of short-term stability analyses when long-term stability is more critical. Regardless of the correctness of the input values the analysis will not be correct if the wrong problem was solved. The significance of the difference between the total stress analysis and effective stress analysis will be separately reviewed in Section 3.2.3.

Another example of such erroneous results is the computation of high tensile stresses near the active zone of a slope in cohesive material. The tensile stresses are correct for the mechanics employed and the assumption of a cohesive material. However, they may not be valid for most soils for which such high tensile strengths cannot be expected. In such cases, where unrealistic tensile stresses develop, the problem is usually remedied by introducing into the stability analysis a vertical crack near the upper portion of the shear surface. It is important to realize here that the quantitative description of a slope stability analysis in terms of factor of safety is of limited value in itself, as it depends on the various simplifying inputs such as strength parameters and theoretical models.

However, when combined with experience in similar situations and good engineering judgement in the interpretation of the results, it becomes a useful input to the decision-making process.

3.2.2 Factor of Safety

In design of slopes, the factor of safety of a slope should be determined after taking following uncertainties into account. First, uncertainties of shear strength parameters due to soil variability, and the relationship between the strength measured in the laboratory and the field strength. Second, uncertainties in the loading on the slope: surface loading, unit weight, pore pressure distribution. Third, uncertainties in the way the model represents the actual conditions in the slope should be accounted for, which include: (a) the possibility that the critical failure mechanism is slightly different from the one which has been identified, (b) the model is not conservative.

Generally the factor of safety does not allow for the possibility of gross errors, for example a bad choice of failure mechanism, such as ignoring the presence of existing shear surfaces in a slope. It has been pointed out by De Mello (1977) that a factor of safety of 1.0 does not necessarily indicate that failure of a slope is imminent. The real factor of safety is strongly influenced by minor geological details, stress-strain characteristics of the soil, actual pore-pressure distribution, initial stresses, progressive failure, and numerous other factors. Although it is usual for a deterministic analysis to be made, it is good practice for

the analysis to include a study of the sensitivity of the factor of safety to the choice of each parameter over which there is uncertainty. The major design decisions are then taken on the basis of a chosen factor of safety (or factor of ignorance).

If the factors affecting the stability can be identified and their variability defined, it is possible to introduce this into the analysis. For example, if the variability of the material parameters (c , ϕ) and pore pressure distribution can be expressed statistically (Harr, 1977), a probabilistic analysis can then yield a probability of failure. The difficulty with this approach is that some of the most important areas of uncertainty (e.g., bad choice of failure mechanism due to minor geological detail) necessitate the application of extreme value statistics if they are to be included in the analysis, and this is fraught with difficulties (De Mello, 1977). These procedures offer the possibility of a more rational approach to design which is overdue in geotechnical engineering.

3.2.3 Drainage and Loading Conditions

Stability problems have historically been divided into three categories according to the drainage conditions that either exist or are considered critical during construction and during a potential failure. It is further useful to distinguish between loading versus unloading problems to differentiate construction that causes the total normal stresses acting within the soil mass to increase or decrease, respectively (Lambe and Whitman, 1969). Staged

construction projects inherently involve loading problems, whereas excavations entail unloading.

In the case of saturated soils with a compressible soil skeleton (i.e., normally consolidated clay), the increases in shear stress tend to cause the soil skeleton to contract, which in turn are resisted by compressive pore pressures in the voids of the soil. As the pore water is not allowed to flow out of these highly stressed areas for a short period of time, the effective stresses and hence the shear strengths remain unchanged. This type of situation is a short-term stability problem, because the minimum factor of safety against failure occurs immediately after the loads are applied. For example, this case denotes situations where both construction and failure occur rapidly enough to preclude significant drainage. Since there is negligible change in water content, the initial in situ undrained shear strength of the cohesive soil controls stability during construction. It represents the critical condition for loading problems since the factor of safety increases with time due to consolidation.

Long-term stability problems represent the opposite extreme, in that the excess pore pressures caused by loading (or unloading) have dissipated due to a slow rate of construction or sufficient time after construction, and the shear induced pore pressures are also due to a slow rate of shearing during failure. Stability is therefore controlled by the drained strength of the soil corresponding to equilibrium (long-term) pore pressures. This case represents the critical condition for unloading problems that generate negative excess pore pressures

during construction (e.g., excavations in stiff clays) since the factor of safety decreases with time due to swelling. Both these extremes of pore water behavior were originally described by Bishop and Bjerrum (1960).

The intermediate between the two extremes is the partially drained case. This case applies to staged construction since loading problems produce positive excess pore pressures and hence decreases in water content during construction. However, the types of analyses currently used to assess stability during staged construction make different assumptions regarding the drainage conditions during a potential failure. Specifically, will failure occur so slowly that it approaches a drained condition or will it occur so rapidly that it approaches an undrained condition? In other words, will the shear induced pore pressure be essentially zero or significantly greater than zero? This question basically entails treating staged construction either as a consolidated-drained (CD) or a consolidated-undrained (CU) failure.

For some simple cases in which the loading and drainage conditions are straightforward, problems can be analyzed using either undrained stress analysis or effective stress analysis. However, for other cases of staged construction, realistic definition of the fundamental mechanism associated with drainage behavior during failure should first be proceeded in the design phase. Bishop and Bjerrum (1960) proposed that effective stress analysis is a generally valid method for analyzing any stability problem and collected many followers, presumably since it could be readily used to check stability during construction based on measured

pore pressures. However, some other engineers felt this approach to be dangerous (Barron, 1964), believing that staged construction should be treated as a consolidated-undrained (CU) case.

Ladd (1986) argued that undrained conditions prevail during failures of most clays having liquid limits between 30 % and 90 %. Therefore, a conventional effective stress analysis that uses measured pore pressures gives an instantaneous factor of safety corresponding to the effective stress-pore pressure conditions existing prior to failure. It inherently assumes that a potential failure will occur so slowly that the drained shear strength of the soil will resist failure. He finally concluded that the resulting factor of safety is potentially unsafe because it never considers the more critical possibility of an undrained shear failure and generally misleading because most failures during staged construction occurs under essentially undrained conditions.

Alternatively, Ladd (1986) proposed a new approach named undrained strength analysis (USA). His method is conceptually similar to QRS method suggested by Casagrande and Wilson (1960), yet far refined in the treatment of soil. In essence, USA uses either the Recompression (Bjerrum, 1973) or SHANSEP (Ladd and Foott, 1974) technique to minimize the adverse effects of sample disturbance and simulate the stress history of the soil in the laboratory soil testing. The undrained strength profile in the foundation is then obtained from K_0 -consolidated undrained (CK_0U) tests having different modes (compression and extension) of failure via the undrained strength ratio. Finally, the stability analysis

can be conducted using one of limit equilibrium methods. This method is based on an assumption that undrained condition prevails during failures, and it treats the staged construction as a consolidated undrained (CU) case.

In summary, three categories of problems have been reviewed: drained, undrained, and partially drained problems associated with loading conditions. In order to avoid the complexities of partially drained analysis, the problem is customarily simplified into one of the first two problems: drained or undrained problems. In certain cases, it may not be always possible to do so and the partially drained problem must be solved. In such cases, undrained stress analysis (USA) is believed to be the most rational approach based on the field evidence of rapid failure (Jeyapalan et al., 1983) than any other approaches reported. The effective stress analysis must not be carried out since it gives too unsafe results (Ladd, 1991).

3.3 Slope Stability Analysis Methods

3.3.1 Introduction

The slope stability analysis has a long history and vast literature. It is not the author's intention here to include the complete survey of the historical development of the slope stability methods. Instead, this section is designed to provide an idea of where the current finite difference method with the strain softening model can be placed and how it can be compared to others in historical view as well as in its capability and practicality.

Mathematically rigorous methods such as the slip-line method were once considered to be a powerful method in early days. However, they did not appeal to practicing engineers since they were too esoteric and complex in the application. These days, most slope stability analyses are carried out by the limit equilibrium method due mainly to its simplicity, practicality, and experience accumulated with it. For some complicated materials of strain softening, however, the method loses its ground of perfect plasticity and the solution is no longer valid. It was not long ago when the continuum mechanics computer code such as finite element or finite difference method was first introduced to engineering practice. In principle, using the method with an appropriate constitutive model, any well-defined boundary value problems can be solved for which material properties are much more complicated than those of perfectly plastic materials. The emergence of the finite element method has made a turning point in the soil mechanics area and its capability has been proved to be powerful for general purposes.

In the following historical development of the slope stability analysis from the classical plastic equilibrium (slip line) methods to the finite element (or difference) analysis with complicated material models will be briefly reviewed.

3.3.2 Classical Plastic Equilibrium Methods

The plastic equilibrium method deals with the stresses in soil masses at failure. The soil is then in the plastic range. The ideally plastic material at

failure yields and undergoes deformation at a constant rate without change in stress. The behavior of a real soil is of course considerably different from that of an ideally plastic material, and this point should always be remembered.

However, analysis by the plastic theory provides a theoretical basis with which the actual behavior of soil masses may be compared. The basic equations of the plastic theory are derived from the conditions of equilibrium and the condition of yield or failure. These make it possible to solve for the stresses in a soil mass at failure.

At the instant of impending plastic flow, both equilibrium and yield conditions are satisfied in the region near the footing. For soils, the Coulomb criterion is widely used for this yield condition. Combining the Coulomb criterion with the equations of equilibrium gives a set of differential equations of plastic equilibrium in this region. Together with the stress boundary conditions, this set of differential equations can be used to investigate the stresses in the soil beneath the footing or behind a retaining wall at the instant of impending plastic flow. In order to solve specific problems, it is convenient to transform this set of equations to curvilinear coordinates whose directions at every point in this yielded region coincide with the directions of failure or slip plane. These slip directions are known as slip lines and the network is called the slip-line field.

Kotter (1903) was the first to derive these slip-line equations for the case of plane deformations. Prandtl (1920) was the first to obtain an analytical closed form solution to these equations for a footing on a weightless soil. In the analysis,

he developed the solution with a singular point with a pencil of straight slip-lines passing through it. These results were subsequently applied by Reissner (1924) and Novotortsev (1938) to problems on the bearing capacity of footings on a weightless soil, when the slip-lines of at least one family are straight and the solutions have closed form.

However, the important inclusion of soil weight considerably complicates the mathematical solution. Consequently, many approximate methods have been developed. Sokolovskii (1965) adopted a numerical procedure based on a finite difference approximation of the slip-line equations. He obtained a number of interesting problems on the bearing capacity of footings and slopes as well as the pressure of a fill on retaining walls, for which it is impossible to find closed form solutions. De Jong (1957) on the other hand adopted a different approach and developed a graphical procedure for solutions. Other forms of approximate solution include the applications of perturbation methods (Spencer, 1962) and series expansion methods (Dembicki et al., 1964).

One weakness of the slip-line method is the neglect of the stress-strain relationship of the soil. According to the mechanics of deformable solids, this condition must be satisfied for a valid solution. Here, only the equilibrium and yield conditions are utilized. For the case of plane deformation, the two equations of equilibrium and the yield condition produce what appears to be and sometimes is static determinacy in the sense that there are the same number of equations as unknown stress components. In most practical problems, however,

the boundary conditions involve stresses and rates of displacement, and the static determinacy is lost.

The slip-line field analysis described above is often considered to be too esoteric and complex to be a useful tool for engineers. In fact, so much depends on the skill and intuition of the engineer that solving a mixed (displacement and stress) boundary value problem appears to be an art rather than an engineering method.

3.3.3 Limit Equilibrium Analysis

3.3.3.1 Introduction

The limit equilibrium method has traditionally been used to obtain approximate solutions for the stability problems in soil mechanics. These days, this method is most widely used, mainly because of the ease with which it can accommodate complex geometries and variable soil and pore water pressure conditions. This method generally entails assumed failure surfaces of various simple shapes: plane, circular or logspiral. With this assumption, the stability problem is reduced to one of finding the most dangerous position for the failure surface.

A number of limit equilibrium methods have been proposed and can be grouped into three categories based on the main hypothesis. Those hypotheses are regarding (a) the direction of the resultant internal forces (Bishop, 1955; Spencer, 1967; Morgenstern and Price, 1965), (b) the height of the line of thrust (Janbu,

1954), (c) the shape of the distribution of the internal shear force (Sarma, 1973). Although the concepts are basically the same, the nature of the hypotheses used to represent the internal forces distinguishes the different procedures, leading to different expressions for the factor of safety.

The use of computers has helped in speedy evaluation of the stability of the slopes, which used to be a lengthy and slow process. However, this increased reliance on computers coupled with the lack of actual experience and of understanding of the method may lead to meaningless outputs.

3.3.3.2 Principle of Limit Equilibrium Analysis

The principle of limit equilibrium methods can be found in any standard soil mechanics text book (e.g., Das, 1990). The common basis of numerous limit equilibrium methods can be concisely summarized as follows. First, at any local point in a slope, the available shear strength of the material is expressed in terms of the Mohr-Coulomb criterion:

$$\tau_f = c' + \sigma' \tan\phi' \quad (3.1)$$

It is then the most common practice to assume the same degree of mobilization of the soil's cohesion and friction components at all points in the considered soil mass by expressing the shear stress as:

$$\tau = \frac{c'}{F} + \frac{(\sigma' \tan\phi')}{F} \quad (3.2)$$

where σ' and τ represent the applied normal and shear stresses on any section of the potential failure surface, respectively, and F is the factor of safety.

Equation (3.2) thus represents both the presumed local stress conditions and the local expression of the factor of safety.

The integration of the local factors of safety to obtain an estimate of the overall stability is done by writing the factor of safety in terms of the overall equilibrium of the considered soil mass, i.e.,

$$F = \frac{\text{resisting force or moment}}{\text{disturbing force or moment}} \quad (3.3)$$

This equation was originally proposed by Collin (1846). Since then, the equation has been written in such a form that it can be combined with Equation (3.2) to obtain an expression of F satisfying both local and overall equilibrium conditions, not only at failure ($F=1.0$) but theoretically for any stable condition ($F>1.0$), along any selected potential failure surface. This is the common basis of the different limit equilibrium methods of stability analysis available in the literature.

The procedure of the methods is as follows. First, a potential failure surface is selected, which is then considered as a discontinuity between a rigid sliding mass and a rigid stable base. Second, the equation of global equilibrium of the mass is written in terms of either a sum of moment (circular surfaces), or of forces (non-circular surfaces) or both. The active forces are the weight of the sliding mass and any surface loads, whereas the reacting forces are the resisting forces along the failure surface. Third, the equation of equilibrium of the vertical

forces in a vertical slice of the sliding mass is derived. Since the complete state of stresses is normally unknown, simplifying assumptions have to be made concerning the type and magnitude of the internal and external forces acting on the slice.

Forth, the equations for the normal stress and shear stress along the base of the slice are derived, which are all function of F . Lastly, the equations of the normal stress and the shear stress are substituted into the global equilibrium equation obtained in the second step and obtain the expression of the type:

$$F = f(F) \tag{3.4}$$

which will be solved by iteration.

This principle has been followed, for example, by Bishop (1955) for the analysis of circular failure surfaces and by Janbu (1957) for composite failure surfaces. Bishop (1955) considers the equilibrium of a mass along a circular surface. The overall equilibrium of moments, combined with the Mohr-Coulomb criterion, results in the classical implicit expression of the factor of safety. Janbu (1957) considers the equilibrium of a mass sliding on a composite surface.

Writing the overall equilibrium of the mass in terms of horizontal forces as well as the local equilibrium of vertical forces, Janbu finally obtains an equation for factor of safety which is very similar to Bishop's. The solution of the equation suggested by Bishop or Janbu is obtained by iteration of F , which is generally carried out by means of a computer.

In addition to Bishop's and Janbu's methods, a large number of solutions for the slope stability analysis have been developed on essentially the same

principles but using various sets of assumptions as mentioned previously.

Fredlund and Krahn (1977) have presented an interesting comparison of the common methods of analysis. They clearly evidenced the similarity of the factor of safety equations in all methods. They also showed that the differences between the relatively simple methods (simplified Bishop; simplified Janbu) and the sophisticated ones (Morgenstern and Price) were limited. The use of Bishop's simplified method appeared fully justified in all cases where a circular failure surface was likely, whereas Janbu's simplified method could be use for non-circular surfaces. Similar conclusions were reached by Whitman and Bailey (1967) and Wright et al. (1973).

An implicit assumption in equilibrium analyses of slope stability, however, is that the stress-strain behavior of the soil is ductile, i.e., that the soil does not have a brittle stress-strain curve (where the shearing resistance drops off after reaching a peak). This limitation results from the fact that the methods provide nor information regarding the magnitudes of the strains within the slope, nor any indication about how they may vary along the slip surface. As a consequence, unless the strengths used in the analysis can be mobilized over a wide range of strains (i.e., the stress-strain behavior is ductile) there is no guarantee that peak strength can be mobilized simultaneously along the full length of the slip surface. If the shearing resistance drops off after reaching the peak, progressive failure can occur, and the shearing resistance that can be mobilized at some points may be smaller than the peak strength. The only reliable approach in this case is to use

the residual strength rather than the peak strength in the analysis with conservative results to some extent.

3.3.4 Limit Analysis

The limit analysis method was established firmly less than thirty years ago, but is now recognized as an alternative analytic method. In contrast to slip line and limit equilibrium methods, the limit analysis method considers the stress-strain relationship of a soil in an idealized manner. This idealization, termed normality (or the flow rule), establishes the limit theorems on which limit analysis is based. Within the framework of this assumption, the approach is rigorous and the techniques are competitive with those of limit equilibrium, in some instances being much simpler.

The plastic limit theorems of Drucker et al. (1952) may conveniently be employed to obtain upper and lower bounds of the collapse load for stability problems, such as the critical heights of unsupported vertical cuts, or the bearing capacity of nonhomogeneous soils. The limit analysis is composed of two parts: upper bound theorem and lower bound theorem. The lower bound theorem (static solution) is determined from a distribution of statically admissible stress fields that satisfy the equilibrium equations, stress boundary conditions and nowhere violate the yield criterion. It should be noted here that the strains and displacements are not considered and that the state of stress is not necessarily the

actual state of stress at collapse. By examining different admissible states of stress the static solution (lower bound value) may be improved (i.e., increased).

In the upper bound theorem (kinematic solution), the limit load is determined by equating the external rate of work to the internal rate of energy dissipation in a kinematically admissible velocity field that satisfies velocity boundary conditions and strain and velocity compatibility conditions. In this case the external loads are not necessarily in equilibrium with the internal stresses, and that the mechanism of collapse is not necessarily the actual collapse mechanism. By examining different mechanisms, the upper bound value may be improved (i.e., reduced).

The upper bound theorem solution has been shown to yield reasonable answers when compared with existing limit equilibrium solutions for which validity have been established on the basis of practical experience (Chen and Scawthorn, 1970; Fang and Hirst, 1970). However, the idealization of plastic deformation by the flow rule usually predicts volume expansion which is enormously in excess of that observed (Drucker et al., 1957). In that case, the ground of limit analysis is lost, because of the normality which predicts the same amount of dilation angle as the internal friction angle. In general, the validity of the limit analysis in slopes has been proved and its solution comparable to the one from the limit equilibrium analysis. However, the limit analysis does not seem to strongly appeal to practicing engineers for whom the limit equilibrium methods provide all the convenience and equivalent results in form of well diversified computer software.

3.3.5 Finite Element Analysis

The current study is concerned about the application of the numerical method in the slope of strain hardening and softening materials. The difficulties in appropriate constitutive models are usually the problem. Therefore, the review on the finite element numerical method is mostly focused on various constitutive models implemented in geotechnical engineering area.

3.3.5.1 Linear Elastic Models

The principal advantage of linear elastic analyses is simplicity. Only two elastic parameters, Young's modulus and Poisson's ratio, are needed to characterize the stress-strain behavior of isotropic elastic materials. The shortcoming of linear elasticity is that it is not a good model for the actual stress-strain behavior of soils, except at low stress levels and small strains. Furthermore, it is usually hard to determine the appropriate values of those parameters since they should be representative for all the stress paths and stress conditions possibly encountered in the analysis.

In spite of these shortcomings, linear elastic model have been used in a number of numerical analyses of embankments and excavated slopes and found to be good in comparison to the measured values of deformation (Penman et al., 1971; Eisenstein and Simmons, 1975; Thomas et al., 1976). According to Duncan and Dunlop (1969), slopes with factors of safety of as high as 5.0 may also experience local failure around the highly stressed area in the slope. The local

failure is then immediately accompanied by stress redistribution in order to reach the global equilibrium. Therefore, it is natural that slopes with the factors of safety below 2.0, which is usually the case in design, should always have certain percentage of local failure with readjusted stress distribution in the slope.

3.3.5.2 Multilinear Elastic Models

Modelling constitutive behavior of soils with two or more straight lines improves the accuracy of analysis results. Once the calculated stress exceeds the material strength, much smaller modulus value is assigned to relate the stress increment to the strain. For example, Dunlop and Duncan (1970) used reduced moduli for failed elements which were on the order of one ten thousandth of the initial moduli values. As in the previous case, a number of analyses with the multilinear elastic model were reported to be in good agreement with field measurements of deformation (Clough and Woodward, 1967; Boughton, 1970; Eisenstein et al., 1972; Shibata et al., 1976; Adikari and Parkin, 1981; Miki et al., 1988).

On the other hand, some of the analyses were found to give larger deformations as compared to measurements. Duncan (1992) summarized the reasons for the discrepancy as follows. First, where stress-strain parameter values are determined from tests on samples retrieved from the field, the lab specimens will tend to be less stiff than the material in the field because disturbance will tend to flatten the stress-strain curves and reduce the stiffness. Second, if triaxial

tests are used to develop stress-strain curve for plane strain analysis, the stress-strain curve is not as steep as actual case. The tendency is to underestimate the stiffness of the soil.

3.3.5.3 Hyperbolic Elastic Models

Hyperbolic stress-strain relationships have a great deal in common with the methods discussed in the previous section. This model uses the generalized Hook's law with tangent modulus of stress-strain curve, and relates strain increments to stress increments. The hyperbolic model affords a systematic method for relating modulus values to stresses. The parameters in the hyperbolic model that relate modulus values to stresses have physical meaning, and their values can be determined by means of conventional laboratory tests. Because of their convenience and practicality, they have been used quite widely. In general, this model can give satisfactory results for limited class of problems. For instance, if we are interested in stress-deformation analysis of a soft foundation under a monotonically increasing construction load such as embankment, the results will be acceptable. However, for problems involving loading and unloading, and various stress paths in soil, the results may not be reliable (Desai and Siriwardane, 1984).

Most of hyperbolic model applications use the hyperbolic modulus relationship developed by Duncan and Chang (1970), but they use different methods of characterizing Poisson's ratio or bulk modulus. The simplest method

is to use a constant Poisson's ratio throughout the analysis. A problem with this method is that a single Poisson's ratio can hardly represent the real soil especially during failure. To model the measured volumetric strains in triaxial tests more accurately, Kulhawy and Duncan (1972) developed a procedure for relating the Poisson's ratio to the confining pressure and the deviatoric stress. Although this method affords a logical means of deriving the parameters, it has been found that the method leads to erratic or unstable results in some cases (Cathie and Dungar, 1978). A procedure that involves relating the bulk modulus to the confining pressure was developed by Duncan et al. (1980). However, this was also found to have problems under some conditions (Boscardin et al., 1990). An alternative procedure that involves relating the bulk modulus to the mean normal stress was developed by Boscardin et al. (1990) to avoid many of the problems involved in other formulations.

3.3.5.4 Plasticity Models

3.3.5.4.1 Perfect Plasticity Models

In the preceding sections, several elasticity-based soil models have been reviewed. The fundamental difference between elasticity-based and plasticity-based models lies in the treatment of loading and unloading. In the most fundamental sense, soil behaves as an elastic-plastic material, i.e., soil deformation is basically plastic since upon unloading deformation follows a different path from that followed by loading. Therefore, if an elasticity-based model is used to

describe the soil behavior under a general loading condition, a special loading criteria must be defined to differentiate loading and unloading. In plasticity models, these problems associated with the path-dependent deformation can be overcome by the introduction of the flow theory of plasticity. Existing plasticity models are generally defined by a few material parameters that can usually be determined from standard tests. In general, these models can represent such important soil characteristics as dilatancy, dependency of strength on stress paths, nonlinear hysteretic behavior under cyclic loading.

The perfect plasticity model is most necessary where ductile soils are involved and the conditions analyzed are close to failure. There have been a number of reports in which good agreements between the prediction using this type of model and field measurements can be found (Wroth and Simpson, 1972; Smith and Hobbs, 1976; Snitbhan and Chen, 1976; Thamm, 1979). Basically the perfect plasticity model can be broken into two parts: yield criteria and flow rule. The yield criteria are used to define the onset of plasticity or the point at which elastic relations cease to be valid. Once the yielding starts, the flow rule then takes over to relate the stress to strain during plastic deformation. As mentioned in the previous sections, the current study is deeply related to the application of soil plasticity on which the strain softening and hardening models are based. Therefore, it should be necessary to review the soil plasticity in some details in the following sections.

3.3.5.4.1.1 Yield Criteria

Elasto-plastic model is an idealization of stress-strain behavior of real soils by an elastic behavior up to yield stress and plastic behavior during failure. Therefore, it is necessary to have an idea of what conditions characterize the change of the material from an elastic state to a yield or flow state. This condition, satisfied in the yield state, is called the yield criterion. In order to express the criteria under the multi-axial states of stress, a mathematical expression involving all the stresses is often required. Establishment of this mathematical expression is usually done based on experimental observations. Original experimental work was done on metals, and hence the development of this subject started with metal plasticity.

Numerous criteria have been proposed for the yielding of solids since Coulomb in 1776. However, only a few criteria have been modified to fit for geological materials: Tresca yield criteria and von Mises Criteria. Tresca yield criteria was suggested in 1864. His theory assumes that the yielding will occur when the maximum shear stress reaches the value of the maximum shear stress occurring under simple tension. von Mises yield criteria (1913) is equivalent to assuming that yielding will take place when the distortion or shear strain energy reaches a critical value. In the following a few yield criteria which are most relevant to soils are briefly reviewed.

According to the Mohr-Coulomb criterion, the shear strength increases with increasing normal stress on the failure plane:

$$\tau_f = c' + \sigma' \tan\phi' \quad (3.5)$$

where τ_f is the shear stress on the failure plane, c' the cohesion of the material, σ the normal effective stress on the failure surface, and ϕ' the angle of internal friction. The above equation represents an irregular hexagonal pyramid in the stress space; the projection of this surface on the Π plane is shown in Fig. 3.1a. On the basis of the Tresca criterion for metals, Drucker (1953) proposed a modified Tresca criterion appropriate for the general treatment of three-dimensional problems of soils. In contrast to the irregular hexagonal pyramid of Coulomb, the yield surface proposed by Drucker is a right regular hexagonal pyramid (Fig. 3.1b). A generalization of the von Mises criterion for soils was proposed by Drucker and Prager (1952). Their model accounts for the effects of all principal stresses and the hydrostatic stress using the invariants of the stress tensor (Fig. 3.1c).

Bishop (1966) attempted to correlate all three yielding criteria with experimental data and concluded that the Mohr-Coulomb criterion best predicts failure of soil. However, for the two dimensional plane strain case it can be shown that in the limit or collapse state both the extended von Mises and the extended Tresca criteria reduce to the Mohr-Coulomb rule. This implies that the constants of the extended von Mises and extended Tresca criterion can be adjusted such that all three criteria will give identical collapse loads.

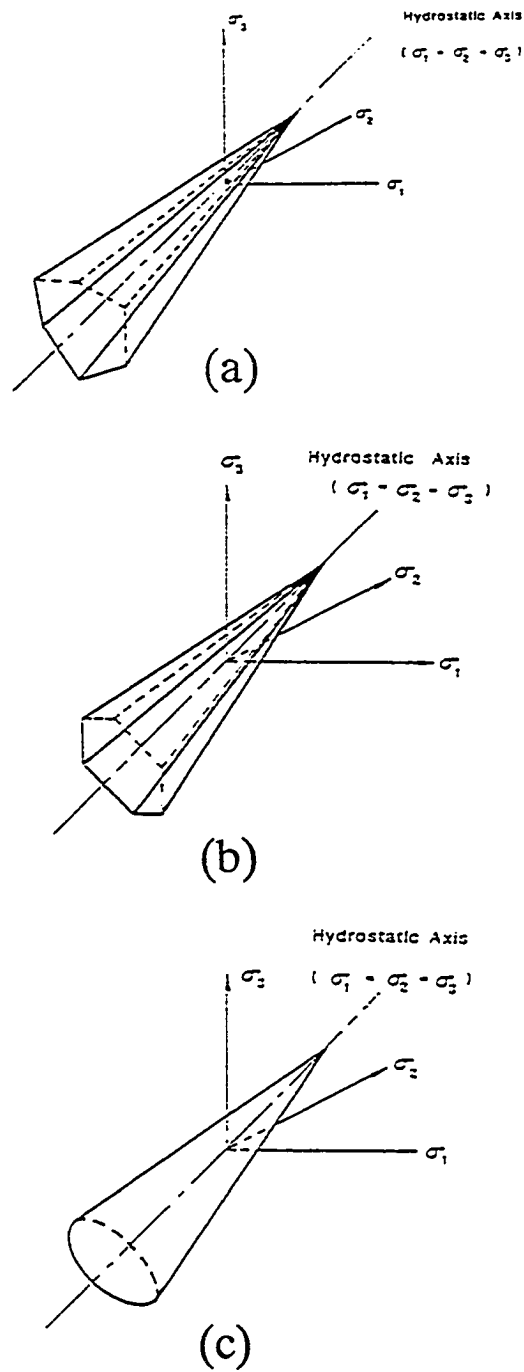


Fig. 3.1 Yield criteria for soils: (a) Mohr-Coulomb criterion; (b) Extended Tresca criterion; and (c) Extended von Mises criterion

3.3.5.4.1.2 Flow Rule

Plastic flow occurs when a stress in a stress space, represented by a vector from the origin, reaches the perfectly plastic yield surface. During the plastic flow, the direction of plastic strain vectors is defined through a flow rule by assuming the existence of a plastic potential function, to which the incremental strain vectors are orthogonal. Then the increments of the plastic strain can be expressed as

$$de^p_{ij} = \lambda \frac{\partial Q}{\partial \sigma_{ij}} \quad (3.6)$$

which is referred to as the normality rule; here, Q is the plastic potential function, and λ is a positive scalar factor of proportionality. For some materials, the plastic potential function, Q , and the yield function can be assumed to be the same. Such materials are considered to follow the associative flow rule of plasticity. However, for many geologic materials, the yield function and the plastic potential function, Q , are often different. These materials are considered to follow non-associative flow rules of plasticity.

One of the stumbling blocks in the further development of the stress-strain relations of soil based on the Drucker-Prager type or Mohr-Coulomb type of yield surfaces to define the limit of elasticity and beginning of a continuing irreversible plastic deformation was the excessive prediction of dilation, which was the result of the use of the associative flow rule. Therefore, it became necessary to extend classical plasticity ideas to a non-associated form (Davis, 1968). However, this

modification created doubts about the uniqueness of solutions. In order to apply the constitutive relations defined in Equation (3.6) to practical problems, the positive scalar factor, λ , should first be determined using some appropriate assumptions. The detailed procedure to determine the factor for Mohr-Coulomb plasticity model will be given in Chapter 5.

3.3.5.4.2 Strain Hardening Models

It has been observed that many geologic materials experience plastic deformations almost from the very beginning of loading. In other words, if the material is unloaded from a given state during loading, it does not return to its original configuration, and experiences plastic deformations. Thus the material undergoes a process of continuous yielding until it finally reaches the conventional failure or ultimate state.

3.3.5.4.2.1 Plasticity Hardening Models

The perfect plasticity theory mentioned in the preceding sections can readily be extended to materials with strain hardening behaviors. The incremental theory of plasticity for hardening materials is based on three fundamental assumptions as follows. First, there exists an initial yield surface and subsequent loading surfaces. Second, an appropriate hardening rule are readily formulated which describes the evolution of the subsequent loading surfaces. Third, a flow rule specifies the general form of the stress-strain relationship. The

first assumption states that a stress function which defines the limit of elasticity of the material exists. It is called the initial yield function before plastic deformations occur and called the loading function beyond the initial yielding. These functions are viewed respectively as the initial yield surface and the subsequent yield surfaces (or loading surfaces) in the multi-dimensional stress space.

For the second assumption, there are a number of hardening rules, such as isotropic hardening, kinematic hardening, and mixed hardening (Chen and Mizuno, 1990). Isotropic hardening rule allows for a uniform expansion of the loading surface, while the kinematic hardening rule permits the loading surface to move as a rigid body in stress space. Mixed hardening, on the other hand, which combines both of these types of hardening, permits the loading surface to expand or to contract uniformly and to translate in stress space. It is well known that the models associated with isotropic hardening rule apply mainly to monotonic loading, while for cyclic loadings effects, the models associated with kinematic hardening rule or mixed hardening rule would be more appropriate.

The third assumption states that the direction of the plastic strain increment vector, de^p_{ij} , is normal to the surface defined by the plastic potential function, Q , as in Equation (3.6). The proportionality factor determining the magnitude of the plastic strain increments can be rewritten as:

$$\lambda = \frac{1}{H'} \left(\frac{\partial f}{\partial \sigma_{ij}} d\sigma_{ij} \right) \quad (3.7)$$

where H' is the hardening modulus, and f is the loading function beyond the initial yielding. As can be understood, the magnitude of λ depends on the magnitude of the hardening modulus and the normal component of a stress increment to the yield surface.

Many of the recent plasticity models appear to be rather complex, difficult to relate to physical behavior, and usually require more detailed experimental result (Chen and Mizuno, 1990). In examining the advantages and shortcomings of the isotropic hardening formulation for soils, Drucker (1966) concluded that yield surfaces are a matter of definition and the choice is not an absolute one, but is rather determined by the most significant features of the problem to be solved. The isotropic work-hardening model suggested by Lade and Duncan (1973, 1975) consists of a shear loading surface which expands asymptotically to the failure surface as the shearing continues. Subsequently, Lade (1977) proposed the modified Lade-Duncan surface to improve on the shortcoming in the previous model. However, both of the models are suitable only for cohesionless soils. It is generally noted that adequate results for monotonic and proportional loading may be obtained from simple isotropic formulations. Difficulties arise, however, when stress paths change directions. Materials with significant anisotropic strength and deformation characteristics are particularly difficult to represent when rotations in the principal stress axis occur.

The fact that the loading surface at large strains is almost independent of loading path leads to the concept of bounding surface models where the

subsequent loading surfaces are allowed to move isotropically inside a limit surface or bounding surface. Various types of strain-hardening plasticity models have been employed based on such bounding surface concept introduced earlier for metals (Dafalias and Popov, 1975; Krieg, 1975). A two-surface model of this type was proposed by Mroz et al. (1978, 1979) for clays. The hardening modulus on the yield surface is assumed to vary with the distance between the yield and bounding surfaces. The bounding surface models have the advantages of a smooth transition from the elastic to the fully plastic state for general loading which is generally observed experimentally on soils.

3.3.5.4.2.2 Cap Hardening Models

Drucker et al. (1957) were the first to suggest that soil might be modeled as an elastic-plastic strain-hardening material. They introduced a spherical end-cap in the stress space to the Drucker-Prager model in order to control the plastic volumetric change of soil, or dilatancy. As the soil strain-hardens, both the cone and cap expand. In the development of their model, there are two important innovations included. The first is the introduction of spherical cap fitted to the cone. The second is the use of current soil density (void ratio) as the strain-hardening parameter to determine the successive loading surfaces. There will be a succession of such surfaces, all geometrically similar, but of different sizes, for different densities. This strain- or work-hardening model was a major step toward a more realistic representation of soil behavior. Roscoe et al. (1963) utilized the

strain-hardening theory of plasticity to formulate a complete stress-strain model for normally consolidated or lightly overconsolidated clay in a triaxial test. These results are presented together in the book entitled "Critical State Soil Mechanics" (Schofield and Wroth, 1968) in which the models for sand and for normally consolidated or lightly overconsolidated clay are named, respectively, Granta-gravel and Cam-clay models. In the former model, volumetric strain and shear strain are both assumed to be irrecoverable. In the latter model, however, only volumetric strain is assumed to be partially recoverable but shearing strain is irrecoverable.

In order to overcome the limitation with Cam-clay models, a modified version of the Cam-clay model was suggested by Burland (1965) replacing the bullet-shaped surface of the Cam-clay model with an elliptic shape and subsequently was extended by Roscoe and Burland (1968) to a model, now known as the modified Cam-clay model, for a general three-dimensional stress state. However, the Modified Cam-clay and Cap models by no means can describe the behavior of materials under all significant conditions and stress paths. Usually, like other currently available models, they may be able to successfully simulate only a limited number of stress paths (Chen and Mizuno, 1990). Often, the global load-displacement behavior of a system predicted by these models can be satisfactory. This may be due to the fact the models simulate satisfactorily a part of the significant stress paths in boundary value problems for a given material (Desai et al., 1981).

3.3.5.4.3 Strain Softening Models

Most soils display a decrease in strength with increasing strain from peak values to the ultimate or residual value. This occurs under both drained and undrained conditions and constitutes an important departure from most plastic idealizations. It is now generally acknowledged that progressive failures occur as a result of strain softening properties of soil and have significant effects on problems such as slope stability and bearing capacities of footings. Therefore, most attempts to analyze the progressive failure problems have been made in the area of constitutive modeling of strain softening behavior of soil. Although a number of viable models have been reported for the strain hardening behavior, very little success in softening models have been reported in the literature. A major part of the problem is that strain softening implies unstable behavior in many instances and can lead non-unique results.

The notion of local constitutive model is a concept wherein stress, strain and material properties exist at every point in a continuum. This assumption implies that the constitutive behavior of an infinitesimal material element will be the same as that of a finite volume of material when the stress and strain fields are homogeneous within the finite volume, i.e. there is no size effect. Under these conditions, the behavior of an infinitesimal element can be determined from finite specimen tested under conditions of homogeneous stress and strain. However, as field conditions deviate from homogeneity, tests on finite specimens become increasingly inappropriate for determining material properties. Therefore,

questions have been raised for years on the validity of the stress-strain relations especially in the post peak region (Lade, 1982; Lade and Tsai, 1985; Finnø and Rhee, 1992).

In spite of these shortcomings, almost all current strain softening models which are practically available in the solutions of boundary value problems are of curve fitting type based on globally derived quantities from laboratory tests. One of the problems associated with strain softening models is that any numerical approach which requires inversion of the tangent stiffness may break down in the presence of negative modulus. For example, Hoeg (1972) applied the strain softening theories on metal plasticity to soils by incorporating a strain softening parameter in the von Mises criterion; his yield criterion is:

$$f_y = k^2 \left(1 + \frac{H}{3G} \right) - J_2 \quad (3.8)$$

where k is the yield stress of a material in the pure shear state, H is the slope of the relation between axial stress and axial plastic strain in a uniaxial loading test, G is the shear modulus of the material, and J_2 is the second invariants of the deviatoric stress tensor. If $H = 0$, the criterion is identical to the von Mises criterion which is perfectly plastic. If $H > 0$, the material is strain hardening, and if $H < 0$, it is strain-softening. The incremental stress-strain relations are identical to the perfectly plastic case with the associated flow rule except the coefficient of the matrix in it.

Subsequently, Lo and Lee (1972) raised some objections to Hoeg's procedure. According to them, Hoeg basically tried to obtain the solution by introducing a negative (H/G) term into the plasticity matrix due to Yamada et al. (1968). This plasticity matrix has been formulated for the purpose of solving elastic plastic problems, and is based on the Prandtl-Reuss hypothesis given by Hill (1956). In the definition the H was designed to relate the generalized stress to generalized strain, which are all positive quantities. Then, it is immediately clear that the negative H can not hold its physical meaning in the context of classical plasticity theory. They continued to discuss the problem with the negative stiffness. For an element which has yielded (or failed), the use of a negative stiffness in the direction of the applied load will result in unrealistic displacements and strains. On the other hand, the use of positive post-peak stiffness will bring in positive shear stress increments even if the post-peak stiffness is very small compared with the pre-peak value, and the case is actually equivalent to that of strain hardening.

Alternatively, Lo and Lee (1973) proposed a multilinear type of model with a numerical procedure based on the Newton-Raphson approach. In their model the emphasis was placed on how to overcome the negative moduli problem in the post peak region of the stress-strain curve. The method first simplifies the stress-strain relation by multilinear curves as shown in Fig. 3.2. In the process of finite element application, the peak strength for each element is compared with the computed maximum shear stress defined by Mohr-Coulomb model. For each of

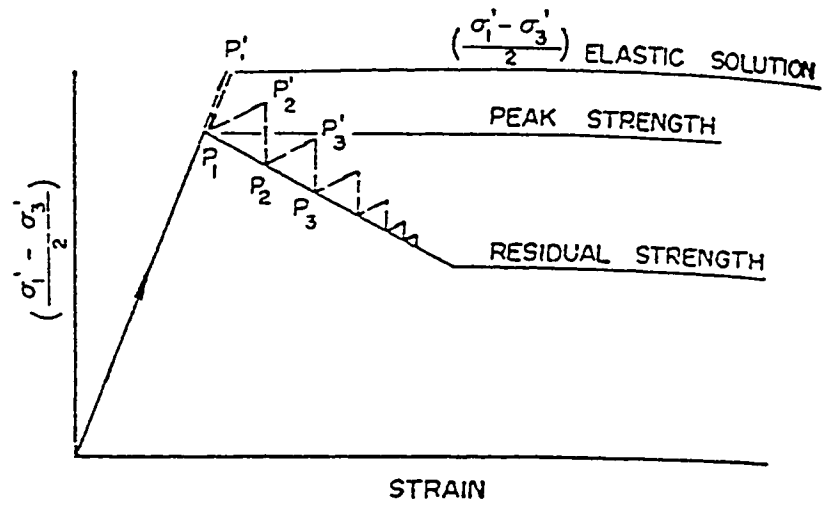


Fig. 3.2 The numerical procedure of iterative process of the stress release and transfer (Lo and Lee, 1973)

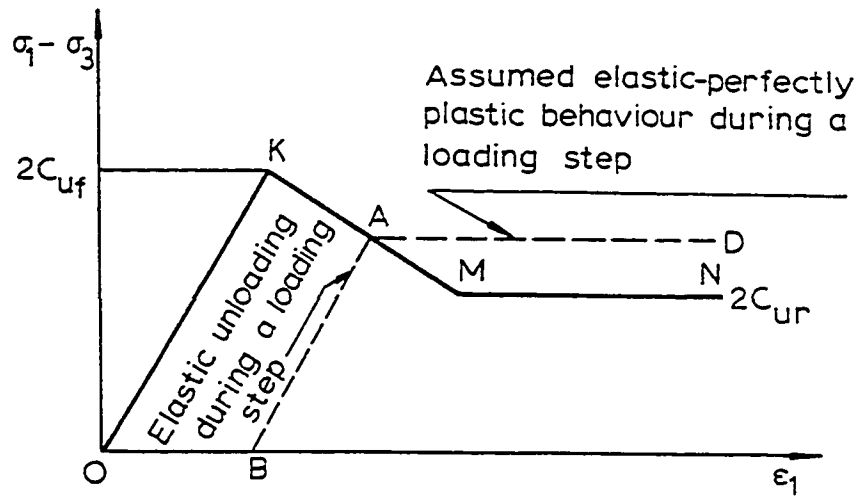


Fig. 3.3 A simplified strain softening model using the elasto-plastic theory (Kalteziotis and Kyrou, 1985)

the over-stressed elements, the shear stress is brought down to the peak condition, i.e. from P'_1 to P_1 in Fig. 3.2 by removing the excess amount of shear stress from the element. The released stresses is then put back into the continuum. Corresponding to these stress increments a new set of nodal forces can be generated by using the principle of virtual work. Simultaneously, the strains for the over-stressed elements are brought to the peak failure condition. A new value of modulus E_2 is assigned to these elements and the half-band stiffness matrix is re-assembled with all pre-peak elements having modulus E_1 . The new stiffness equations are then solved, and the stress and strain increments corresponding to the new set of nodal forces are computed. Since a positive modulus E_2 has been used resulting in P'_2 , the stress condition at P'_2 , is brought to that at P_2 on the descending portion of the stress-strain curve by removing the excess shear stress from the element.

Following Hoeg's attempt (1972), the theoretical justification for using the classical theories of plasticity to simulate strain-softening behavior was provided by Prevost and Hoeg (1975) who proved the existence of uniqueness and stability of solution. However, their model is complex and hard to use in practice. Sture and Ko (1976) used a similar constitutive model to Lo and Lee's (1973) to see the influence of strain softening behavior on the bearing capacity of footing. Biondi et al. (1976) analyzed the influence of the degree and rate of softening behavior on the extent of plastic yield under footing foundation. They employed two

parameters to describe the strain softening behavior: c/c_p , which is the ratio between the residual and the peak cohesions, and H/G , which is the ratio between the slope of the shear stress-strain curve in post-peak (H) and in pre-peak (G) regions.

Kalteziotis and Kyrou (1985) pointed out that strain softening models associated with sophisticated plasticity theory are complex such that practical applications in design offices are usually difficult. Alternatively, they proposed a simplified application of elasto-plastic theory with the associated flow rule and Tresca yield criterion. The strength of an element in post peak region was considered to remain constant throughout a computational step and behave just like an elasto-plastically (B-A-D in Fig. 3.3). Unloading on the element causes elastic rebound (A-B) and loading results in associated flow (A-D). By this way the problem dealing with strain softening model was reduced to the one with the elastic-perfectly plastic model. They found that the peak bearing capacity of strain softening clay foundation significantly depends on the strain softening rate, yet the ultimate residual strength does not.

Potts et al. (1990) used a strain softening model implemented in finite element method to analyze Carsington embankment which had failed during construction. In their model, the pre-failure and unloading-reloading behavior were modelled by isotropic elastic theory, and failure and post-failure strain softening were modelled by plasticity using the Mohr-Coulomb yield criterion.

Softening behavior is introduced by allowing the angle of shearing resistance, ϕ' , and the cohesion intercept, c' , to vary with the deviatoric plastic strain invariant.

3.4. PSEUDO-PROGRESSIVE FAILURE ANALYSES

3.4.1 Introduction

It has been repeatedly confirmed that the ratio of the actually mobilized strength to the laboratory-determined strength of undrained samples decreases significantly with increasing stiffness of the soil due to the progressive failure. The mechanism of the progressive failure is complex and extremely difficult to deal with. As pointed out by Peck (1967), finite element method with an appropriate constitutive model describing the complex soil behavior of strain softening is necessary for the complete analysis of progressive failures of slopes. However, appropriate constitutive modeling itself is a formidable task and very little success in the area have been reported. Therefore, in practice, there have been alternative attempts to use limit equilibrium methods for the designs of slopes in strain softening materials. Commonly, the average operational strengths along the failed surface is obtained by back-analysis of already-failed slopes using the limit equilibrium methods. They are obviously different from the peak strengths measured in laboratory tests depending on the brittleness and strain softening rate of the soil. Correction factors can then be used to relate these two strengths for the same soil. This approach was adopted for embankments on the undrained soft clay foundation (Bjerrum, 1973). It has been applied also to cut

slopes in stiff fissured brown London clay and Upper Lias clay (Chandler and Skempton, 1974; Skempton, 1977). This approach is believed to provide a design guide for the particular soils under consideration, but can not be a universal design methodology.

In the following section, several attempts to analyze the progressive failures of slopes using limit equilibrium methods have been reviewed. Although none of these attempts have proved strictly valid, their approaches are especially useful in interpreting the results from numerical analysis such as finite element or finite difference analysis. Since the analyses using the limit equilibrium method cannot be of complete form, they are termed "pseudo-progressive failure analysis" of slopes.

3.4.2 Progressive Failure Analyses Using LEA Methods

3.4.2.1 Residual Method

Skempton (1964) back calculated the average shear strengths along the failure surfaces in already failed slopes in unweathered Selset Boulder clay with no fissures or joints as well as in weathered London clays with fissures and joints. The slopes were all in overconsolidated clay and the time to failure took more than 20 years from the cut construction due partly to weathering and pore pressure equilibrium. He compared back calculated strengths to the residual strengths and drew the following conclusions. The Selset Boulder clay developed its peak strength along the nearly entire length of the failure surface. The

weathered London clay, on the other hand, shear strength parameter decreases below the peak values and the average shear strength along the failure surface eventually moves toward the residual level with sufficient time. As a consequence of this finding, Skempton concluded that in natural slopes, where sufficient time is available for the development of sliding surfaces by progressive failure, the ultimate stability depends on the residual shear strength only.

Although Skempton's suggestion represents a way of handling the progressive failure in a simple way using the residual strength, it may be in many cases unnecessarily conservative and enormously expensive solution. Consequently, Bjerrum (1967) raised the questions "under what conditions are we compelled to use the residual shear strength in the design of slopes, and when can we rely upon some proportion of the peak strength?" Answers to these questions require first a fundamental understanding of the mechanism of progressive failure and of the factors that are involved. Secondly, a fundamental knowledge of the properties of the various types of material that we are dealing with.

3.4.2.2 Conlon's Approach

An attempt to quantitatively solve the progressive failure problem was made by Conlon as cited by Peck (1967). His approach is of interest such that it deserves a review in detail. Conlon considered the compressibility of the soil and hypothesized that the displacement along the surface of sliding is not uniform from one end to the other. He developed an idealized slope with ideally defined

effective normalized stress distribution from which the shearing forces along the failure surface were obtained. He used the conventional method of slices without taking into account the forces between the slices. It was found that near the upper portion of the failure surface the shearing forces are somewhat greater than the shearing resistances corresponding to any amount of deformation. Therefore, it was postulated that the portion of the sliding mass near the upper part of the failure surface moves downward a distance sufficient to pass the peak strength of the materials and to approach the residual value. However, the soil near the central portion of the failure surface, where the normal stresses are highest and consequently the strains to the peak value are also rather high, may be exhibiting its peak strength. Near the lower portion of the surface of sliding, the deformations are determined primarily by those required to bring the central portion of the surface to the peak strength. Therefore, the strengths are intermediate between the peak and residual values.

This hypothesis led Conlon to make an interesting suggestion. He proposed to establish a numerical measure of the available shearing resistance by taking the shearing resistance on the upper portion of the failure surface equal to the residual value, by taking the resistance for the central zone of maximum normal stress at the peak value, and by taking the shearing resistance for the lower portion of the failure surface consistent with the shear deformation for the peak shearing resistance for the maximum normal stress. In this fashion, although judgement is still required in estimating the length of the various portions of the

surface of sliding, a quantitative procedure is set forth for estimating the available shearing resistance along the surface of sliding. Conlon's suggestion is certainly an interesting attempt to predict the degree to which the shear strength may be mobilized along the failure surface. Peck (1967) states that Conlon's suggestion does not necessarily imply that failure always starts at the head of a slide. Although there are undoubtedly several other factors to be considered, it seems that refinements of this sort of approach may be promising on the basis of theories of the limit equilibrium.

3.4.2.3 Bishop's Approach

According to Bishop (1967), the magnitude of the possible error involved in the slope stability analysis without considering the progressive failure is directly related to the brittleness of the soil (Fig. 3.4) defined by the parameter I_B where

$$I_B = \frac{\tau_f - \tau_r}{\tau_f} \quad (3.9)$$

in which τ_f and τ_r are the shear stresses at the peak and the residual states, respectively. The parameter is strongly influenced by consolidation stress level, and in anisotropic soils it depends also on the orientation of the principal stresses. At the point of limiting equilibrium, on some part of the slip surface the peak drained strength will be mobilized while the post-peak and pre-peak strengths will be operative over the remainder of the slip surface.

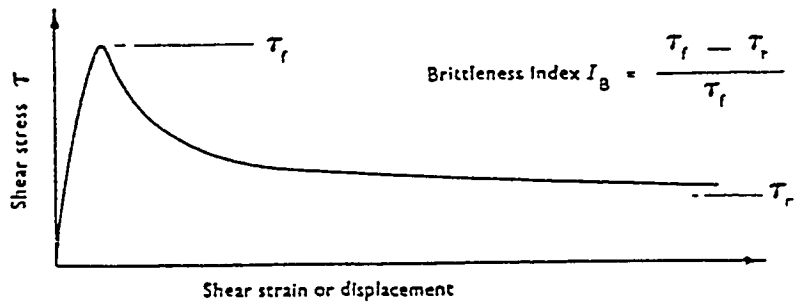


Fig. 3.4 The definition of brittleness index of soil

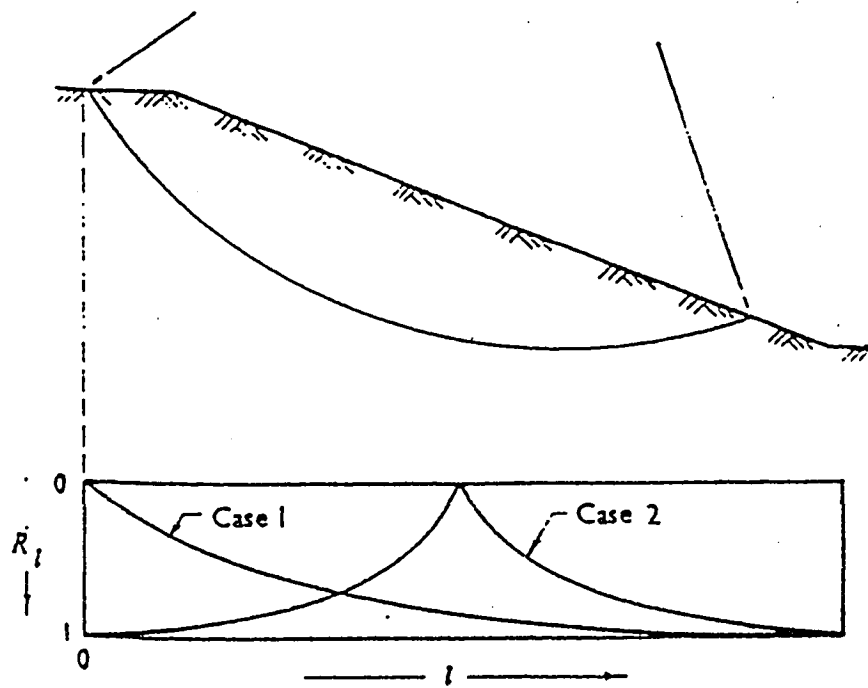


Fig. 3.5 Possible local residual factor distributions

At this stage the shear strength mobilized may be represented as shown in Fig. 3.5 by a local residual factor R_1 similar to that defined by Skempton (1964) but varying along the slip surface. The value of R_1 denotes the proportional drop from the peak to the residual strength at any point along the surface, that is, $R_1=0$ at the peak strength and $R_1=1$ at the residual strength. Although at least some part of the surface must be at an R_1 value of zero (i.e. it is just passing the peak of the stress-strain curve), it is less certain whether any other part will have reached the residual state. A few intuitively chosen R_1 distributions were suggested and reviewed as a guide to the practical relevance of this approach. Bishop (1967) suggested that under drained conditions progressive failure advances from both ends of the rupture surface inward. Field observations with an inclinometer installation (de Beer, 1967, 1969) suggest that rupture may progress predominantly from the toe towards the top of the slope. These may be simplified to the two R_1 distributions (case 1 and case 2) shown in Fig. 3.5. The rapid initial drop in strength with relative displacement across the rupture surface suggests that the R_1 values will fall off rapidly on moving into the post-peak zone.

In conclusion, a reasonable distribution of local residual factor R_1 can adequately account for the progressive failure problems of first time slides in overconsolidated clay. The distribution of local residual factors around the slip surface at failure will be a function of the following factors: (a) strength drop-off rate in post peak regime, (b) swelling characteristics, (c) coefficient of earth pressure at rest, and (d) geometry and scale of the slope.

3.4.2.4 Chandler and Skempton's Approach

Chandler and Skempton (1974) back calculated a number of failed slopes in brown London clay and Upper Lias clay to obtain the average effective internal friction angles and cohesion intercepts which were mobilized during failures. They obtained small cohesions and friction angles which were the same as the ones determined from the conventional laboratory test. Therefore, the determination of the cohesion intercept in the design of slopes in overconsolidated clay was suggested to be the key point. While zero cohesion intercept obviates the problem of determining the true value, they believed that it is not realistic answer as the assumption leads to the conclusion that the limiting slope of a cut in clay is independent of depth, which is contrary to practical experience.

They concluded that for brown London clay and weathered Upper Lias clay residual strength does not have any relevance in first time slides, which is in contradiction to Skempton's conclusion (1964). For fissured clays, large specimens were suggested to be used in the laboratory testing rather than conventional small samples, which was believed to give too high values of strength parameters. It is interesting here to note that Skempton (1964) used strength parameters which were determined from conventional size specimens. Then there could be a possibility that Skempton's shear strength parameters were all overestimates for peak as well as residual strengths. This possibility implies that the residual

strengths that he thought could have been somewhere between the peak and residual values.

3.4.2.5 Lo & Lee's Approach

As pointed by Peck (1967) and Bishop (1967), Lo and Lee also agree that a complete solution to the progressive failure problem would require a finite element analysis with strain softening constitutive model. Consequently, they developed a finite element method to solve problems with strain softening materials using an iterative process of stress release and transfer. The numerical scheme has been separately reviewed in section 3.3.5.4.3. Lo and Lee applied the finite element method to an excavated slope of 25° inclination and 30 ft height and obtained results in which failure zone can be identified in the slope. Then, they suggested that the result be combined with limit equilibrium analysis in the following manner in order to determine the factor of safety of the slope of strain softening material. First, the residual factor R_r is used which was defined as proportion of the total failure surface in the clay along which its strength has fallen to the residual value. In other words, $R_r = D/L$, where L is the length of the slip surface and D is the portion in which the residual strength operates.

By using an appropriate limit equilibrium method, whether circular or non-circular, the critical failure surface is obtained. Then a relationship between the factor of safety and the residual factor R_r for the surface is computed. This can be achieved by letting the slices of the critical circle fail successively, starting from

the toe towards the crest, and the corresponding correct factor of safety (F_c) is computed. The method basically assumes that the failure initiates from the toe of the slope and propagates toward the crest. The relationship between F_c and the residual factor R_r for the critical circle of the 30 ft slope is plotted in Fig. 3.6. Using the residual factor obtained from the finite element analysis, the factor of safety can then be directly evaluated in the graph depicting the relationship between F_c and the residual factor R_r .

The method implicitly divides the strength distribution along the critical failure surface into two sections, peak and residual strengths, based on finite element analysis. Then, the method assumes that the failure initiates from the toe of the slope and propagates toward the crest. This assumption was found to be consistent with the field observations by de Beer (1969) on slopes of stiff overconsolidated clays, if not applicable to general cases. Once the way of failure propagation is defined, then the factor of safety of the slope directly depends on the proportion along which the peak strength has fallen into residual state.

3.4.2.6 Koutsoftas and Ladd's Approach

Koutsoftas and Ladd (1985) developed the strain compatibility technique as an approximate methodology to account for progressive failure when conducting the undrained strength analysis. It seems that they owe much of the strain compatibility technique to a similar concept first suggested by Leonards (1962). Fig. 3.7 plots normalized stress-strain data of normally consolidated AGS marine

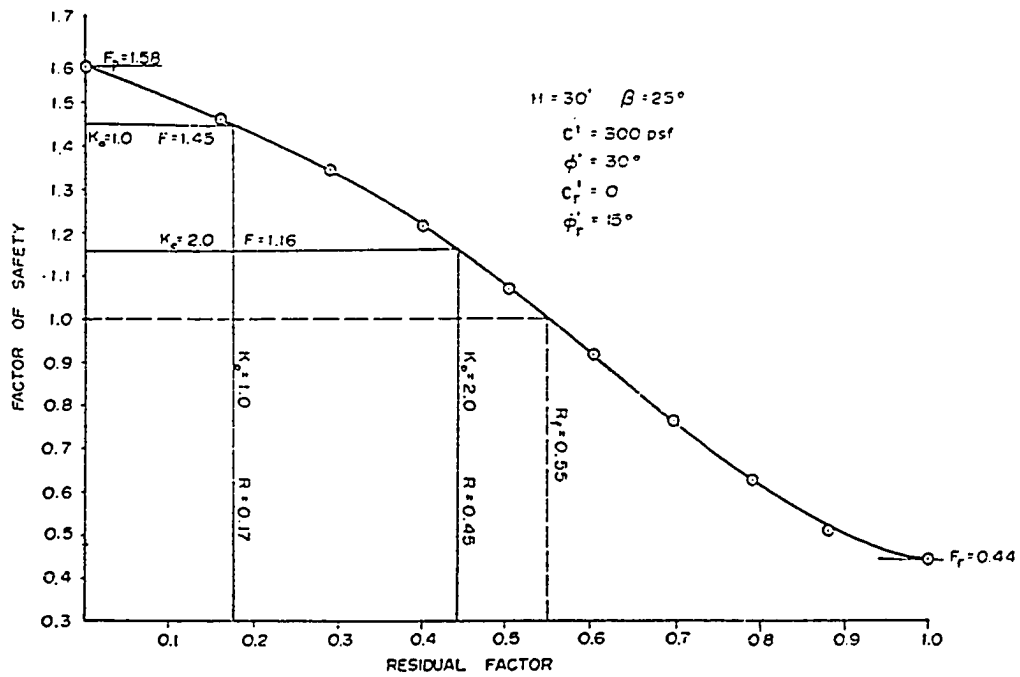


Fig. 3.6 Relationship between the correct factor of safety and the residual factor

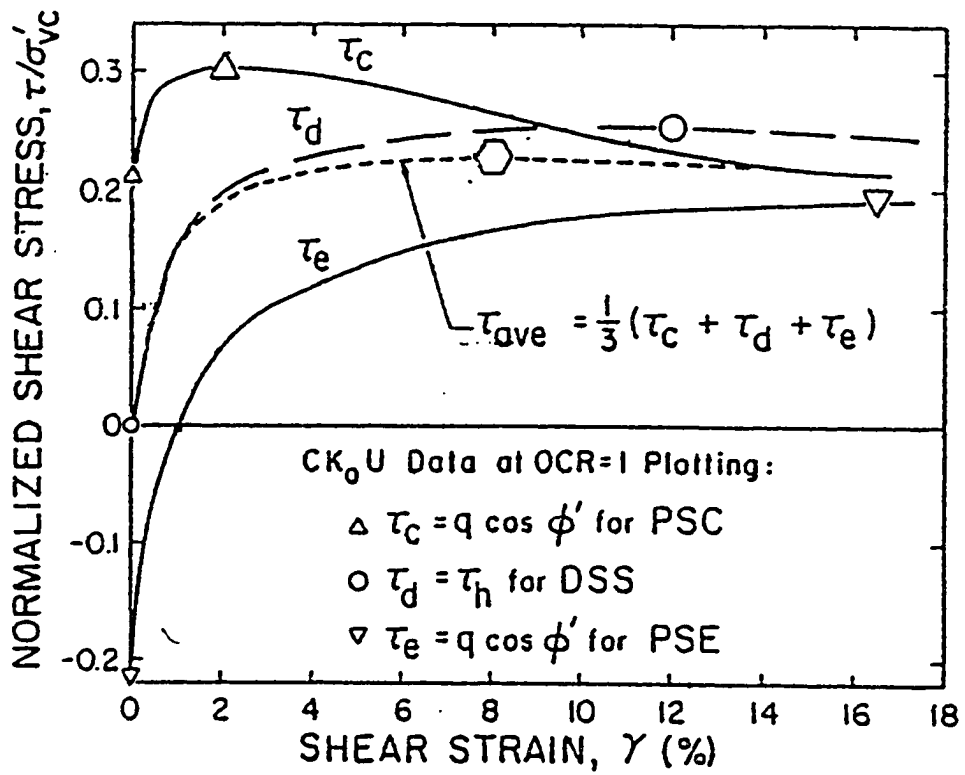


Fig. 3.7 Anisotropic stress-strain relations of AGS clay

clay which were determined from the K_0 -consolidated undrained (CK₀U) plane strain compression and the extension and the direct simple shear tests. For a wedge-shaped failure surface, τ_c represents the shear resistance of the active (compression) portion, τ_d simulates shear on the horizontal segment, and τ_e represents shear resistance within the passive (extension) zone. In the plot it can be noted that each stress path has a different shear strain level at which the maximum shear stress occurs.

Koutsoftas and Ladd (1985) assume that the shear strain all along a potential failure surface will be uniform at the moment of actual failure, which takes place when the maximum average resistance is mobilized. Based on this premise, the average resistance that can be mobilized at any given strain equals $\tau_{ave} = 1/3 \times (\tau_c + \tau_d + \tau_e)$ for a failure surface having equal contributions of τ_c , τ_d , and τ_e . The average resistance for the clay in Fig. 3.7 reaches a maximum value of $\tau_{ave}/\sigma'_{vo} = 0.225$ at $\gamma_{max} = 8\%$, compared to an average of the peak strengths equal to $1/3 \times (0.305 + 0.255 + 0.19) = 0.25$. Thus, progressive failure reduces the available resistance in this case by 10%.

It is very important here to note that Ladd and Koutsoftas's suggestion can be immediately applied in such a way that the stress-strain-strength anisotropy of soil is taken into consideration to some degree in the limit equilibrium analysis. Application of his suggestion to all progressive failure analyses, however,

represents a loss of ground in certain cases, where the strains along the failure surface are nonuniform to a great extent. The strain non-uniformity along the failure surface of slopes is a well confirmed fact as reported by a number of engineers.

3.4.2.7 Mesri and Abdel-Ghaffar's Method

Mesri and Abdel-Ghaffar (1992) noticed that the best estimate of the shear strength mobilized in full-scale field situations is obtained by back-analysis of slope failures. They collected and re-analyzed 40 already-failed slopes and embankments in soft and stiff clays. The results suggested that a closer agreement between the computed critical slip surface and actual slip surface is obtained when the peak shear strength rather than the mobilized strength is used to determine the critical slip surface, which is a confirmation of previous finding (Abdel-Ghaffar, 1990). When the exact location of the failure surface is known, the mobilized shear strength on the surface is computed using a limit equilibrium method (Spencer or Bishop's method). In the absence of information on the observed slip surface, a critical slip surface is computed using the reported peak shear strength data. Then, the mobilized shear strength on the critical slip surface is determined.

The results are summarized in Fig. 3.8 in terms of a reduction factor η to the peak strength. The figure indicates that for soft clays, such as those from Norway, and stiff boulder clays, with plasticity indices (I_p) less than 20 %, $\eta = 1$

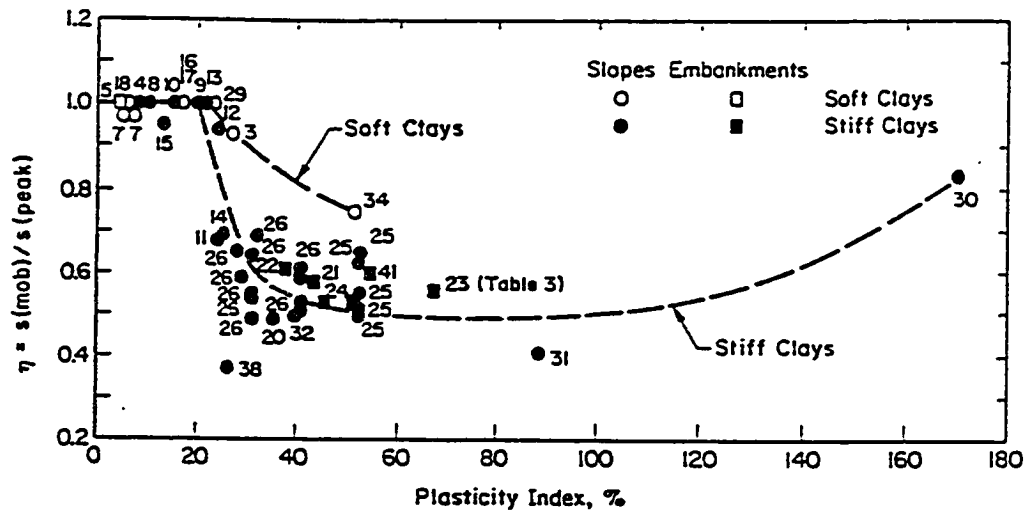


Fig. 3.8 Relations between the correction factor (η) and the plasticity index (I_p)

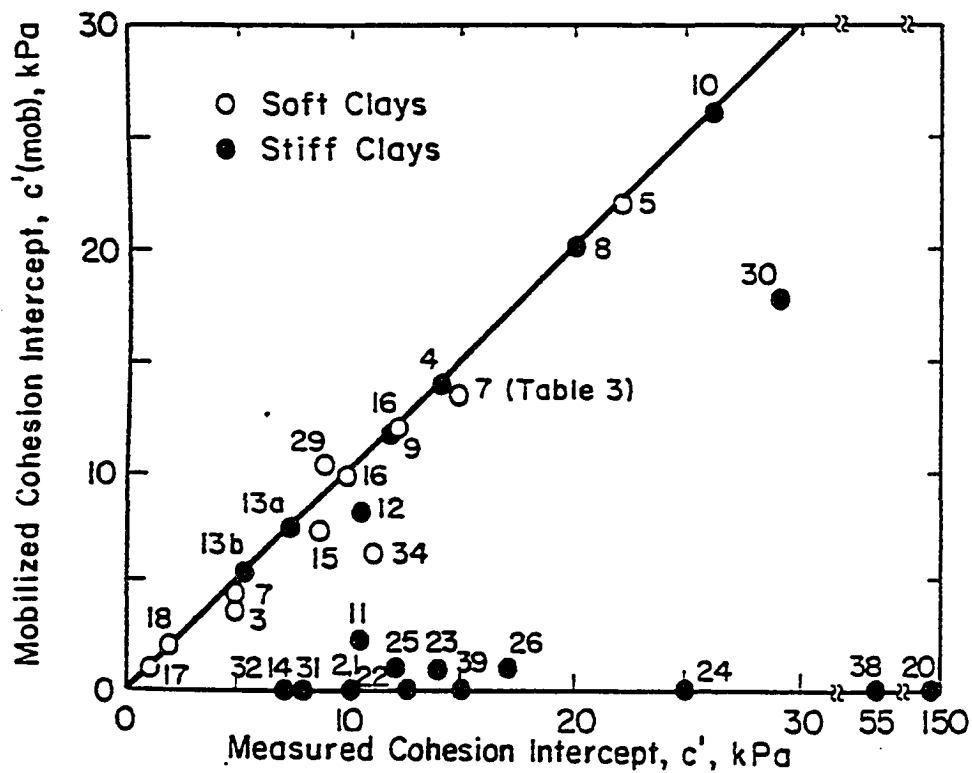


Fig. 3.9 Relations between mobilized cohesion intercept (c'_{mob}) and measured cohesion intercept (c')

and the mobilized shear strength is equal to the laboratory-measured peak strength. They claimed that the result was consistent with the previous conclusions (Kenney, 1967; Chandler, 1984) on the same clays. On the other hand, at higher I_p , values of η are less than one and may be as small as 0.4. Using the assumption that the mobilized internal friction angle (ϕ'_{mob}) is the same as ϕ' , the values of average c'_{mob} were computed and compared with c' . This procedure is based on the assumption that the average resistance along the failure surface drops as the cohesion intercept drops, yet the internal friction angle is likely to remain constant even at an extreme strain level, i.e. residual strength level. Fig. 3.9 shows that full magnitude of c' is mobilized during the global instability in low-plasticity soft and stiff clays, which is in agreement with Fig. 3.8.

Finally, the results (Fig. 3.8) were suggested to be used in an effective stress stability analysis of the first-time initial slips in soft and stiff clays. For clays of similar type, peak strength envelope is measured using either the triaxial compression or the direct shear tests on undisturbed specimens subjected to effective stresses similar in magnitude to those in the field. Then the peak strength parameters are used to determine the critical slip surface and the corresponding factor of safety. The computed factor of safety is then corrected by η based on the plasticity index, I_p , in Fig. 3.8. However, the assumption of constant internal friction angle during failure may be questionable. According to Bjerrum (1967) the residual shear resistance has a frictional character although the ϕ' , is

not necessarily independent of the normal pressure. Skempton (1964) reviewed the knowledge on the residual shear strength and concluded that the residual shear strength parameter, ϕ'_r , is independent of the original strength of the clay and such factors as water content and liquidity index. The value of ϕ'_r , of a clay seems to depend only on the size, shape, and mineralogical composition of the constituent particles.

3.5 Stress-Strain-Strength Relations of Soils

3.5.1 Introduction

For a normally consolidated clay deposited under the level ground, the effective overburden pressure is usually greater than the horizontal effective stress. Therefore, the clay is consolidated one-dimensionally under an anisotropic system of stresses. Studies of the structure of clays (Mitchell, 1976) have shown that clay particles tend to become oriented perpendicular to the major principal stress (effective overburden pressure) direction during the one-dimensional consolidation. Parallel orientation of clay particles causes both the strength and compressibility of the clay to vary with direction.

Therefore, when an undrained failure occurs in a deposit of clay in the field, the shear strength mobilized on a failure surface may vary with the orientation of the failure surface as a result of anisotropy of the clay. Because the failure plane has a different orientation at every point along the sliding surface, it

can be said that the undrained strength ratio, S_u/σ'_{vo} , will also vary from point to point along the sliding surface. In addition, it is well known that deformation characteristics of soil also greatly depend on the orientation of the sliding surface (major principal stress direction). Therefore, in order to perform a proper slope stability analysis, it would be necessary to know the relations between the undrained strength ratio, stress-strain characteristics and the orientation of the failure plane.

3.5.2 Plastic Yielding Behavior of Soils

Stress-strain behavior of a material can be idealized as follows: (a) perfectly elastic, (b) rigid, perfectly plastic, (c) rigid, linear strain hardening, (d) elastic, perfectly plastic, (d) elastic, linear strain hardening, (f) elastic, linear strain softening. Physical and graphical representations of these idealized models are shown in Fig. 3.10. As described in the previous sections, the phenomenon of progressive failure is governed by plastic yielding behavior of the material: perfectly plastic, strain hardening and strain softening. The perfectly plastic behavior is, however, a drastic idealization of plastic deformation for most soils such that it cannot account for the progressive nature of failure. Therefore, the following review will be focused on the strain hardening and softening behaviors observed in the laboratory testing in the literature.

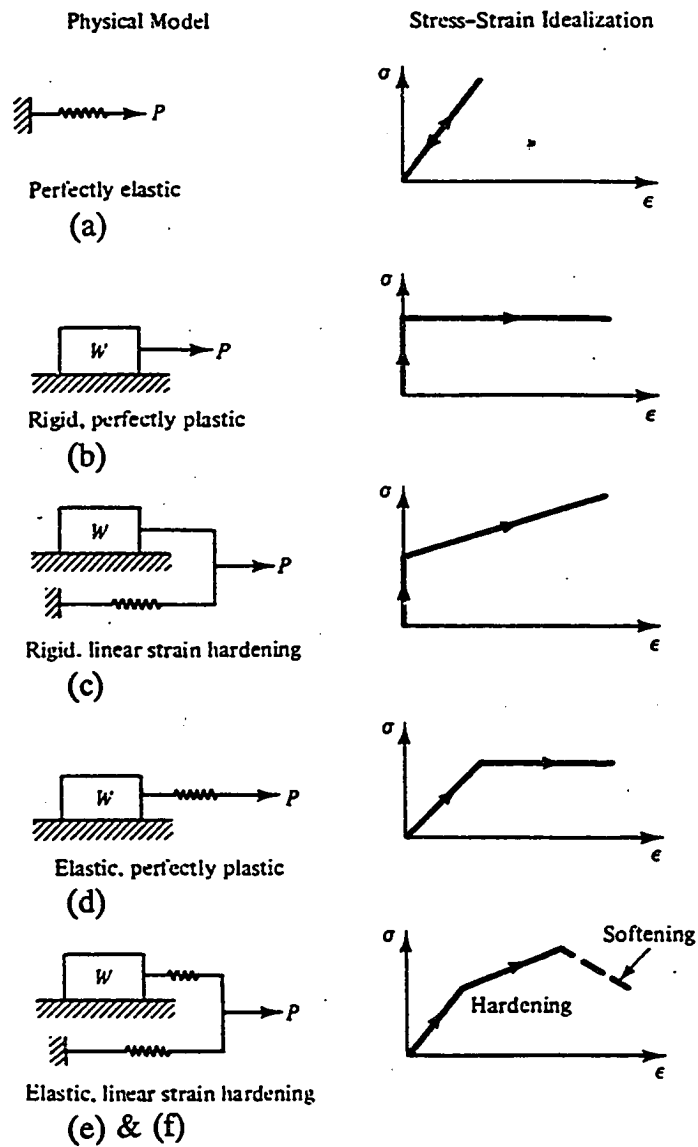


Fig. 3.10 Idealized stress-strain models

3.5.2.1 Strain Hardening Behavior

It is a well known fact that most soils experience plastic deformations almost from the very start of loading. When soil is unloaded from a given state in the process of loading, it does not return to its original configuration, and experiences plastic deformation. Most soils undergo a process of continuous yielding and hardening (strength increment) until they finally reach the conventional failures or ultimate states so that stress-strain relations up to the peak is close to a convex curve. However, it has been a practice to approximate the initial portion of the stress-strain relation as a linear-elastic and assume that the perfectly plastic deformation occurs thereafter (Fig. 3.11). Then, the whole stress-strain relation is simply represented by two linear lines. This sort of simplification in practice has been the most usual way of modelling the stress-strain relations of soils. The simplified model then often gives good agreement with expected results leading to less attention to the hardening aspect of soil behavior.

The whole stress-strain curve itself up to the peak stress represents a strain hardening process. Therefore, the strain hardening behavior also depends on the stress path for anisotropic soils. A comparative review of strain hardening patterns up to the peak stress of the three typical stress paths of the plane strain compression (PSC), the plane strain extension (PSE), and the direct simple shear (DSS) will later be provided with detailed experimental data (Section 3.5.5).

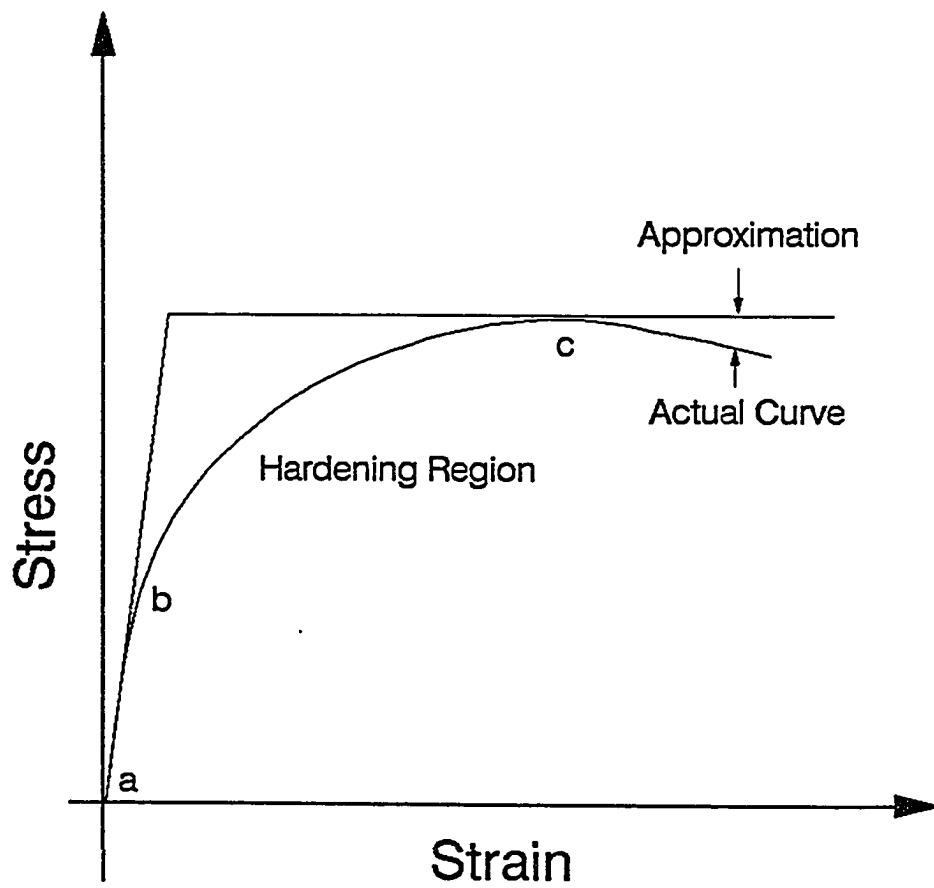


Fig. 3.11 Approximation of stress-strain relations by elasto-plastic model

3.5.2.2 Strain Softening Behavior

The strain softening phenomenon in the post peak region critically influences the overall behavior of structure and must be carefully modelled. The modelling of the strain softening is generally more difficult and has challenged engineers for years leading to plenty of researches concerning softening phenomena. There are a variety of soils that exhibit a phenomenon called strain softening under certain loading conditions. Soils which exhibit such softening are characterized by a global constitutive response in which the stress rises monotonically with strain to the peak, and then decreases with further increase in strain. A good amount of data exist that show apparent strain-softening behavior of a variety of soils. For example, Lee and Seed (1967) clearly showed that dense sand dilates when sheared at low confining pressures and exhibits strain softening behavior. Castro (1975) showed that contractive granular soils exhibit global strain-softening behavior during the undrained triaxial compression. Similarly, strain softening has been observed to occur when heavily overconsolidated clays are sheared under drained conditions (Bjerrum, 1967). Strain softening behavior is often observed with sensitive and structured clays under undrained conditions (Leroueil et al., 1979). To a lesser degree, it is also found with a relatively insensitive, normally overconsolidated clay such as Boston blue clay in the undrained triaxial and the plane strain compression tests (Ladd, 1971).

The mechanism of strain softening in ideal conditions can be considered in the following two cases. First, for dried sand with void ratio smaller than the

critical value, the shearing stress of certain magnitude will cause the whole specimen to dilate homogeneously, resulting in less density and therefore less strength. Upon reaching a critical state, the soil skeleton stops dilating and the strength approaches to the residual state. This kind of ideal mechanism of strain softening is very hard to observe due mainly to the nonuniform density and nonuniform stress and strain distributions in the specimen during laboratory testing.

Second, saturated sand with void ratio higher than the critical value may exhibit a different strain softening mechanism, which is related to pore water pressure increase due to shearing. For example, the collapse of the soil structure in triaxial tests can cause the load to be suddenly transferred from the sand skeleton to pore water, resulting in a sharp increase in pore water pressure. Consequently, the shear strength is reduced substantially, and the sand undergoes large deformations in a short period of time (Alarcon-Guzman et al., 1988).

The general understanding of the softening behavior is that soils that tend to dilate will strain soften when sheared under drained condition and soils that tend to contract strain soften when sheared under undrained conditions. These conclusions are based on assumptions of uniform stress and strain within the specimen during all phases of shearing, even in the post-peak region. In reality, however, the specimen in the laboratory testing undergoes deformation which is far from uniform. Therefore, it should be in order to review actual laboratory

testing conditions, resulting failure modes and their implications in the stress-strain-strength characteristics in the following section.

3.5.3 Failure Modes

It is well known fact that the stress-strain-strength characteristics determined from laboratory testing are strongly influenced by the mode of specimen failure: zone failure and line failure. Zone failure occurs under the uniform stress and strain conditions. In this type of failure, multiple failure planes traverse the specimen along the planes of the possible maximum shear stress which is oriented at $\pm (45 + \phi/2)$ degree from the minor principal stress direction. Line failure occurs under the nonuniform stress and strain conditions. In this type of failure, two practically solid bodies slide past each other along a single failure plane whose orientation is the same as that of the zone failure.

The terms 'zone failure' and 'line failure' were first used by Jacobson (1967) in a study of the behavior of Boulder clay in the triaxial compression tests. He found that the undrained shear strengths of preconsolidated Boulder clay determined from tests with zone failure were comparable in magnitude with those determined from vane shear tests. Tests with line failure, however, resulted in substantial scatter with average strengths of about 40% of those determined from vane tests.

Lade and Tsai (1985) studied failure modes of the triaxial testing specimens and their effects on the strength characteristics using triaxial tests on

remolded EPK clay. The tests results showed that line failures resulted in stiffer stress-strain relations and higher strengths for the compression test, while zone failure produced stiffer stress-strain relations and higher strengths for the extension tests. It was concluded that the comparisons of stress-strain, and strength characteristics should only be made if these have been obtained under the same strain and failure condition, preferably those of uniform strains and consequent zone failure. They also pointed out that the stress-strain curve must be associated with the type of failure mode: line failure or zone failure.

It is interesting to consider the failure mode of the specimen in association with the causing factors in the laboratory test. According to Lade (1982) and Lade and Tsai (1985) the failure mode depends on three factors: uniformity of density, dilatancy, and boundary condition. First, non-uniformity in the density of a specimen promotes development of line failures. Zones with low densities constitute zones of weakness, and single failure planes may develop through such parts of the soil. Second, a tendency to dilate during shear aggravates initial non-uniformity of density and makes line failure more likely. A tendency to contract during shear has the opposite effect. If sufficient densification occurs, the soil in the failure plane could become as dense and strong as some other parts of the specimen. This would result in increasing uniformity of density thus promoting conditions for zone failure.

Lastly, regardless of the uniformity of density of the specimen and the changes in density resulting from volume changes, zone failure will occur if the

boundary conditions enforce uniform strains throughout the specimen. The best boundaries for enforcing uniform strains are stiff, lubricated flat surfaces. Such boundaries reduce friction greatly, resulting in essentially uniform stresses. They also prevent development of line failures provided that the potential planes of sliding are oriented such that they would have to intersect the boundary.

From above examples, it is clear that the line failure in the laboratory occurs as a result of testing conditions in association with one or more of the factors: density, dilatancy, and boundary condition. Therefore, it is important to check the implication of the line failure in the specimen with regard to global response of the material. Atkinson and Richardson (1987) discussed strain softening behavior with line failure mode of stiff overconsolidated clay. They explained that since soil in a shear zone is softer and weaker than soil elsewhere, and continuing straining will continue to soften and weaken it. Once a shear zone has formed, its direction is found to be fixed, and continue to dilate until it reaches the critical state. Therefore, the strength measured in a specimen with the line failure is only representative of the density of the soil actually involved in the failure, which is often less than the average for the whole specimen. Their study supports that the highly concentrated strain along the shear zone strongly influences the stress-strain relations obtained in the average sense for the whole specimen.

Because natural soil deposits are seldom uniform with regard to density, line failure will occur in the field when the soil is expanding and when zone

failure is not imposed by the boundary conditions. Line failure and localized deformation may also be promoted by the boundary conditions and stress concentrations produced in the particular field problem under investigation. However, it should be realized that the boundary conditions and stress concentrations particular to the laboratory soil tests in which line failure develops will seldom be representative of those in the field (Taylor, 1948), and it is therefore unlikely that the results from such tests would be appropriate for analyses of field problems. It should be emphasized that zone failure tests provide the best means of establishing the stress-strain and strength relations of soil elements. The development of line failure and localized deformation then can be determined from numerical analyses (FEM or FDM) which takes into account the proper boundary conditions, stress concentrations, possible non-uniformities in the soil, and an appropriate constitutive model with material parameters determined from tests with zone failure.

3.5.4. Undrained Shear Strength Anisotropy

3.5.4.1 Normalized Shear Strength Behavior of Clays

Most short-term stability analyses for structures on soft clay deposits are carried out by the undrained strength analysis. The undrained strength (\bar{S}_u) of clay is proportional to the vertical effective consolidation stress (σ'_{vo}) so that the relation between them is commonly expressed in terms of the undrained strength

ratio, S_u/σ'_{vo} . For a normally consolidated clay, the undrained strength ratio is found to remain constant for a given stress path. In the literature, a number of studies have been reported in which the undrained strength ratio is related to the basic index properties of clay such as plasticity index (I_p) or liquid limit (LL). It is consistently found that clay with higher plasticity index or liquid limit usually has higher undrained strength ratio as can be seen in the following equations.

$$S_u/\sigma'_{vo} = 0.37 I_p + 0.11 \text{ (Skempton, 1957)} \quad (3.10)$$

based on field vane, UC and UU triaxial tests.

$$S_u/\sigma'_{vo} = 0.05 I_p + 0.20 \text{ (Ladd, 1975)} \quad (3.11)$$

based on the strain compatibility concept, i.e., the average strength.

$$S_u/\sigma'_{vo} = 0.45 LL \text{ (Larson, 1980)} \quad (3.12)$$

based on field vane shear tests.

In these equation, plasticity index and liquid limit are input as fractions rather than percentages. These equations imply that most normally consolidated clays have the undrained strength ratio (S_u/σ'_{vo}) ranging from 0.22 to 0.28.

The undrained strength ratio increases with overconsolidation ratio. Ladd and Foott (1974) presented experimental results for the variation of the ratio with varying overconsolidation ratio for five clays (Fig. 3.12) based on K_o -consolidated undrained direct simple shear (CKoU DSS) tests. Subsequently, Ladd et al., (1977) demonstrated that, for overconsolidated clays, the following relation holds approximately true:

$$(S_u/\sigma'_{vo})_{oc}/(S_u/\sigma'_{vo})_{nc} = (OCR)^{0.8} \quad (3.13)$$

where OCR stands for overconsolidated ratio.

3.5.4.2 Sources of Anisotropy

For a given clay, the undrained strength ratio of most clay depends on the stress paths in the load application, which must be fully addressed in the slope stability analysis especially for highly anisotropic clays. The term "anisotropy" is used to describe the dependence of strength and deformation characteristics of a material with respect to different stress paths and the direction of shearing. Historically, Casagrande and Carillo (1944) were the first to study the variation of shear strengths of soils with respect to different directions of the major principal stress. For natural clays having a one-dimensional strain history (e.g. K_o -consolidation), the resulting cross-anisotropic behavior has two components: inherent anisotropy and initial shear stress anisotropy.

An inherent anisotropy arises from the "soil structure" developed at the microlevel (preferred particle orientations and inter-particle forces) and also at

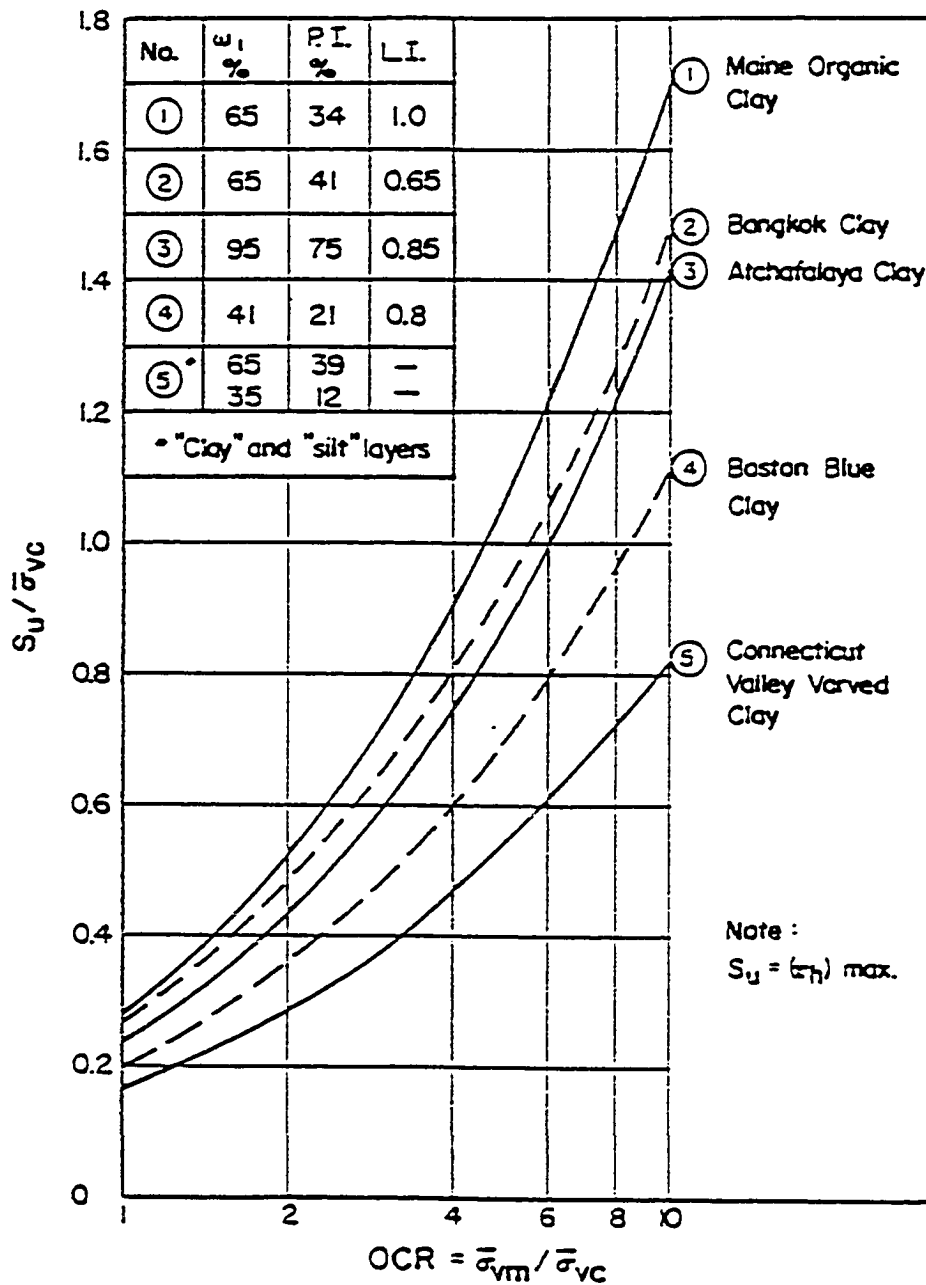


Fig. 3.12 Undrained strength ratios with varying OCR for several clays (Ladd and Foott, 1974)

the macrolevel for certain soils such as stiff fissured clays and varved glacial-lake deposits containing alternating layers of silt and clay. This type of anisotropy is commonly termed inherent anisotropy. In any case, inherent anisotropy will lead to directional changes in basic material properties governing elastic behavior and plastic behavior at yielding.

Clays also exhibit directionally dependent undrained strengths whenever shearing starts from a $K_0 \neq 1$ condition, as first predicted by Hansen and Gibson (1949) and called initial shear stress anisotropy by Jamiolkowski et al. (1985). The theoretical expressions for the variations in undrained strengths with stress paths for normally consolidated clays are functions of initial K_0 , the Hvorslev strength parameters, and Skempton's pore water pressure parameter A_r . For example, the undrained strength ratios of clay with initial $K_0 = 0.5$ can be predicted by the theoretical derivation as 0.331 and 0.193 for the compression and the extension tests, respectively. It should be emphasized that these strength ratios were computed using isotropic material properties, i.e. assuming no inherent anisotropy. The initial shear stress anisotropy helps explain the undrained behavior of soils and it should be considered when conducting test programs or interpreting test data. Since this effect can be theoretically computed from a knowledge of material properties, it is not a material anisotropy (Jamiolkowski et al., 1985). The combined effect of both components of anisotropy, inherent and initial shear stress anisotropies, is of prime interest in

practice, where soil elements are monotonically sheared in various stress paths as in slope stability problems.

When the loading condition is of cyclic nature, additional sources of anisotropy, which are induced anisotropy, should be taken into account. The induced anisotropy is related to how the initial anisotropy of a soil changes due to subsequent stressing or straining. For example, the initial cross-anisotropic properties of a K_0 -consolidated sample will become less pronounced if unloaded and then subjected to a large hydrostatic compression, i.e. the initial anisotropy will evolve towards isotropy in this case.

3.5.4.3 Observation of Undrained Strength Anisotropy

In 1960's, the most popular way for an experimental study on the undrained strength anisotropy of clays was to perform laboratory testing (UU or direct shear test) on the specimens which were trimmed with their axes at different angles to the depositional direction. Since the laboratory testing methods have limitations, the reliability of the test results were uncertain. Currently, there exist a few advanced testing methods with which experimental anisotropy studies can be made for a spectrum of stress paths, but they are seldom used in practice and very little data are available on them. In the following, laboratory testing data obtained from some of the most typical testing methods in practice will be presented to overview the anisotropic nature of the undrained shear strength of natural clays.

Fig. 3.13 plots peak undrained strength ratios obtained from three different stress paths: the CK_0U triaxial compression, the CK_0U extension, and Genor direct simple shear tests performed on various normally consolidated clays and silts (Ladd, 1991). The figure indicates that the undrained strength ratio significantly depends on the stress path, in which the triaxial compression and the extension tests give the highest and the lowest values, respectively, with direct simple shear test coming in between. Generally, the degree of strength anisotropy seems to decrease as the plasticity index increase, since K_0 values become close to unity for highly plastic clays. These data clearly demonstrate that most normally consolidated soils exhibit significant undrained strength anisotropy that generally becomes most important in lean and sensitive clays.

In the literature, there exist a few empirical expressions describing the directional dependence of undrained shear strength of natural clays which are mostly based on the experimental observation. Casagrande and Carrillo (1944) proposed the following equation for the directional variation of the undrained shear strength:

$$S_{u(i)} = S_{u(h)} + [S_{u(v)} - S_{u(h)}] \cos^2 i \quad (3.14)$$

in which $S_{u(h)}$ and $S_{u(v)}$ correspond to the undrained strengths of specimens with the major principal stress directions in the horizontal and vertical at failure, respectively. The i is defined as the angle between the major principal stress direction and the vertical. The coefficient of strength anisotropy can be defined

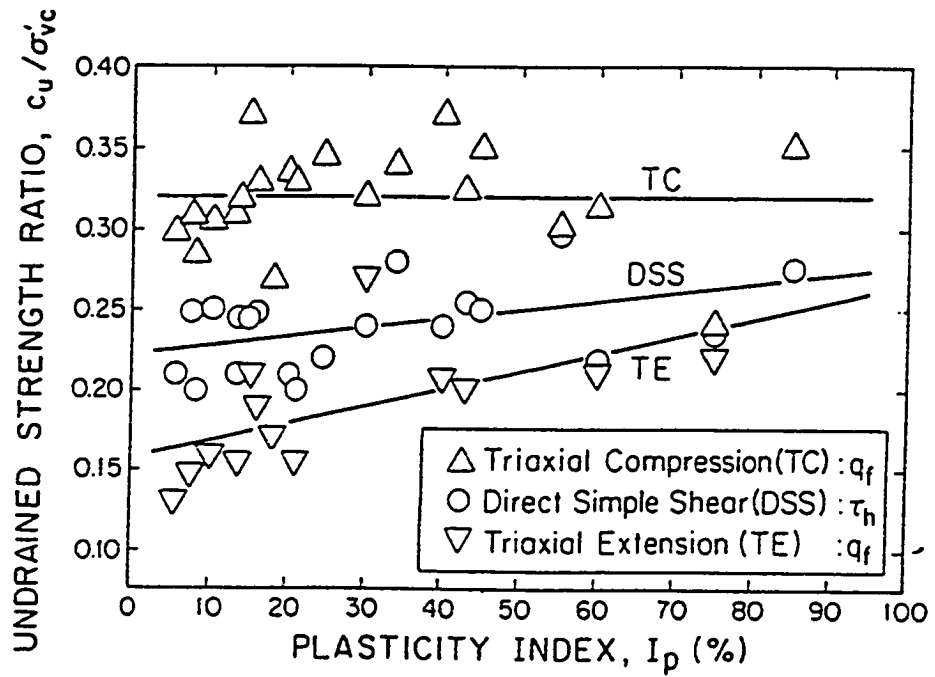


Fig. 3.13 Undrained strength anisotropy from K_0 -consolidated undrained (CK_0U) Tests on normally consolidated clays and silts (Ladd, 1986)

as $K=S_{u(h)}/S_{u(v)}$. In the case of natural soil deposits, the value of K can vary from 0.5 to 1.3. K is generally less than unity in normally or lightly overconsolidated clays.

Richardson et al. (1975) used field vane test devices to study the anisotropic undrained strength of a soft deposit of marine clay in Thailand and proposed the following equations:

$$S_{u(i)} = \frac{S_{u(h)}S_{u(v)}}{\sqrt{S_{u(h)}^2 \sin^2 i + S_{u(v)}^2 \cos^2 i}} \quad (3.15)$$

Fig. 3.14 shows the undrained strength variation patterns obtained by using the two empirical equations (Eqs. 3.14 and 3.15) along with experimentally determined data points. Three direct simple shear test data points, which were obtained by the pure shear assumption, are also shown in the figure. It is seen that the undrained strength generally decreases with the major principal stress rotation. In order to cover the experimentally observed data points, the equation suggested by Casagrande and Carrillo (1944) was slightly modified by changing the power of the cosine term in Equation 3.14 to obtain number three and number four curves.

Overconsolidated clays also exhibit pronounced anisotropic behavior, as illustrated by Fig. 3.15a. The data were obtained by SHANSEP CK_u tests on AGC clay which is moderately plastic marine clay ($I_p=43.0\%$, $I_L=0.6$). The figure shows a consistent strength decrease and very large increase in the shear strain at

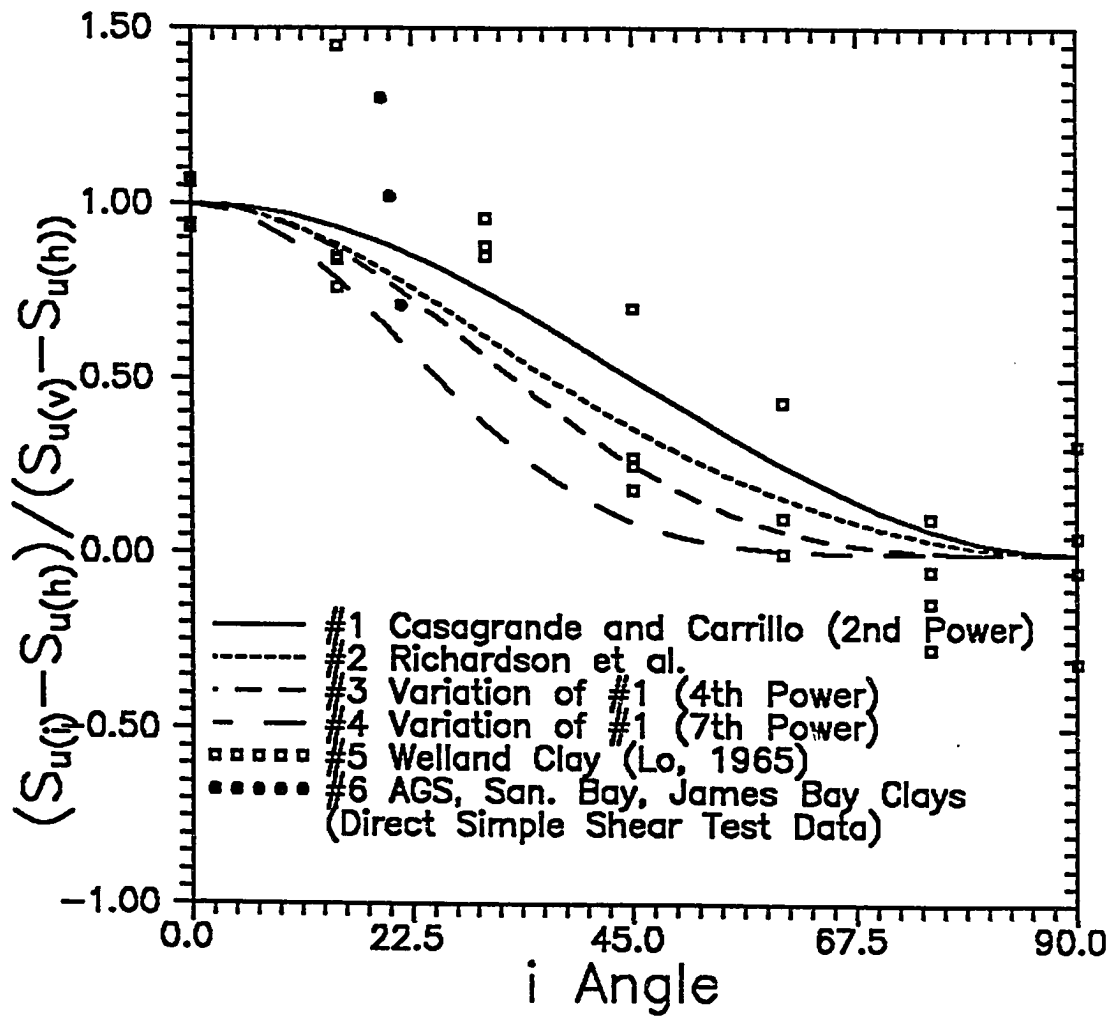


Fig. 3.14 Undrained strength variation with the major principal stress direction (i angle)

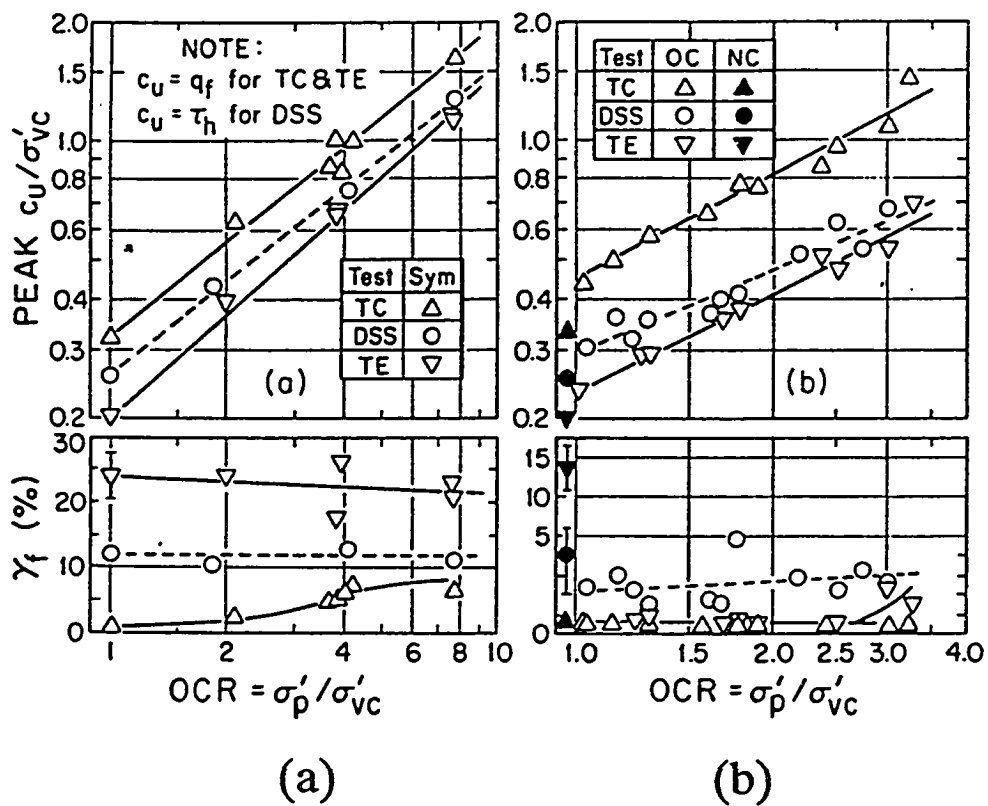


Fig. 3.15 OCR vs. undrained strength ratio and shear strain at failure from K_0 -consolidated undrained (CK_0U) tests: (a) AGS plastic marine clay; and (b) James Bay sensitive marine clay (Ladd, 1886)

failure (γ_f) in going from TC to DSS to TE, especially at low OCR. Fig. 3.15b plots data obtained from Recompression CK_u tests performed on block samples of a highly sensitive, cemented lean marine clay from James Bay ($I_p = 13.0\%$, $I_L = 1.9$), Quebec, Canada. The figure shows very high strengths in TC compared to DSS and TE and much smaller γ_f values compared to the AGS clay. For normally consolidated clay, wherein large consolidation strains presumably destroyed most of the cementation bonds, the solid symbols in Fig. 3.15b show somewhat less strength anisotropy, but much greater differences in γ_f .

The study on the stress-strain-strength anisotropy by Sambhandharaksa (1977) proposed the following equation for strength variation with OCR for a given stress path.

$$S_u / \sigma'_{vo} = S(\text{OCR})^m \quad (3.16)$$

where S_u = for a particular mode of failure; S = normally consolidated value of undrained strength ratio; OCR = overconsolidation ratio; and m = the strength increase exponent. The strength parameters for James Bay clay shown in Fig. 3.15b were $S = 0.225, 0.14$ and $m = 1.0, 1.0$ for the compression and the extension tests, respectively. When these parameters were used, the coefficient of strength anisotropy ($K = S_{u(h)} / S_{u(v)} = S_{u(e)} / S_{u(c)}$) turned out to be constant (0.62) with OCR as can be seen in Fig. 3.15b. Similar pattern is shown in Fig. 3.15a for AGS clay where strength anisotropy slightly decrease with increasing OCR. It seems that the compression strength is constantly greater than the extension strength for

lightly to moderately overconsolidated clays, while the opposite may be true for highly overconsolidated clays. The pattern of strength variation with i angle for overconsolidated clays are relatively uncertain with little laboratory testing data. However, as a crude approximation, it may be approximated with the empirical equations suggested for normally consolidated clays for a given coefficient of strength anisotropy.

3.5.5 General Stress-Strain Behavior of Soils

3.5.5.1 Data Collection of Stress-Strain Relations

3.5.5.1.1 Normally Consolidated Clay

Due to the progressive nature of slope failure, all the elements along the failure surface do not necessarily exercise the peak strength at the same time. Consequently, the relative patterns of stress-strain relations for varying stress paths in addition to the peak strength are also important factors which must be fully addressed in the slope stability analysis.

Soil elements in the cut slope, which were initially consolidated under the anisotropic state of stress ($K_o \neq 1.0$), are often assumed to be loaded in the plain strain condition. Therefore, laboratory soil testing should be performed in the plain strain condition on the specimen which has been consolidated back to the anisotropic state of stress. In the past, however, the most popular laboratory soil testings were the isotropically consolidated triaxial compression (CITC) and the extension (CITE) tests due mainly to the practical difficulties arising with the K_o .

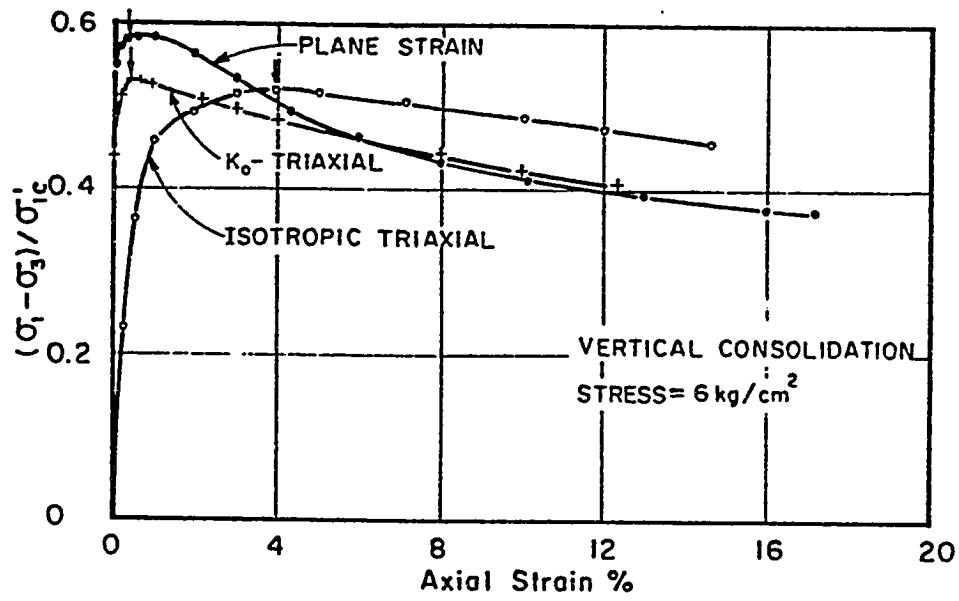
consolidation and the lack of plane strain devices. The abundance of the conventional testing data was followed by a number of attempts to establish the relationships between the testing results from the conventional and advanced testing methods. It has been repeatedly observed that the triaxial test underestimates the undrained strength determined by the plane strain test and Ladd et al. (1977) quantified the extent of underestimates for a limited number of clays as follows:

$$S_u \text{ (TC)}/S_u \text{ (PSC)} = 0.92 \pm 0.05 \text{ (several clays)} \quad (3.17)$$

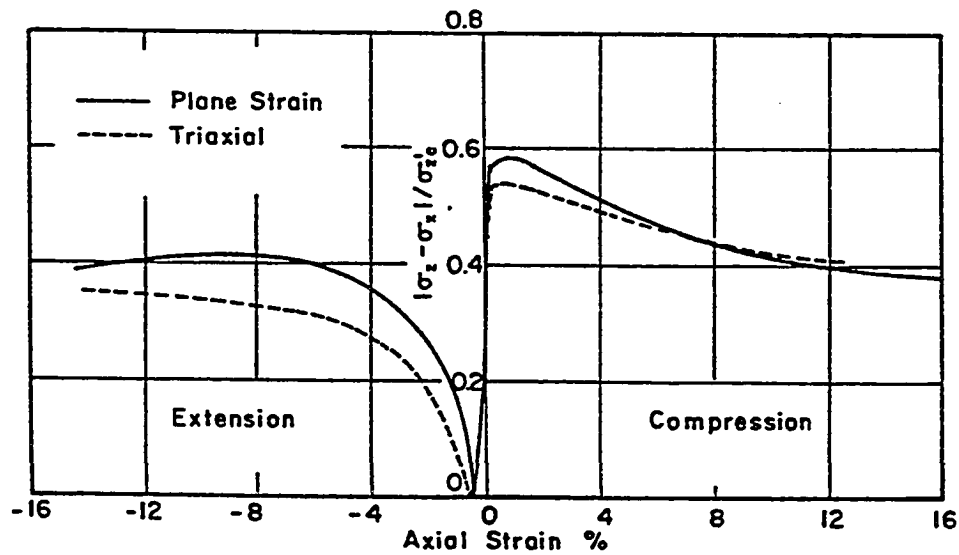
$$S_u \text{ (TE)}/S_u \text{ (PSE)} = 0.82 \pm 0.02 \text{ (only four clays)} \quad (3.18)$$

where TC, TE, PSC, and PSE represent the triaxial compression, the triaxial extension, the plane strain compression, and the plane strain extension tests, respectively.

It should be noted that stress-strain data collected herein are not only obtained from the advanced testing methods (PSC, PSE, and DSS), but also gathered from the conventional testing methods. Whenever the data from the conventional testing methods are presented, discussion will be made on the influence of the different testing condition on the resulting stress-strain-strength relations. A comparison of undrained stress-strain relations of a normally consolidated clay (Haney clay) was made by Vaid and Campanella (1974) among three types of laboratory tests: isotropically and anisotropically (K_o) consolidated triaxial tests and anisotropically (K_o) consolidated plane strain tests. The liquid limit of the clay was 44.0%, plasticity index 18.0%, sensitivity 6.0-10.0. Fig. 3.16a



(a)



(b)

Fig. 3.16 Comparison of stress-strain relations: (a) plane strain, K_0 triaxial, and isotropic triaxial compression tests; and (b) triaxial and plane strain tests (Vaid and Campanella, 1974)

shows the range of stress-strain relations of the clay due to differences in initial consolidation conditions and differences in stress changes during the subsequent shear. It is observed that the stress-strain behavior of the clay considerably depends on the initial consolidation condition. Especially, isotropically consolidated specimen shows a completely different stress-strain pattern from that of anisotropically consolidated specimens. The strain at the peak shear stress for K_0 -consolidated triaxial test is smaller than that for isotropically consolidated triaxial test by a factor of about 10, whereas it is almost the same as that for K_0 -plane strain test. The plane strain compression data shows somewhat higher degree of strain softening than the triaxial compression data, while both of them follow a similar pattern.

Fig. 3.16b shows the comparison between the triaxial and plane strain test data on anisotropically consolidated Haney clay. It is shown that the maximum shear stress for the plane strain compression (PSC) test occurs at the axial strain (1.0%) which is about twice greater than that for the triaxial compression (TC) test. The strain softening for both tests are remarkable until the stress reaches the residual level at about 20% of axial strain. On the other hand, stress-strain curves from the extension tests show continuously increasing stresses with the plastic strain (strain hardening) such that peak stresses occur at strains of about 10.0% and 14.0% for the plane strain extension (PSE) and the triaxial extension (TE) tests, respectively. It is shown for Haney clay that the strengths from the

triaxial test are 6% and 18% smaller than those from the plane strain tests for the compression and the extension tests, respectively.

The evidence of the consolidation condition effects on the stress-strain relations can also be found elsewhere (Ladd, 1964). Normalized stress-strain curves for five normally consolidated clays of plasticity index ranging from 25.0% to 42.0% are shown in Fig. 3.17. First five curves were all obtained from the anisotropically consolidated undrained triaxial compression tests, yet the initial stress anisotropy is very little so that the curves are very close to those obtained from the initial isotropic consolidation state. Most of these curves show similar patterns in which shear stresses continuously increase at axial strains of about 3.0% as in the previous case (Fig. 3.16a). On the other hand, the sixth curve shows stress-strain curves of Boston blue clay obtained from the K_0 -consolidated compression test. As in Haney clay case, the stress-strain curve from the K_0 -consolidated compression test shows considerable strain softening behavior after the peak stress at a very small strain. Ladd (1965) also confirmed the same brittle and pronounced strain softening behavior of anisotropically consolidated clays as shown in Fig. 3.18. The data presented herein show a consistent pattern in which the triaxial compression tests produce the peak stress at a very small strain and pronounced strain softening thereafter whenever the specimen is consolidated anisotropically (K_0) prior to shearing.

It seems that for the same anisotropic consolidation condition the pattern of stress-strain curves of plane strain and triaxial tests are similar each other,

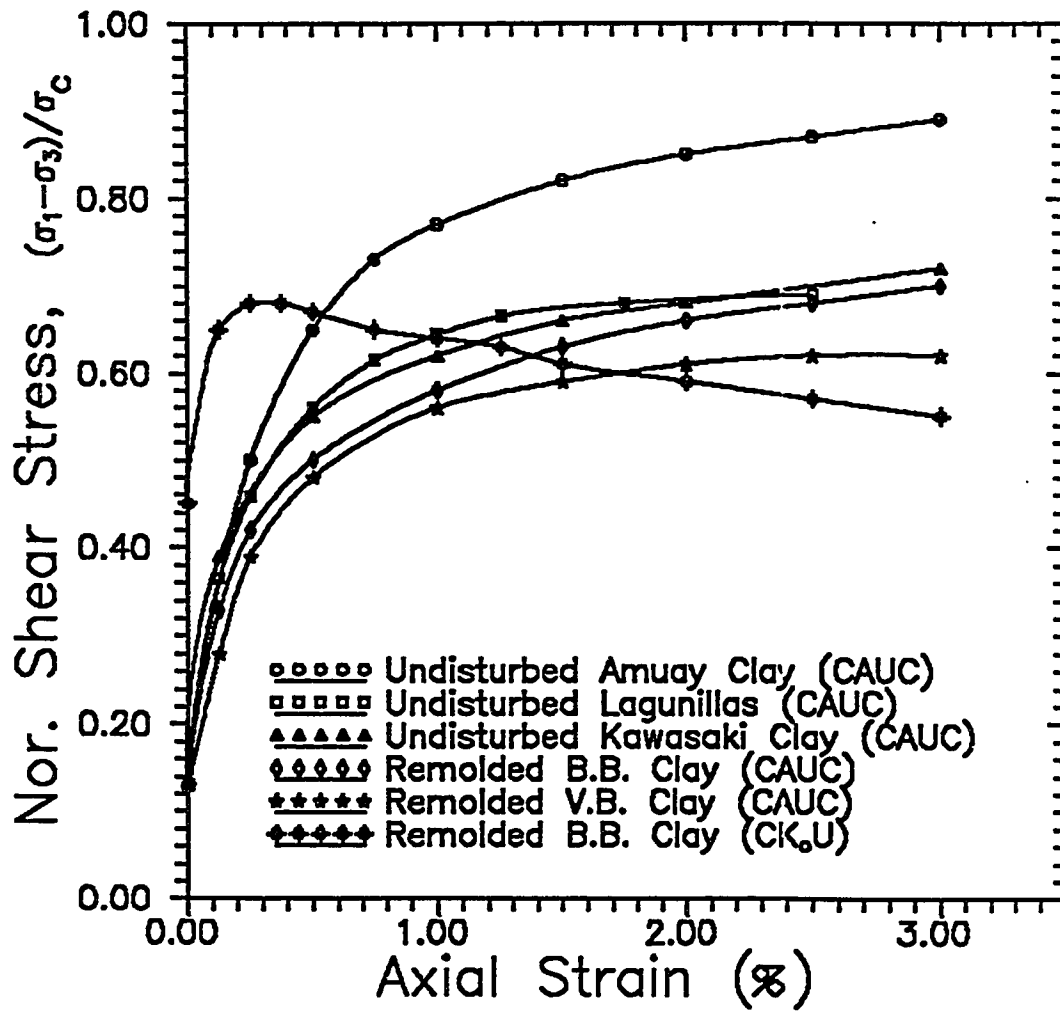


Fig. 3.17 Effect of anisotropic consolidation stress on the stress-strain relations (Ladd, 1964)

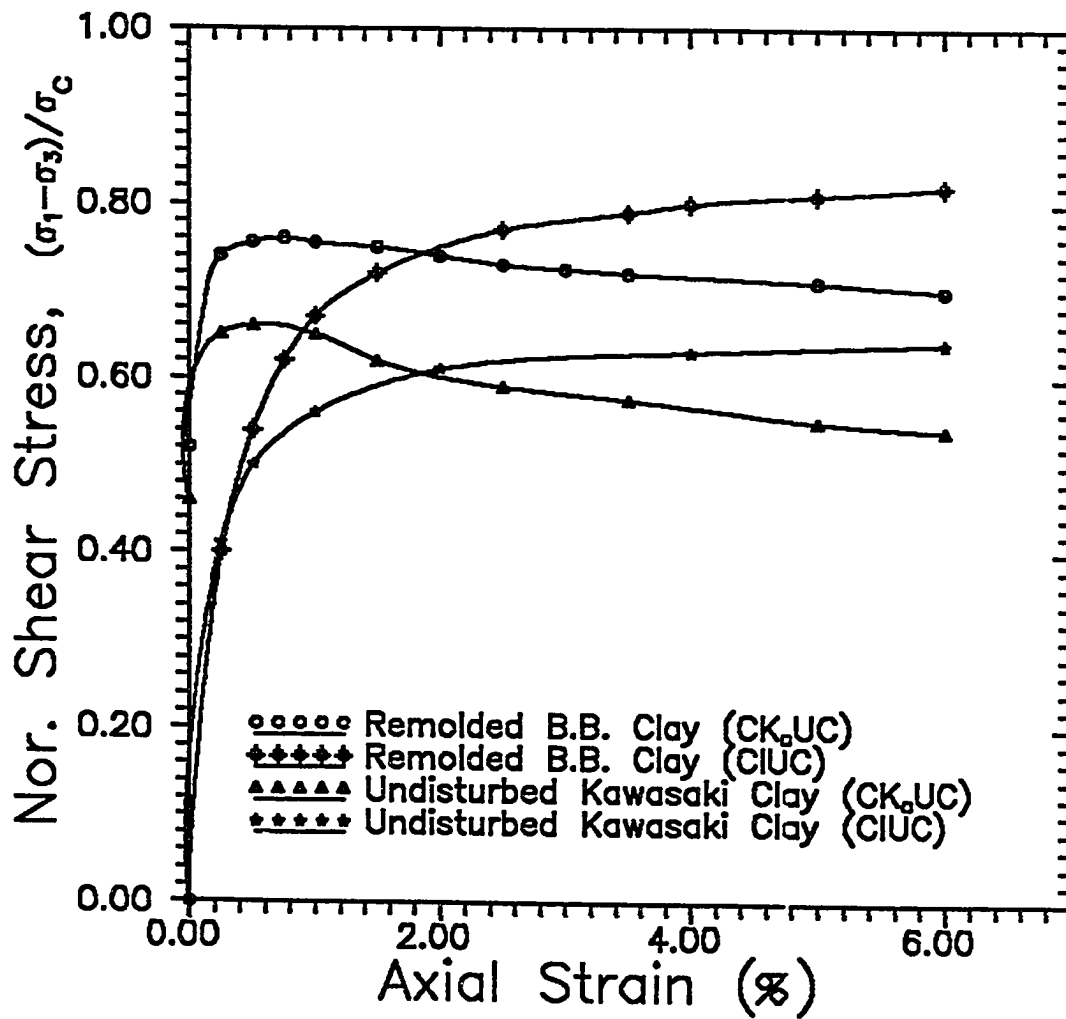


Fig. 3.18 Effect of anisotropic consolidation stress on the stress-strain relations (Ladd, 1977)

whereas the strength predictions from the TC and TE tests are always smaller than those from the plane strain tests (Ladd et al., 1977). For a given type of test, whether it is a plane strain or triaxial test, the stress-strain patterns of the compression and the extension tests are drastically different for a given soil. The compression mode always gives brittle behavior, where the shear stress reaches its peak at very small shear strain with strain softening in the post peak region. The extension mode is, on the other hand, always accompanied by resilient behavior where the peak shear stress occurs at a great shear strain level in the order of about 15.0 to 20.0%. The distinct stress-strain behavior of the compression and extension tests is analogous to the relation between the lateral earth pressure and wall movement in which the active and passive modes correspond to the compression and the extension tests, respectively as seen in Fig. 3.19.

It should be noted that the laboratory compression and extension tests, which are most frequently performed in practice, can only approximately simulate the loading conditions for elements located in the crest and toe. Particularly, soil elements around the bottom of the failure plane are subjected to the loading condition which is somewhat intermediate between the two extremes. It is generally agreed that the direct simple shear (DSS) test best simulates the stress and failure conditions for those bottom elements. Therefore, relative patterns of stress-strain relations for the typical laboratory tests, the plane strain compression, the plane strain extension, and the direct simple shear tests, are of practical importance.

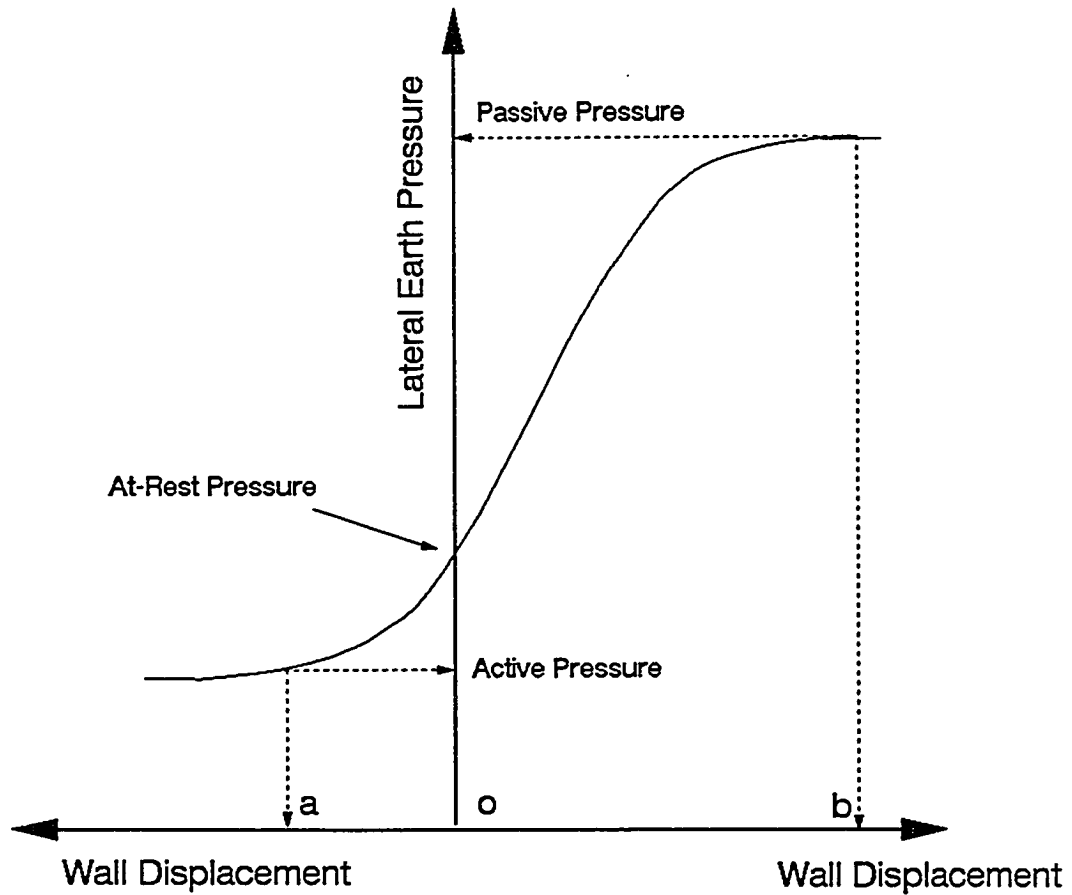


Fig. 3.19 Analogy of stress-strain behavior of compression and extension tests to the earth pressure-displacement pattern of active and passive modes

It should be noted that the stress condition in the specimen during the direct simple shear test is nonuniform and largely unknown. Therefore, it is a usual practice that the applied shear stress (τ_d) on the horizontal plane of the specimen is related to the shear strain (γ_d) to obtain a practical estimate of the undrained stress-strain relations in the direct simple shear test. Alternatively, it may be assumed that the stress condition in the DSS is closely approximated by the pure shear case (Duncan and Dunlop, 1969). Then, the assumption enables theoretical evaluation of the stress-strain curve which starts from the initial state of stress point as in the compression and extension cases. In the following figures (Figs. 3.20 through 3.22), the stress-strain data of DSS obtained by the two methods are presented.

A comparison of the stress-strain relations among the three typical laboratory testings was made on AGS clay (Koutsoftas and Ladd, 1985) in Fig. 3.20. It is shown that the shear strains at the peak stresses occur in an increasing order from the plane strain compression, the direct simple shear, to the plane strain extension tests. The pronounced strain softening behavior for PSC is contrasted to those of PSE and DSS. The curve of DSS₍₂₎ (i.e., the pure shear assumption) seems to be intermediate between the two extremes of PSC and PSE in its pattern. Similar pattern of stress-strain relations for the stress paths are also shown in Fig. 3.21, which was obtained from San Francisco bay mud (Duncan and Dunlop, 1969).

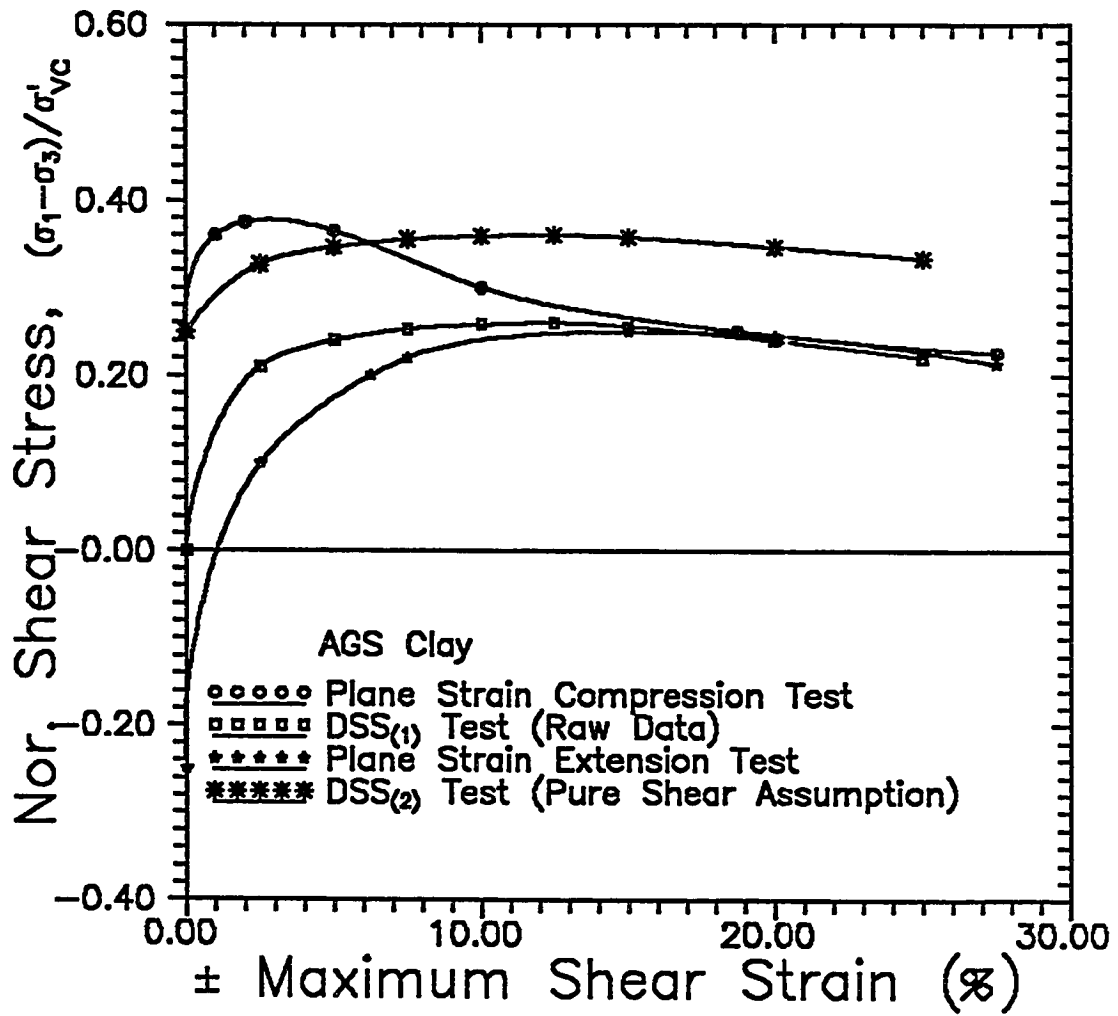


Fig. 3.20 Stress-strain relations of AGS clay (Ladd, 1986)

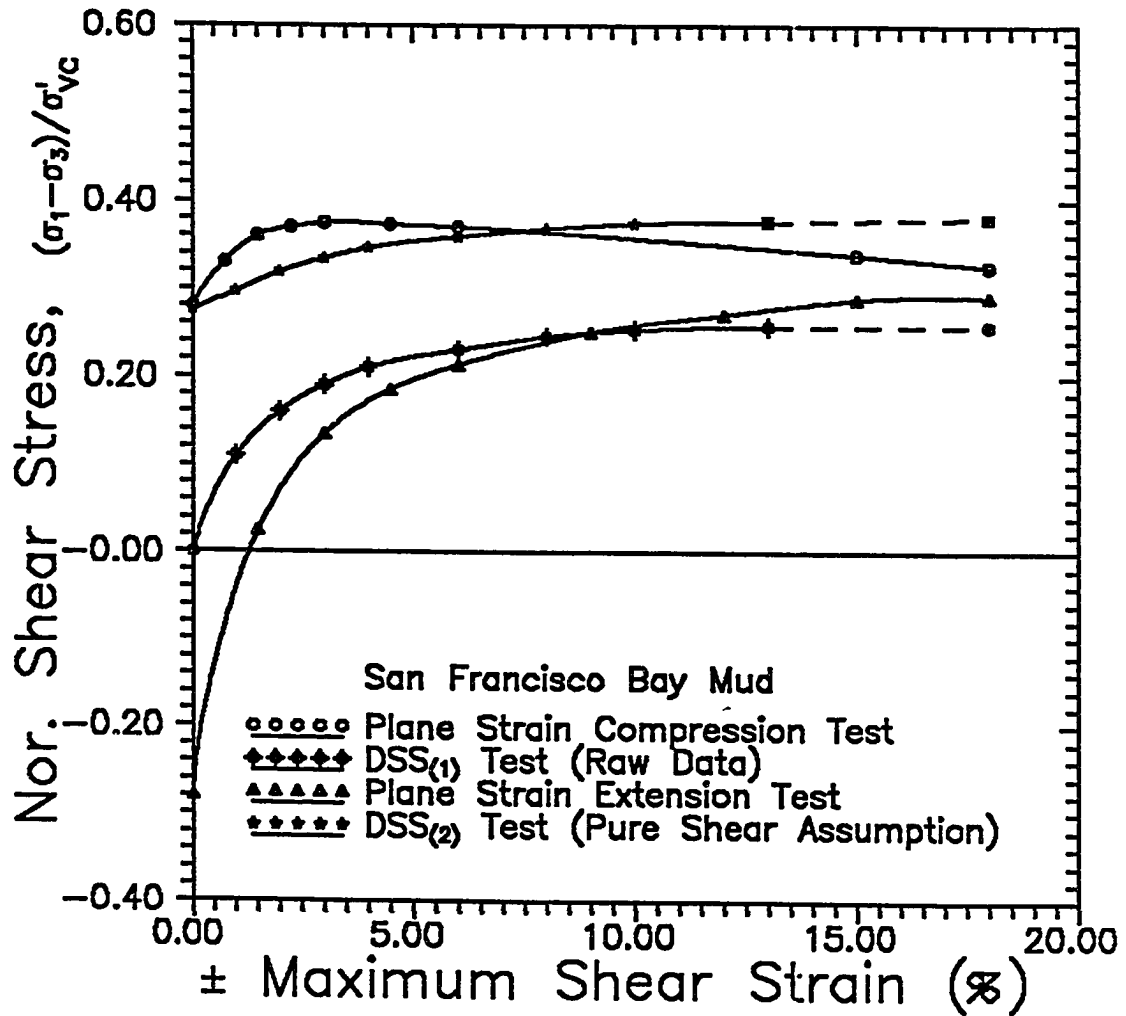


Fig. 3.21 Stress-strain relations of San Francisco Bay mud (Duncan and Dunlop, 1969)

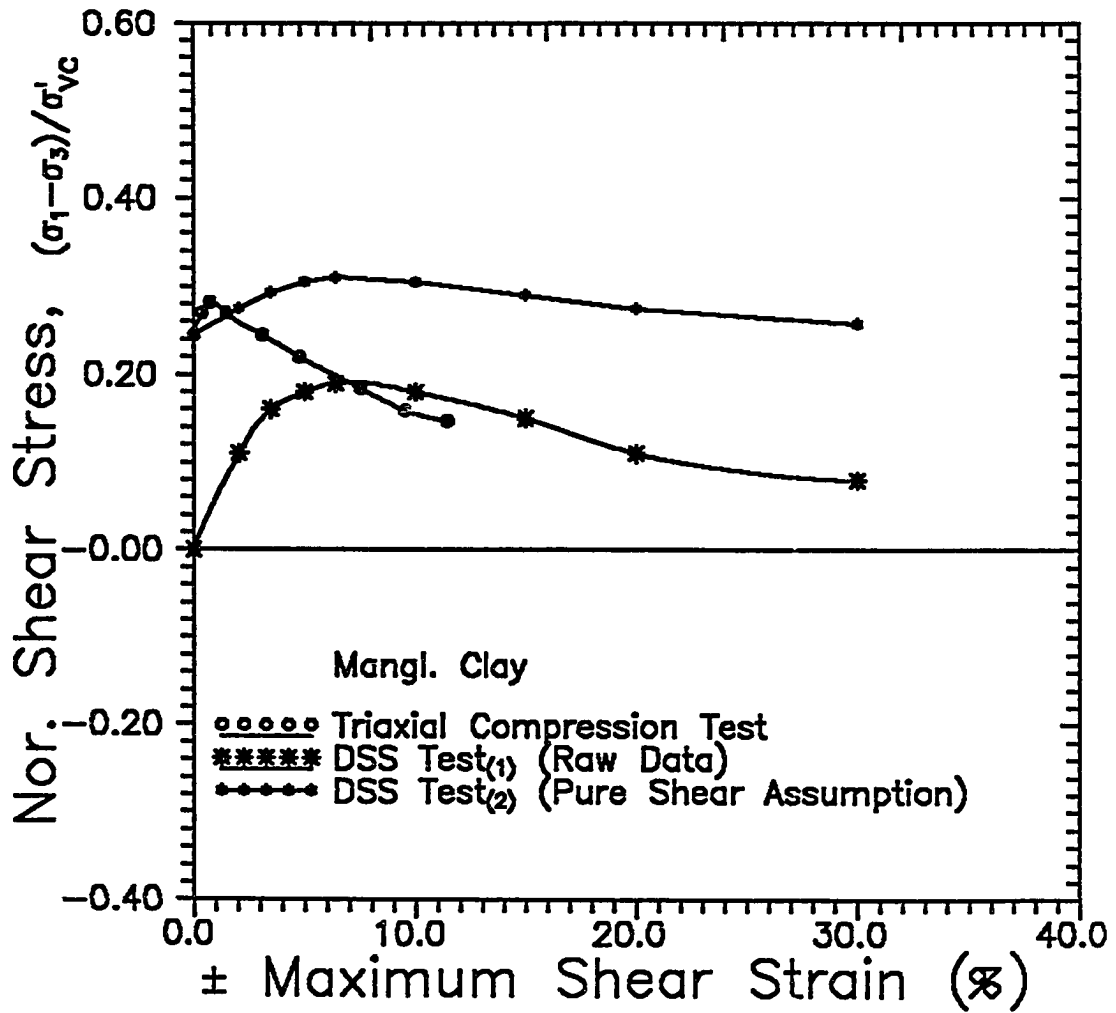


Fig. 3.22 Stress-strain relations of Mangle clay (Bjerrum and Landva, 1966)

Another example of the relative patterns of the stress-strain relations of direct simple shear (NGI type) tests in comparison to the triaxial compression tests is shown in Fig. 3.22, which was obtained from Norwegian quick clay (Bjerrum and Landva, 1966). It is found that the peak shear stress for the compression test takes place at a small shear strain of about 0.8% and rapidly drops, while that of DSS test smoothly increases up to the peak at a large strain, which is followed by a strain softening to some extent. Considering the type of clay, it seems that the quick characteristics might also depend on the stress path. It should be noted that the peak strength of the DSS test obtained by using the pure shear assumption is even greater than the compression strengths, which is rather unusual.

In this section, stress-strain relations of normally consolidated clays have been comparatively reviewed for the initial consolidation conditions as well as subsequent shear conditions. It was desired to define the stress-strain patterns for the most relevant testing methods in the slope stability analysis: the plane strain compression, the plane strain extension, and the plane strain direct simple shear tests. It can be summarized that the specimen loaded in the compression test always shows brittle behavior in which the peak stress occurs at a small strain level. In the post peak region, the shear stress decreases remarkable until it reaches the residual strength level at a large shear strain level of about 20%. In contrast, the specimen loaded in the extension test is characterized by the pronounced strain hardening in which the peak stress occurs at a large strain. It

seems that the shear stress level at practically large shear strain (15 to 20%) remains approximately the same (i.e. perfectly plastic) in this case. The specimen subjected to the loading conditions of the DSS test produces the stress-strain curve which is somewhat intermediate between the two extremes of PSC and PSE tests. The slight strain softening in the post peak region also seems to be intermediate between the pronounced softening of the compression and the perfect plastic of the extension modes. Table 3.1 summarizes the stress-strain-strength relationship of various normally consolidated clays reviewed in this section.

3.5.5.1.2 Overconsolidated Clays

In the literature, it is hard to find the stress-strain data of intact overconsolidated clays with undisturbed particle structures created by the complex geological history. It is well known that the stress-strain-strength behavior of natural clay is considerably affected by the natural structures. Once clay specimen is consolidated beyond the in-situ stress in the laboratory, the stress-strain relations determined from the disturbed clay is no longer representative of natural clay due to destructuration of the in-situ clay structure. Therefore, overconsolidated clay specimen prepared in the laboratory testing program such as SHANSEP program (Ladd and Foott, 1974) cannot be considered to be equivalent to the naturally created overconsolidated clay. When the clay specimen is mechanically compressed beyond the in-situ stress, the slope of the

Table 3.1 Summary of the stress-strain-strength relations of various clays.

No. (1)	Soil (2)	σ'_{vo} , kPa (3)	K_o (4)	Undrained Strength Ratios and Strains at the Peak Stresses						Source (11)
				PSC (5)	γ_{max} , % (6)	DSS (7)	γ_{max} , % (8)	PSE (9)	γ_{max} , % (10)	
1	AGS clay	-	0.50*	0.38	2.0	(0.25) 0.34	12.5	0.25	17.5	Ladd (1986)
2	Haney clay	589.0	0.56.	0.29	1.50	0.28	-	0.21	13.5	Vaid and Camp. (1974)
3	San Franc. Bay clay	245.0	0.45	0.37	4.50	(0.25) 0.37	≈ 13.0	0.28	≈ 19.5	Duncan & Dunlop (1969)
4	Craney Island clay	150.0	0.52	0.33**	1.50	0.29	-	0.22**	≈ 22.5	Ishibashi & Choi (1994)
5	Boston Blue clay	392.0	0.54	0.35**	0.45	0.29	-	-	21.0	Ladd (1964)
6	Haney clay	589.0	0.56	0.29**	0.75	0.26	-	0.21**	21.0	Vaid and Camp. (1974)
7	James Bay clay	-	0.44*	0.36**	1.00	(0.26) 0.36	4.0	0.24**	14.0	Ladd (1986)
8	Mangl. clay	-	0.51	0.34**	0.55	(0.19) 0.31	6.6	-	-	Bjerrum & Land. (1966)
9	Kawas. clay	295.0	0.51	0.49**	1.20	0.37	-	-	-	Ladd (1964)

1. Values in column #7 were obtained by the pure shear assumption (values in parentheses are of τ/σ'_{vo}).
2. K_o values with * were obtained by using empirical relations between P_r and ϕ' (Mesri & Ghaffar, 1993), and $K_o = 0.95 - \sin\phi'$ (Brooker and Ireland, 1965).
3. Values with ** reflect that the triaxial tests results were modified for PSC and PSE conditions by using Eqs. 3.18 and 3.19.

stress-strain curve reduces with flattening of the curve at the peak stress (Tavenas and Leroueil, 1985). The clear effect of destructuration on the stress-strain behavior of overconsolidated clay can be illustrated by laboratory testing data presented by Jamiolkowski et al. (1985) in Fig. 3.23. The stress-strain curves from three CK_oUC tests on overconsolidated James Bay B-6 Marine clay ($OCR=2.5$), which is a very brittle and highly structured quick clay, are shown. In order to measure the effect of destructuration, the ratio of laboratory consolidation stress to the preconsolidation stress was varied from 0.34 to 1.33. It can be seen that at the in-situ OCR, the intact clay is extremely brittle with pronounced strain softening behavior in the post peak region. Such behavior is very different from that of a mechanically overconsolidated clay.

Overconsolidated clay can be prepared by resedimenting clay particles in a slurry oedometer. For example, Ladd et al. (1985) investigated anisotropy effect of natural clay using directional shear cell (DSC) on overconsolidated clay samples ($OCR=4.0$). Clay specimens in the study were prepared by resedimenting Boston Blue clay which were all K_o -consolidated in a slurry

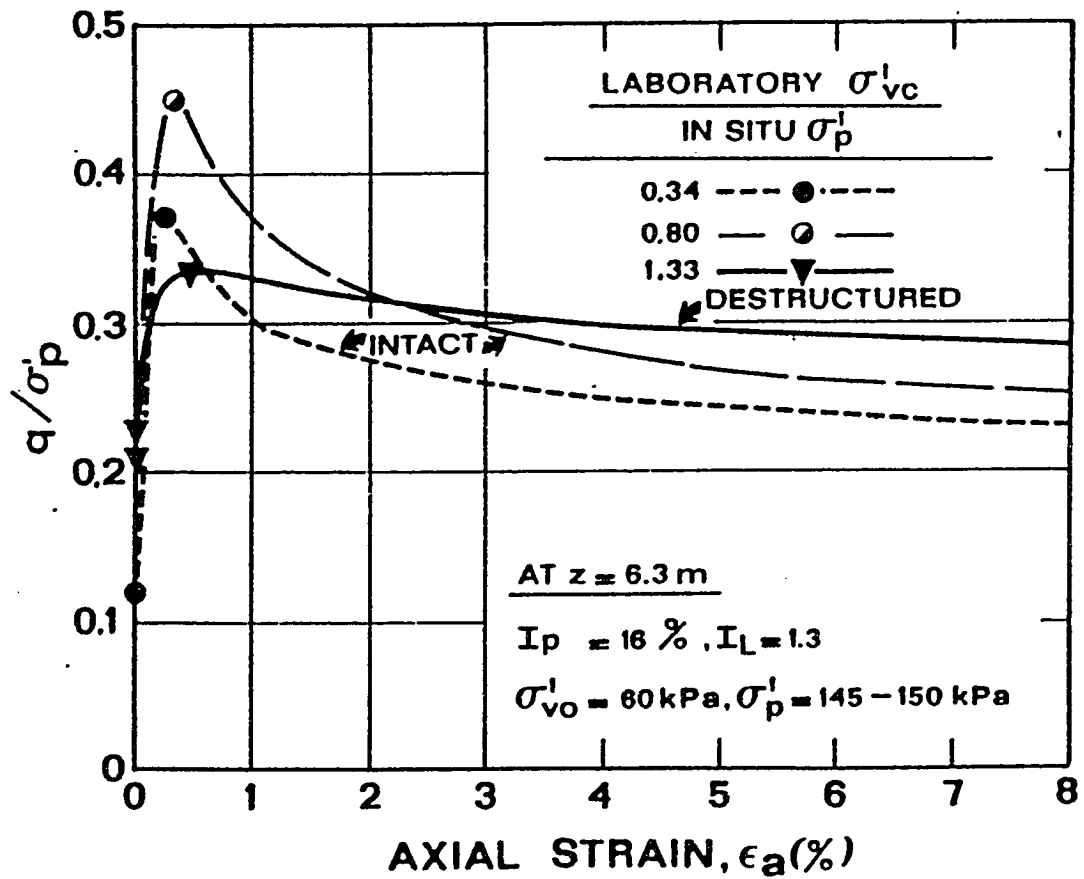


Fig. 3.23 Stress-strain relations of intact overconsolidated clay with varying ratios of laboratory σ'_{vc} to in situ σ'_p (Lefebvre et al., 1983)

oedometer to varying consolidation pressures. Fig. 3.24 shows the stress-strain curves obtained from undrained DSC tests with varying i angles in which decreasing strength with increasing i angle is striking. It appears that the peak stress occurs at strains gradually increasing from the compression ($i=0^\circ$) to the extension ($i=90^\circ$) tests. Although resedimented clay cannot be considered as representative of natural clays, it can give at least the general pattern of stress-strain relations with varying i angle. It should be noted that the data were all obtained from tests having an initial isotropic state of stress. Hence, the observed anisotropy must have resulted entirely from a preferred soil structure developed during the one-dimensional deposition.

It is generally found that the strength of overconsolidated clay decreases with increasing i angle (Figs. 3.15a, 3.15b, 3.24) as in normally consolidated clay. When considering the stress-strain relations of lightly overconsolidated clay, it should be noted that K_0 values are usually closer to the unity than normally consolidated clay case such that the initial point of the shear stress-strain curve is closer to the origin. Then, the difference in the strains at the peak stress between the two opposite stress paths (compression and extension tests) should not be as great as in the normally consolidated clay. The little different strains at the peak stresses in the triaxial compression and extension tests observed on overconsolidated James Bay clay (Fig. 3.15b) may be partly explained by the location of the initial state of stress. For overconsolidated James Bay clay, the stress-strain curve of the intact clay was extremely brittle for the compression test

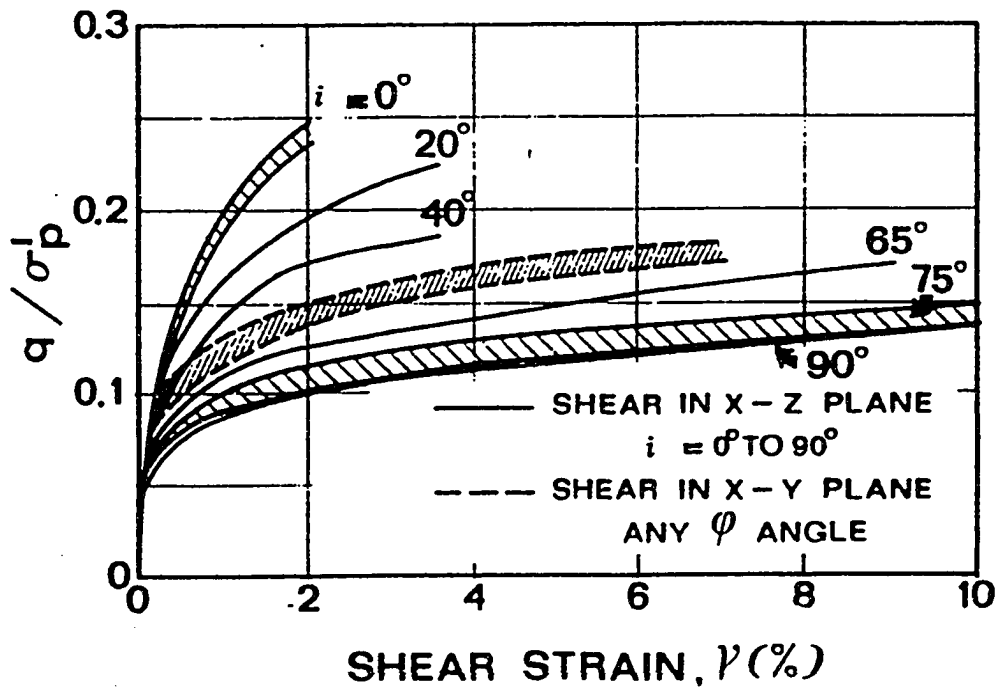
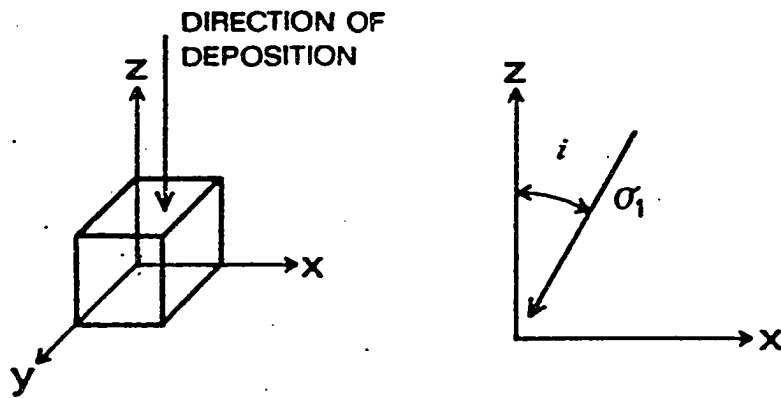


Fig. 3.24 Variation of stress-strain relations with varying i values of overconsolidated clay prepared with directional shear cell (Ladd et al., 1985)

as compared to those of normally consolidated clays reviewed in the previous section. Although it could be only the case of the sensitive clay, the generality of the brittle nature of overconsolidated clay cannot be completely eliminated. Therefore, it is necessary that evaluation of the effect of such brittle stress-strain curve on the slope stability should be included in the analysis.

3.5.5.2 Generalization of Stress-Strain Curves

3.5.5.2.1 Correlation of Stress-Strain Curves

In this section, the stress-strain curves of the three different stress paths are compared and their relative patterns are quantified using a couple of parameters. The stress-strain curve of the compression mode is used as a reference frame to relatively describe the behavior of clay in other stress paths such as the extension and direct simple shear modes. In order to quantify the relative pattern of the stress-strain curves of the extension mode in comparison to that of the compression mode, following two factors are introduced: (a) the ratio of strains at the peak stresses (γ_p/γ_c) and (b) the ratio of the undrained strengths (τ_p/τ_c). The former gives the idea of relative shear strain levels of the peak shear stresses and the latter provides the relative strengths in the two stress paths. Once the initial modulus is determined and the manner is prescribed in which how the peak strength is arrived, the two independent parameters can concisely describe the pattern of stress-strain curves in the two different stress paths up to the peak shear stresses.

Table 3.2 (Col. 6 and 7) summarizes the parameters obtained from the stress-strain curves of the compression and extension modes on the clays reviewed in this study. It should be noted that the average strength of the compression modes is higher than that of the extension mode by about 33%. It is shown that the average strain ratio (7.36) at the peak stress obtained from the comparison between the plane strain compression and the plane strain extension tests are much smaller than that (29.9) obtained from the triaxial compression and triaxial extension tests. The great discrepancy of the strain ratio (γ_c/γ_e) between the two types of tests can be expected from the fact that the plane strain extension test produces the peak stress at strain far smaller than that of the triaxial extension test while the strain at peak stress in compression tests are similar whether it is the plane strain or the triaxial test (Fig. 3.16b).

Similarly, the stress-strain relations determined from the direct simple shear test can be contrasted to that of the plane strain compression. However, there exist fundamental uncertainties regarding the stress-strain-strength determined from the direct simple shear test due to the basic configuration of the test device causing nonuniform stress-strain conditions within the specimen (Roscoe, 1953, Duncan and Dunlop, 1969). Therefore, the stress-strain curves of direct simple shear tests are usually reported in plots where the applied shear (Roscoe, 1953, Duncan and Dunlop, 1969). Therefore, the stress-strain curves of direct simple shear tests are usually reported in plots where the applied shear stresses (τ_h) on the plane are related to the shear strains. It is clear that when

Table 3.2 Summary of the parameters of the stress-strain-strength relations

No. (1)	Soil (2)	Index Properties		σ'_{vo} , kPa (5)	Com. vs. Ext.		Com. vs DSS		Testing Methods
		I_p % (3)	I_p (4)		$\frac{\gamma_e}{\gamma_c}$ (6)	$\frac{S_{u(e)}}{S_{u(c)}} (7)$	$\frac{\gamma_d}{\gamma_c}$ (8)	$\frac{S_{u(d)}}{S_{u(c)}} (9)$	
1	AGS clay	43.0	0.6	---	8.8	0.66	6.25	0.90	PSC, PSE, DSS
2	Haney clay	18.0	LL=44.0	589.0	9.0	0.72	---	---	PSC, PSE
3	San Franc. Bay clay	---	---	245.0	-4.3	0.76	2.89	1.00	PSC, PSE, DSS
4	Craney Island clay	41.4	0.98	150.0	-15.0	0.67	---	---	TC, TE
5	Boston Blue clay	15.0	0.38	392.0	46.7	0.49	---	---	TC, TE
6	Haney clay	18.0	LL=44.0	589.0	28.0	0.72	---	---	TC, TE
7	James Bay clay	---	---	---	---	0.72	4.10	1.10	TC, DSS
8	Mangl. clay	8.0	2.2	85.0	---	---	8.10	0.91	TC, DSS
9	Average of PSC vs. PSE or DSS				7.36	0.71	4.6	0.95	---
10	Average of TC vs. TE or DSS				29.9	0.63	6.1	1.00	---
11	Average of Entire Data				18.6	0.67	5.3	0.98	---

the initial stress condition of the specimen is anisotropic, the applied shear stress, τ_h , is not the maximum shear stress, nor is it the shear stress on the failure plane. Either the shear stress on the failure plane or the maximum shear stress might be used as a measure of shear strength, and both of these values are larger than the shear stress on the horizontal plane, τ_h . Consequently, Duncan and Dunlop (1969) suggested to use the assumption that the stress condition in the direct simple shear test can be closely approximated by pure shear case. The assumption enables a theoretical equation possible and its use increases the shear stress value to some extent. In certain case, however, the equation results in even higher strengths than that obtained from the plane strain compression tests, which is not realistic considering the experimental observation.

In addition to the strength uncertainty, the stress-strain relation is also uncertain to some extent. Assuming that the stress-strain curve of the applied shear stress (τ_h) and the shear strain at the peak stress (γ_d) gives the correct strain at the peak stress, ratios of strains (γ_d/γ_c) at the peak stresses were obtained for four clays as shown in Table 3.2 (Col. 8 and 9, respectively). It is shown that on the shear strains at the peak stress for DSS are 5.3 times greater than that of PSC on the average. The ratio of the undrained strengths is found to be very close to the unity, which is believed to be overestimated by the pure shear assumption to some extent.

3.5.5.2.2 Consolidation Pressure Effects on the Stress-Strain Relations

In the previous sections, the stress-strain-strength relations of soils have been reviewed. If the relations can be uniquely expressed in terms of the consolidation stress, that will be of great importance in practice. Generally speaking, the strain at the maximum shear stress varies with the effective consolidation stress on the specimen. Peck (1967) cited two experimental observations of Patton (1966) and Conlon (1967), both of whose papers are not currently available. According to Peck, Patton experimentally proved that for a given soil the strain at the peak stress is dependent on the effective normal stress. At a low normal stress, the strain is small. At higher pressures, it increases; whereas at even higher pressures, the strain to the peak stress again decreases. Peck continued to cite that the observation were confirmed by subsequent experiments by Conlon, who carried out direct shear tests on undisturbed Lake Agassiz clay. The stress-strain curves at various normal consolidation pressures are shown in Fig. 3.25. It is noted that all the curves exhibit peaks, but that the strain at the peak stress occurs depending on the normal stress, increasing with the normal stress increment and decreasing back for even high normal stress (72 psi). In the slope stability analyses of cuts in normally consolidated clay, the heights of the slopes, which are most frequently encountered in practice, may range from 10 to 30 feet. In such cases, the effective consolidation stresses for the elements around the potential failure surface range from 6.0 to 25.0 psi. Therefore, the strain at the peak stress in the range may be considered to

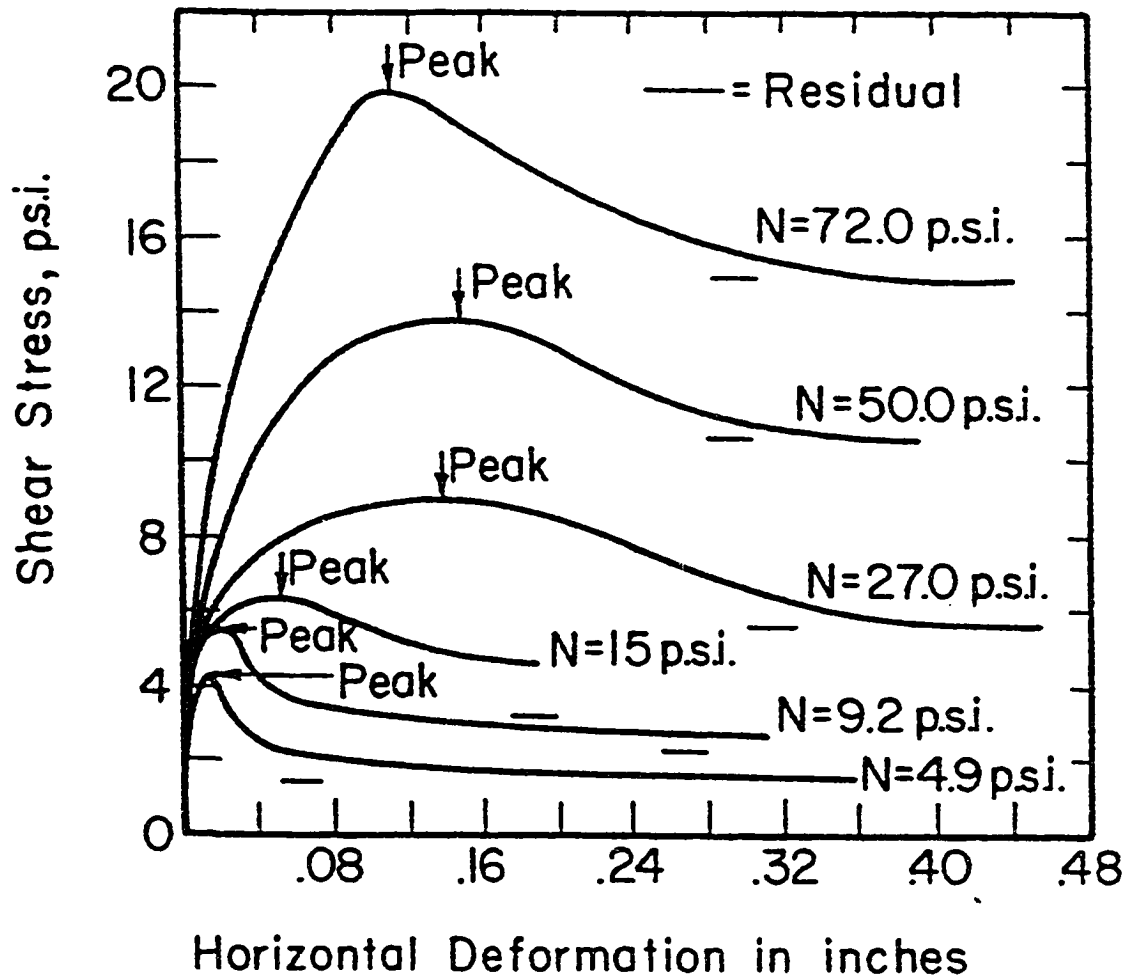


Fig. 3.25 Variation of strain at peak stress depending on the consolidation stress (Peck, 1967)

continuously increase with the consolidation stress increase so that reduction in the strain in higher stress can be practically ignored.

For a given peak stress and the corresponding strain level, it is also important to know the manner in which the stress reaches the peak. In the stress-strain curve shown in Fig. 3.11, the stress range from the initial point (a) to the peak point (c) can be broken into two pieces for a practical purpose: initial elastic region and strain hardening region. Then, the material's elastic modulus should be the most influencing parameter to determine the stress-strain relations up to the peak stress. For normally consolidated clays, it is often assumed that the modulus is proportional to the consolidation stress, i.e., the stress at any strain is proportional to the consolidation stress. Fig. 3.26 presents the results of the undrained triaxial tests in the form of stress paths through which axial strain contours have been drawn (Lambe, 1964). If the effective stress paths are geometrically similar and the strain contours are straight radial lines for a group of tests, then a plot of q/σ'_w versus strain would be unique and the stress-strain relations can be nicely normalized by the consolidation stress. If the plot is unique, the modulus is then proportional to the consolidation stress. The plots indicate that there is variation from this unique relationship. In general, the modulus is less than proportional, i.e., the strain contours curve downward, especially the contours for the smaller strains. The general trend of the modulus can also be seen from the empirical equation suggested by Hardin and Black

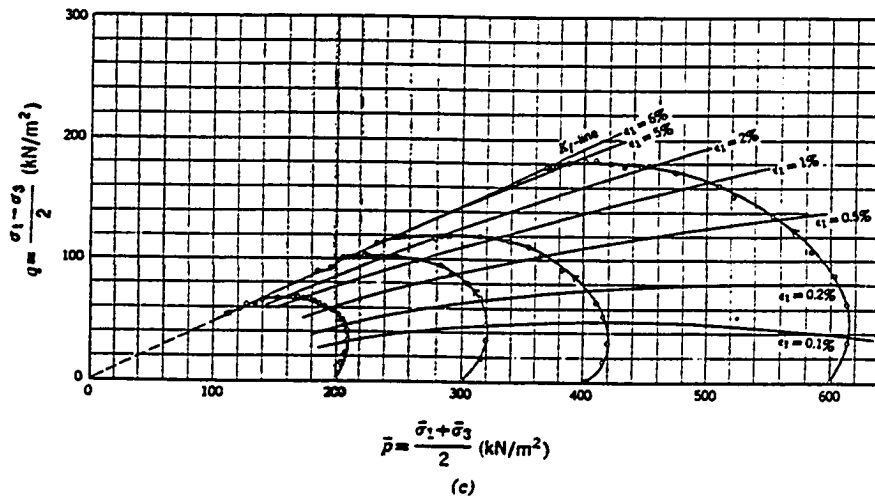
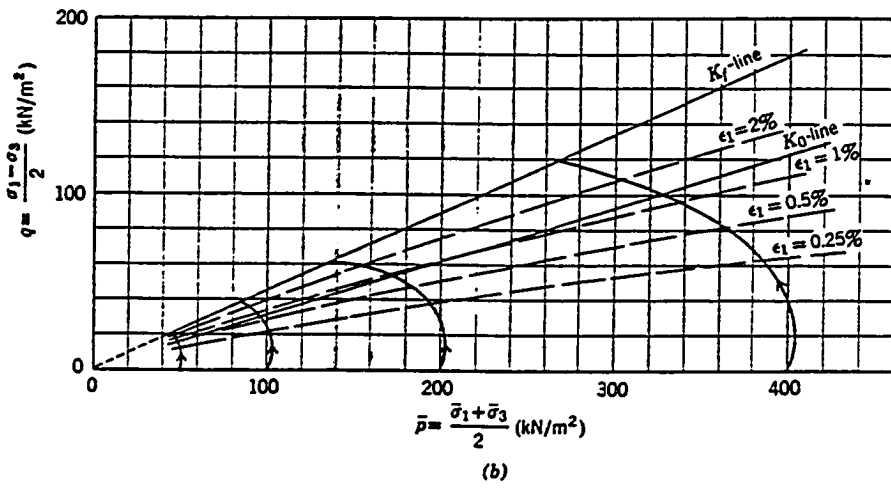
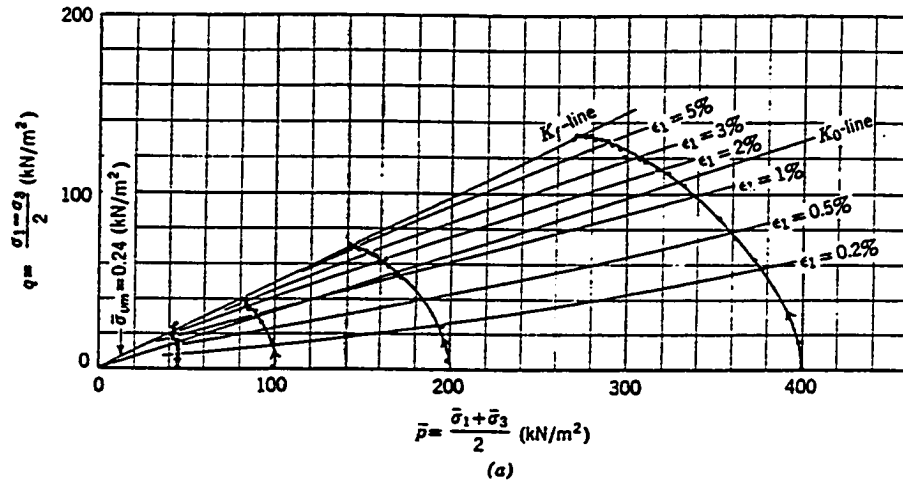


Fig. 3.26 Contours of equal strain for three normally consolidated clays: (a) Amuay clay; (b) Remolded Boston blue clay; and (c) Lagunillas clay (Lambe, 1964)

(1968) relating the void ratio and effective consolidation stress to the dynamic shear modulus as follows:

$$G = 1230 \frac{(2.973 - e)^2}{1 + e} \sqrt{\sigma'_c} \quad (3.19)$$

where σ'_c is the average principal stress to which the soil has been consolidated.

The shear moduli and the stress are in the unit of pound per square inch (psi) in Equation 3.19. The equation predicts that the dynamic shear modulus, which is analogous to the initial moduli, is less than linearly proportional to the consolidation stress so that the rate of moduli increase decreases with the consolidation stress.

4. LOADING MODE AND STRESS-STRAIN MODELLING

4.1 Analysis of Loading Mode

In a slope of normally consolidated clay with a potential failure surface extending below the toe, elements near the toe are subjected to the passive mode loading while those near the crest to the active mode loading. In the passive mode the major principal stress is in near the horizontal direction, while it is in near the vertical direction in the active mode. It has been shown in the previous section (Section 3.5.5) that the soil loaded in the active mode shows relatively brittle behavior with higher strength than that in the passive mode so that implementing appropriate constitutive relations based on the stress path for individual element is very important in the slope analysis.

The following examples of FLAC analyses are presented in order to observe the variations of the stress paths of soil elements during the process of slope excavation. Fig. 4.1 shows a slope of 30 degree inclination angle and 15 meters of excavation height. It is divided into 480 elements for finite difference analyses. Isotropic Mohr-Coulomb elasto-plastic constitutive model was used in the analyses of slope excavation of total 6 layers (15.0 meters) in an initially level ground with $K_0=0.85$. The soil strengths were designed to be constant along the depth. The equal depth of soil layers were then removed layer by layer until a

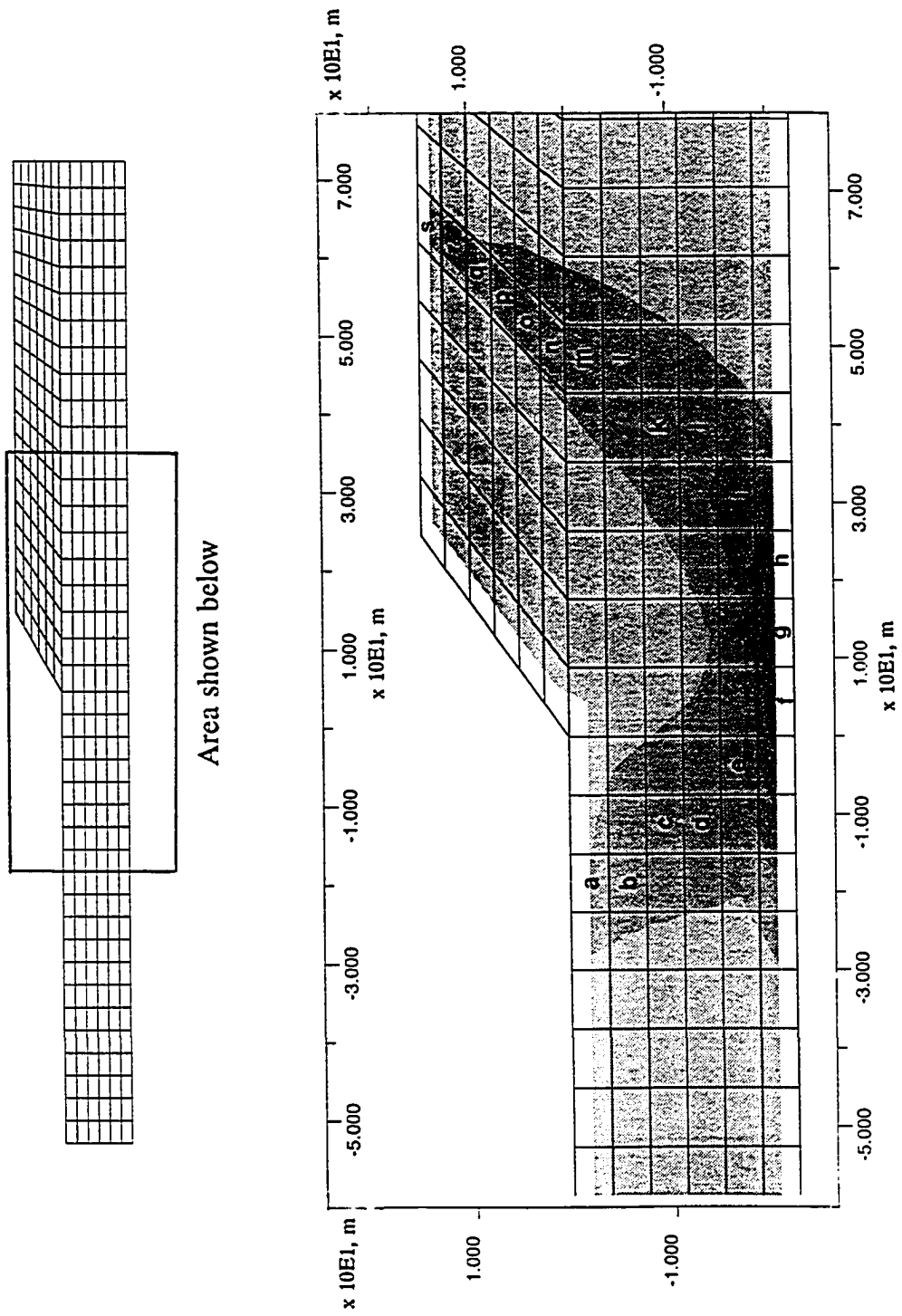


Fig. 4.1 Finite difference mesh

clear failure is noticed by monitoring the displacement of a nodal point at the tip of the crest as shown in Fig. 4.2. The elements along the potential failure surface were labeled 'a' through 's' from the toe to the crest for identification and are indicated in the finite element mesh (Fig. 4.1). Fig. 4.3 shows the history of maximum unbalance force with respect to computational time steps, in which it jumps to a peak right after a layer of excavation and gradually dies out with computational time steps. This figure will be used as an indication when relating the time steps to a specific layer of excavation. Note that at the last layer excavation, the structure takes about 50% more computational time steps to get to the equilibrium state, indicating that structure is in the state of near failure.

In the presentation of analysis results, y axis coincides with the direction of gravity acceleration, which makes a plane in the plane strain direction with x axis, while z axis is in the out of plane direction. Figs. 4.4a and 4.4b show the variations of σ_h and σ_v , along with the computational time steps, respectively.

Fig. 4.5a shows the variation of τ_{xy} and Fig. 4.5b shows the shear stress ratio (τ_{xy}/τ_{max}), from which the contribution of the shear stress component (τ_{xy}) to the maximum shear stress (τ_{max}) can be evaluated. For clarity, only three representative elements from each area of the crest, bottom and toe of the potential failure surface were used in the figures. It can be seen that the soil elements (o,p,q) around the crest are subjected to the active mode of loading in which the horizontal normal stress decreases (Fig. 4.4a), while the vertical normal

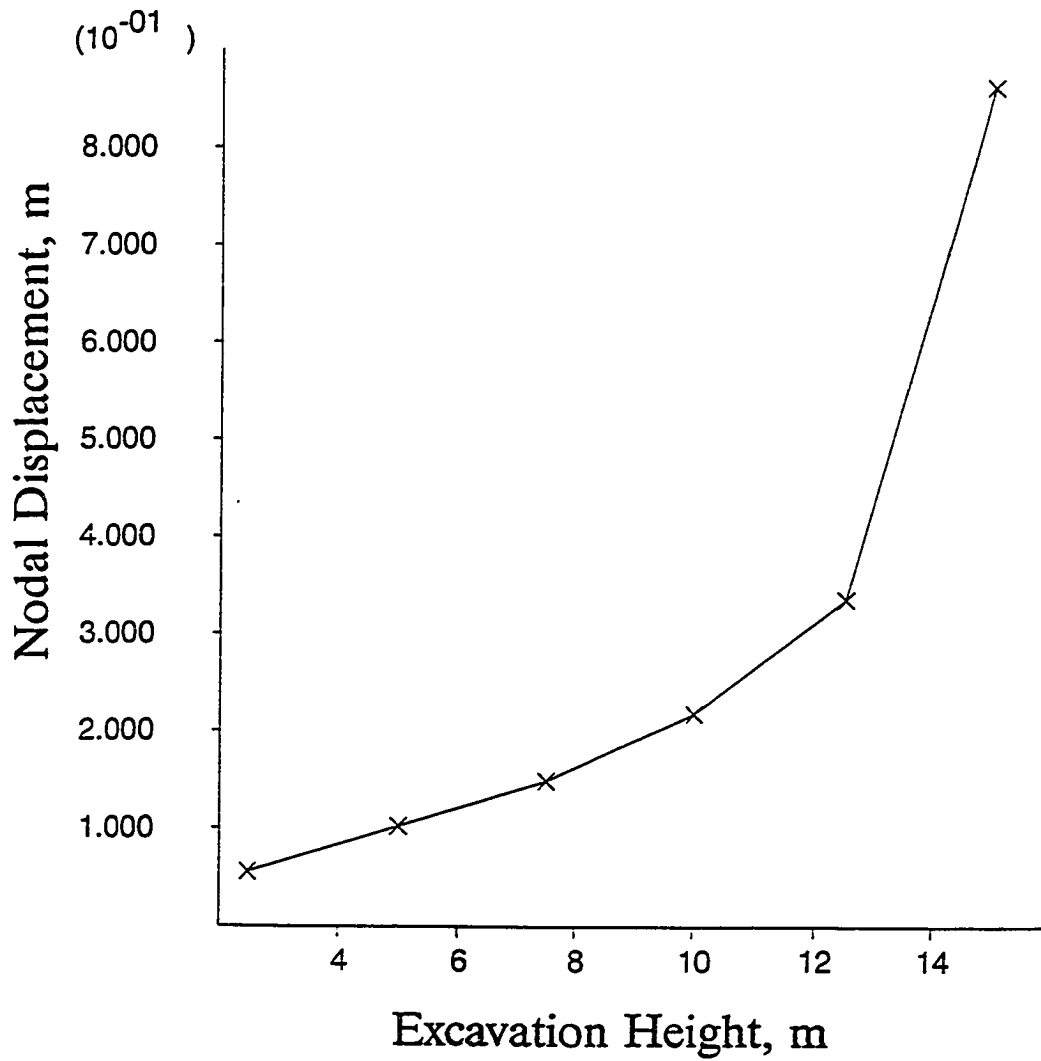


Fig. 4.2 Nodal displacements with increasing excavation heights

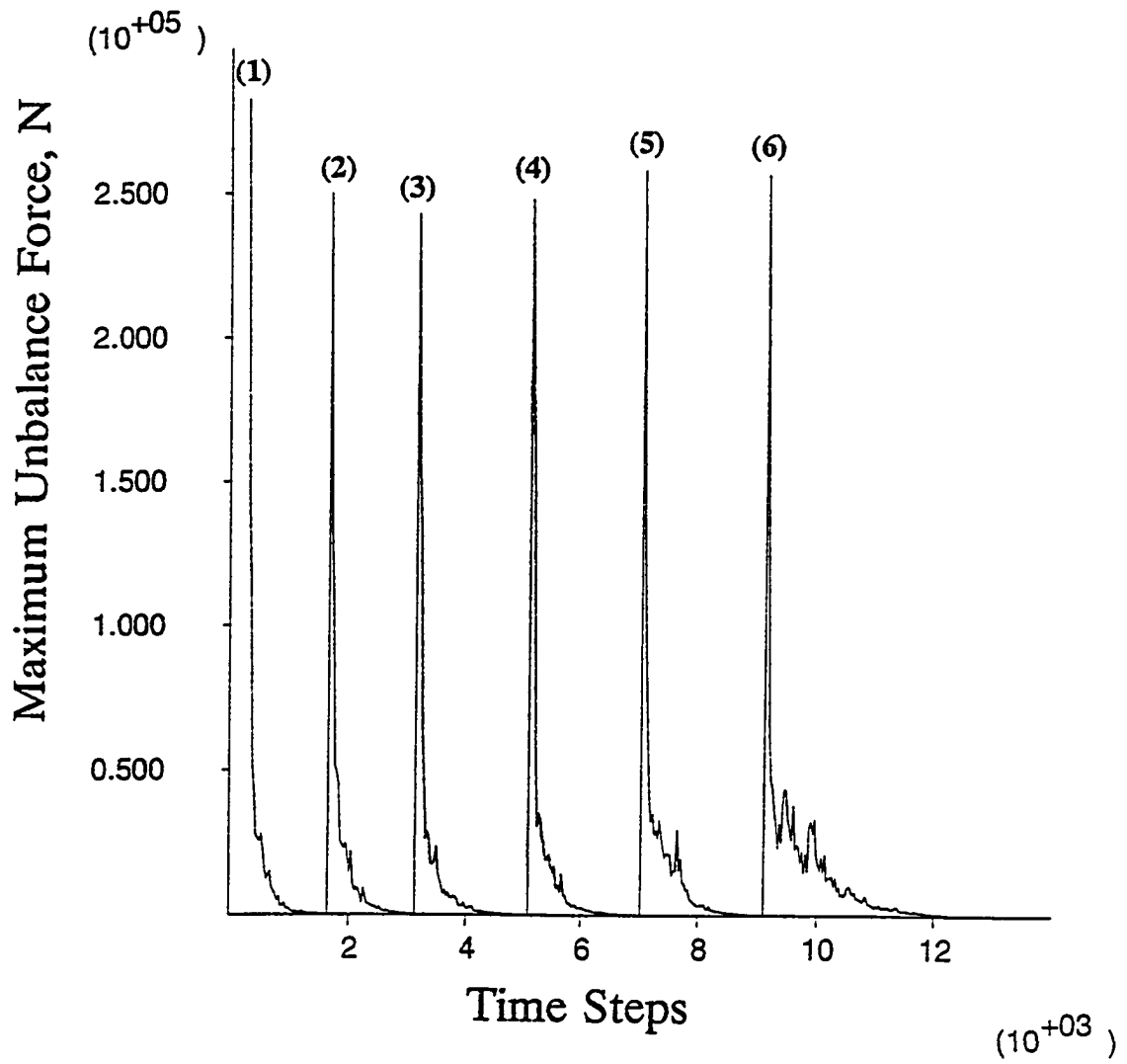


Fig. 4.3 History of maximum unbalance force

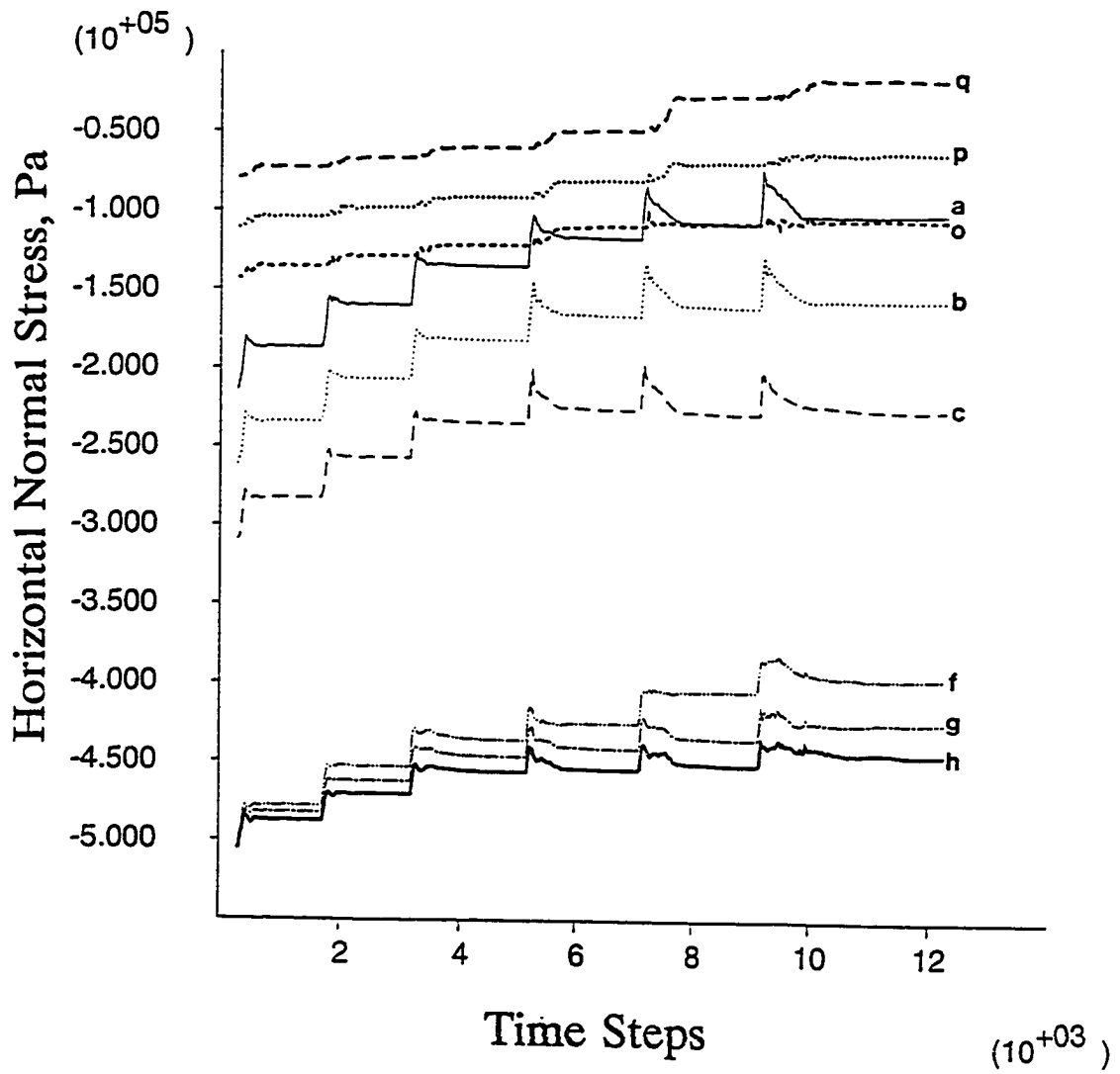


Fig. 4.4a Variation of normal stresses in the horizontal with excavations

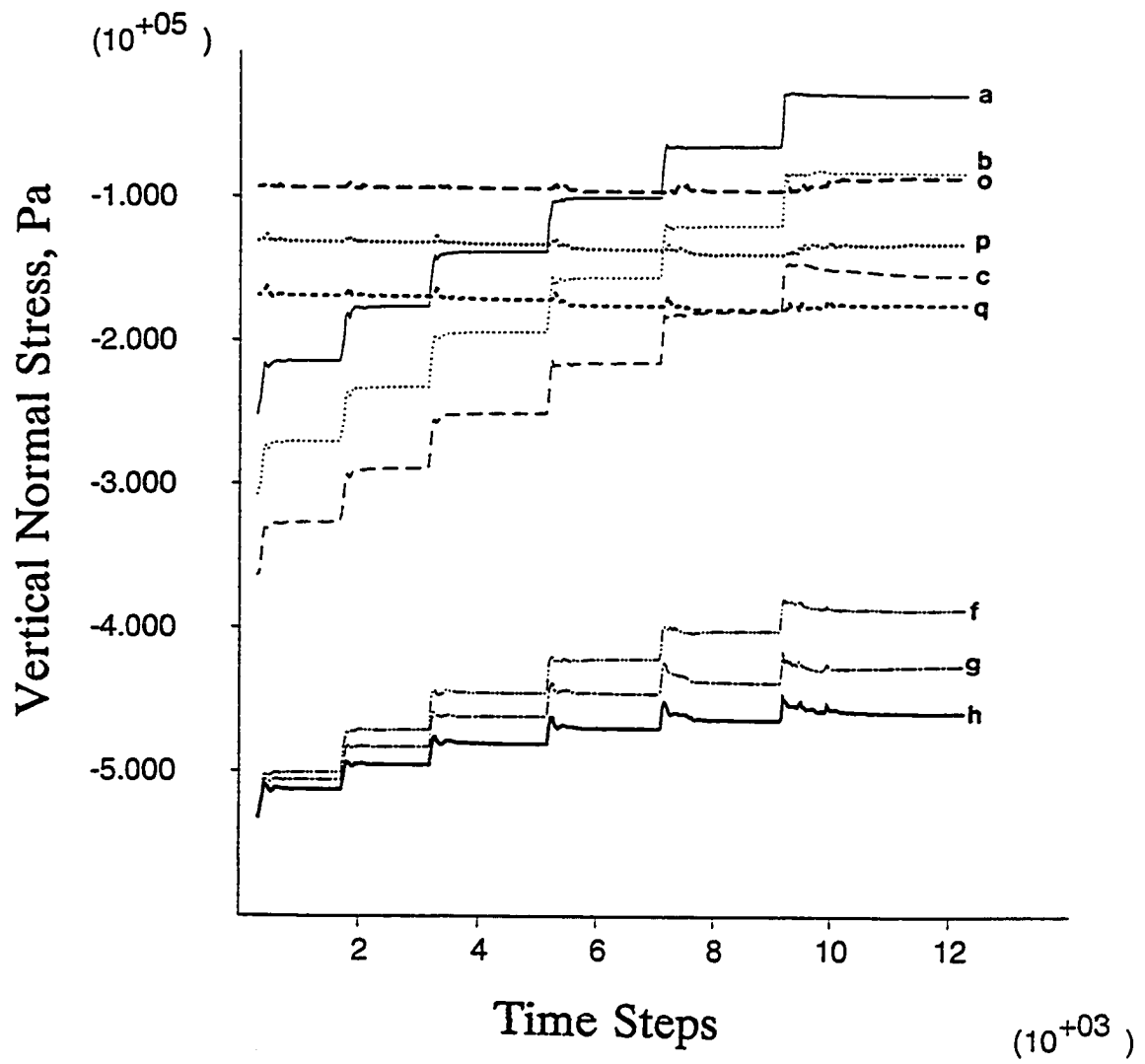


Fig. 4.4b Variation of normal stresses in the vertical with excavations

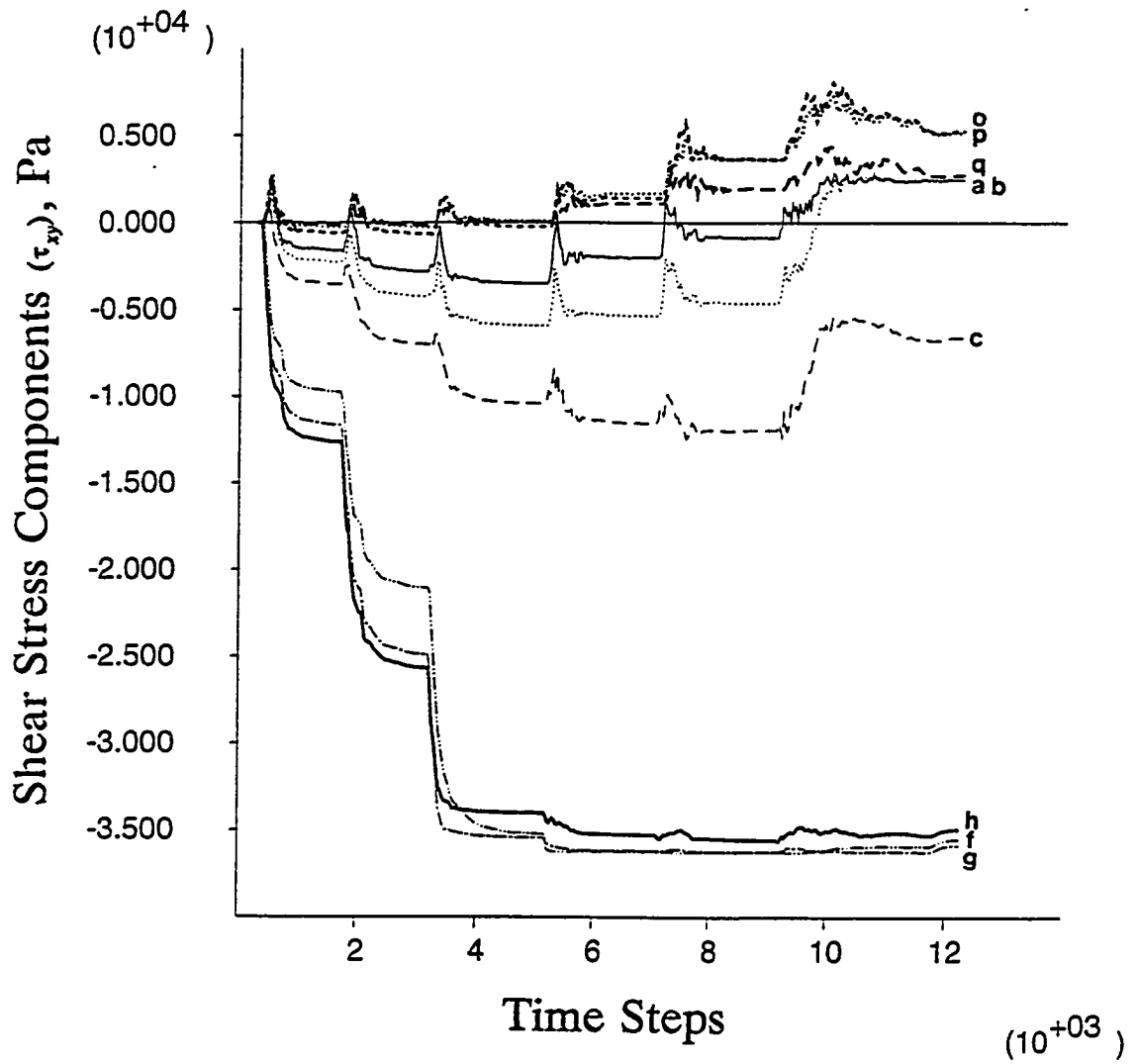


Fig. 4.5a Variation of shear stress components with excavations

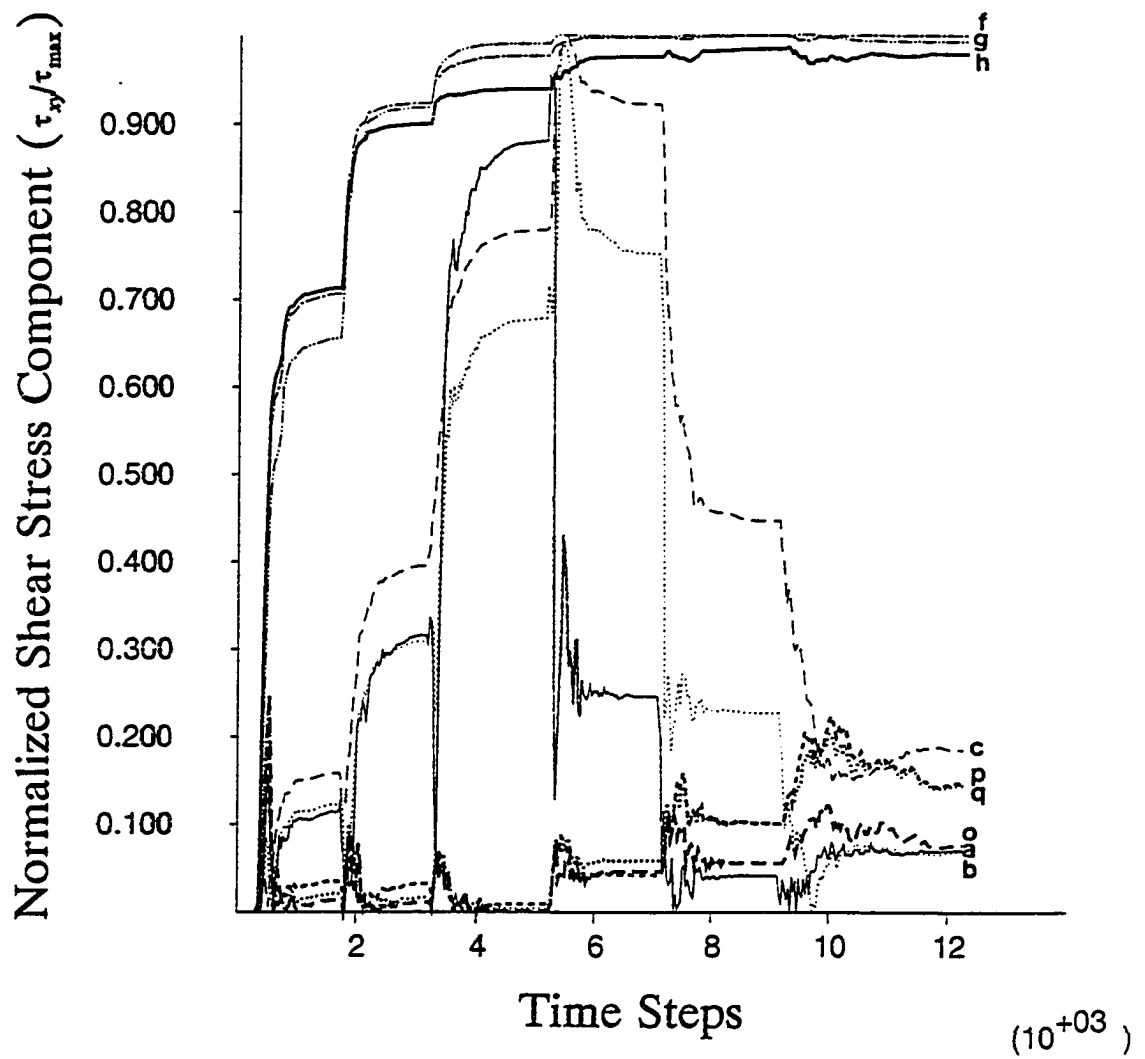


Fig. 4.5b Variation of normalized shear stresses with excavations

stress is kept virtually constant (Fig. 4.4b) for those elements. Fig. 4.5b shows that the shear stress ratios for those three crest elements at the failure are very little indicating that increments of shear stress components during the excavation have nominal contributions to the maximum shear stresses for these elements. Therefore, the main cause of the shear failure for these elements are the horizontal normal stress reduction which is similar to the laboratory compression test as illustrated in Fig. 4.6a.

In contrast, soil elements (a,b,c) around the toe are subjected to the opposite mode of loading (passive) in which the normal stress reductions in the vertical (Fig. 4.4b) are much greater than those in the horizontal (Fig. 4.4a). The shear stress ratios (τ_{xy}/τ_{max}) of the elements are seen to increase continuously up to values close to unity after which they drop to very small values (Fig. 4.5b), while the actual magnitude of the (τ_{xy}) remains nearly constant Fig. 4.5a. It means that during the initial stage of the excavation (up to the third layer) the maximum shear stress increment mainly comes from both the shear stress component increment and the vertical normal stress reduction. In the later stage, however, the maximum shear stress is mainly increased due to the vertical normal stress decrease, leading to the shear failure at the end of excavation. This process is analogous to the laboratory extension test (Fig. 4.6b).

The elements around the bottom (f,g,h) deserve a special attention. In Figs. 4.4a and 4.4b, it can be seen that both the horizontal and the vertical normal stresses are slightly reduced. At a glance, it appears that the elements are

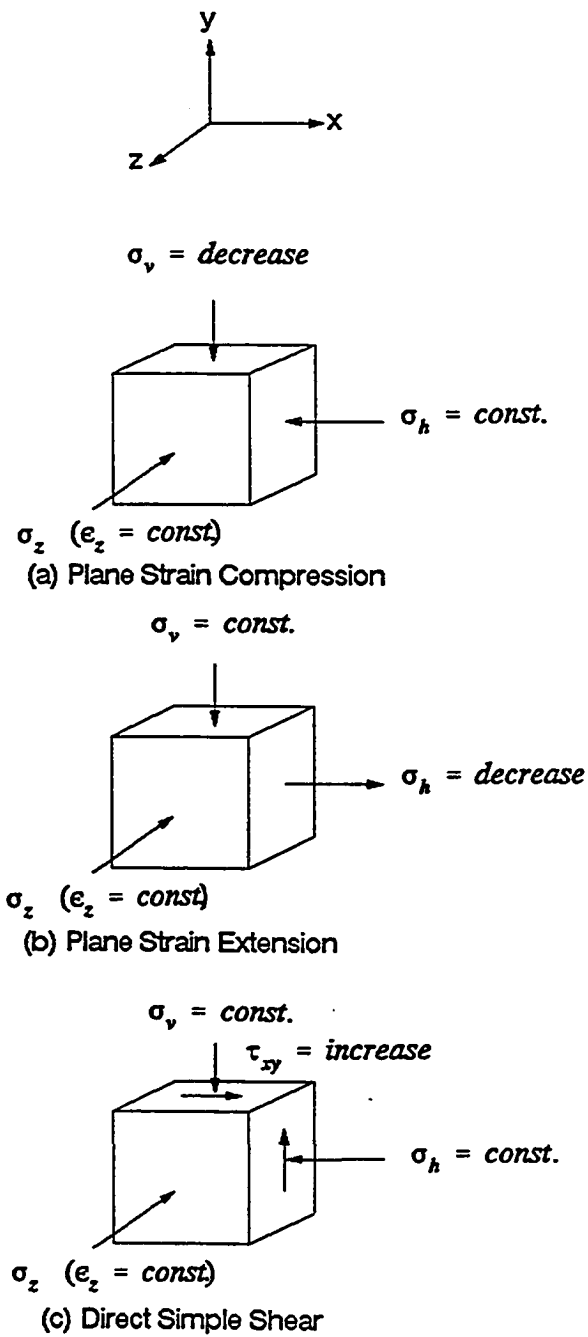


Fig. 4.6 Loading conditions in the laboratory soil testings

subjected to a mode of loading in which the Mohr circles are just shifted toward left while keeping the same diameters. However, the shear stress ratios for those elements at the end of the second layer excavation reached as high as unity, reflecting the fact that the shear failures of those elements are induced by the shear stress increment on the horizontal plane as in the laboratory direct simple shear test (Fig. 4.6c). Only difference in the mode of loading between the laboratory direct simple shear test and this case is that in the laboratory the initial horizontal and vertical normal stresses are kept constant, whereas they were both reduced in this case during the process of excavation.

Fig. 4.7 shows variations of the maximum shear stresses normalized by the initial maximum shear stresses during the excavation for three representative elements in each group. It is seen that the elements near the toe (a, b, c) initially undergo shear stress reduction before moving into the negative shear stress domain. In addition, it is interesting to find in the same figure that the shear stress of element "f" shows little increase up to a certain point and fluctuates between the active and the passive regions thereafter. The reason for the fluctuation is due to the sign convention of the shear stress in which shear stress takes on the negative sign when the vertical normal stress is smaller than the horizontal normal stress. It can be also shown that the fluctuation of the shear stress between positive and negative signs reflects the fact that the major principal stress directions fluctuate around 45 degree.

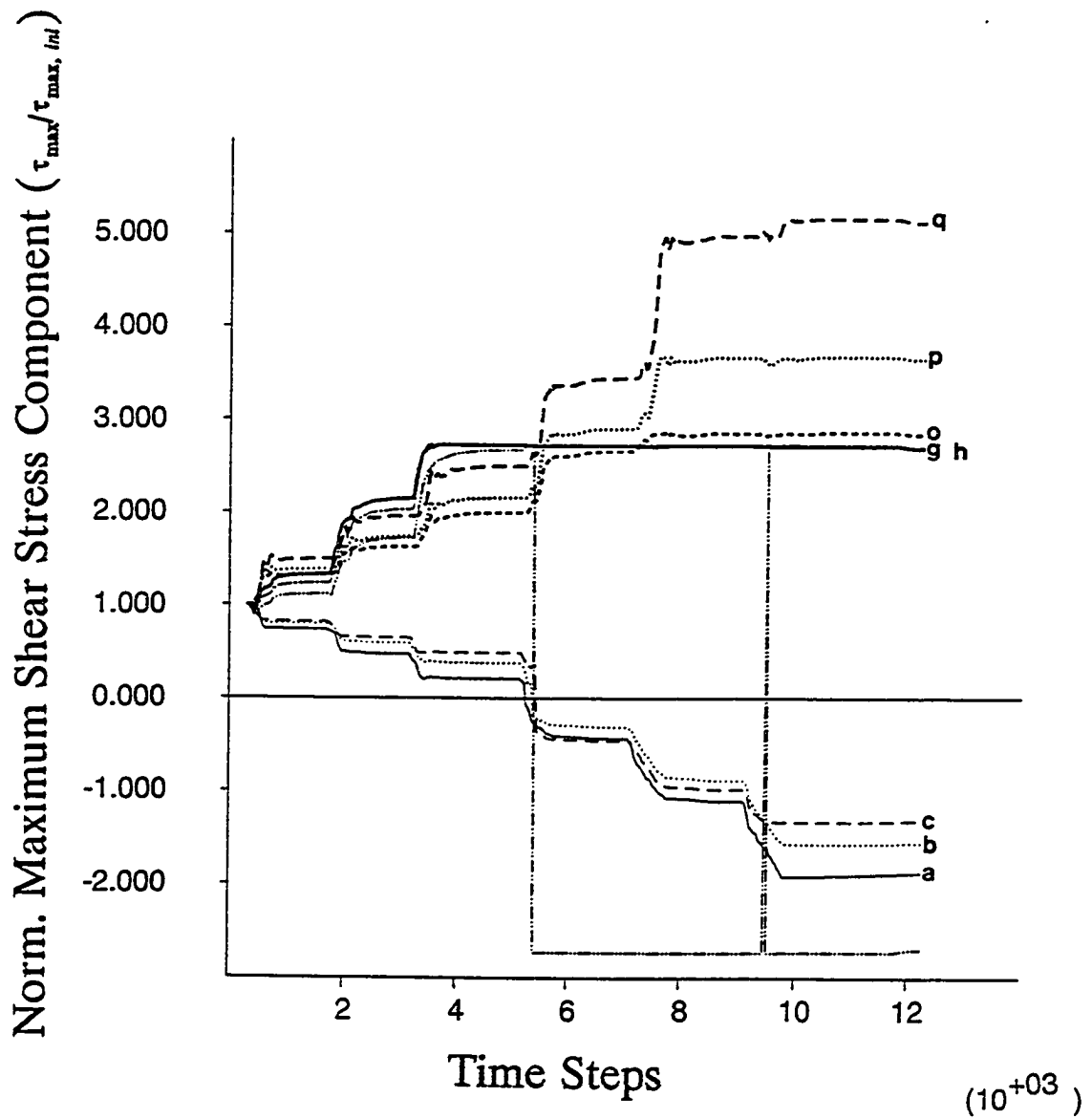


Fig. 4.7 Variation in the normalized shear stresses with excavations

The variation of the major principal stress direction during the excavation is of prime interest. The angle between the vertical and the major principal stress is defined herein as i angle as appeared in Fig. 3.24 in Section 3.5. In order to compare the i angle variation patterns for varying initial stress conditions, three different cases with different initial K_o values ($K_o=0.85$, $K_o=1.00$, and $K_o=1.15$) were analyzed with other conditions kept the same. The variation of i angles of the elements along the potential failure surface during the excavation is shown in Figs. 4.8a, 4.8b and 4.8c for those different K_o cases. It is noticed that the final i angles at the end of the excavation increase as the location of the element is close to the toe from the crest. Based on those figures clear groups can be identified, i.e., the toe group: a, b, c, d, e; the bottom group: f, g, h; the crest group: i, j, k, l, m, n, o, p, q, r, s (from "m" to "s" are not shown in the figures for clarity). In addition, it is interesting to note that the final i angles of the elements in Figs. 4.8a, 4.8b and 4.8c are almost the same without regard to the initial state of stress.

In the level ground of $K_o=0.85$ case, all the major principal stress directions are initially in the vertical, which rotate with the subsequent excavation. Since i angles at the final stage of excavation are different depending on the location of the element, the rates of i angle rotation should be different. In a normally consolidated clay with K_o less than unity, the elements around the toe experience greater amount of changes in i angles as compared to others from the level ground to the end of excavation. Therefore, the rates of rotation for the toe elements for this case are much higher than those of elements near the crest. In

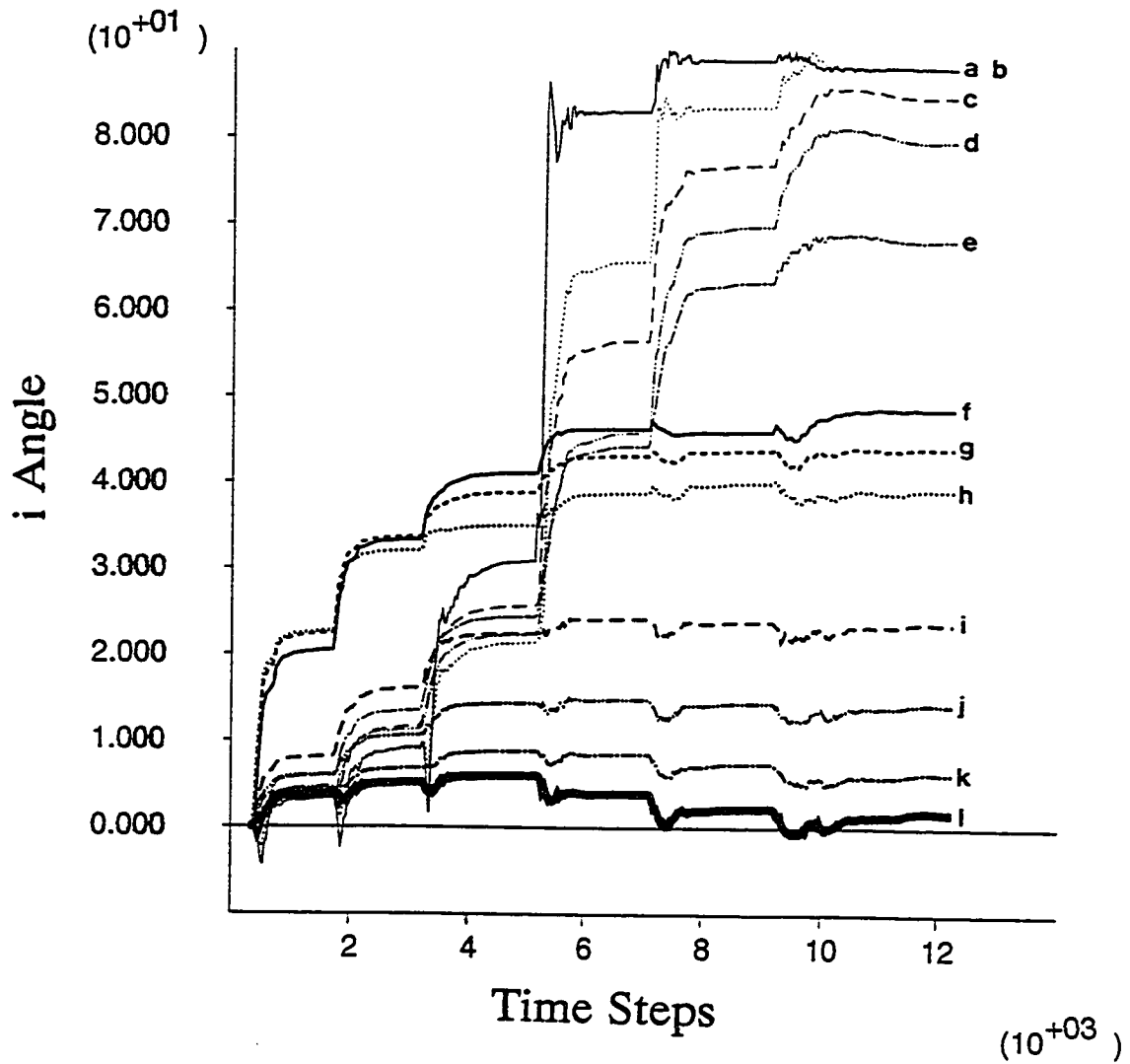


Fig. 4.8a Variation of i angles with excavations ($K_p=0.85$)

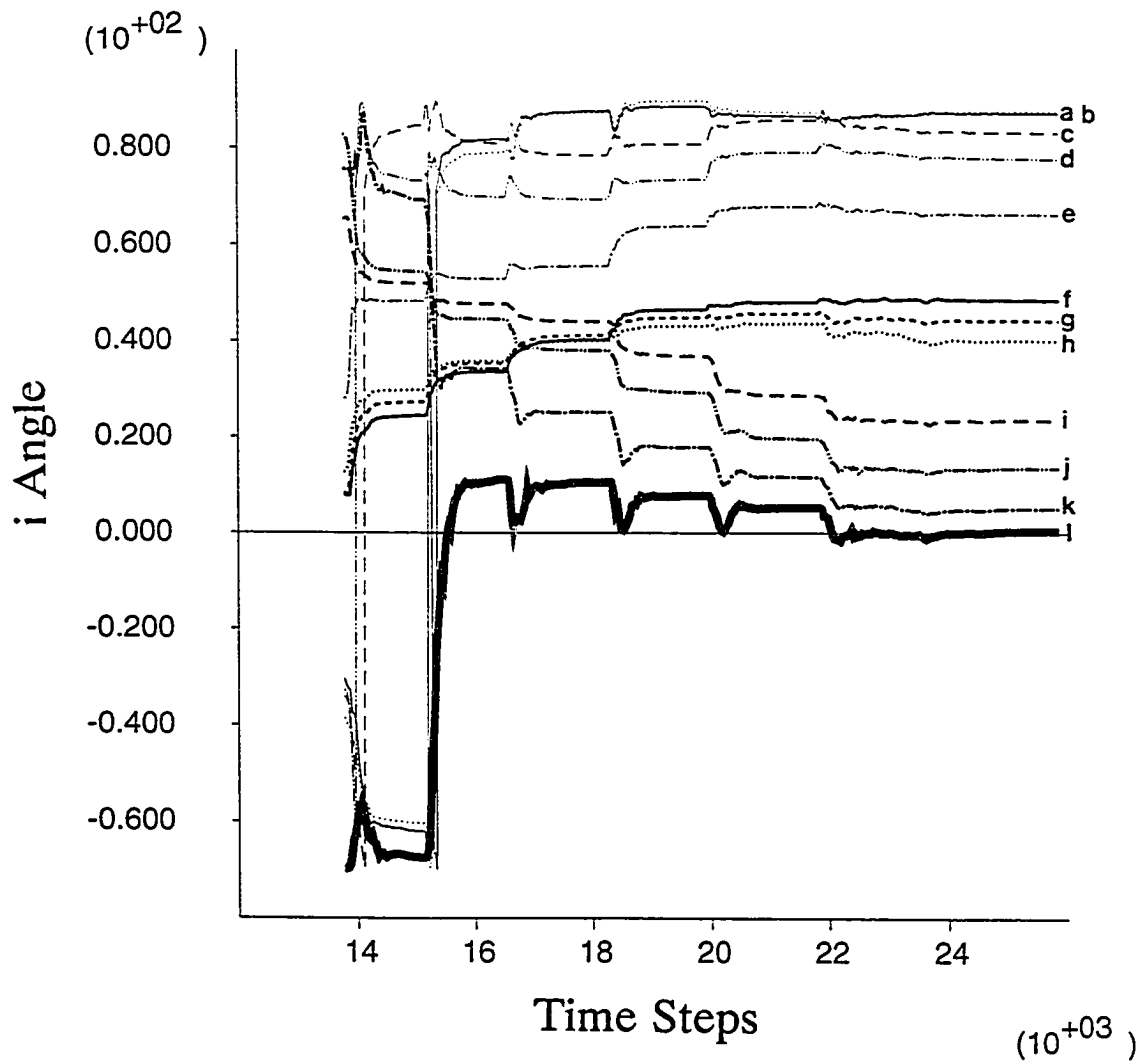


Fig. 4.8b Variation of i angles with excavations ($K_o=1.00$)

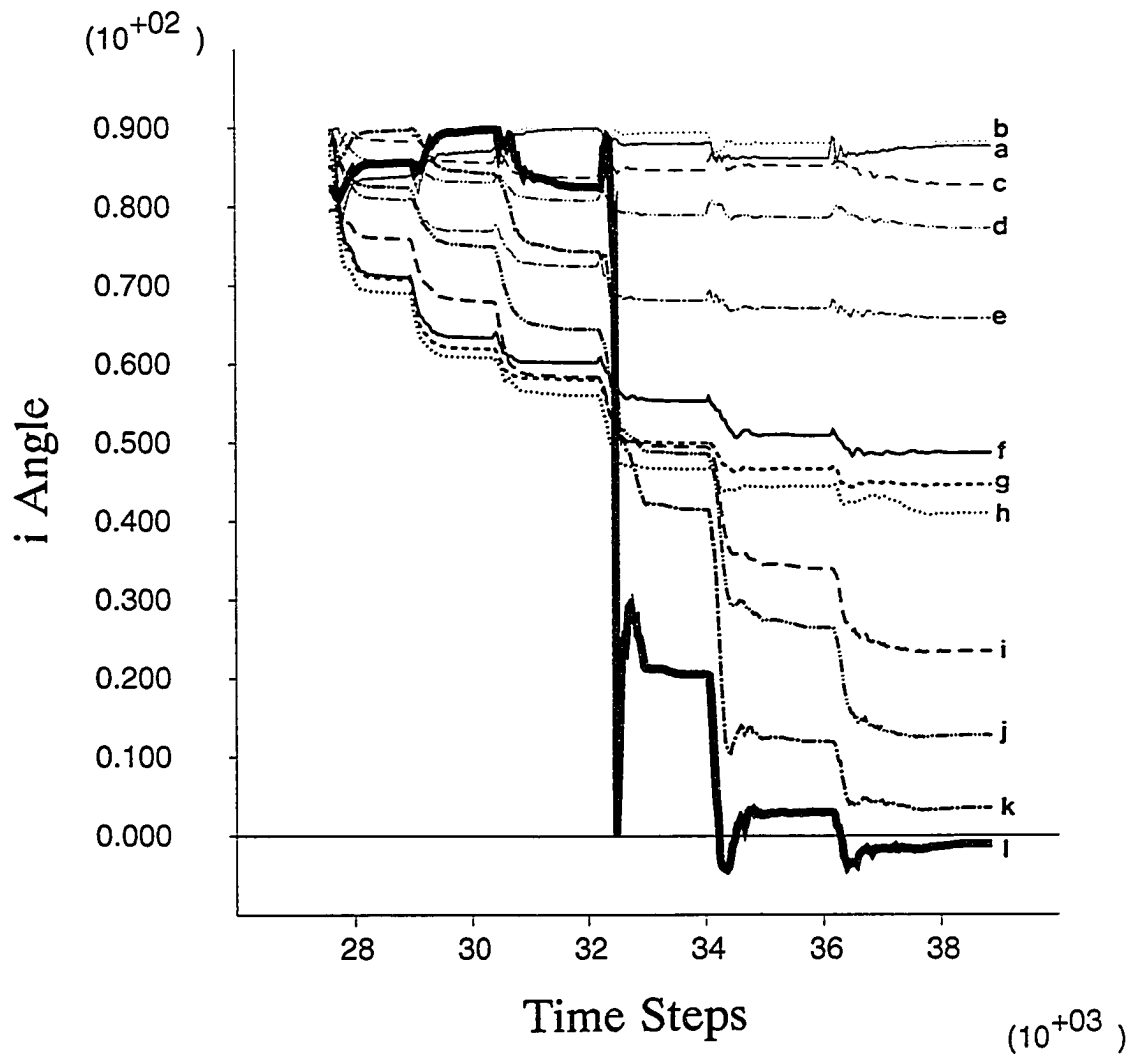


Fig. 4.8c Variation of i angles with excavations ($K_0=1.15$)

contrast, since the major principal stresses for overconsolidated clays ($K_o = 1.15$) are initially in the horizontal, the i angles are much greater for the elements near the crest as compared to those around the toe. Therefore, those elements have higher rates of i angle rotations during the excavation for this case (Fig. 4.8c). Comparing the above two cases, it is interesting to find that the patterns of i angle rotation of elements in the toe and crest groups for the first case ($K_o = 0.85$) are quite similar to those of elements in the crest and toe groups of the third case ($K_o = 1.15$), respectively.

The i angle rotation pattern for the initially isotropic state ($K_o = 1.0$) is an interesting case to examine in comparison to the above two cases (initial stress anisotropy). In this case, the soil elements are initially in the hydrostatic state of stress such that i angles at the level ground are not definable in the plane strain direction. As the state of stress deviates from the initial state upon excavation, elements take on certain i angles which range from 0 to 90 degrees depending on the location of the element. Fig. 4.8b shows i angle rotation variations during the excavation for this case. It can be seen that the patterns of i angle variations of elements in the toe group are similar to those of elements in the crest group in a symmetric manner with the variations of the bottom elements (f,g,h) at the center.

4.2 Stress-Strain Modelling

It has been shown that the major principal stress directions at the failure state considerably deviate from their initial vertical directions. Therefore, it is

desired that the strengths, which can be mobilized with certain i angles at the incipient failure, are actually used in the slope stability analysis. In addition to the strength variation, it has been observed in the experimental data that the stress-strain pattern also varies with i angle at the failure. If the stress-strain pattern is assumed to vary systematically with respect to i angle at the incipient failure, it may be possible that the stress-strain curve for any i angle can also be interpolated using the stress-strain relations determined by the typical laboratory testings: the plane strain compression, the plane strain extension and the direct simple shear tests. In the following, detailed description of how to determine the i angles for the entire elements at the incipient failure, and how to interpolate the stress-strain curves for the i angles which based on the results from the typical laboratory testings.

4.2.1 Stress-Strain Model in the Anisotropic Analysis

4.2.1.1 Anisotropy of the Undrained Strength

In the analysis aimed at the evaluation of anisotropic strength effect, isotropic Mohr-Coulomb constitutive model was slight modified in the implementation, which is herein called the pseudo-anisotropic model. Unlike usual isotropic elasto-plastic models shown in Fig. 4.9, the strengths of the elements in the pseudo-anisotropic model are continuously adjusted based on the major principal stress direction (i angle) until the incipient failure is reached as illustrated in Fig. 4.10. In the model, the stress-strain relations for the passive

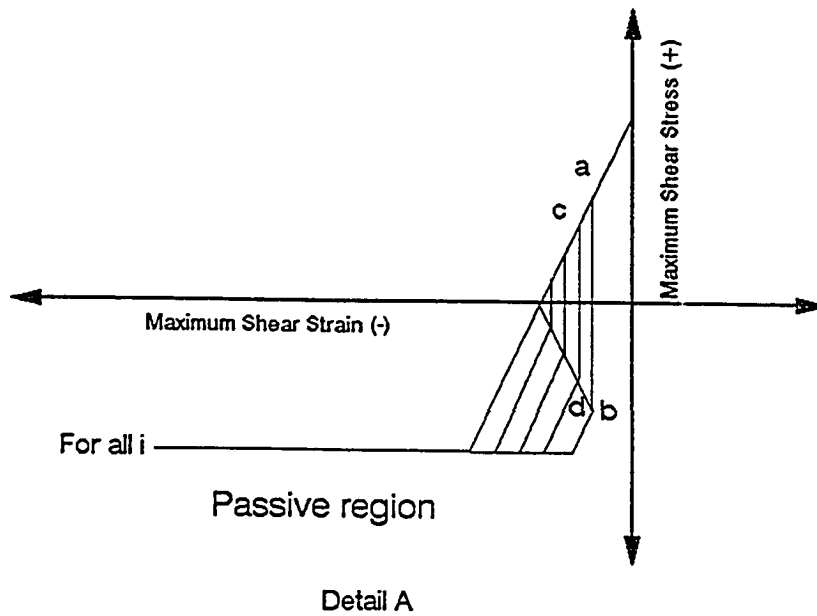
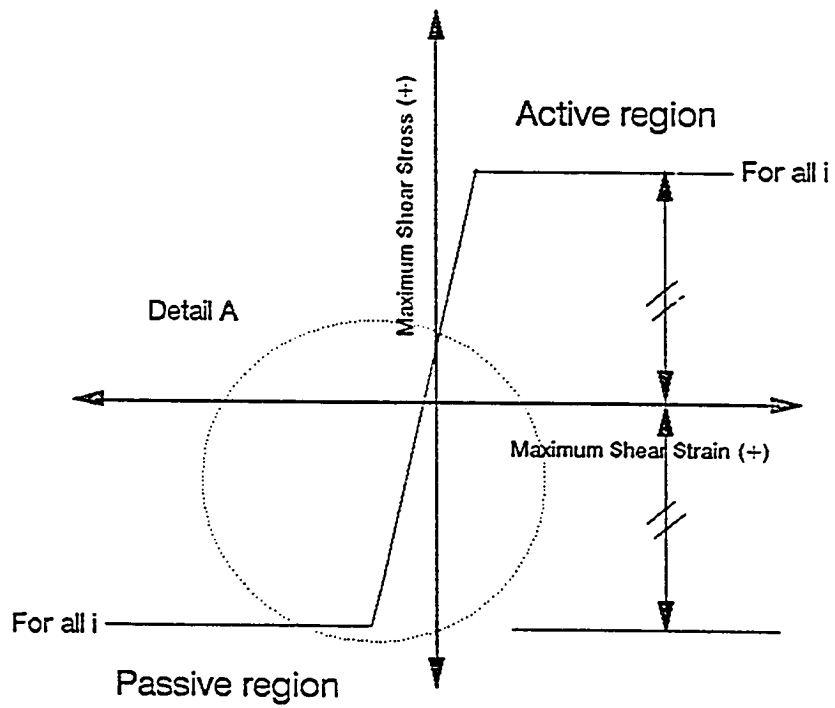


Fig. 4.9 Isotropic elasto-plastic model

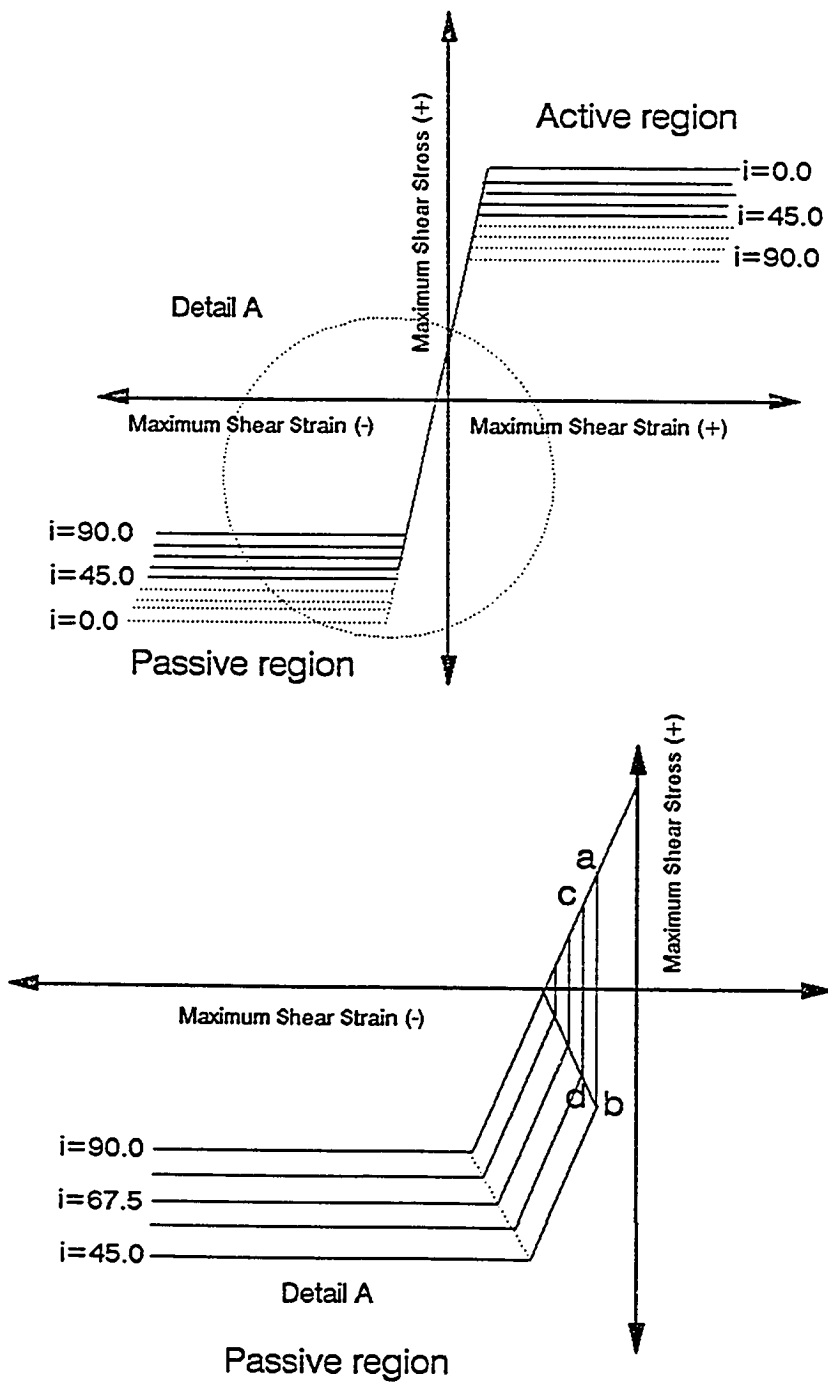


Fig. 4.10 Pseudo-anisotropic elasto-plastic model

elements experience jumps in moving from the active to the passive regions. The reason for the jump is explained in the following.

Let us consider a state of stress (Fig. 4.11) of an element, which will eventually fail in the passive region, is experiencing the shear stress reduction from the initial K_0 condition toward the passive state. The i angle of the element in the figure can be expressed as

$$i = \tan^{-1} \left(\frac{\sqrt{((\sigma_v - \sigma_h)^2 + (2\tau_{xy})^2) - (\sigma_v - \sigma_h)}}{2\tau_{xy}} \right) \text{ for } \tau_{xy} > 0 \quad (4.1)$$

and the radius of the Mohr circle (maximum shear stress) is

$$R = 1/2 \sqrt{((\sigma_v - \sigma_h)^2 + (2\tau_{xy})^2)} \quad (4.2)$$

It can be seen that as $(\sigma_v - \sigma_h)$ is reduced toward zero, the radius of the Mohr circle is also reduced, but the reduction is constrained by the magnitude of τ_{xy} .

Therefore, the element never experiences the isotropic state of stress, unless τ_{xy}

also vanishes at the same time. Once $(\sigma_v - \sigma_h)$ vanishes, the maximum shear

stress becomes equal to the shear stress component (τ_{xy}) and i angle becomes

45.0 degree. When σ_v becomes smaller than σ_h ($(\sigma_v - \sigma_h) < 0$), the maximum

shear stress takes on negative sign accompanied by the jump in the shear stress

domain and hence in the stress-strain relations. At the same time i angle

continuously increases. It should be noted that the element with a high τ_{xy} jumps

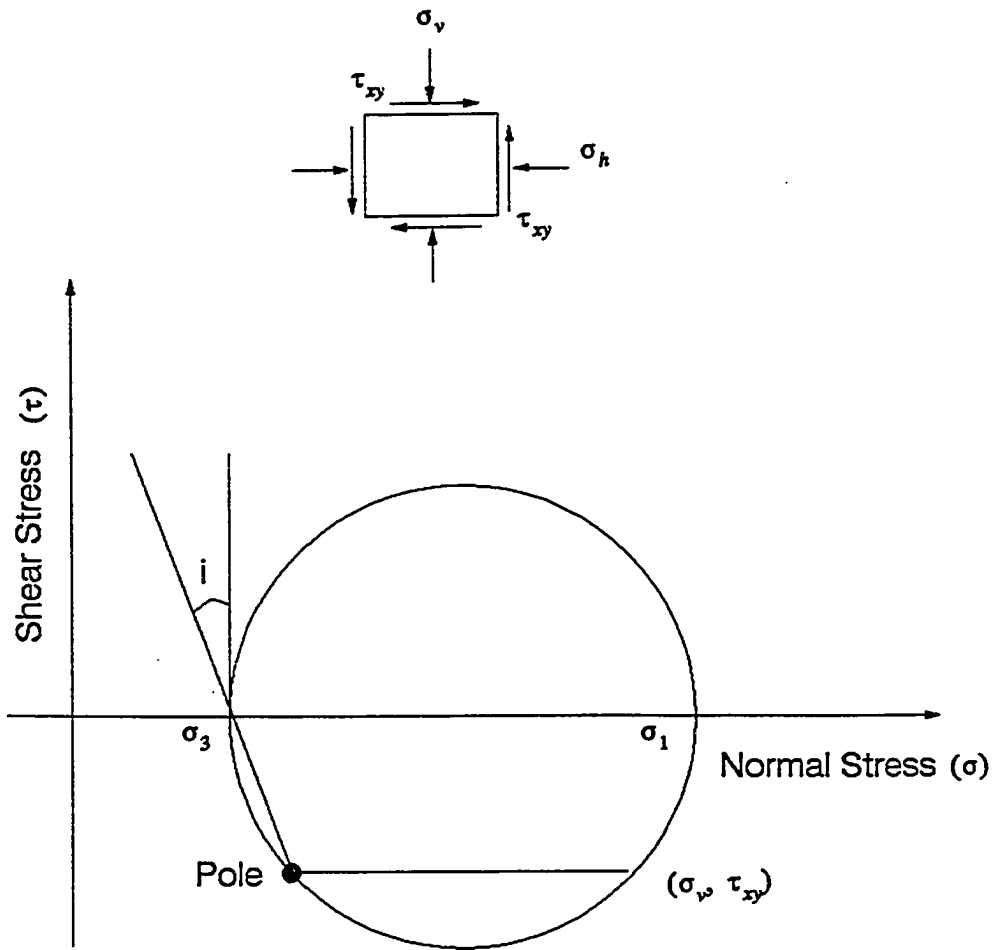


Fig. 4.11 The Mohr circle stress presentation of an element

at a high level of the maximum shear stress (i.e., "a" to "b" in comparison to "c" to "d" in Fig. 4.10b).

Initially, the major principal stresses of elements under the level ground are all in the vertical so that all the elements have potential maximum strengths corresponding to the compression mode ($i=0^\circ$). As excavation proceeds, however, the major principal stress directions (i angles) deviate from the vertical and strengths which would be exercised by the elements at the particular i angles are somewhat less than those at $i=0^\circ$ due to strength anisotropy. Therefore, after each block (30 time steps) of computational time steps, the current i angles are computed and the strengths of the elements are reassigned based the relations between the strength and i angle as defined Fig. 3.14 in Section 3.5.3.3. The cycle of i angle computation and strength reassignment continues until the slope reaches the state of incipient failure, after which the strengths for the entire elements are fixed at the values determined by the lastly determined i angles. Fig. 4.12 shows the relations between the i angle and the plastic shear strain for the elements along the failure surface of the slope, which were obtained from the analysis in Section 4.1. The plastic shear strain is defined as the shear strain accumulated during the plastic flow obtained by using the flow rule. It is shown that at the point of initial plastic yielding the i angles have already increased considerably from the initial zero.

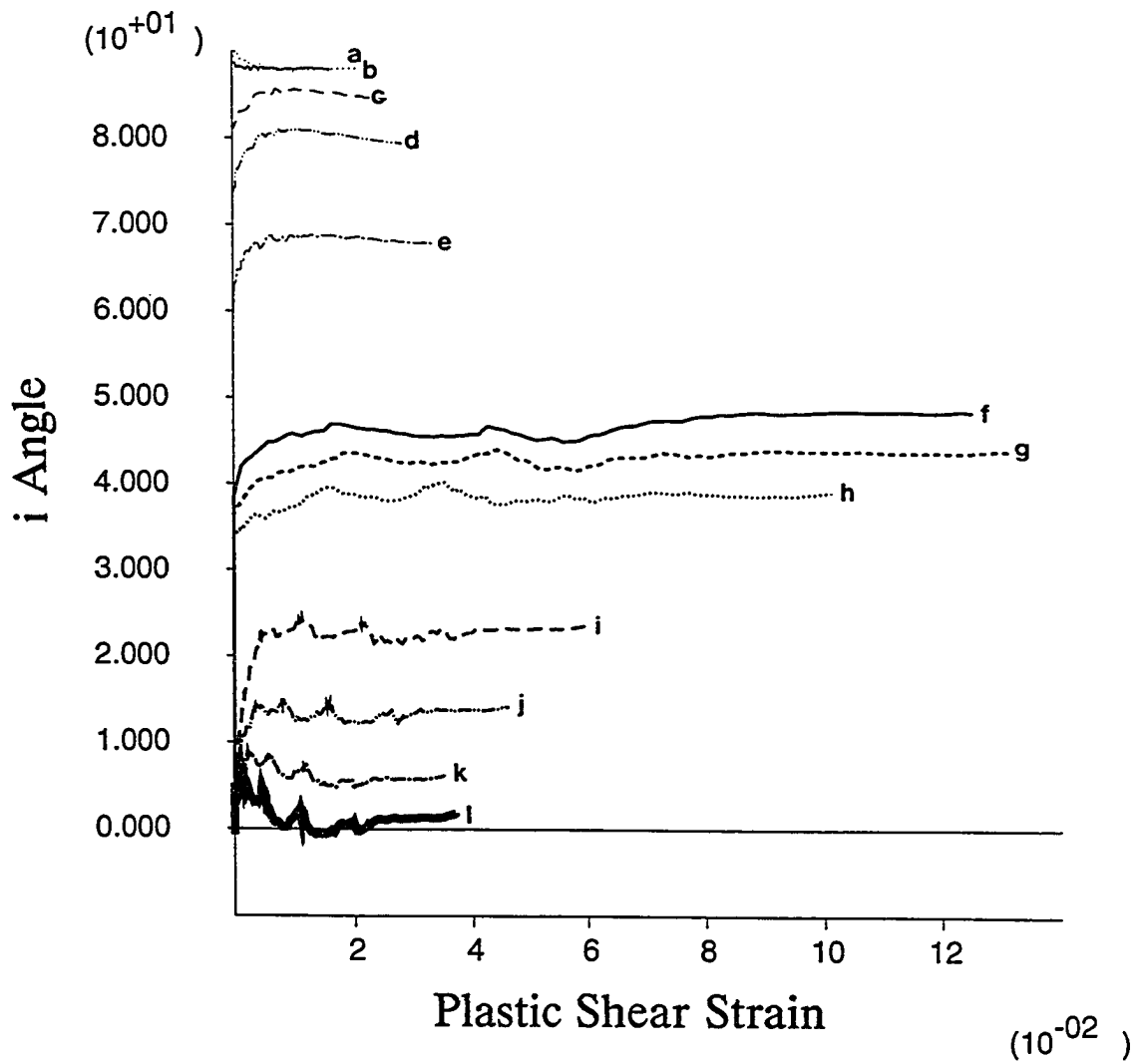


Fig. 4.12 Relations between the plastic shear strains and i angles

4.2.1.2 Determination of i Angle

It has been already mentioned that strengths in the pseudo-anisotropic model are varied based on i angles after each block of computational time steps until the slope reaches the state of incipient failure. Once the slope reaches the failure state, then i angles are saved and corresponding constant strengths are continuously used in the subsequent failure process. Therefore, the saved i angles determine the peak strengths which can be mobilized in the failure for the entire elements. In order to catch the state of incipient failure during the slope excavation process, the slope behavior should be carefully observed. It may be subjective to determine the failure moment to some extent, but it should not be too much different from person to person. In this study, the incipient failure state was caught by a combination of the following criteria: (1) the peak shear strength mobilization ratio (τ_{\max}/S_u) along the potential failure surface, (2) the plastic shear strain level along the potential failure surface, (3) the displacement behavior of a nodal point at the tip of the crest, and (4) the number of time steps required to reach the equilibrium state after a layer of excavation.

For example, the nodal displacement at the tip of the crest for the slope analyzed in Section 4.1 was shown in Fig. 4.2. It can be seen that the magnitude of the nodal displacement accelerates at the sixth layer excavation. In addition, the computational time steps to reach the equilibrium state for the sixth layer excavation takes almost 1.5 times those of the previous layers excavation (Fig. 4.3). Based on those two criteria, it can be said that the slope at the 5th layer

excavation is at the incipient failure state. Consequently, i angles determined at the equilibrium state after the 5th layer excavation are saved for the computational process for the last layer excavation. Figs. 4.13 and 4.14 show the distribution of i angles along the failure surface and contour of i angles in the slope, respectively, at the state of incipient failure of the slope analyzed in Section 4.1. It should be noted that the state of incipient failure caught by the pseudo-anisotropic strength analysis may depend on the prescribed relation between the peak strength and i angle. The relation which was used to catch the failure state in this study was the same as the one suggested by Casagrande and Carrillo (1944).

4.2.1.3 Elastic Properties Determination

In order to define the stress-strain relations in the elasto-plastic constitutive model, it is necessary to determine the elastic modulus of the material in addition to the peak strength. The elastic modulus used in the model is not necessarily the initial elastic modulus, nor is it the secant modulus determined at the strain corresponding to the peak stress. It is somewhat in between them to adequately approximate the actual stress-strain relations with two linear lines. The modulus increases with increasing consolidation stress such that the elements in the deeper location should have higher moduli as compared to those of shallow elements. In order to obtain the relations between the modulus and the consolidation stress, the shear strain levels at the peaks in Table 3.1 in Section 3.5.5.1.2 were first

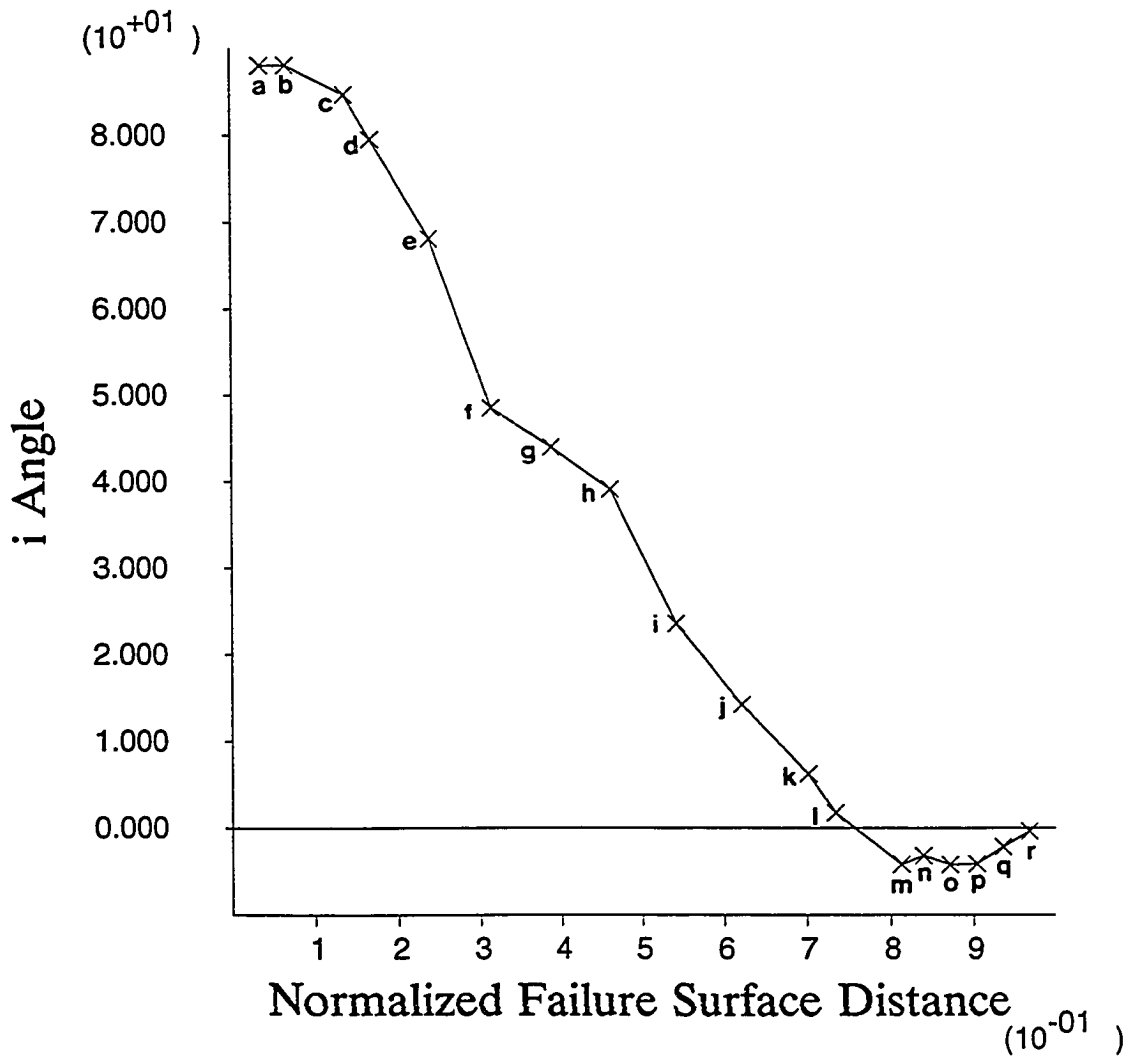


Fig. 4.13 Distribution of *i* angles along the normalized failure surface distance at the state of incipient failure

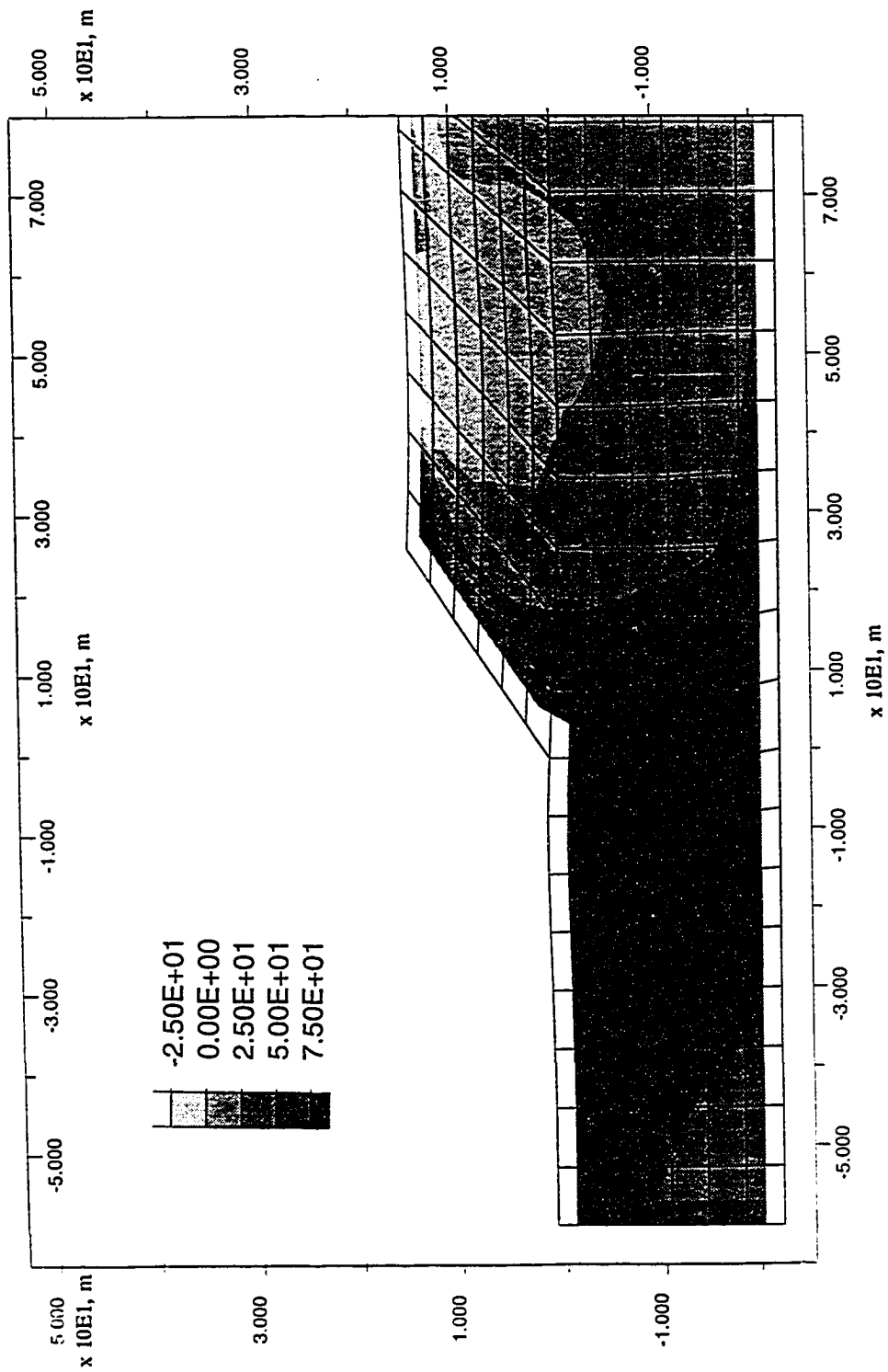


Fig. 4.14 Distribution of i angles in the slope at the state of incipient failure

consulted. However, for the nine different clays, any consistent variation of the strain at the peak shear stress or initial (or secant) modulus was not found with respect to the consolidation stress ranging from 150 kPa to 590 kPa.

Alternatively, it was assumed that the elastic modulus and the secant modulus at the peak stress vary with the same pattern with the consolidation stress such that they can be related by a constant parameter for a given consolidation stress. It should be recalled here that even for limited data the strain at the peak stress was found to increase with increasing consolidation stress (Figs. 3.25 and 3.26 in Section 3.5). It implies that the increasing rate of the secant modulus decreases with the increasing consolidation pressure. Therefore, it is reasonable to assume that the rate of elastic modulus increase with the increasing consolidation pressure also decreases. Next question is then how to define the manner in which the strain at the peak stress increases with the consolidation stress. Since there is no experimental data available for a consolidation stress range in which any consistent variation can be found, a series of linearly increasing strains at the peak stresses in the consolidation stress range from 30 kPa to 590 kPa were assumed as shown in Fig. 4.15. In the figure scattered experimental data from Table 3.1 also were shown for a reference purpose only. Fig. 4.15 was then converted to the relations between the consolidation stress and the secant shear modulus (not shown here).

In order to determine the relations between the secant modulus and the elastic moduli, which will be used to represent the initial stress-strain curve with a

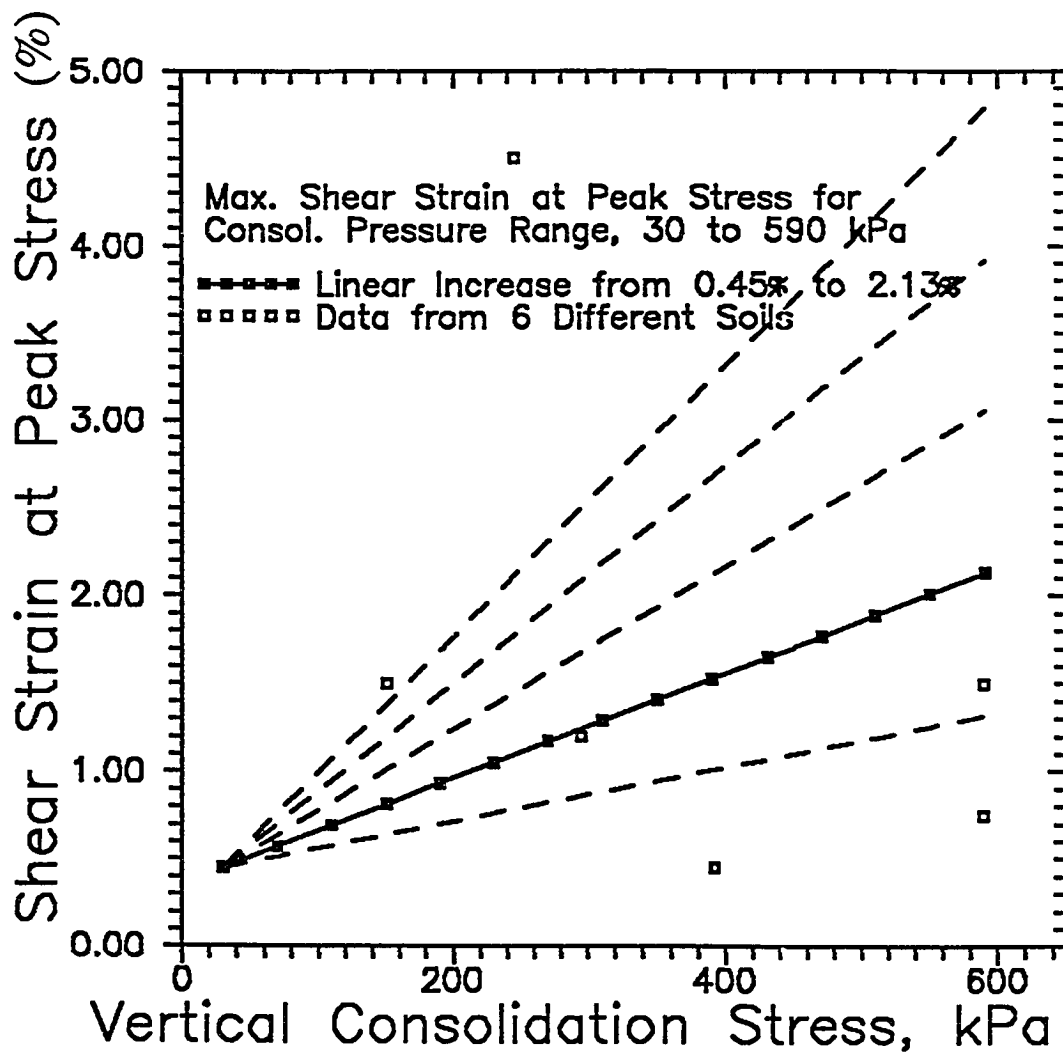


Fig. 4.15 Relations between the vertical consolidation stress and the shear strain at the peak stress

linear line, laboratory determined stress-strain curves were consulted. It was found that the elastic modulus is about 5.5 times greater than the secant modulus on the average based on six clays (Table 3.1 in Section 3.5.5.1.2.). Consequently, the relations between the consolidation stress and the secant modulus were converted to the relations between the consolidation stress and the elastic modulus using the constant parameter (5.5) in Fig. 4.16. In order to choose the most reasonable relation among them, they were compared to the typical values of elastic moduli for soft clay (1.9 MPa-9.6 MPa) used in the calculation of foundation settlement (Bowles, 1982). It was found that the solid lines in Figs. 4.15 and 4.16 resulted in the most reasonable moduli variation ranging from 1.8 MPa to 7.7 MPa for consolidation stress ranging from 30 kPa to 650 kPa, which is the maximum working stress range of the current slope analysis. The elastic shear moduli determined as above are used for a given consolidation stress without regard to stress path (i.e., isotropic elastic shear modulus).

The Poisson's ratio is another important elastic property of soil in the numerical analysis with the elasto-plastic constitutive model. Studies have been made to determine appropriate values of Poisson's ratio for various conditions (Dunlop et al., 1968, Hwang et al., 1969). For the analysis of undrained conditions in saturated clays, the Poisson's ratio is usually chosen to be as nearly equal to 0.5 as is consistent with numerical stability of the computer solution. For the drained condition, Poisson's ratios are estimated from the relationship

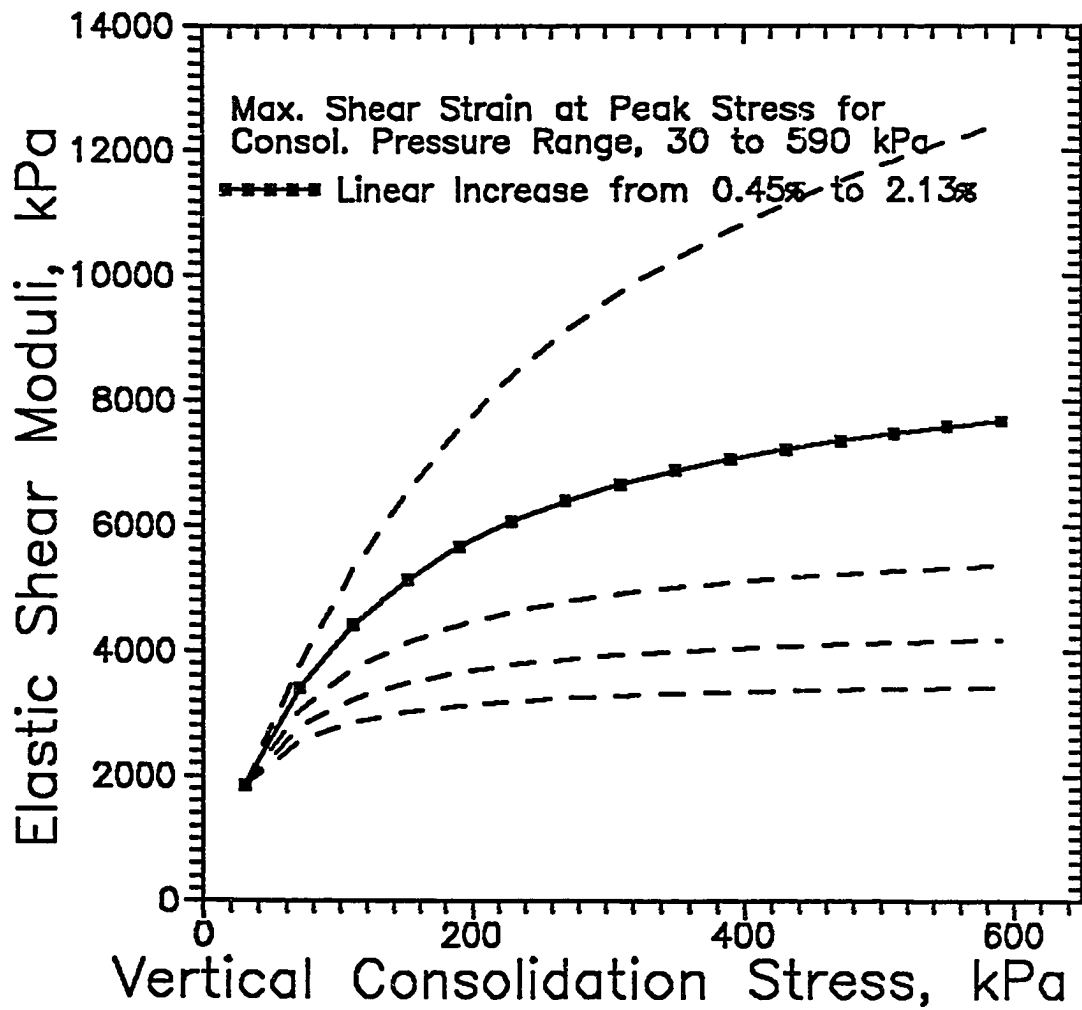


Fig. 4.16 Relations between the vertical consolidation stress and the elastic shear moduli

$\mu = K_o / (1+K_o)$, where K_o is the coefficient of earth pressure at rest, expressed in terms of effective stresses.

For the current analysis, the initial level ground was assumed to have reached an equilibrium state on the fully drained condition before any construction. The level ground was then subjected to the construction of excavation on the fully undrained condition with the corresponding Poisson's ratio (0.49). The shear deformations in the elements under the construction are directly computed based on the two elastic properties: elastic shear moduli and Poisson's ratio in the elastic range. Once an element experiences shear stress which is greater than the undrained strength, the plastic flow rule takes over to control the plastic deformation of the element.

4.2.2 Stress-Strain Modelling in the Strain Hardening and Softening Analysis

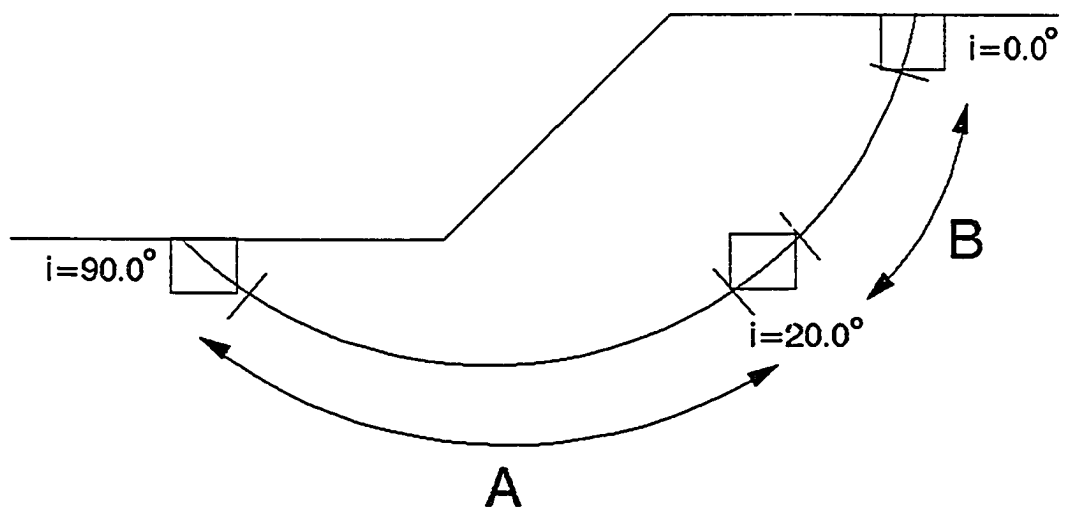
4.2.2.1 Basic Approaches

The analysis in the previous section (4.2.1) was focused on the evaluation of only strength anisotropy effects on the stability of slope in which the stress-strain relations were a simple elastic-plastic. However, when the evaluation of the strain softening as well as hardening effects are the thrust of the study, the input stress-strain relation should be as closely fitted as possible to the experimentally observed data.

In Section 3.5, the stress-strain patterns of three typical laboratory testings were collected such that they can be directly used when the element is loaded in

one of the typical modes of loading as in the laboratory testing. However, it needs to be pointed out that not all the elements are subjected to those typical modes of loading. In order to define the stress-strain relations for a spectrum of i angles, the three modes of loading are correlated with a parameter, and the resulting stress-strain relations are varied systematically. To correlate the mode of loading of the typical laboratory testings, it is considered that individual test has its own i angle at failure. Then, it is subsequently assumed that the i angle during the laboratory test continuously increases from the initial zero to the final i angle in an increasing order from the compression test ($i=0^\circ$ to 0°), the direct simple shear test ($i=0^\circ$ to 20°), to the extension test ($i=0^\circ$ to 90°).

It has been shown in the previous section that the stress-strain pattern varies from the compression ($i=0^\circ$) to the extension ($i=90^\circ$) tests. If the variation is originated from different i angles at failure, the stress-strain patterns for elements with varying i angles in the slope excavation can also be assumed to vary systematically. Then, the stress-strain relations for elements in between those typical stress paths were interpolated as illustrated in Fig. 4.17. In order to determine the systematic variation of the stress-strain relation with varying i angle, general observation on the stress-strain patterns are utilized, which are (a) the peak strength of the clay decreases as i angle increases, and (b) the shear strain at the peak strength increases with increasing i angle. It has been previously shown that the mode of loading of the elements in the toe was similar to the laboratory extension test, yet somewhat different in terms of i angle variation pattern. It has



A and B: Interpolation regions

Fig. 4.17 Regions for the stress-strain relations interpolation

been shown that the i angles for those elements during the excavation gradually increase from initial zero to 90 degree at failure, while that of the specimen in the laboratory extension test remains fixed at zero up to the isotropic state of stress and jumps to 90° thereafter. Therefore, i angle in the laboratory test is not precisely simulating the field loading condition except at the beginning and at the end of the test. If those i angle variation patterns during the loading process makes considerable differences in the pattern of stress-strain relation, then the use of the laboratory extension test for the elements in the toe may not be fully justified.

Consequently, the comparison was made of the patterns of i angle variation during the loading process between the field condition and the laboratory testing. Fig. 4.18a shows the relations between the maximum shear stress (τ_{max}) and the shear stress components (τ_{xy}), and Fig. 4.18b shows the relations between the maximum shear stress (τ_{max}) and i angle for elements "a" and "b" with those of the laboratory extension test. It is clearly shown that the laboratory test is a simplification of the loading conditions of the elements in the toe. It has been shown in Fig. 4.5 that elements in the toe are subjected to the shear stress components (τ_{xy}) increase in addition to the loading condition similar to the laboratory extension test. Therefore, it is clear that the discrepancy in the i angle variation pattern was mainly caused by the existence of the shear stress components (τ_{xy}). In order to see the relations between the magnitude of (τ_{xy})

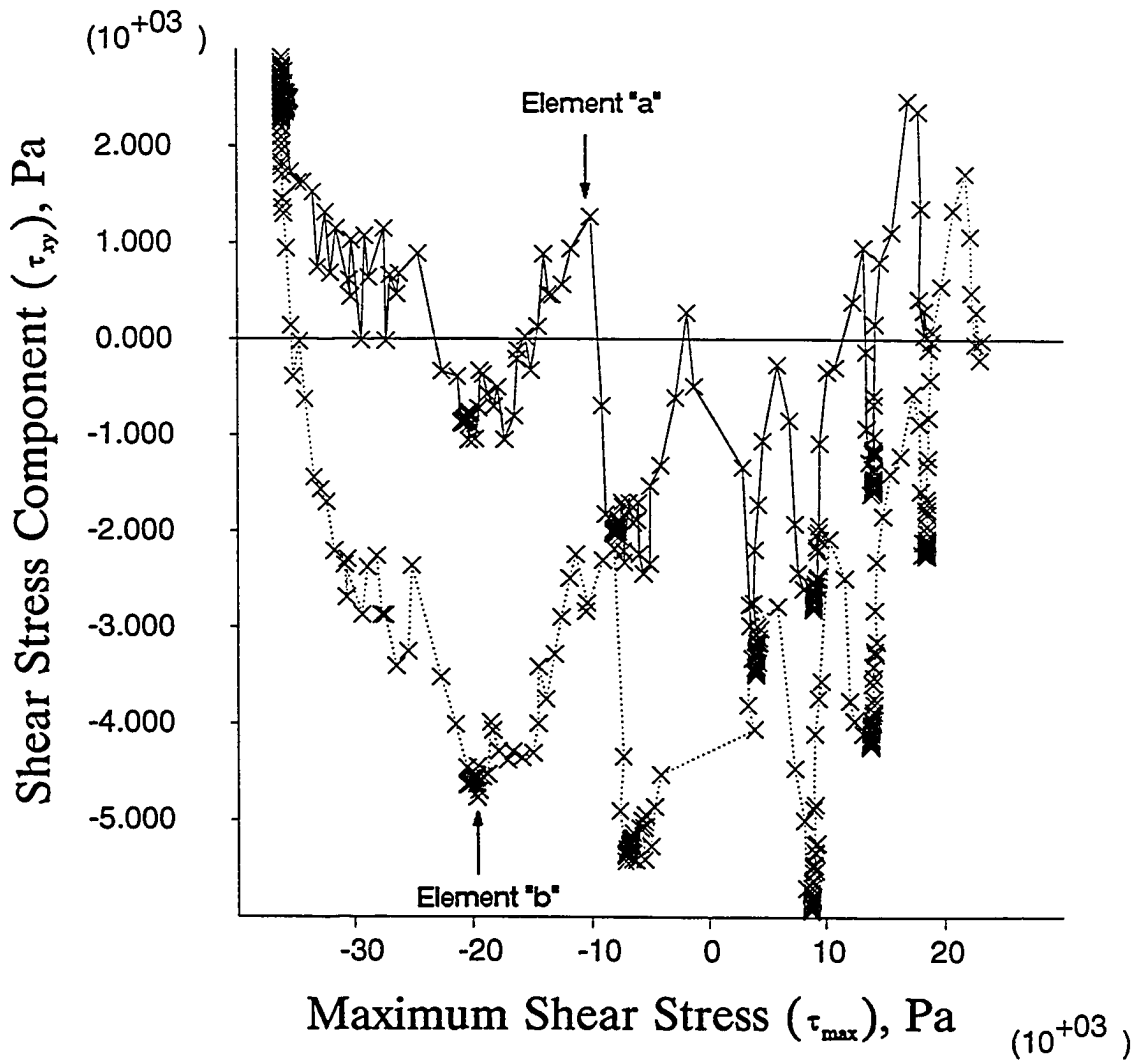


Fig. 4.18a Variation of shear stress components of the toe elements with excavations

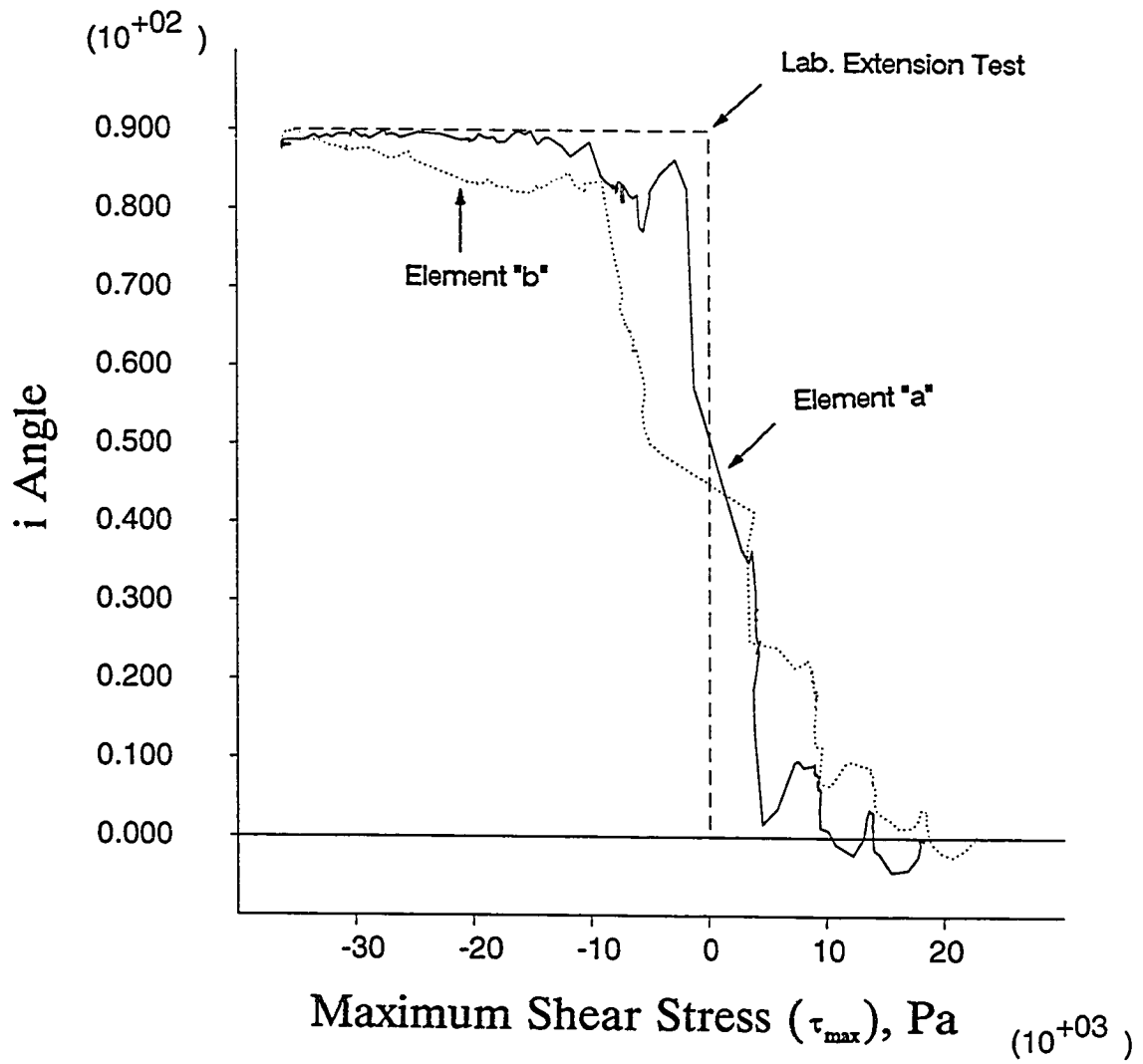


Fig. 4.18b Comparison of *i* angle variations between the toe elements and the laboratory extension test

and i angle variation pattern, four imaginary laboratory tests were considered which are exactly the same as the extension tests except that they have four different constant τ_{xy} on the top of the specimens as seen in Fig. 4.19. It is clearly seen that the discrepancy in the i angle variation pattern is mainly caused by the magnitude of τ_{xy} in the element. When τ_{xy} is very small (curve number one), which is close to the laboratory extension test case, i angle variation occurs in a small stress range near the isotropic state of stress. Meanwhile, for the case of relatively high τ_{xy} (curve number four), i angle variation occurs rather uniformly throughout the entire stress range. It should be noted here that τ_{xy} in the imaginary tests are kept constant from the beginning for all cases, while those in the field continuously vary from zero to certain final values throughout the excavation process.

Theoretically, it is possible to conduct laboratory shear tests in which exact i angle rotation and the maximum shear stress increment pattern can be precisely simulated as in the field, but none of them are currently in use in practice. Therefore, in order to determine the stress-strain relations for elements in the toe, the use of the laboratory extension test data which are closest in the mode of loading will be the only possible alternative. It is not known, however, how much difference the exact simulation of varying i angle during the test will induce in the stress-strain relations in comparison to the extension test case.

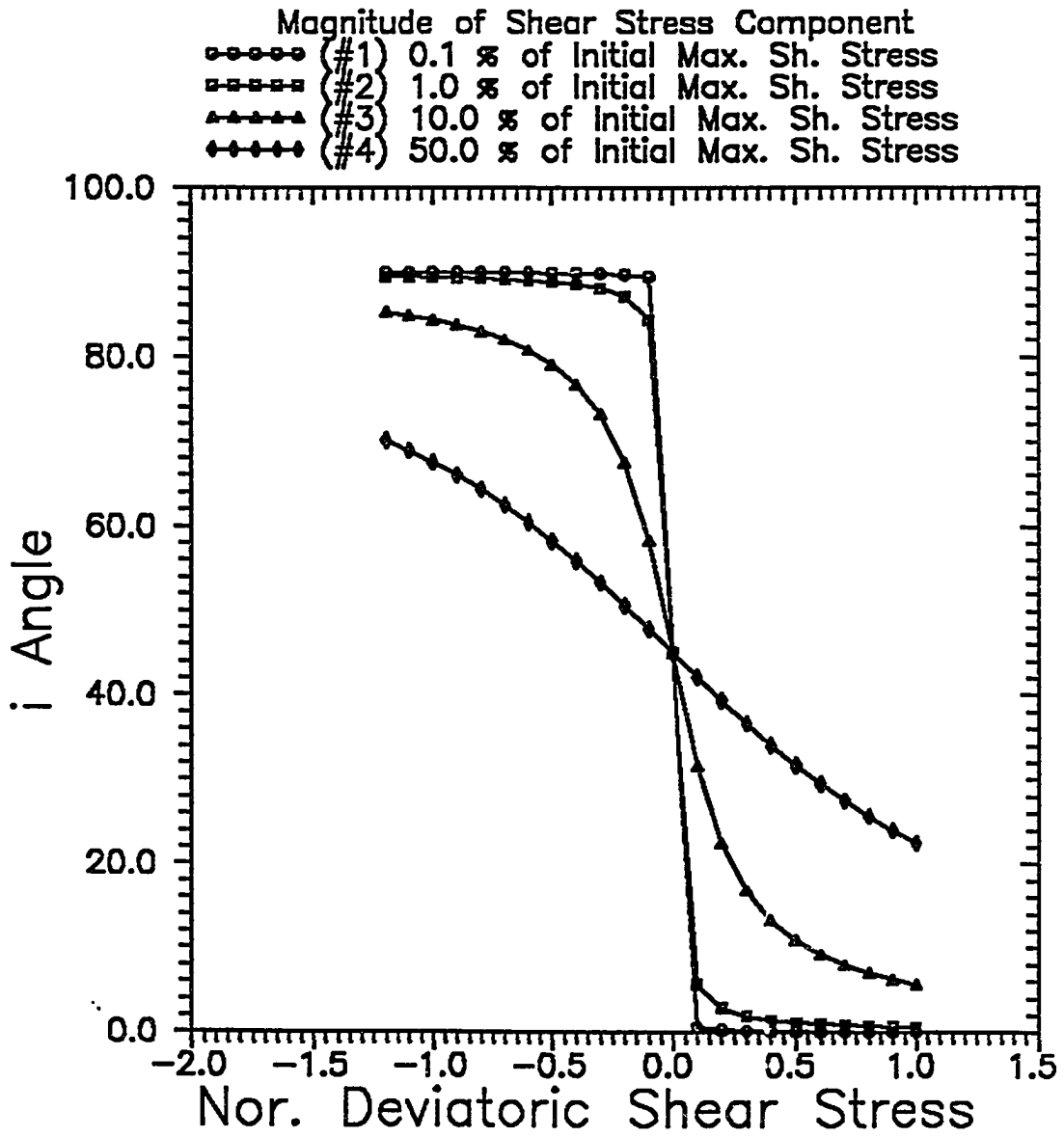


Fig. 4.19 Pattern of i angle variations depending on the magnitudes of the shear stress components (τ_{xy})

The i angle of direct simple shear test at failure is not as definite as in the compression and the extension tests and is an intermediate case of them. Fig. 4.20 illustrates i angles at failure in the direct simple shear test for various conditions in which pure shear assumption was used. In the figure, the parameter, ϕ' , is the drained internal friction angle of soil. The maximum i angle which is theoretically attainable in the direct simple shear test is 45 degree when the initial state of stress is isotropic ($K_0=1.0$). It is seen that for cases with $K_0=0.50-0.85$ and $\phi'=20$ degree, which are most frequently encountered values for normally consolidated clays, i angle at failure ranges from 7.0 to 38.0 degree. The direct simple shear data collected from four different clays in this study (Table 3.1 in Section 3.5.5.1.1) show that i angles at failure are very close to 20 degree using the pure shear assumption. Therefore, $i=20$ degree was used as the representative value for the direct simple shear tests during this study.

In this section, an attempt has been made to correlate the typical laboratory testings with i angle variation, and the resulting stress-strain relations have been viewed as a consequence of the i angle variation at failure. Therefore, for a given i angle, corresponding unique stress-strain relation can be interpolated. The detailed description of the interpolation will be given in the following.

4.2.2.2 Stress-Strain Modelling in the Active Region

The laboratory testings in the category of the active mode with available data are the plane strain compression and the direct simple shear tests. A curve-

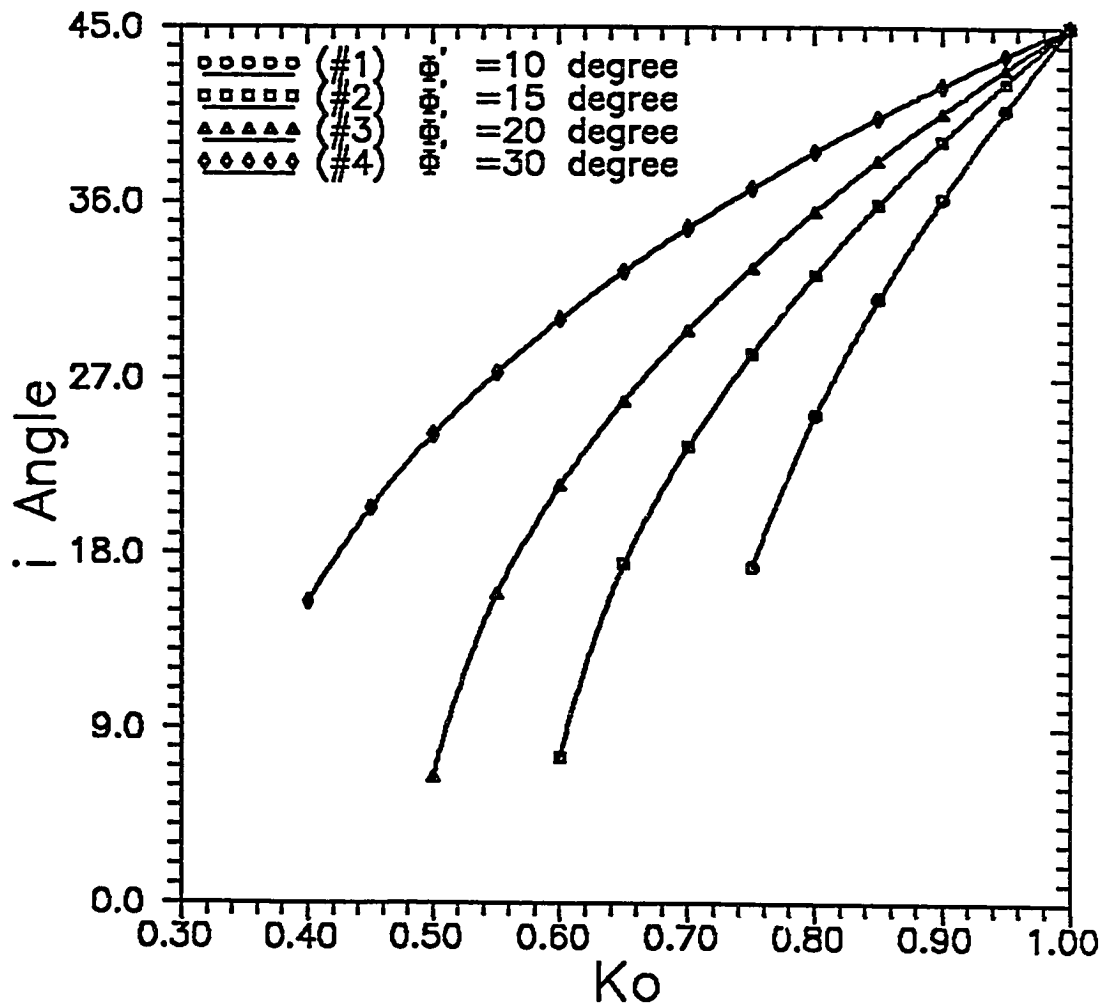


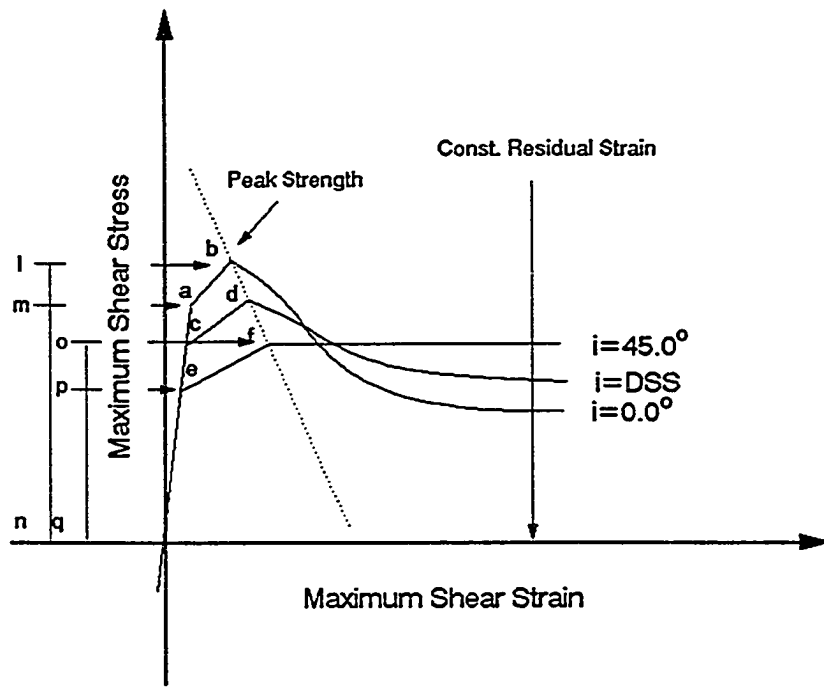
Fig. 4.20 i angles at failure in direct simple shear test using the pure shear assumption

fitting method is used to model the stress-strain curves for these cases.

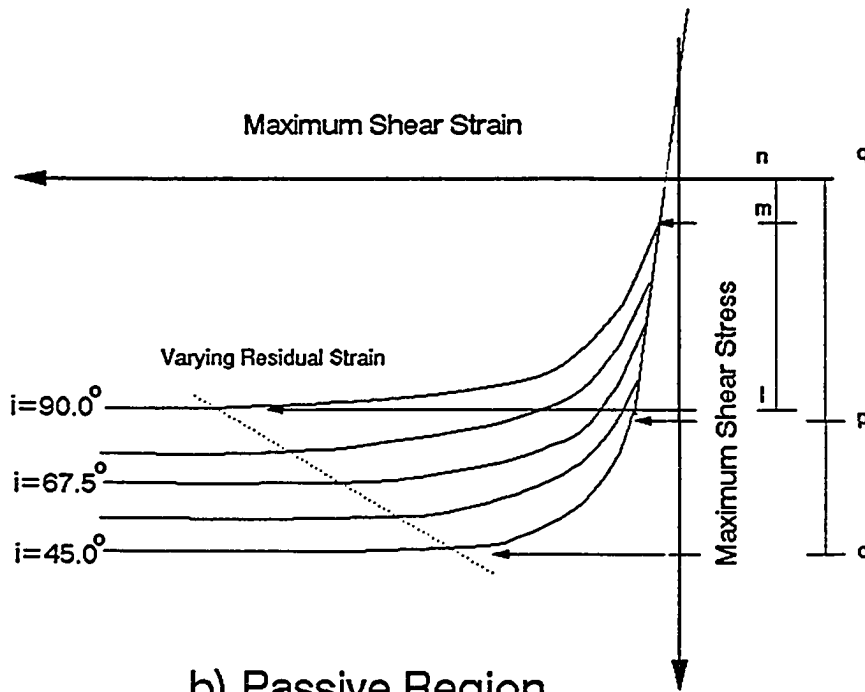
Subsequently, the procedure for determining the stress-strain curve for any varying i angle at the incipient failure ranging from 0 to 45 degrees is described in the following.

It has been observed that the stress-strain curve for the plane strain compression test is characterized by a combination of the peak strength at a small strain (about 1.5% of maximum shear strain) and a pronounced softening in the post peak region. The elastic shear modulus which is used in the current analysis is too high to meet the peak strength at the desired failure strain level. Thus, the element under the compression mode of loading ($i=0^\circ$) is designed to behave elastically up to a certain percentage (e.g., $m_n/\ln=0.85$ in Fig. 4.21a) of the peak undrained strength (e.g., up to point "a"). Then, the element undergoes plastic yielding with the strength increment (strain hardening) to point "b" as a linear function of the plastic strain.

In the post peak region, the strength is modelled to remain constant or to reduce with the plastic shear strain increment depending on the type of analysis. For the softening model, the reduction of the strength continues down to the residual strength at a large strain. The pattern of softening behavior of soil in the post peak region is conveniently described by (a) the degree of softening (the ratio of the residual strength to the peak strength) and (b) the rate of softening (the slope of softening in the stress-strain curve). In order to match the softening pattern in the post peak region, following equations suggested by Vermeer and



a) Active Region



b) Passive Region

Fig. 4.21 Stress-strain modelling (a) Active region and (b) Passive region

Borst (1984) are used, in which two parameters, c_r and ϵ_c , are introduced to vary the degree of softening and the rate of softening, respectively.

$$c = c_r + (c_p - c_r) \exp\left[-\left(\frac{\bar{\epsilon}_p}{\epsilon_c}\right)^2\right] \quad \text{for } \bar{\epsilon}_p < 2.5 \epsilon_c \quad (4.3)$$

$$c = c_r \quad \text{for } \bar{\epsilon}_p > 2.5 \epsilon_c \quad (4.4)$$

where c is the mobilized cohesion, c_p is the peak cohesion, c_r is the residual cohesion, $\bar{\epsilon}_p$ is the plastic shear strain, and ϵ_c is a constant strain parameter controlling the rate of softening behavior. Fig. 4.22 shows softening patterns for a number of different constant strain parameters. In the figure it is clearly shown that a smaller parameter (ϵ_c) results in a faster reduction of the cohesions. It can be observed in the equation that the reduction of the cohesion completes when the total plastic strains reach about 2.5 times the constant strain parameters.

The stress-strain relations of elements for which i angles are greater than 0 degree should be different from that of the compression test ($i=0^\circ$). In the active mode i angle ranges from 0 to 45 degree. It has been noted that the stress-strain pattern varies with the mode of loading such that the strain at the peak stress increases and the degree of softening decreases as i angle increases. It was also found that the softening is most pronounced for the compression case ($i=0^\circ$) and it reduces as i angle increases leading to absolutely no softening at the passive mode. Therefore, it is likely that the degree of softening for $i=45^\circ$ case, which is

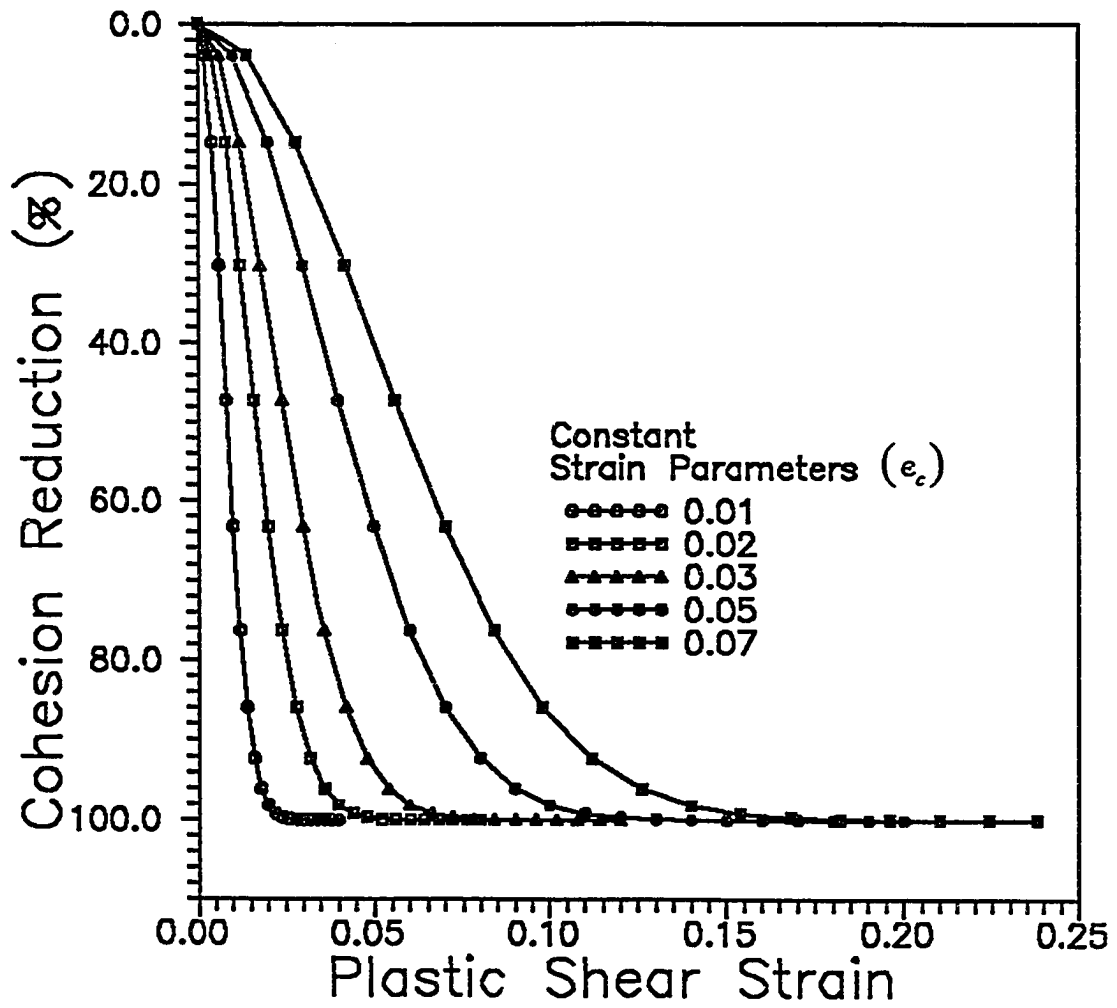


Fig. 4.22 Strain softening pattern depending on the constant strain parameters, e_c

the boundary between the active and the passive modes, is negligible at best. It is assumed that the strain at the peak strength increases linearly from the compression case ($i=0^\circ$) to the direct simple shear case ($i=20^\circ$), which is then continuously extended to the $i=45^\circ$ case (Fig. 4.21a). The peak strength is related to the i angle using Casagrande and Carrillo's curve or its variation (Fig. 3.14 in Section 3.5). As in the compression case, a certain percentage of the peak strength is designed to increase through the plastic yielding (strain hardening). The percentage of strain hardening to the peak strength is also assumed to decrease linearly from the compression case (15.0%) to the direct simple shear case (10.5%), which is then extended to $i=45^\circ$ case (5.0%). Then, for a given i angle among 0° , 20° , and 45° , the slope of hardening and the peak strength can be automatically determined.

Once the three backbone stress-strain curves (i.e., for $i=0^\circ$, 20° and 45°) are established, then it is straightforward to define the remaining stress-strain curve for general angles. It should be noted that the slope of the strength increment during the strain hardening process in the active region is not strictly speaking moduli and has little physical meaning except satisfying the desired strain level at the peak stress. The degree of softening in the post peak region is reduced as a linear function of the peak strength from the compression to $i=45^\circ$ case so that at the boundary case of $i=45^\circ$ perfect plasticity takes over (zero softening). Fig. 4.23a illustrates examples of the stress-strain curves for varying i

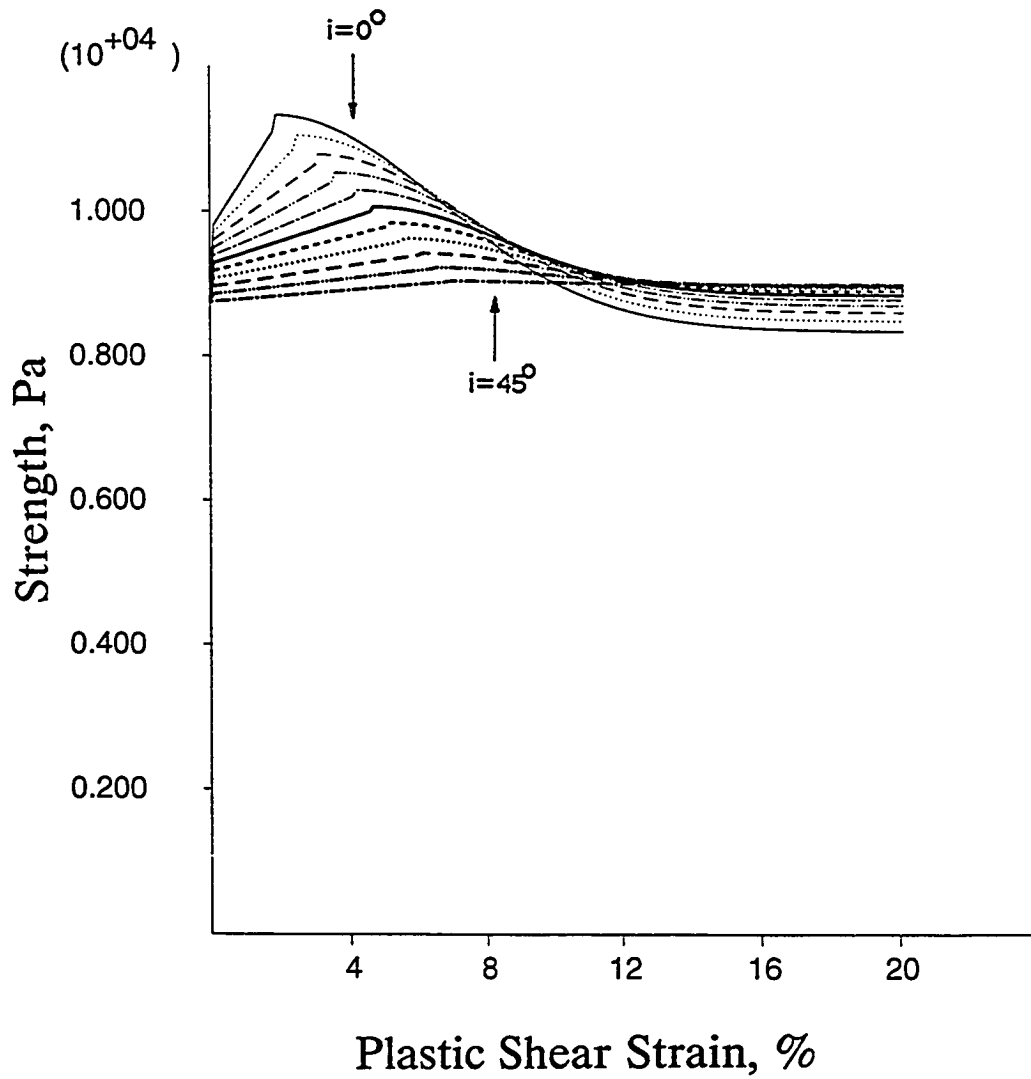


Fig. 4.23a Examples of stress-strain relation: Active region

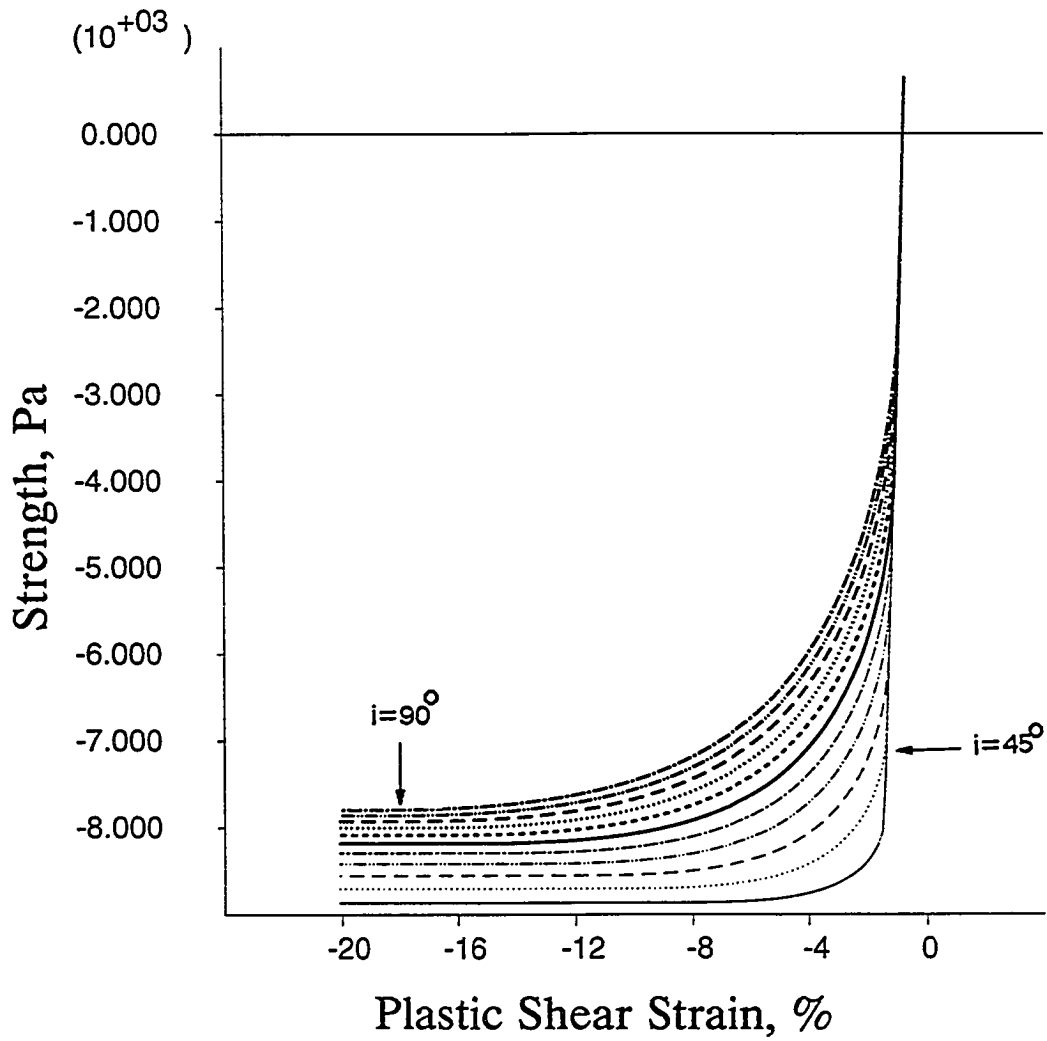


Fig. 4.23b Examples of stress-strain relation: Passive region

angles in the active region for a given consolidation stress. The degree of softening for the compression mode ($i=0^\circ$) was 30% ($(c_p - c_r)/c_p = 0.3$) in this case.

4.2.2.3 Stress-Strain Modelling in the Passive Region

It has been observed that the strain hardening phenomenon is particularly pronounced in the plane strain extension test in which the strength continues to increase with the strain leading to a large strain at the peak strength. In order to match the stress-strain pattern for the elements loaded in the extension mode, only 15.0% of the cohesion (e.g., $mn/\ln = 0.15$ in Fig. 4.21b) based on the experimental data was taken to vary elastically and the remaining 85.0% plastically (strain hardening process). During the plastic deformation, the strength is increased as a function of the plastic strain so that the peak strength is reached at the desired strain level based on the experimental data.

As in the active mode, the strain hardening behavior can also be simulated by increasing the undrained strength using the following equation (Vermeer and Borst, 1984).

$$c = 2 \frac{\sqrt{(\bar{e}_p e_c)}}{\bar{e}_p + e_c} c_p \quad \text{for } \bar{e}_p < e_c \quad (4.5)$$

$$c = c_p \quad \text{for } \bar{e}_p > e_c \quad (4.6)$$

where c_p is the peak cohesion and the $\bar{\epsilon}_p$ and ϵ_c are the plastic strain and the constant strain parameter controlling the hardening pattern, respectively. When the total plastic strain becomes greater than the constant strain parameter, the strain hardening ends and perfectly plastic flow takes over. Fig. 4.24 shows the hardening pattern for a number of constant parameters in which the hardening reaches peaks at the total plastic strain values which equals the constant strain parameters. Therefore, the smaller constant strain parameter will lead to faster hardening process.

In the interpolation of the stress-strain for those elements subjected to modes of loading other than the exact extension ($i=90^\circ$), its pattern is assumed to vary systematically in the passive region. The hardening ratio (the ratio of the strength increase through the plastic flow to the peak strength) and the strain at the peak strength are assumed to vary linearly with respect to the peak strength from $i=45^\circ$ case to the exact extension case of $i=90^\circ$ (Fig. 4.21b). As in the active case, the peak strength is related to i angle using Casagrande and Carrillo's curve or its variations shown in Fig. 3.14 in Section 3.5. It should be noted that the peak strength for $i=45^\circ$ case is the same as that defined in the active region (Fig. 4.21a) and it reaches the peak at the same strain level. Fig. 4.23b illustrates examples of stress-strain relations for varying i angles in the passive region for a given consolidation and initial modulus.

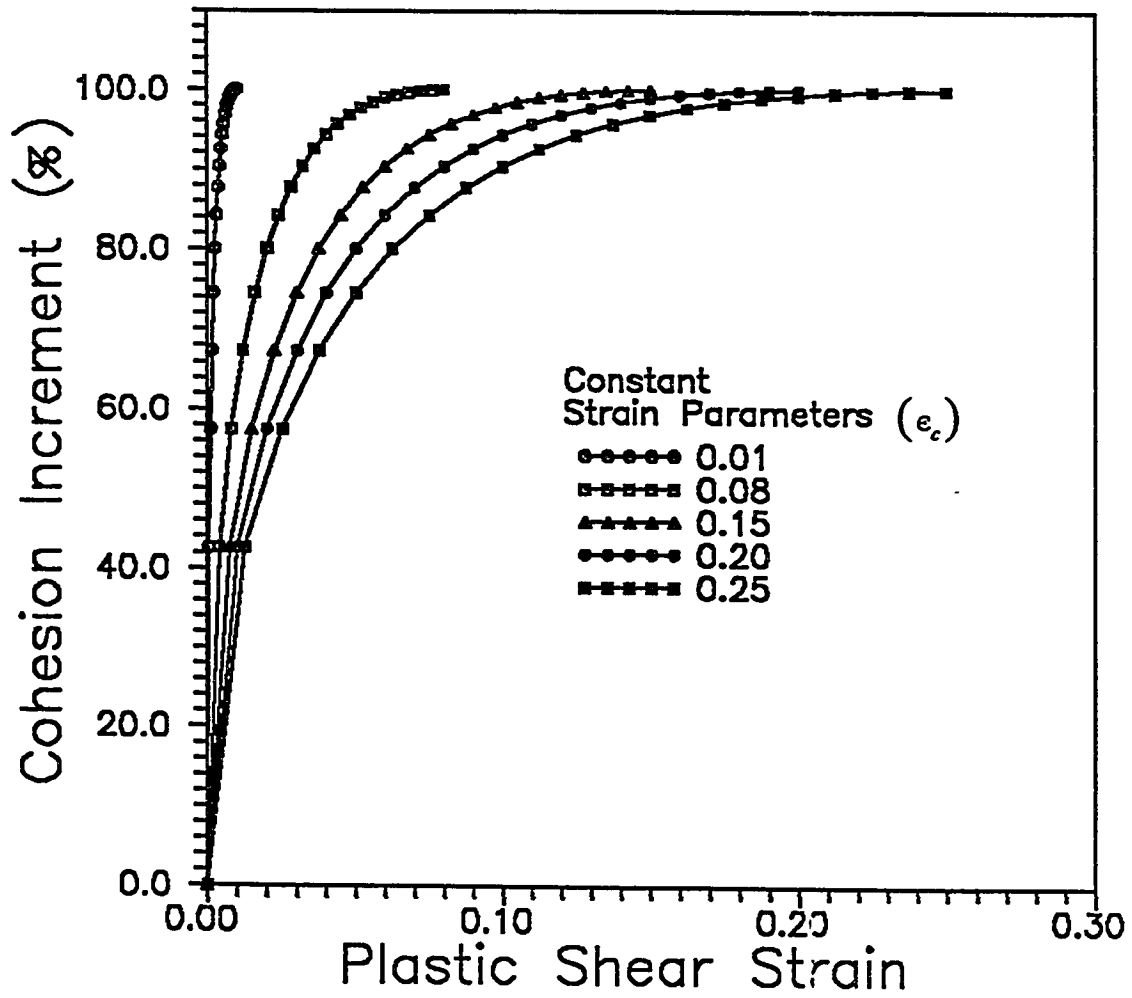


Fig. 4.24 Strain hardening pattern depending on the constant strain parameters, e_c

4.3 Analyses Procedure

4.3.1 Anisotropic Strength Analyses

The stress-strain relation used in the analysis is basically elasto-plastic (Fig. 4.13). Isotropic shear moduli of elements are determined by the consolidation stresses while undrained shear strengths are determined by i angle using predetermined relations between them (Fig. 3.14 in Section 3.5). The procedure in evaluating the anisotropic strength effects are composed of a preliminary analysis and subsequent analyses. Fig. 4.25 shows a flow chart for the anisotropic strength analysis procedure.

The main goal of the preliminary analysis is to determine the representative i angles for the entire elements. Under the level ground, i angles of all elements are initially zero so that every element has the highest shear strength potentials. However, as the excavation proceeds, the horizontal normal stress reduces, the shear stress components are induced on the horizontal plane, and the i angles increase particularly for elements near the slope surface. Once i angle increases, the shear strength that the element can exercise is reduced according to the predetermined relations between i angle and shear strength (e.g., curve number one by Casagrande and Carrillo in Fig. 3.14 in Section 3.5). The computations of i angles are carried out after each block (30 time steps) of computational steps and strengths are reassigned to the entire elements accordingly. The cycle of step computation- i angle computation-strength assignment continues until the incipient failure is encountered in the process of

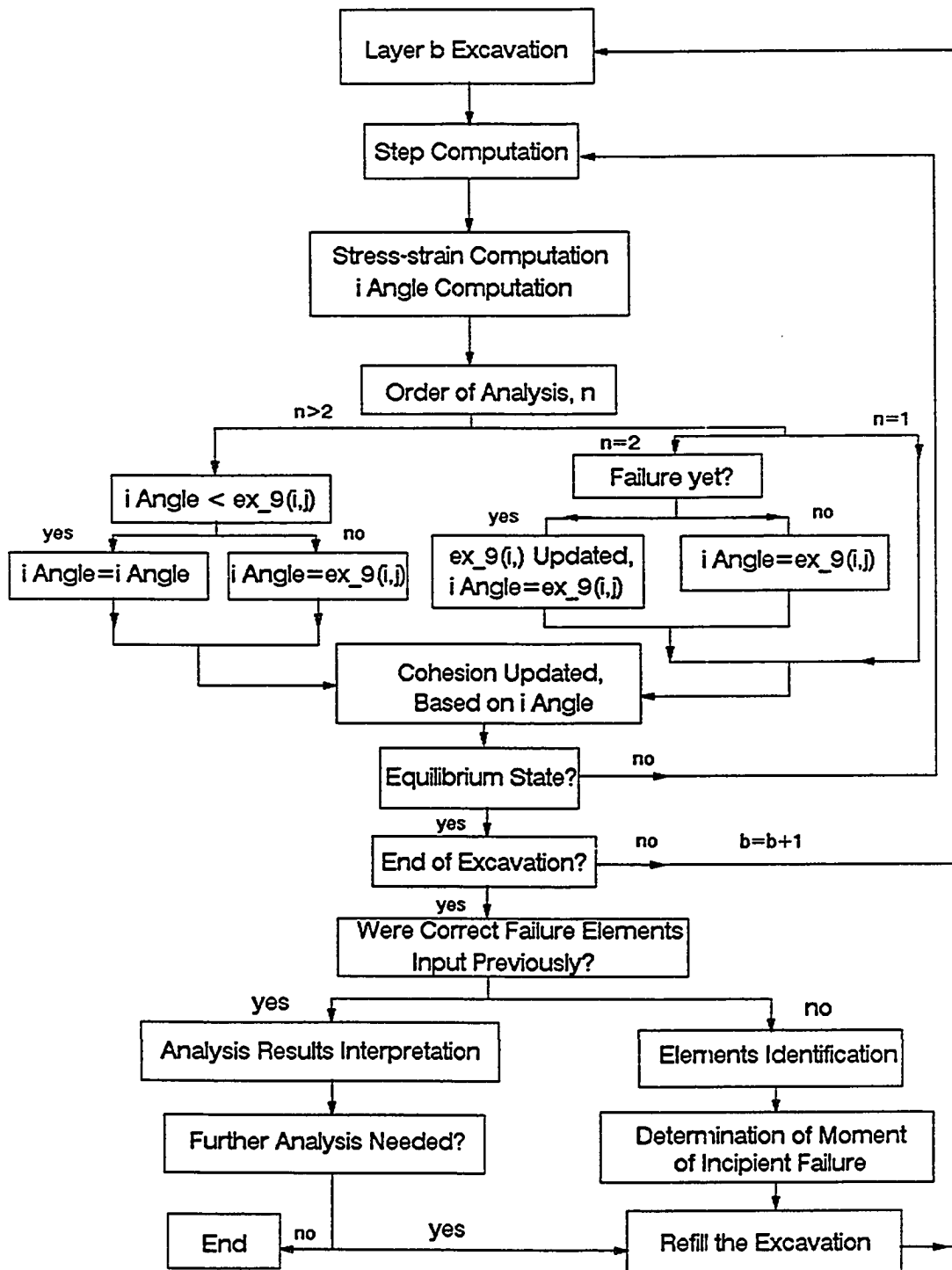


Fig. 4.25 Flow chart for the pseudo-anisotropic strength analysis

layer by layer excavation. Upon reaching the incipient failure state, i angle distribution of the entire elements are saved in an array ($ex_9(i,j)$ appeared in Fig. 4.25 is the array designation). From this point on, the strengths of elements are no longer varied as functions of i angles and the constant values at the failure are continuously used to the end of analysis.

In the subsequent analyses, different relations between the strength and i angle (anisotropic strength curve) are used (Fig. 3.14 in Section 3.5). As in the preliminary analysis, i angles are computed after each block of computational time steps and the corresponding strengths are reassigned to the elements. However, during this analysis the strength reassignments are carried out until the i angles reach the final values determined at the incipient failure in the preliminary analysis. Once an i angle for an element becomes greater than that at the failure ($ex_9(i,j)$), then the strength is fixed at the corresponding value for the i angle. The subsequent analyses are repeated as many as the anisotropic strength curve numbers that are needed to be analyzed. It should be noted here that the i angle distribution for the entire elements are determined by the preliminary analysis in which a particular relation between the strength and i angle (anisotropic strength curve number one) is used. Therefore, it may be argued that the i angle distribution at the state of incipient failure for a given relations between the strength and i angle is not necessarily valid for another. However, it was found that the distributions of i angles for different anisotropic strength curves shown in Fig. 3.14 (Section 3.5) are virtually the same.

After a complete series of analyses (one preliminary analysis and three or four subsequent analyses) with different anisotropic strength curves have been carried out, saved results are analyzed to identify the elements along the most possible failure surface for each analysis. In most cases, the plastic shear strain distribution is sufficient to determine the potential failure surface. Then, the addresses of elements are input in the next series of identical analyses such that various quantities (e.g., local factors of safety, shear strain level, etc.) of the elements are monitored during the subsequent series of analyses.

4.3.2 Anisotropic Strength with Strain Softening Analyses

The preliminary analysis results from the previous pseudo-anisotropic strength analysis are used for the i angle distribution at the incipient failure state for the subsequent series of analyses which are aimed at the evaluation of hardening and softening effects on the stability of slopes. The flow chart for the analysis is shown in Fig. 4.26. It should be noted here that the stress-strain model in the preliminary analysis is pseudo-anisotropic elasto-plastic in which only the strength anisotropy is accounted for. On the other hand, the stress-strain models used in the subsequent series of analyses are a combination of strength anisotropy and strain hardening and softening to be closely fitted to laboratory testing data. It is assumed that i angle distribution in the state of incipient failure in the preliminary analysis is the same for the cases in which the strain hardening and softening model is used with the same anisotropic strength. Then, the

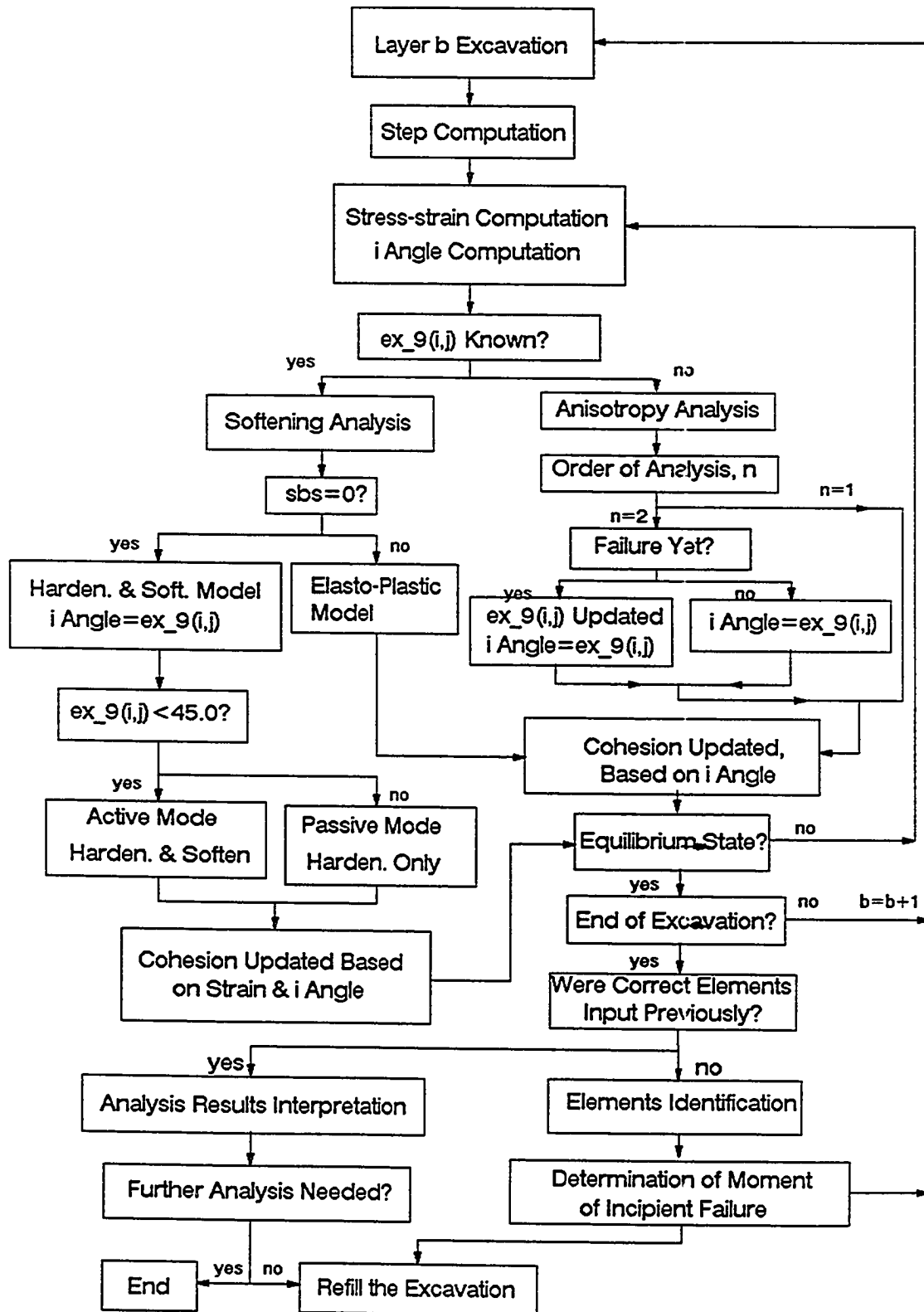


Fig. 4.26 Flow chart for the anisotropic strain hardening/softening analysis

corresponding stress-strain relation for a given element is selected based on the constant i angle and is utilized in the computational process.

It should be noted here that i angles of elements in this series of analyses have already been determined from the preliminary pseudo-anisotropic strength analysis so that corresponding stress-strain-strength relations are directly utilized in the computational process. However, when strengths are fixed especially for the passive elements from the beginning of the excavation, a problem associated with the isotropic constitutive model may arise. In the beginning of the excavation, the maximum shear stresses of the entire elements are positive ($\sigma_v > \sigma_h$) so that they are plotted in the active region (Fig. 4.10). As excavation progresses, the shear stresses of the active elements gradually increase toward the failure envelope in the positive shear stress domain, while those of the passive elements decrease toward the failure envelope in the negative shear stress domain. In the process, it is quite possible that the shear stresses induced in the passive elements still in the positive shear stress domain are higher than the strength levels. In that case, the passive elements begin to yield in the positive shear stress domain leading to erroneous results.

This problem is caused by the use of the isotropic stress-strain model for the anisotropic strength implementation. When a strength is assigned for an element, the computer program accept it as isotropic such that the failure envelopes are equally located from the isotropic state line. Therefore, the element starts to yield whenever the failure condition is satisfied whether it is in

the passive or the active region. In order to keep the passive elements from yielding in the active region, the shear stresses of the passive elements are carefully monitored in the preliminary analysis so that the layer of excavation is caught at which shear stresses of the passive elements are crossing the isotropic states in the process of stress reduction. Then, up to the layer of excavation, the passive elements in the positive shear stress domain should behave elastically without regard to the input strength. To this end, the assignment of corresponding strengths to the ϕ angles are temporarily delayed until the shear stresses of the passive elements moved to the passive region. In the computer program, a parameter called "sbs" is assigned a value 1 or 0. When sbs=0, the strength assignment is delayed to protect the element from yielding. As in the anisotropic strength analyses, elements identified along the failure surface in the first series of analyses are re-input in the second series of analyses to obtain quantities specific to those elements.

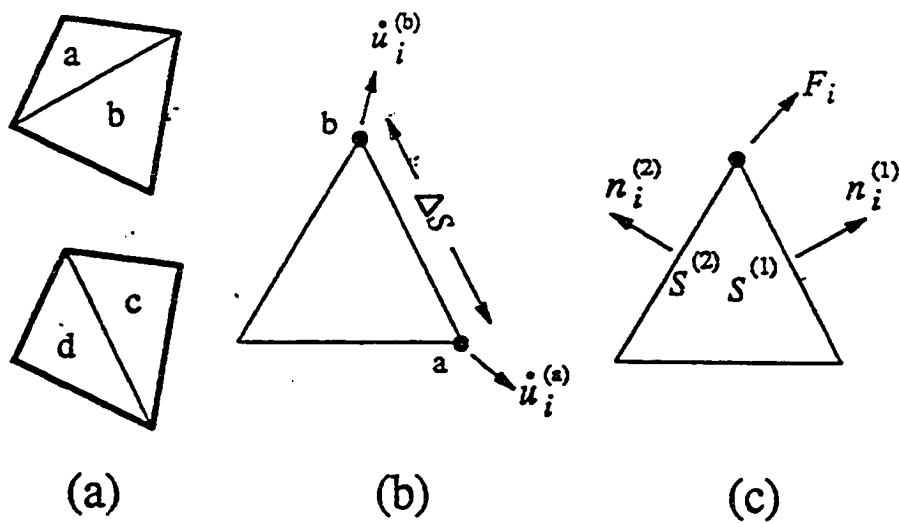
5. EXPLICIT FINITE DIFFERENCE METHOD (FLAC)

5.1 FLAC (Fast Lagrangian Analysis of Continua) Formulation

FLAC models continuum behavior with a formulation derived from finite difference techniques. The formulation is explicit in time, using an updated Lagrangian scheme to account for large strains. FLAC is believed to offer advantages over conventional finite element schemes in cases where flow and material instability can occur (Cundall, 1987). Complete descriptions of the numerical formulation of FLAC are given by Cundall (1989). The constitutive model in FLAC used in this study is the elasto-plastic in which the Mohr-Coulomb yield criteria and the flow rule are used. The description given here is adapted from Cundall (1989).

Each quadrilateral element of FLAC is represented as two overlaid pairs of constant-strain triangles (Fig. 5.1). Each node receives a force vector that is the average of two vectors, one from each overlaid quadrilateral. The response of the composite element is symmetric, in contrast to the response of a single pair of triangles. The difference equations for a generic triangle are derived from Gauss's divergence theorem:

$$\int_S n_i f dS = \int_A \frac{\partial f}{\partial x_i} dA \quad (5.1)$$



(a) *Overlaid quadrilateral elements used in FLAC*
 (b) *Typical triangular element with velocity vectors;*
 (c) *Nodal force vector*

Fig. 5.1 Composition of the finite difference element in FLAC

where S is the path around the element
 A is the element area
 n_i is the outward unit normal vector
 x_i is the position vector, and
 f denotes a scalar, vector, or tensor.

Defining the average value of the derivative over A as

$$\left\langle \frac{\partial f}{\partial x_i} \right\rangle = \frac{1}{A} \int_A \frac{\partial f}{\partial x_i} dA \quad (5.2)$$

the following equation is obtained:

$$\left\langle \frac{\partial f}{\partial x_i} \right\rangle = \frac{1}{A} \int_S n_i f dS \quad (5.3)$$

For a polygon, such as the triangular element shown in Fig. 5.1b, the finite difference formula becomes

$$\left\langle \frac{\partial f}{\partial x_i} \right\rangle = \frac{1}{A} \sum_S \langle f \rangle n_i \Delta S \quad (5.4)$$

where the summation is over the three sides, and $\langle f \rangle$ is the mean value of the scalar, vector or tensor f over a side. This formula enables the strain increments, Δe_{ij}

for a zone, to be written in terms of nodal velocities, by substituting the velocity vector \dot{u}_i for f in Eq. (5.4):

$$\frac{\partial \dot{u}_i}{\partial x_j} = \frac{1}{2A} \sum_s (\dot{u}_i^{(a)} + \dot{u}_i^{(b)}) n_j \Delta S \quad (5.5)$$

$$\Delta e_{ij} = \frac{1}{2} \left[\frac{\partial \dot{u}_i}{\partial x_j} + \frac{\partial \dot{u}_j}{\partial x_i} \right] \Delta t \quad (5.6)$$

where Δt is the time step, and (a) and (b) denote two consecutive nodes on the boundary of the triangle (see Fig. 5.1b).

Element stresses are modified by applying a standard elastic-plastic, Mohr-Coulomb constitutive model M with non-associated flow rule:

$$\sigma_{ij} := M(\sigma_{ij}, \Delta e_{ij}) \quad (5.7)$$

When stresses in all elements have been recalculated, nodal forces are summed from all surrounding elements. A typical expression is given below for the force on one node of the triangle shown in Fig. 5.1:

$$F_i = \frac{1}{2} \sigma_{ij} (n_j^{(1)} S^{(1)} + n_j^{(2)} S^{(2)}) \quad (5.8)$$

where S is the length of the boundary segment over which the stress σ_{ij} acts.

The summation of all such forces acting on a node is used to derive an acceleration that is integrated by central finite differences to provide new velocities:

$$\dot{u}_i^{(t+\Delta t/2)} = \dot{u}_i^{(t-\Delta t/2)} + [\Sigma F_i^{(t)} - \alpha \{\Sigma F_i^{(t)}\} \text{sign}(\dot{u}^i)] \frac{\Delta t}{m} + g_i \Delta t \quad (5.9)$$

where m =inertial mass of the node,

α =damping factor, and

g_i =gravitational acceleration.

Note that the damping force vanishes for steady flow and at equilibrium.

Equations 5 to 7 are evaluated for all elements and then Eqs. 8 and 9 are evaluated for all nodes. This cycle is repeated until equilibrium state is reached for each perturbation such as a layer of excavation. Since the scheme is an explicit one, no sub-iterations are necessary when applying the constitutive model (Eq. 7).

The explicit solution procedure is conditionally stable; the speed of the calculation front must be larger than the maximum speed at which information propagates. A time step must be chosen that is smaller than some critical time step. The stability condition for an elastic discretized into elements of size Δx is

$$\Delta t < \Delta x/C \quad (5.10)$$

where C is the maximum speed at which information can propagate (typically, the p wave speed).

5.2 Mohr-Coulomb Plasticity Model

5.2.1 Yield Criteria

Both shear and volumetric yield surfaces are formulated in three-dimensional terms, with the out-of-plane stress, σ_z , being taken as a principal stress. The shear yield surface corresponds to the Mohr-Coulomb criterion in which only the major and minor principal stresses are active in the formulation and the intermediate principal stress has no effect. The Cartesian stress components are resolved into principal stresses, and ordered so that $\sigma_1 < \sigma_2 < \sigma_3$. It should be recalled that compressive stresses are negative, so that σ_1 is the major principal compressive stress. The shear yield function f_s is:

$$f_s = \sigma_1 - \sigma_3 N_\phi + 2c\sqrt{N_\phi} \quad (5.11)$$

where $N_\phi = (1+\sin\phi)/(1-\sin\phi)$. In the equation, ϕ is the friction angle and c is the cohesion. Shear yield is detected if $f_s < 0$. In this case, plastic flow is allowed to occur in order to restore the condition $f_s = 0$. The volumetric yield function is:

$$f_v = \frac{1}{3}(\sigma_1 + \sigma_2 + \sigma_3) + p_c \quad (5.12)$$

where p_c is the cap pressure, which is the current location of the volumetric yield surface. Volumetric yield is detected if $f_v < 0$.

5.2.2 Flow Rule

In what follows, it is assumed that elastic stress increments have been computed, and that both the shear and the volumetric yield conditions are exceeded. The usual assumption is made that the overall strain increment of an element can be decomposed into elastic and plastic parts and, further, it is assumed that the plastic contributions of shear and volumetric yielding are additive. The principal axes of both plastic and elastic strain increments are taken to be coaxial with the principal axes of stress (only valid if elastic shear strains are small compared to plastic strains), and the maximum shear strain increments obtained are:

$$\Delta e_i = \Delta e_i^e + \Delta e_i^{ps} + \Delta e_i^{pv} \quad (5.13)$$

where $i = 1, 3$ and superscripts ps and pv stand for plastic shear and plastic volume, respectively. The flow rules for shear and volumetric yielding are:

$$\Delta e_i^{ps} = \lambda_s \frac{\partial g_s}{\partial \sigma_i}, \quad \Delta e_i^{pv} = \lambda_v \frac{\partial f_v}{\partial \sigma_i} \quad (5.14)$$

It can be shown that the volumetric flow rule is associated and the shear flow rule is non-associated. The plastic potential for shear yielding is :

$$g_s = \sigma_1 - \sigma_3 N_\varphi + 2c\sqrt{N_\varphi} \quad (5.15)$$

where $N_\varphi = (1+\sin\varphi)/(1-\sin\varphi)$, and φ is the dilation angle. Differentiating Eqs.

12 and 15 with respect to σ_i , and substituting in Eqs. 14 and 13,

$$\begin{aligned}\Delta e_1 &= \Delta e_1^e + \lambda_s + \lambda_v/3 \\ \Delta e_2 &= \Delta e_2^e + \lambda_v/3 \\ \Delta e_3 &= \Delta e_3^e - \lambda_s N\varphi + \lambda_v/3\end{aligned}\tag{5.16}$$

The multipliers, λ_s and λ_v , can be determined using the fact that stress increments $\sigma_i' - \sigma_i^o$ are related to the elastic strain increments Δe_i^e by the elasticity equations:

$$\begin{aligned}\sigma_1' &= \sigma_1^o + A\Delta e_1^e + B(\Delta e_2^e + \Delta e_3^e) \\ \sigma_2' &= \sigma_2^o + A\Delta e_2^e + B(\Delta e_1^e + \Delta e_3^e) \\ \sigma_3' &= \sigma_3^o + A\Delta e_3^e + B(\Delta e_1^e + \Delta e_2^e)\end{aligned}\tag{5.17}$$

where $A = K + 4G/3$ and $B = K - 2G/3$.

In addition, initial estimate of the new stresses (before testing for yield) were also derived from the applied strain increments and the same elasticity relations:

$$\begin{aligned}\sigma_1^I &= \sigma_1^o + A\Delta e_1 + B(\Delta e_2 + \Delta e_3) \\ \sigma_2^I &= \sigma_2^o + A\Delta e_2 + B(\Delta e_1 + \Delta e_3) \\ \sigma_3^I &= \sigma_3^o + A\Delta e_3 + B(\Delta e_1 + \Delta e_2)\end{aligned}\tag{5.18}$$

Substituting Δe_i^e from Eq. 16 into Eq. 17 and replacing Δe_i from Eq. 18, we obtain, after some rearrangement,

$$\begin{aligned}
\sigma_1' &= \sigma_1^I - \lambda_s(A - BN_\phi) - \lambda_v K \\
\sigma_2' &= \sigma_2^I - B\lambda_s(A - N_\phi) - \lambda_v K \\
\sigma_3' &= \sigma_3^I - \lambda_s(B - AN_\phi) - \lambda_v K
\end{aligned} \tag{5.19}$$

Finally, we note that if yielding occurs, the final stresses (σ_i') must lie on both yield surface; i.e., $f_s = 0$ and $f_v = 0$. Substituting Eq. 19 into Eqs. 11 and 12, and solving for λ_s and λ_v ,

$$\lambda_s = \frac{f_s^I - f_v^I(1 - N_\phi)}{A - BN_\phi - BN_\phi + AN_\phi N_\phi - K(1 - N_\phi)(1 - N_\phi)} \tag{5.20}$$

$$\lambda_v = \frac{f_v^I}{K} - \lambda_s(1 - N_\phi) \tag{5.21}$$

In these equations, the notation f^I stands for the function f evaluated for the initial trial stresses. Equations 20 and 21 can now be used to evaluate the new stresses from Eq. 19 and these stresses simultaneously satisfy both yield conditions and flow rules.

5.2.3 Strain Softening/Hardening Implementation

Both yield surfaces can harden (or soften) according to hardening rules that are specified by look-up tables. Entry to the tables is by hardening

parameters that record some measure of accumulated plastic strain. In shear, the hardening parameter is

$$\Delta e^{ps} = \left[\frac{1}{2}(\Delta e_1^{ps} - \Delta e_m^{ps})^2 + \frac{1}{2}(\Delta e_m^{ps})^2 + \frac{1}{2}(\Delta e_3^{ps} - \Delta e_m^{ps})^2 \right]^{\frac{1}{2}} \quad (5.22)$$

where $\Delta e_m^{ps} = \frac{1}{3}(\Delta e_1^{ps} + \Delta e_3^{ps})$. In the volumetric direction, the hardening

parameter is

$$\Delta e^{pv} = |\Delta e_1^{pv} + \Delta e_2^{pv} + \Delta e_3^{pv}| \quad (5.23)$$

These hardening parameters are used in look-up tables to determine new values of friction, cohesion, dilation or cap pressure. The new parameters are only updated after the plastic calculations are done and the hardening or softening thus lags one time step behind the corresponding plastic flow. In an explicit code, this error is small because the time steps are small.

6 SLOPE STABILITY ANALYSIS USING FLAC

6.1 Classification of Analyses Based on Material Types

Slope analyses were carried out on two types of materials based on the stress history: (a) normally consolidated clay and (b) overconsolidated clay. Normally consolidated clay is further classified into two types in which the undrained strength is homogeneous and linearly increasing with depth. On each type of the material, four different stress-strain relations are used as shown in

Table 6.1 Analysis classification based on stress-strain relations

Symbol	Stress-strain relations
A	Isotropic elasto-plastic
B	Anisotropic elasto-plastic
C	Anisotropic elasto-plastic strain hardening/softening
D	Anisotropic elasto-plastic strain hardening/softening (brittle)

Table 6.1. The first analysis (A) is the same as the conventional analysis in which isotropic elasto-plastic model is utilized without regard to the stress path. The second analysis (B) is carried out using the pseudo-anisotropic elasto-plastic model in which anisotropic strength is explicitly addressed. The third analysis (C) uses a material model which is basically elasto-plastic for a given computational time step but is strain hardening/softening for the global stress-strain relations as

discussed in detail in Section 4.2.2.2. The residual strengths of active elements are designed to be reached at a unique maximum shear strain level of 18.6% based on the laboratory testing data. The last analysis (D) is the same as the third analysis (C), but the active elements are designed to reach residual strengths in an increasing strain level from 6.0% for $i=0^\circ$ case to 18.6% for $i=45^\circ$ case. This case is to represent the brittle behavior of soil particularly for elements with low i angles. The brittle behavior is particularly possible for sensitive clay in which intact clay structure is carefully maintained prior to shearing in the laboratory tests.

The analysis codes B, C and D shown in Table 6.1 is further classified based on the undrained strength variation with i angle and the degree of strain softening as shown in Tables 6.2 and 6.3, respectively. In Section 3.5.3.3 four different undrained strength relations with i angle, termed anisotropic strength curves, have been defined using the suggestion made by Casagrande and Carrillo (1944) and its slight modification (Fig. 3.14 in Section 3.5). The degree of softening has also been defined as the ratio of the residual strength to the peak strength in Section 4.2.2.2. In C and D analyses, the maximum degree of strain softening for $i=0^\circ$ element is varied (0%, 15% and 30%) to measure the net effects of strain softening with exactly the same stress-strain relations up to the peak stress. Note that the degree of strain softening decreases from $i=0^\circ$ element to $i=45^\circ$ element as a linear function of i angle such that it vanishes at $i=45^\circ$

Table 6.2 Analysis classification based on the strength anisotropy variation.

Symbol	Anisotropic strength curve number (Fig. 3.14 in Section 3.5)
1	Curve number one
2	Curve number two
3	Curve number three
4	Curve number four

Table 6.3 Analysis classification based on the degree of strain softening.

Symbol	Degree of strain softening
a	0%
b	15%
c	30%
d	60%

element. In order to simulate the drastic strength drop for highly brittle soil, extremely high degree of strain softening, 60% (case d), is utilized only for overconsolidated clay.

A complete code to represent the type of analysis consists of a single letter for A analysis, two letters for B analysis (i.e., no softening) and three letters for C and D analyses. For example, code C-2-a represents the case in which anisotropic elasto-plastic strain hardening/softening model (C) is used with anisotropic strength curve number two (2) and 0% strain softening (a) for element with $i=0^\circ$. Table 6.4 shows the summary of FLAC analyses covered in this study.

6.2 Normally Consolidated Clay

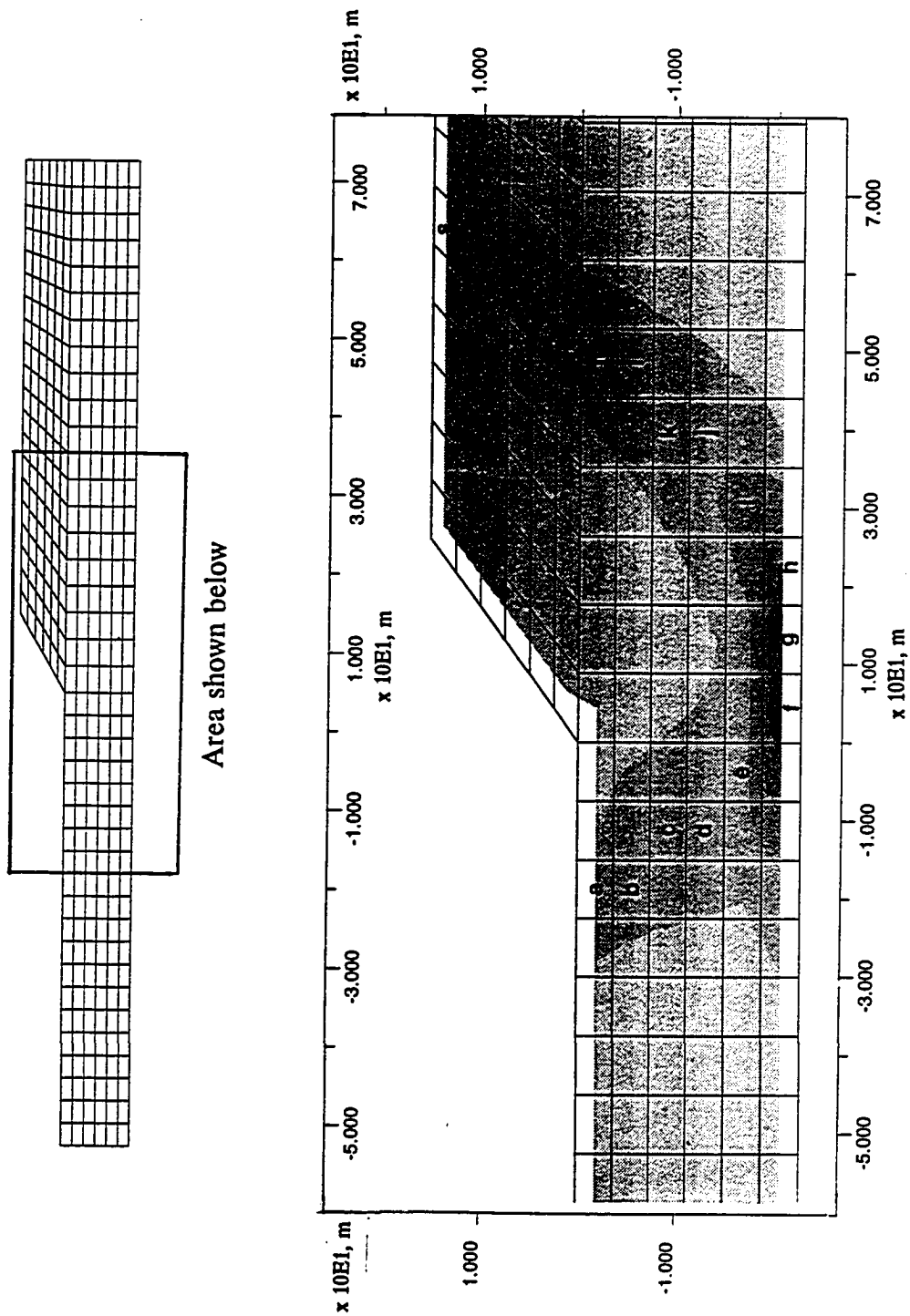
6.2.1 Homogeneous Strength Profile

This type of material represents the case in which the undrained strength is homogeneous with depth. In normally consolidated clay, when the rate of strength increase with depth is negligible, the strength can be conveniently

Table 6.4 Summary of FLAC analyses

Material type	Strength profile	Slope inclination angle, degree	Analyses types
Normally consolidated clay	Homogeneous	30	A, B, C, D
	Linear increase with depth	30	A, B, C, D
		60	A, B, C, D
Over consolidated clay	Function of OCR	60	A, B, C, D

assumed to be constant along the depth. Then the computation becomes simple and the fast evaluation of slope stability is possible since complete analytical solutions exist. A slope of 30 degree inclination angle was analyzed in the process of layer by layer excavation from the initial level ground to the final excavation height of 15.0 meters. The excavation heights corresponding to the number of excavation layer are summarized in Table 6.5. The constant undrained strength was 36304.2 Pa, the total unit weight of soil was 14935.0 N/m³, and K_o was 0.85. The finite difference grid at the final excavation is shown in Fig. 6.1 with element identification along the failure surface. The lateral boundaries were conservatively chosen to minimize the boundary interference. The bottom



Area shown below

Fig. 6.1 Finite difference mesh

boundary represents the firm base in the soil profile. The lateral boundaries are rollers and the bottom is fixed against any displacement.

6.2.1.1 Isotropic Strength Case (A Analysis)

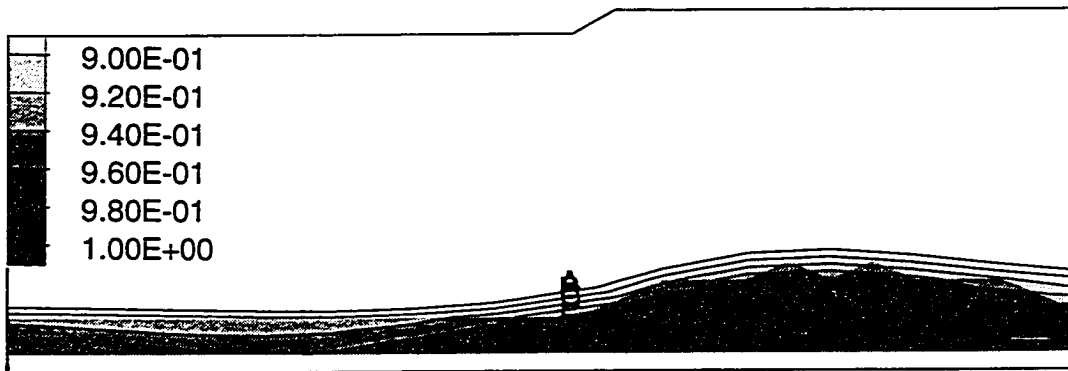
The slope failure mechanism can be understood by examining the nonuniform stress/strain distributions in the slope. The stress distribution in the

Table 6.5 Summary of excavation heights with number of layer excavation

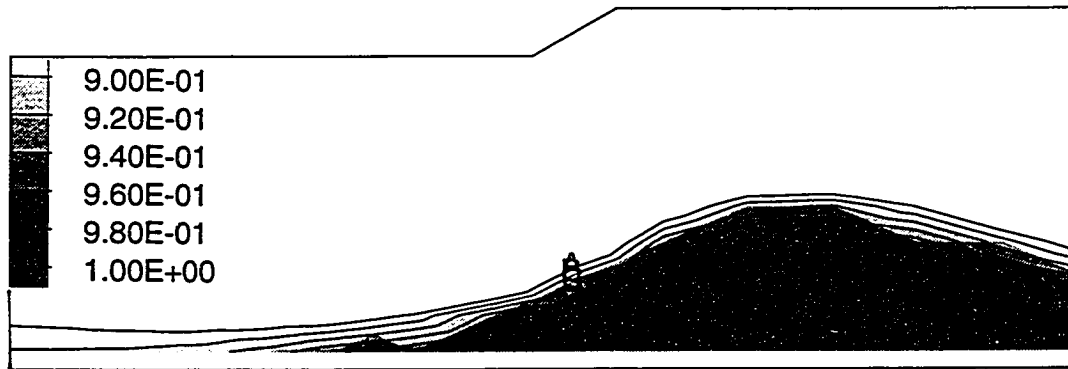
No. of excavation	1st	2nd	3rd	4th	5th	6th
Excavation height, meters	2.50	5.00	7.50	10.00	12.50	15.00

slope of constant strength profile is far from uniform and the zone of overstress is located at the bottom of the slope. The zone of overstress may be regarded as the zone in which the mobilized maximum shear stress ratios (τ_{\max}/S_u) are in excess of the average. The maximum shear stresses at the both ends of a potential failure surface are very low in comparison to that at the interior section. Therefore, failure usually commences within the soil mass and propagates towards the ends of the failure surface.

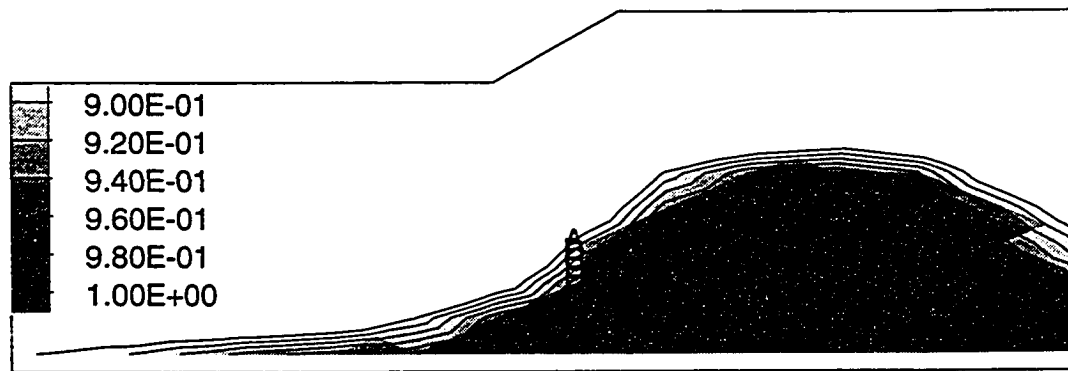
The nonuniform maximum shear stress distribution in the slope throughout the entire excavation process can be seen in Figs. 6.2a through 6.2f. At the first layer excavation (Fig. 6.2a), the high concentration of maximum shear stress starts to develop at the bottom of the model especially below the crest. The overstressed zone is gradually expanding toward the crest as the excavation continues



(a) 1st layer ($H_{ox} = 2.50$ m); Contour Interval = $2.0E-02$ (A: $9.00E-01$, E: $9.80E-01$)

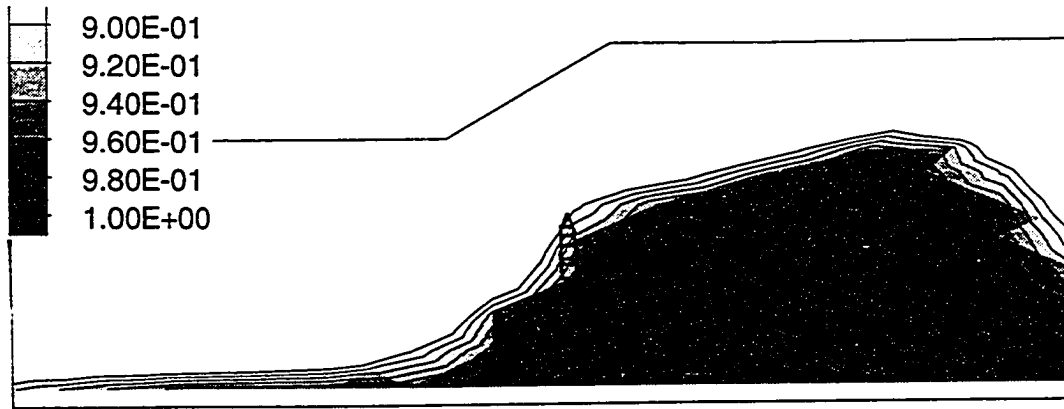


(b) 2nd layer ($H_{ox} = 5.00$ m); Contour Interval = $2.0E-02$ (A: $9.00E-01$, E: $9.80E-01$)

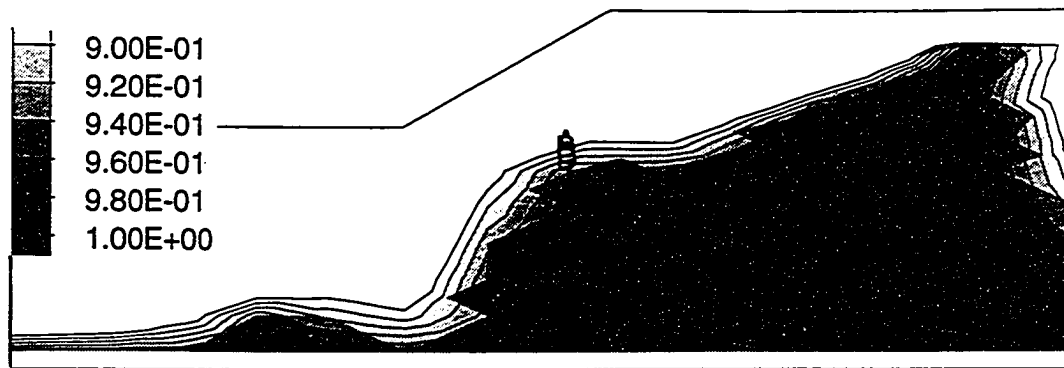


(c) 3rd layer ($H_{ox} = 7.50$ m); Contour Interval = $2.0E-02$ (A: $9.00E-01$, E: $9.80E-01$)

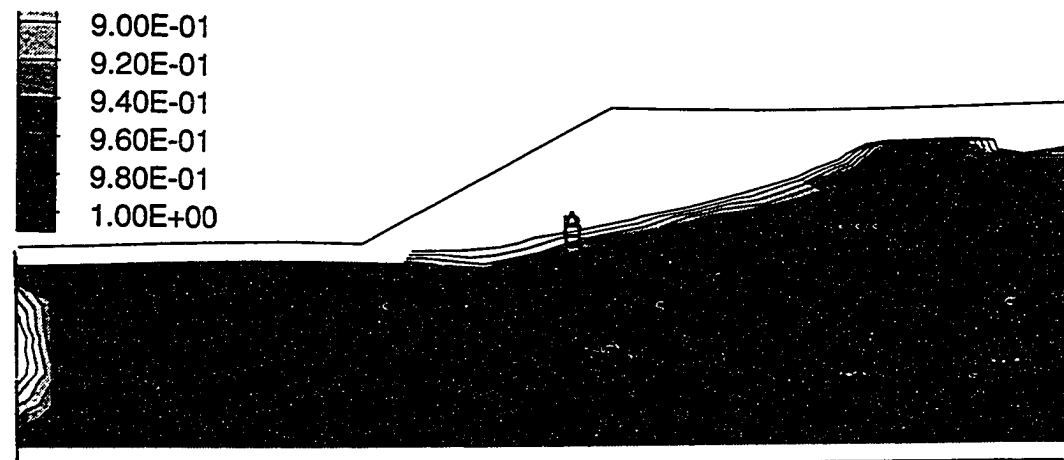
Fig. 6.2 Maximum shear stress ratio (τ_{max}/S_u) distribution, A analysis
189



(d) 4th layer ($H_{ex} = 10.0$ m); Contour Interval = $2.0E-02$ (A: $9.00E-01$, E: $9.80E-01$)



(e) 5th layer ($H_{ex} = 12.5$ m); Contour Interval = $2.0E-02$ (A: $9.00E-01$, E: $9.80E-01$)

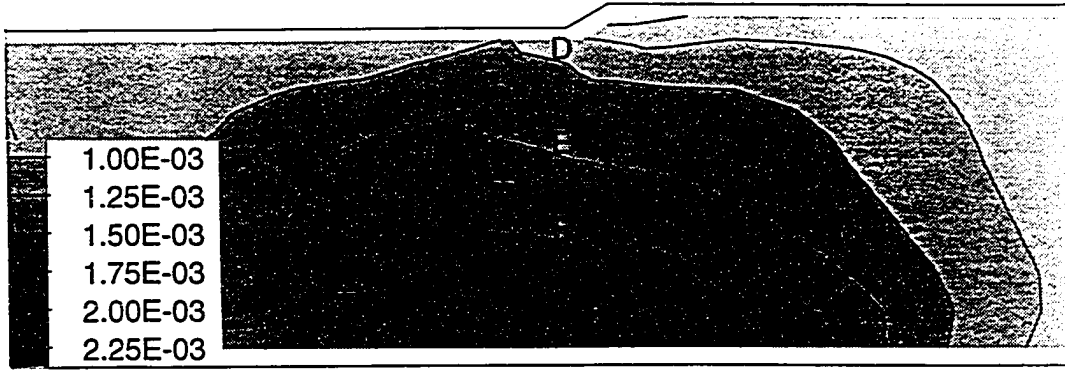


(f) 6th layer ($H_{ex} = 15.0$ m); Contour Interval = $2.0E-02$ (A: $9.00E-01$, E: $9.80E-01$)

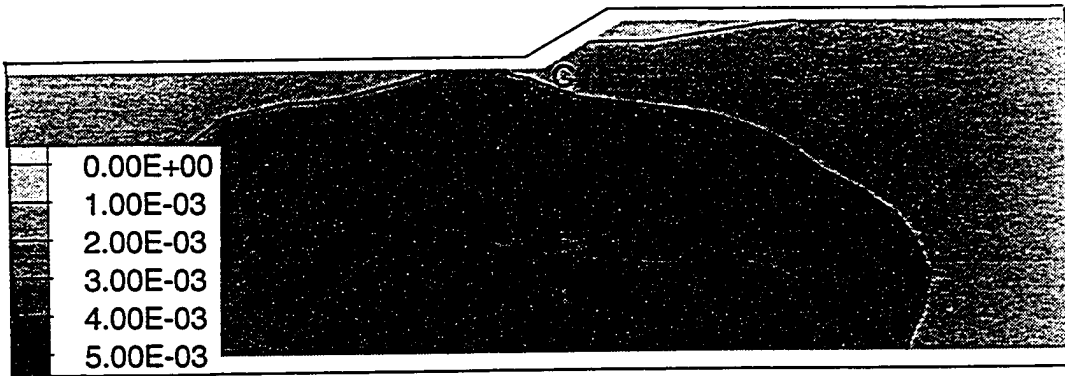
Fig. 6.2 Maximum shear stress ratio (τ_{max}/S_u) distribution, A analysis

(Figs. 6.2b through 6.2d). At the fifth layer excavation (Fig. 6.2e), the over-stressed zone reaches near the top of the crest. The reason that the zone is not fully expanded to the crest in Fig. 6.2e is because the top layer has already been failed by tension. Note that when the element is failed by tension, then it can no longer take stress anymore so that the mobilized maximum shear stress ratios (τ_{\max}/S_u) are usually very low for the element. Once the over-stressed zone is expanded to the crest, the remaining elastic zone near the excavated bottom is the next area to be stressed. Consequently, at the last layer excavation, the whole region below the slope is in yielding (Fig. 6.2f). It is clearly seen that the failure first propagates from the bottom layer to the crest and subsequently from the bottom layer to the bottom of the excavation.

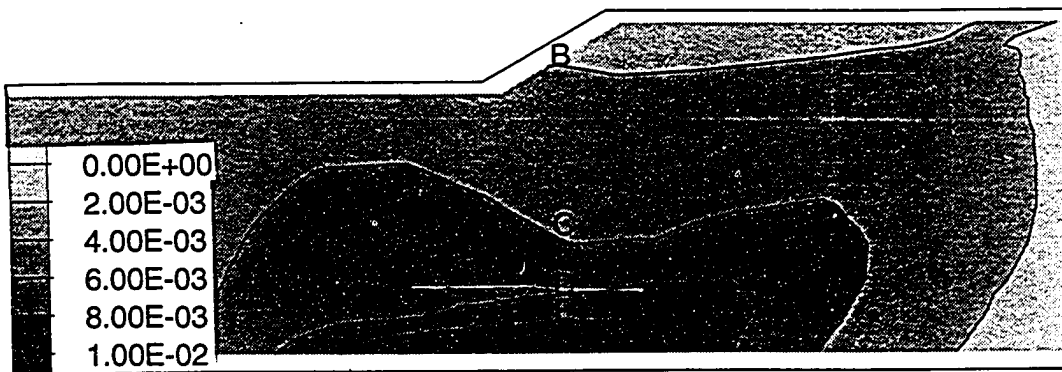
The nonuniform maximum shear strain development in the slope excavation process can be seen in Figs. 6.3a through 6.3f. The maximum shear strain has been defined as the summation of the elastic shear strain and the plastic shear strain (the plastic volumetric strain is zero in the undrained strength analysis) in Section 4.2.2. As has been observed in the maximum shear stress distribution, the maximum shear strain starts to develop from the bottom of the model and gradually increases toward the both sides. It is seen that the highly strained region remains in the bottom of the model (contained failure) up to the fifth layer excavation (Fig. 6.3e), which is finally expanded to the crest as well as the toe of the slope at the final layer (6th) of excavation (Fig. 6.3f). The sequence of failure propagation is not as clear as in the stress development



(a) 1st layer ($H_{ox} = 2.50$ m); Contour Interval = $2.5E-04$ (D: $1.00E-03$, I: $2.25E-03$)

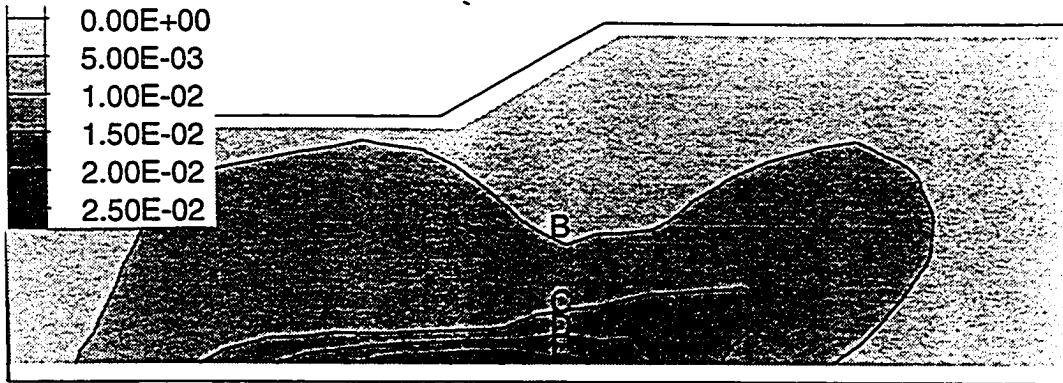


(b) 2nd layer ($H_{ox} = 5.00$ m); Contour Interval = $1.0E-03$ (C: $2.00E-03$, F: $5.00E-03$)

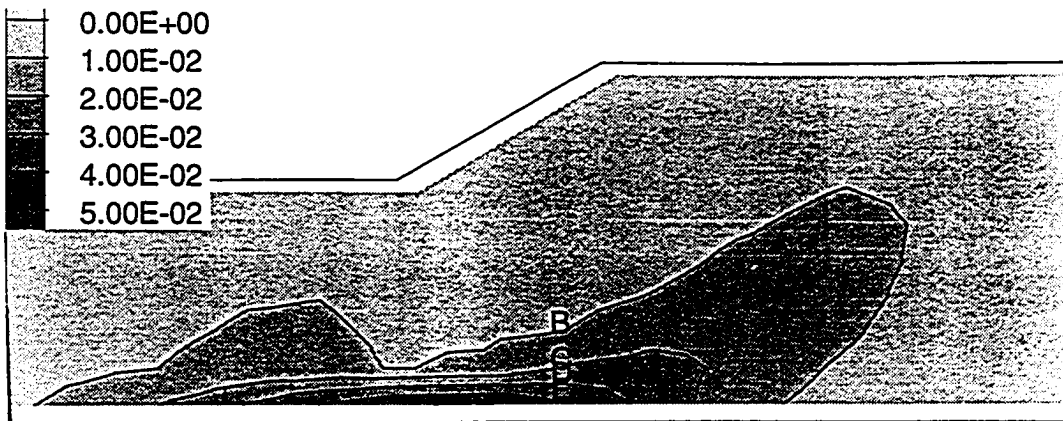


(c) 3rd layer ($H_{ox} = 7.50$ m); Contour Interval = $2.0E-03$ (B: $2.00E-03$, E: $1.00E-02$)

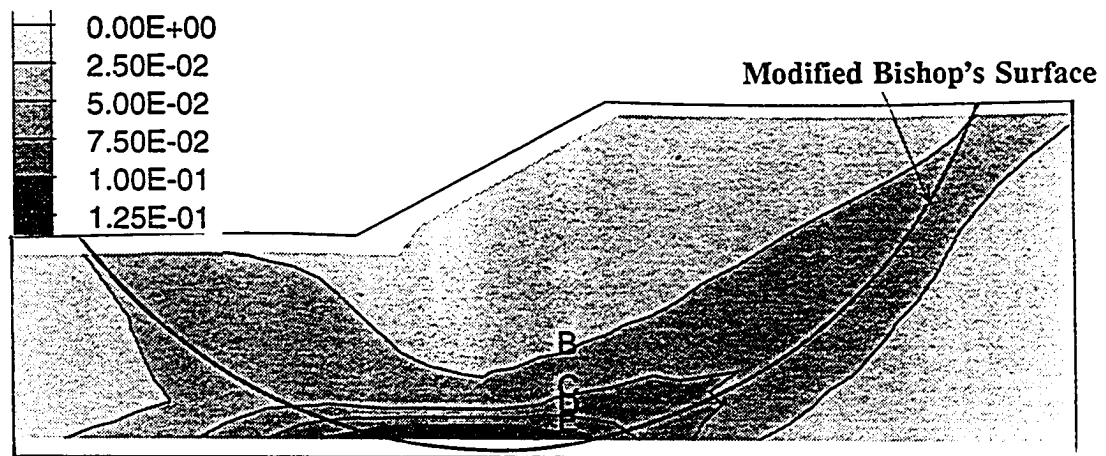
Fig. 6.3 Maximum shear strain distribution, A analysis



(d) 4th layer ($H_{ox} = 10.0$ m); Contour Interval = $5.0E-03$ (B: $5.00E-03$, E: $2.00E-02$)



(e) 5th layer ($H_{ox} = 12.5$ m); Contour Interval = $1.0E-02$ (B: $1.00E-02$, E: $4.00E-02$)



(f) 6th layer ($H_{ox} = 15.0$ m); Contour Interval = $2.5E-02$ (B: $2.50E-02$, E: $1.00E-01$)

Fig. 6.3 Maximum shear strain distribution, A analysis

pattern. At the last layer excavation (Fig 6.3f), the maximum shear strain along the failure surface reaches 2.5% (contour B). It is also seen that the failure surface prediction from this analysis is in close agreement with that of Modified Bishop method.

Numerical analyses (FEM and FDM) of slopes do not automatically provide factors of safety as in limit equilibrium methods. Therefore, in order to determine the global factor of safety in FLAC analysis, it is necessary to take average out of local factors of safety with appropriate weights (proportional lengths in the direction of the failure surface) of the elements involved in the failure surface. However, the failure surface in the numerical analysis is not as definite as in the limit equilibrium analysis so that the proportional length (weight) of individual element become dependent to some extent upon the manner in which the failure surface is assumed even for a given series of failed elements. As an approximation, factor of safety can be roughly calculated without weights (or equal weights) for the entire elements. Fig. 6.4 shows the comparison between the factors of safety variations along the fixed failure surface with and without weights accounted for. It is seen that the two lines are very close each other particularly near the failure state (FS=1.005). Therefore, the factor of safety determined without weights is alternatively used to provide the level of slope stability in the interpretation of FLAC analyses in most cases except it is mentioned.

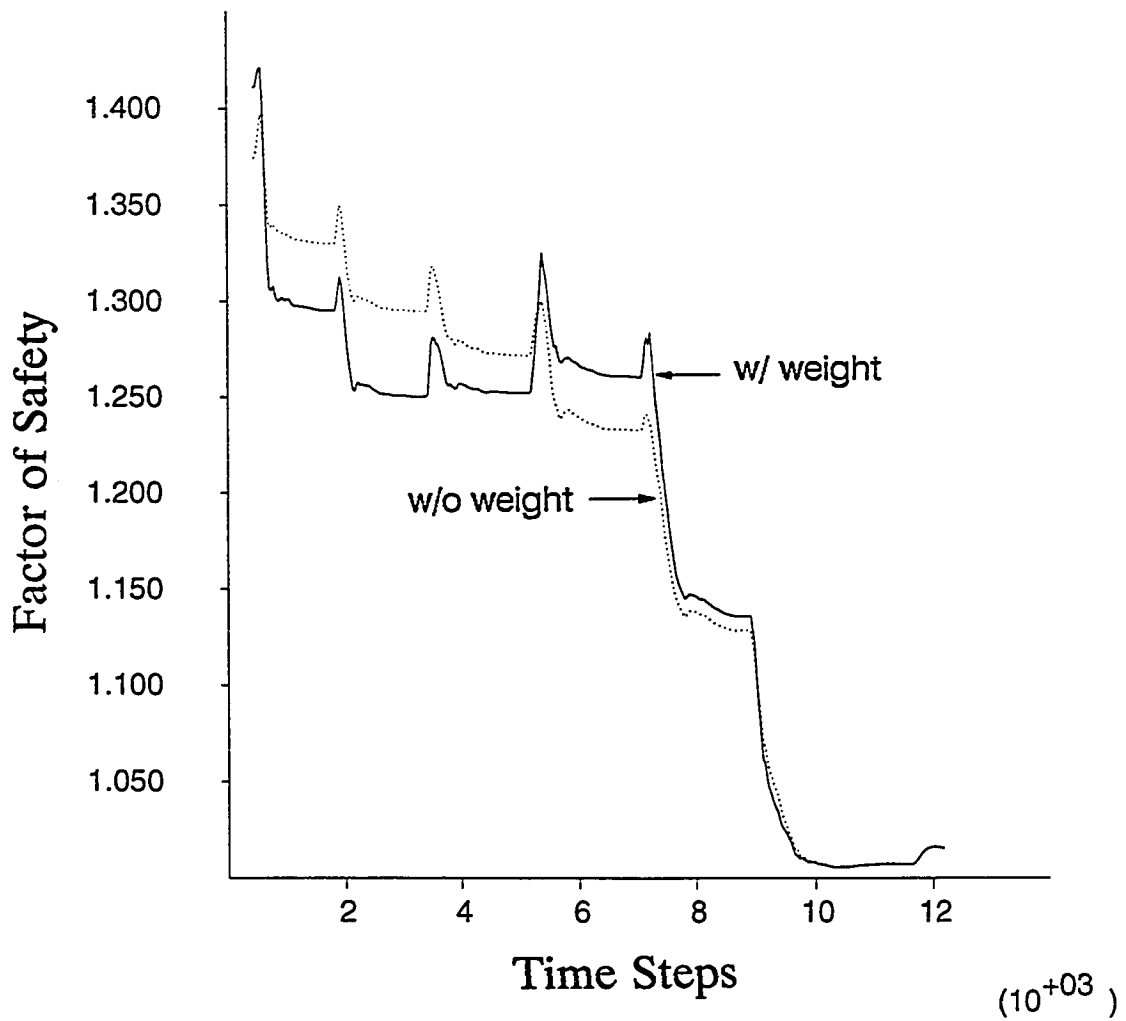


Fig. 6.4 Variation of factors of safety at the Modified Bishop's surface, A analysis

The local factors of safety distribution at the 5th layer excavation along the normalized distances of the elements from the toe to the crest along the failure surface is shown in Fig. 6.5. The elements at the toe of the slope have much higher factors of safety than the rest of the elements, which are at yield (i.e., factor of safety = 1.0). Note that the global factor of safety, 1.037, determined by taking average out of local factors of safety at the stage gives the level of slope stability on the average sense, whereas the distribution of local factors of safety is highly non-uniform to be represented by a single safety factor (Fig. 6.5).

6.2.1.2 Anisotropic Strength Case (B Analysis)

FLAC analyses were carried out in which four different anisotropic strength curves (Fig. 3.14 in Section 3.5.4.3) were respectively implemented. Fig. 6.6, which was obtained from B-1 analysis, shows the i angle distribution at the incipient failure along the normalized distance of the failure surface from the toe. Note that the normalized distance which is slightly shorter than unity at the end of x axis is due to the fact that tension-failed elements in the crest are always excluded in the figure. It is seen that i angle ranges from about 90 degree at the toe to about negative 5 degree near the crest of the slope. The i angles for the bottom elements (f,g,h,i) are located in the middle of the extremes. Fig. 6.7 shows the i angle distribution at the state of incipient failure, in which i angles near the toe are close to 90 degree reflecting the mode of loading close to the laboratory extension test. The displacements of a nodal point on the tip of the

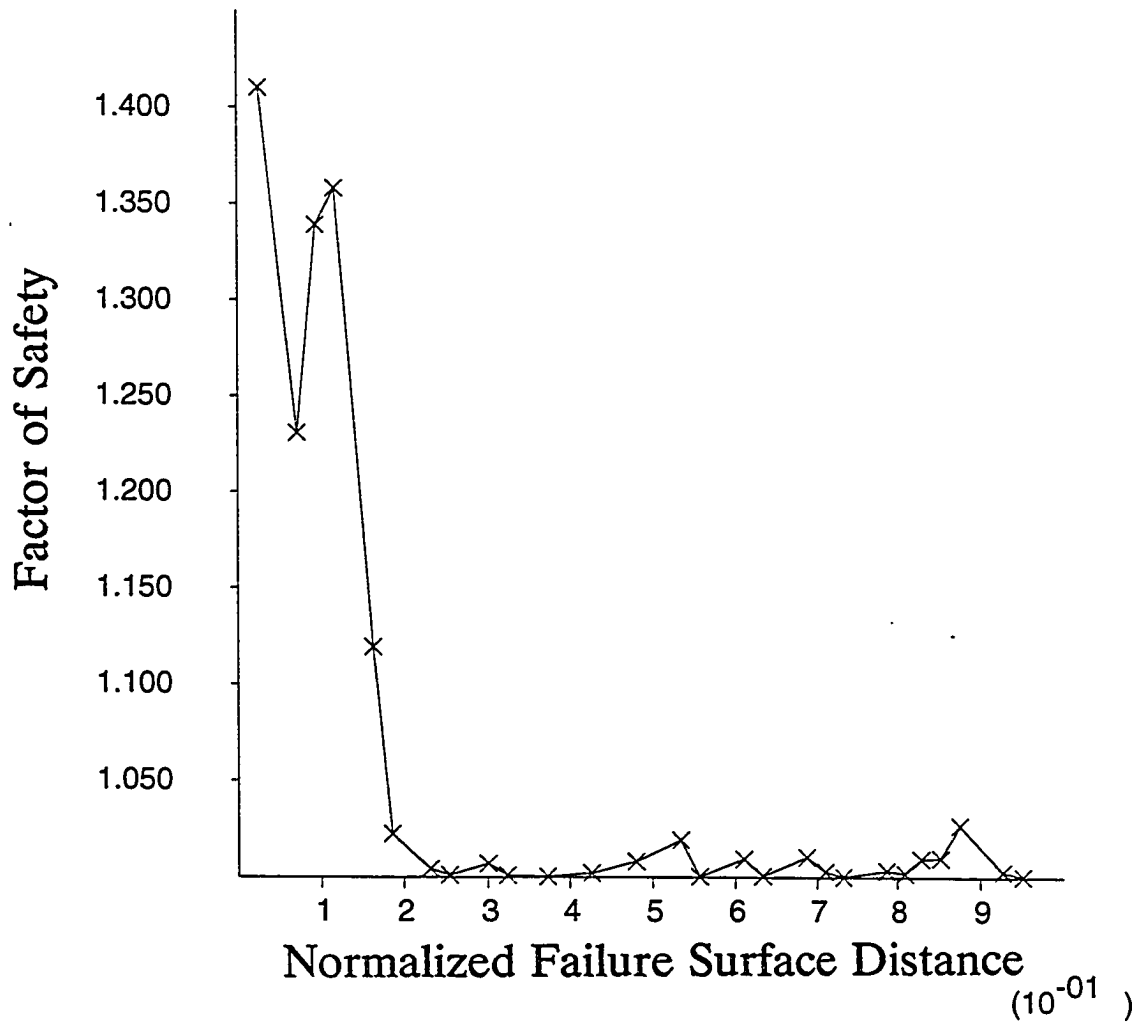


Fig. 6.5 Distribution of local factors of safety along the Modified Bishop's surface (5th layer excavation), A analysis

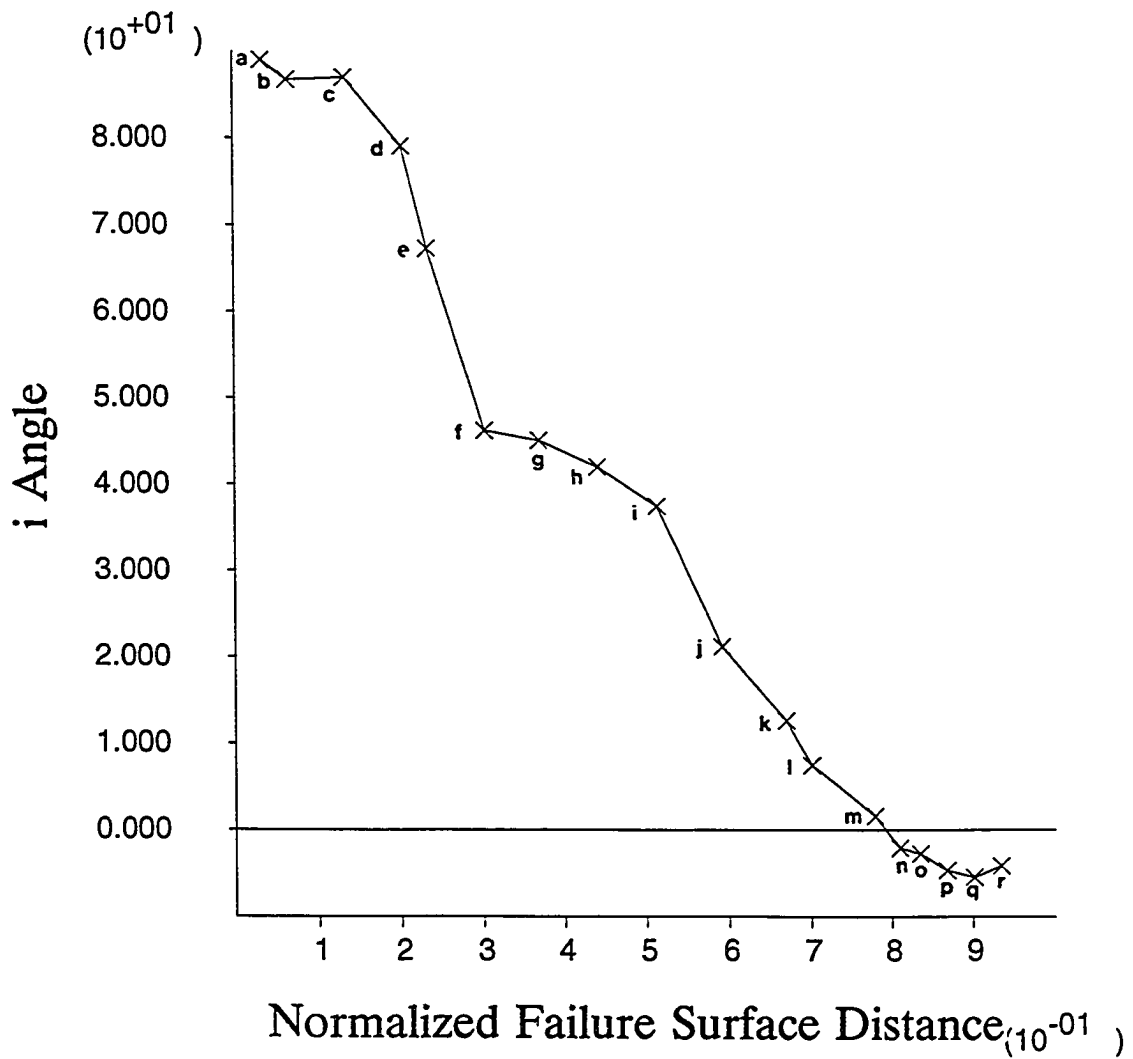


Fig. 6.6 Distribution of i angles along the normalized failure surface distance (5th layer excavation), B-1 analysis

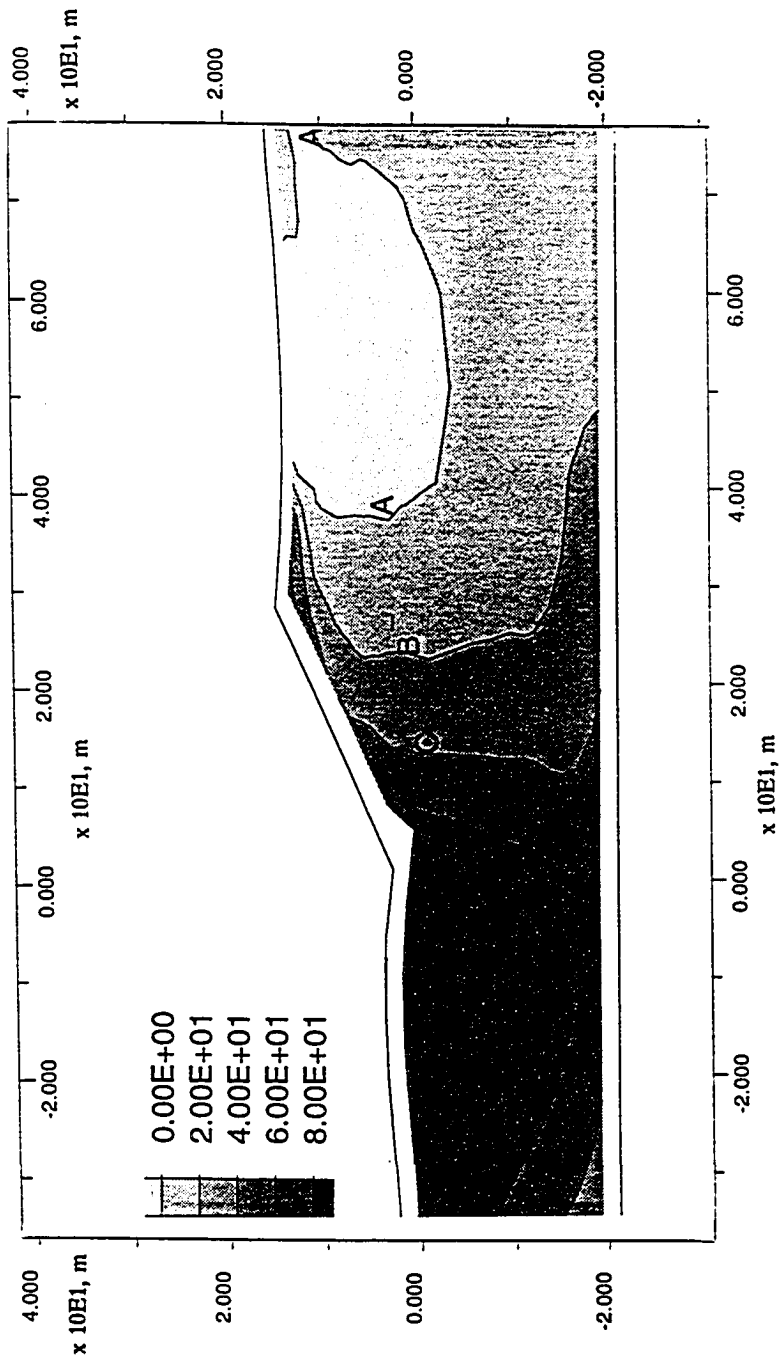


Fig. 6.7 Distribution of i angles in the slope (5th layer excavation), B-1 analysis
(Contour interval: 2.00E+01)

crest (Fig. 6.1) with the gradual excavation are shown in Fig. 6.8, which includes results from A, B-1 through B-4 analyses. It can be seen that the magnitude of the nodal displacement at the last layer excavation is greatly increased from A analysis to B series analyses. In addition, it is clearly seen that the magnitude of the displacement continuously increases with increasing anisotropic strength curve number. Since the undrained strength of an element with i angle greater than 0° is smaller than the compression strength, the total strength mobilized in the failure state in B series of analyses should be somewhat less than that of A analysis. Therefore, the global structural resistance against failure is also less than that of A analysis case leading to greater deformation of the structure.

In the process of excavation, the summation of the peak strengths of the elements along the failure surface decreases as i angles gradually increase for those elements. When the summation of the peak strengths are expressed as a ratio to the summation of the isotropic compression strengths, termed "the available strength ratio", the total strength available at a moment along the failure surface can be obtained in proportion to the isotropic compression strength case. Fig. 6.9 shows the variations in the available strength ratios in B series analyses. It is clearly shown that as excavation proceeds for a given analysis, the available strength ratio along the failure surface continuously decreases due to increasing i angles of the elements. At the last layer excavation at which elements are already at failure, the strength ratio becomes constant due to the fixed i angles. The summary of the available strength ratios at failures are shown in

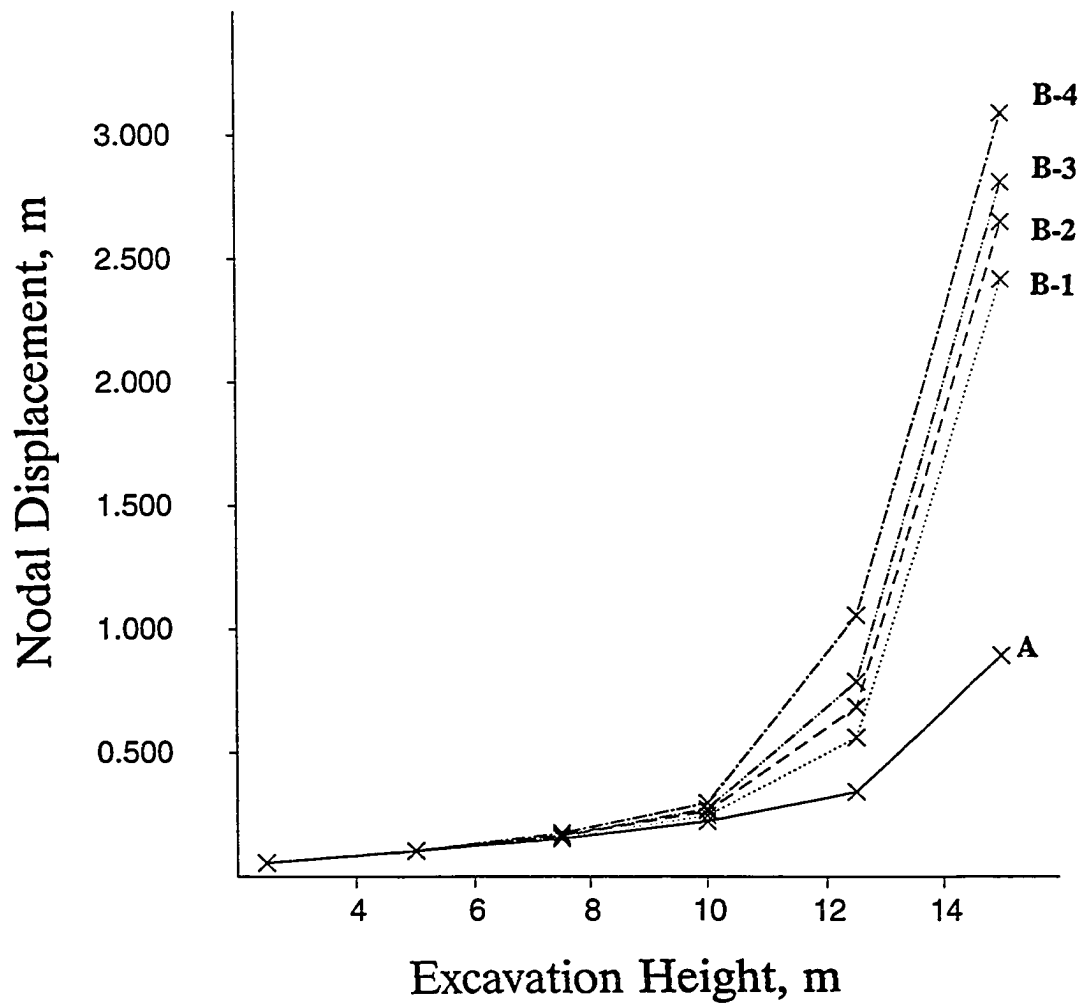


Fig. 6.8 Nodal displacements with increasing excavation heights, A and B series analyses

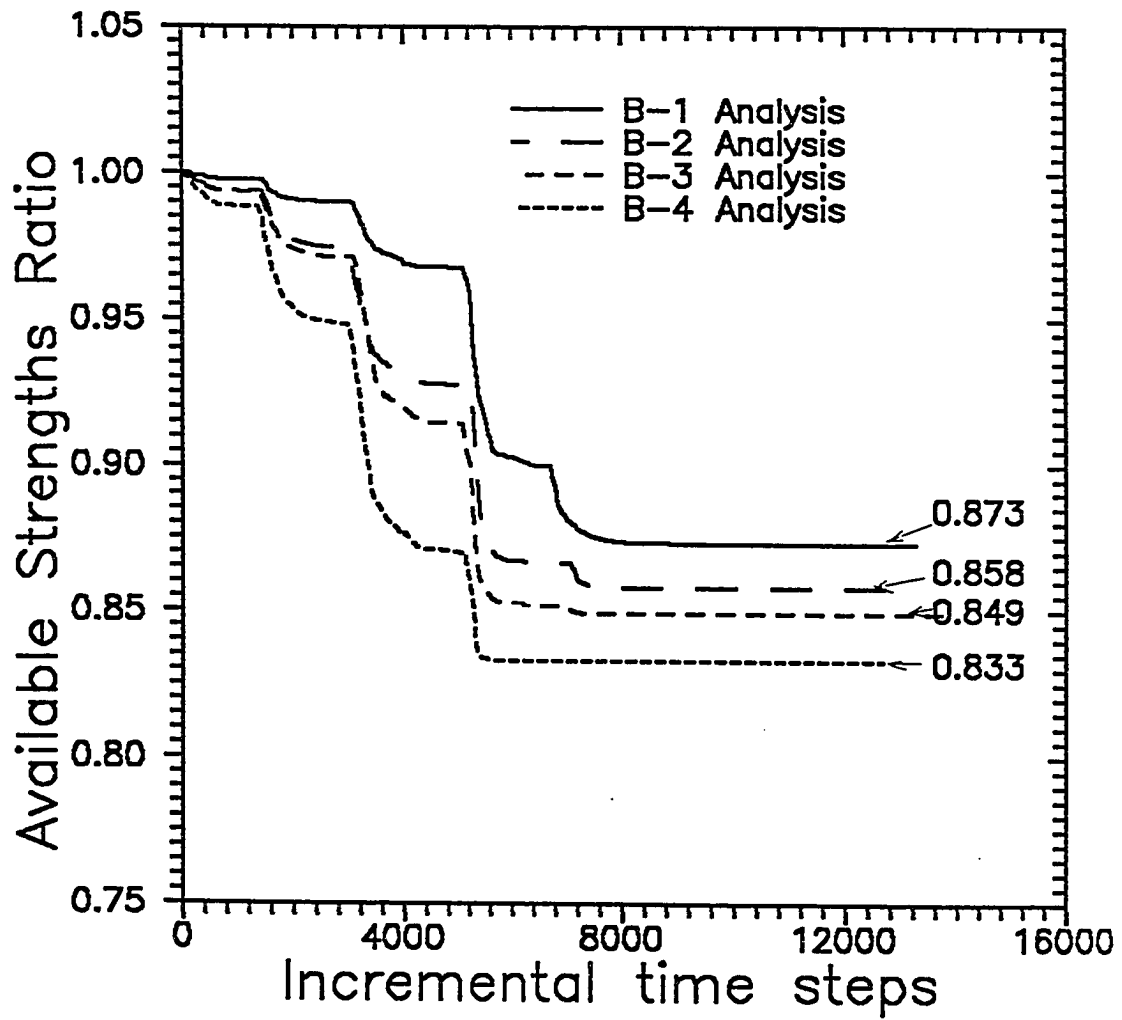


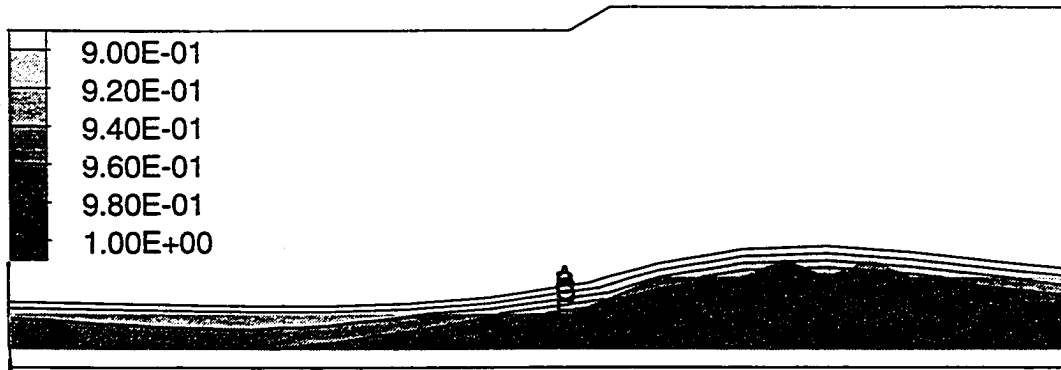
Fig. 6.9 Variation of the available strength ratio, B series analyses

Table 6.6. It can be seen that the available strength ratio at failure continuously decreases from 0.873 for B-1 analysis to 0.833 for B-4 analysis. This means that the total strengths available along the failure surface at failure are reduced by 12.7% and 16.7% for B-1 and B-4 analyses, respectively, as compared to A analysis.

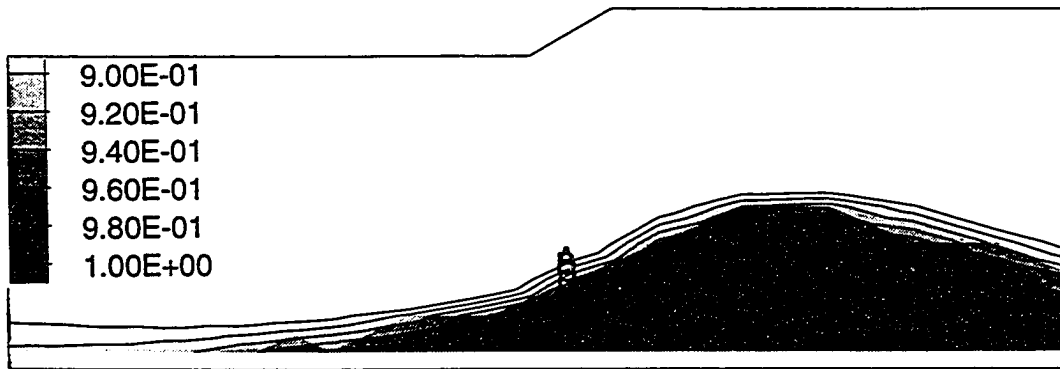
Table 6.6 Summary of the available strength ratio at failure

Analysis	Available strength ratio
B-1	0.873
B-2	0.858
B-3	0.849
B-4	0.833

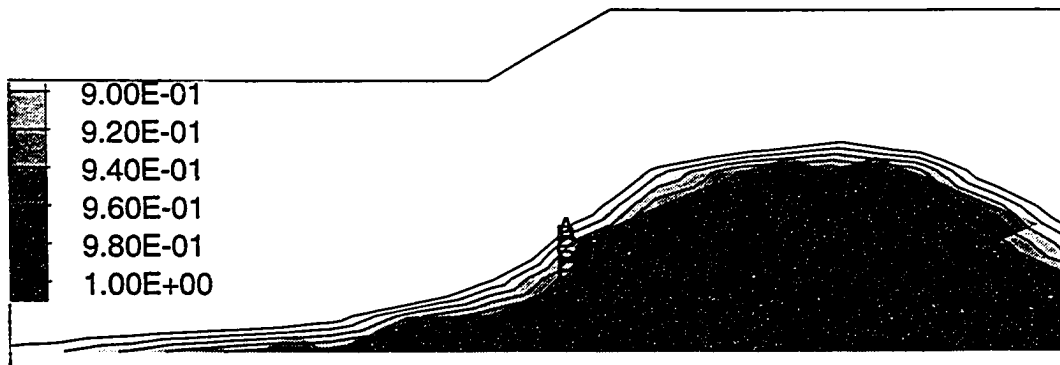
The pattern of maximum shear stress development in B-1 analysis (Figs. 6.10a through 6.10f) is similar to that of A analysis (Figs. 6.2a through 6.2f) except the fact that the global failure occurs at the 5th layer excavation (Fig. 6.10e) this time. It is interesting to note that elements in the upper part of the crest are far from the plastic yield (i.e., the maximum shear stress ratio, τ_{\max}/S_u , is less than 0.9) so that a rigid body rotation type of failure occurs along the failure surface. It is seen that at the end of the last layer excavation (Fig. 6.10f), the intensity of the stress ratio distribution is somewhat reduced, reflecting that the stresses of elements are released by the considerable slope failure. The fact that the slope already failed at the fifth layer excavation can be seen in the history of unbalance force (Fig. 6.11). It is seen that the unbalance force is at the peak right after a



(a) 1st layer ($H_{cx} = 2.50$ m); Contour Interval = $2.0E-02$ (A: $9.00E-01$, E: $9.80E-01$)

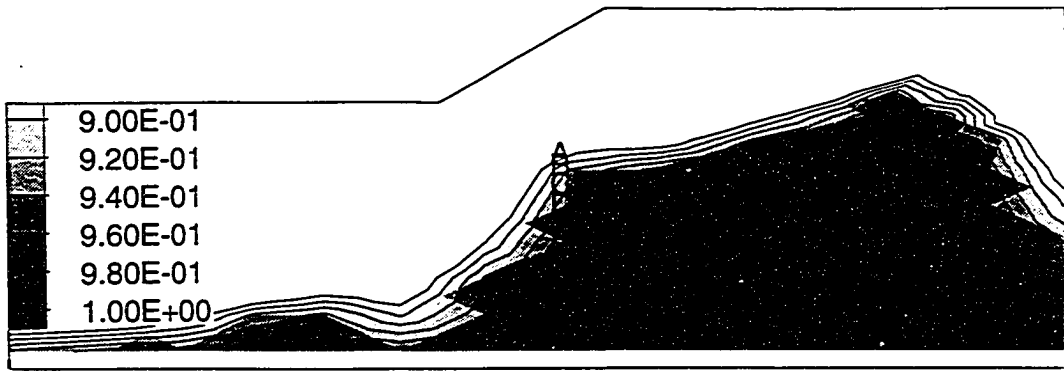


(b) 2nd layer ($H_{cx} = 5.00$ m); Contour Interval = $2.0E-02$ (A: $9.00E-01$, E: $9.80E-01$)

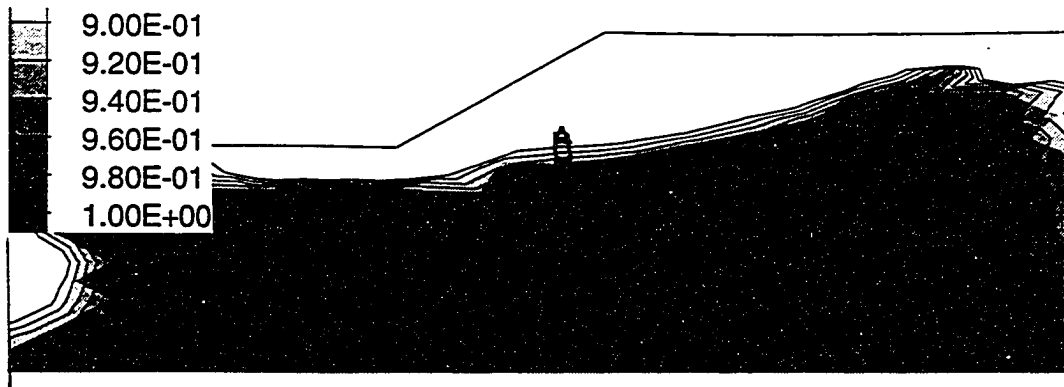


(c) 3rd layer ($H_{cx} = 7.50$ m); Contour Interval = $2.0E-02$ (A: $9.00E-01$, E: $9.80E-01$)

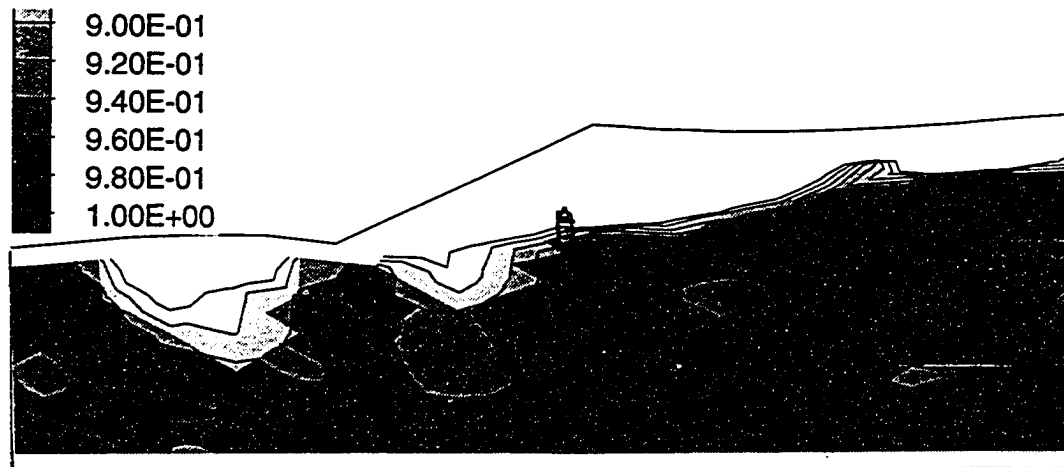
Fig. 6.10 Maximum shear stress ratio (τ_{max}/S_u) distribution, B-1 analysis



(d) 4th layer ($H_{ox} = 10.0$ m); Contour Interval=2.0E-02 (A: 9.00E-01, E: 9.80E-01)



(e) 5th layer ($H_{ox} = 12.5$ m); Contour Interval=2.0E-02 (A: 9.00E-01, E: 9.80E-01)



(f) 6th layer ($H_{ox} = 15.0$ m); Contour Interval=2.0E-02 (A: 9.00E-01, E: 9.80E-01)

Fig. 6.10 Maximum shear stress ratio (τ_{max}/S_u) distribution, B-1 analysis

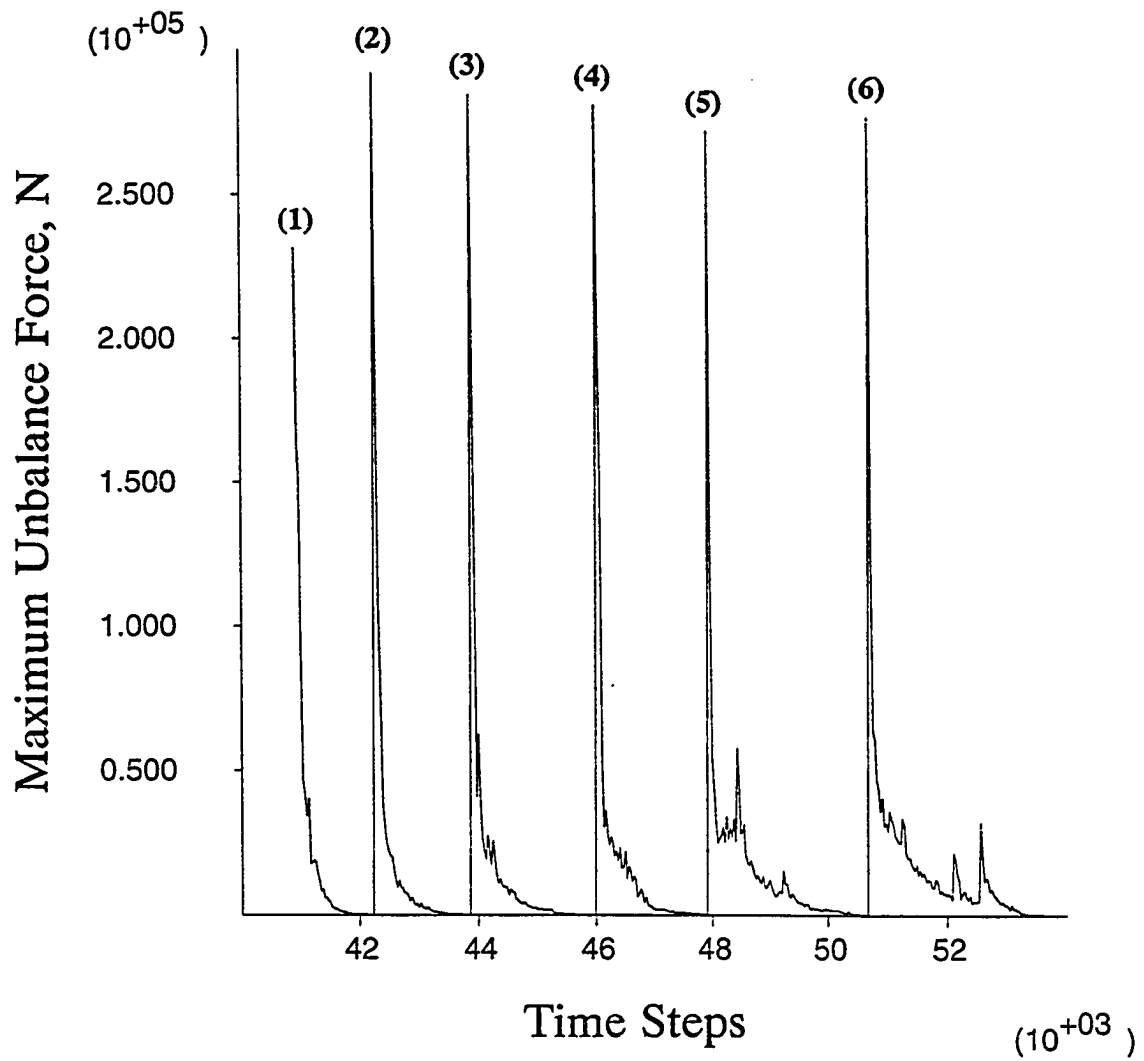


Fig. 6.11 History of maximum unbalance force, B-1 analysis

layer of excavation and converges to a smaller value at the equilibrium. At the 5th layer excavation, the slope takes twice as many time steps as usual to get to an equilibrium state due to plastic flow. The already failed slope is then further loaded by the last layer excavation which is accompanied by further plastic flow.

6.2.1.3 Anisotropic Strength with Straining Hardening and Softening Cases (C and D Analyses)

The types of analyses considered in this section are C-1-a through C-1-c and D-1-a through D-1-c, which implies that only anisotropic strength curve number one is used for varying degrees and patterns of strain softening. The relations between nodal displacements and excavation heights in C-1-a through C-1-c and D-1-a through D-1-c analyses are shown in Fig. 6.12a and 6.12-b along with those of A and B-1 analyses, respectively. The magnitudes of nodal displacements at the final layer excavation in C and D analyses become greater as the degree of strain softening increases. However, overall displacement patterns in these analyses are very close to each other in which failures are evident at the 5th layer excavation.

Figs. 6.13 shows the maximum shear strain distribution at the end of excavation obtained in D-1-b analysis. The pattern of maximum shear strain development from the beginning of the excavation to the end was similar to those of the previous cases (A and B analyses) except the magnitudes of the maximum shear strain distribution at failures. Since the peak strength is mobilized at higher

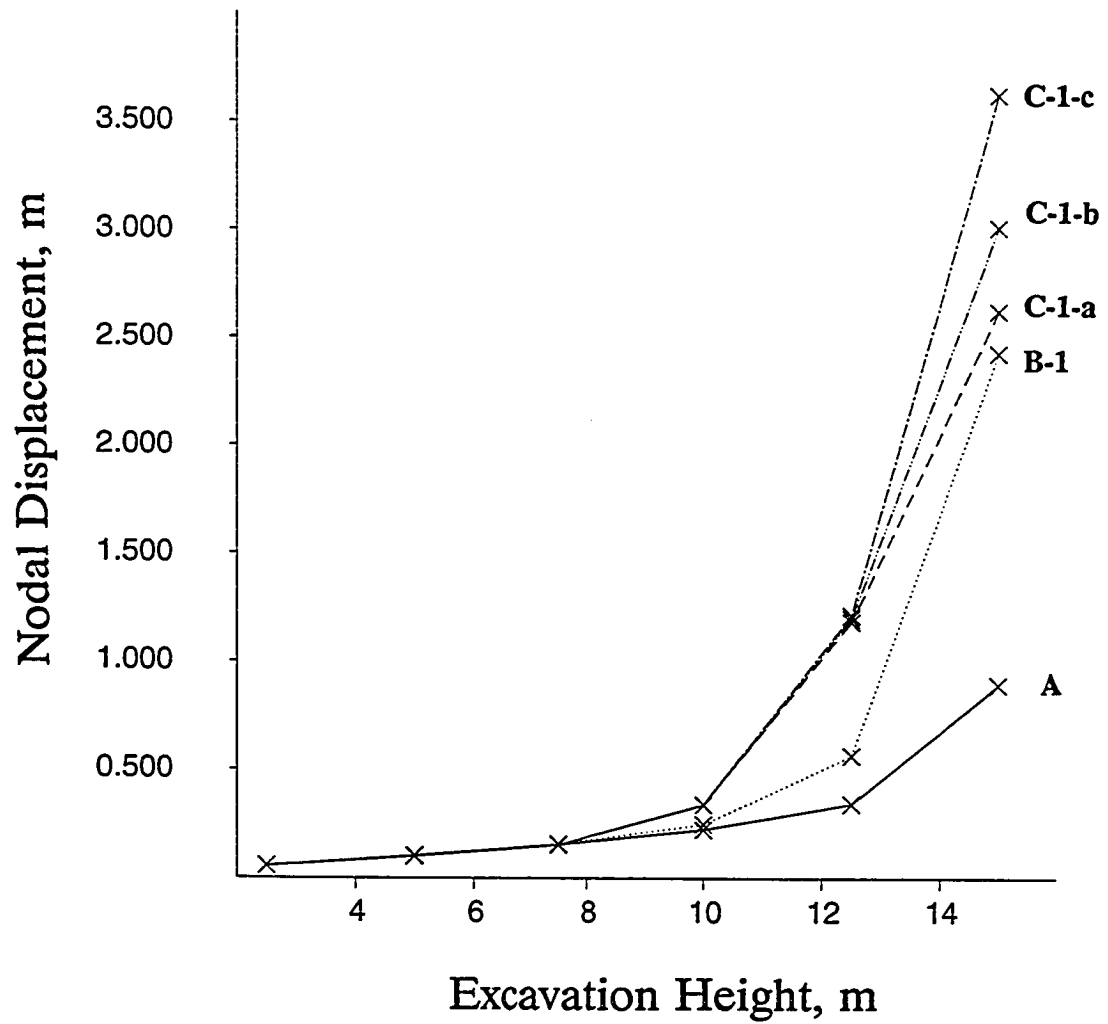


Fig. 6.12a Nodal displacements with increasing excavation heights, A, B-1 and C series analyses

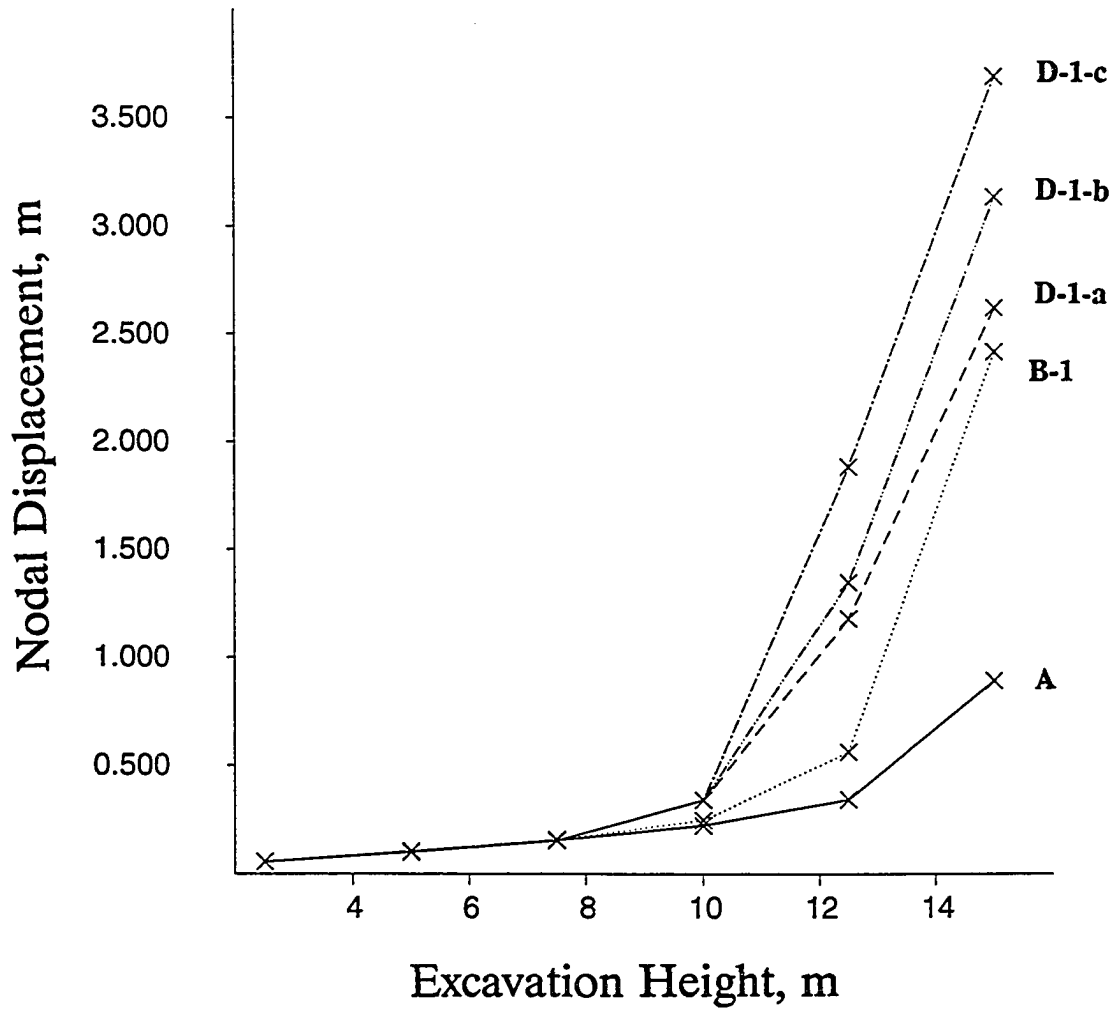


Fig. 6.12b Nodal displacements with increasing excavation heights, A, B-1 and D series analyses

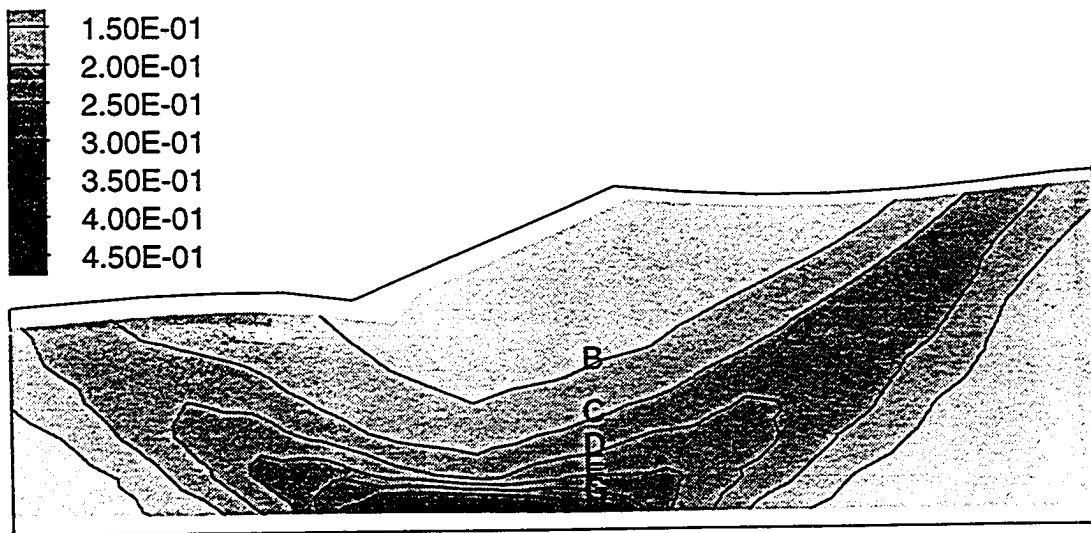


Fig. 6.13 Distribution of maximum shear strain (6th layer excavation), D-4-b analysis ($HH_{ex} = 15.0$ m; contour interval = $5.0E-02$, B: $5.0E-02$, H: $3.5E-01$)

strain level in C and D analyses as compared to the previous cases (A and B analyses), the magnitude of the maximum shear strain (10%, contour B) at failure along the failure surface should be much higher than those of A analysis (2.5%) and B analysis (5.0%). The maximum shear strain distribution obtained from the rest of C and D analyses were very similar to that of D-1-b analysis.

Figs. 6.14a and 6.14b demonstrate the sequence of the peak strength mobilization of the elements along the failure surface for D-1-c analysis. (c is the currently mobilized strength and S_u is the peak strength.) Since there are too many elements in the surface to be presented in a figure, two separate figures are used. It is seen that the passive elements (elements "a", "b", "c" and "d") arrive at the peak strengths at larger time steps at which strength of active elements (elements "o", "p", "q", "r" and "s") have already fallen to residual levels. It is also observed that the active elements arrive at the peak strengths for a short duration (Fig. 6.14b).

The summation of mobilized strengths of the elements along the failure surface can be expressed as a ratio to the summation of the isotropic compression strengths of those elements at a given time. As the elements experience strain hardening and softening, the ratio varies. When the peak in the ratio takes place, the slope is exercising the maximum shear strength possible along the failure surface for given anisotropic strengths and stress-strain relations. The ratio at a given time is herein termed "the mobilized strength ratio" and the peak in the ratios is herein termed "the peak mobilized strength ratio". Curves "a" in Figs.

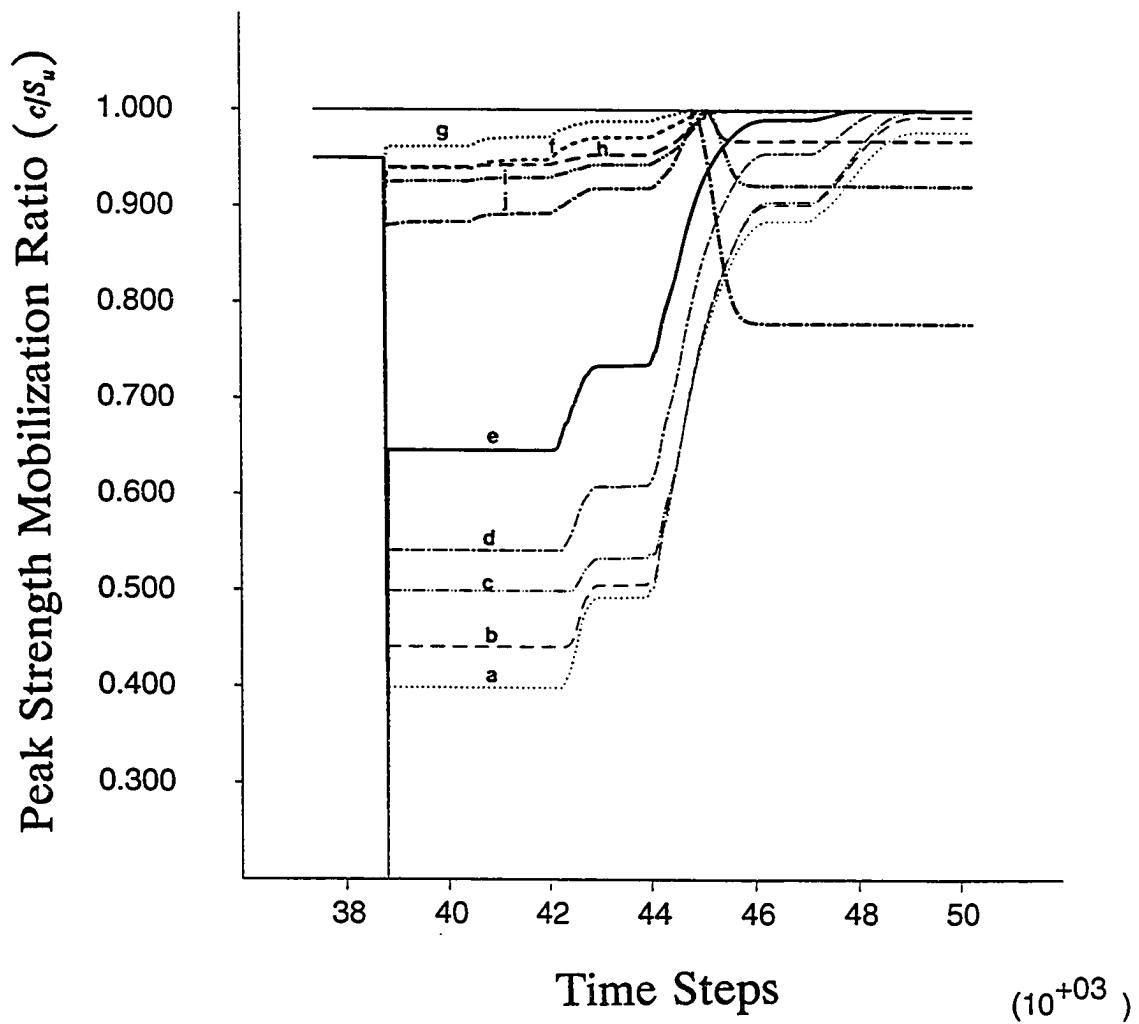


Fig. 6.14a Sequence of the peak strength mobilization with time steps, D-1-c analysis

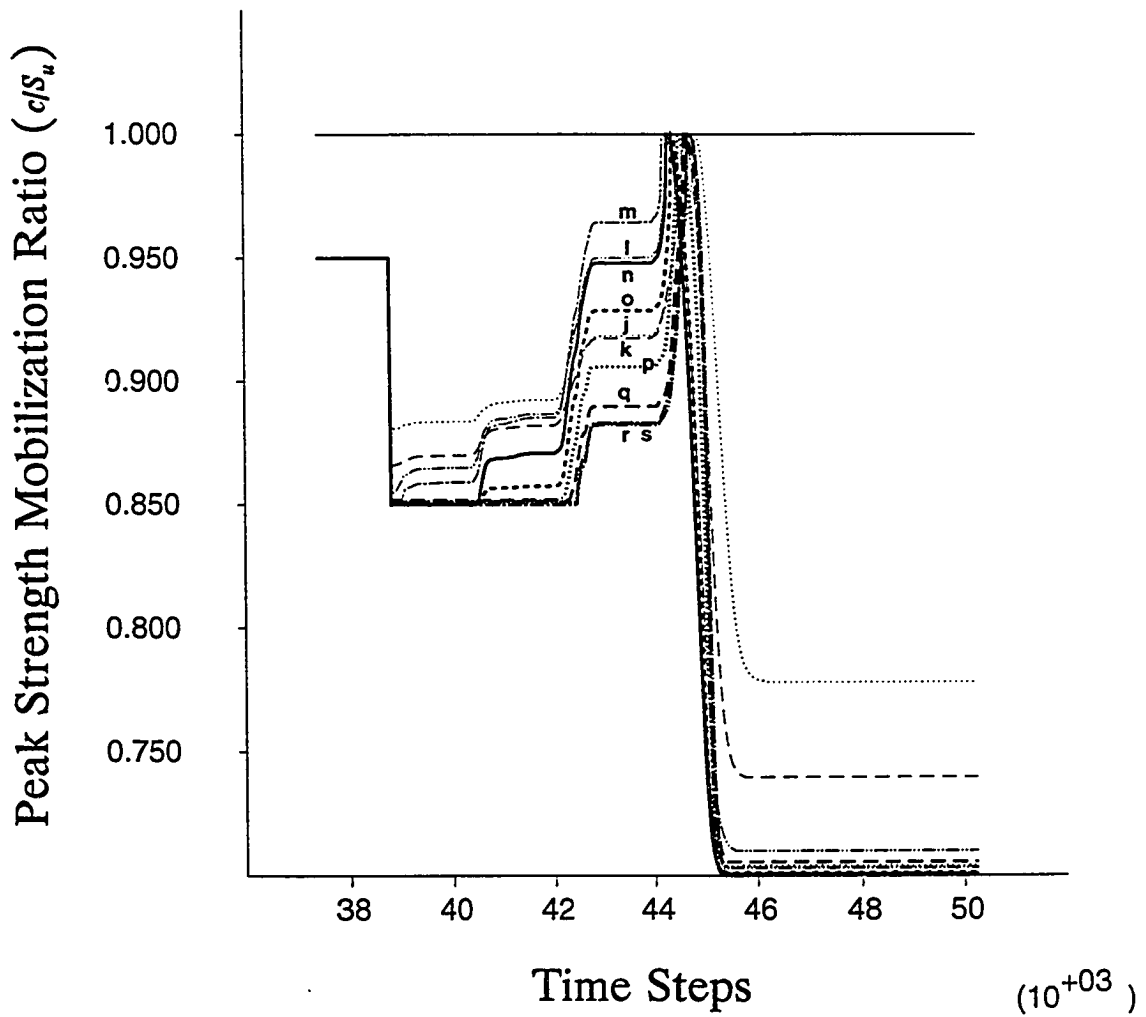


Fig. 6.14b Sequence of the peak strength mobilization with time steps, D-1-c analysis

6.15a, 6.15b and 6.15c show the variation in the mobilized strength ratios in C-1-a, C-1-c and D-1-c analyses, respectively. In the same figures, the variations in the ratios of the summation of the maximum shear "stresses" of the elements to the summation of the isotropic compression strengths, which is termed "the mobilized stress ratio" are also presented as curve b. In addition, the three horizontal lines in the figures are limit lines which would be obtained by (a) the summation of the isotropic compression ($i=0^\circ$) strengths (the top line), (b) the summation of the anisotropic strengths of varying i angles (the middle line), (c) the summation of the isotropic extension ($i=90^\circ$) strengths (the bottom line) in proportion to the summation of the isotropic compression strengths, respectively. In other words, the middle line represents the limit line which is the total strength mobilizable in B analysis in proportion to that in A analysis, and is also asymptotically approached by the curve "a" in C-1-a analysis (zero degree strain softening case) at a large strain level.

It can be seen in Fig. 6.15a that the mobilized strength ratio becomes equal to the mobilized stress ratio at the 4th layer excavation (point a) after which they are virtually the same (i.e., flow state) for a while. At point b, which corresponds to the last layer excavation, the global failure releases maximum shear stresses in the elements so that the mobilized stress ratio starts to drop. After the failure the mobilized stress ratio is rebuilt (point c) so that further shear deformation occurs. It is seen that the mobilized strength ratio is approaching the middle line, since the degree of strain softening is zero in C-1-a analysis. When strain softening is

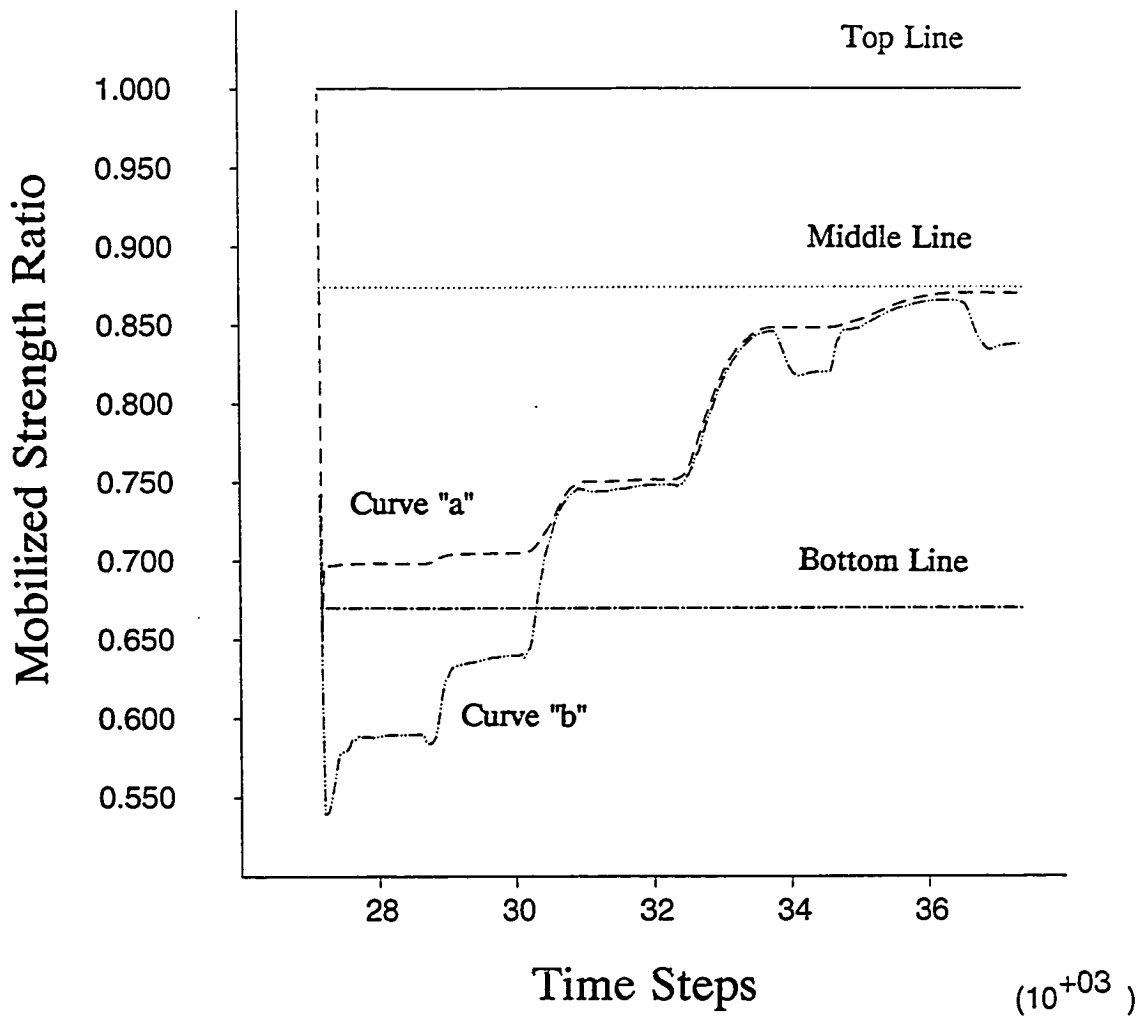


Fig. 6.15a Variation of the mobilized strength ratio with time steps, C-1-a analysis

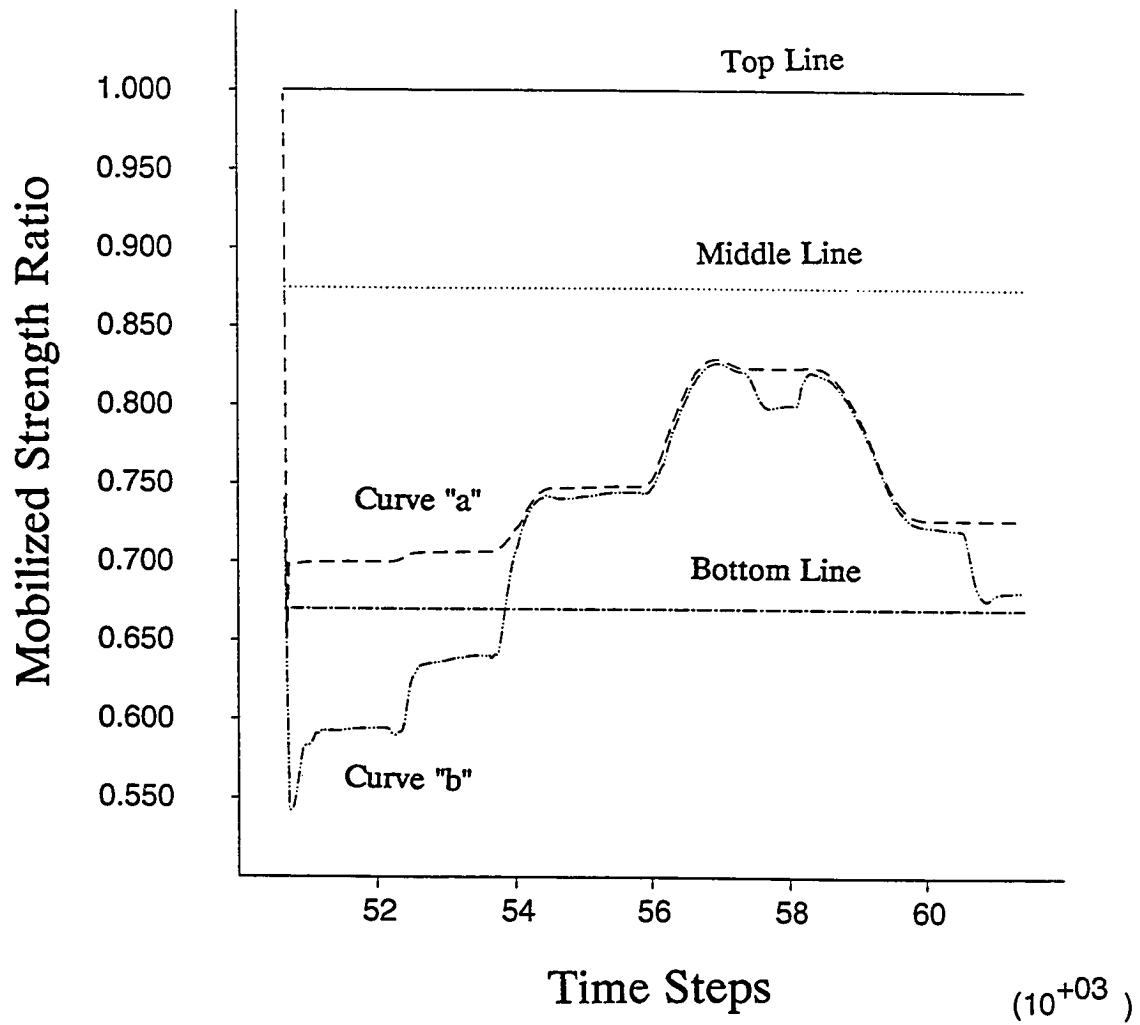


Fig. 6.15b Variation of the mobilized strength ratio with time steps, C-1-c analysis

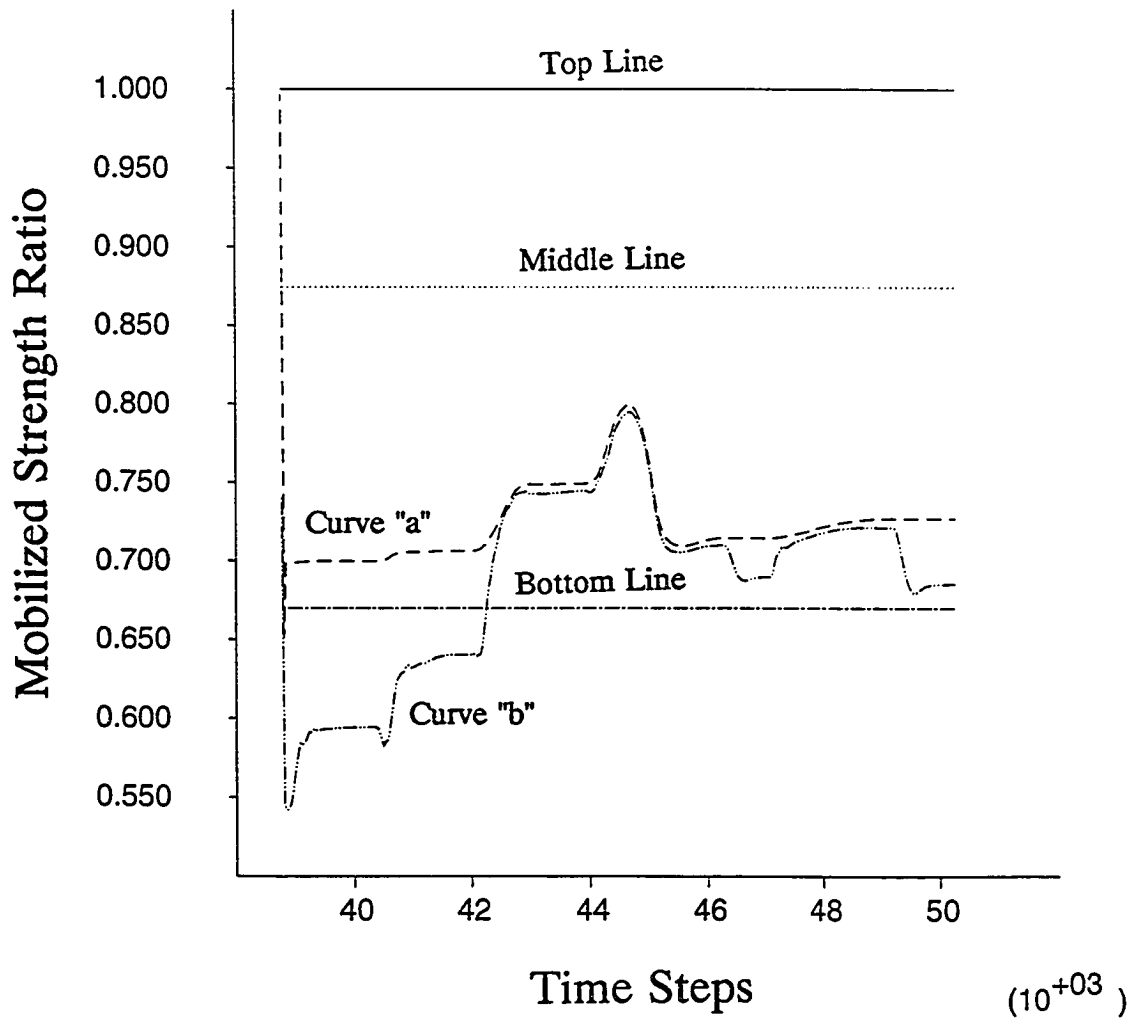


Fig. 6.15c Variation of the mobilized strength ratio with time steps, D-1-c analysis

incorporated in the stress-strain relations in C-1-c and D-1-c (Figs. 6.15b and 6.15c), however, the peak mobilized strength ratio is somewhat below the middle horizontal line due to the strength drops in the post peak region in the stress-strain relations for active elements, while the passive elements experience peaks at large strains (progressive failure effect). Figs. 6.15b and 6.15c show that the peak mobilized strength ratios are 0.831 for C-1-c case and 0.800 for D-1-c case, respectively. In addition, it can be seen that the peak mobilized strength ratio is maintained for a relatively shorter duration in D-1-c (Fig. 6.15c) analysis as compared that in C-1-c analyses (Fig. 6.15b).

The peak mobilized strength ratios for the entire analyses are summarized in Table 6.7. In the table R^1 represents the level of the middle horizontal line which is the peak mobilized strength ratio in B analysis and R^2 corresponds to the peak mobilized strength ratios in C or D analyses. In addition, OE^1 is the

Table 6.7 Summary of the peak mobilized strength ratios

Case	C-1-a	C-1-b	C-1-c	D-1-b	D-1-c
R^1	0.873	0.873	0.873	0.873	0.873
R^2	0.873 (0.873)	0.839 (0.829)	0.831 (0.818)	0.816 (0.799)	0.800 (0.791)
OE^1	14.54%	19.20%	20.33%	22.55%	25.0%
OE^2	0%	4.05%	5.05%	6.99%	9.13%

overestimate in the peak mobilized strength due to neglecting both the progressive failure effect and anisotropic strength effect, by simply using isotropic strength parameters as in A analysis. The values of OE^1 were computed as the

difference in the peak mobilized strength ratios between A analysis and C or D analysis (R^2) divided by the peak mobilized strength ratio (R^2) of C or D analysis (e.g., $OE^1 = (1.0 - 0.839) / 0.839 = 19.2\%$ in C-1-b analysis). On the other hand, OE^2 is the overestimate in the peak mobilized strength due to neglecting only the progressive failure effect, by simply employing anisotropic strength parameters as used in B series analyses. For example, in C-1-b analysis, the difference (0.873-0.839) in the peak strength ratios between B ($R^1 = 0.873$) and C ($R^2 = 0.839$) analysis is divided by the peak strength ratio ($R^2 = 0.839$) of C-1-b analysis to obtain 4.05%.

Based on C and D series of analyses on the slope with a constant strength profile, it can be concluded that when the undrained strength is determined by a compression type of the laboratory test alone and the stability analysis is carried out by one of limit equilibrium methods, the overestimate in the total strength mobilization along the potential failure surface may be as large as 25.0% (D-1-c). When the anisotropic strength is correctly addressed, while ignoring the anisotropic stress-strain pattern and strain softening, the resulting overestimate may be as large as 9.13% (D-1-c). In addition, the overestimate which would be caused by using anisotropic strength parameters without consideration of anisotropic stress-strain relations for ductile material (0 % strain softening even for active elements) would be 14.54% (C-1-a), which is much less than 25.0% for strain softening material case (D-1-c).

The plastic shear strain distributions along the failure surface at distinct stages of the excavation in D-1-c analysis are shown in Fig. 6.16. The plastic shear strain is the difference between the maximum shear strain and the elastic shear strain as has been defined in Section 4.2.2. The elastic shear strain is only small fraction of the plastic shear strain so that the plastic shear strain itself is practically the same as the maximum shear strain. It is seen that the plastic shear strains distribution is highly nonuniform in which bottom elements (g,h,i) (or at the normalized failure surface distance $\approx 0.3-0.6$) have higher strain concentrations than the rest of the elements. Fig. 6.17 shows relations between the strength and plastic shear strain for $i=0^\circ$ (element "r"), $i=20^\circ$ (element "j"), and $i=90^\circ$ (element "a") elements along the failure surface, which were obtained in D-1-c analysis. It is shown that the strength of passive element "a" is on the rise while those of active elements "j" and "r" reach their residual levels at a large strain level (10.0%).

The strain compatibility concept, which was explained in Section 3.4.2.6, was applied to the entire stress-strain relations involved in the failure surface. The strengths of all elements along the failure surface at a given maximum shear strain level were added and divided by the summation of the anisotropic peak strengths of those elements, which is herein termed "the strength ratio". The strength ratio varies as a function of the maximum shear strain and reaches the peak at a certain strain level, which is defined as "the peak strength ratio". Figs. 6.18a and 6.18b show the variations of the strength ratios for C and D series of analyses, respectively. The peak strength ratios for C and D series of analyses are

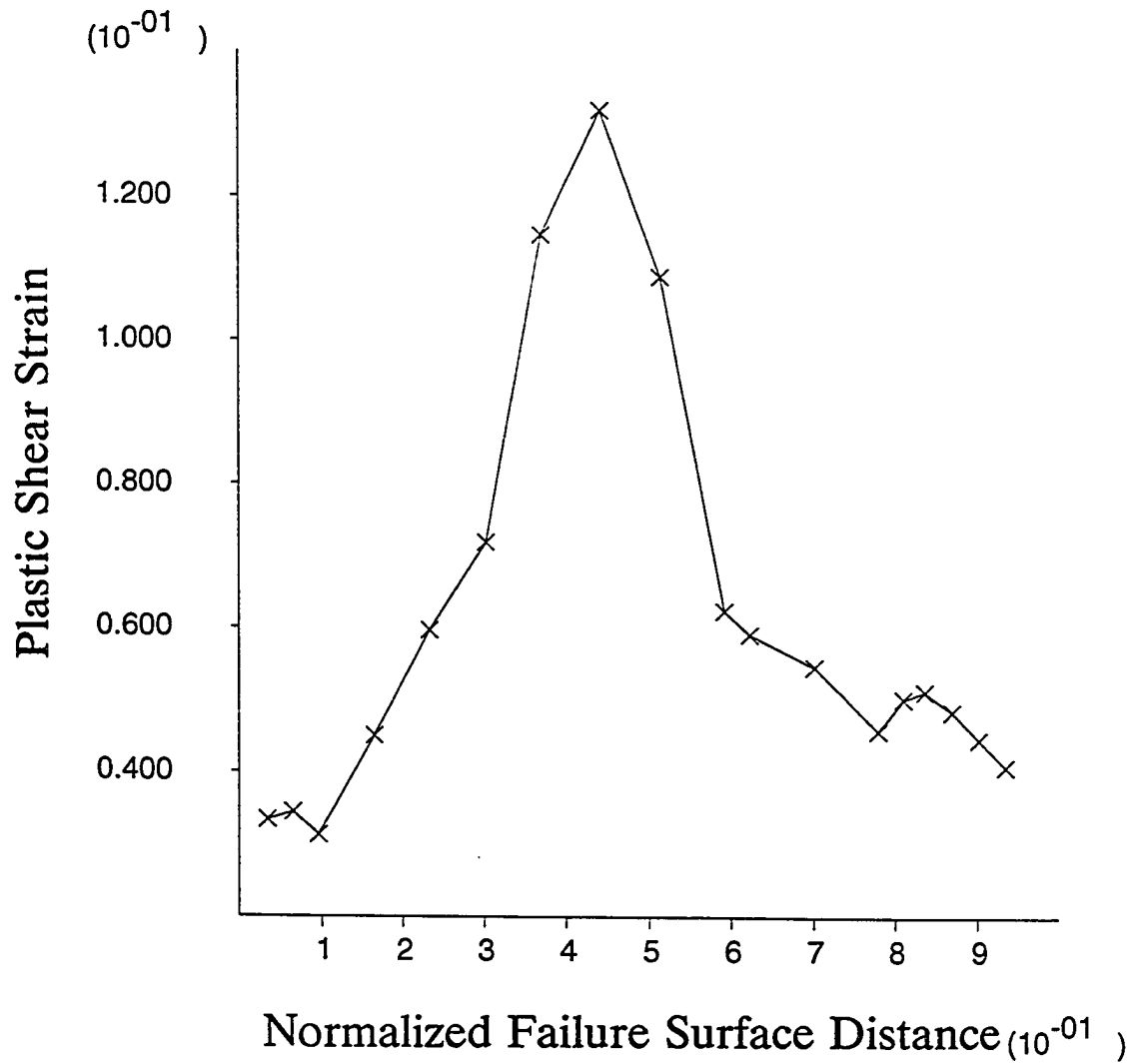


Fig. 6.16 Distribution of plastic shear strain along the normalized failure surface distance, C-1-c analysis

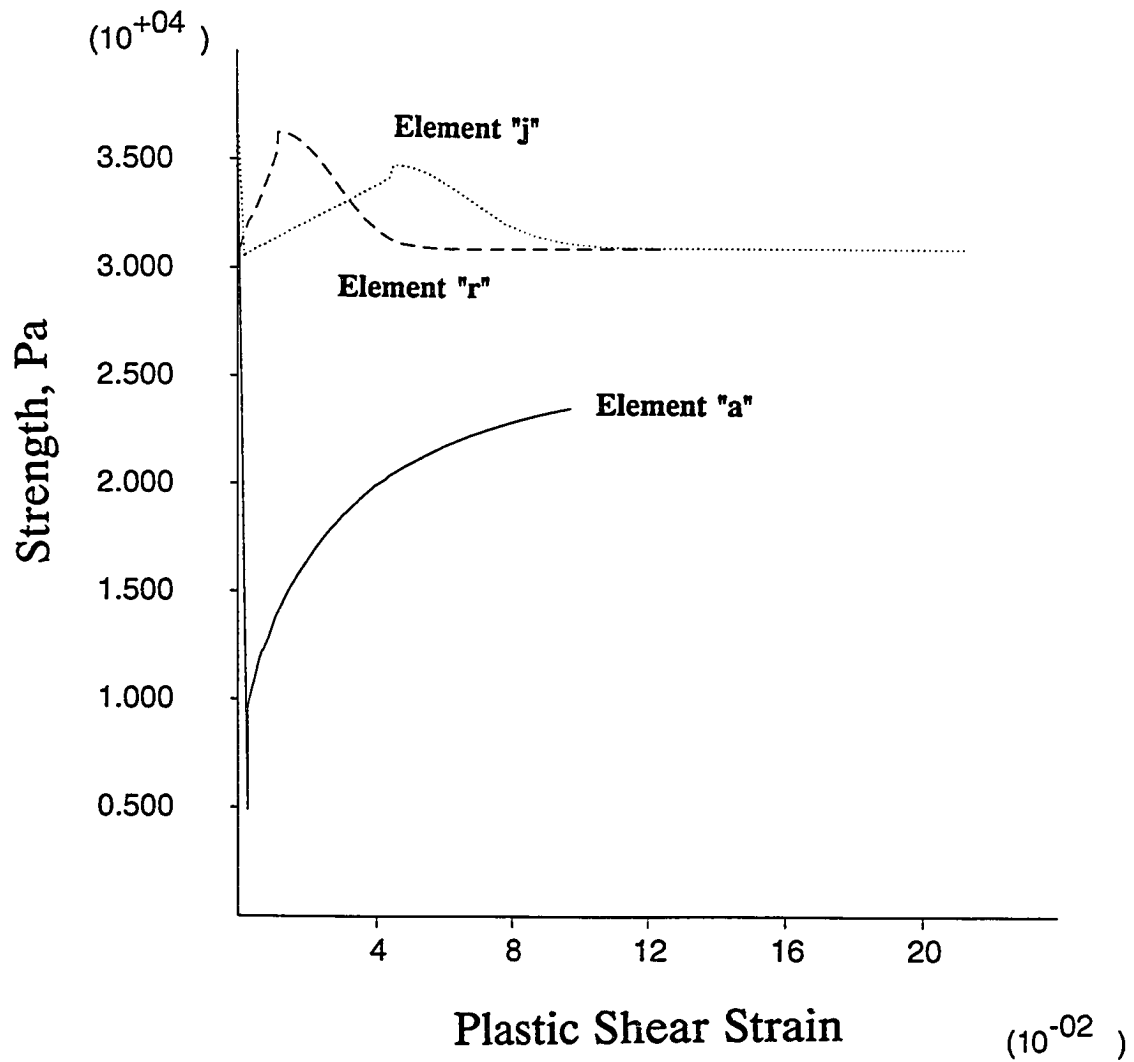


Fig. 6.17 Examples of strength and plastic shear strain relations, C-1-b analysis

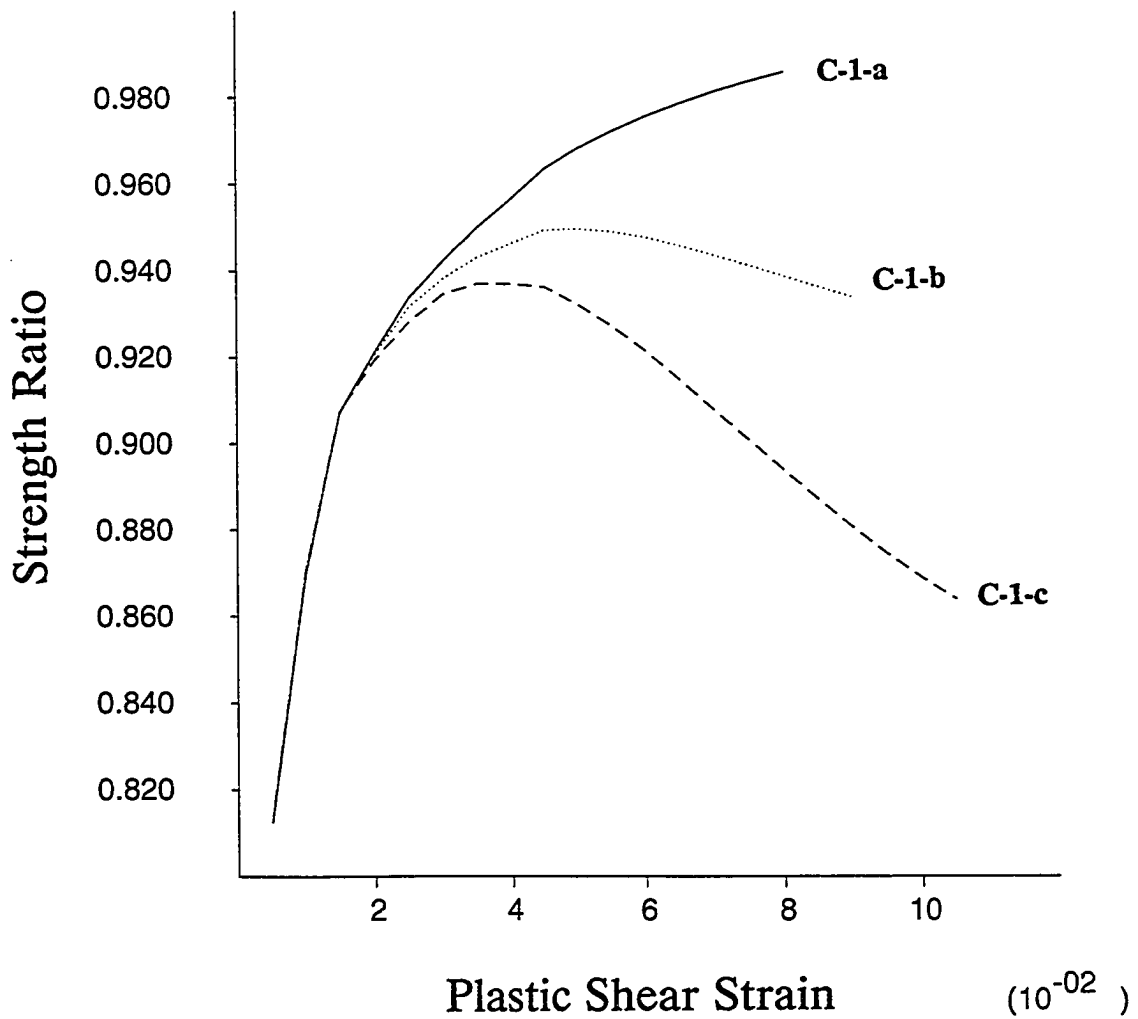


Fig. 6.18a Variation of strength ratios (strain compatibility concept), C-1 analyses

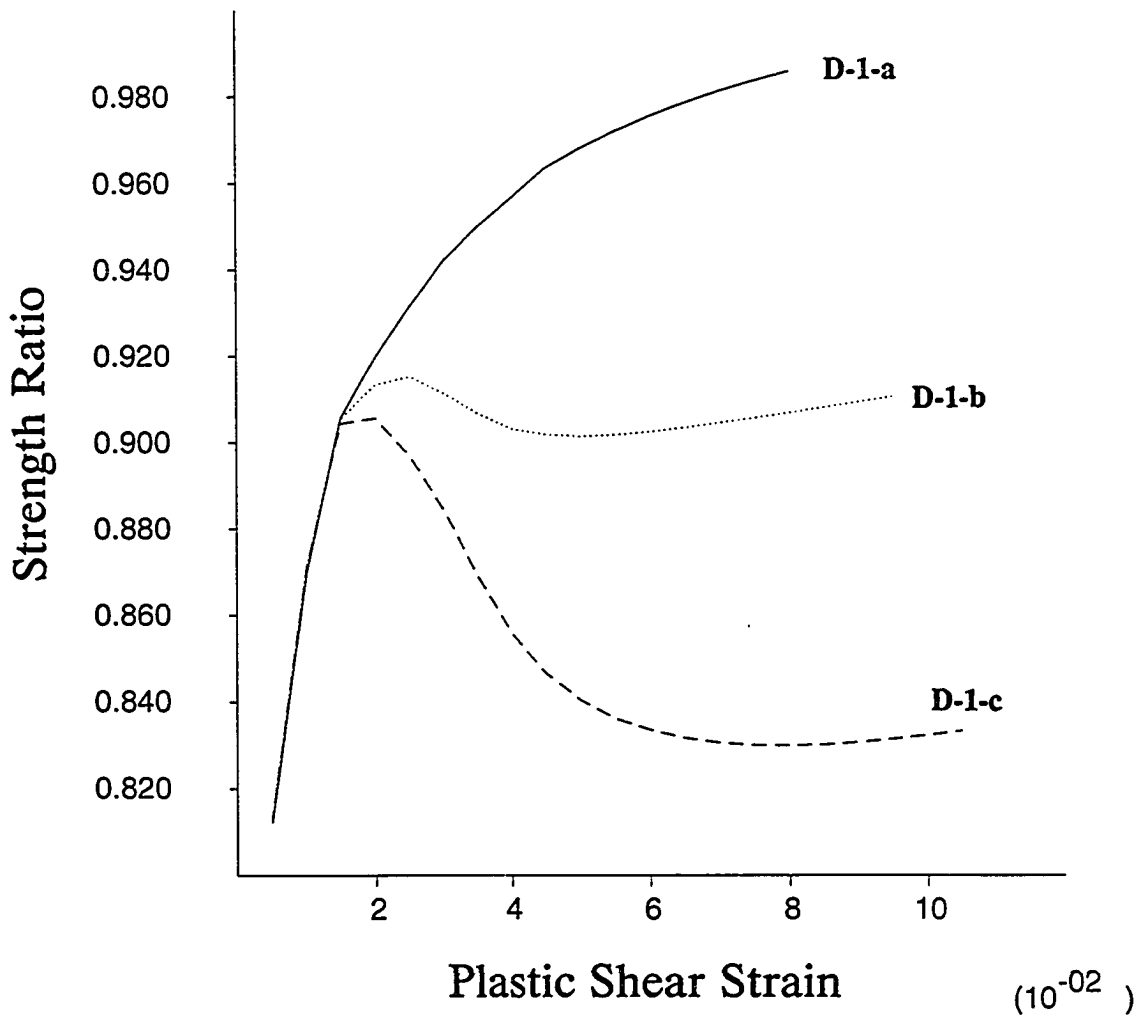


Fig. 6.18b Variation of strength ratios (strain compatibility concept), D-1 analyses

summarized in Table 6.8. Fig. 6.18a (C-1-a) shows that the peak strength ratio is approaching the unity, which is a consequence of no strain softening, whereas

Table 6.8 Summary of the peak strength ratios using the strain compatibility technique.

Code	C-1-a	C-1-b	C-1-c	D-1-b	D-1-c
Peak strength ratio	1.00	0.950	0.937	0.915	0.906

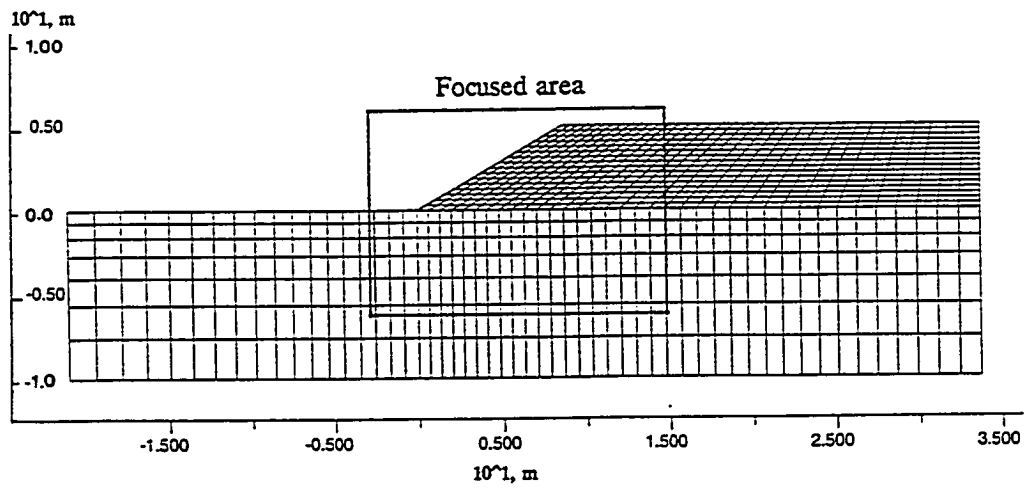
those of C-1-b and C-1-c cases reach the peak values at 0.950 and 0.937, respectively. This implies that if the uniform maximum shear strain is assumed along the failure surface as in the strain compatibility technique to obtain the peak in the summations of strengths at varying strains, then only 95.0% and 93.7% of the summation of the anisotropic strengths (B-1 case) are obtained for the stress-strain relations utilized in C-1-b and C-1-c analyses, respectively.

The peak strength ratios in Table 6.8 were recalculated such that they are comparable to the peak mobilized strength ratios in Table 6.7 (i.e., the ratios were re-scaled based on the summation of the isotropic strengths rather than the summation of the anisotropic strengths). The recalculated values are shown in the parentheses in the third row in Table 6.7. It appears that the strain compatibility concept application consistently result in slightly lower strength mobilization predictions as compared to those of rigorous C and D analyses. In addition, it was found that the levels of plastic shear strain at which the peak strength ratios take place are almost twice greater (3.5% and 4.4%) for C-1-b and C-1-c analyses

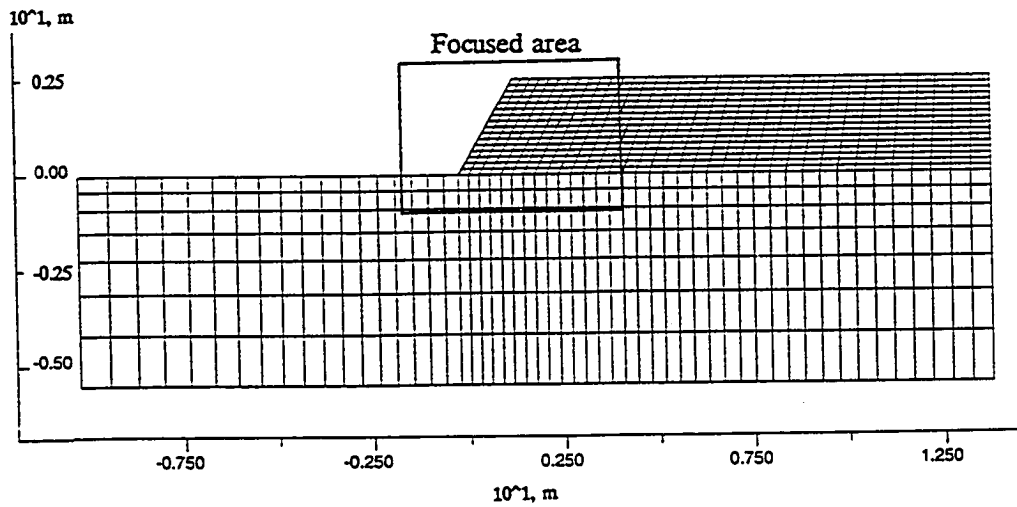
than those (2.0% and 2.5%) for D-1-b and D-1-c analyses (Figs. 6.18a and 6.18b). The higher strain levels at the peak strength ratios for C analyses are a consequence of the difference in the stress-strain relations between C and D analyses.

6.2.2 Linearly Increasing Strength Profile

The slopes considered here in this section have linearly increasing strength profiles with two inclination angles: 30 and 60 degrees. The finite difference meshes of the two slopes are shown in Figs. 6.19a and 6.19b, respectively. The location of lateral and bottom boundaries were conservatively chosen to minimize the boundary interference. The lateral boundaries are rollers and the bottom boundaries are fixed against any displacement. In the following an additional number in the parentheses after an analysis code, such as (30) in C-1-a (30), indicates the inclination angle of the slope in degree. In order to simulate the gradual excavation process in the field, layers of elements are sequentially removed (excavated) from the model, which is followed by computational time steps to bring the slope to the equilibrium state. After the slope reaches the equilibrium state, additional layer of excavation is carried out and further time steps are taken. The cycle of excavation and computational time steps continues until the excavation height reaches the intended final height. In the initial stage where the impact of excavation is relatively small, two layers of elements were removed for each excavation. As the total excavation height approaches the



(a)



(b)

Fig. 6.19 Finite difference meshes: (a) 30 degree slope; and (b) 60 degree slope

critical value, a single layer of elements were removed (from the 10th layer). The excavation heights for the number of excavation layer are summarized in Table 6.9.

Table 6.9 Summary of excavation heights (meters) with the number of layer excavation

Slope	2nd	4th	6th	8th	10th	11th	12th	13th	14th	15th	16th
30°	0.64	1.27	1.89	2.52	3.14	3.46	3.77	4.08	4.39	4.70	5.06
60°	0.32	0.63	0.94	1.26	1.57	1.72	1.89	2.04	2.19	2.35	2.50

6.2.2.1 Isotropic Strength Case (A analysis)

This case represents slopes of isotropic material properties in which both the strength and modulus increase with depth of the soil element from the initial level ground. Table 6.10 shows soil parameters of the slopes. The analytical solution by Kenny (1963) for this case shows that the factor of safety does not depend on the height of the excavation, but only on the strength increment ratio

Table 6.10 Slope information

Inclination of Slope	Undrained Strength Ratio	Unit Weight of Soil, N/m ³	Final Excavation Height, meters	K _o
30 degree	0.20	19651.4	5.0	0.70
60 degree	0.30	19651.4	2.5	0.70

and slope inclination angle. The critical failure surface continues to expand as excavation proceeds. However, after a certain depth of excavation it becomes

fixed with a constant factor of safety even for further excavation (i.e., the failure becomes of mid-slope type). The critical slip surface for slopes with strength profiles which increase with depth from zero at the surface are typically toe or mid-slope failures (Gibson and Morgenstern, 1962; Kenney, 1963; Booker and Davis, 1972). In most practical cases there exist an intercept strength (S_{uo}) at the ground surface and an strength increment ratio with depth ($\delta S_f/\delta D$). If the increase of strength with depth is sufficient, a toe failure is critical. Fig. 6.20 delineates the conditions when a toe or base failure is more critical for slopes with a linearly increasing strength profile (Deschamps, 1993). The actual magnitudes of shear strength do not affect the location of the critical surface, but the rate of the shear strength increase does.

In the literature, it has often been assumed that failure in cut slopes begins at the toe or the bottom of a potential failure surface (Chowdhury, 1978). This assumption is a consequence of the fact that stress concentration is likely to be highest at the toe in such slopes. On the other hand, Peck (1967) raised a doubt on the widely held belief and suggested the possibility of the failure initiating at the crest. In many cases, the first sign of impending slope failure in slopes of cohesive soil is the opening of tension cracks at the crest. It is often observed, however, that a potential failure mass in the slope has already suffered a significant extent of deformation before cracks open up. In such cases, the initial failure point is in the interior of the slope.

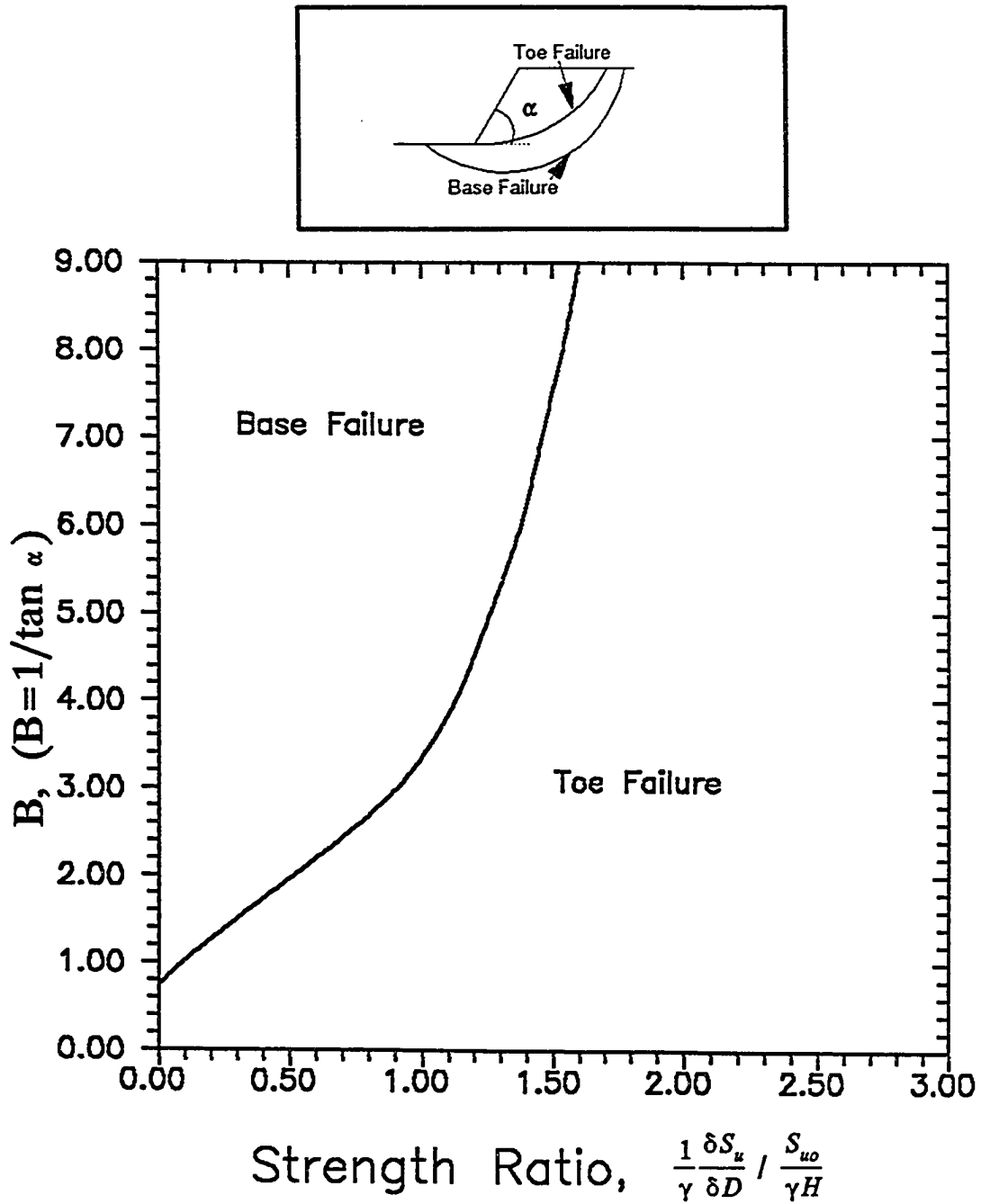
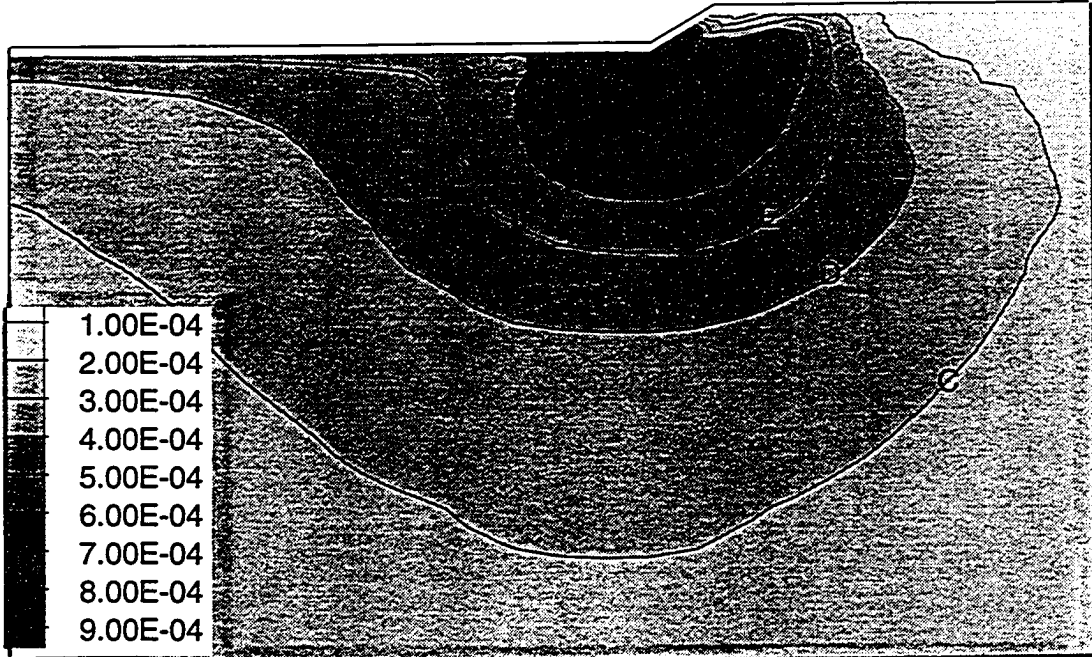


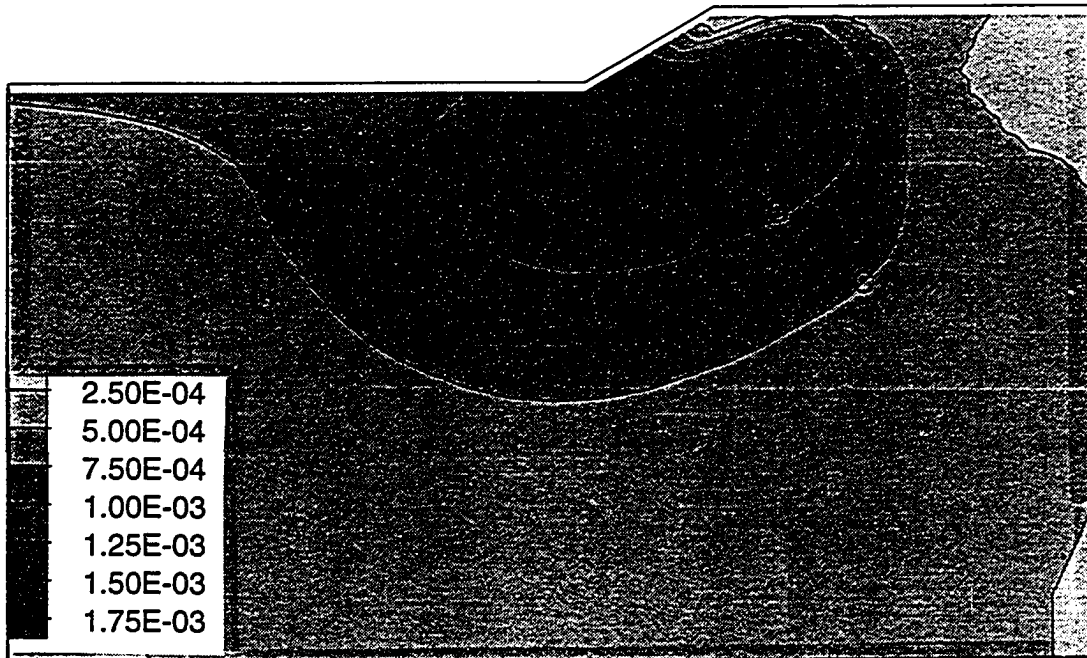
Fig. 6.20 The position of critical surface based on the slope inclination and the strength increment ratio

Figs. 6.21a through 6.21e show the pattern of the maximum shear strain development in the process of layer by layer excavation in A (30) analysis. It is seen that the maximum shear strain starts to concentrate below the toe of the slope at the second layer excavation (Fig. 6.21a). With further excavations the strain concentration is expanded toward interior of the slope. At the sixth layer excavation (Fig. 6.21c), the region somewhat below the crest has the highest concentration of the maximum shear strain, which is then continuously expanded in the size and intensity as excavation continues. If failure occurs in this case, it is likely to develop from the region somewhat below the crest where the strain is highest. Figs. 6.22a through 6.22e show the pattern of maximum shear strain development in the slope of 60 degree inclination (A (60) analysis). It is also observed that the maximum shear strain concentration is highest at the toe in the initial stage of excavation. It is then gradually expanded toward the crest of the slope with further excavations. If failure occurs in this case, it is likely to develop from the toe of the slope based on the maximum shear strain development pattern.

It turned out that both the slopes in A analyses are safe after the 16th layer excavation so that failure surfaces predicted by Modified Bishop method were used to determine the elements which would be involved in the potential failure. Then individual local factor of safety was weighted by the length of the element in the potential failure surface to obtain the global factors of safety for the slopes. Fig. 6.23a shows variations of the factors of safety with and without weights

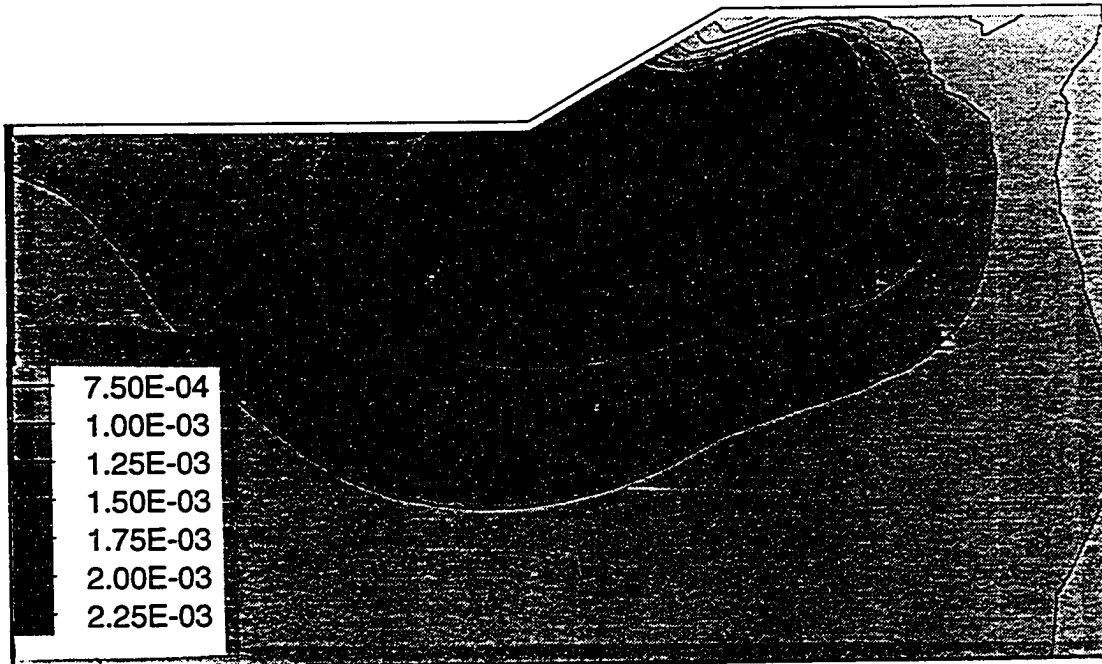


(a) 2nd layer ($H_{ex} = 0.64$ m); Contour Interval = $1.0E-04$ (C: $3.00E-04$, H: $8.00E-04$)

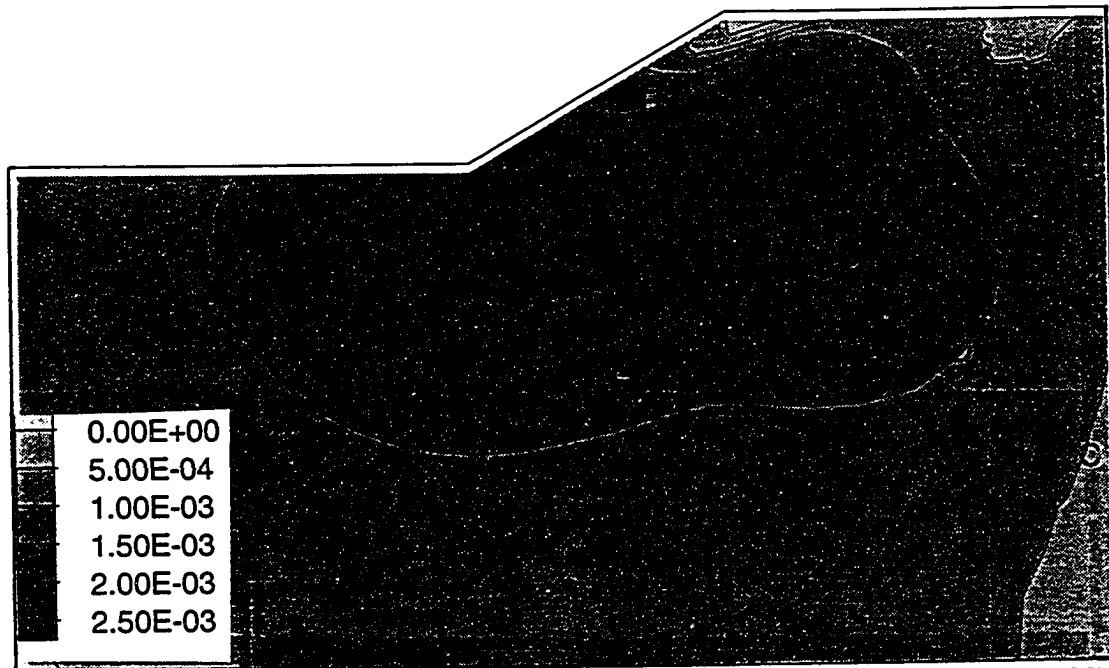


(b) 4th layer ($H_{ex} = 1.27$ m); Contour Interval = $2.5E-04$ (B: $5.00E-04$, F: $1.50E-03$)

Fig. 6.21 Maximum shear strain distribution, A (30) analysis



(c) 6th layer ($H_{\alpha} = 1.89$ m); Contour Interval = $2.5E-04$ (D: $7.50E-04$, I: $2.00E-03$)



(d) 8th layer ($H_{\alpha} = 2.52$ m); Contour Interval = $5.0E-04$ (C: $1.00E-03$, F: $2.50E-03$)

Fig. 6.21 Maximum shear strain distribution, A (30) analysis

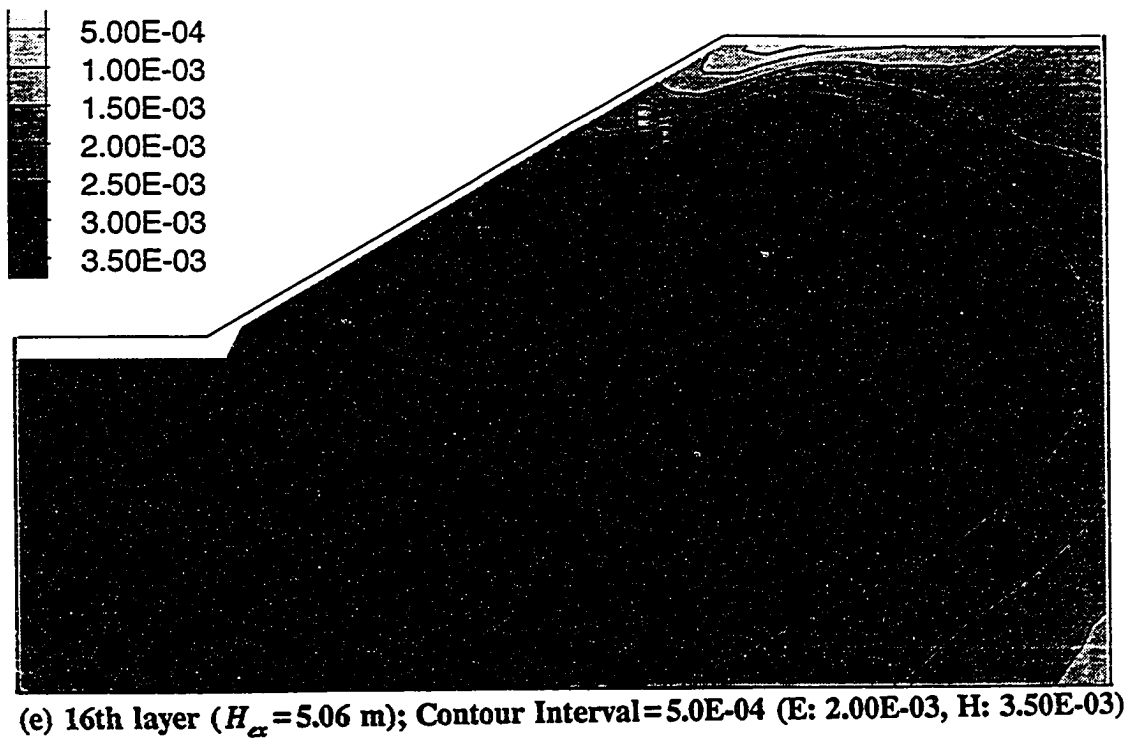
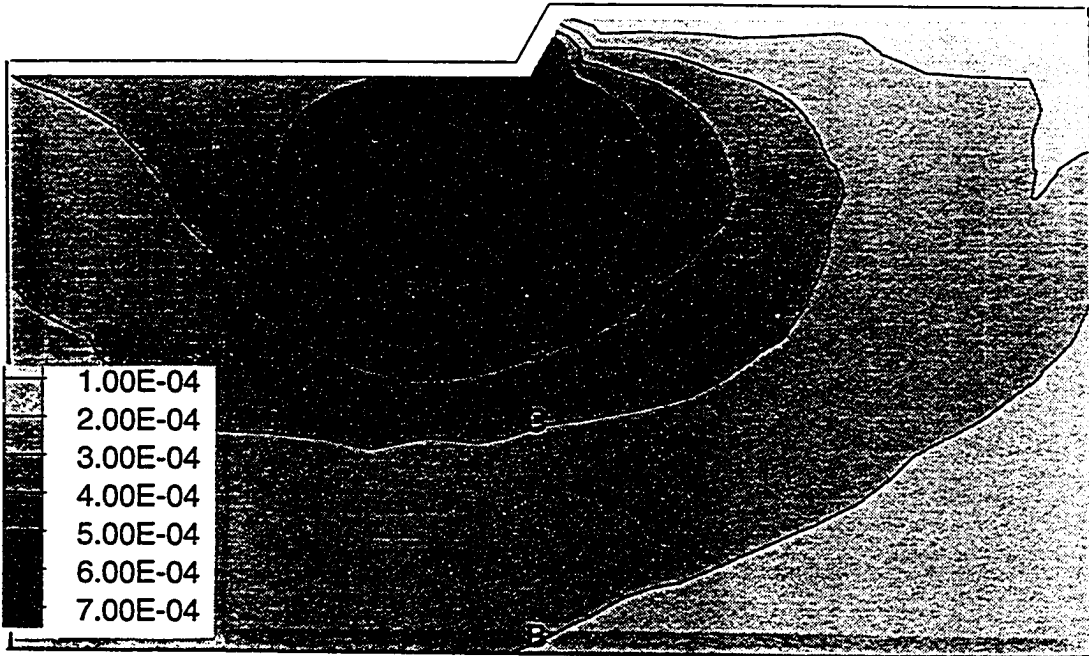
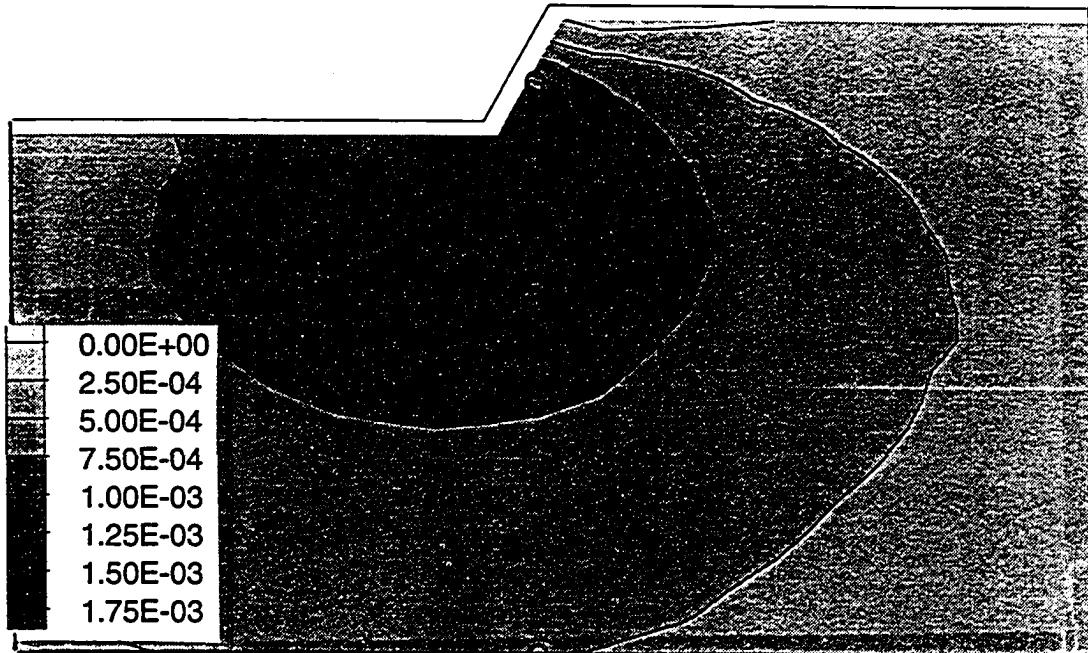


Fig. 6.21 Maximum shear strain distribution, A (30) analysis

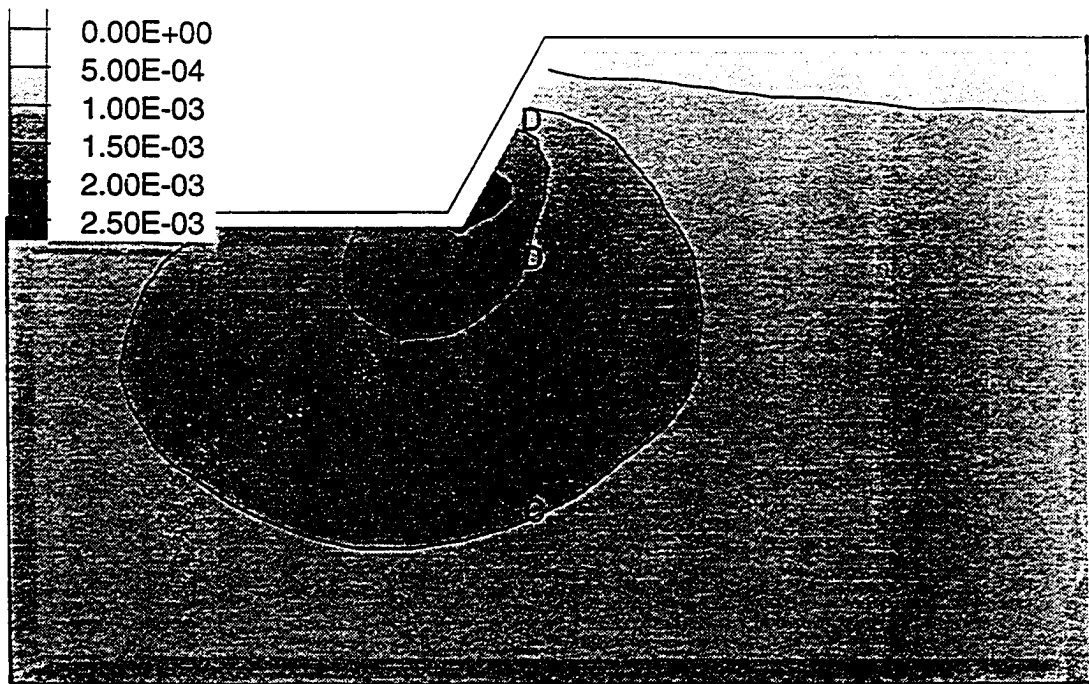


(a) 2nd layer ($H_{\alpha} = 0.32$ m); Contour Interval = $1.0E-04$ (B: $2.00E-04$, G: $7.00E-04$)

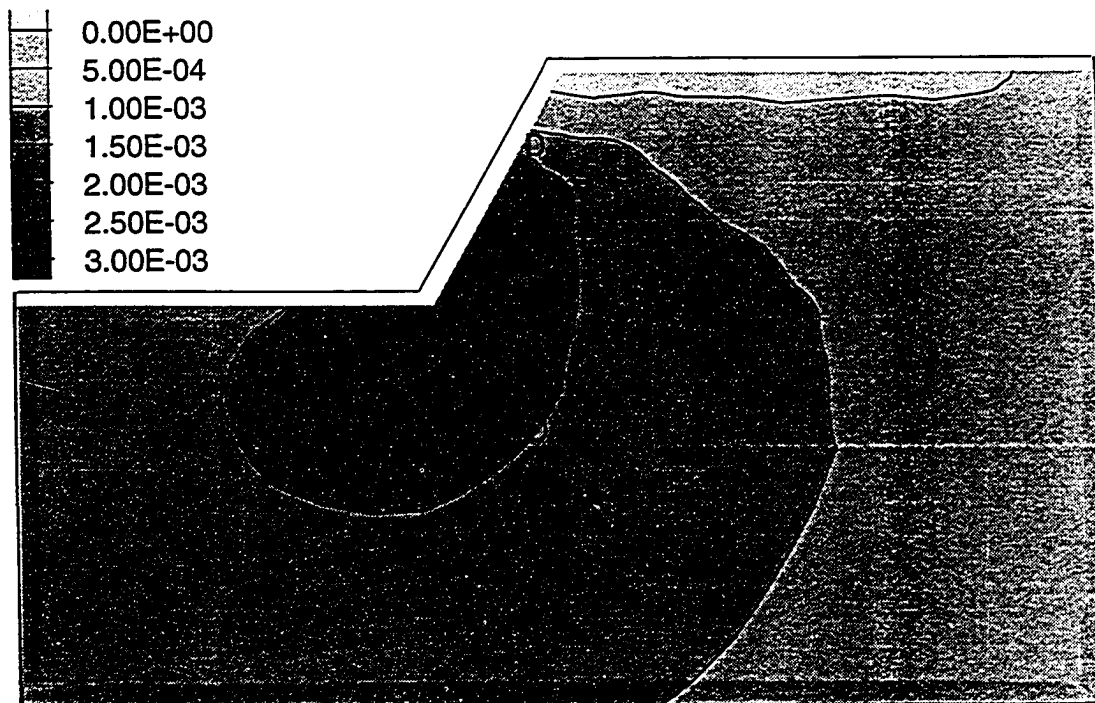


(b) 4th layer ($H_{\alpha} = 0.63$ m); Contour Interval = $2.5E-04$ (C: $5.00E-04$, G: $1.50E-03$)

Fig. 6.22 Maximum shear strain distribution, A (60) analysis

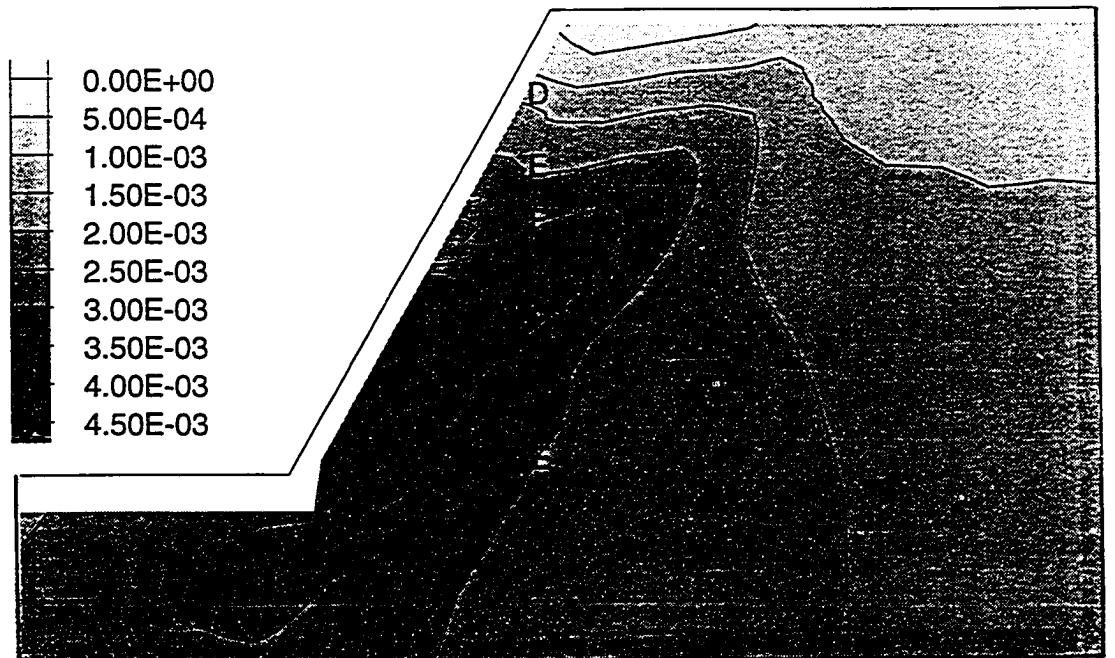


(c) 6th layer ($H_{\alpha} = 0.94$ m); Contour Interval = $5.0E-04$ (C: $1.00E-03$, D: $1.50E-03$)



(d) 8th layer ($H_{\alpha} = 1.26$ m); Contour Interval = $5.0E-04$ (C: $1.00E-03$, D: $1.50E-03$)

Fig. 6.22 Maximum shear strain distribution, A (60) analysis



(e) 16th layer ($H_{ex} = 2.50$ m); Contour Interval = $5.0E-04$ (D: $1.50E-03$, F: $2.50E-03$)

Fig. 6.22 Maximum shear strain distribution, A (60) analysis

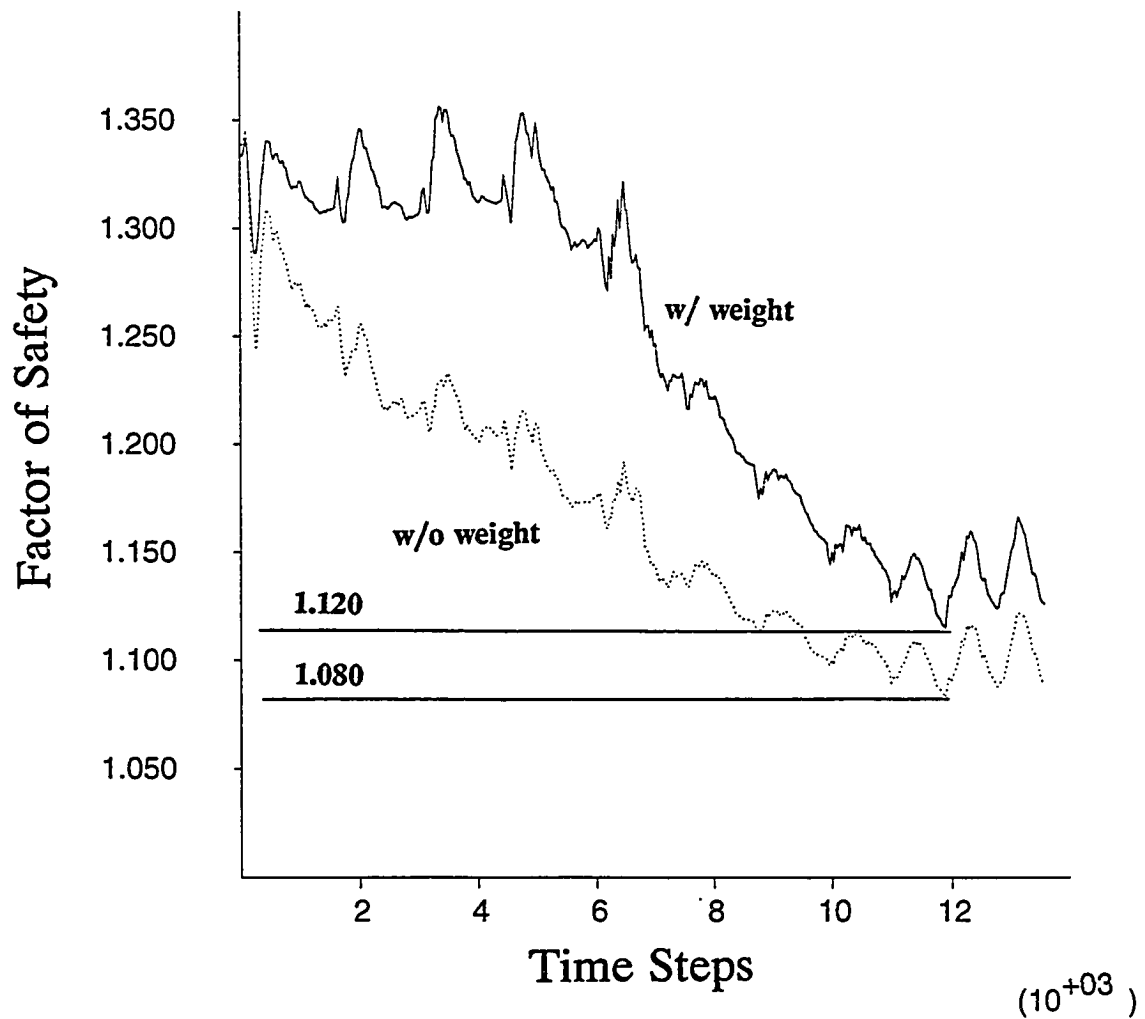


Fig. 6.23a Variation of factors of safety at the Modified Bishop's surface, A (30) analysis

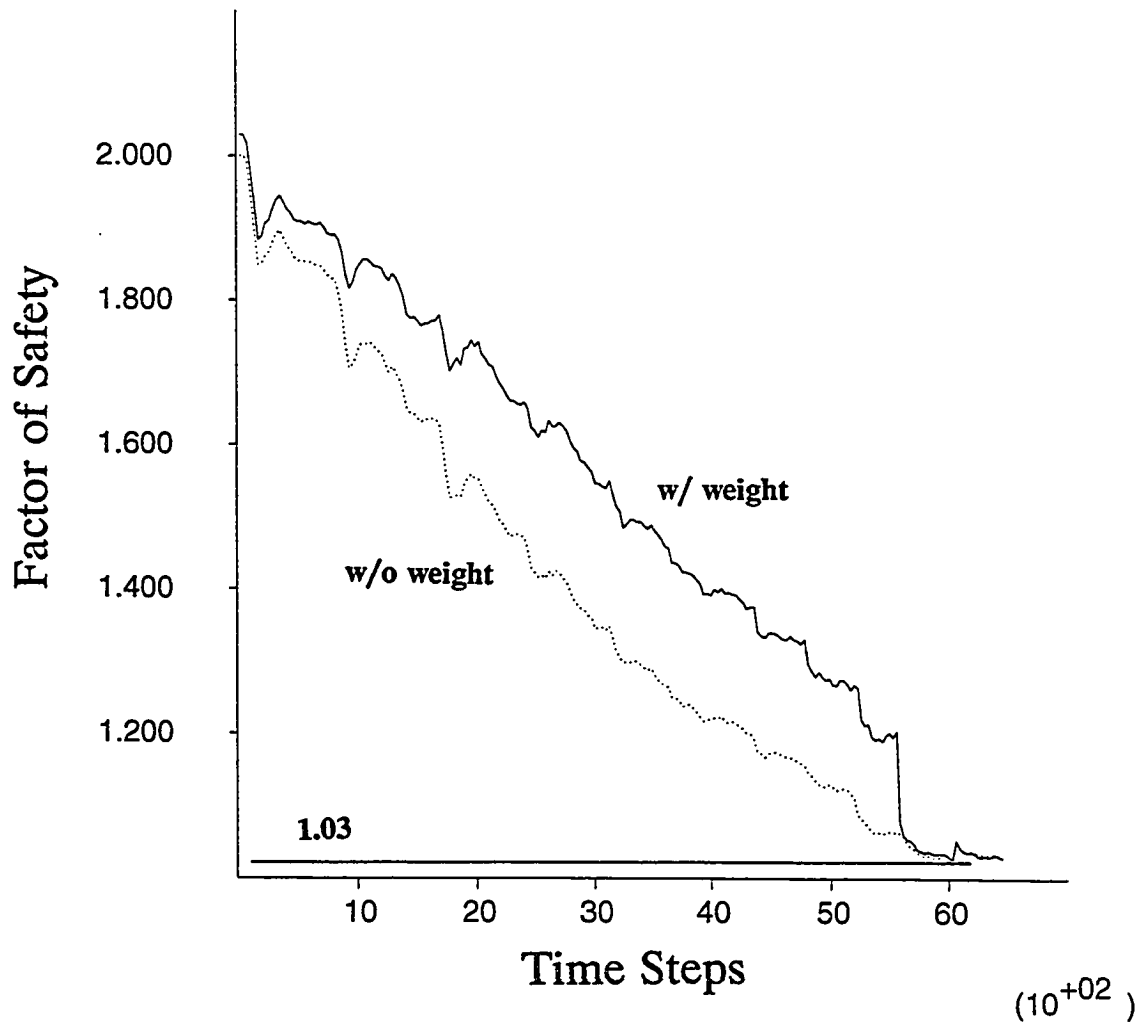


Fig. 6.23b Variation of factors of safety at the Modified Bishop's surface, A (60) analysis

accounted for in A (30) analysis. At the final stage the two factors of safety are 1.12 and 1.08 with and without weight, respectively. Fig. 6.23b shows variations of the factors of safety in A (60) analysis. At the final excavation, the two factors of safety become identical, 1.03 during the final stage of excavation. It should be noted here that the actual critical failure surface during the excavation is continuously expanding downward, but the potential failure surface at the final stage was used to determine the variation of factors of safety during various levels of excavation. The factors of safety from A (30) and A (60) analyses, 1.12 and 1.030, are in good agreement with 1.102 and 0.991, respectively, obtained by Modified Bishop method.

Figs. 6.24a and 6.24b show the distribution of local factors of safety along the normalized failure surface distance at the end of final (16th) excavation in A (30) and A (60) analyses, respectively. In spite of the high concentration of the maximum shear strains near the toe in both of the slopes, it is interesting to find that the toe elements have factors of safety much greater than unity, while the rest of elements are at yield (factor of safety = 1.0). It should be recalled here that limit equilibrium methods are based on the assumption that the local factors of safety are uniform along the potential failure surface. The assumption of uniform distribution of local factors of safety is demonstrated to be unrealistic to a great extent for a stable slope as shown in these figures. However, if a slope enters into a failure state along a failure surface, then the whole elements may have uniform local factors of safety, unity, satisfying the assumption. Therefore, it can be said

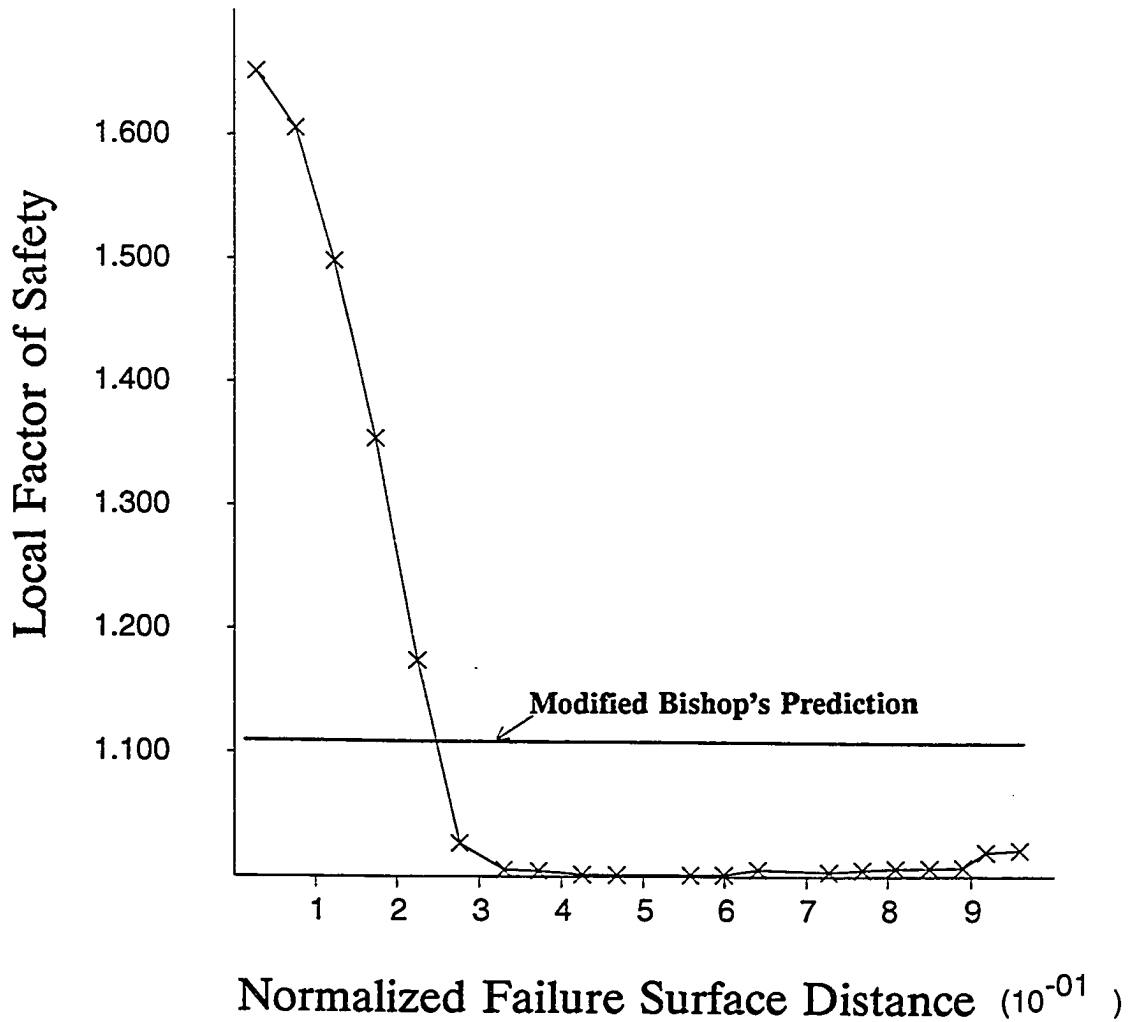


Fig. 6.24a Distribution of local factors of safety along the Modified Bishop's surface (16th layer excavation), A (30) analysis

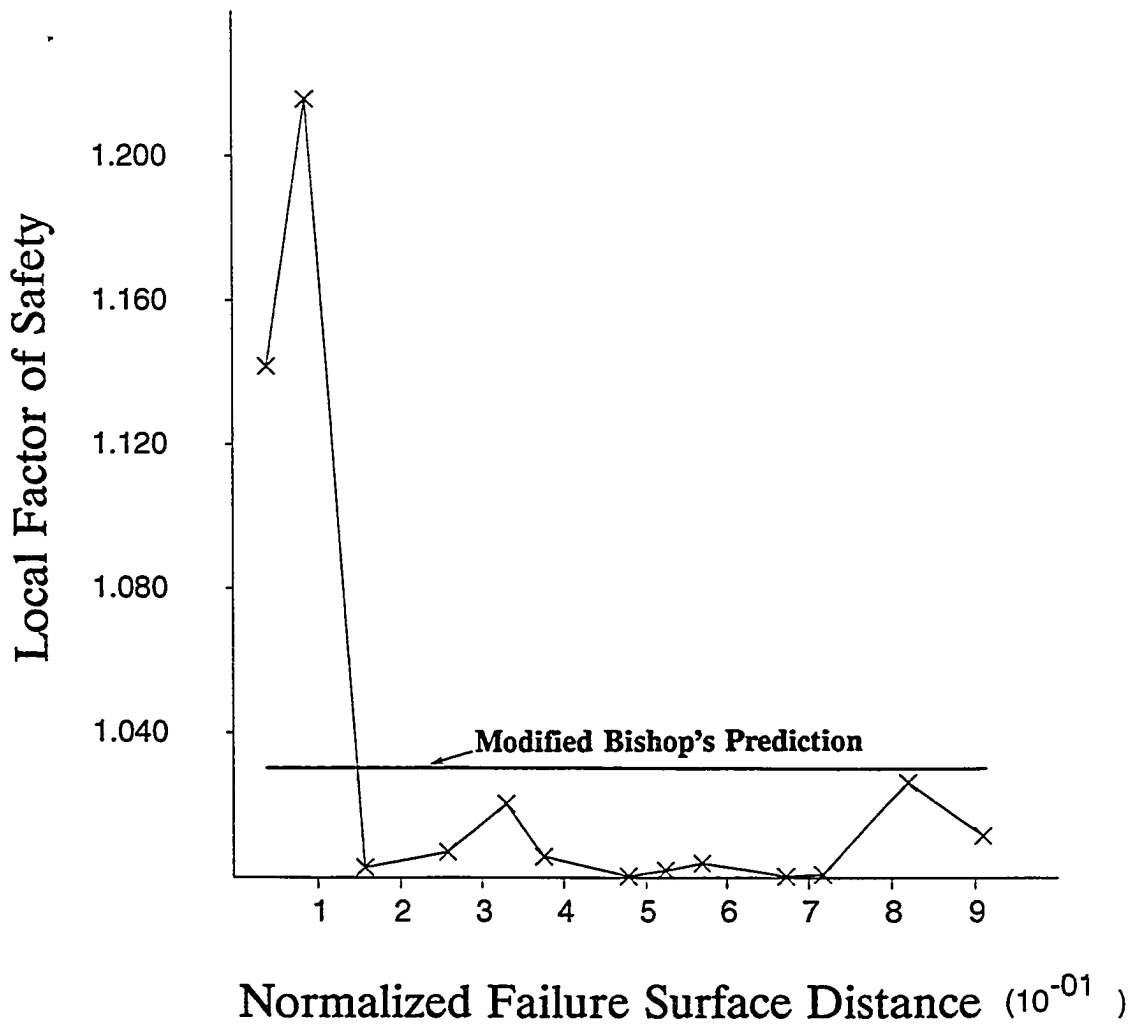


Fig. 6.24b Distribution of local factors of safety along the Modified Bishop's surface (16th layer excavation), A (60) analysis

that the assumption of uniform distribution of local factors of safety (uniform ratio of strength mobilization) is valid only at the critical state especially for ductile materials.

6.2.2.2 Anisotropic Strength Cases (B analyses)

In these series of analyses, major principal stress directions of the entire elements at the state of incipient failure are required in order to determine the corresponding peak strengths. The states of incipient failure were obtained at the 15th layer excavation in B-1 (30) and B-1 (60) analyses. Figs. 6.25a and 6.25b show i angle distributions at the states of incipient failures over the elements along the potential failure surfaces determined from B-1 (30) and B-1 (60) analyses, respectively. The i angle for the 30 degree slope (B-1 (30)) ranges from about -3 to 62 degrees, whereas that of the 60 degree slope (B-1 (60)) ranges from about -6 to 35 degrees. The wider i angle distribution for B-1 (30) is due to the fact that for this case elements involved in the failure surface near the toe are subjected to the passive mode of loading, while those of B-1 (60) are all under the active mode due to the high inclination angle of the slope. Even in B (30) case, only three elements at the toe belong to the passive mode. Therefore, it can be readily said that the active mode strengths (e.g., compression and direct simple shear strengths) are most influential in the stability of slopes in which toe failures are most possible. Figs. 6.26a and 6.26b show the distribution of i angles at the final stages of excavation for the two slopes, respectively. The i angles in the

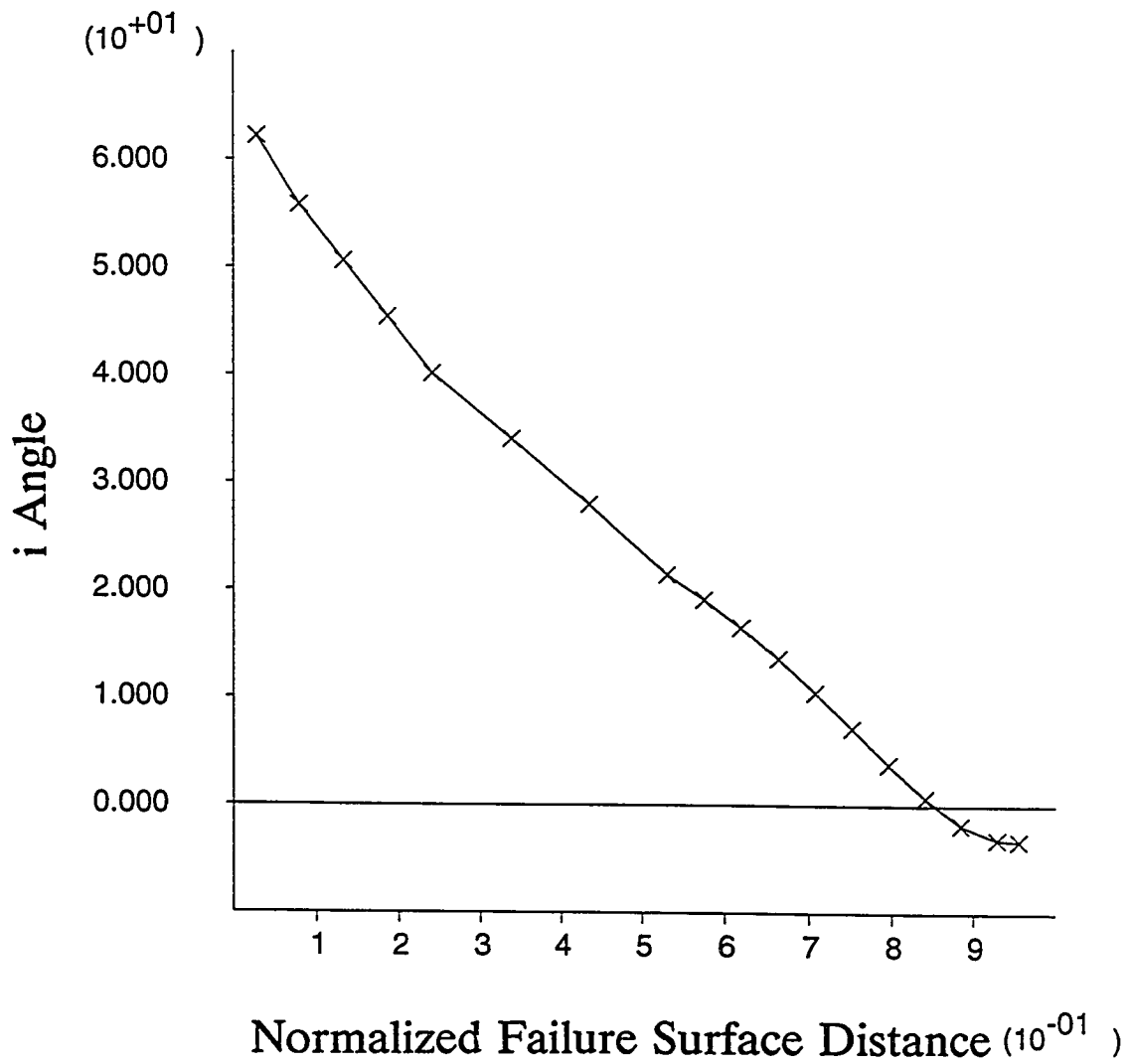


Fig. 6.25a Distribution of *i* angles along the normalized failure surface distance (15th layer excavation), B-1 (30) analysis

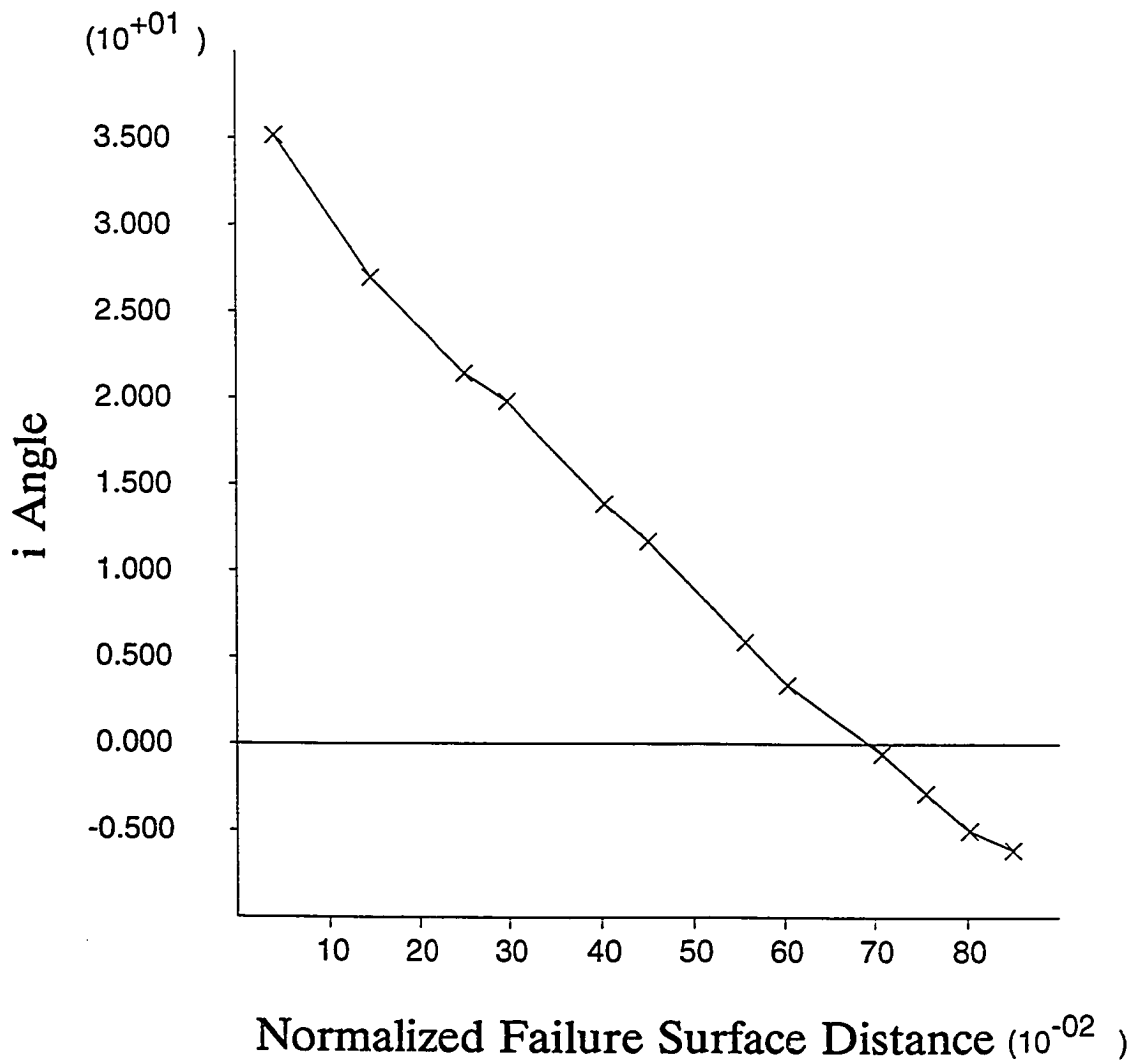
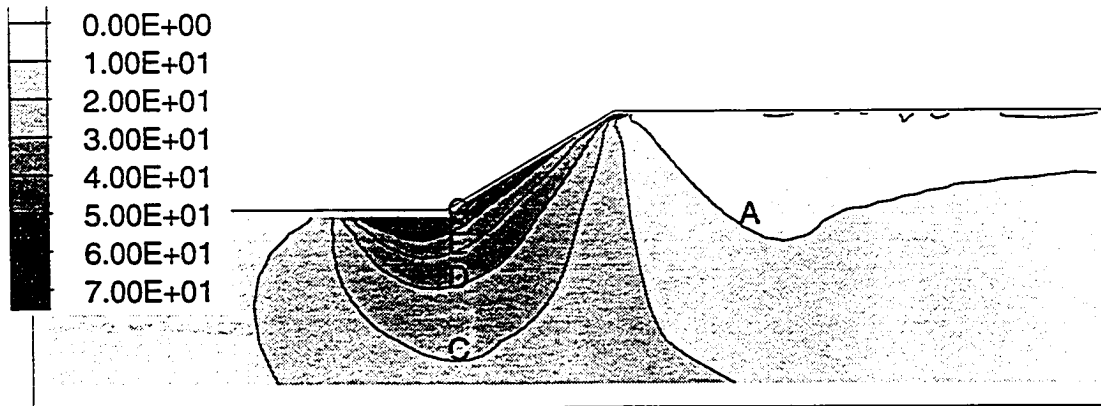
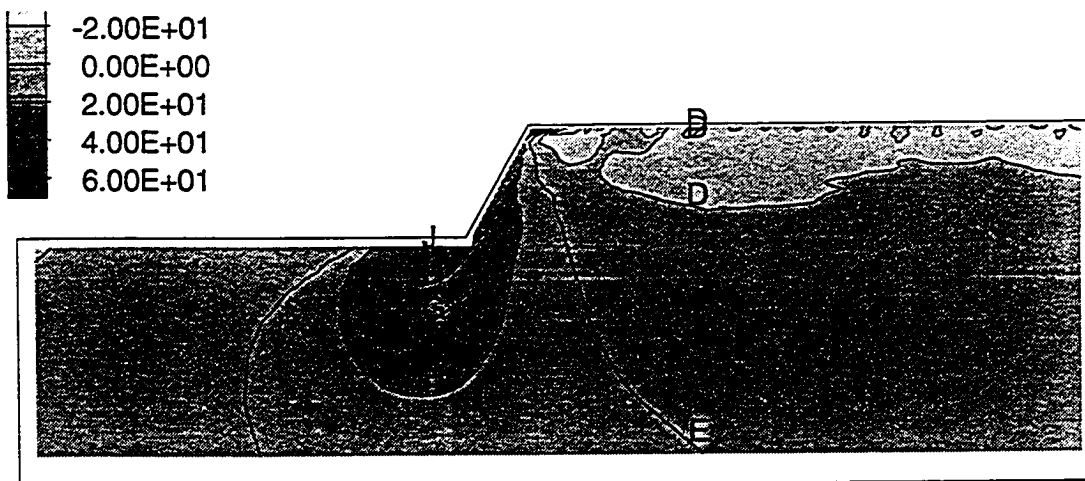


Fig. 6.25b Distribution of *i* angles along the normalized failure surface distance (15th layer excavation), B-1 (60) analysis



(a) B-3 (30); Contour Interval=2.50E-02 (B: 2.50E-02, E: 1.00E-02)



(b) B-4 (60); Contour Interval=5.00E-02 (B: 5.00E-02, D: 1.50E-01)

Fig. 6.26 Distributions of i angles in the slopes: (a) B-1 (30) analysis; and (b) B-1 (60) analysis

bottom of the excavation near the toe are greatest in both cases, but those elements are not actually involved in the failure.

Figs. 6.27a and 6.27b show the relations between the displacement of a nodal point at the tip of the crest (Fig. 6.19) and increasing excavation height in A (30) and B-1 (30) through B-3 (30), and in A (60) and B-1 (60) through B-4 (60) analyses, respectively. It is seen that A and B-1 analyses on both slopes predict almost linear increments of the nodal displacement, which is an indication of stable elastic deformation. The magnitude of nodal displacement at the final layer of excavation continues to increase with higher anisotropy strength curve number. When strength anisotropy curve numbers three and four are used for 30 degree and 60 degree slopes, respectively, the nodal displacement accelerates after a certain excavation depth (3.1 meters for B-3 (30) and 1.6 meters B-4 (60)), reflecting the slopes in failure states. It appears that the implementation of strength anisotropy curve number one (i.e., B-1 analysis) proposed by Casagrande and Carrillo (1944) produces little difference in the nodal displacement behavior as compared to that of A analysis.

Figs. 6.28a through 6.28e show the pattern of mobilized maximum shear stress ratio (τ_{\max}/S_u) development obtained from B-3 (30) analysis. At the second layer excavation, a very high concentration of maximum shear stress is found in the area right below the crest. The contour of the high maximum shear stress ratio simply continues to expand downward inside the slope with further excavations. Note that the contour never expands beyond the toe of the slope,

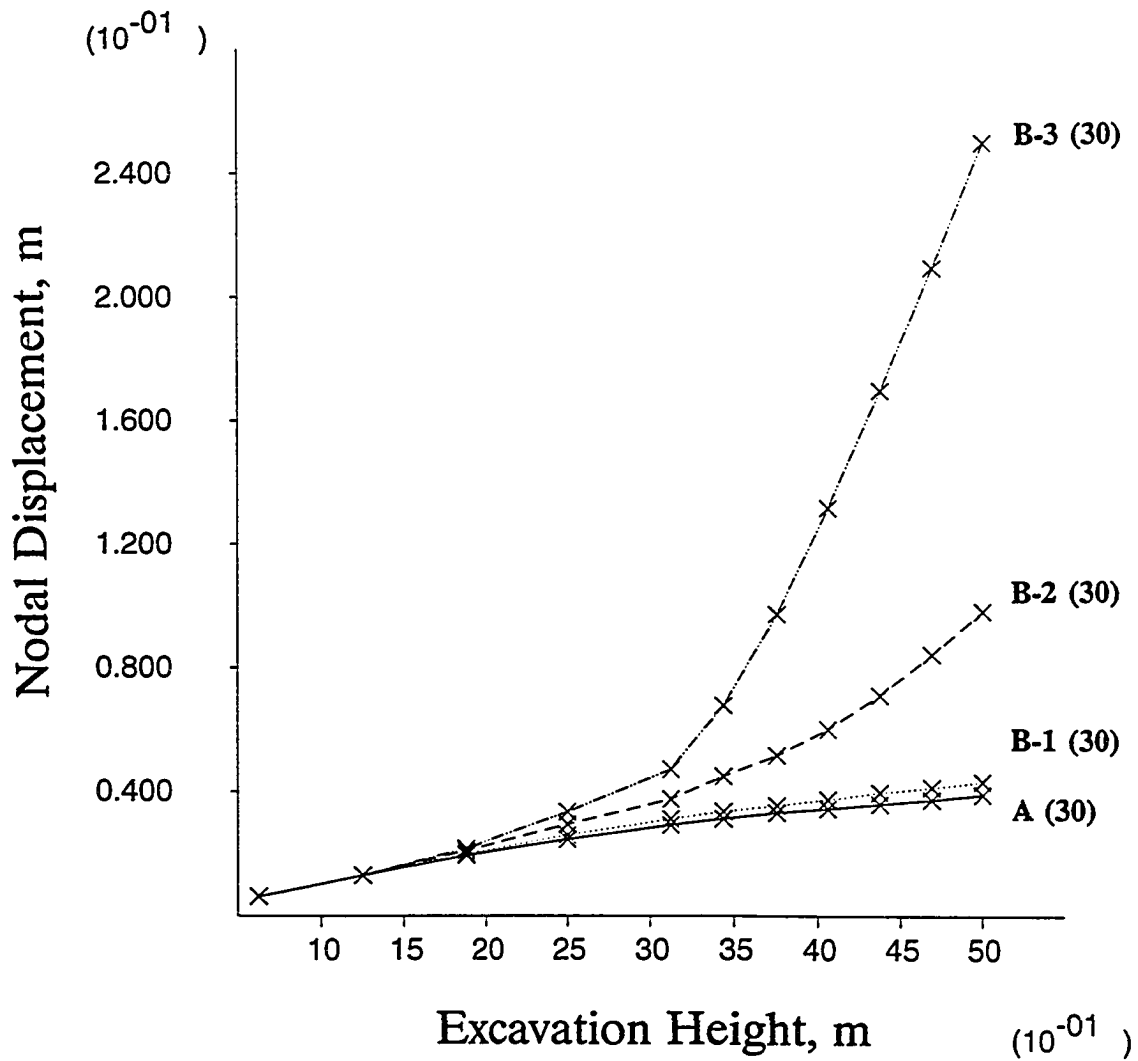


Fig. 6.27a Nodal displacements with increasing excavation heights, A and B (30) series analyses

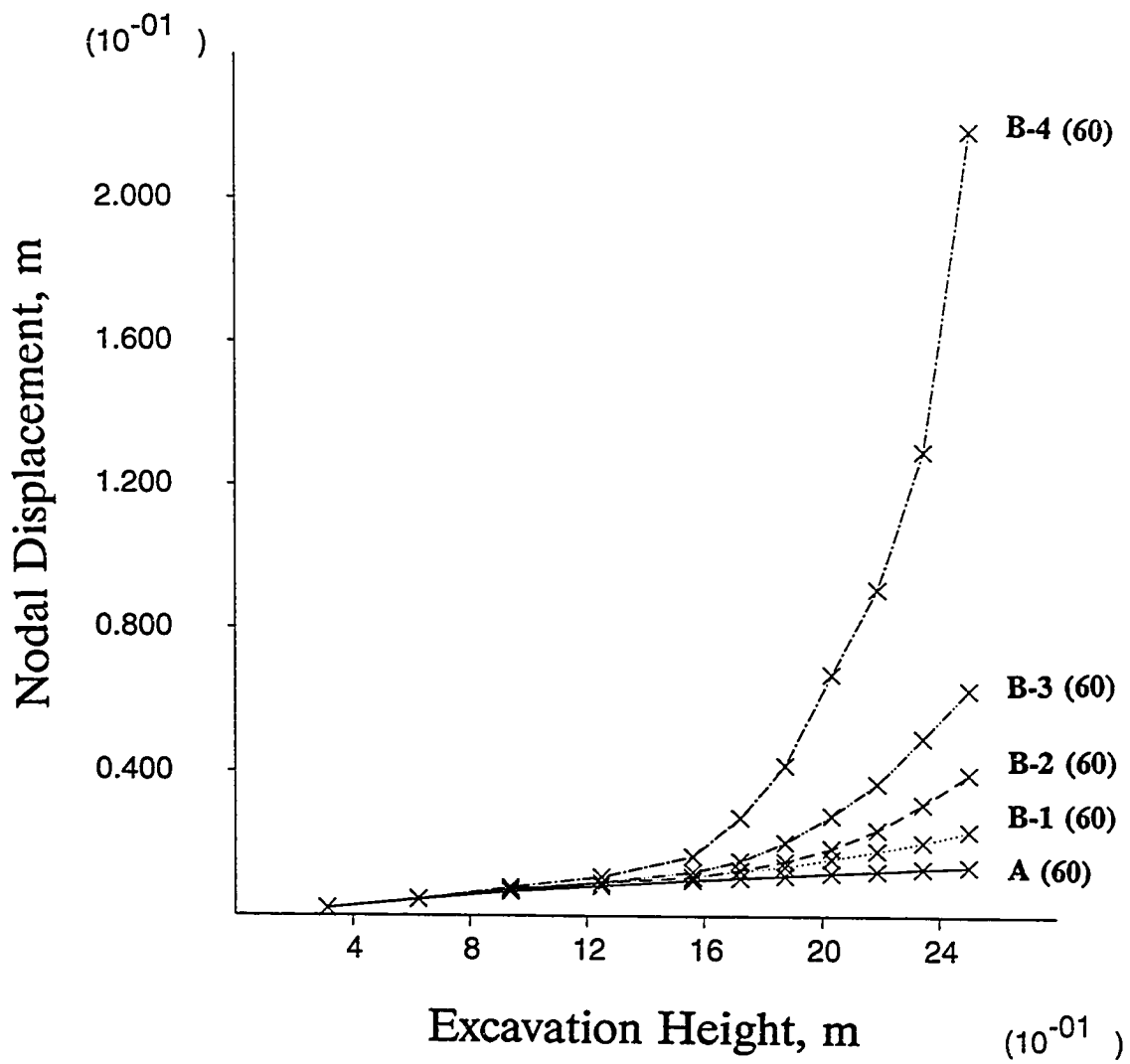
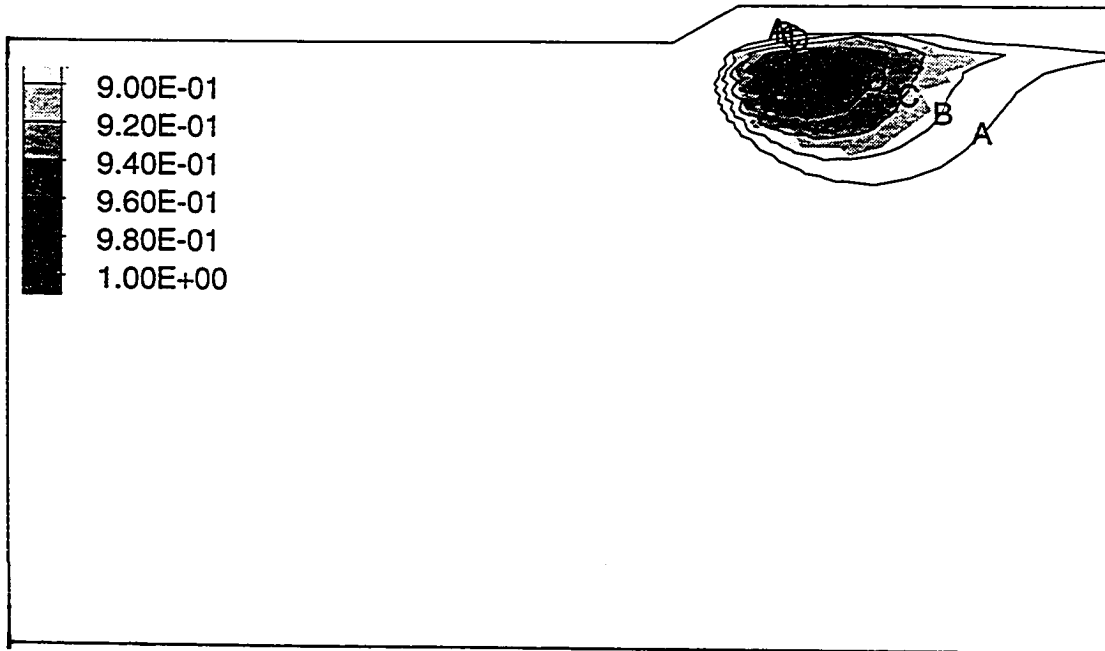
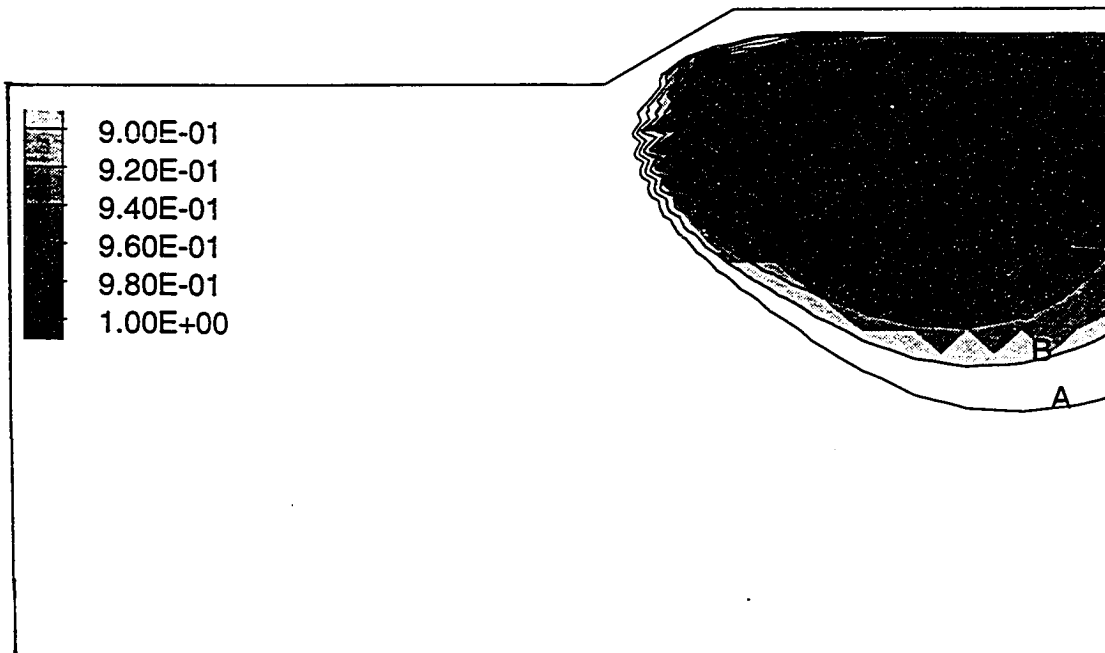


Fig. 6.27b Nodal displacements with increasing excavation heights, A and B (60) series analyses

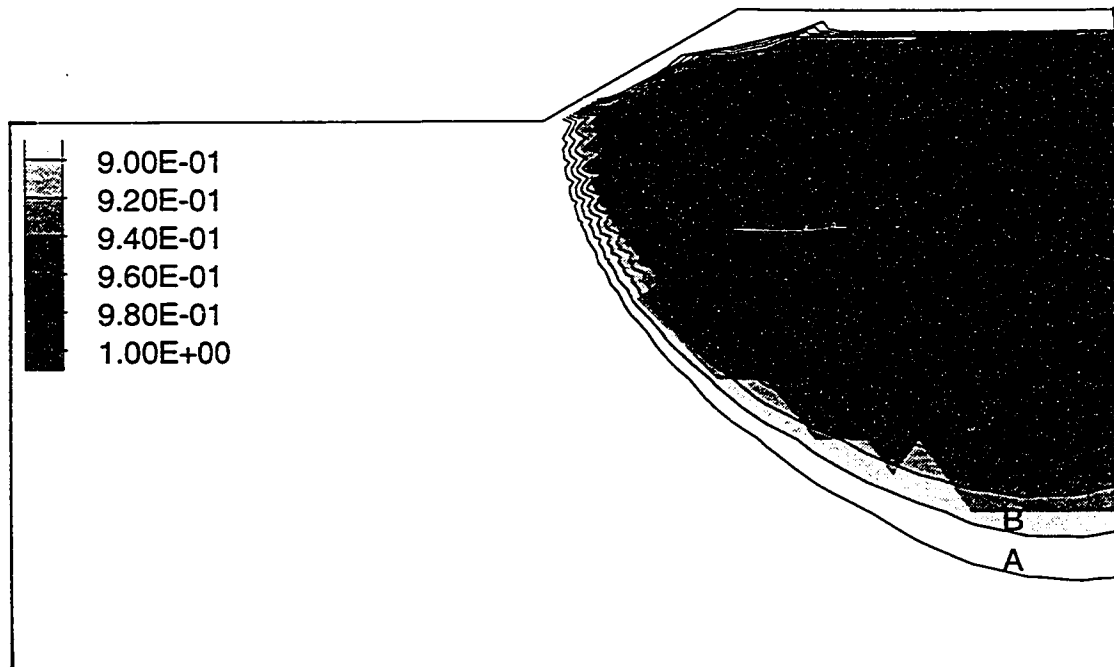


(a) 2nd layer ($H_{ex} = 0.64$ m); Contour Interval = $2.0E-02$ (A: $9.0.0E-01$, D: $9.60E-01$)

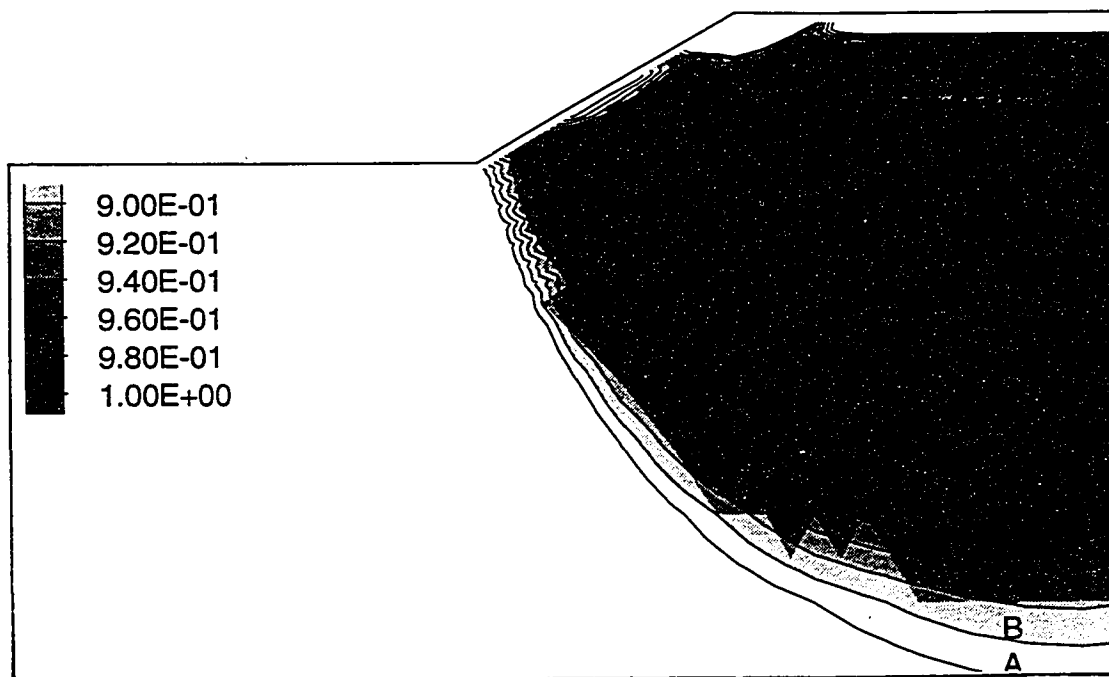


(b) 4th layer ($H_{ex} = 1.27$ m); Contour Interval = $2.0E-02$ (A: $9.0.0E-01$, E: $9.80E-01$)

Fig. 6.28 Maximum shear stress ratio (τ_{max}/S_u) distribution, B-3 (30) analysis



(c) 6th layer ($H_{ex} = 1.89$ m); Contour Interval = $2.0E-02$ (A: $9.0.0E-01$, E: $9.80E-01$)



(d) 8th layer ($H_{ex} = 2.52$ m); Contour Interval = $2.0E-02$ (A: $9.0.0E-01$, E: $9.80E-01$)

Fig. 6.28 Maximum shear stress ratio (τ_{max}/S_u) distribution, B-3 (30) analysis



(e) 16th layer ($H_x = 5.06$ m); Contour Interval = $2.0E-02$ (A: $9.0.0E-01$, E: $9.80E-01$)

Fig. 6.28 Maximum shear stress ratio (τ_{max}/S_u) distribution, B-3 (30) analysis

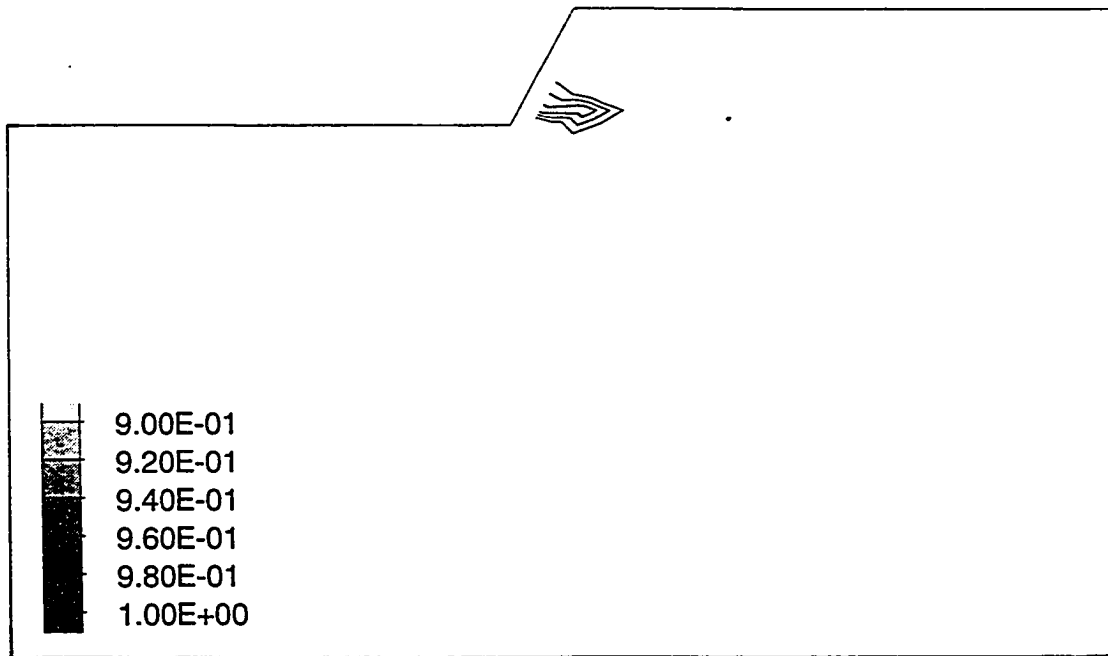
eliminating the possibility of base failure. At the end of final excavation (Fig. 6.28e), almost the whole region below the crest experiences the shear failure. This figure, however, does not give any clue regarding the potential failure surface.

Figs. 6.29a through 6.29d show the pattern of mobilized maximum shear stress ratio (τ_{\max}/S_u) development obtained from B-4 (60) analysis. The pattern is similar to that in B-3 (30) analysis, but the over-stressed region is confined to the area close to the face of the slope. At the last layer excavation (Fig. 6.29d), the entire region near the slope face is at yield. As in B-3 (30) analysis, the maximum shear stress ratio contour does not provide the location of the failure surface.

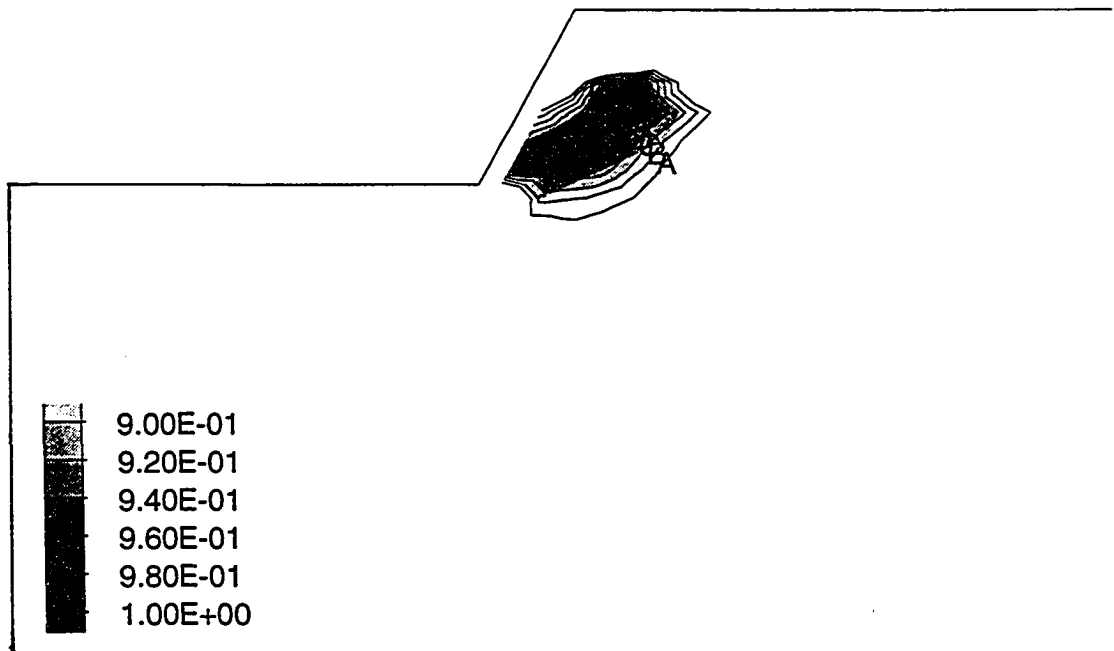
Table 6.11 Summary of factors of safety from A and B series analyses.

Slope Inclination	30 degree				60 degree				
	A	B-1	B-2	B-3	A	B-1	B-2	B-3	B-4
Type of Analysis									
Factor of Safety	1.11	1.01	1.00	1.00	1.03	1.00	1.00	1.00	1.00

Table 6.11 summarizes the global factors of safety determined from such curves as in Fig. 6.23a and 6.23b in A and B analyses. It is seen that factors of safety from B analyses are all unity except B-1 (30) case, which all represent a state of failure. It is interesting to find, however, that individual case shows different levels of slope stability from the observation of the nodal point displacement (e.g., Figs. 6.27a and 6.27b), implying that the factor of safety alone

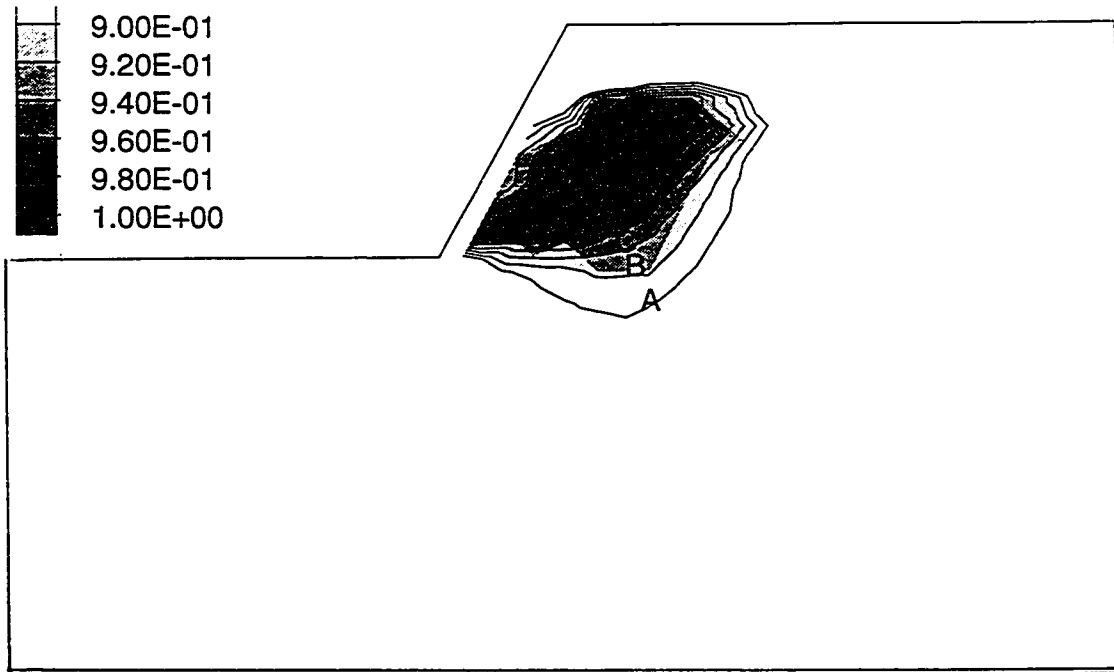


(a) 4th layer ($H_{\alpha} = 0.32$ m); Contour Interval = $2.0E-02$

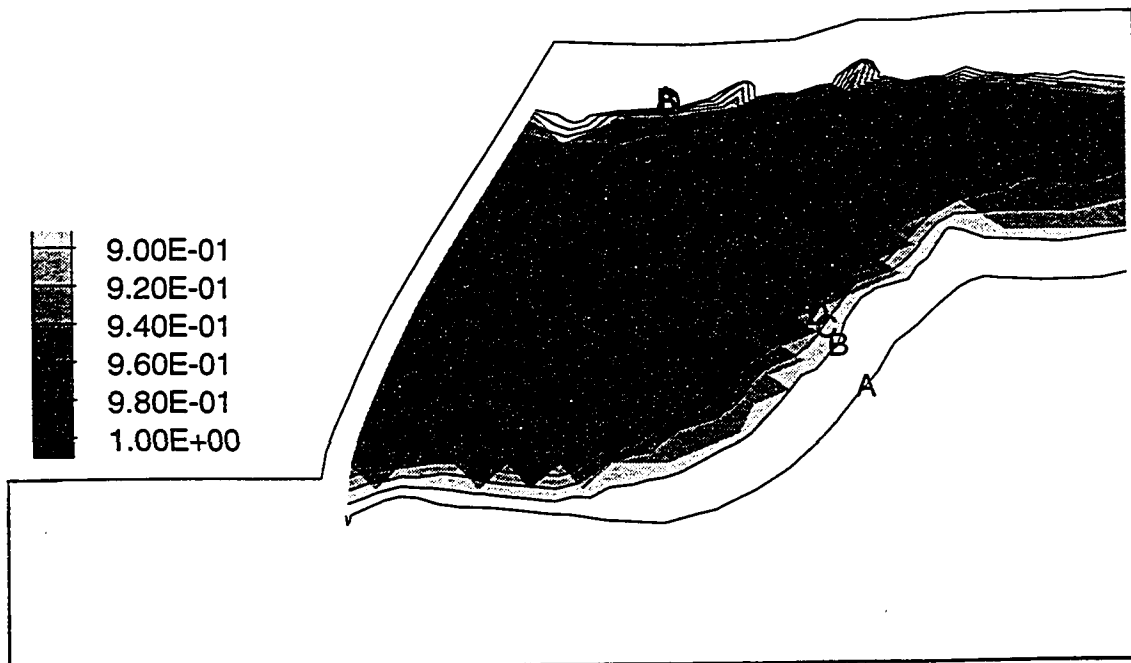


(b) 6th layer ($H_{\alpha} = 0.94$ m); Contour Interval = $2.0E-02$ (A: $9.0.0E-01$, E: $9.80E-01$)

Fig. 6.29 Maximum shear stress ratio (τ_{\max}/S_u) distribution, B-4 (60) analysis



(c) 8th layer ($H_{\alpha} = 1.26$ m); Contour Interval = $2.0E-02$ (A: $9.00E-01$, E: $9.80E-01$)



(d) 16th layer ($H_{\alpha} = 2.50$ m); Contour Interval = $2.0E-02$ (A: $9.00E-01$, E: $9.80E-01$)

Fig. 6.29 Maximum shear stress ratio (τ_{\max}/S_u) distribution, B-4 (60) analysis

cannot fully provide the total picture of slope stability. Fig. 6.30a and 6.30b show the variations of local factors of safety distributions along the normalized failure surface distance at the final excavations in B (30) and B (60) analyses, respectively. The elements in the middle section of the failure surface are constantly at yield without regard to the anisotropic strength curve number. It is clearly shown that as the anisotropic strength curve number increases, the factors of safety of toe and crest elements drop to unity, causing the whole structure to fail.

Figs. 6.31a and 6.31b show the relations between the elements numbered from the toe to the crest and the time steps at which the maximum shear stress becomes equal to the peak strength (i.e., $\tau_{max}/S_u = 1.0$) in B-3 (30) and B-4 (60) analyses, respectively. Figs. 6.31a shows that the failure of element first starts at element "n" and it propagates to elements "m", "o" and "l". Upon reaching the crest elements (element "p"), the failure moves down toward the toe so that failure successively occurs in a well organized manner. It is clearly shown that the failure near the crest (elements "k" to "p") occurs in a short period of time. Fewer number of elements were involved in the failure surface in B-3 (60) analysis (Figs. 6.31b), since the length of the failure surface is relatively short. It appears that failure occurs first at the element (element "i") which is located a few elements below the crest. Then, the elements around the element "i" are alternately failed before the failure moves down toward the toe elements.

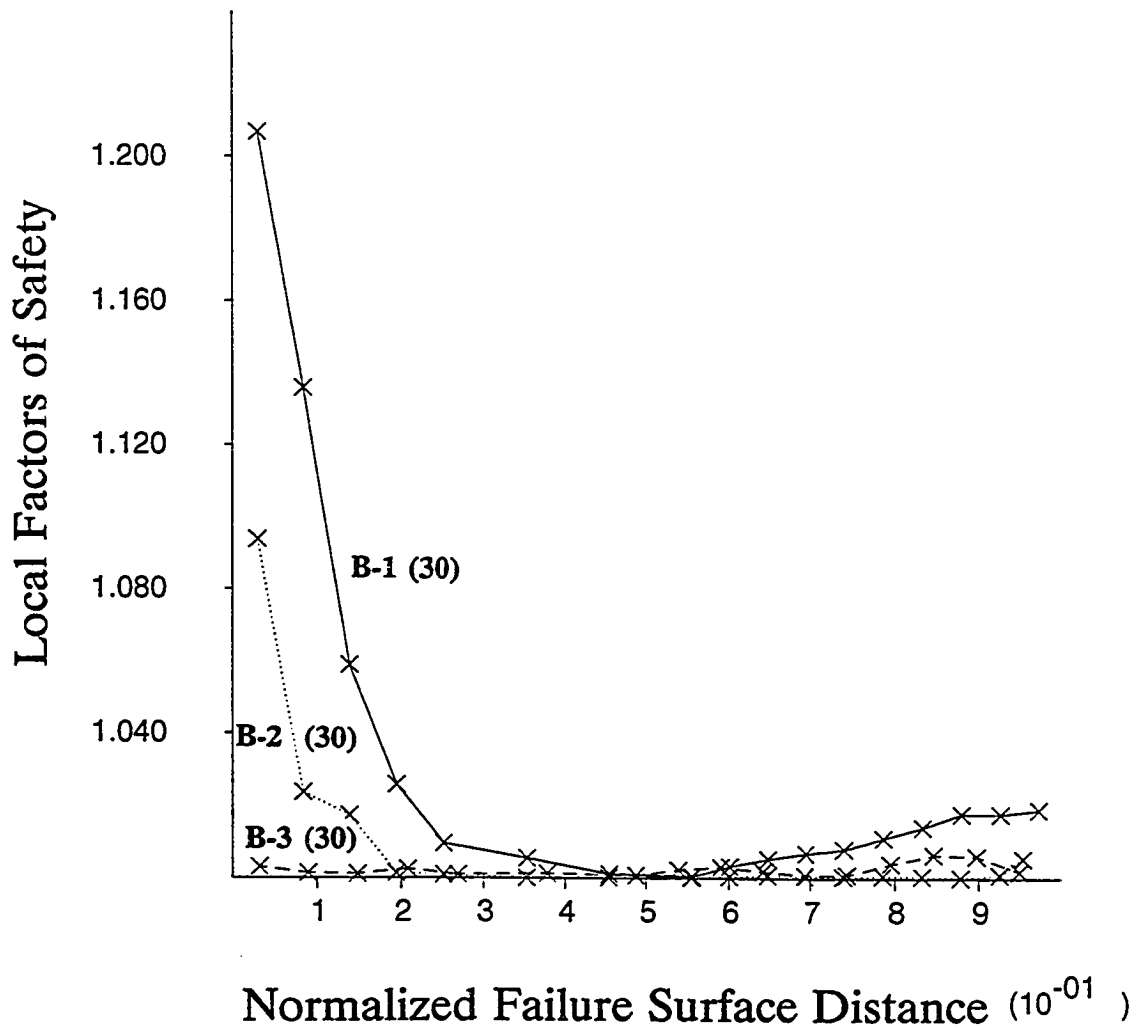


Fig. 6.30a Variation of local factors of safety distribution (16th layer excavations), B (30) analyses

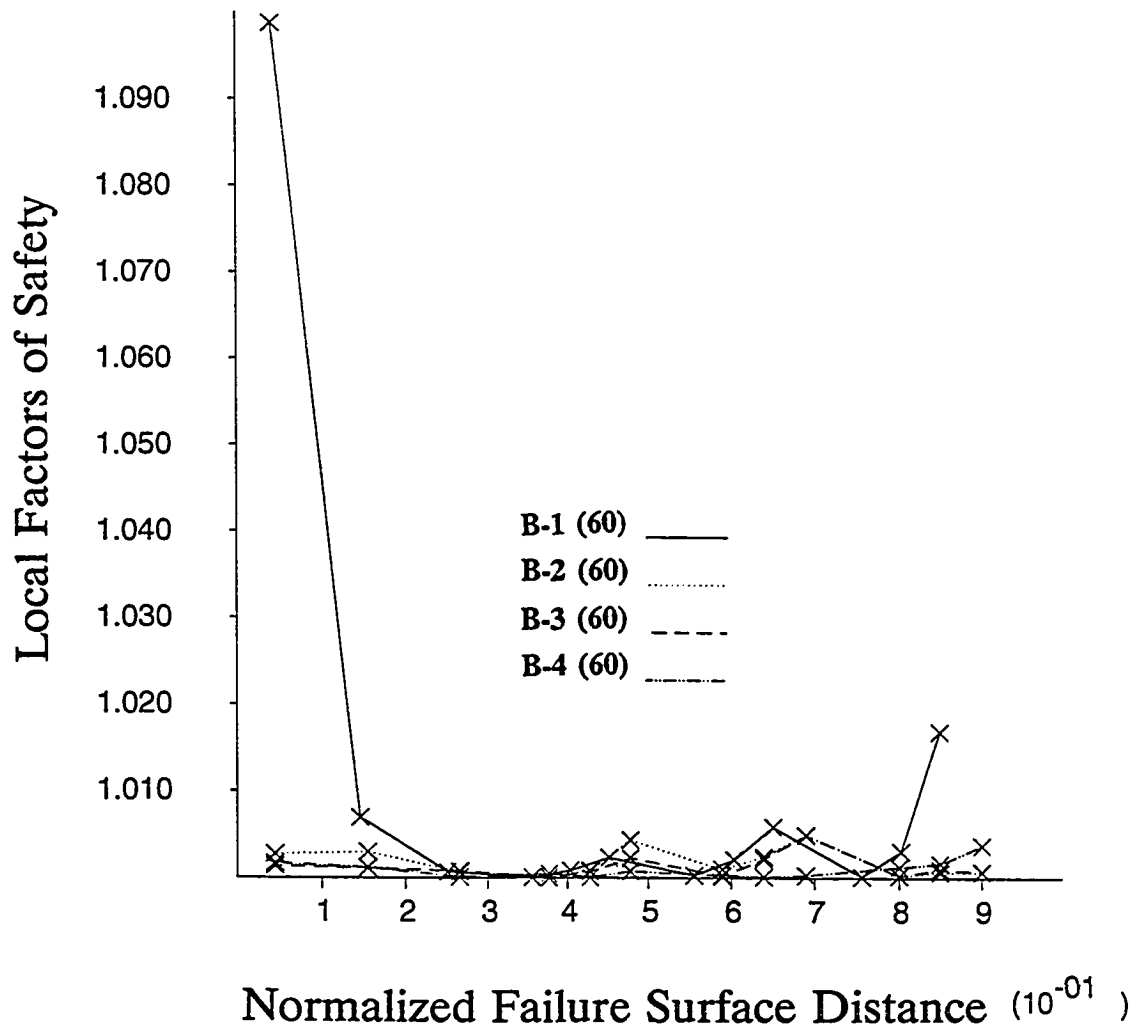


Fig. 6.30b Variation of local factors of safety distribution (16th layer excavations), B (60) analyses

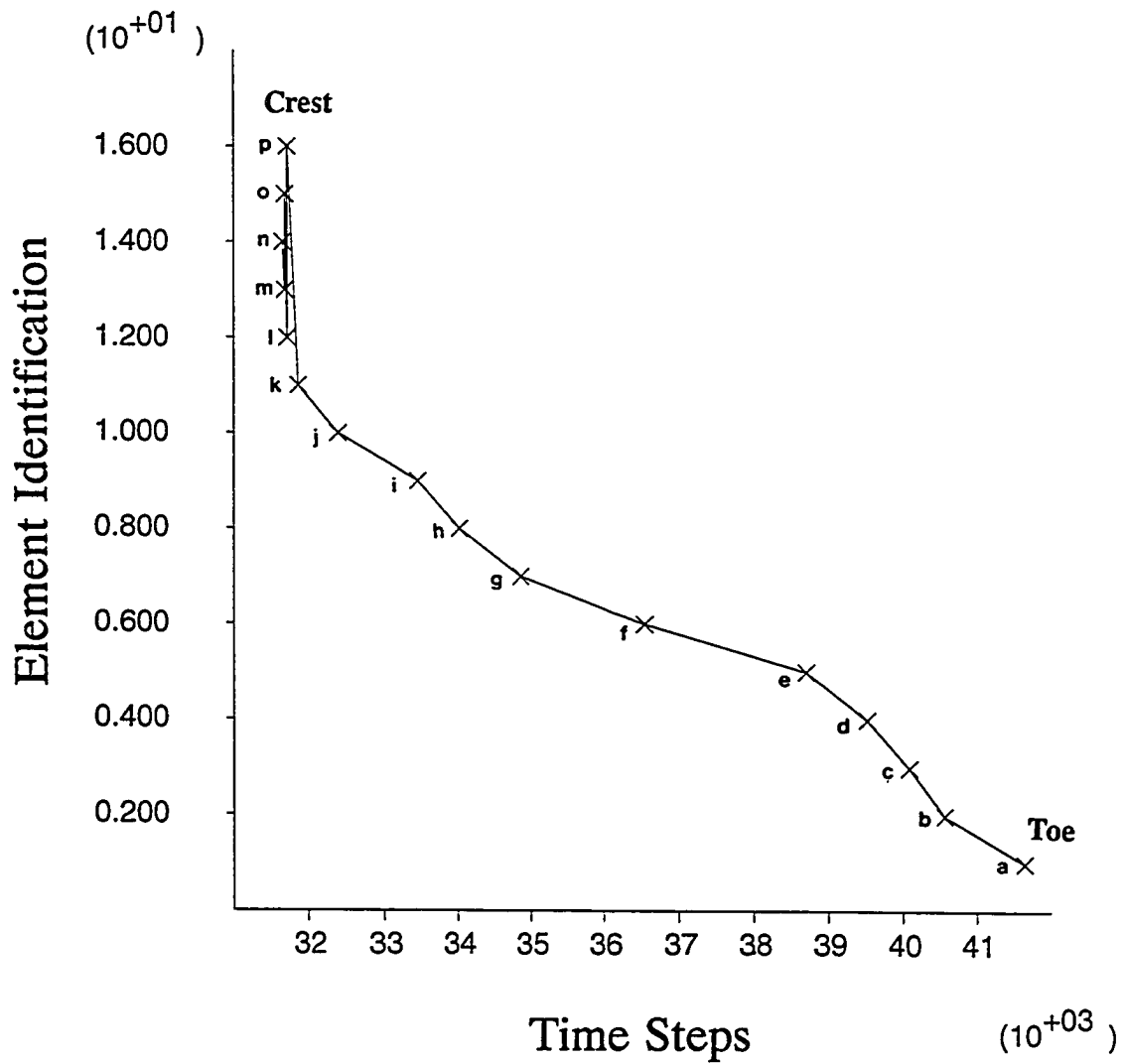


Fig. 6.31a Failure sequence of the elements along the failure surface, B-3 (30) analyses

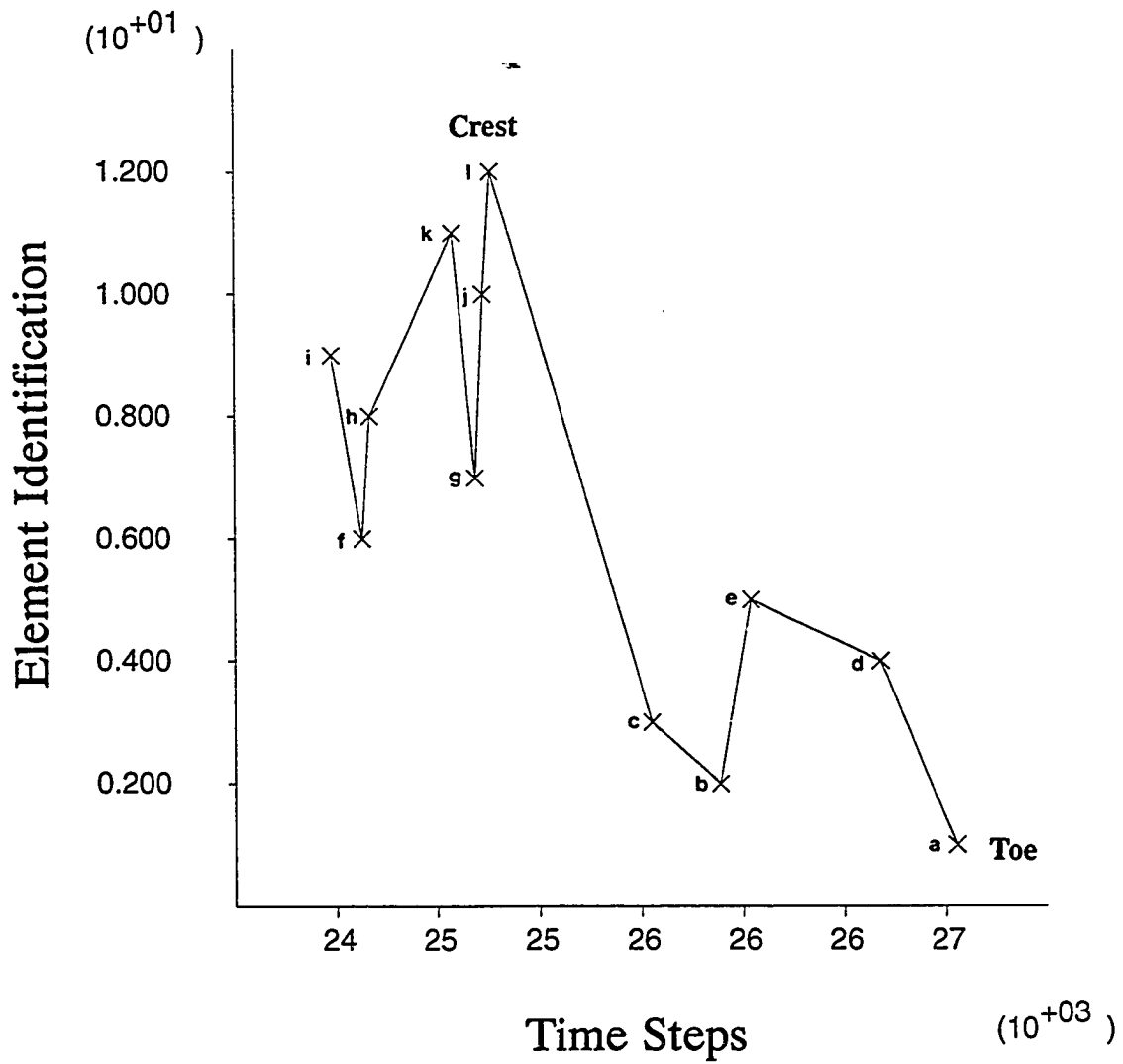
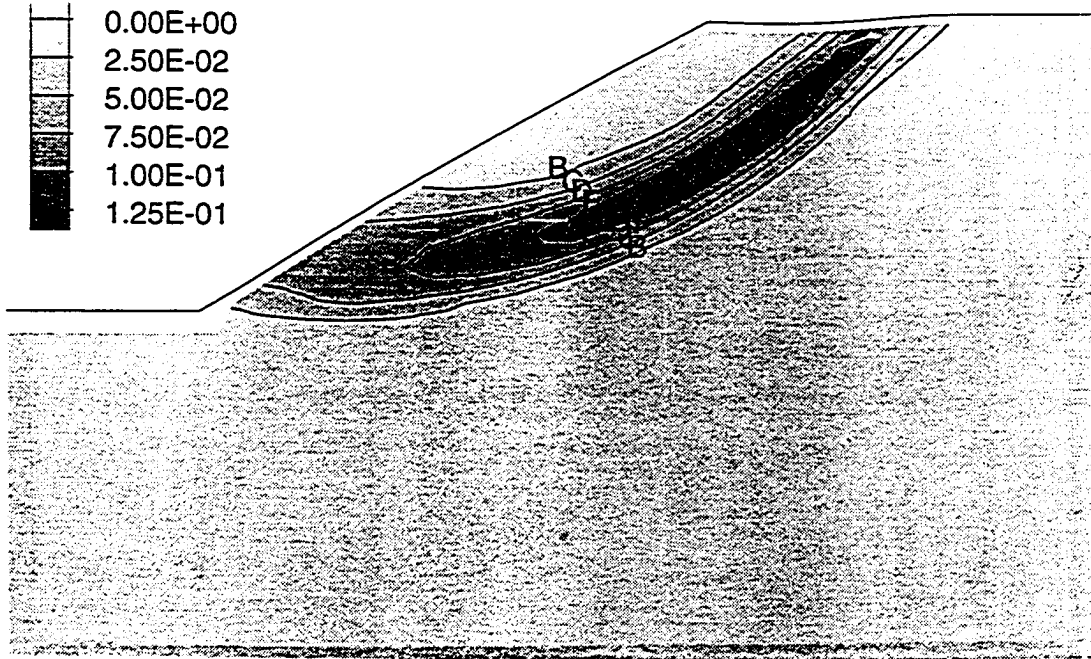


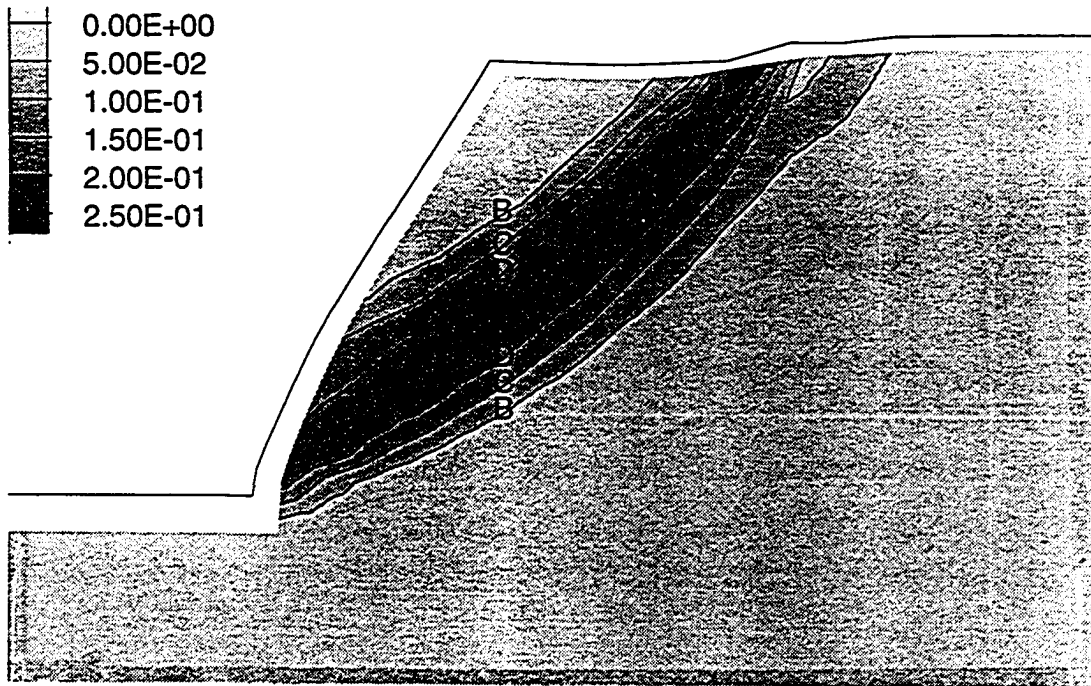
Fig. 6.31b Failure sequence of the elements along the failure surface, B-4 (60) analyses

Figs. 6.32a and 6.32b show the ~~maximum~~ shear strain distribution at the last layer excavation in B-3 (30) and B-4 (60) analyses, respectively, in which a series of shear bands can be clearly seen from the toe to the crest. Figs. 6.33a and 6.33b show the failure surfaces determined in B (30) and B (60) series analyses in comparison to those determined by Modified Bishop method, respectively. In order to present the failure surfaces together for a given series of analyses, individual failure surface was fitted by a circle of the same radius as has been determined by Modified Bishop method, yet with different centers of the circle. It appears in Fig. 6.33a that the failure surface predicted by Modified Bishop method is shallower at the toe, yet deeper at the crest than those of B (30) series analyses. However, the variation of the failure surfaces among B (30) series analyses is considered to be practically negligible. The failure surfaces predicted in B (60) analyses are fairly close to that determined by Modified Bishop method, yet the latter is deeper than the formers to some degrees.

Figs. 6.34a and 6.34b show the variation in the available strength ratios, which was defined in Section 6.2.1.2, for B (30) and B (60) analyses, respectively. The ratios at failures are summarized in Table 6.12. The available strength ratios at the end of the last layer excavation for both slopes are seen to continuously decrease as the strength anisotropy curve number increases from B-1 up to B-4 analyses. It is noted that the ratios for B (60) cases are much higher as compared to those for B (30). This is reflecting much less effect of the strength anisotropy for B (60) cases due to the fact that only narrow range of stress paths close to the



(a) 16th layer ($H_{\alpha} = 5.06$ m); Contour Interval = $2.50E-02$ (B: $2.50E-02$, E: $1.00E-01$)



(b) 16th layer ($H_{\alpha} = 2.50$ m); Contour Interval = $5.0E-02$ (B: $5.0E-02$, D: $1.50E-01$)

Fig. 6.32 Maximum shear strain distribution: (a) B-3 (30) analysis; and (b) B-4 analysis

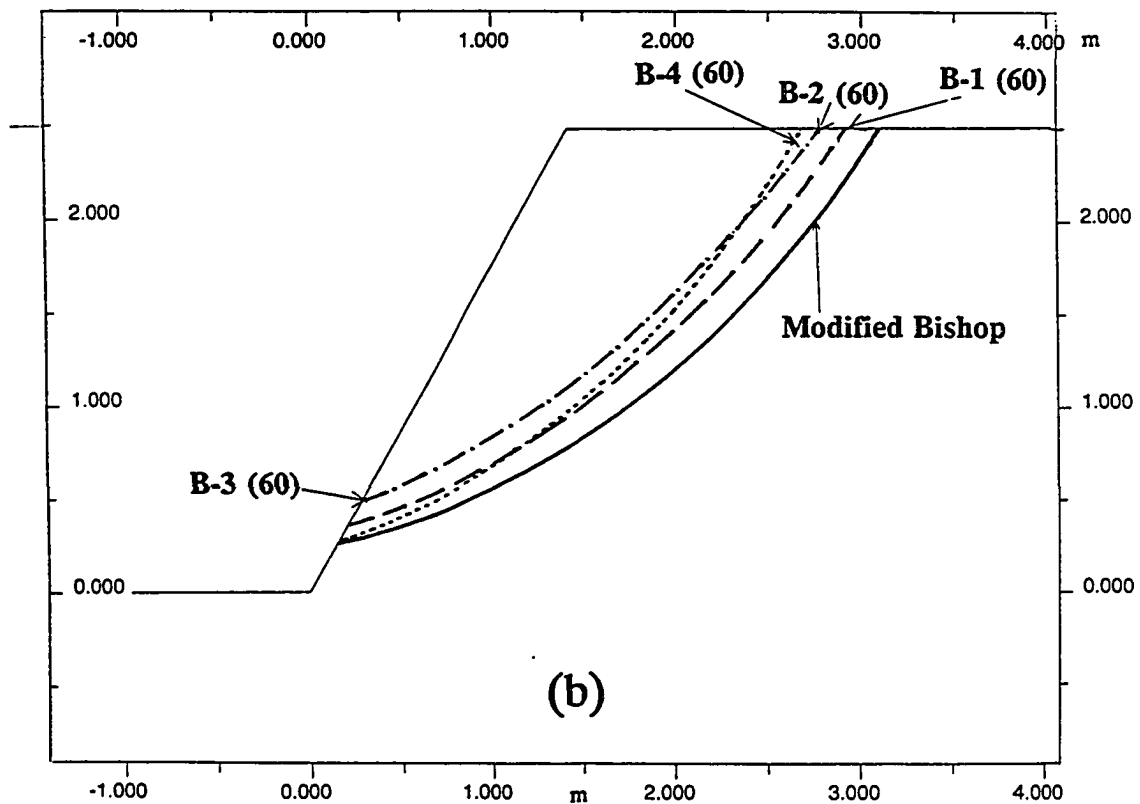
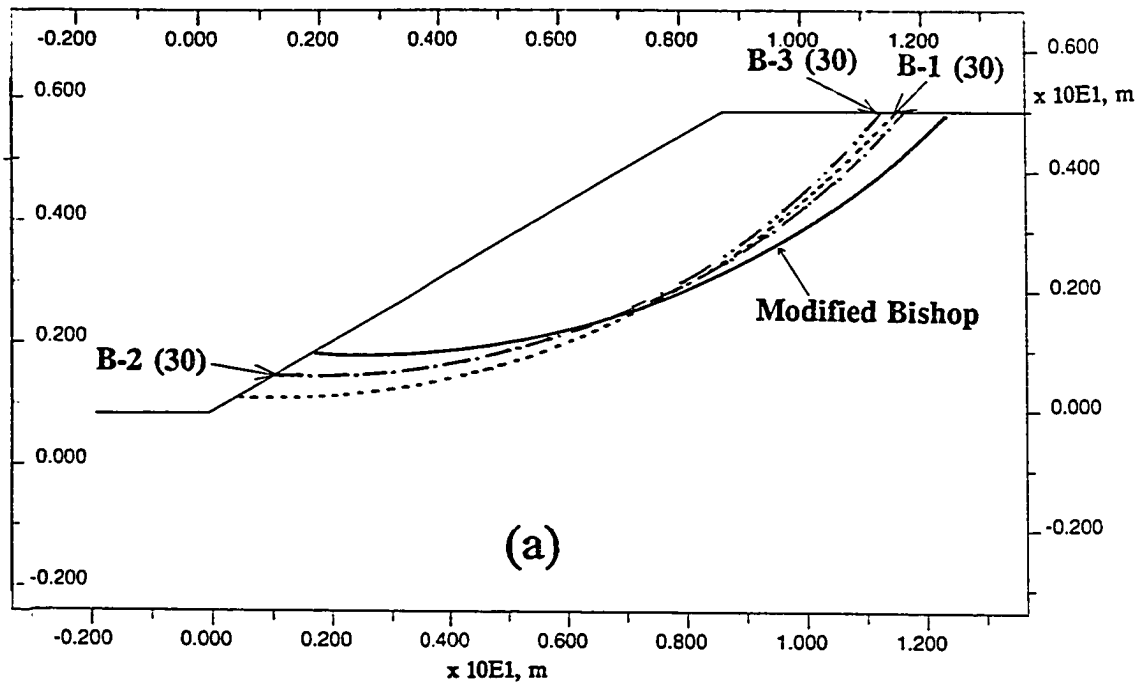


Fig. 6.33 Comparison of failure surface locations: (a) B (30) analyses; and (b) B (60) analyses

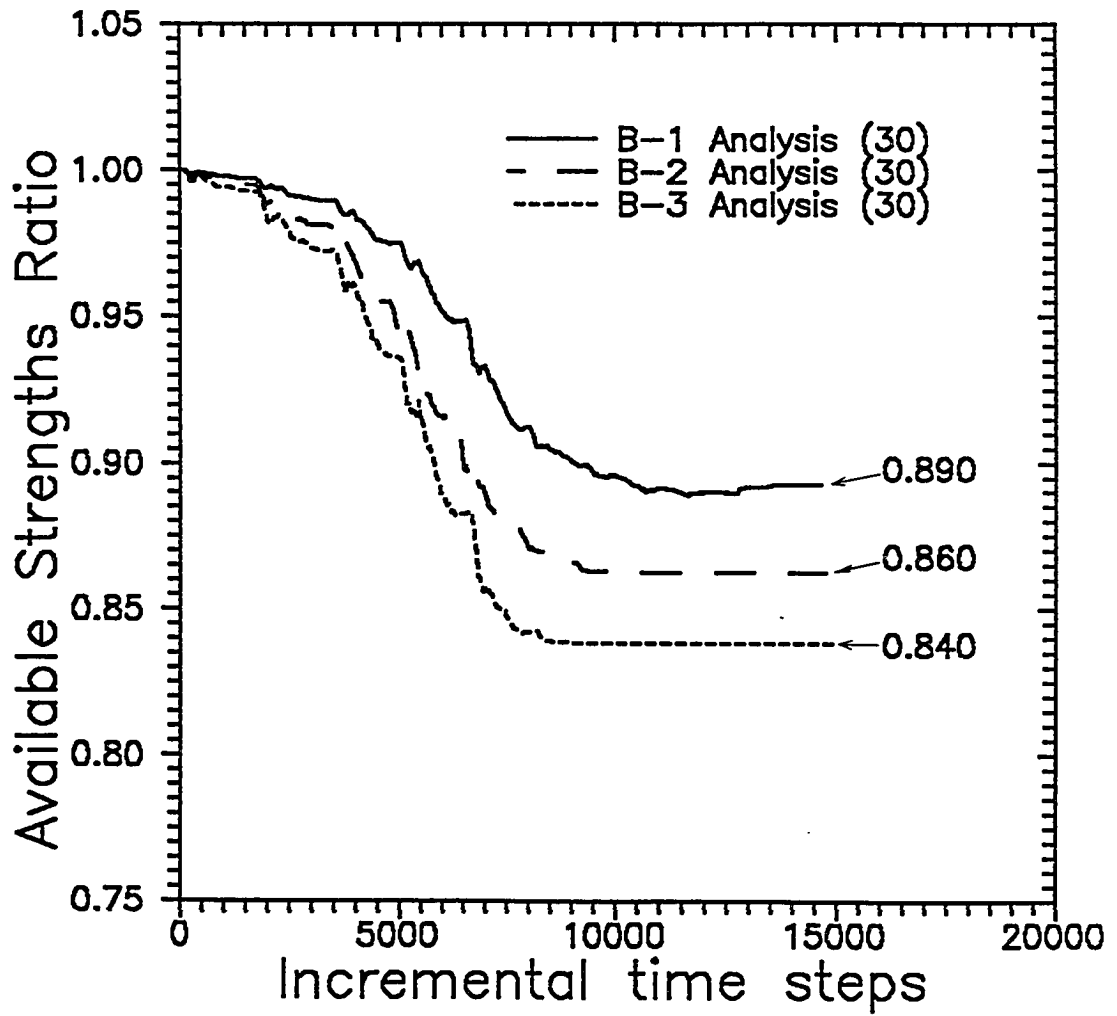


Fig. 6.34a Variation of the available strength ratio, B (30) analyses

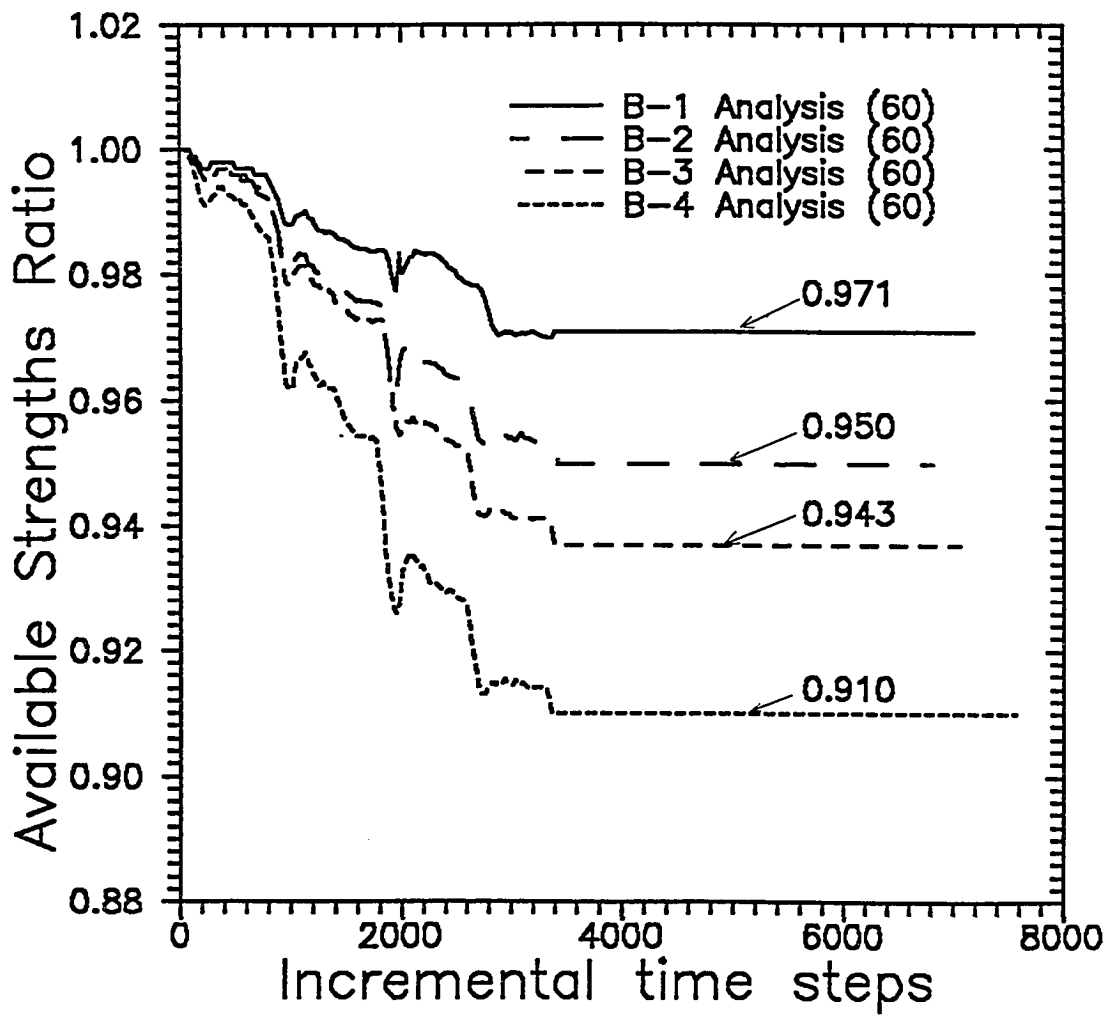


Fig. 6.34b Variation of the available strength ratio, B (60) analyses

compression mode ($i=0^\circ$) are involved in the slope failure in B (60) series of analyses.

Table 6.12 Summary of the available strength ratios from B (30) and B (60) analyses

Analysis	Available strength ratio	Analysis	Available strength ratio
B-1 (30)	0.890	B-1 (60)	0.971
B-2 (30)	0.860	B-2 (60)	0.950
B-3 (30)	0.840	B-3 (60)	0.943
---	---	B-4 (60)	0.910

Fig. 6.35 shows the variations of the maximum shear stresses normalized by the initial maximum shear stresses under the initial level ground condition for B-1 (60). It is seen that elements close to the crest (e.g., elements "h" through "j") experience maximum shear stress increments right after the excavation begins, while those close to the toe elements (e.g., elements "a" through "g") undergo slight reductions in the maximum shear stress before moving up to higher stress levels.

6.2.2.3 Anisotropic Strength with Straining Hardening and Softening Cases (C and D Analyses)

Fig. 6.36a shows the displacements of the nodal point at the tip of the crest in the process of excavation for C-1-a (30), C-1-b (30), and C-1-c (30) analyses along with those of A (30) and B-1 (30) analyses. The magnitudes of C-1-a (30)

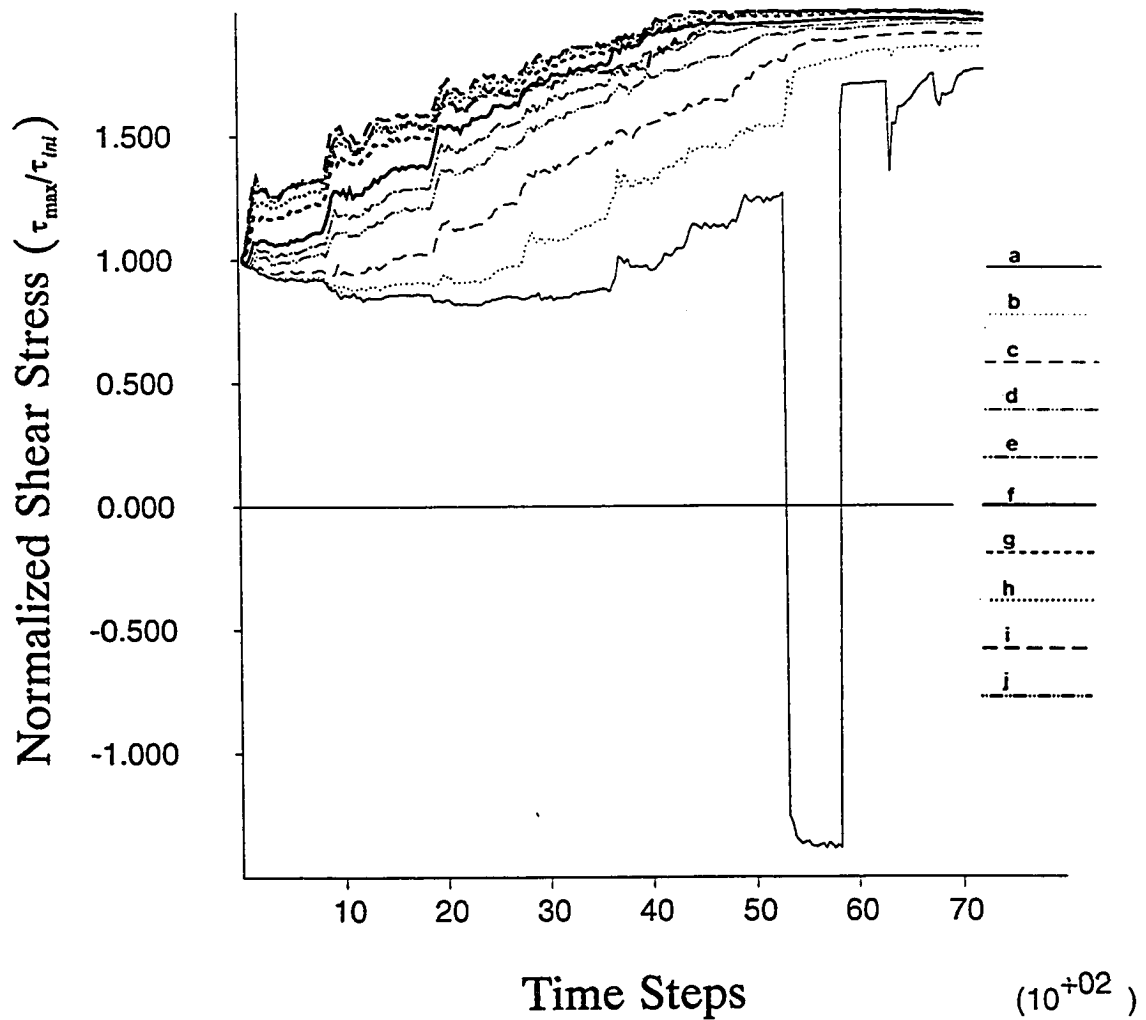


Fig. 6.35 Variation of normalized shear stress of the elements along the failure surface, B-1 (60)

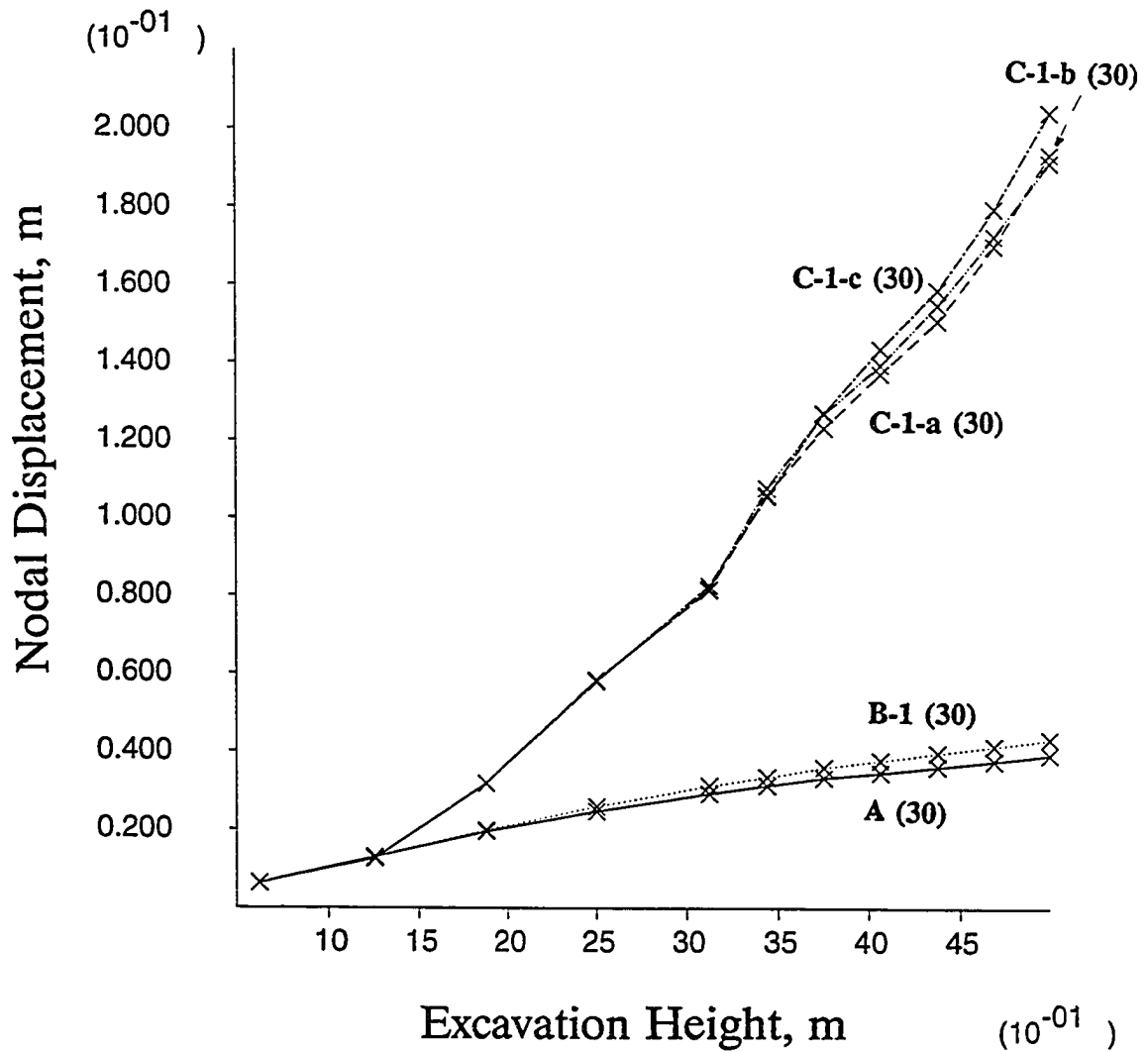


Fig. 6.36a Nodal displacements with increasing excavation heights, A, B-1 and C-1 (30) series analyses

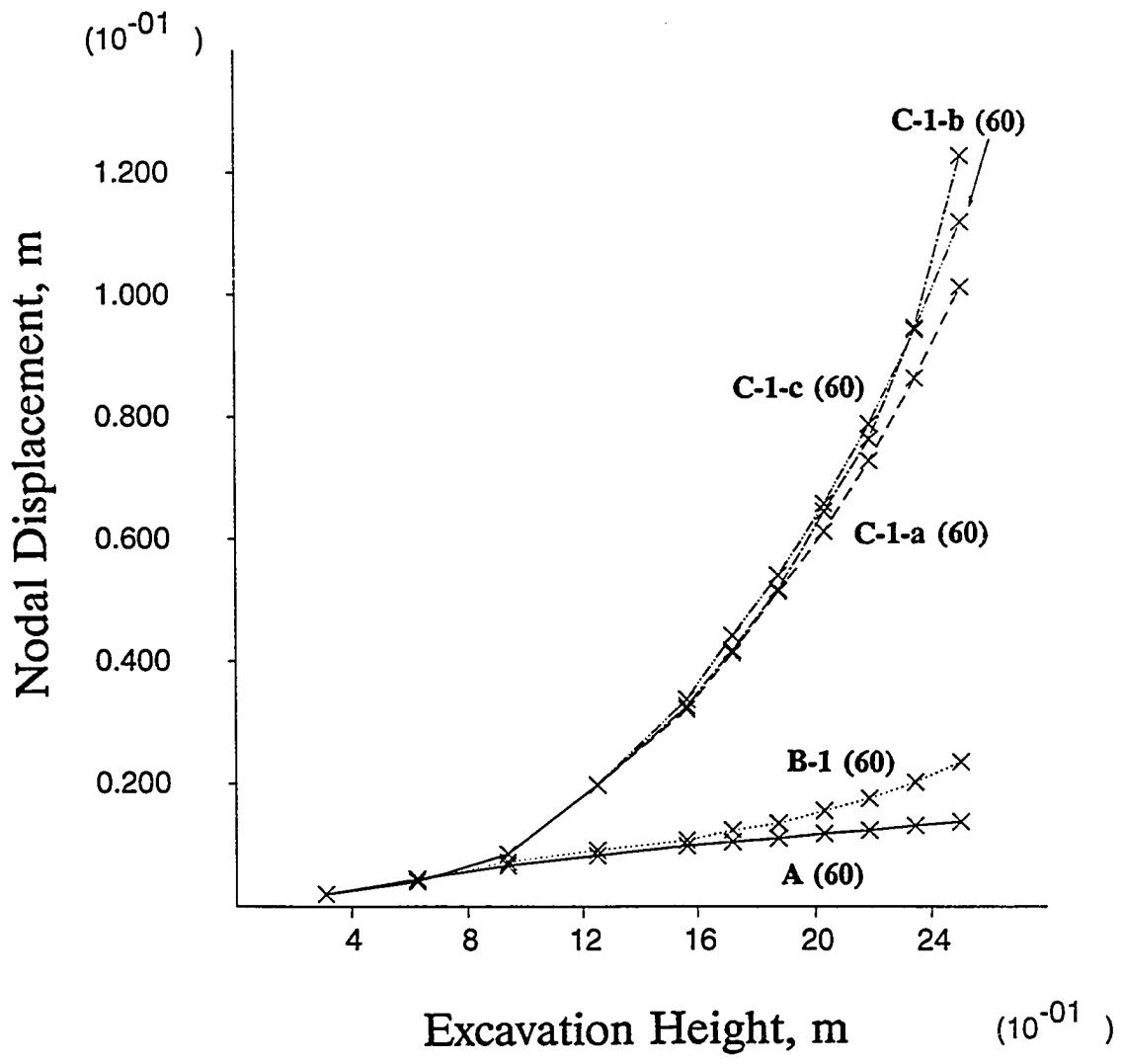


Fig. 6.36b Nodal displacements with increasing excavation heights, A, B-1 and C-1 (60) series analyses

through C-1-c (30) analyses at the end of the final excavation are about five times as great as those of A (30) and B-1 (30) analyses. The discrepancy is completely attributed to the fact that C analyses use the stress-strain relations in which the peak strength is mobilized at higher strain levels than those of A and B analyses. Although the final magnitudes of the nodal displacement are greatly increased for C analyses, failures of the slopes do not seem imminent upon considering the patterns of the nodal displacements (i.e., no abrupt change in the displacement rate). In addition, the close displacement patterns in C-1-a (30) through C-1-c (30) analyses indicate that varying degrees of strain softening of the active elements have little effect due to insufficient shear strain levels to reach the residual strengths. Fig. 6.36b shows the patterns of the nodal displacements in C-1-a (60), C-1-a (60), and C-1-c (60) analyses along with those in A (60) and B-1 (60) analyses. The patterns of nodal displacements are similar to those in 30 degree cases so that a similar interpretation is possible.

Since the slopes in C-1 (30) and C-1 (60) series of analyses did not show clear failures, C-3 (30) and C-4 (60) series of analyses were carried out to study the progressive failure effects. Note that C-4 (30) series of analyses were not performed because some of the elements with low i angles would have the undrained strengths which are even less than the initial maximum shear stresses. Figs. 6.37a and 6.37b show the nodal displacement patterns in C-3-a (30), C-3-b (30), C-3-c (30) and C-4-a (60), C-4-b (60), C-4-c (60) analyses with those of A (30), B-1 (30) and A (60), B-1 (60) analyses, respectively. The changes in the

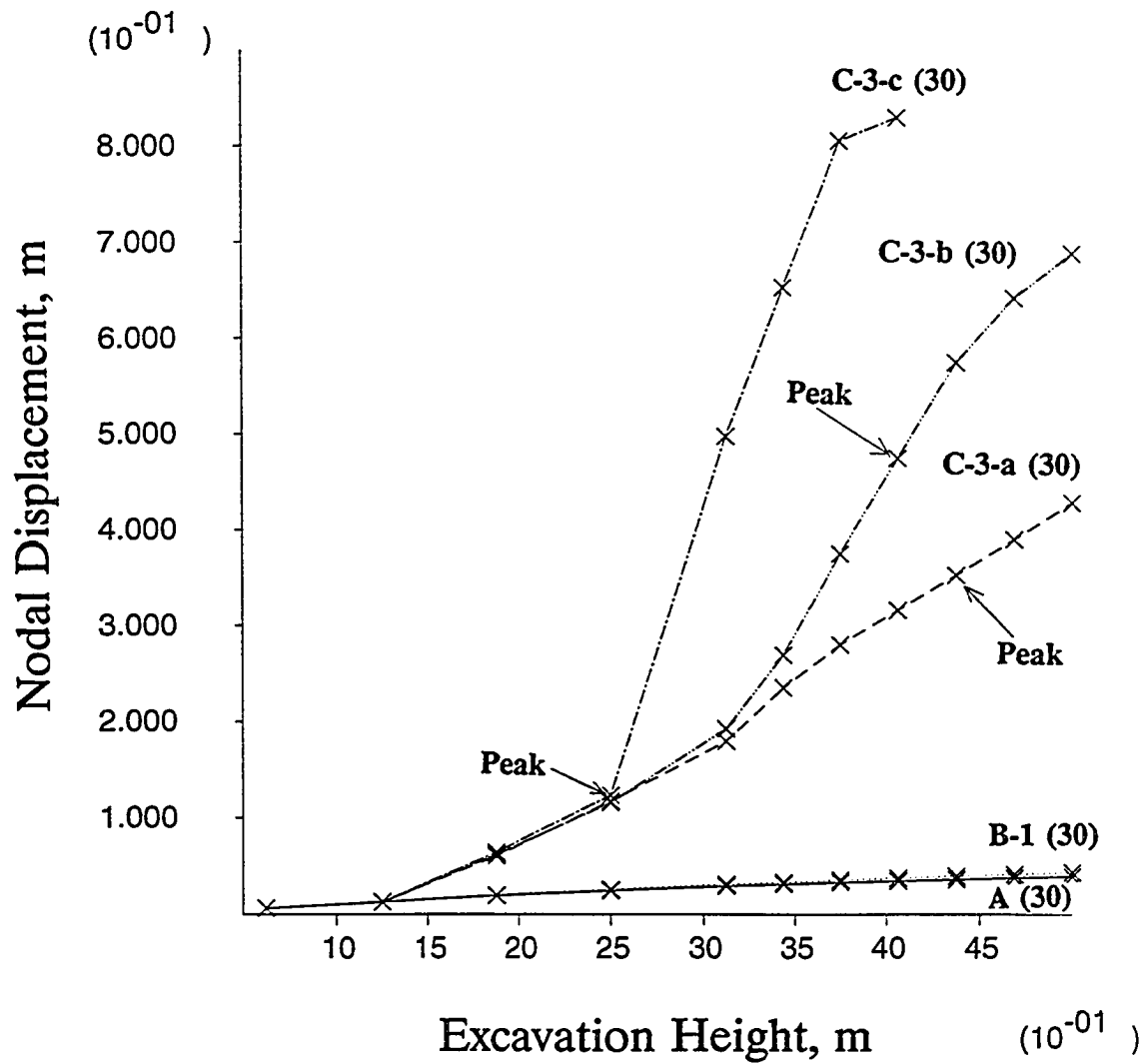


Fig. 6.37a Nodal displacements with increasing excavation heights, A, B-1 and C-3 (30) series analyses

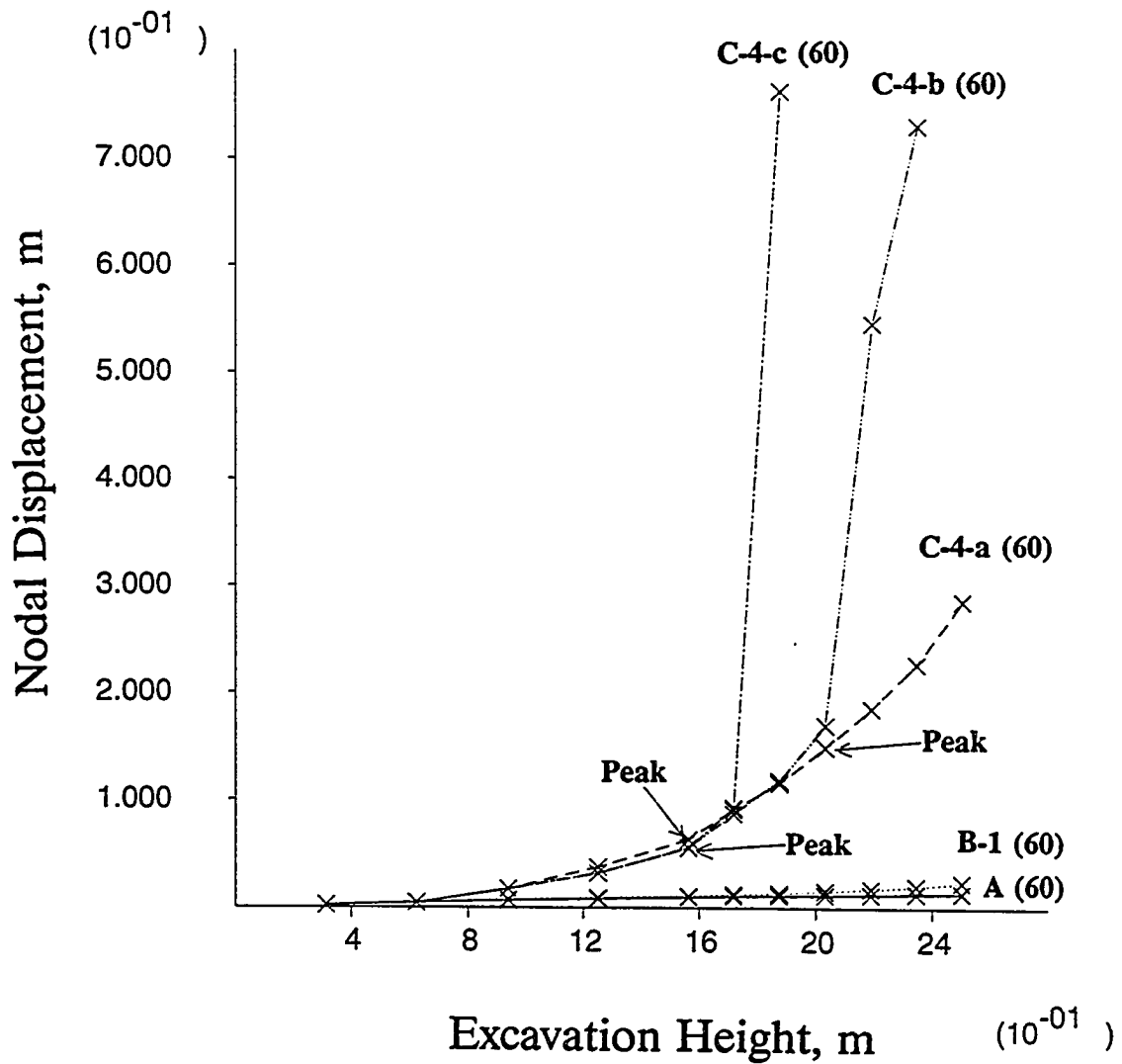


Fig. 6.37b Nodal displacements with increasing excavation heights, A, B-1 and C-4 (60) series analyses

displacement patterns caused by the change of anisotropic strength curve number are evident for both cases. The sudden changes in the nodal displacement rates indicate global slope failures for C-3-b (30) and C-3-c (30) and C-4-b (60) and C-4-c (60) cases. The nodal displacement patterns in D (30) and D (60) series analyses are shown in Figs. 6.38a and 6.38b, respectively. The patterns are very similar to those of C-3 or C-4 series analyses for the same slope inclination angle.

Figs. 6.39a through 6.39f show the pattern of maximum shear strain development for C-3-b (30) analyses. At the second layer excavation (Fig. 6.39a), a clear maximum shear strain concentration is seen near the toe as in A analysis. At the fourth layer excavation (Fig. 6.39b), a series of shear bands are formed from the toe to the crest, which are then continuously expanded downward with further excavations. It is noted that the shear band always passes through the toe of the slope up to the 13th layer excavation (Fig. 6.39c). Beyond that point, however, the shear bands remain fixed approximately at the constant location, which is in good agreement with the analytical prediction (Kenney, 1963). Figs. 6.40a through 6.40d show the pattern of maximum shear strain development in C-4-b (60) analysis. At the second layer excavation (Fig. 6.40a), the maximum shear strains are highly concentrated at the toe of the slope. At the fourth layer excavation (Fig. 6.40b), the maximum shear strain determines the direction of propagation from the toe toward inside the slope. At the sixth layer excavation (Fig. 6.40c), a clear series of maximum shear strain bands are formed from the toe to the crest in which the toe has still the highest concentration of the strain.

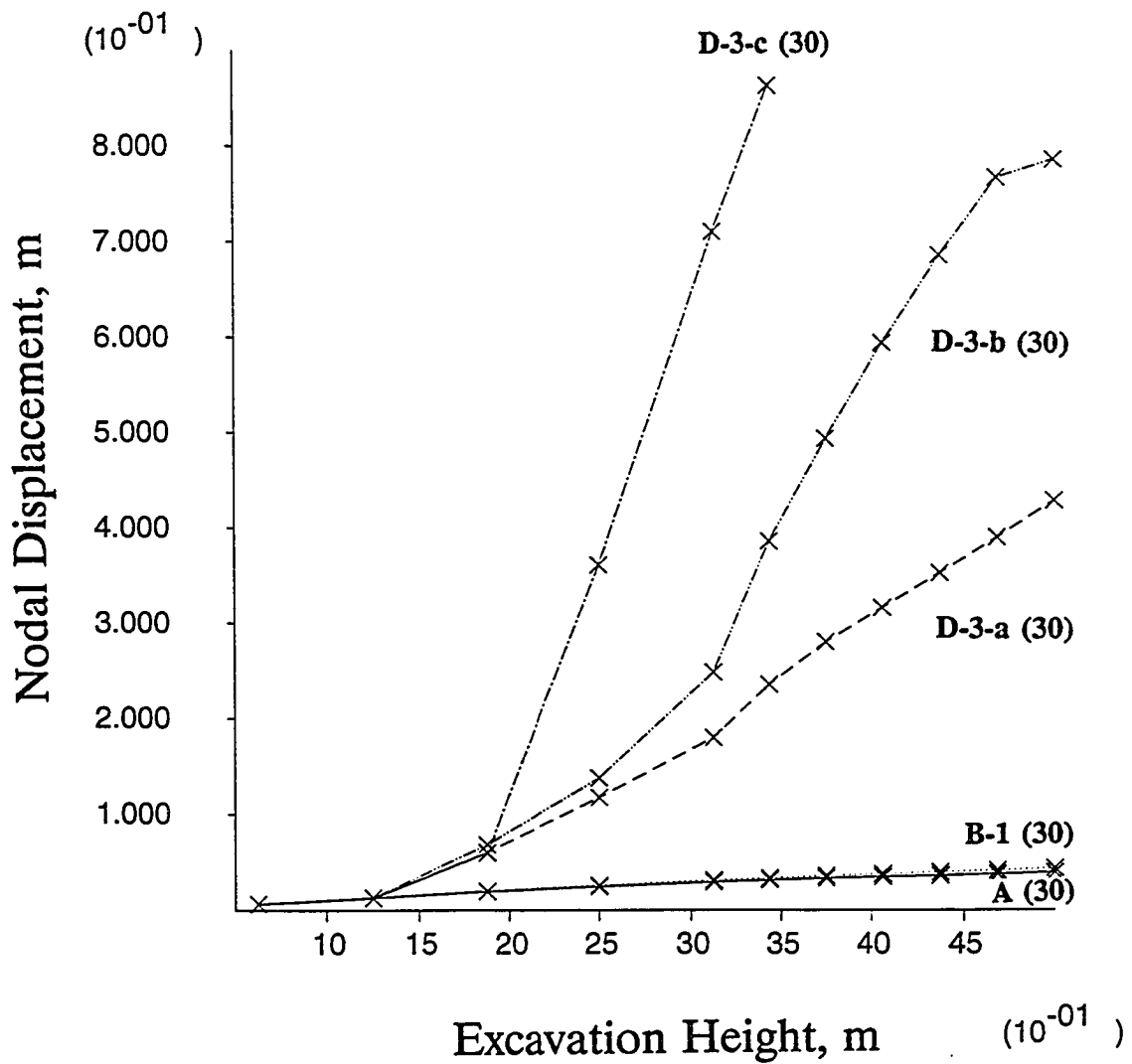


Fig. 6.38a Nodal displacements with increasing excavation heights, A, B-1 and D-3 (30) series analyses

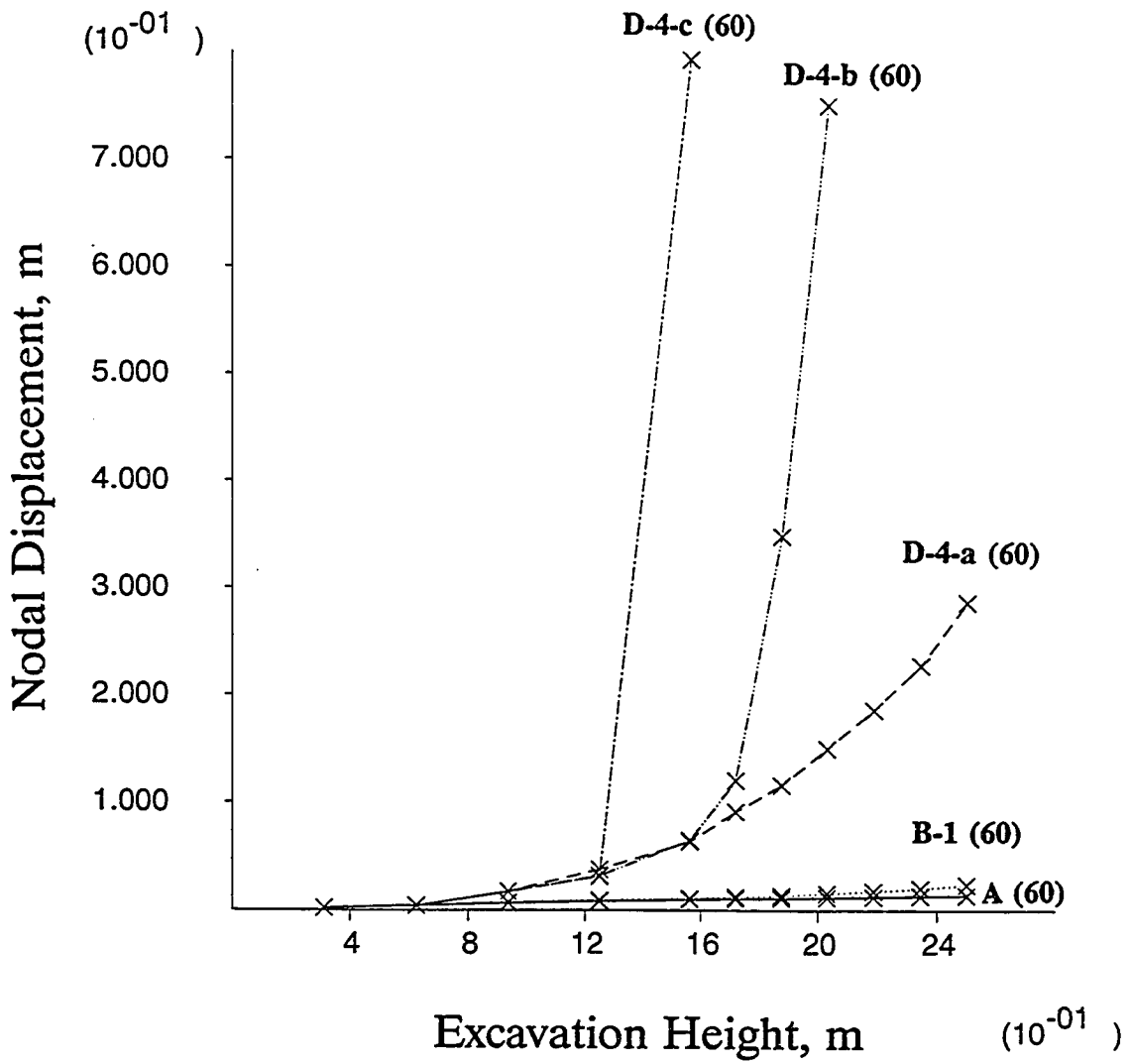
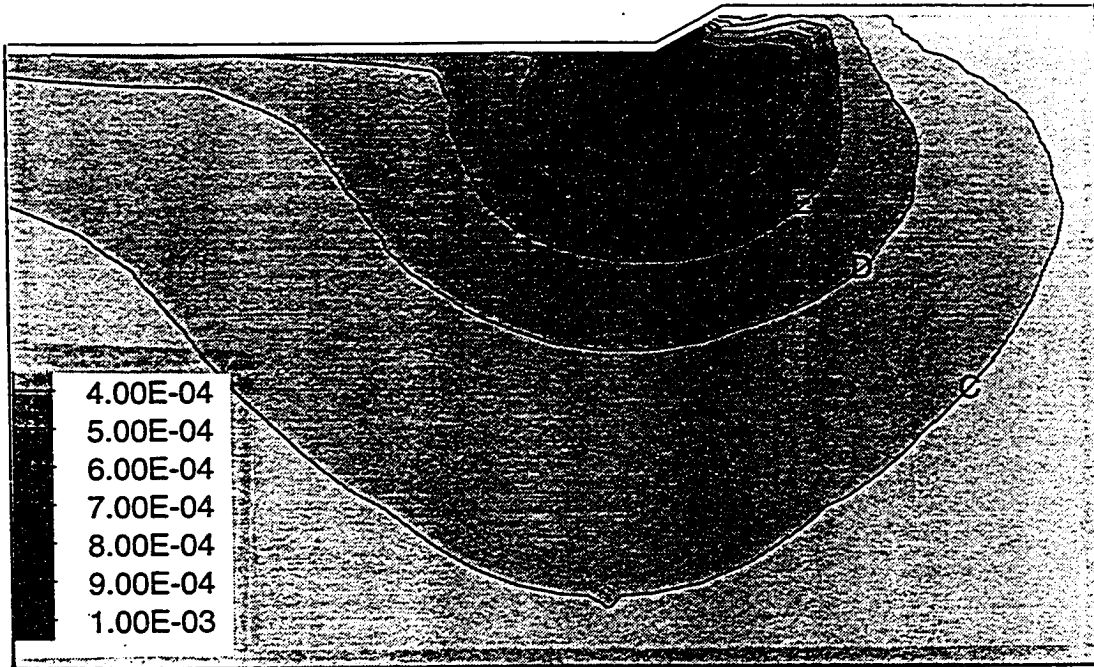
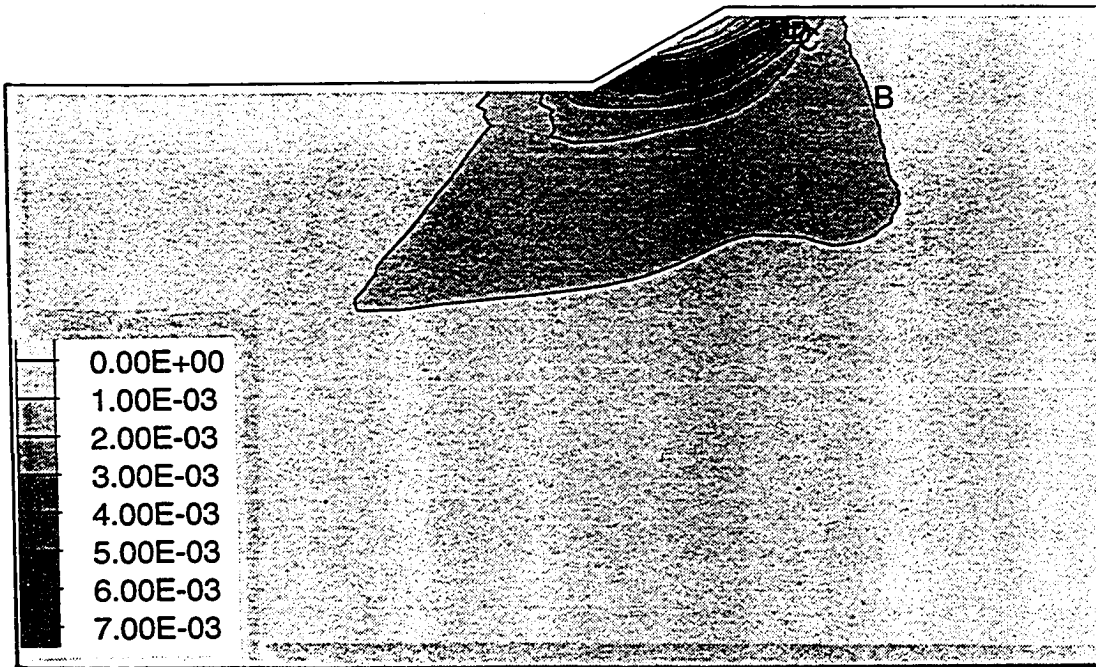


Fig. 6.38b Nodal displacements with increasing excavation heights, A, B-1 and D-4 (60) series analyses

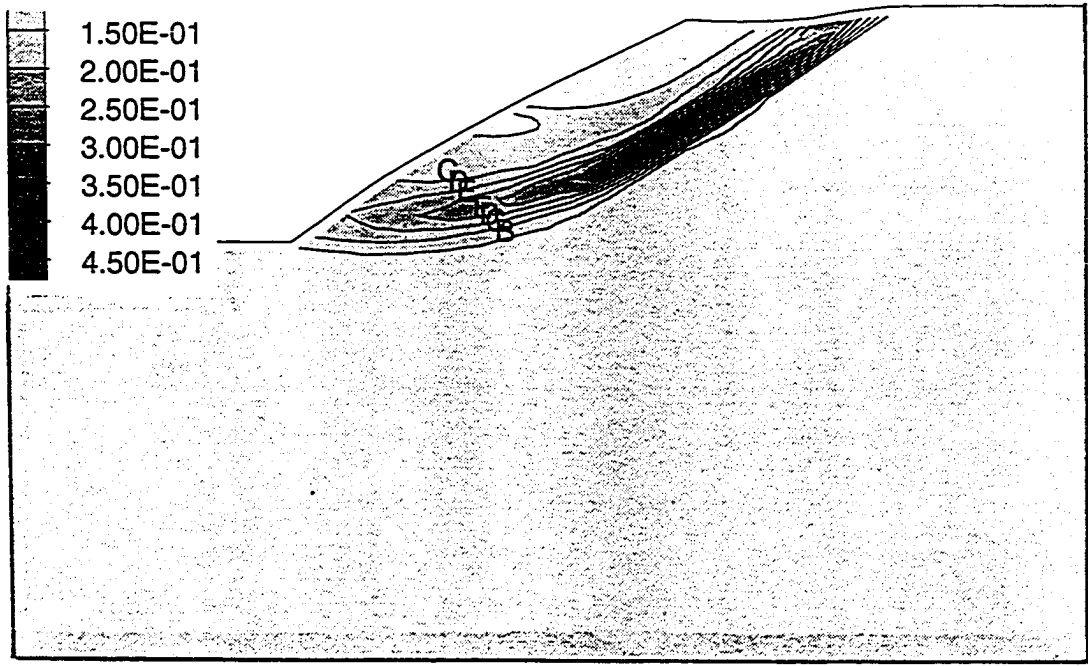


(a) 2nd layer ($H_{\alpha} = 0.64$ m); Contour Interval = $1.0E-04$ (C: $3.00E-04$, I: $9.00E-04$)

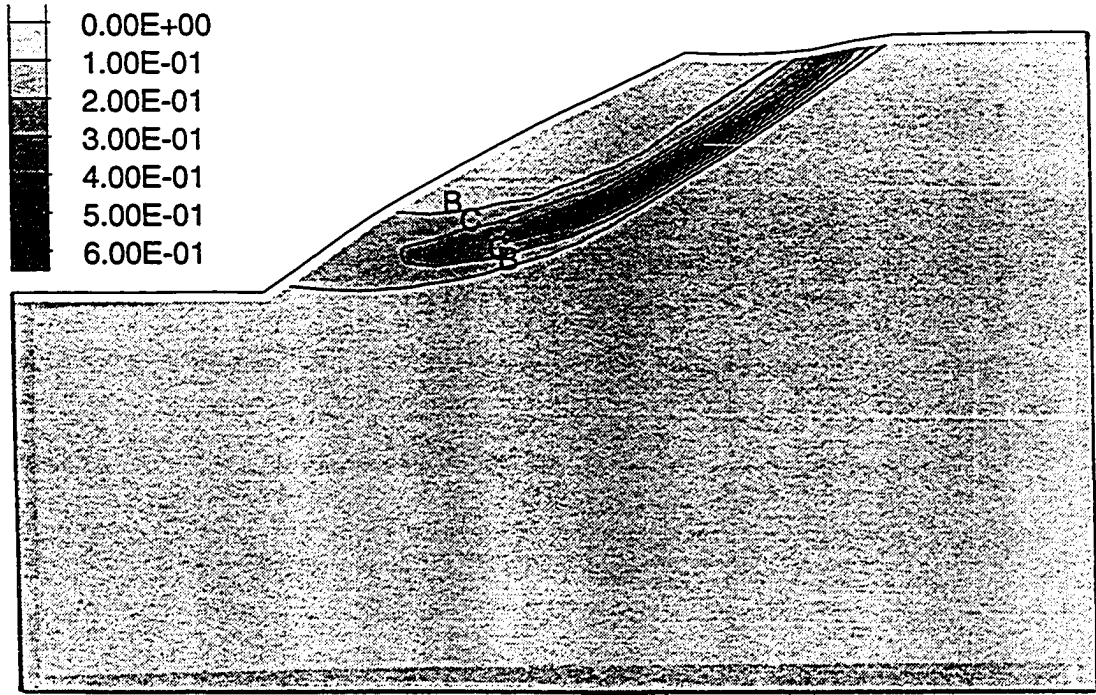


(b) 4th layer ($H_{\alpha} = 1.27$ m); Contour Interval = $1.0E-03$ (B: $1.00E-03$, E: $4.00E-03$)

Fig. 6.39 Maximum shear strain distribution, C-3-b (30) analysis

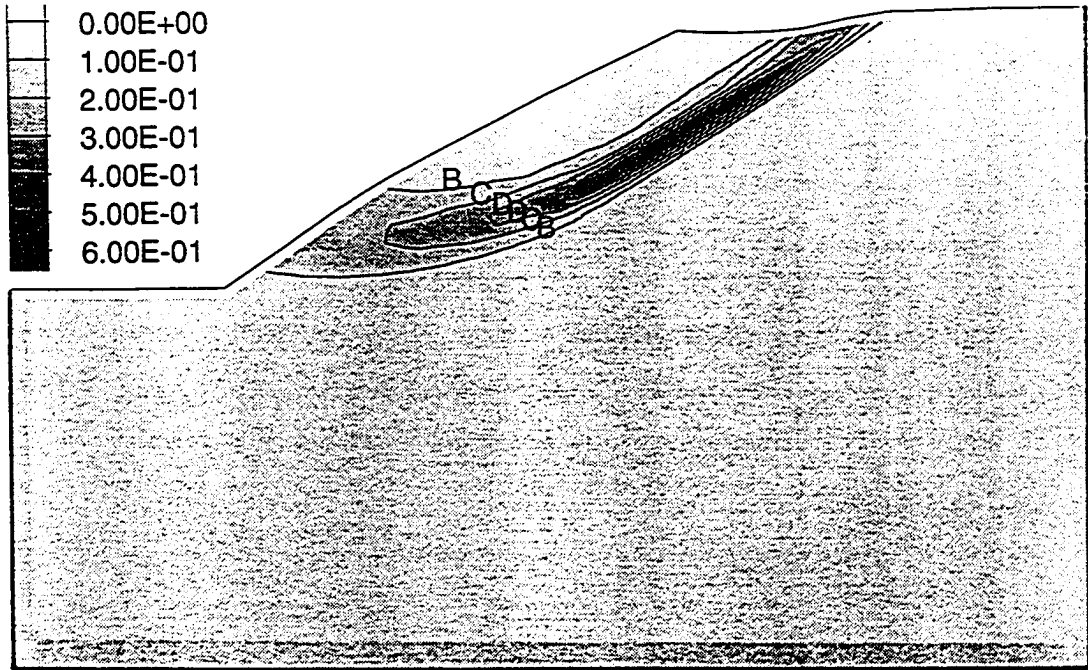


(c) 13th layer ($H_{\alpha} = 4.08$ m); Contour Interval = $5.0E-02$ (B: $5.00E-02$, E: $2.00E-01$)

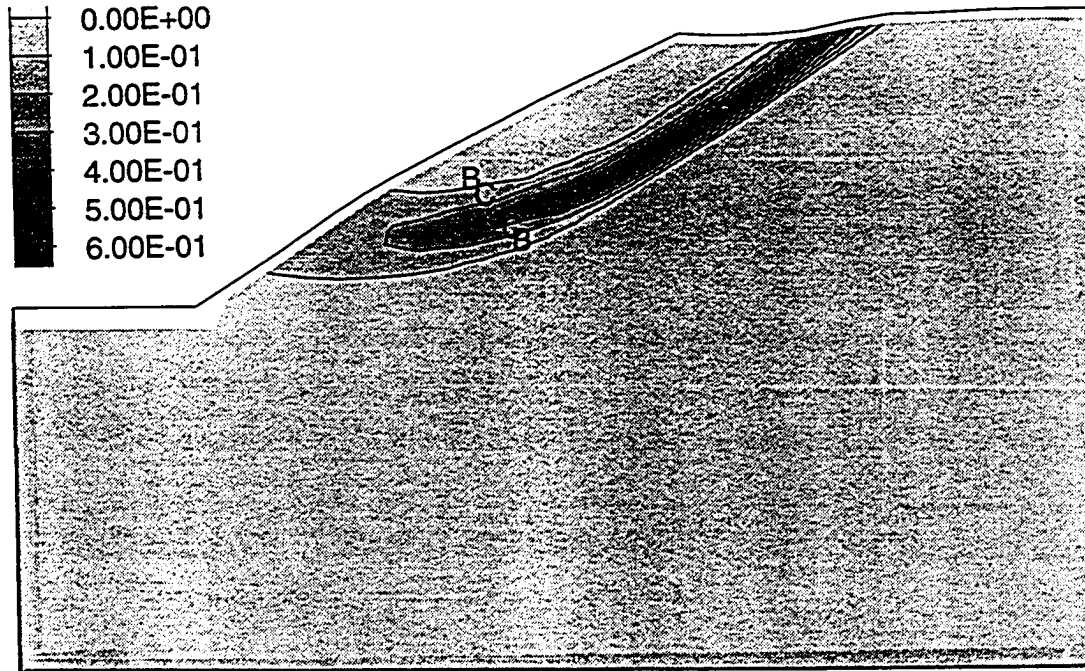


(d) 14th layer ($H_{\alpha} = 4.39$ m); Contour Interval = $1.0E-01$ (B: $1.00E-01$, C: $2.00E-01$)

Fig. 6.39 Maximum shear strain distribution, C-3-b (30) analysis

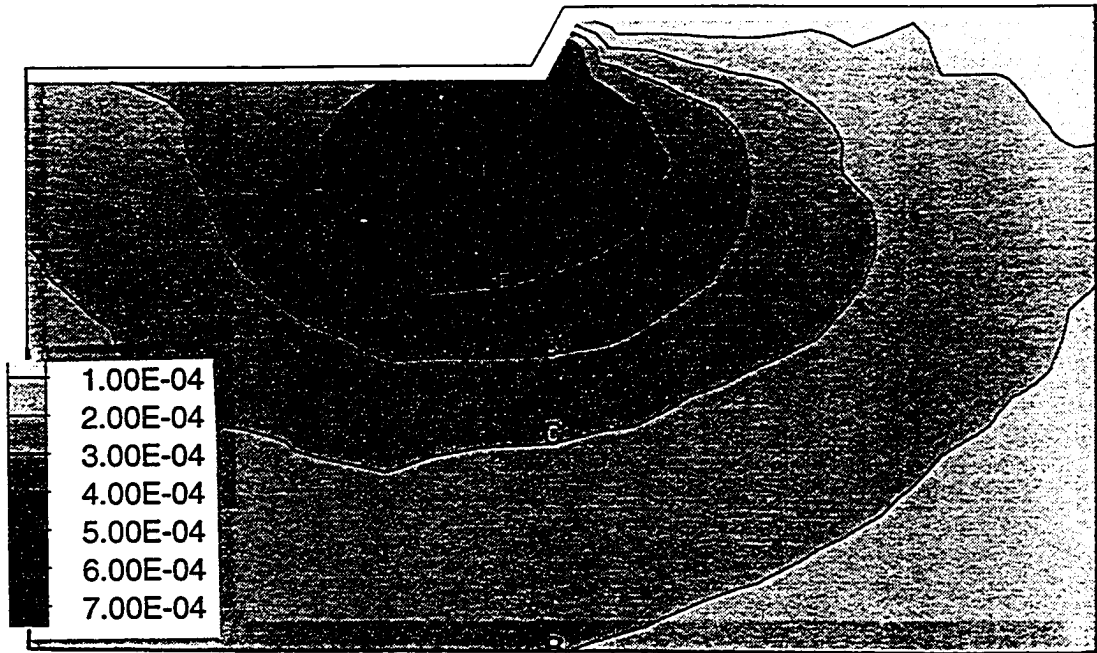


(e) 15th layer ($H_{ex} = 4.70$ m); Contour Interval = $1.0E-01$ (B: $1.00E-01$, D: $3.00E-01$)

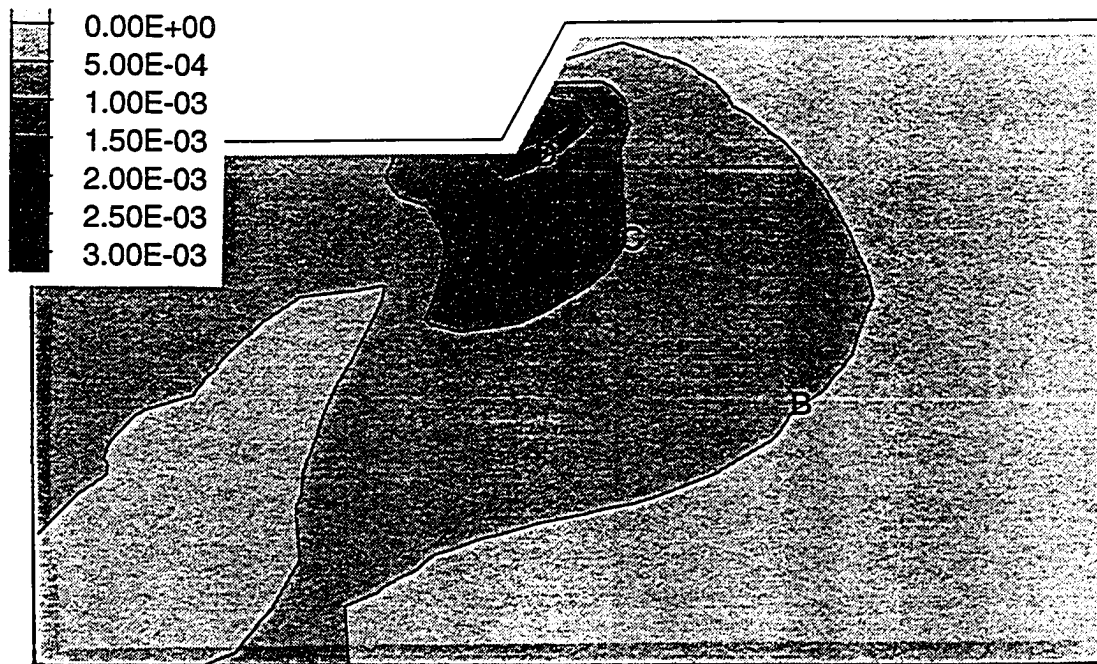


(f) 16th layer ($H_{ex} = 5.06$ m); Contour Interval = $1.0E-01$ (B: $1.00E-01$, C: $2.00E-01$)

Fig. 6.39 Maximum shear strain distribution, C-3-b (30) analysis

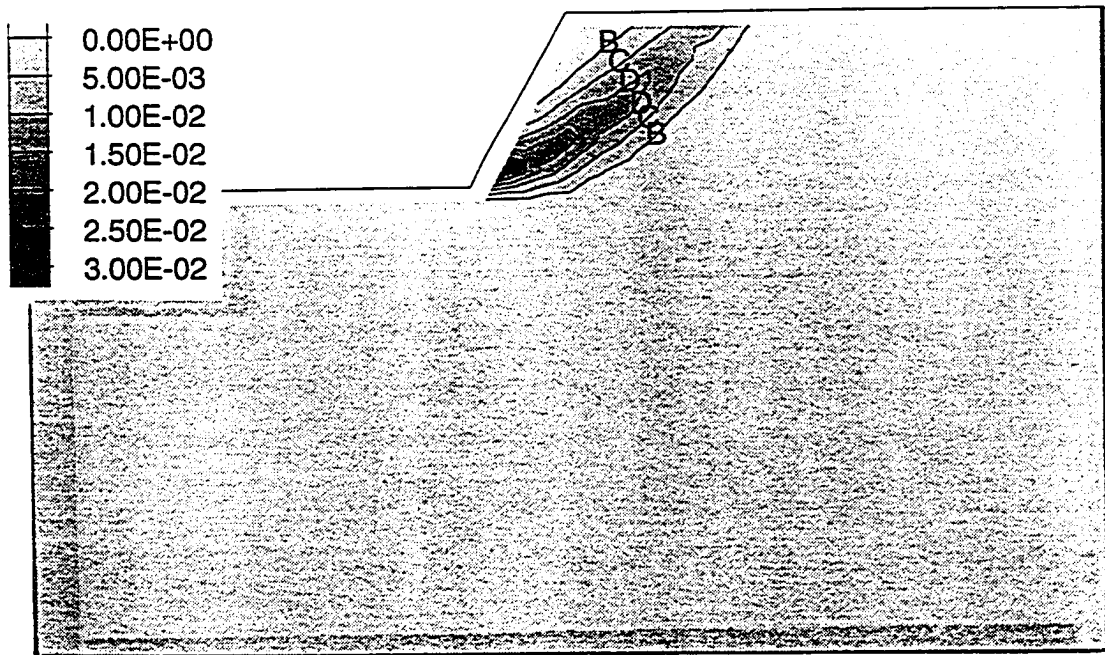


(a) 2nd layer ($H_{ex} = 0.32$ m); Contour Interval = $1.0E-04$ (B: $2.00E-04$, G: $7.00E-04$)

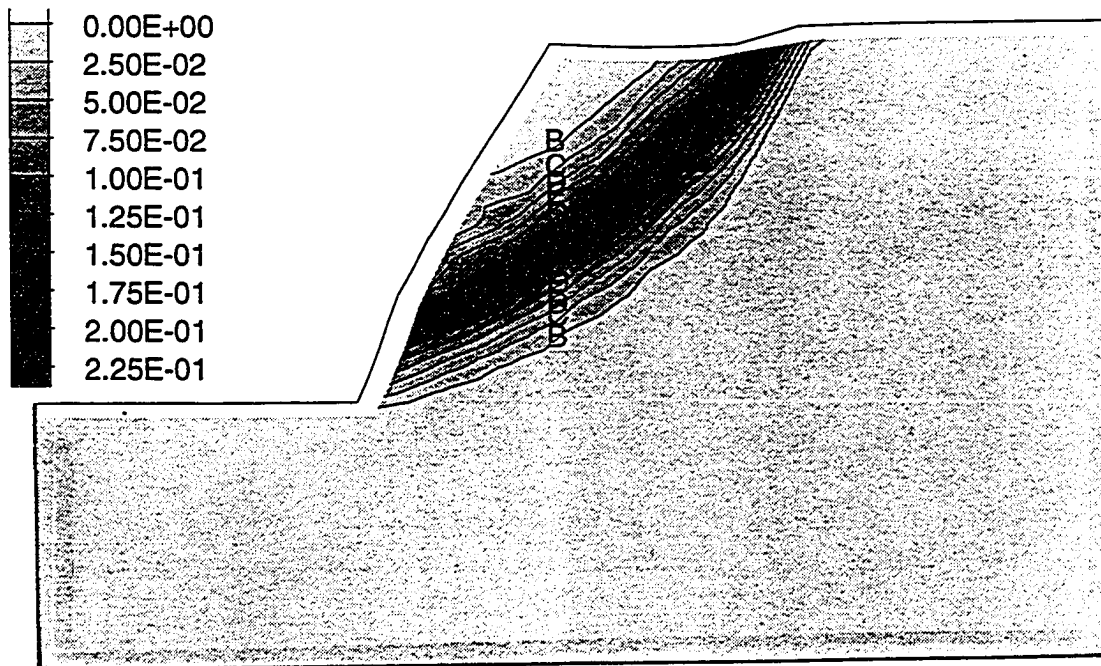


(b) 4th layer ($H_{ex} = 0.63$ m); Contour Interval = $5.0E-04$ (B: $5.00E-04$, D: $1.50E-03$)

Fig. 6.40 Maximum shear strain distribution, C-4-b (60) analysis



(c) 6th layer ($H_{\alpha} = 0.94$ m); Contour Interval = $5.0E-03$ (B: $5.00E-03$, D: $1.50E-02$)



(d) 13th layer ($H_{\alpha} = 2.04$ m); Contour Interval = $2.50E-02$ (B: $2.500E-02$, H: $1.75E-01$)

Fig. 6.40 Maximum shear strain distribution, C-4-b (60) analysis

From this stage to the end (Fig. 6.40d), the maximum shear strain bands continuously move downward as excavation proceeds so that it is always passing through near the toe of the slope, but the failure surface passes through slightly above the toe as seen in C-3-b (30) analysis. The slope at the last layer excavation is not presented, because it is excessively deformed.

Figs. 6.41a and 6.41b demonstrate the sequence of the peak strength mobilization of the elements along the failure surface in C-3-b (30) analysis, in which sequential patterns of elements reaching the peak strengths are evident (c is the currently mobilized strength and S_u is the peak strength). It can be seen that when the shear strength of an element is at the peak, the rest of the elements are at either hardening or softening stage. This results in reduction of the peak in the summation of the strengths along the failure surface. Fig. 6.42a and 6.42b show the variation in the distributions of the peak strength mobilization ratios (c/S_u) along the failure surface during the failure process (the 16th layer) for C-3-b (30) and C-3-c (30) analyses, respectively. Each curve in the figures shows a distribution of the peak strength mobilization ratios (c/S_u) at a given time steps. It is clearly demonstrated that while the passive elements near the toe are experiencing strength increments (strain hardening), the active elements near the crest are at their residual strengths (i.e., no strength changes) for C-3-b (30) analysis (Fig. 6.42a) and are undergoing strength reduction (i.e., strain softening) for C-3-c (30) analysis (Fig. 6.42b). Figs. 6.43a and 6.43b show the failure

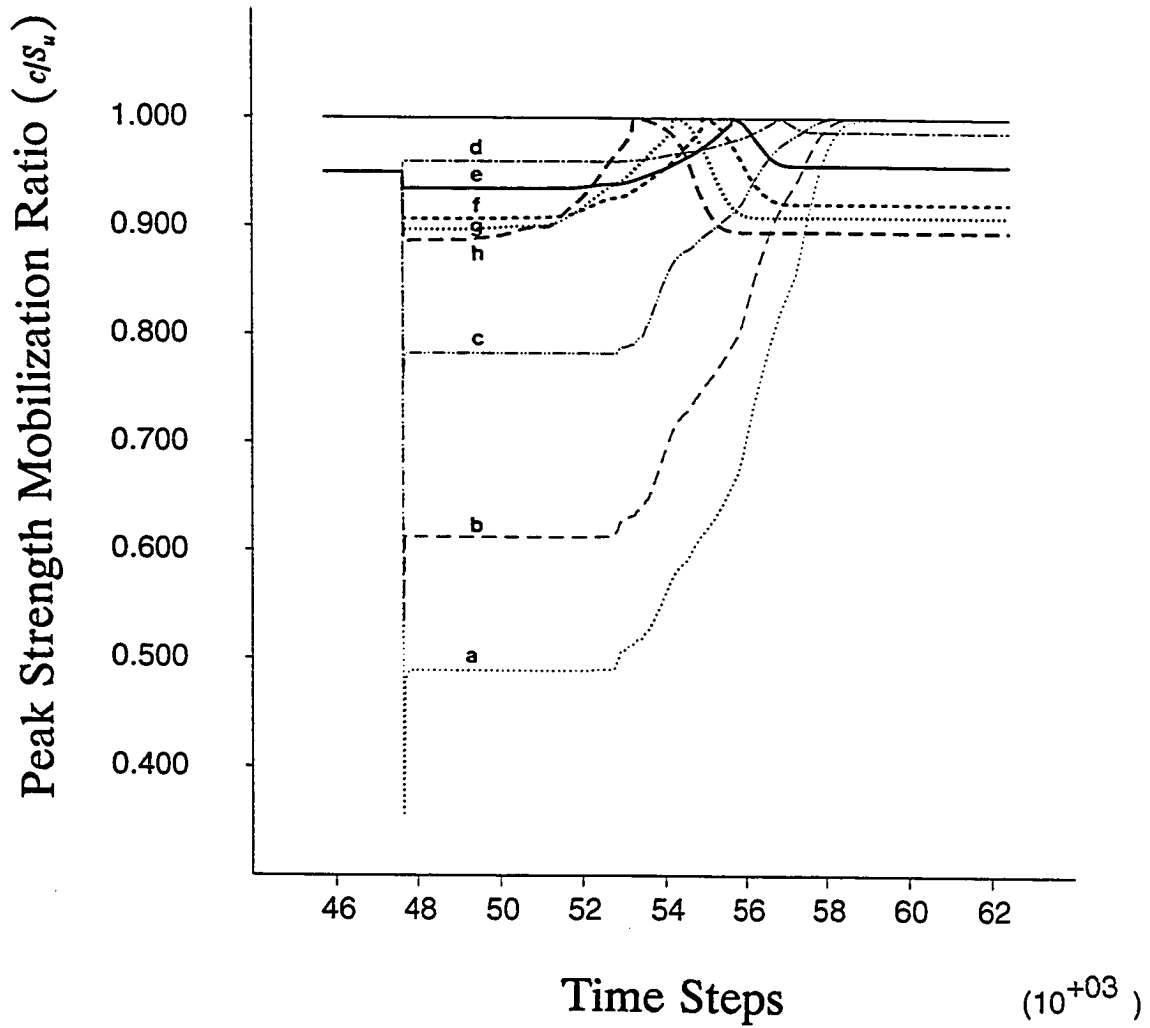


Fig. 6.41a Sequence of the peak strength mobilization with time steps, C-3-b (30) analysis

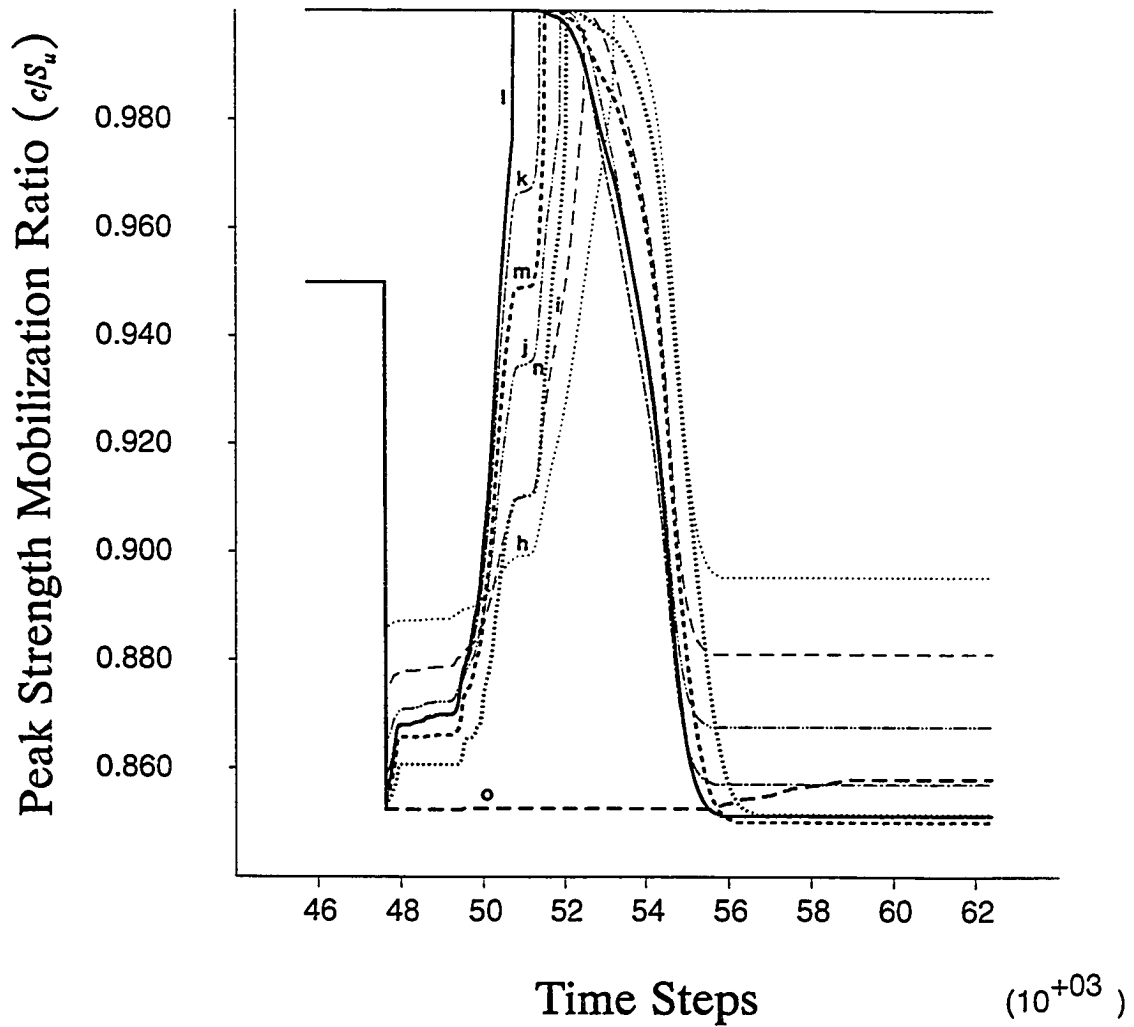


Fig. 6.41b Sequence of the peak strength mobilization with time steps, C-3-b (30) analysis

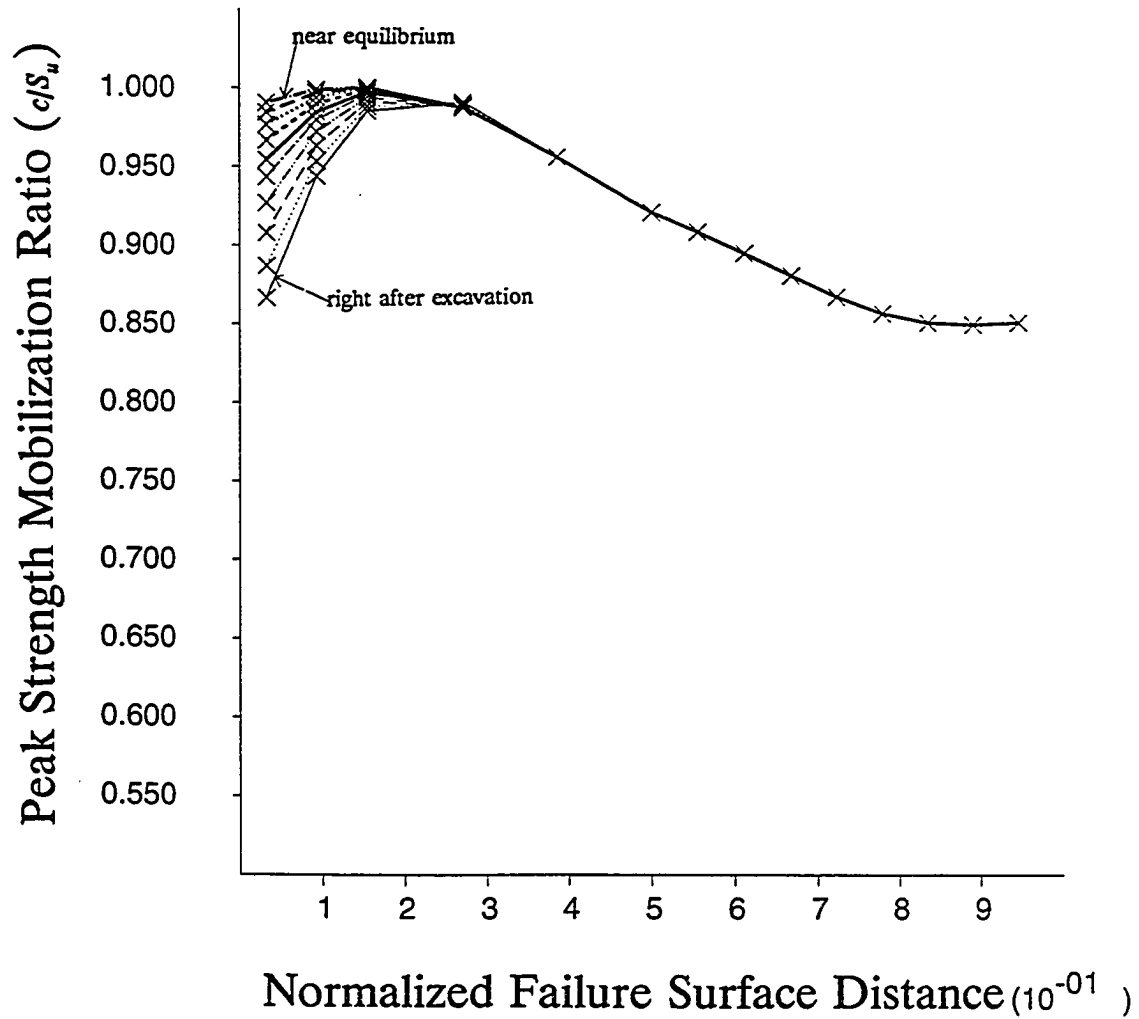


Fig. 6.42a Variation in the distribution of the peak strength mobilization ratios along the failure surface (16th layer excavation), C-3-b (30) analysis

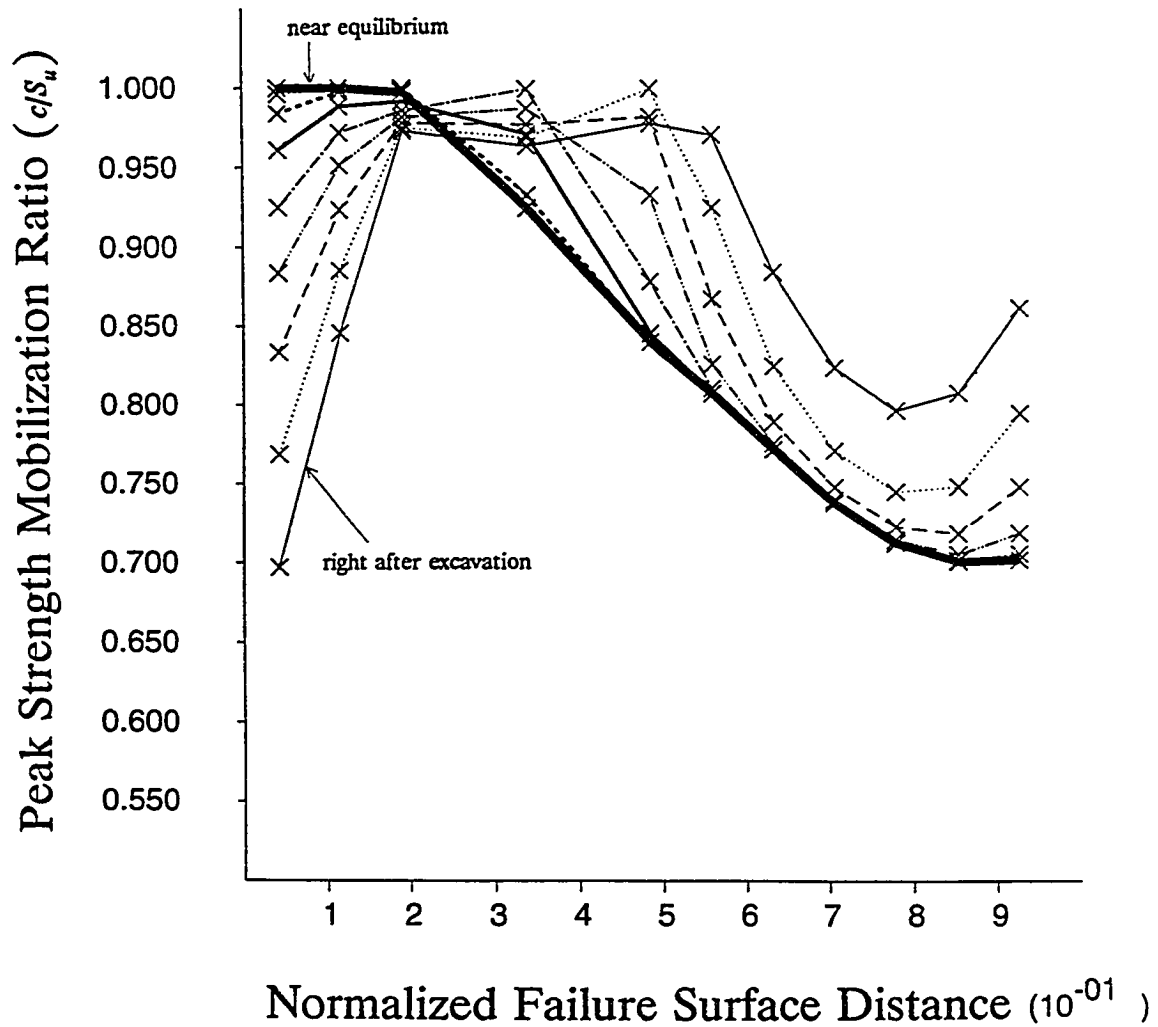


Fig. 6.42b Variation in the distribution of the peak strength mobilization ratios along the failure surface, (16th layer excavation) C-3-c (30) analysis

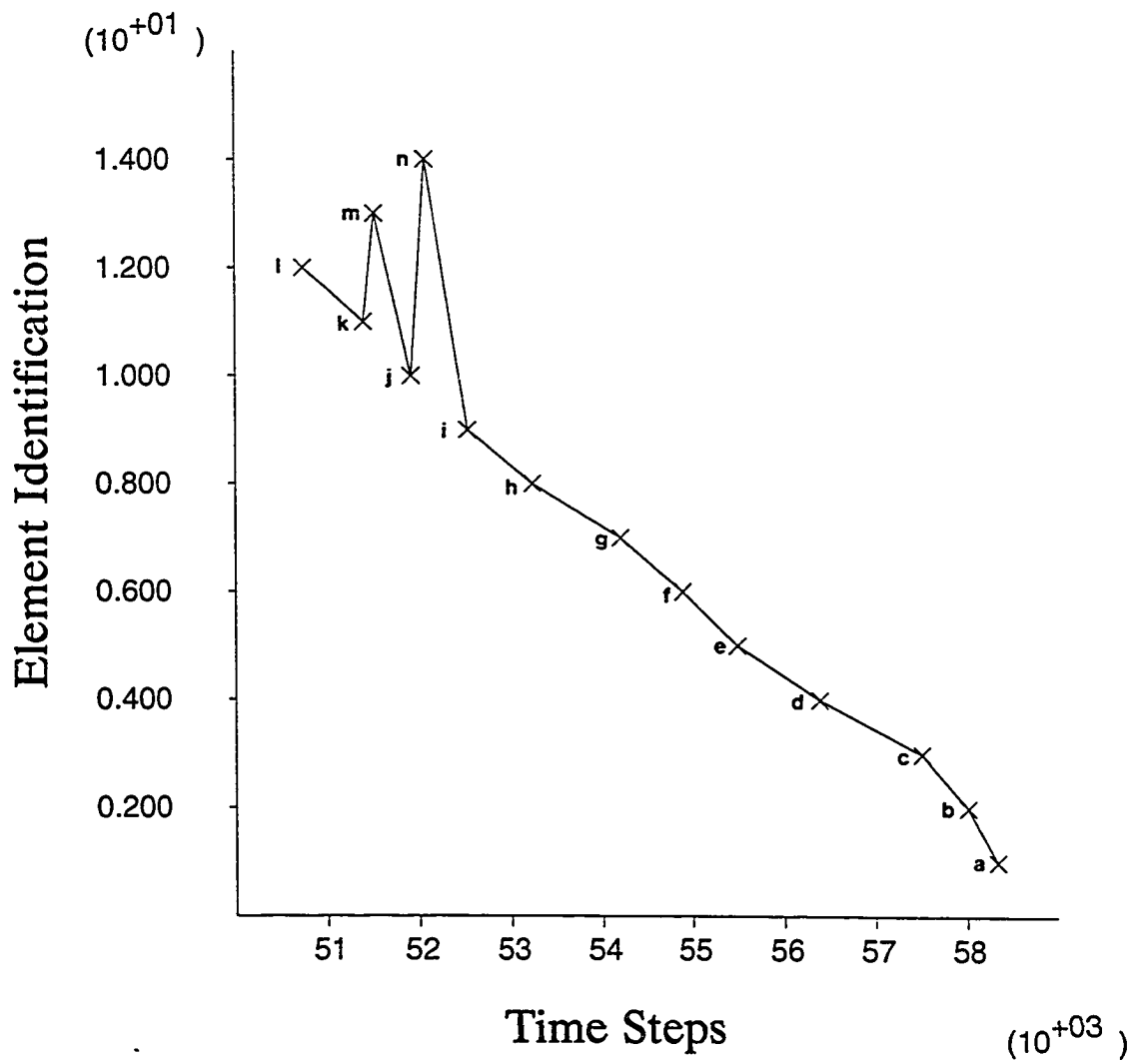


Fig. 6.43a Failure sequence of the elements along the failure surface, C-3-b (30) analysis

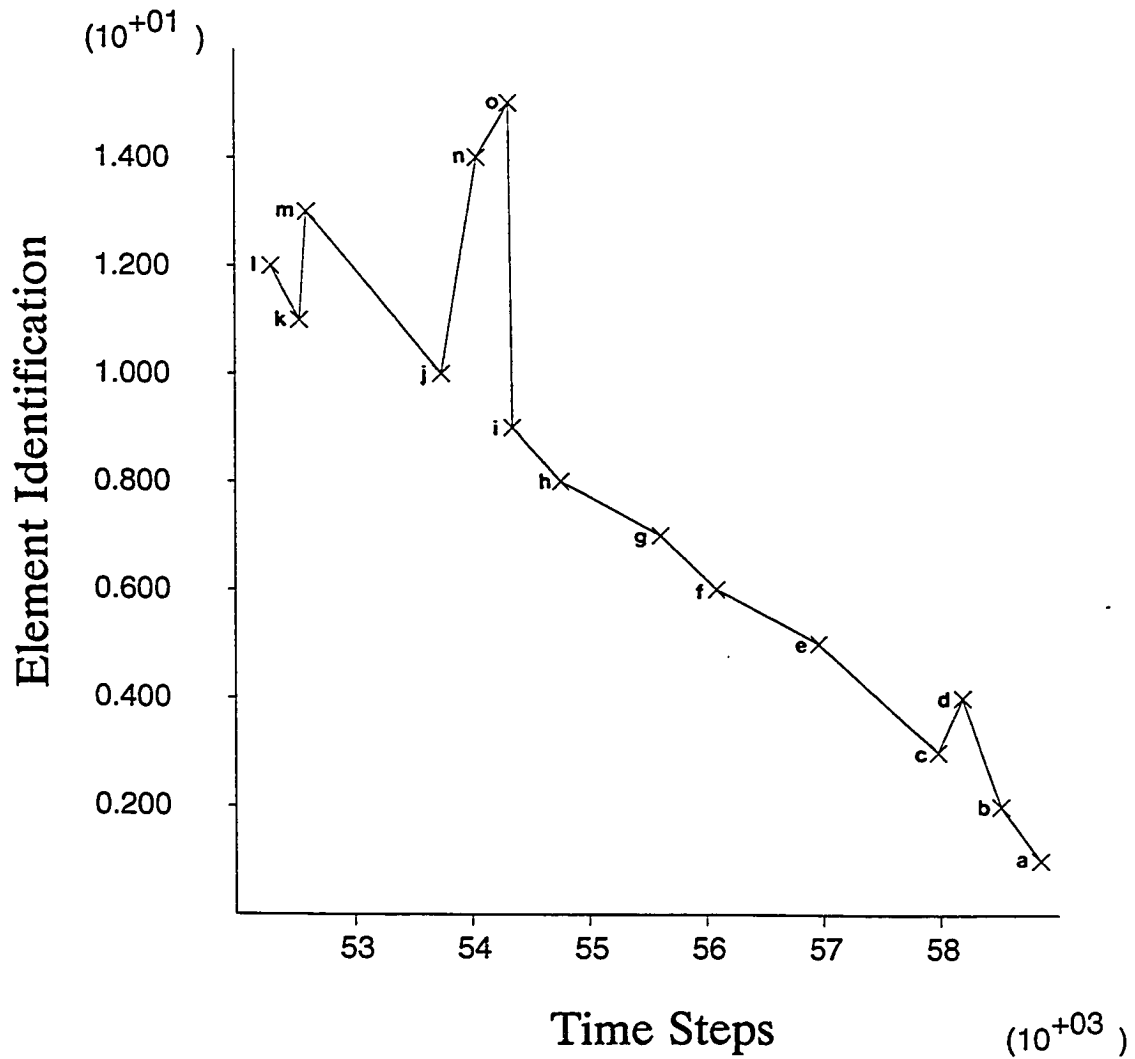


Fig. 6.43b Failure sequence of the elements along the failure surface, D-3-b (30) analysis

($\tau_{\max}/S_u=1.0$) sequence of elements along the failure surface in C-3-b (30) and D-3-b (30) analyses, respectively. As in B series of analyses, the failures in C and D series analyses also occur first at an element which is located somewhat below the crest and spread toward the toe elements as a general trend. This is also valid observation in C-4-b (60) and D-4-b (60) analyses (Figs. 6.44a and 6.44b). This observation is in contradiction to general belief that failure propagates from the over-stressed zone which is the toe of the slope to the crest.

Upon comparing the failure sequence of soil elements along the failure surface, the possible progressive failure mechanism suggested by Peck (1967) was reexamined. His postulate of the failure initiating from the crest and propagating toward the toe of a slope is based on the laboratory determined stress-strain relations in which the strain at the peak stress increases as the normal stress (effective consolidation pressure) increases up to a certain level. Since the soil elements near the ground surface have less consolidation stresses as compared to those in the interior of the sliding mass, he thought that shallow elements would reach the peak strengths faster than those in the interior elements. However, it is interesting to find that despite the fact that B and C series analyses use two distinct patterns of stress-strain relations, the resulting failure sequences are essentially the same (compare Fig. 6.31 to Fig. 6.43 and Fig. 6.44). This means that the failure sequence is strongly influenced by the maximum shear stress ratio (τ_{\max}/S_u) distribution rather than by the shear strain level at the peak stress.

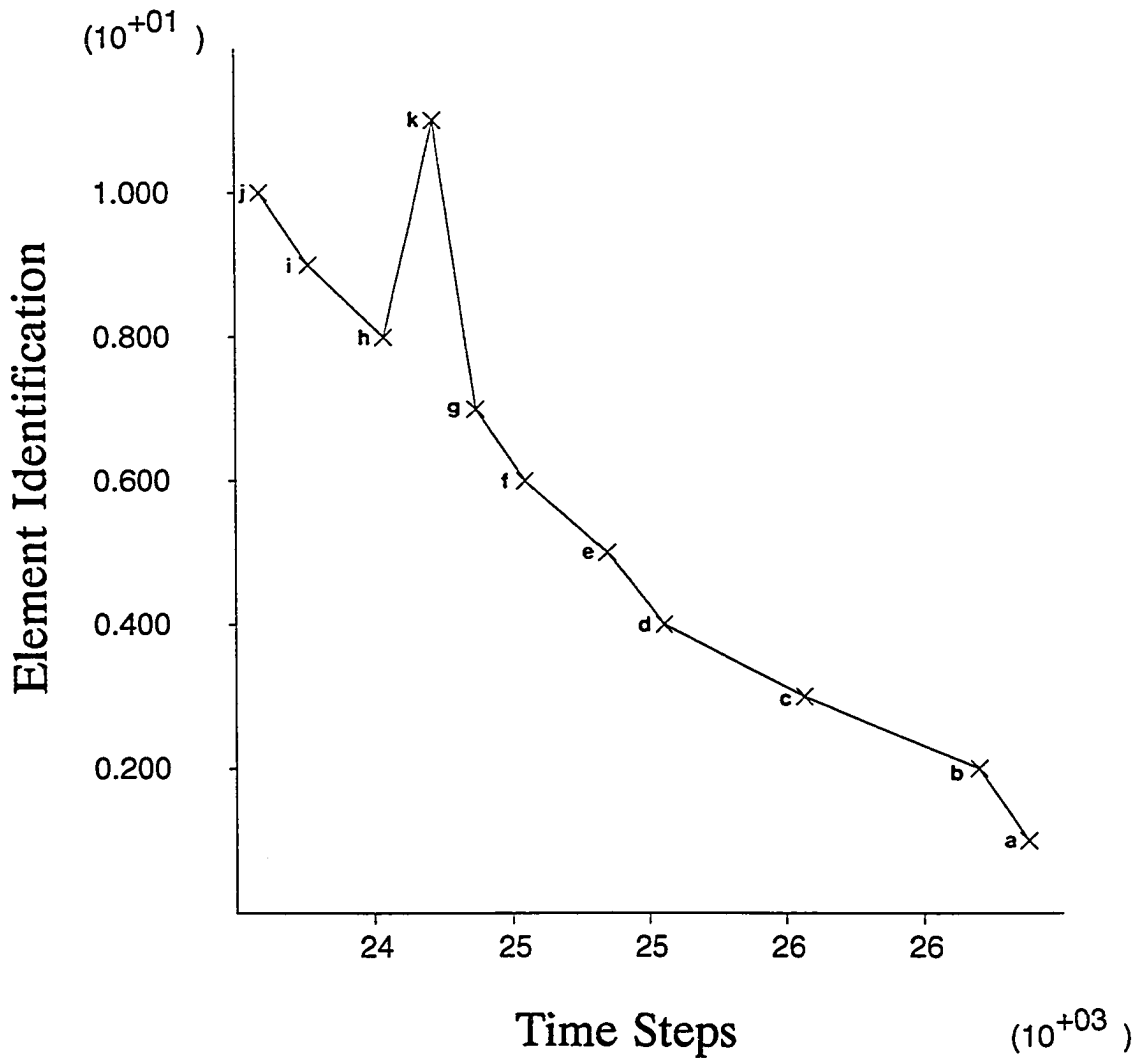


Fig. 6.44a Failure sequence of the elements along the failure surface, C-4-b (60) analysis

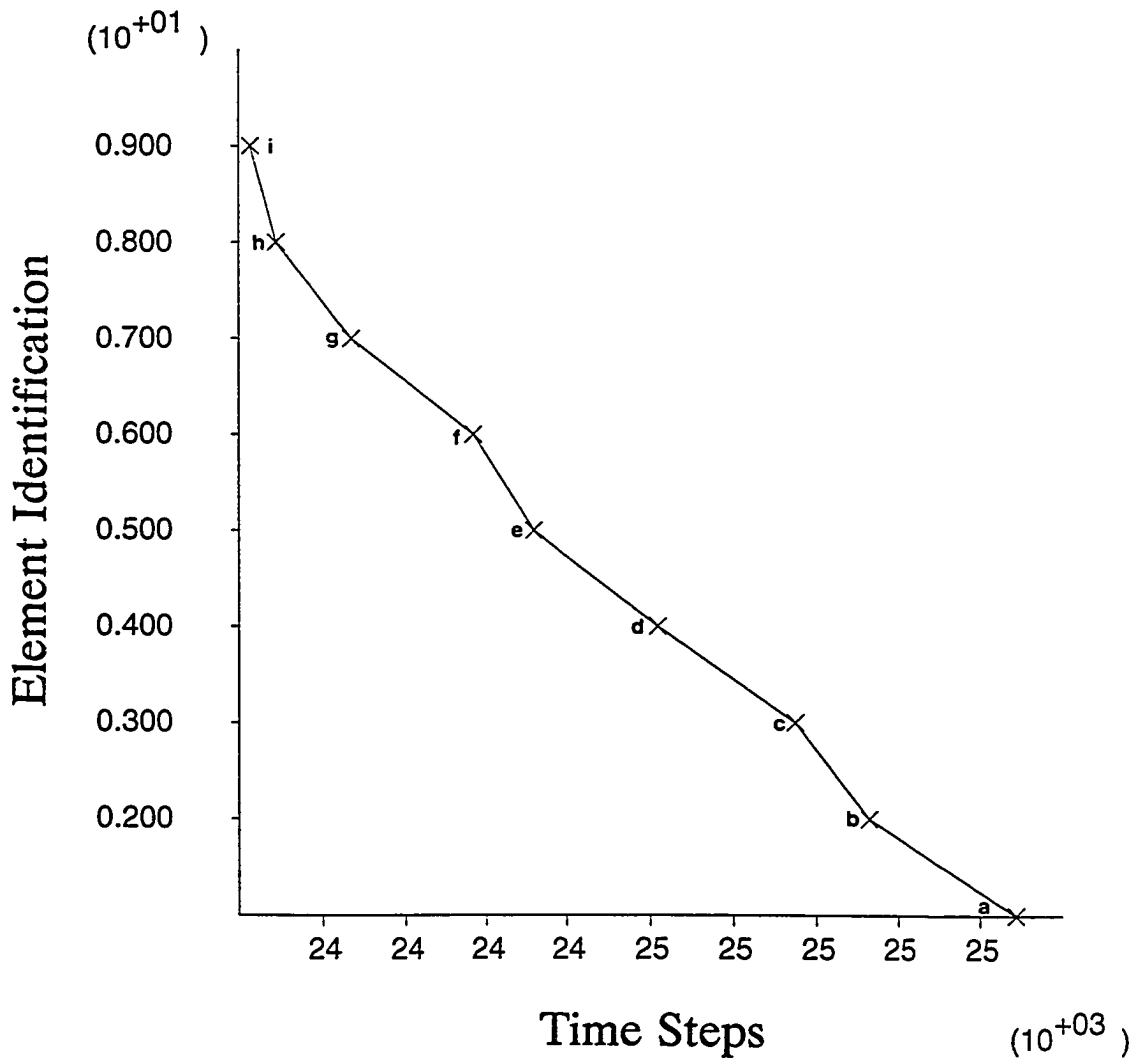


Fig. 6.44b Failure sequence of the elements along the failure surface, D-4-b (60) analysis

The summation of strengths of the elements along the failure surface can be expressed as a ratio to the summation of the isotropic compression strengths of those elements at a given time. As the elements experience strain hardening and softening, the ratio varies and experiences a peak in the process of failure. When the peak in the ratio takes place, the slope is exercising the maximum shear strength possible along the failure surface for given anisotropic strengths and stress-strain relations. The ratio at a given time and the peak ratio have already been termed "the mobilized strength ratio" and "the peak mobilized strength ratio", respectively, in Section 6.2.1.3.

Figs. 6.45a and 6.45b show the examples of variations in the mobilized strength ratios for C-3-c (30) and D-4-c (60) analyses, respectively. The explanation for the three horizontal lines in the figures has also been given in Section 6.2.1.3. The peak mobilized strength ratios for the entire cases are summarized in Tables 6.13a and 6.13b. In the table R^1 represents the level of the middle horizontal line, which is the peak mobilized strength ratio in B analysis, and R^2 corresponds to the peak mobilized strength ratios in C or D analyses. In addition, OE^1 is the overestimate in the peak mobilized strength ratio due to neglecting both the progressive failure effect and anisotropic strength effect, by simply using isotropic strength parameters as in A analysis. On the other hand, OE^2 is the overestimate due to neglecting only the progressive failure effect, by using anisotropic strength parameters as used in B series analyses.

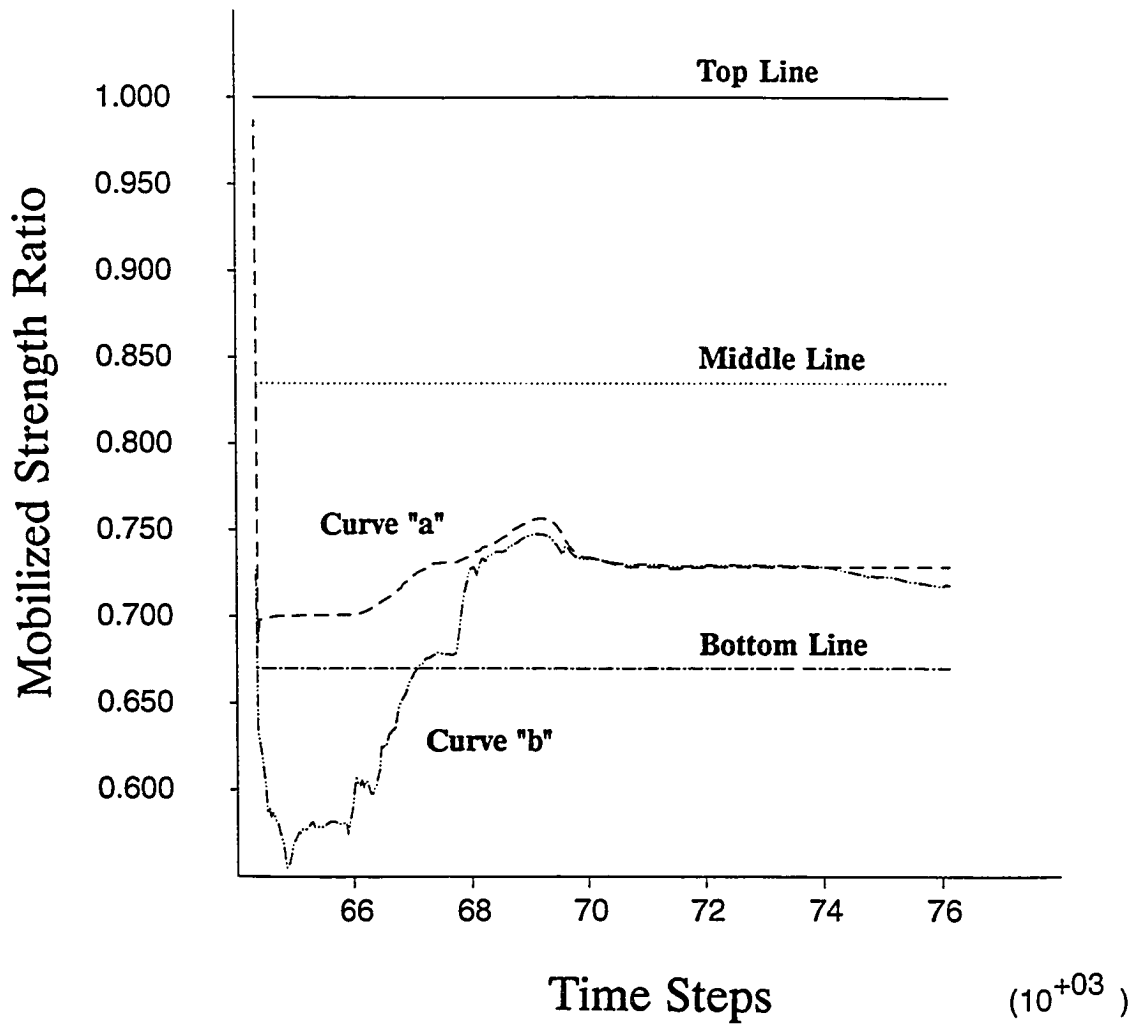


Fig. 6.45a Variation of the mobilized strength ratio with time steps, C-3-c (30) analysis

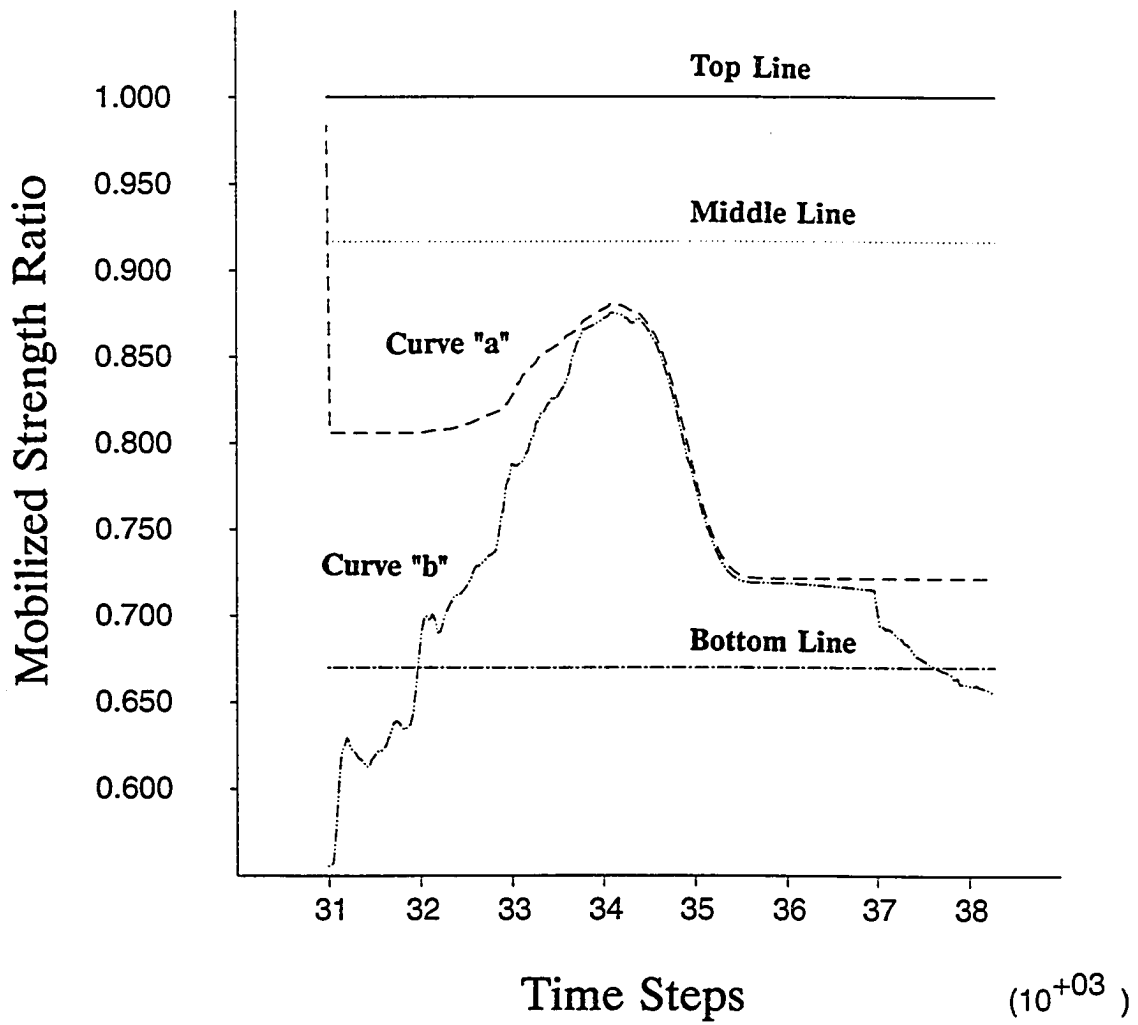


Fig. 6.45b Variation of the mobilized strength ratio with time steps, C-4-c (60) analysis

It can be seen in the tables that the overestimates (OE¹) in the peak mobilized strength ratio which would be accompanied by the isotropic compression strength analysis (i.e., ignoring both the anisotropic strength and progressive failure effects) may be as large as 32.3% for C-3-c (30) and 17.0% for C-4-b (60) cases. In addition, the overestimates (OE²) which would be resulted by

Table 6.13a Summary of the peak mobilized strength ratios (30 degree slope)

Case	C-1-a	C-1-b	C-1-c	C-3-a	C-3-b	C-3-c	D-3-b	D-3-c
R ¹	0.891	0.892	0.891	0.840	0.830	0.835	0.841	0.850
R ²	0.860	0.847	0.835	0.830	0.775 (0.805)	0.756 (0.804)	0.782 (0.795)	0.773 (0.780)
OE ¹	----	----	----	20.5%	29.0%	32.3%	27.9%	29.4%
OE ²	----	----	----	1.20%	6.60%	9.00%	7.54%	9.96%

* In C-1-a, C-1-b and C-1-c analyses, the peak strengths have not been fully mobilized

Table 6.13b Summary of the peak mobilized strength ratios (60 degree slope)

Case	C-1-a	C-1-b	C-1-c	C-4-a	C-4-b	C-4-c	D-4-b	D-4-c
R ¹	0.972	0.970	0.973	0.917	0.893	0.917	0.917	0.933
R ²	0.962	0.941	0.934	0.917	0.855 (0.870)	0.880 (0.896)	0.860 (0.880)	0.887 (0.892)
OE ¹	3.95%	6.27%	7.07%	9.05%	17.0%	13.6%	16.3%	12.7%
OE ²	1.00%	3.00%	4.00%	0.00%	4.00%	5.00%	6.62%	5.19%

anisotropic strength analysis (i.e., ignoring the progressive failure effect) may be as large as 9.96% for D-3-c (30) and 6.62% for D-4-b analyses. Based on the

results, the potential errors which would be induced by ignoring the strength anisotropy and the relative pattern of stress-strain relations (progressive failure effect) appear to be one of the most influential factors which must be fully addressed in the slope stability analysis.

It is found that OE^1 for D series analyses are slightly smaller than those of C series analyses when comparison is made between the analyses of the same degree of softening for both slope inclination angles. This is somewhat contradicting to our expectation, since D series of analyses should have more progressive failure effect so that OE^1 for D series analyses should be at least greater than those of C series analyses. However, it should be noted here that failure surfaces determined in C and D series analyses are not exactly the same so that elements involved in the failure surface are different from analysis to analysis to some extent, if not totally varied. Therefore, the strict comparison of the magnitudes of overestimates among different series of analyses is not valid.

The time steps at which the peak mobilized strength ratio takes place (e.g., in Fig. 6.45) can be used to find the excavation stage at which the peak occurs. Those excavation stages are marked as "peak" in the previous figures (Figs. 6.37a and 6.37b) The mobilized strength ratio reaches the peak at the 14th and the 13th layer excavations in C-3-a (30) and C-3-b (30) analyses, respectively. The stage at which the summation of the strengths is maximized in C-3-c (30) analysis is somewhat different from those of the two analyses. Meanwhile, in C-3-c (30) analysis, the peak mobilized strength ratio occurs at a relatively small nodal

displacement level (the 8th layer excavation). The discrepancy in the stage at which the peak mobilized strength ratio occurs is probably caused by the fact that in C-3-c (30) case the failure surface is moved up toward the crest three layers as compared to that of C-3-b (30) analysis so that much less range of stress paths were involved in the failure process. When the stress paths involved in the failure are concentrated near the compression mode ($i=0^\circ$), the peak mobilized strength ratio can occur at relatively smaller strain level (smaller displacement level). For the same reason, the moments of the peak mobilized strength ratio in C-4 (60) series analyses occur at considerably smaller magnitudes of nodal displacements as seen in Fig. 6.37b.

Figs. 6.46a and 6.46b show the plastic shear strain distributions along the normalized failure surface distances from the toe when the mobilized strength ratios become maximized for C-3-c (30) and C-4-c (60) analyses, respectively. It is clearly shown that the plastic shear strains along the failure surface in C-3-b (30) analysis are highly non-uniform (Fig. 6.46a). The fashion in which the plastic shear strains are distributed in C-4-c (60) analysis (Fig. 6.46b) is relatively rough due to shorter distance of failure surface and fewer elements involved in the surface. Relatively speaking, the non-uniformity of the plastic shear strain distribution in C-4-c (60) analysis is not as high as that in C-3-b (30) analysis.

Fig. 6.47 shows the examples of the stress-strain relations for elements with $i=0.90^\circ$, 26.4° and 61.8° degrees, which were actually used in C-3-b (30) analysis. The relative patterns of the stress-strain relations are well illustrated. Using the

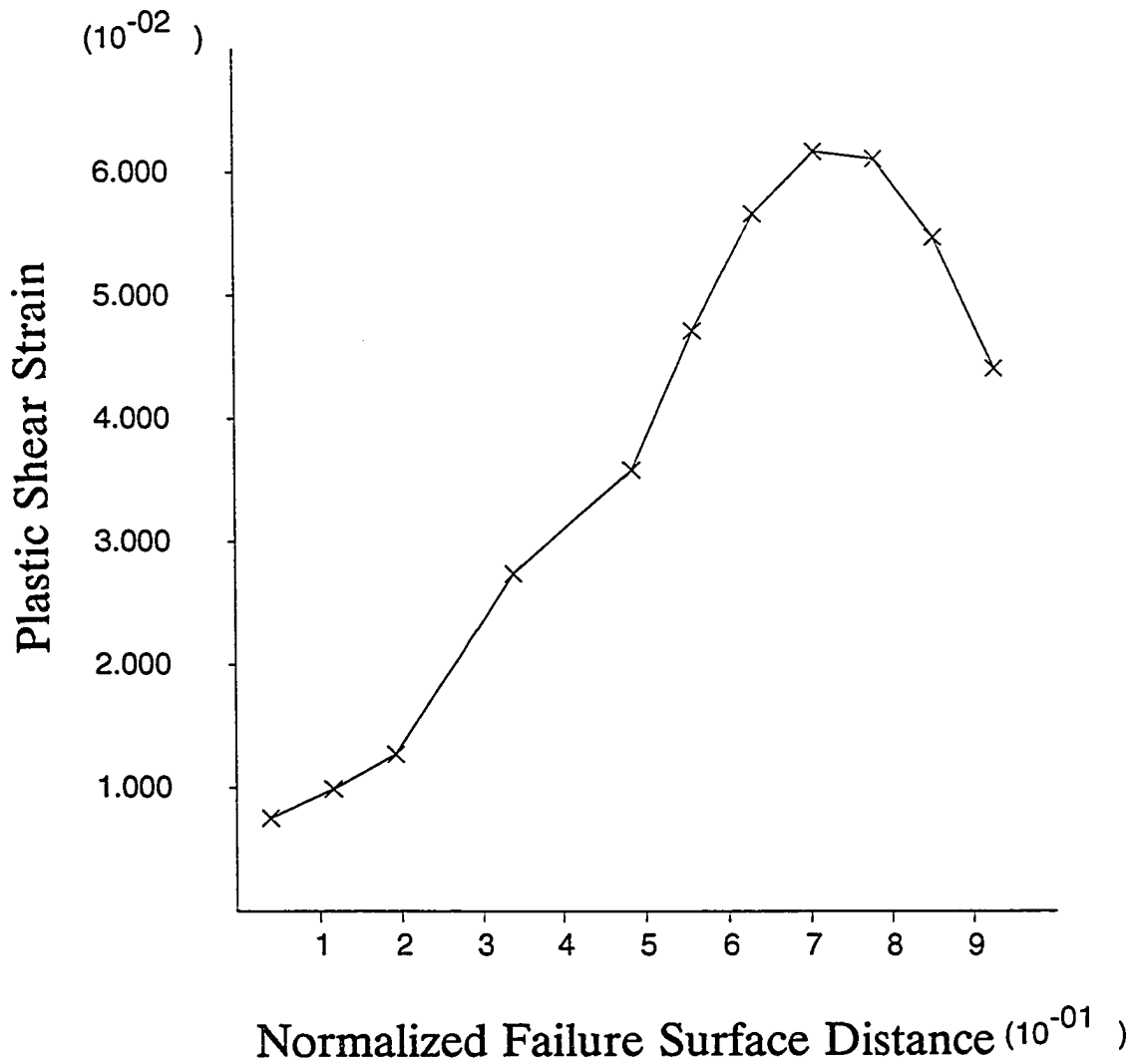


Fig. 6.46a Distribution of plastic shear strain along the normalized failure surface distance, C-3-c (30) analysis

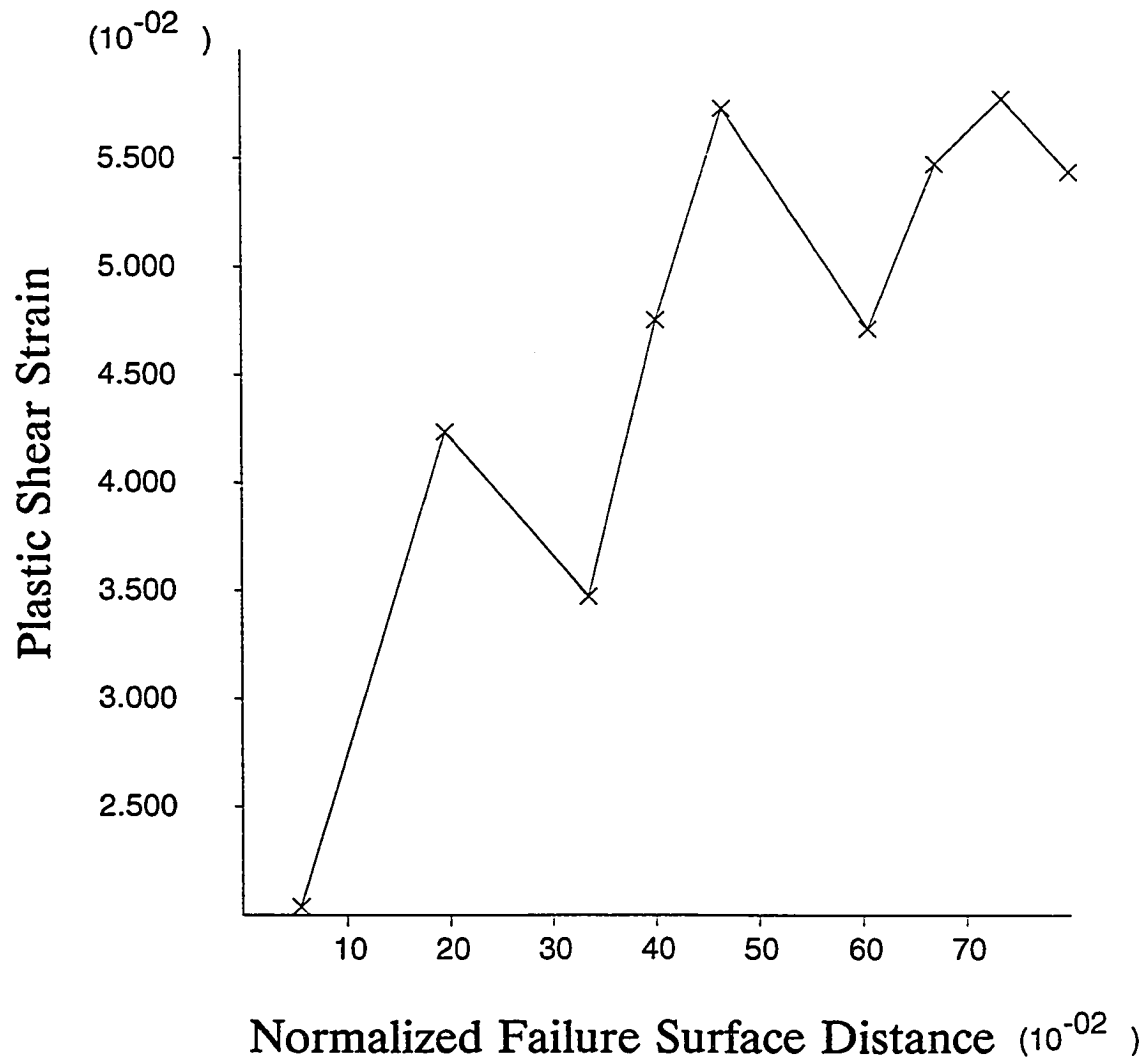


Fig. 6.46b Distribution of plastic shear strain along the normalized failure surface distance, C-4-c (60) analysis

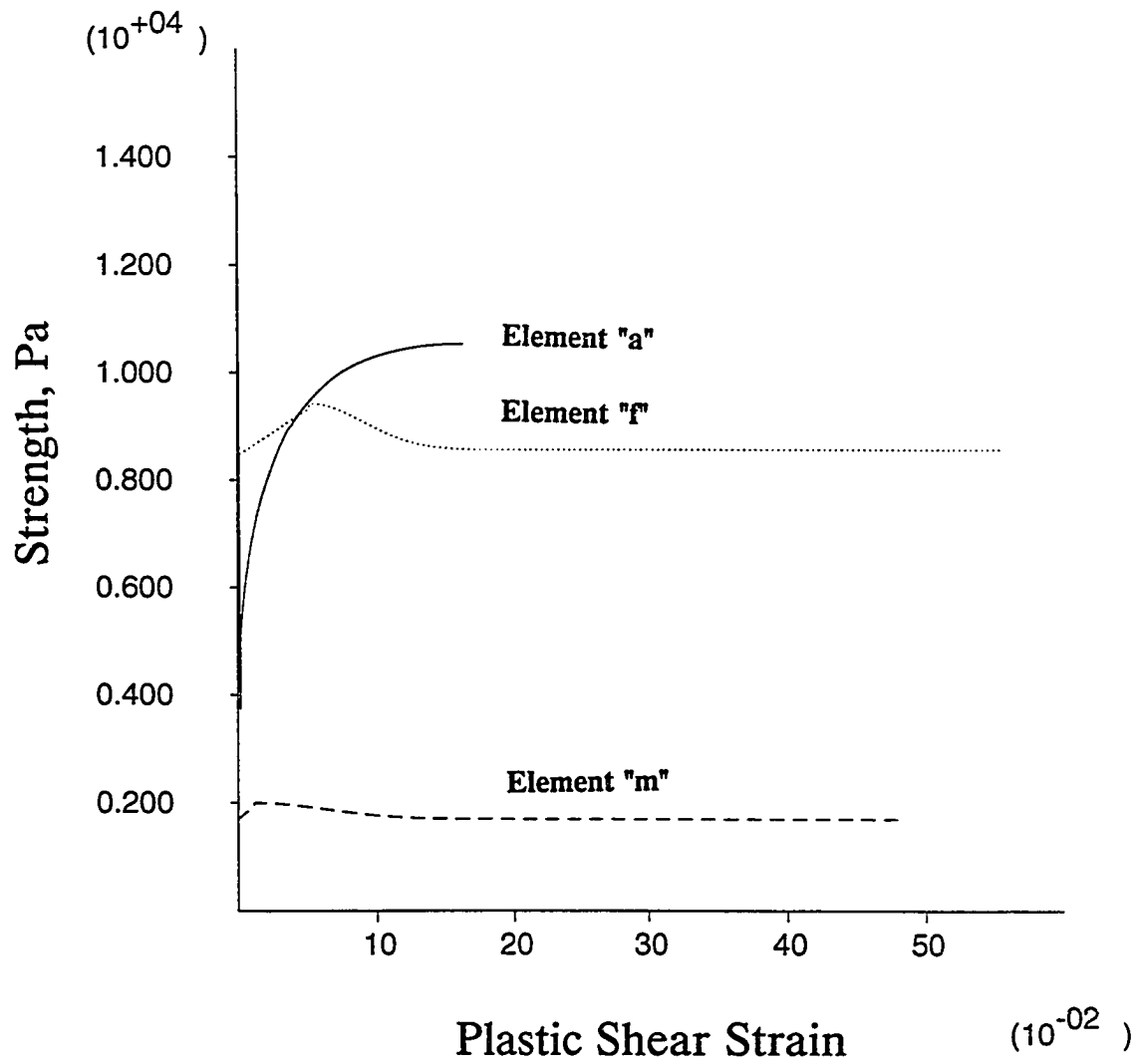


Fig. 6.47 Examples of strength and plastic shear strain relations, C-3-b (30) analysis

stress-strain relations of the entire elements along the failure surface, the summations of the stresses at varying strain levels were obtained (strain compatibility technique). Then, they were expressed as ratios to the summation of the anisotropic peak strengths of those elements (i.e., the strength ratio) as discussed in Section 6.2.1.3. Figs. 6.48a and 6.48b, respectively, show for C-3 (30) and C-4 (60) series analyses the variations of the strength ratios to the summation of the anisotropic peak strengths in B-3 (30) and B-4 (60). It is seen that the ratios in C-3-a (30) and C-4-a (60) eventually approach the unity, while others show less than unity. The peak strength ratios in those figures are summarized in Table 6.14, which also includes similar analyses made for D series of analyses. It is found that the summations of the stresses are consistently smaller than that of anisotropic peak strengths. When the peak strength ratios are converted to the equivalent to those in the third row in Tables 6.13a and 6.13b, it turns out that the predictions of strength mobilizations based on the assumption of uniform strain distribution (strain compatibility technique) are always slightly higher than those from more rigorous C and D analyses. Note that it was opposite way in slopes with uniform strength profiles as seen in Table 6.7 in Section 6.2.1.3.

In the numerical analysis, it is sometimes not clear to determine whether the slope is in failure or not. A sudden increase of deformation rate of a nodal point is often used as a criterion for that purpose. When the structure is experiencing a large deformation, more computational time steps are required to bring the structure to the equilibrium state at which maximum unbalance force is

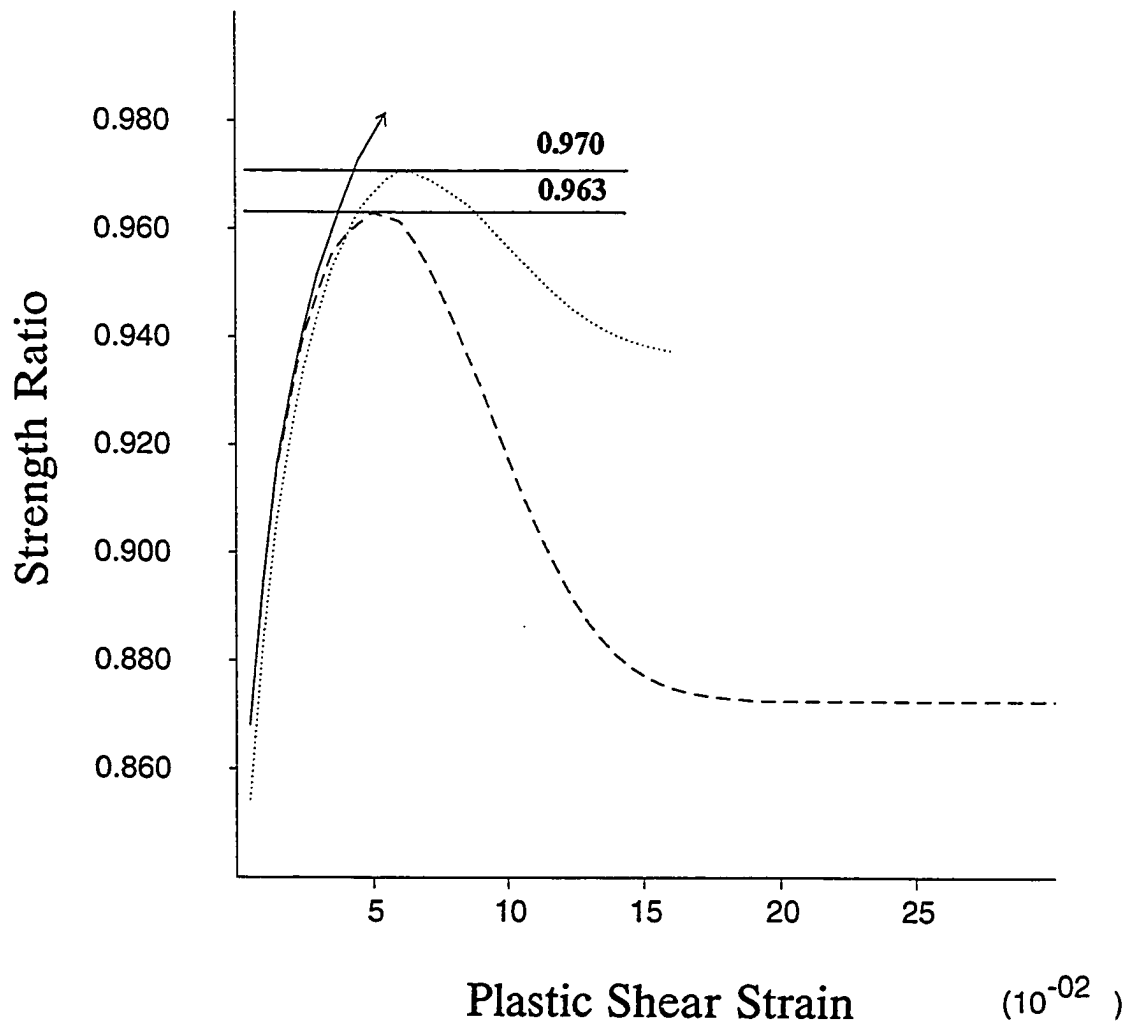


Fig. 6.48a Variation of strength ratios (strain compatibility concept), C-3 (30) analyses

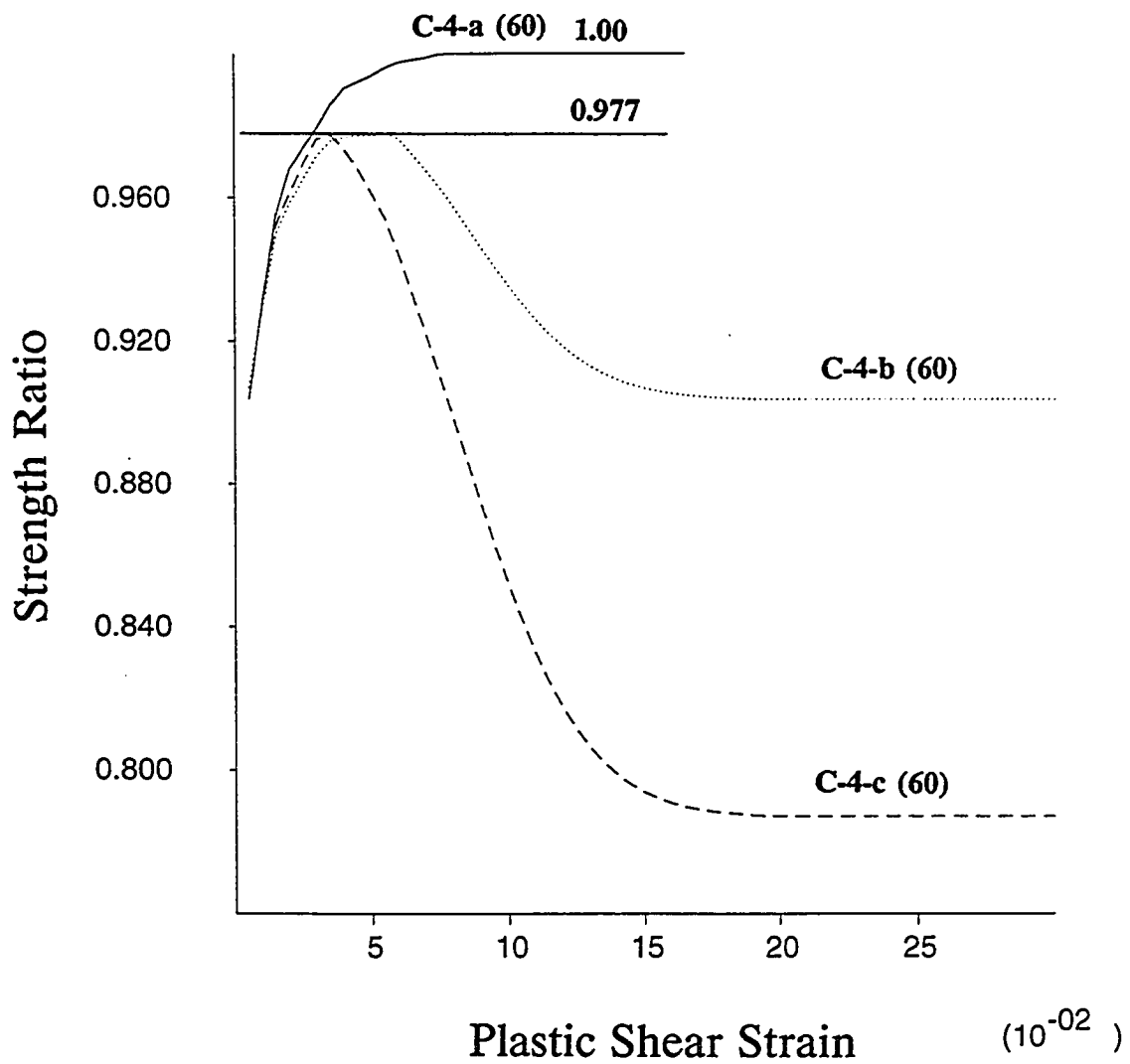


Fig. 6.48b Variation of strength ratios (strain compatibility concept), C-4 (60) analyses

less than a specified value (100.0 N in the current study). Fig. 6.49a shows an example of the history of unbalance force in the process of layer by layer excavation (C-3-c (30) analysis). The numbers at peaks represent the number of

Table 6.14 Summary of the peaks of summations of the undrained strengths using the strain compatibility technique.

slope	C-3-b	C-3-c	C-4-b	C-4-c	D-3-b	D-3-c	D-4-b	D-4-c
30°	0.970	0.963	---	---	0.945	0.937	---	---
60°	---	---	0.977	0.977	---	---	0.960	0.956

excavation layer. It is noted in the figure that at the end of the 10th layer excavation the structure takes greater number of time steps to get to the equilibrium state, which is an indication that the structure is in a flow state. The structural instability at the 10th layer excavation can also be seen in the history of velocity (meter/time step) in the horizontal direction of the nodal point at the crest (Fig. 6.49b). It is shown that at the start of 10th layer excavation, the velocity almost linearly increases, indicating that the soil mass is experiencing a large deformation. After a large number of computational time steps, the maximum unbalance force becomes less than a specified value, but the absolute of the velocity is still very high. The high magnitude of the velocity at this stage (1.2e-4 m/step) can be realized by comparing it to the value (about -0.1e-4 m/step), which was caused by a layer of excavation in the early stage of excavation. It is noted in the figure that even with the small unbalance force at the end of the 10th layer excavation (time steps: 73500), the velocity is still high,

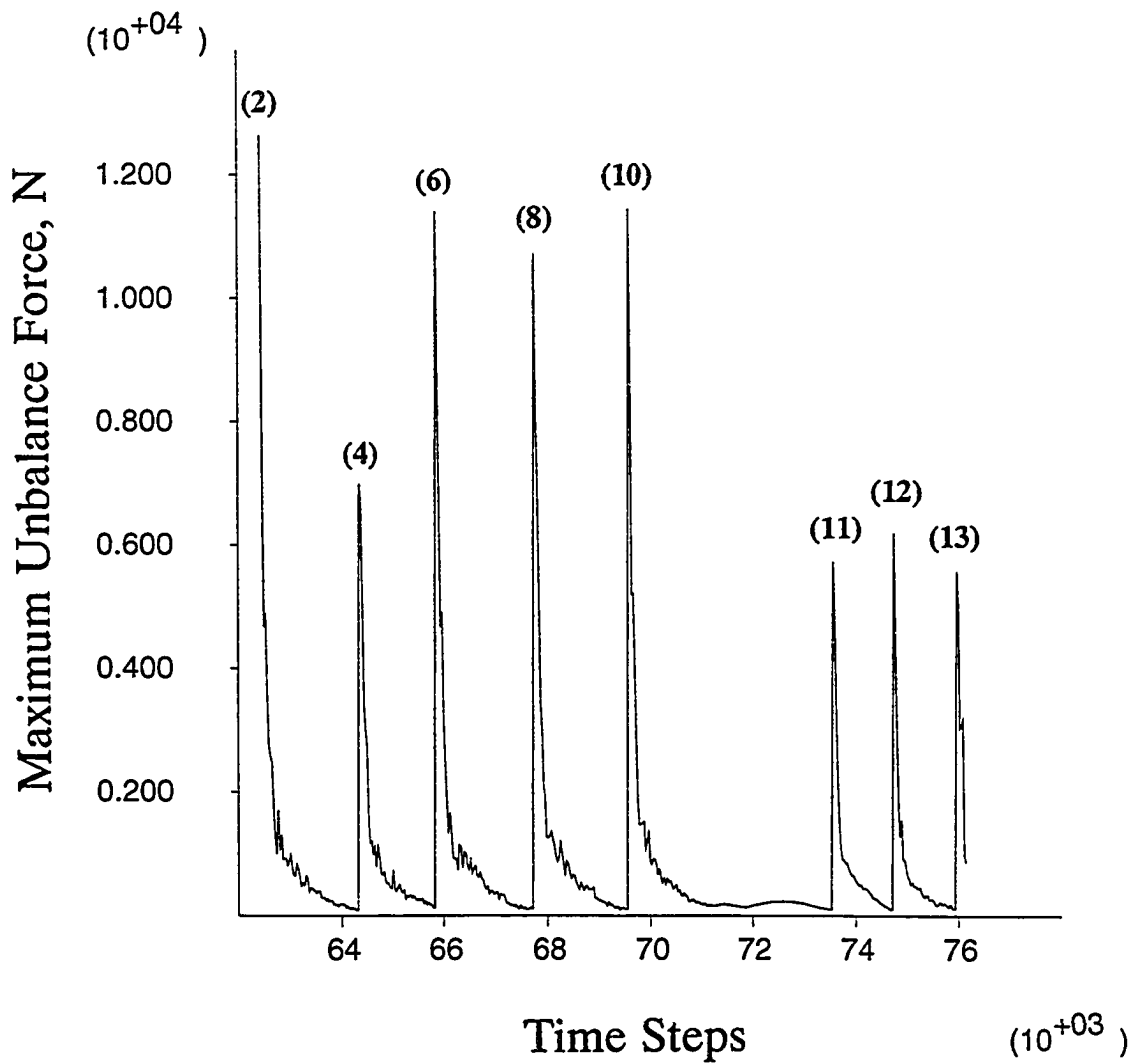


Fig. 6.49a History of maximum unbalance force, C-3-c (30) analysis

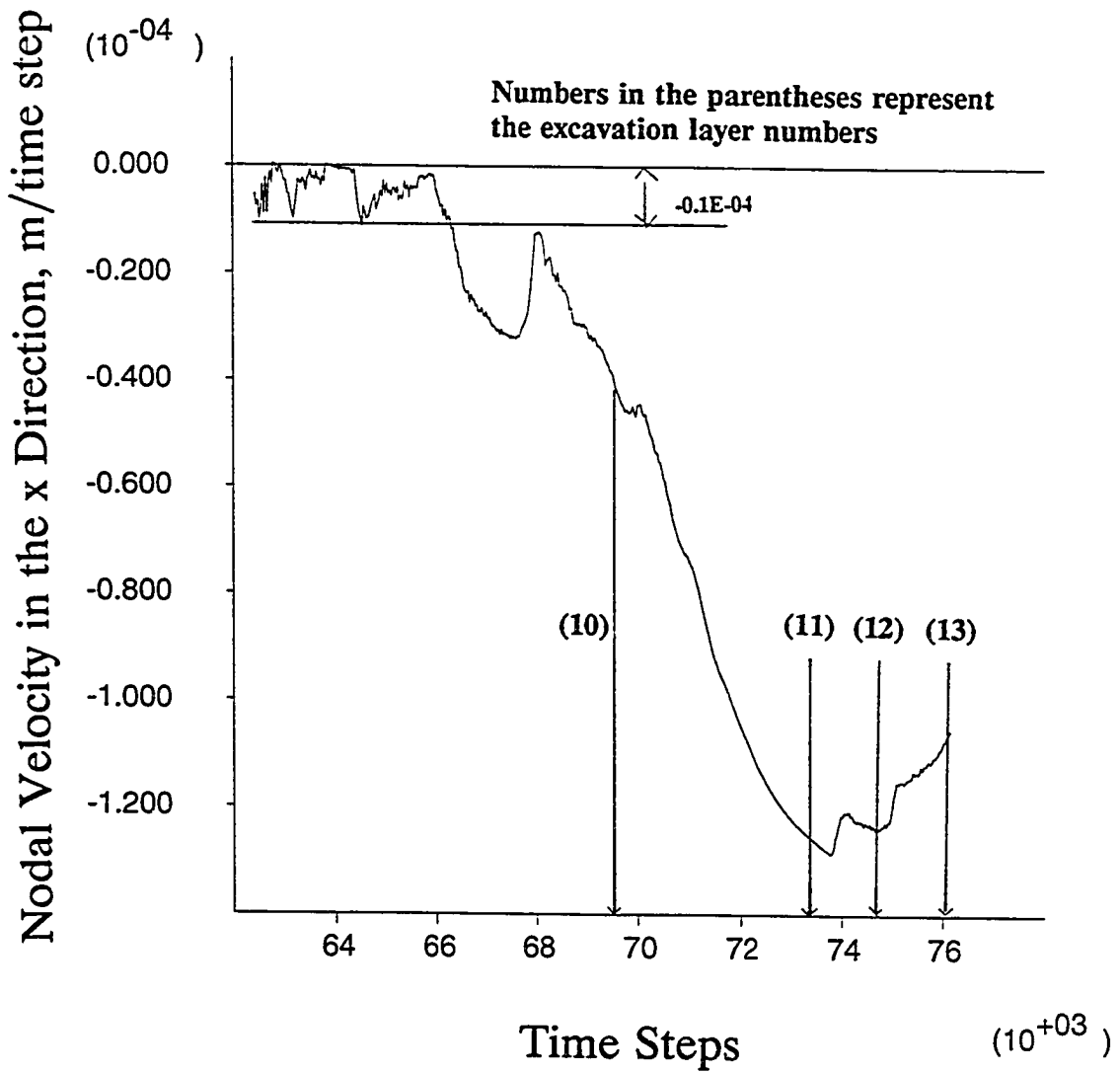


Fig. 6.49b History of nodal velocity in the horizontal direction, C-3-c (30) analysis

which means that the soil mass is in a flow state. (In a perfect plastic flow, the unbalance force is zero, yet a constant velocity exists.) Additional layers of excavation cause the velocity to reduce to some extent, yet the magnitude at the end of final excavation is still substantial. In order to save the computational effort during the unnecessarily excessive deformation of the slope, computational time steps in the analyses were automatically stopped when the magnitude of the nodal displacement is greater than a specified value (usually 0.5 to 1.0 meter). This explains the unnatural patterns of nodal displacements at the end of excavation in C-3-c (30) analysis (Fig. 6.37a). It should be pointed out here that a slope in the analysis does not necessarily either remain elastic or fail plastically. There is always a case in which the slope is experiencing an intermediate state of the extremes with a global factor of safety greater than unity. In such cases, acceptable magnitude of the slope deformation becomes an important design criterion in addition to the factor of safety.

Figs. 6.50a and 6.50b show the failure surfaces determined in C-3 (30), D-3 (30) and C-4 (60), D-4 (60) analyses in comparison to those determined by Modified Bishop method. It is interesting to note in the figures that in both slopes (30 and 60 degrees) the locations of the failure surfaces seem to be depending on the degree of strain softening. When relatively high strain softening (30% softening) is employed, the final failure surface becomes much shallower as compared to those of low strain softening cases (0 and 15% softening). As mentioned previously, the critical surface (i.e., surface with the least factor of

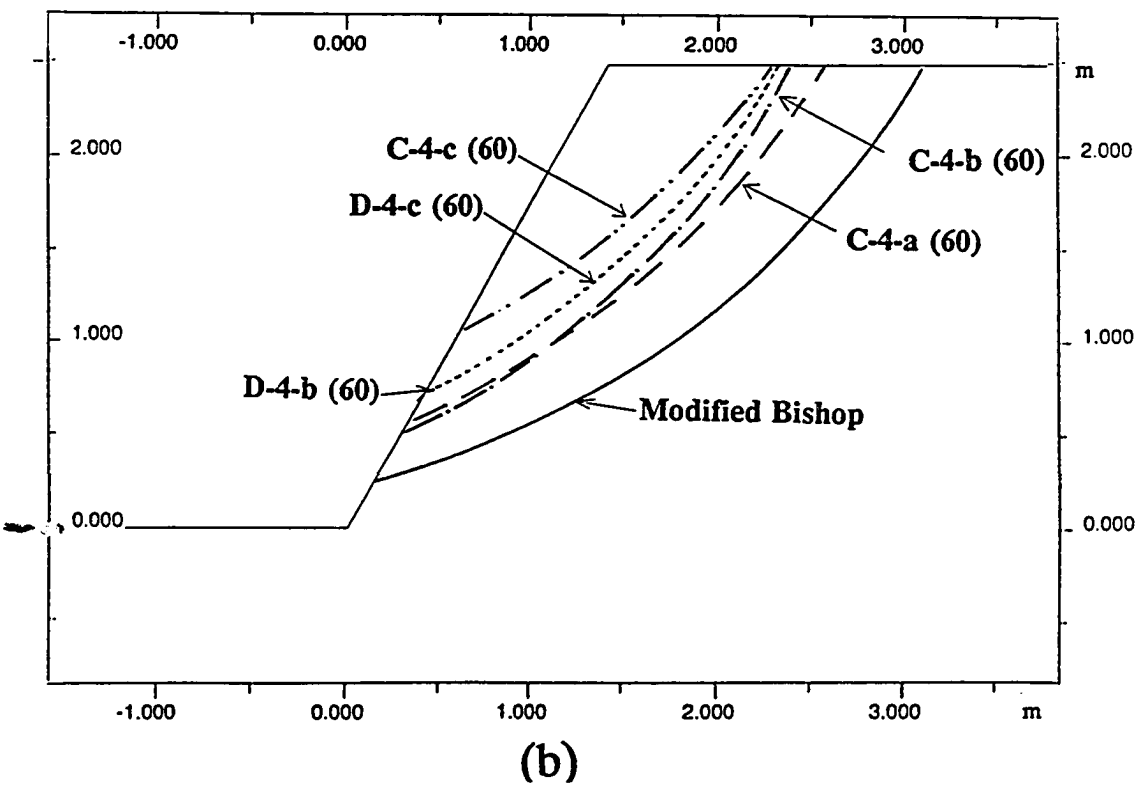
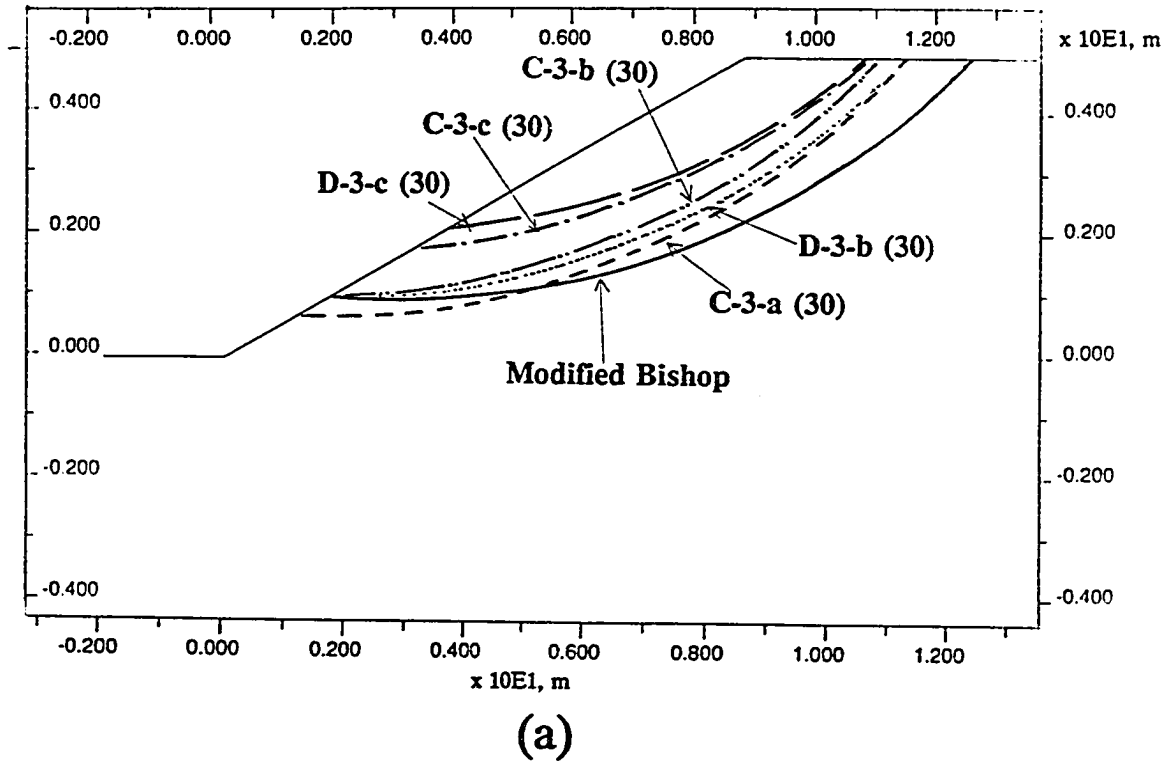


Fig. 6.50 Comparisons of failure surfaces: (a) C-3 (30) and D-3 (30) analyses; and (b) C-4 (60) and D-4 (60) analyses

safety) in the slope with a linearly increasing strength profile usually moves down until the final failure surface is encountered in the process of layer by layer excavation. Therefore, the failure in the analysis with high degree of strain softening should occur at much earlier stages of excavation involving less soil mass in the failure. The failure surfaces determined by Modified Bishop method are usually located below the groups of failure surfaces determined by C and D series analyses for both slopes.

6.3 Overconsolidated Clay

6.3.1 Introduction

Nearly constant strengths (or very little strength increase) up to a certain depth are frequently encountered in overconsolidated clays. The overconsolidation of a cohesive soil due to changes in the effective stress during the geological history may be caused by a variety of factors. For example, the surface layer in dry season exposed to the air can be dried (desiccation) resulting in the increase of effective consolidation pressure. Subsequently, the ground water table in wet season rises and the effective overburden pressure is reduced, leading to a overconsolidated clay. The strength profile representing this case can be characterized by relatively high strengths near the surface, where the effect of overconsolidation would be greatest, which gradually approach the strength of the normally consolidated clay near the base of the overconsolidated clay layer.

One of the main characteristics in overconsolidated clay is the relatively high lateral earth pressure. Unlike the normally consolidated clay, the coefficient of earth pressure at rest, K_o , for overconsolidated clay is not constant and can be approximated as a function of overconsolidation ratio, OCR, (Das, 1990):

$$K_o \text{ (overconsolidated clay)} = K_o \text{ (normally consolidated clay)} \sqrt{(OCR)} \quad (6.1)$$

Equation 6.1 was used to calculate the initial K_o values for the overconsolidated clay in this study.

The variation of OCR with respect to depth, which was used in this study, is shown in Fig. 6.51. It was adapted with slight modification from Deschamps and Leonards (1991). The undrained strength ratio of overconsolidated clay is usually higher than that of normally consolidated clay and can be expressed as a function of OCR (Ladd et al., 1977):

$$S_u/\sigma'_{vo} \text{ overconsolidated clay} = (OCR)^{0.8} \times S_u/\sigma'_{vo} \text{ normally consolidated clay} \quad (6.2)$$

Accordingly, the undrained strength profile corresponding to the OCR variation in Fig. 6.51 is shown in Figs. 6.52. The point where the change in the strength increment ratio occurs in Fig. 6.52 corresponds to the boundary between overconsolidated clay and normally consolidated clay. The undrained compression strength ratio (S_u/σ'_{vo}) for the normally consolidated clay used in this study was 0.152, the total unit weight of the entire soil was 19651 N/m³, and K_o of the normally consolidated clay was 0.8. The ground water table was assumed to

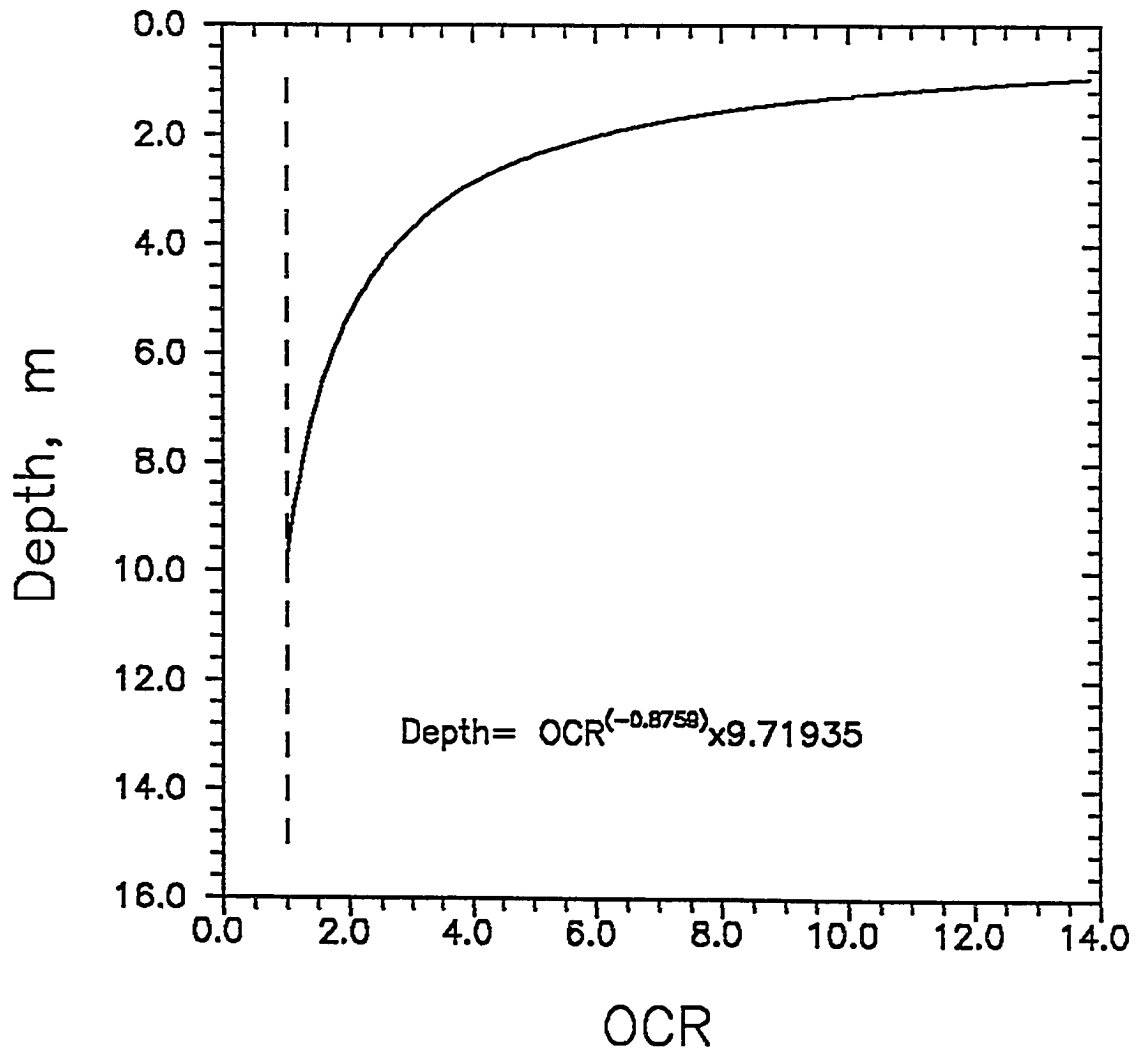


Fig. 6.51 Variation of OCR with depth

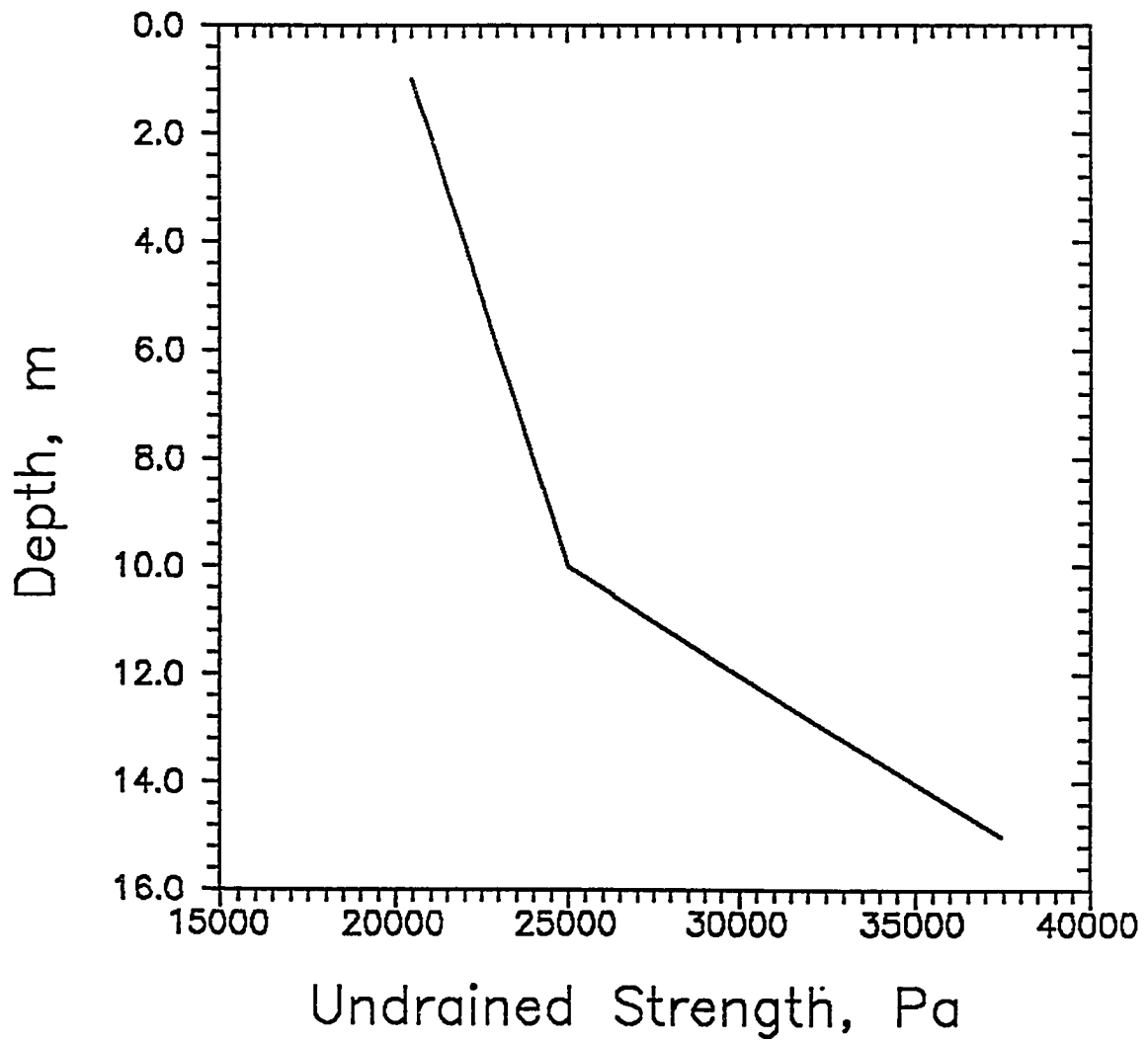


Fig. 6.52 Undrained strength profile

be located below the bottom of the model. The excavation heights corresponding to the number of excavation layer are summarized in Table 6.15. The slope considered in this section has an inclination angle of 60 degree. The finite difference meshes of the slope is shown in Fig. 6.53.

Table 6.15 Summary of excavation heights (meters) with the number of layer excavation

Slope Angle	1st	2nd	3rd	4th	5th	6th	7th	8th
60°	0.84	1.69	2.54	3.40	4.24	5.09	5.94	6.71

6.3.2 Isotropic Strength Analysis (A Analysis)

This case is similar to other A analyses in that isotropic elasto-plastic model is used, but initial lateral stresses in the overconsolidated clay layer were varied based on K_0 values, which is a function of OCR. Figs. 6.54a through 6.54h show the pattern of maximum shear strain development in the focused area near the slope face during the layer by layer excavation. It is seen that the maximum shear strain is highly concentrated near the toe with a trend of moving downward in the initial stage of excavation (Figs. 6.54a through 6.54e). At the sixth layer excavation (Fig. 6.54f), the concentration of the maximum shear strain is rather shifted toward the interior of the slope. At the final layer excavation (Fig. 6.54h), the maximum shear strain development toward the crest is evident. If failure occurs, it is likely a toe failure based on the maximum shear strain distribution.

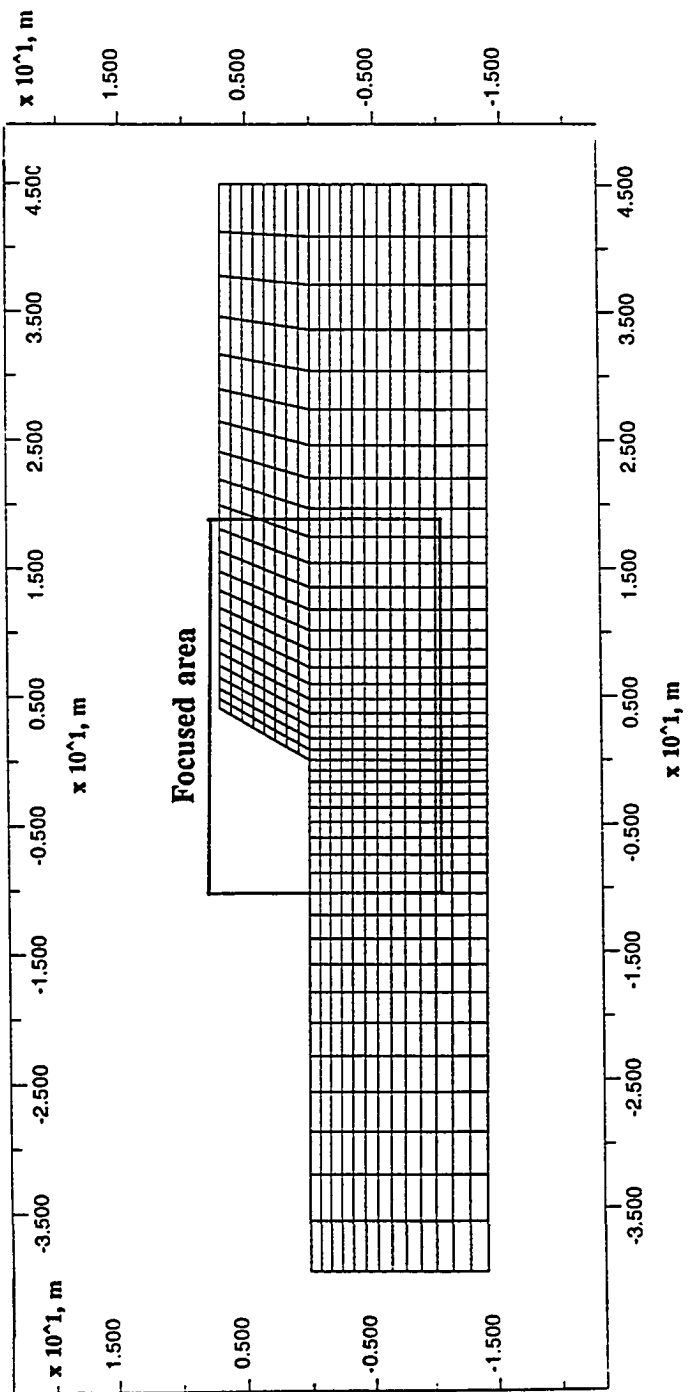
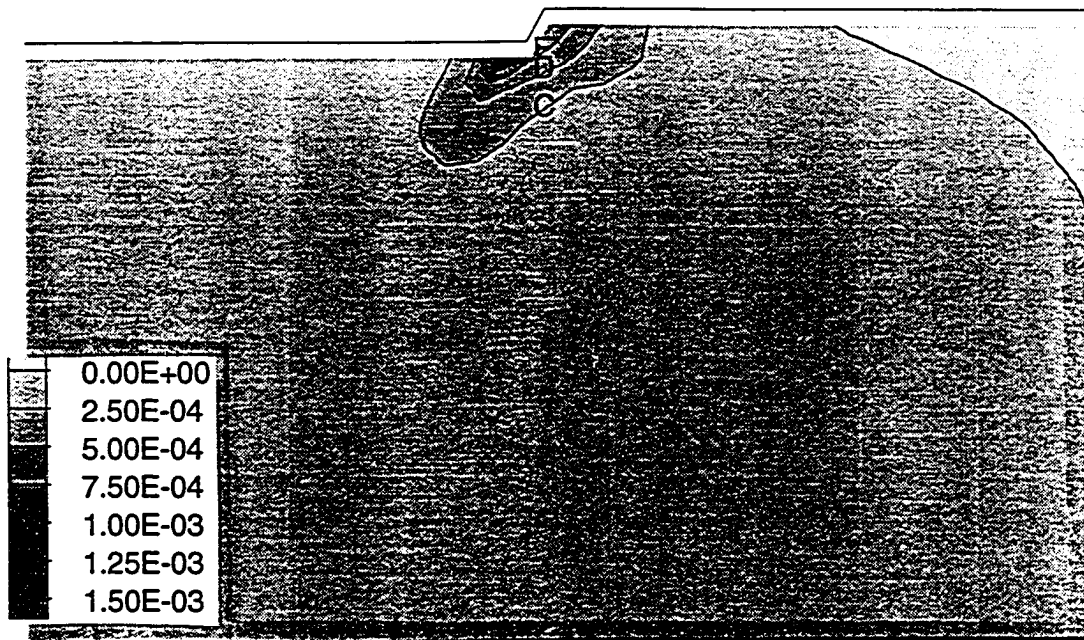
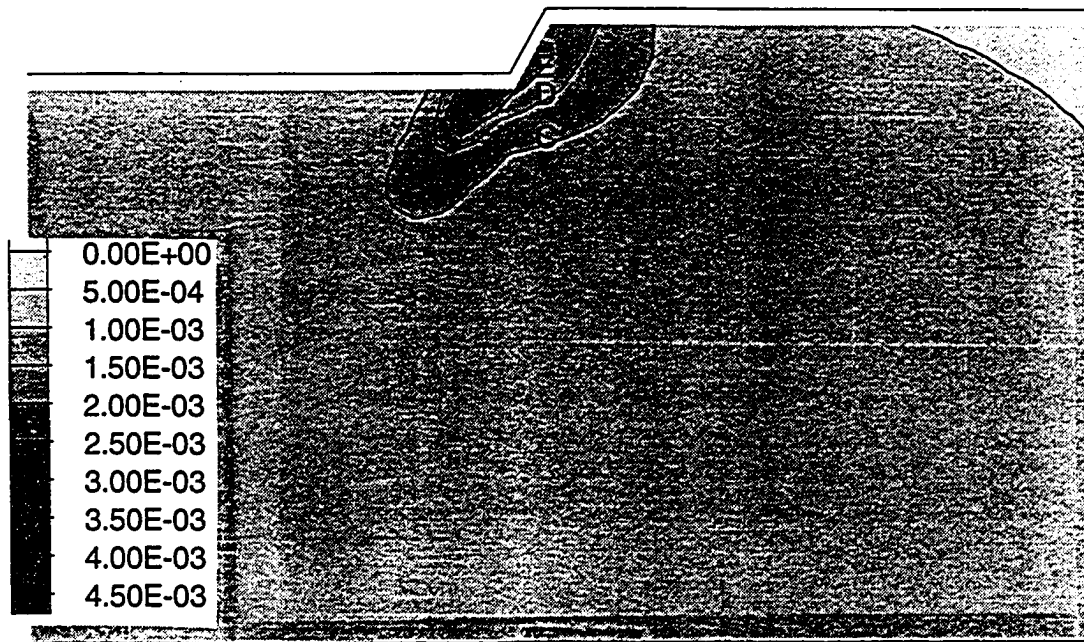


Fig. 6.53 Finite difference mesh

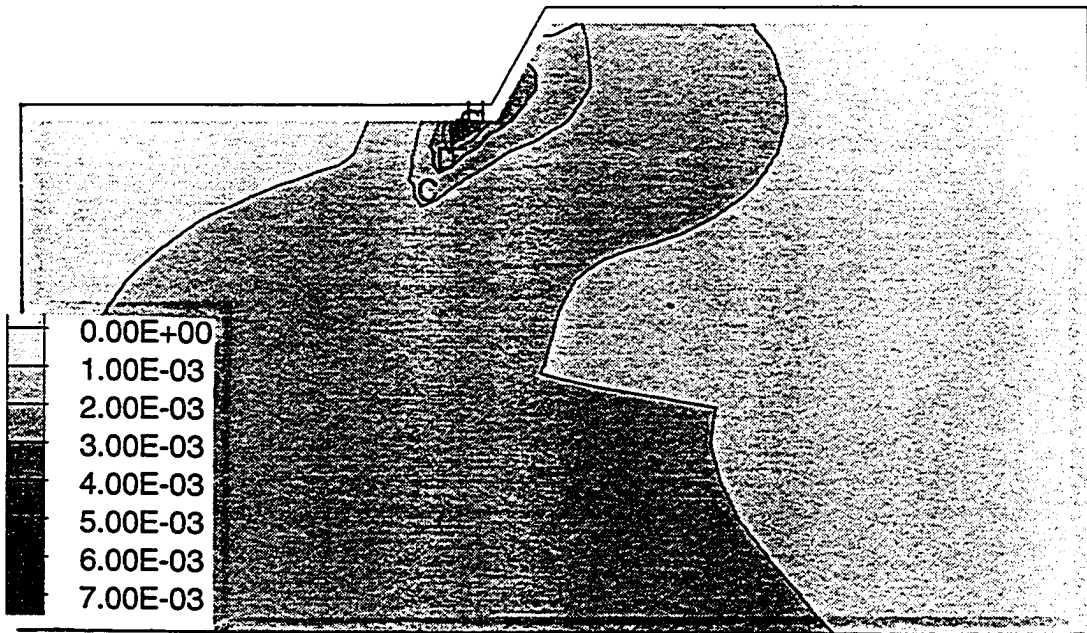


(a) 1st layer ($H_{\alpha} = 0.84$ m); Contour Interval = $2.5E-04$ (C: $5.00E-04$, E: $1.00E-03$)

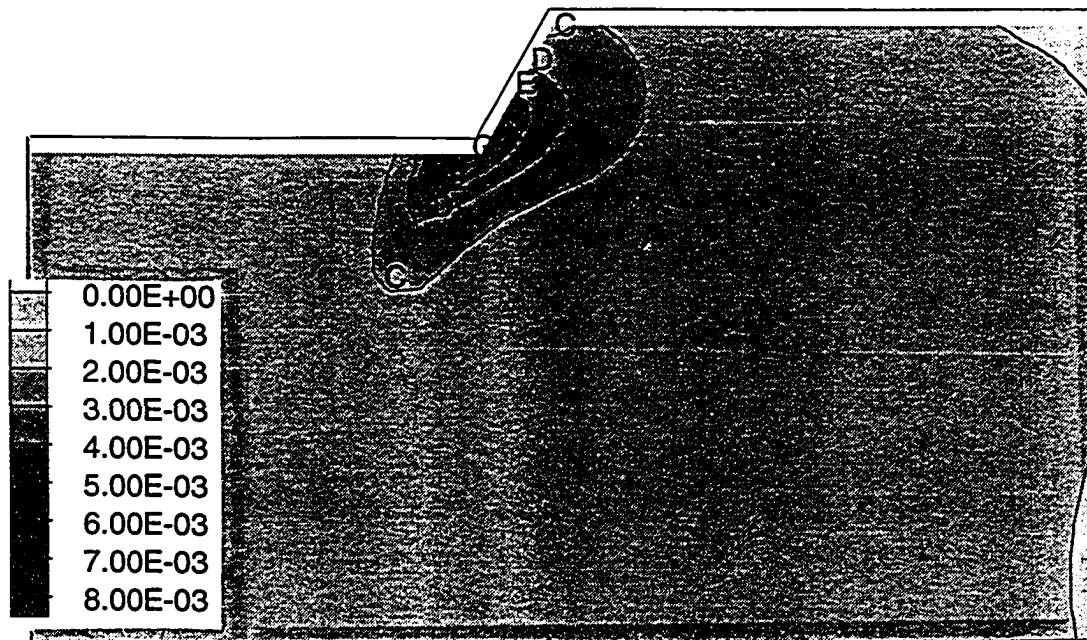


(b) 2nd layer ($H_{\alpha} = 1.69$ m); Contour Interval = $5.0E-04$ (C: $1.00E-03$, E: $2.00E-03$)

Fig. 6.54 Maximum shear strain distribution, A analysis

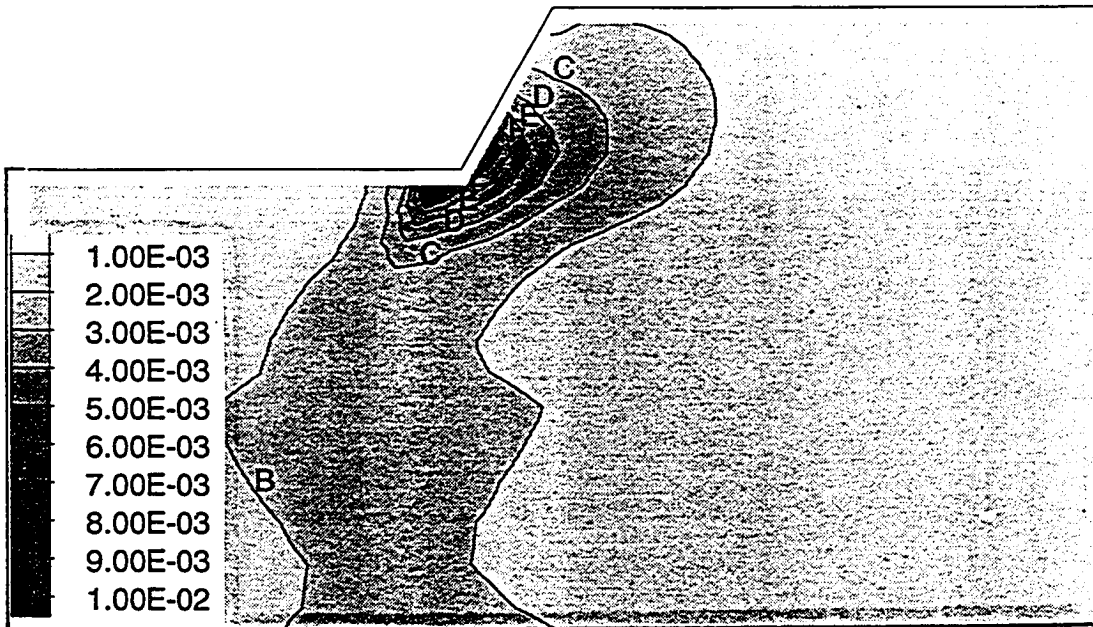


(c) 3rd layer ($H_{ex} = 2.54$ m); Contour Interval = $1.0E-03$ (B: $1.00E-03$, H: $7.00E-03$)

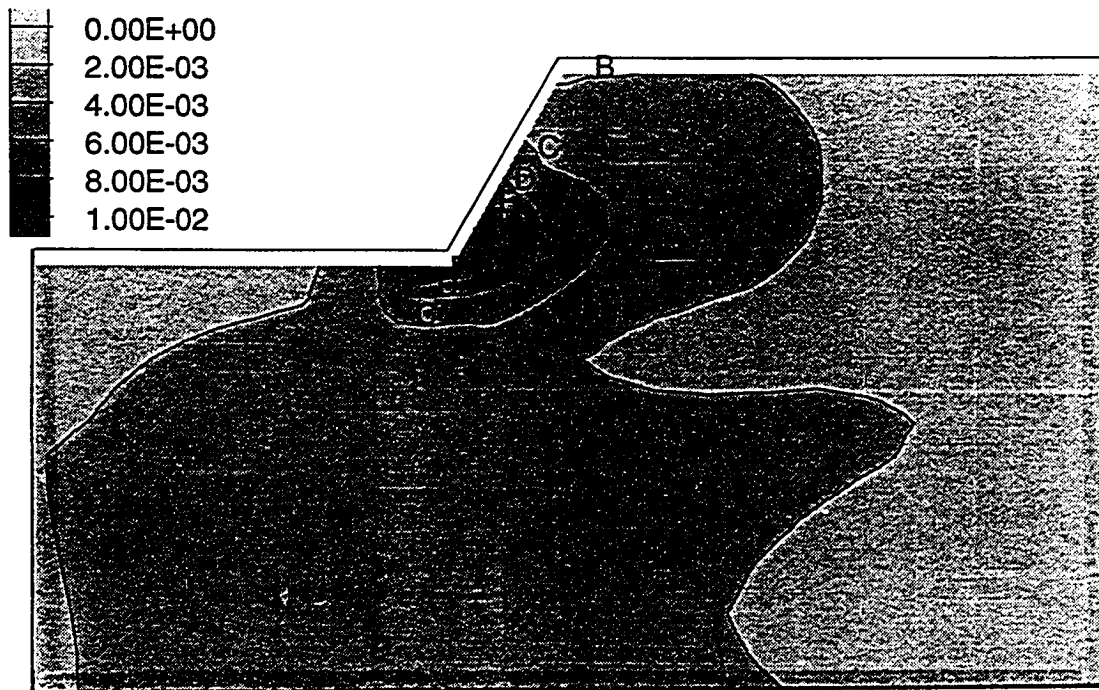


(d) 4th layer ($H_{ex} = 3.40$ m); Contour Interval = $1.0E-03$ (C: $2.00E-03$, G: $6.00E-03$)

Fig. 6.54 Maximum shear strain distribution, A analysis

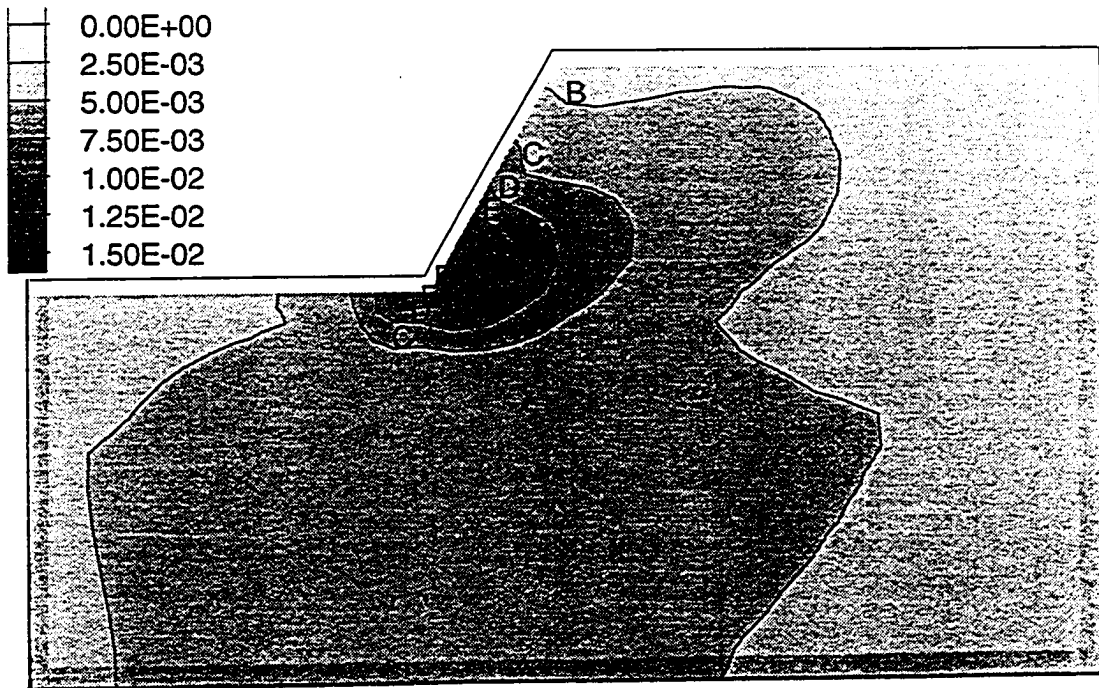


(e) 5th layer ($H_{ex} = 4.24$ m); Contour Interval=1.0E-03 (B: 2.00E-03, F: 4.00E-03)

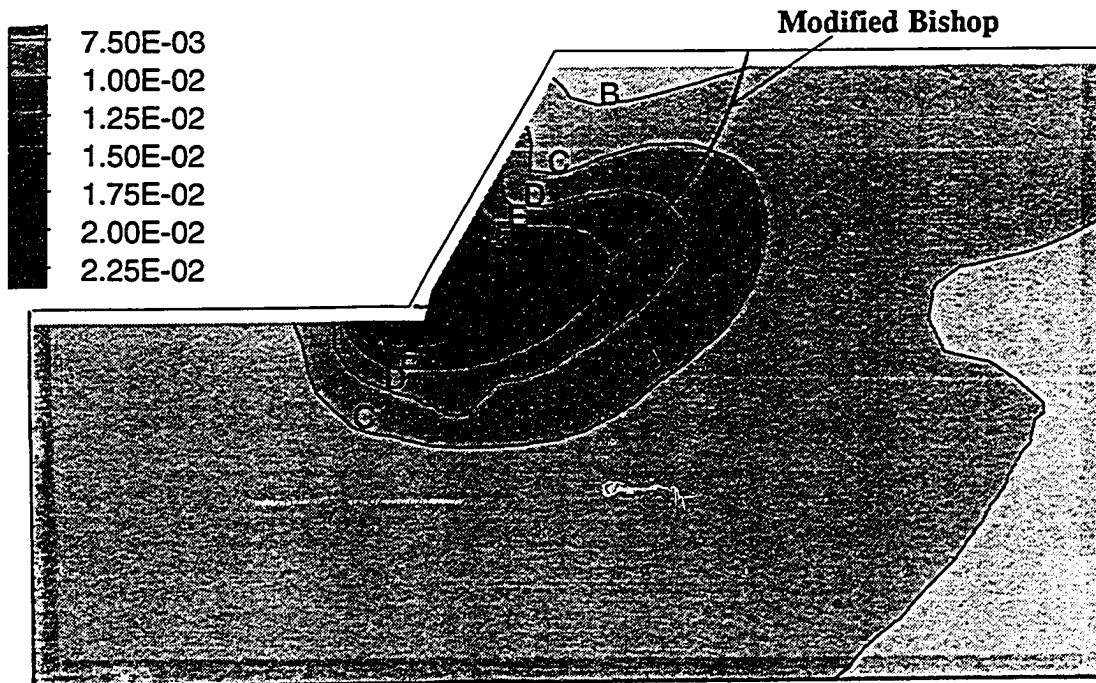


(f) 6th layer ($H_{ex} = 5.09$ m); Contour Interval=2.0E-03 (B: 2.00E-03, F: 1.00E-02)

Fig. 6.54 Maximum shear strain distribution, A analysis



(g) 7th layer ($H_{\alpha} = 5.94$ m); Contour Interval = $2.5E-03$ (B: $2.50E-03$, G: $1.50E-02$)



(h) 8th layer ($H_{\alpha} = 6.71$ m); Contour Interval = $2.5E-03$ (B: $2.50E-03$, I: $2.00E-02$)

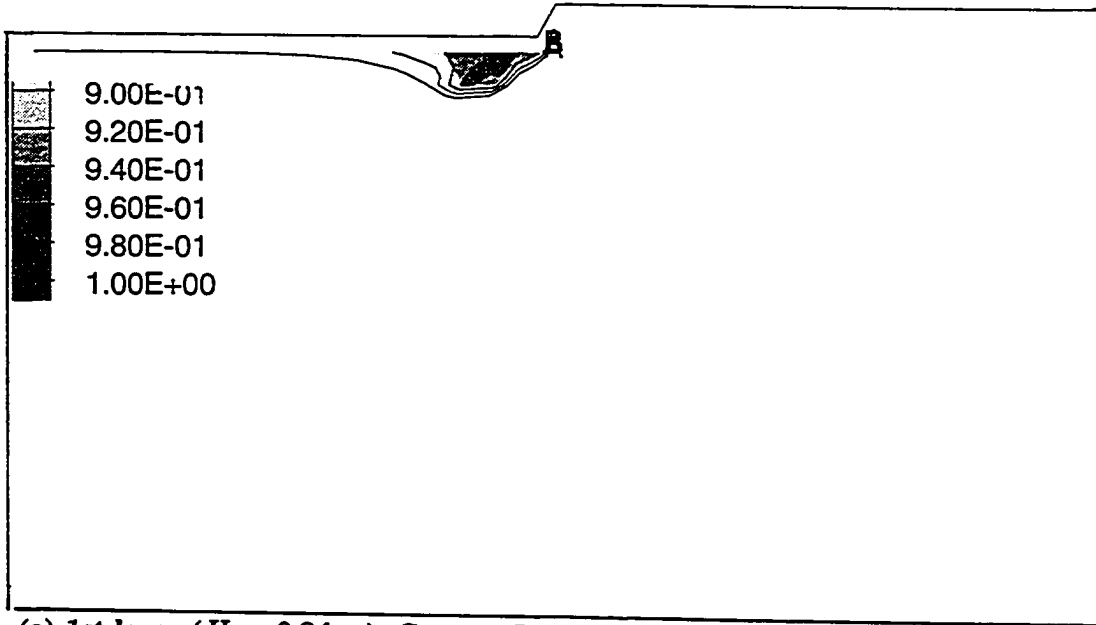
Fig. 6.54 Maximum shear strain distribution, A analysis

The failure surface predicted by Modified Bishop method is compatible with the maximum shear strain distribution (Fig. 6.54h).

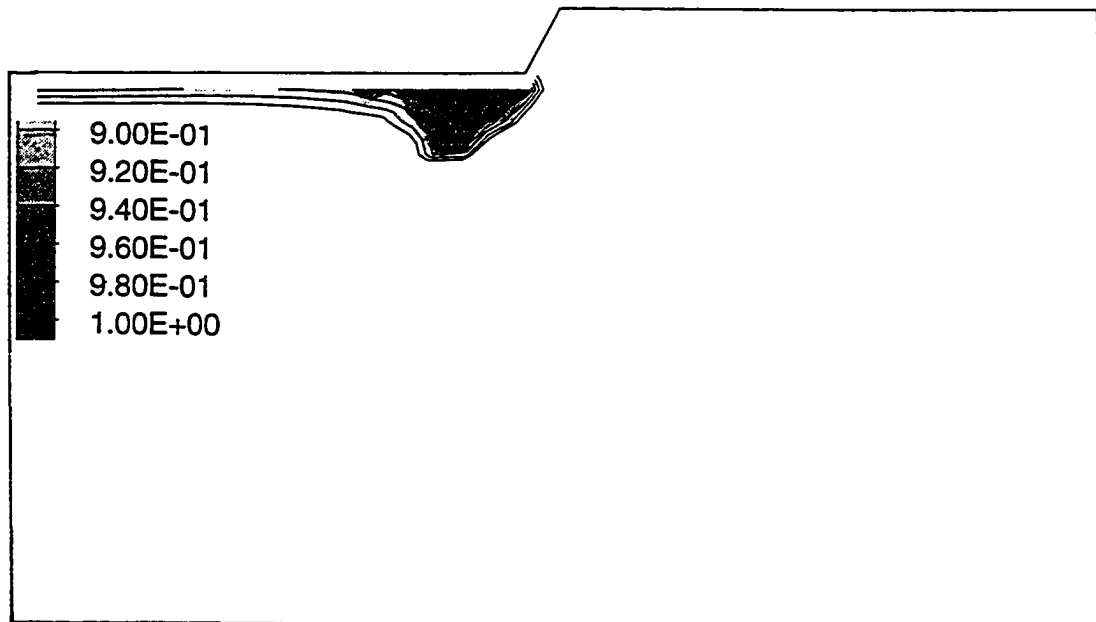
Figs. 6.55a through 6.55h show the pattern of the maximum shear stress ratio (τ_{\max}/S_u) development. It is seen that the high stress ratio is concentrated at the area which is right below the toe up to the second layer excavation (Fig. 6.55b). At the third layer excavation (Fig. 6.55c), the high stress ratio development at the boundary between the overconsolidated clay layer and normally consolidated clay layer appears in addition to the one below the toe. As excavation continues, the two regions of high stress ratio expand such that they are merged at the sixth layer excavation (Fig. 6.55f). At the final layer excavation (Fig. 6.55h), a considerably large area under the slope is in yielding status. It appears that the slope in A analysis is not failing based on both maximum shear strain and maximum shear stress distributions. The factor of safety determined by Modified Bishop method, 1.104, is moderately higher than 1.001, which was determined by taking average of elements' local factors of safety with weights of the element lengths accounted for (Fig. 6.56a). Fig. 6.56b shows the distribution of local factors of safety along the failure surface which was determined by Modified Bishop method at the last layer of excavation.

6.3.3 Anisotropic Strength Case (B analysis)

In overconsolidated clay the coefficient of strength anisotropy K ($S_{u(h)}/S_{u(v)}$) is not constant as in normally consolidated clay. Figs. 3.15a and 3.15b

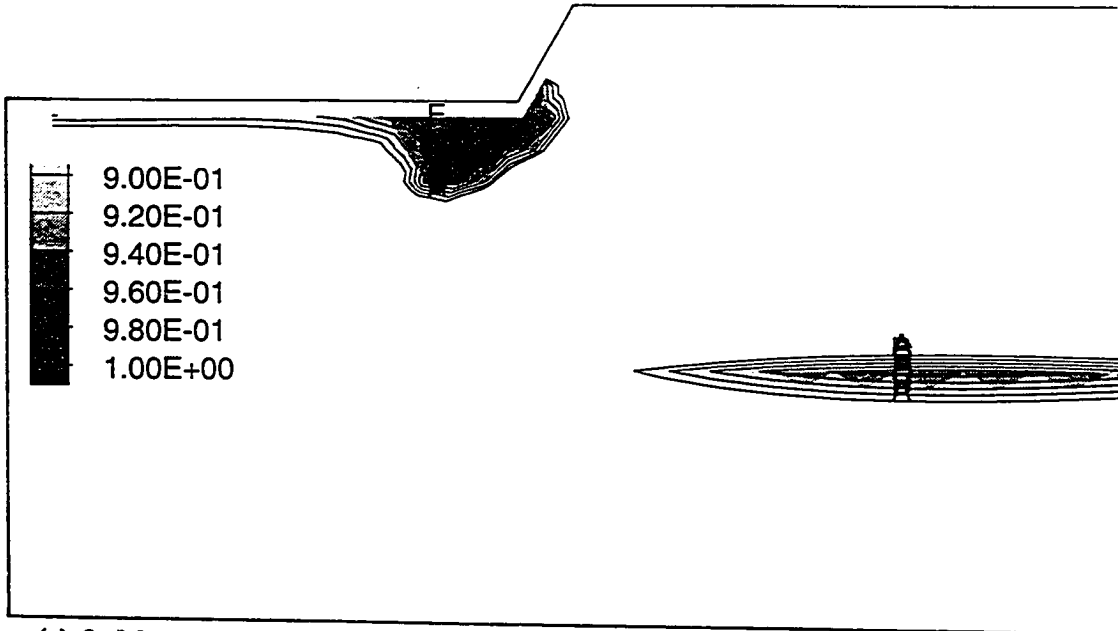


(a) 1st layer ($H_{\alpha} = 0.84$ m); Contour Interval = $2.0E-02$ (A: $9.00E-01$, B: $9.20E-01$)

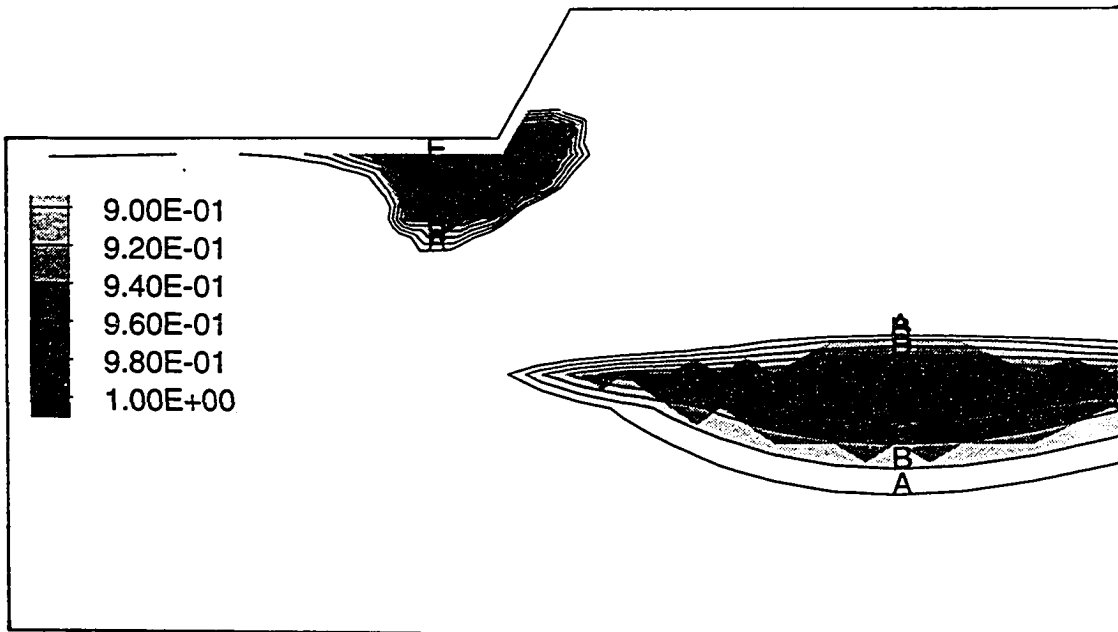


(b) 2nd layer ($H_{\alpha} = 1.69$ m); Contour Interval = $2.0E-02$ no contour to be noted

Fig. 6.55 Maximum shear stress ratio (τ_{\max}/S_v) distribution, A analysis

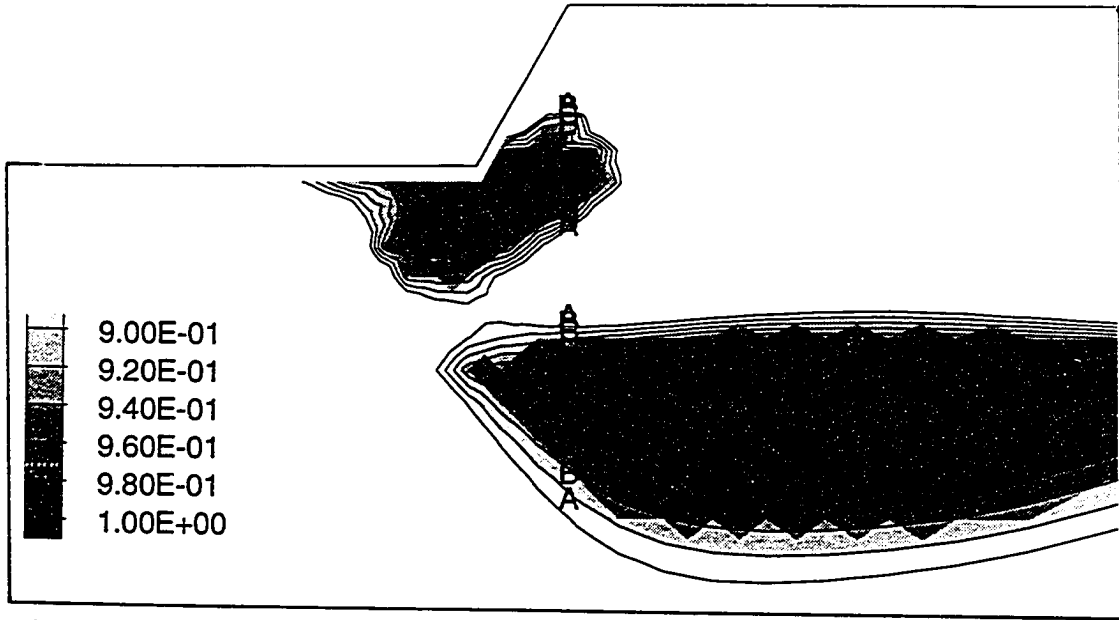


(c) 3rd layer ($H_{\alpha} = 2.54$ m); Contour Interval = $2.0E-02$ (A: $9.00E-01$, E: $9.80E-01$)



(d) 4th layer ($H_{\alpha} = 3.40$ m); Contour Interval = $2.0E-02$ (A: $9.00E-01$, E: $9.80E-01$)

Fig. 6.55 Maximum shear stress ratio (τ_{\max}/S_u) distribution, A analysis

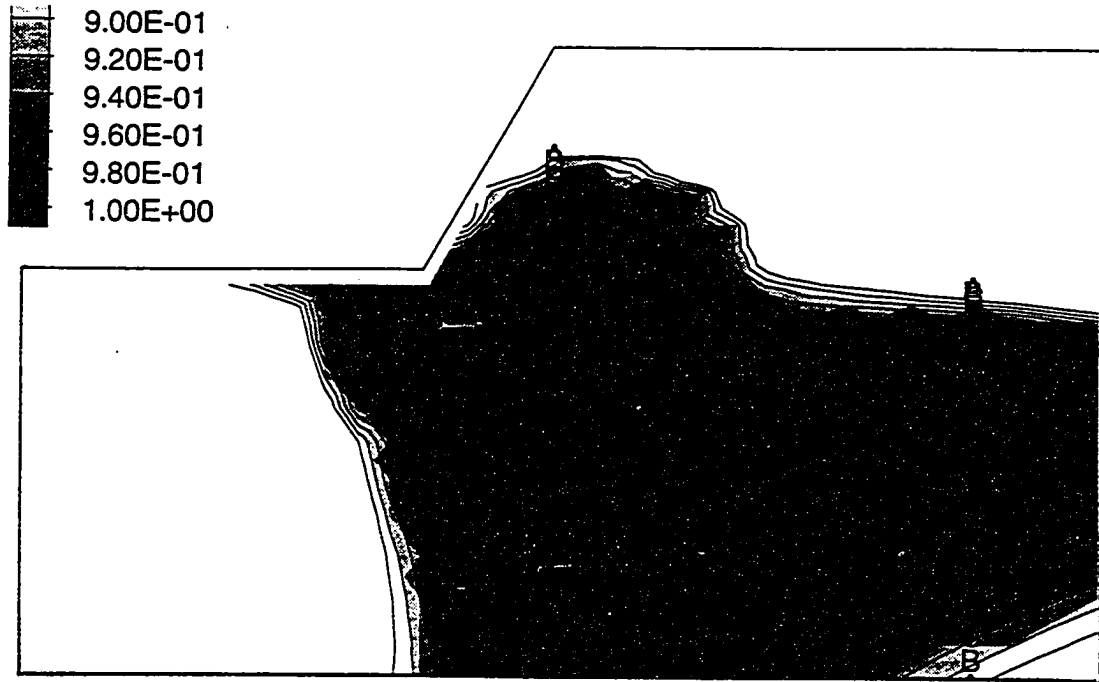


(e) 5th layer ($H_{ex} = 4.24$ m); Contour Interval = $2.0E-02$ (A: $9.00E-01$, E: $9.80E-01$)

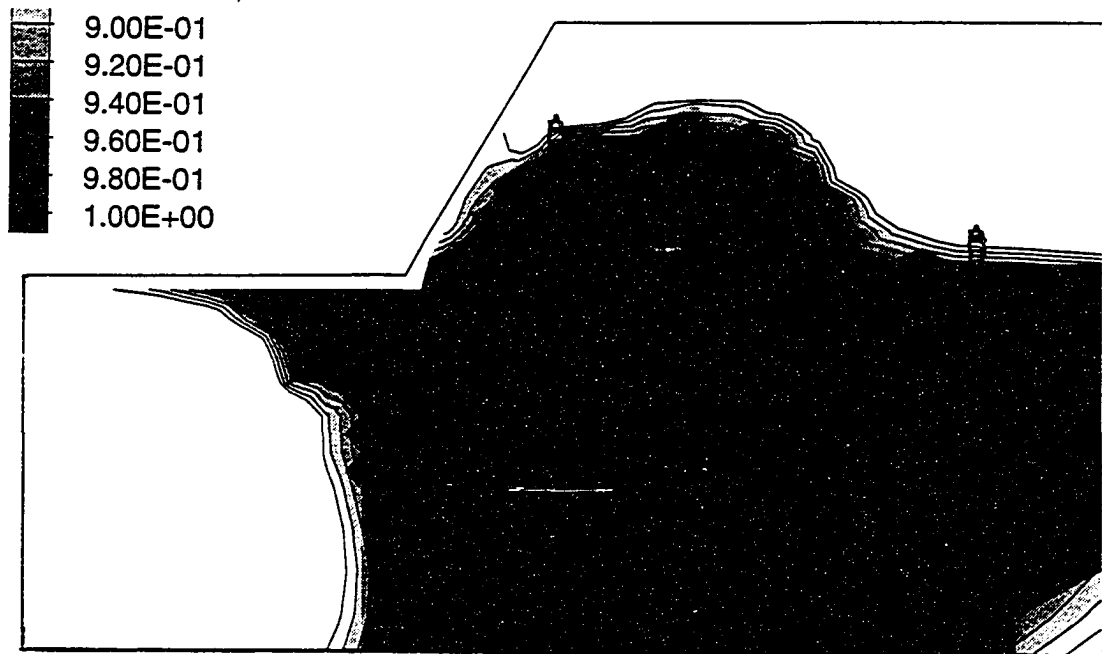


(f) 6th layer ($H_{ex} = 5.09$ m); Contour Interval = $2.0E-02$ (A: $9.00E-01$, E: $9.80E-01$)

Fig. 6.55 Maximum shear stress ratio (τ_{max}/S_u) distribution, A analysis



(g) 7th layer ($H_{ex} = 5.94$ m); Contour Interval = $2.0E-02$ (A: $9.00E-01$, E: $9.80E-01$)



(h) 8th layer ($H_{ex} = 6.71$ m); Contour Interval = $2.0E-02$ (A: $9.00E-01$, E: $9.80E-01$)

Fig. 6.55 Maximum shear stress ratio (τ_{max}/S_u) distribution, A analysis

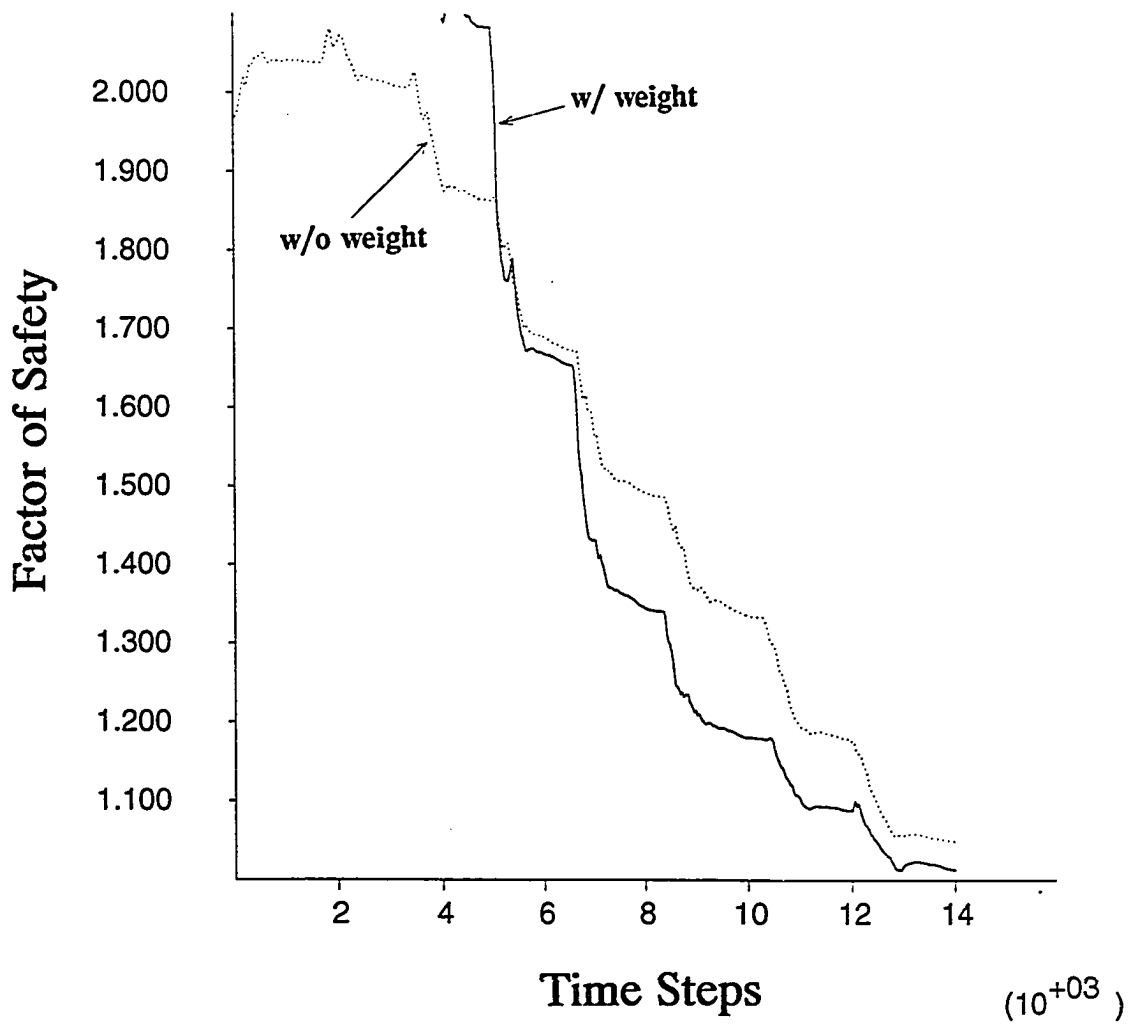


Fig. 6.56a Variation of factors of safety at the Modified Bishop's surface, A analysis

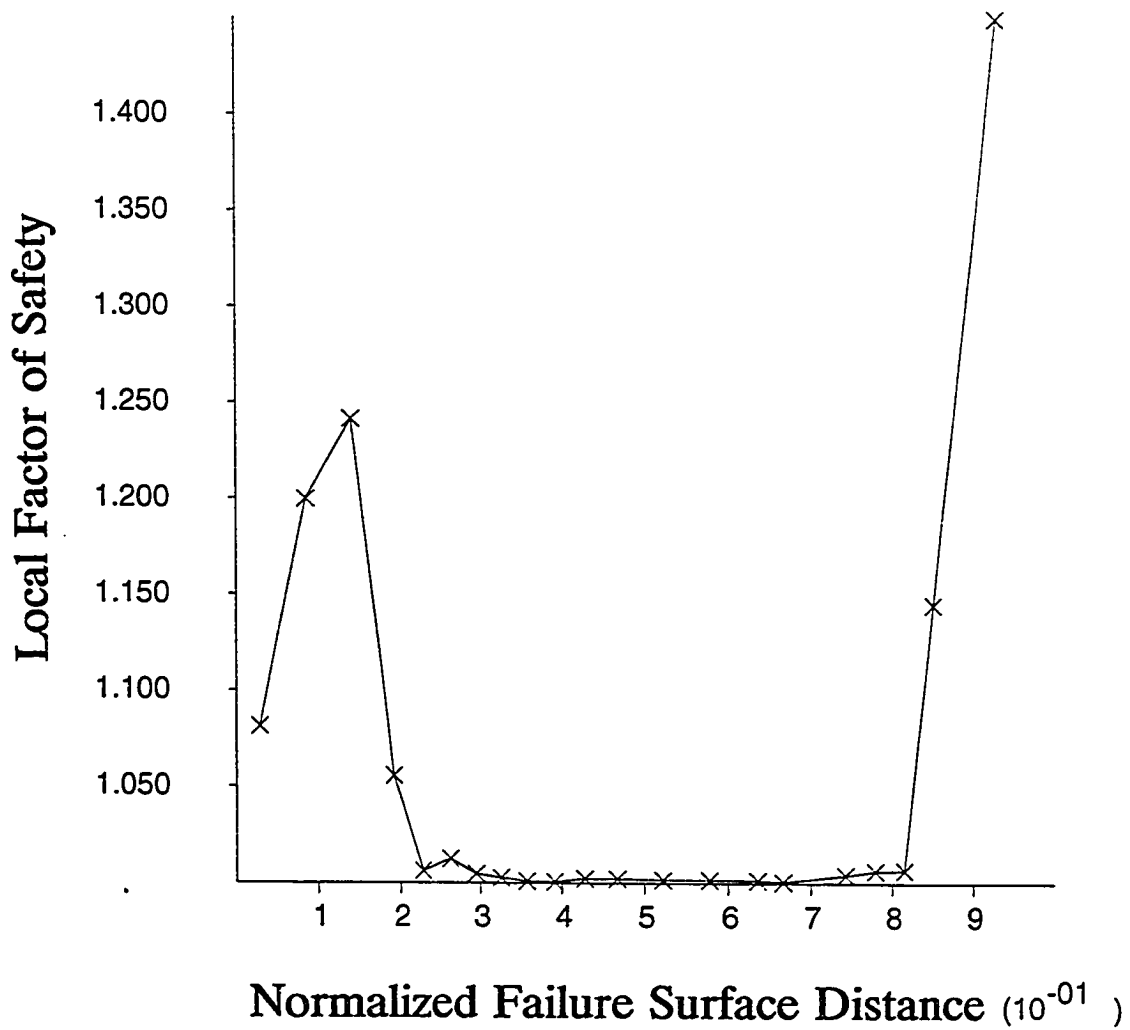


Fig. 6.56b Distribution of local factors of safety along the Modified Bishop's surface (7th layer excavation), A analysis

in Section 3.5.3.3 showed the examples of the variations of undrained strengths, determined by the three typical laboratory tests: the triaxial compression, the triaxial extension and the direct simple shear tests, with varying OCR (overconsolidation ratio). In the figures the coefficient of strength anisotropy, K , at $OCR = 1.0$ are 0.63 and 0.60 for AGS (Atlantic Generating Station) clay and James Bay clay, respectively. As OCR increases, the coefficient, K , varies such that it reduces to 0.48 at $OCR = 4$ for James Bay clay, while it increases to 0.70 at $OCR = 8$ for AGS clay. The two clays show an opposite trend of the coefficient variation with increment of OCR. It is often encountered in practice that the extension strengths of highly overconsolidated clays are even greater than the compression strengths. In lightly overconsolidated clay, however, the coefficient may be close to that established for normally consolidated clay as seen in Section 3.5.4.2.1.

As a simplification, the coefficient, K , in this study was assumed to be constant (0.67) without regard to OCR as in normally consolidated clay. For a given coefficient of strength anisotropy, the fashion in which undrained strength varies with i angle may be different from clay to clay as in normally consolidated clay. However, the anisotropic strength curve (curve number one in Fig. 3.14) suggested by Casagrande and Carrillo (1947), was only used for the overconsolidated clay considered in this study. It was thought that the constant coefficient of strength anisotropy for overconsolidated clay itself was a simplified assumption so that further parametric study did not seem to be meaningful.

Fig. 6.57a shows the distribution of i angles of the elements along the failure surface predicted in B-1 analysis. It is interesting to find that the i angle generally decreases from the toe toward the crest, but it jumps back up at the last two elements. It is noted that initial K_0 values in overconsolidated clay may be larger than unity for shallow elements so that the initial i angles in those elements are 90 degree rather than 0 degree as in normally consolidated clay. Especially, the elements near the surface have high OCR so that the initial normal stresses in the horizontal are much greater than those in the vertical. Therefore, the normal stress releases in the horizontal and maximum shear stress increases due to the excavation may not be sufficient to reduce the i angles from 90 degree to small values for those elements. The distribution of i angles in the slope is shown in Fig. 6.57b. As mentioned, high i angle concentrations are shown on the crest away from the slope face as well as the bottom of the excavation.

Figs. 6.58a through 6.58h show the pattern of the maximum shear strain development. As in A analysis, the maximum shear strain is highly concentrated near the toe up to the fifth layer excavation (Fig. 6.58e). At the sixth layer excavation (Fig. 6.58f), the maximum shear strain front is at contact with the boundary between the two layers of soil. At the seventh layer excavation (Fig. 6.58g), the concentration of maximum shear strain at the toe is expanded into the slope leading to clear shear bands. During the 8th layer excavation (Fig. 6.58h), the level of the maximum shear strain bands is more than 20.0% (contour C), indicating the global failure in progress. Note that the elasto-plastic model (B

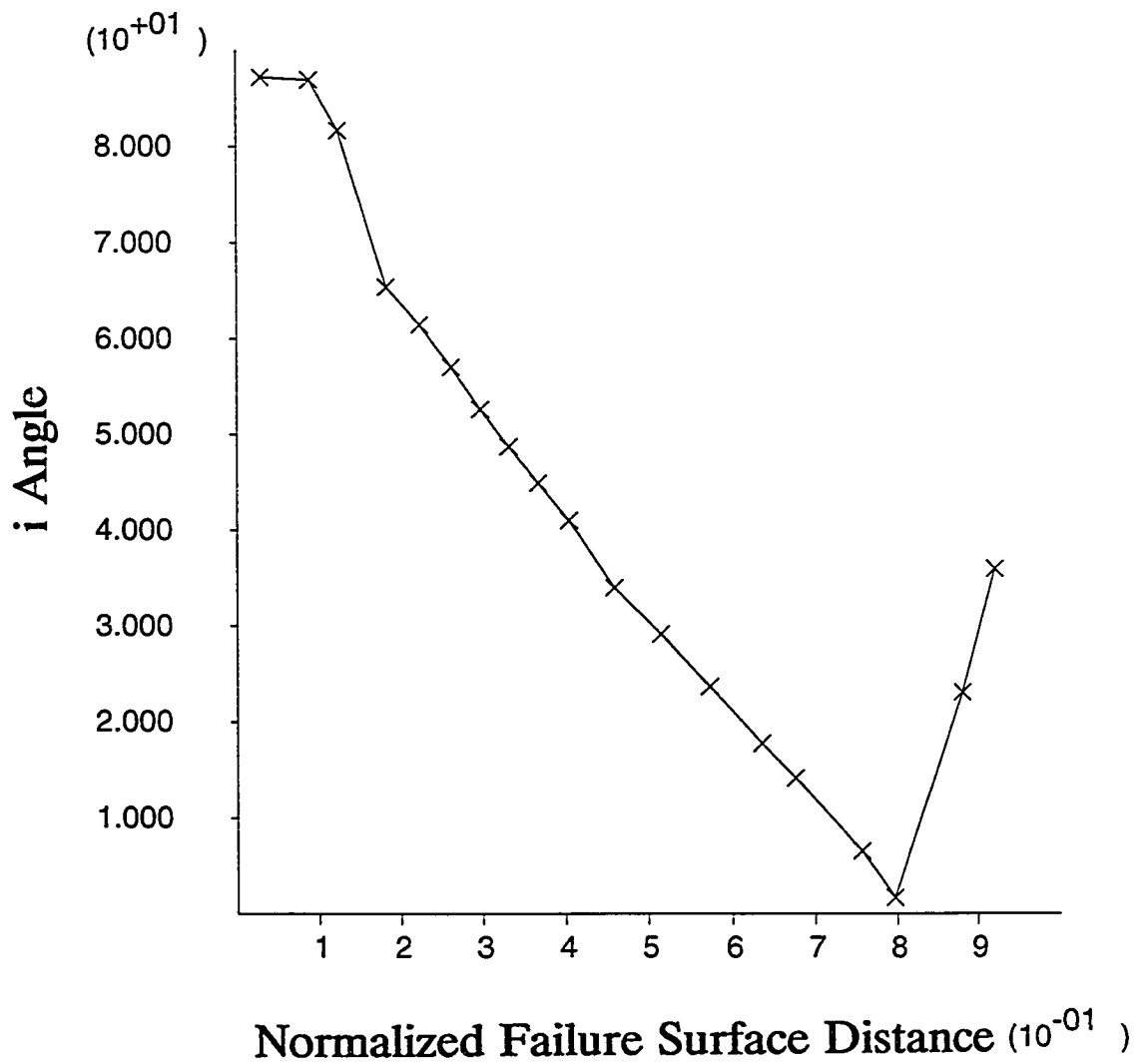


Fig. 6.57a Distribution of *i* angles along the normalized failure surface distance (7th layer excavation), B-1 analysis

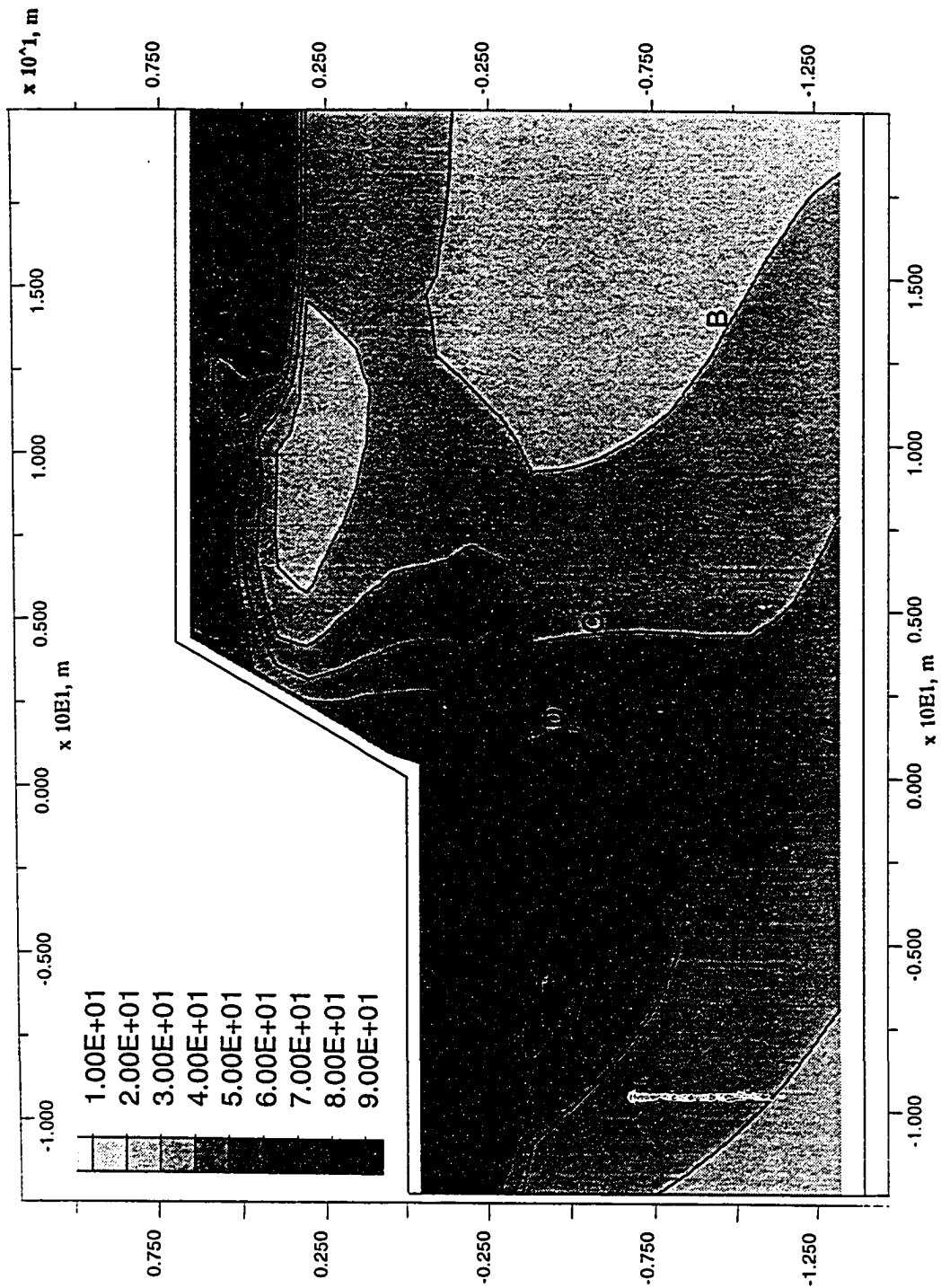
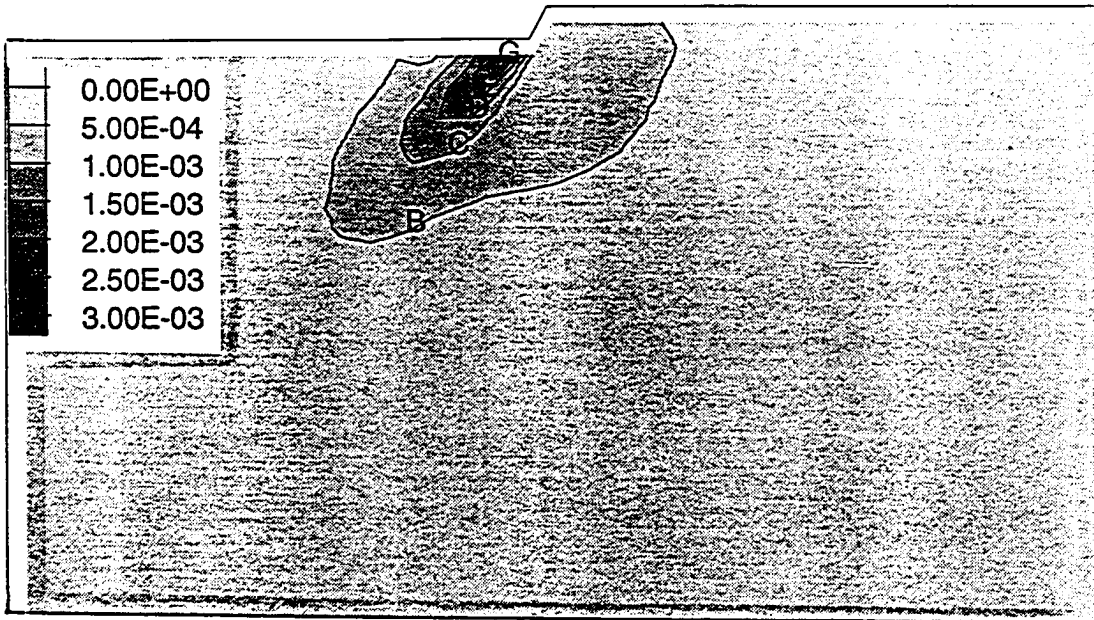
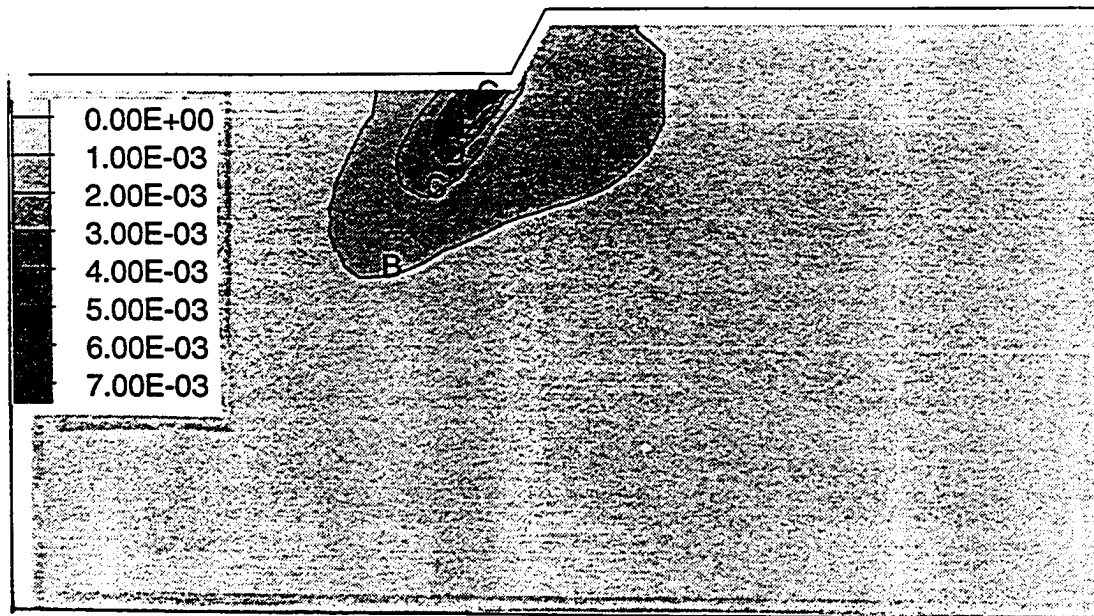


Fig. 6.57b Distribution of i angles in the slope at the 7th layer excavation, B-1 analysis, Contour Interval = 1.0E+01 (B: 1.0E+01, I: 8.0E+01)

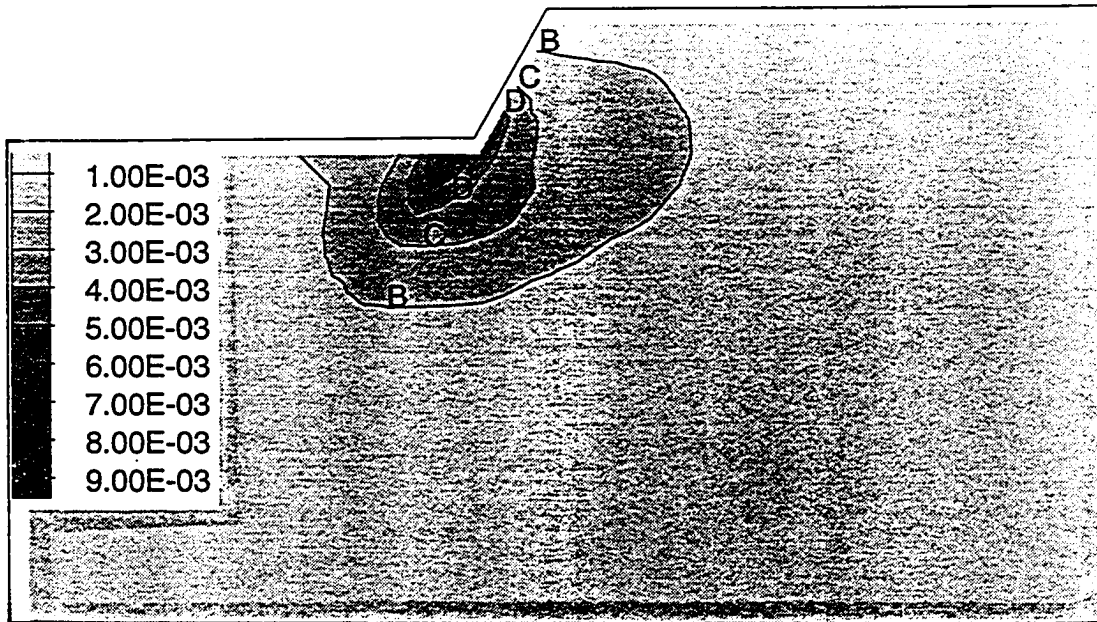


(a) 1st layer ($H_{\alpha} = 0.84$ m); Contour Interval = $5.0E-04$ (B: $5.00E-04$, G: $3.00E-03$)

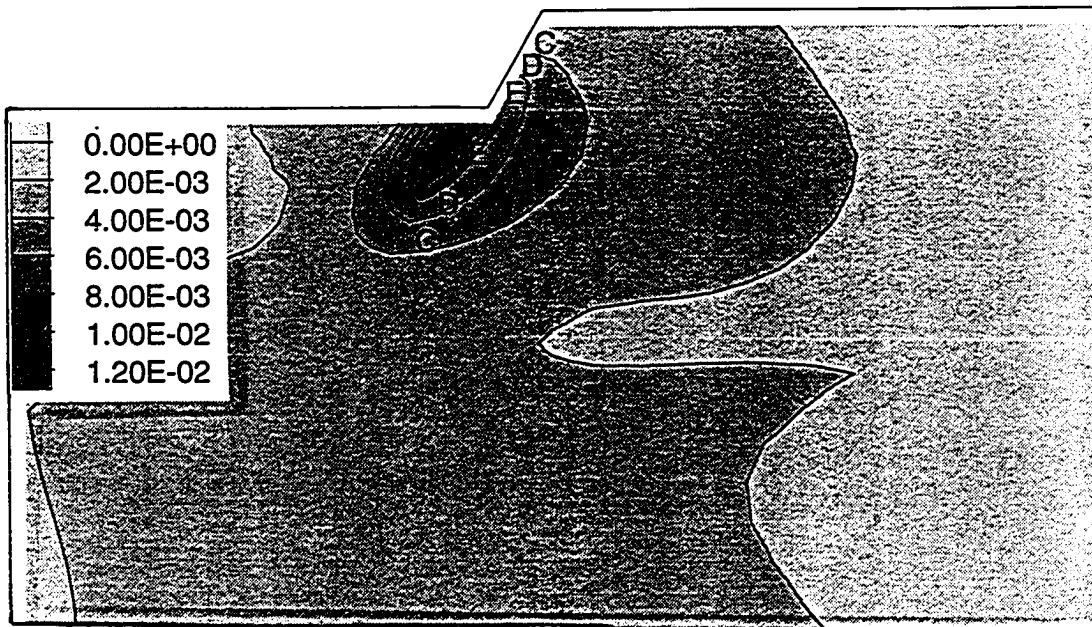


(b) 2nd layer ($H_{\alpha} = 1.69$ m); Contour Interval = $1.0E-03$ (B: $1.00E-03$, G: $6.00E-03$)

Fig. 6.58 Maximum shear strain distribution, B-1 analysis

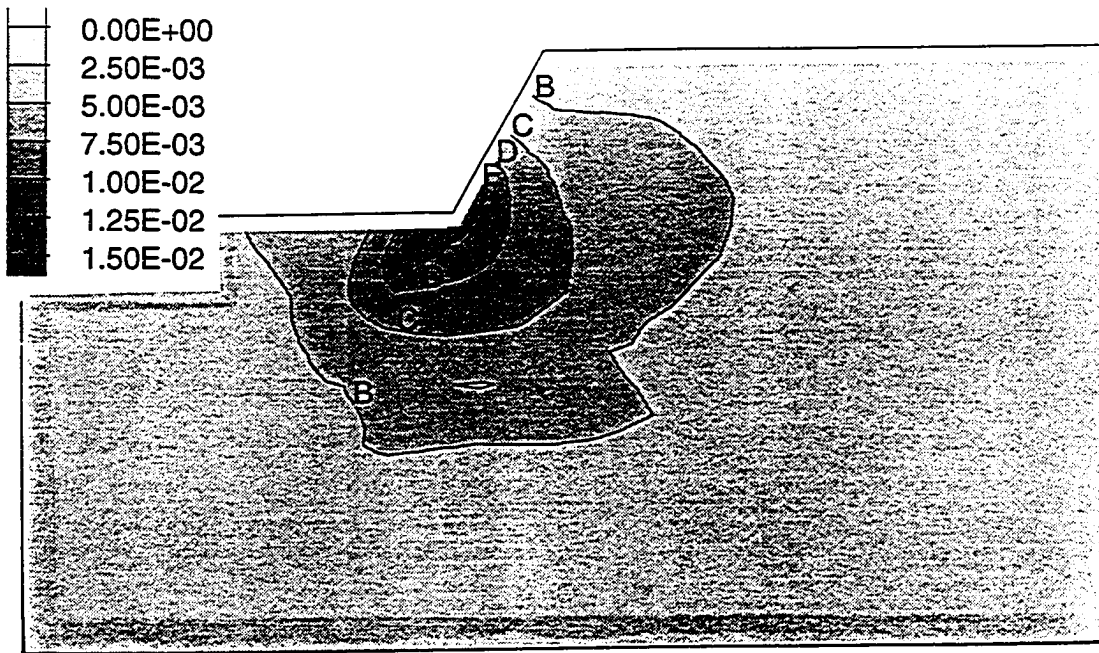


(c) 3rd layer ($H_{\alpha} = 2.54$ m); Contour Interval = $1.0E-03$ (C: $2.00E-03$, E: $4.00E-03$)

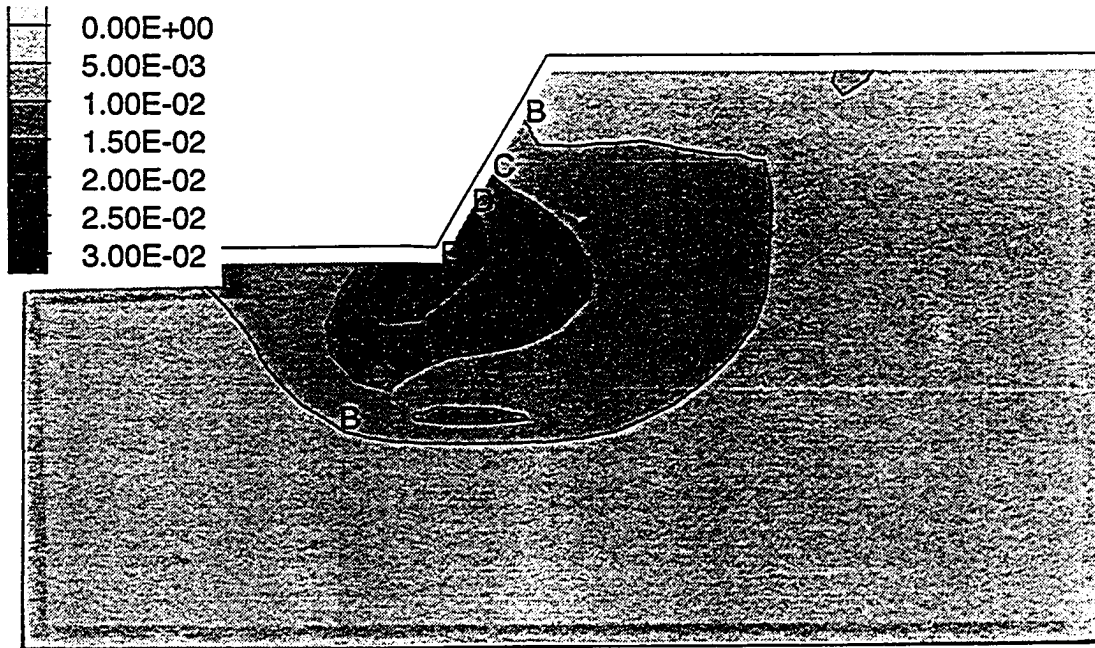


(d) 4th layer ($H_{\alpha} = 3.40$ m); Contour Interval = $2.0E-03$ (B: $2.00E-03$, D: $6.00E-03$)

Fig. 6.58 Maximum shear strain distribution, B-1 analysis

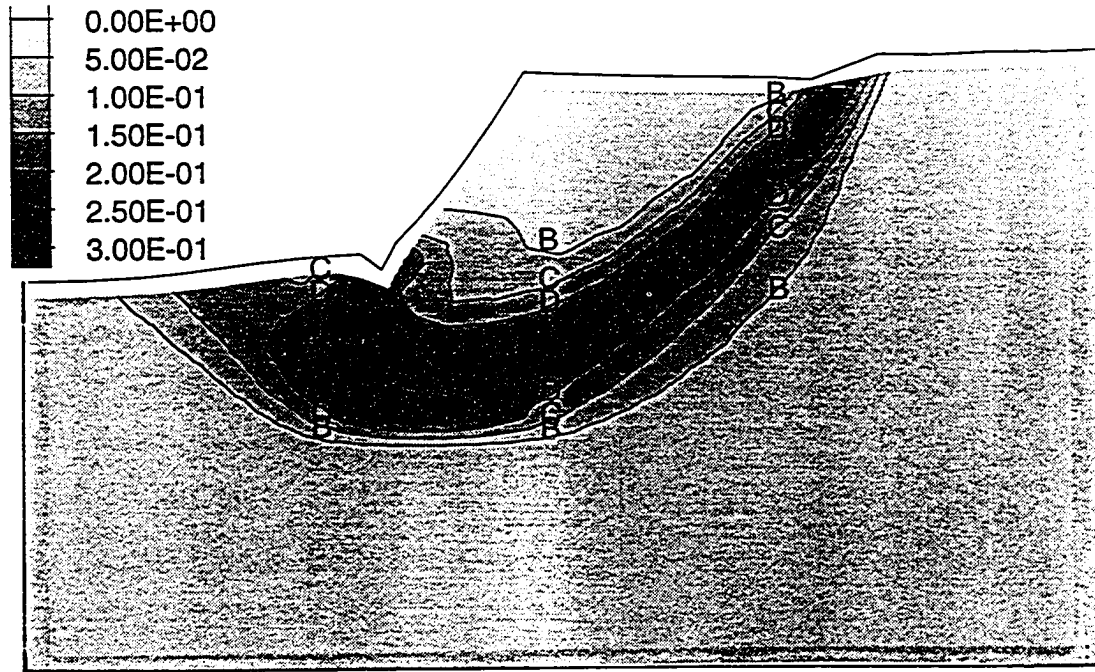


(e) 5th layer ($H_{\alpha} = 3.24$ m); Contour Interval = $2.5E-03$ (B: $2.50E-03$, E: $1.00E-02$)

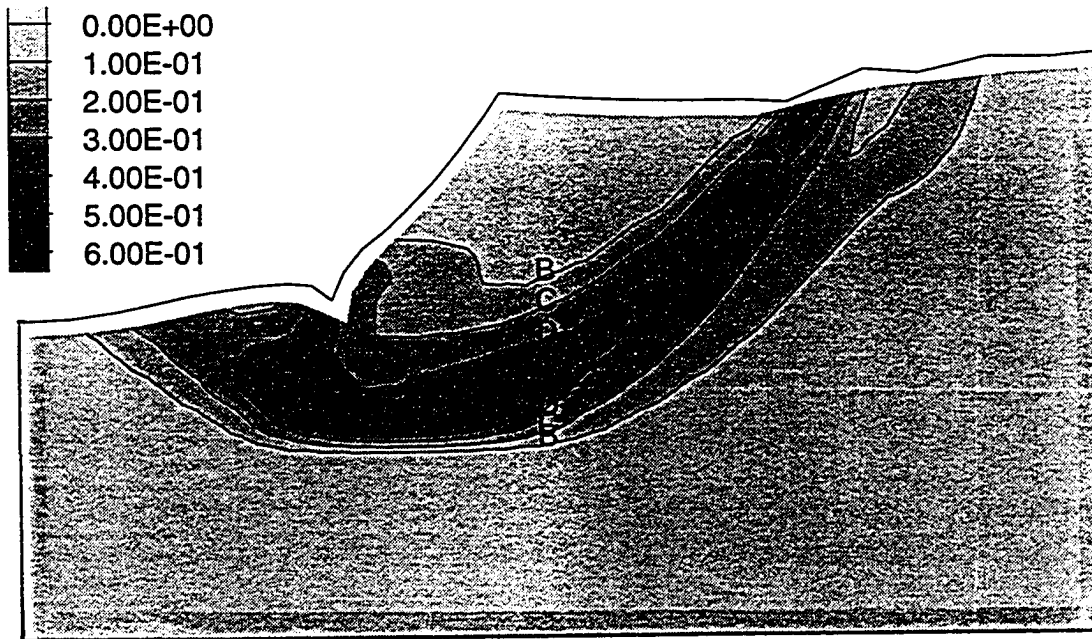


(f) 6th layer ($H_{\alpha} = 5.09$ m); Contour Interval = $5.0E-03$ (B: $5.00E-03$, E: $2.00E-02$)

Fig. 6.58 Maximum shear strain distribution, B-1 analysis



(g) 7th layer ($H_{ex} = 5.94$ m); Contour Interval = $5.0E-02$ (B: $5.00E-02$, D: $1.50E-01$)



(h) 8th layer ($H_{ex} = 6.71$ m); Contour Interval = $1.0E-01$ (B: $1.00E-01$, D: $3.00E-01$)

Fig. 6.58 Maximum shear strain distribution, B-1 analysis

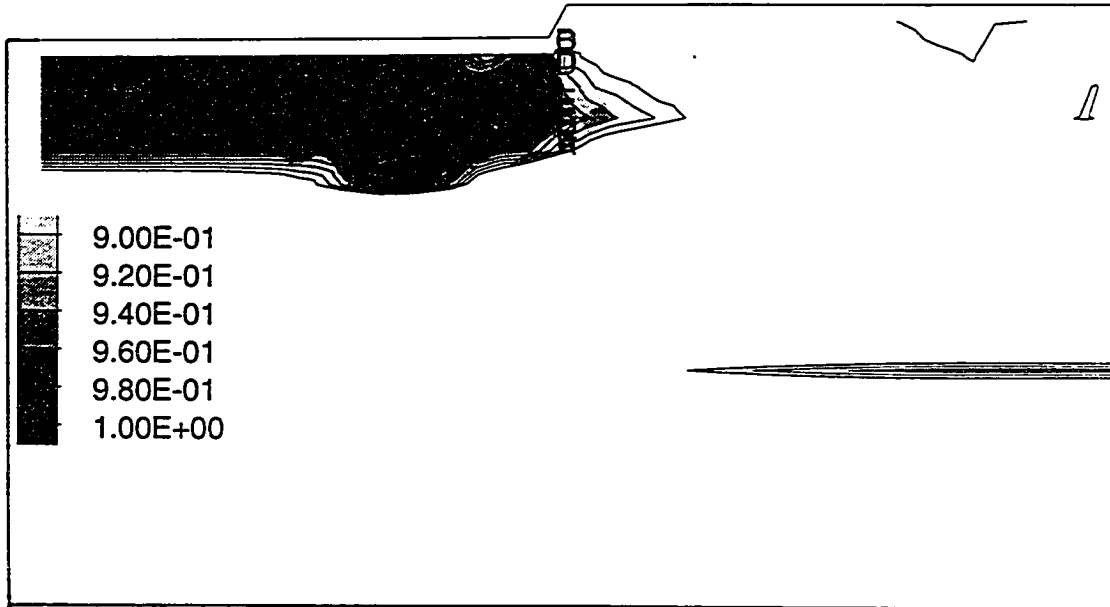
analysis) used in this analysis reaches the peak strength at a maximum shear strain far less than 1.0%. It is interesting to note that the location of the failure surface evolved in the final excavation is quite different from that predicted by Modified Bishop method or A analysis.

It has been repeatedly shown that the maximum shear strain of a slope in failure state is concentrated in narrow shear bands in B, C and D analyses. It is useful to understand the mechanism of shear bands formation in both physical situations and numerical analyses. First consider a body composed of material that softens (becomes weaker) with strain. Let us suppose the boundary of the body is deformed and that the strain distribution within the body is very slightly non-uniform. The element that carries most strain then becomes weaker than the rest and it carries less stress. Since its neighbors carry the original stress, the boundaries of the weakened element are thrown out of equilibrium (because the internal and external stresses do not balance). The weak element, therefore, starts straining more, which only causes it to soften more. This weak link process is responsible for the localization in a strain-softening material. Any small initial perturbations are amplified, causing strain to be concentrated in one place, or band. Although localization is expected in a strain-softening material, the same process can occur in a perfectly-plastic (non-softening) material. Such a material can mimic the required stress drop through a readjustment of stress rather than by a loss of material strength. The shear bands shown in B series analyses (e.g., Fig. 6.58g) are the examples of this case. It should be noted here that the shear bands

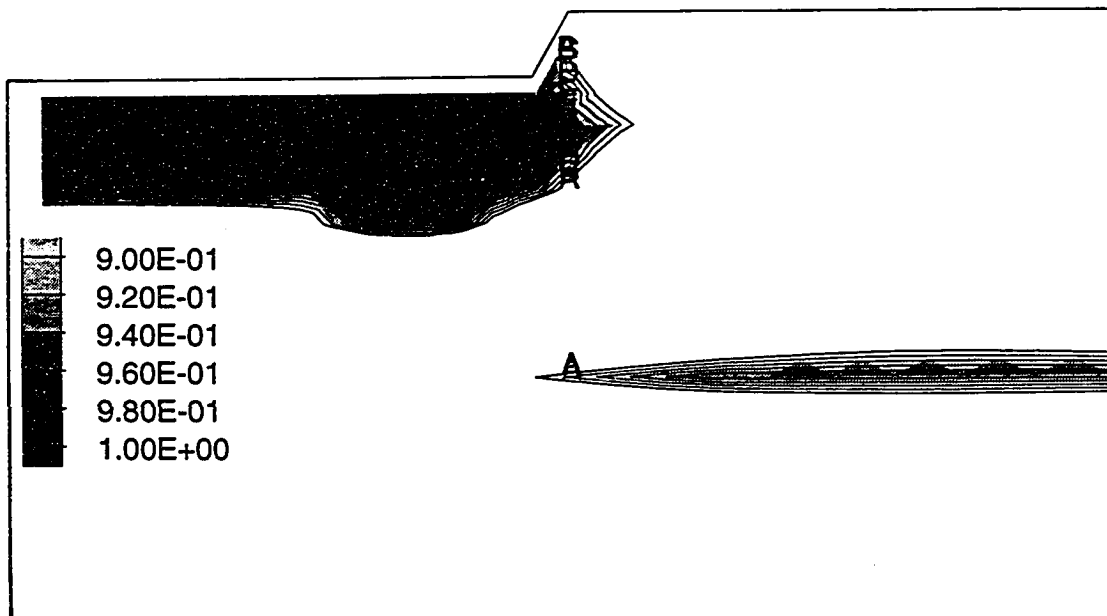
formation in numerical simulations is influenced to some extent by the artificial conditions imposed by the numerical grid, the orientation and the element size.

Figs. 6.59a through 6.59h show the pattern of the maximum shear stress ratio (τ_{\max}/S_u) development. At the first layer excavation (Fig. 6.59a), a large area below the excavation bottom is at yield which remained elastic in A analysis. The discrepancy in the yielding patterns between A and B analyses is certainly caused by the reduction of peak strengths due to high i angles in that area. The high maximum shear stress ratios at the boundary between the two clay layers are also shown. From this point, the pattern of high maximum shear stress evolution is very similar to that of A series except the fact that at the seventh (Fig. 6.59g) and eighth layer excavations (Fig. 6.59h), the levels of maximum shear stress ratios are greatly reduced by the global failure. Note that the maximum shear stress ratios of the elements in the middle of the failure surface are even less than 0.9 so that they are represented by the white zones.

The failure ($\tau_{\max}/S_u=1.0$) sequence of elements along the failure surface is shown in Fig. 6.60a. It is seen that element "j" (see Fig. 6.60b) is first subjected to failure after which elements around the first-failed one are alternately failed in a symmetric fashion. The variation of global factors of safety along the failure surface is shown in Fig. 6.61a. It is seen that at the sixth layer excavation, the factor of safety becomes very close to unity. Although the slope is in failure state right after the 7th layer excavation based on criteria of velocity and displacement, all the elements along the failure surface are not simultaneously at yield. Some of

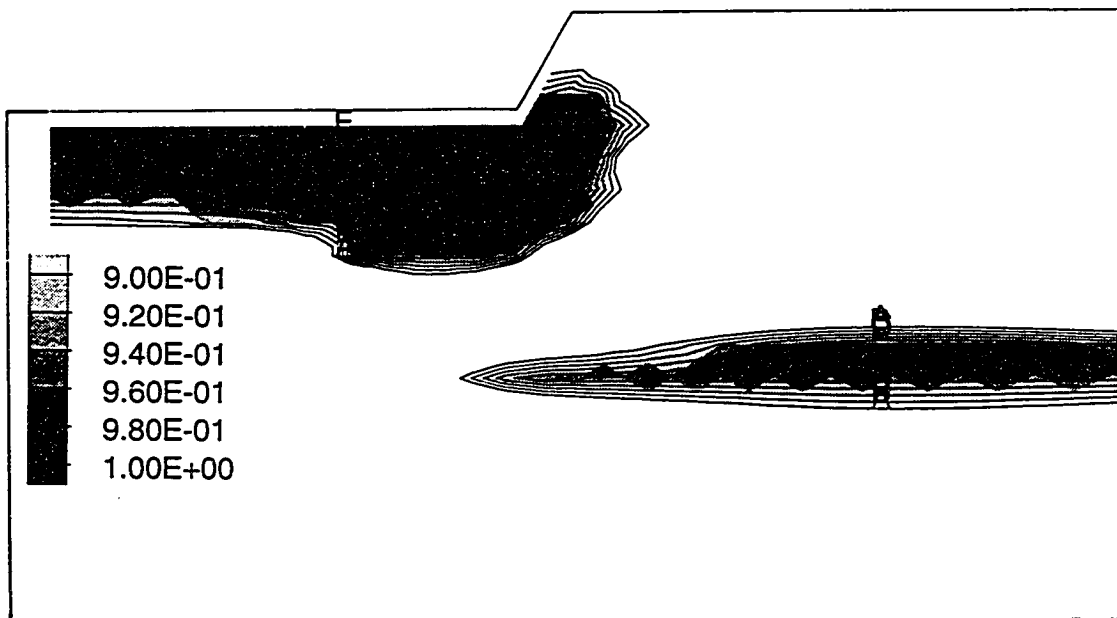


(a) 1st layer ($H_{ex} = 0.84$ m); Contour Interval = $2.0E-02$ (A: $9.00E-01$, E: $9.80E-01$)

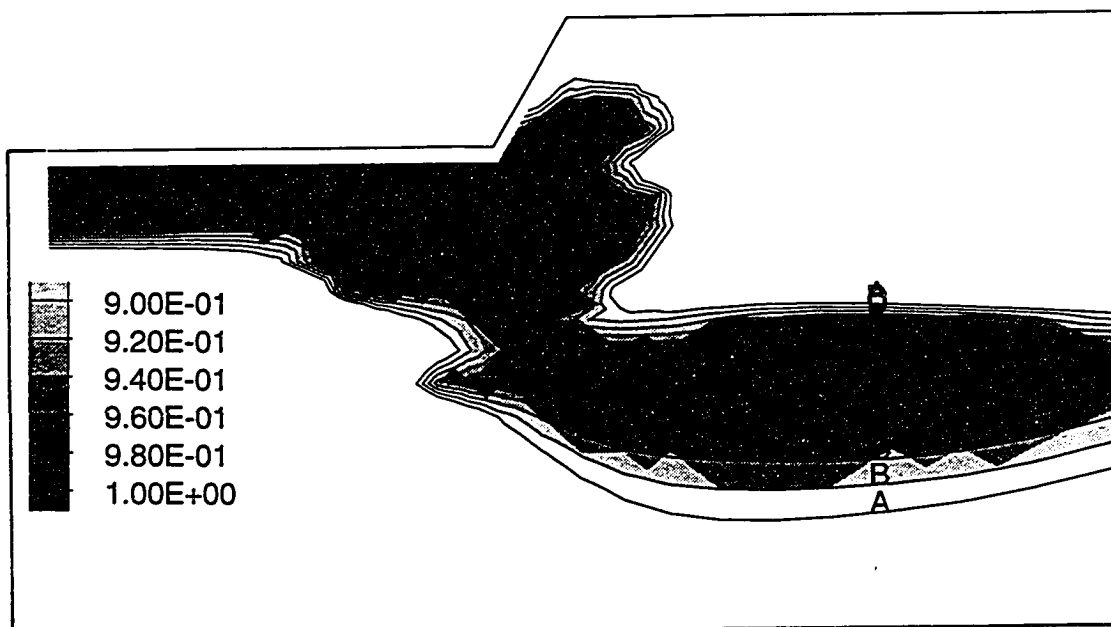


(b) 2nd layer ($H_{ex} = 1.69$ m); Contour Interval = $2.0E-02$ (A: $9.00E-01$, E: $9.80E-01$)

Fig. 6.59 Maximum shear stress ratio (τ_{max}/S_u) distribution, B-1 analysis



(c) 3rd layer ($H_{ex} = 2.54$ m); Contour Interval = $2.0E-02$ (A: $9.00E-01$, E: $9.80E-01$)

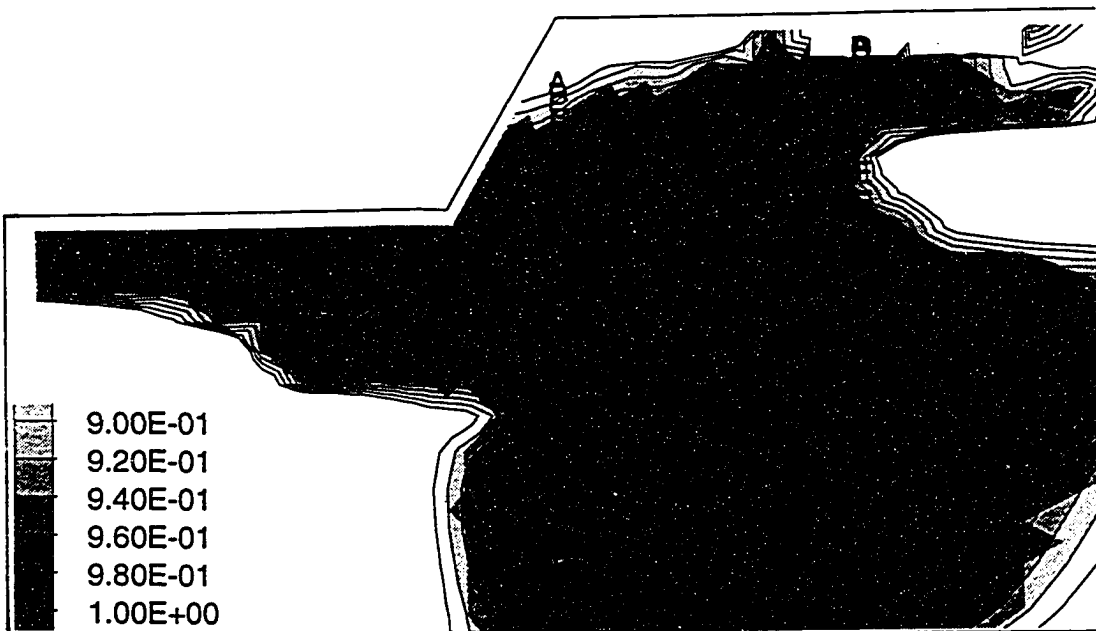


(d) 4th layer ($H_{ex} = 3.40$ m); Contour Interval = $2.0E-02$ (A: $9.00E-01$, E: $9.80E-01$)

Fig. 6.59 Maximum shear stress ratio (τ_{max}/S_u) distribution, B-1 analysis

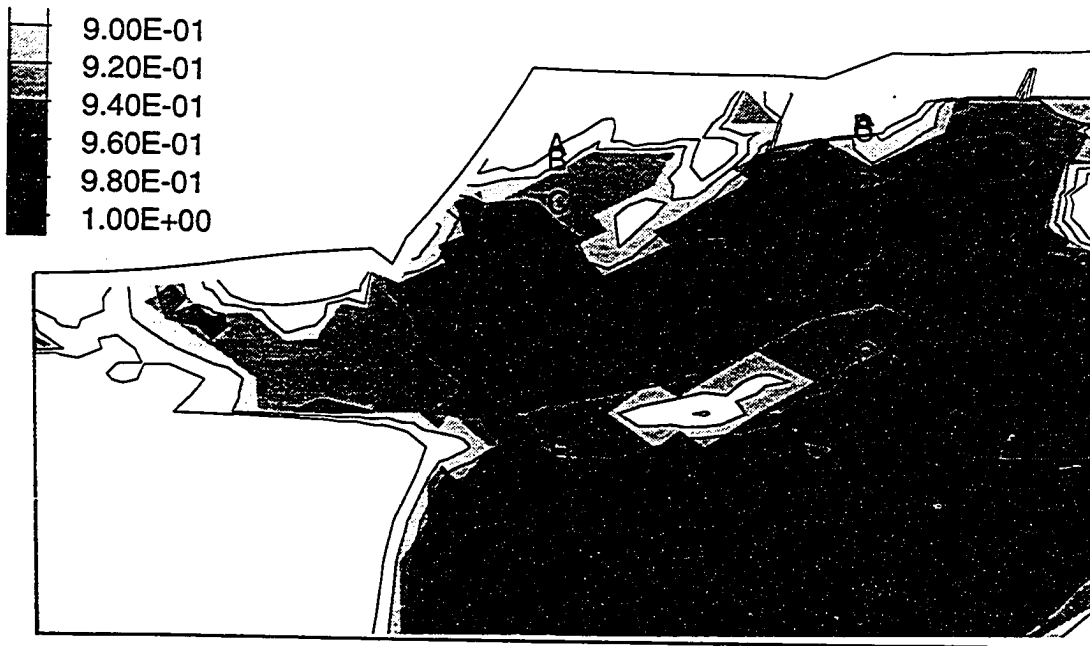


(e) 5th layer ($H_{ex} = 4.24$ m); Contour Interval = $2.0E-02$ (A: $9.00E-01$, E: $9.80E-01$)

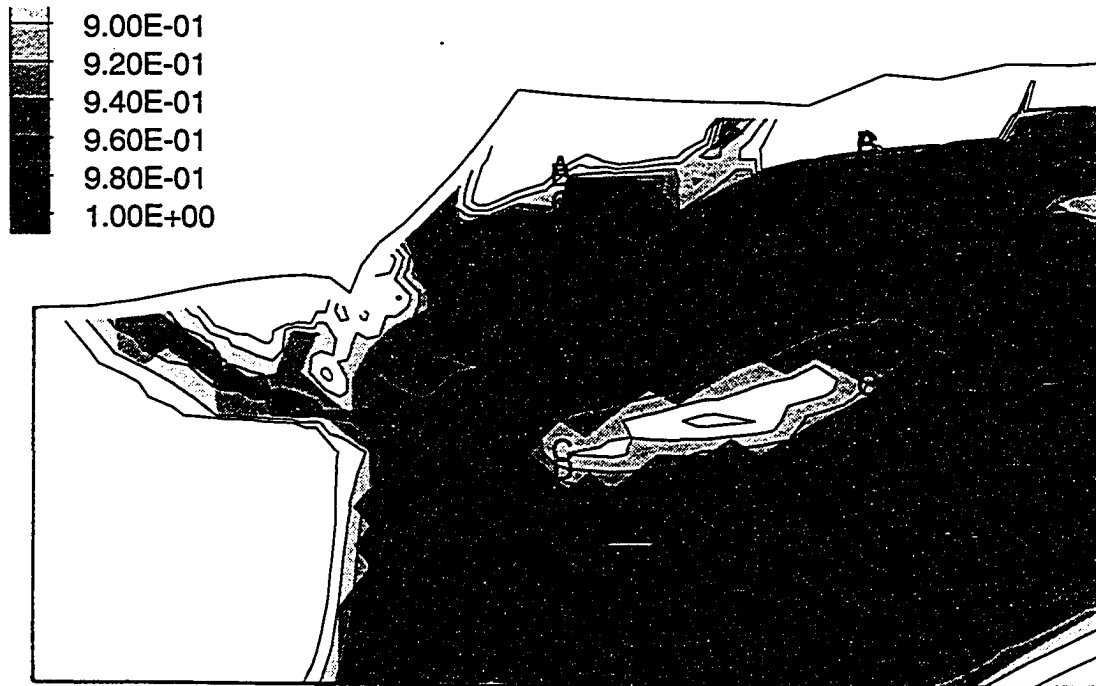


(f) 6th layer ($H_{ex} = 5.09$ m); Contour Interval = $2.0E-02$ (A: $9.00E-01$, E: $9.80E-01$)

Fig. 6.59 Maximum shear stress ratio (τ_{max}/S_u) distribution, B-1 analysis



(g) 7th layer ($H_{\alpha} = 5.94$ m); Contour Interval = $2.0E-02$ (B: $9.00E-01$, E: $9.80E-01$)



(h) 8th layer ($H_{\alpha} = 6.71$ m); Contour Interval = $2.0E-02$ (B: $1.00E-01$, E: $9.80E-01$)

Fig. 6.59 Maximum shear stress ratio (τ_{\max}/S_u) distribution, B-1 analysis

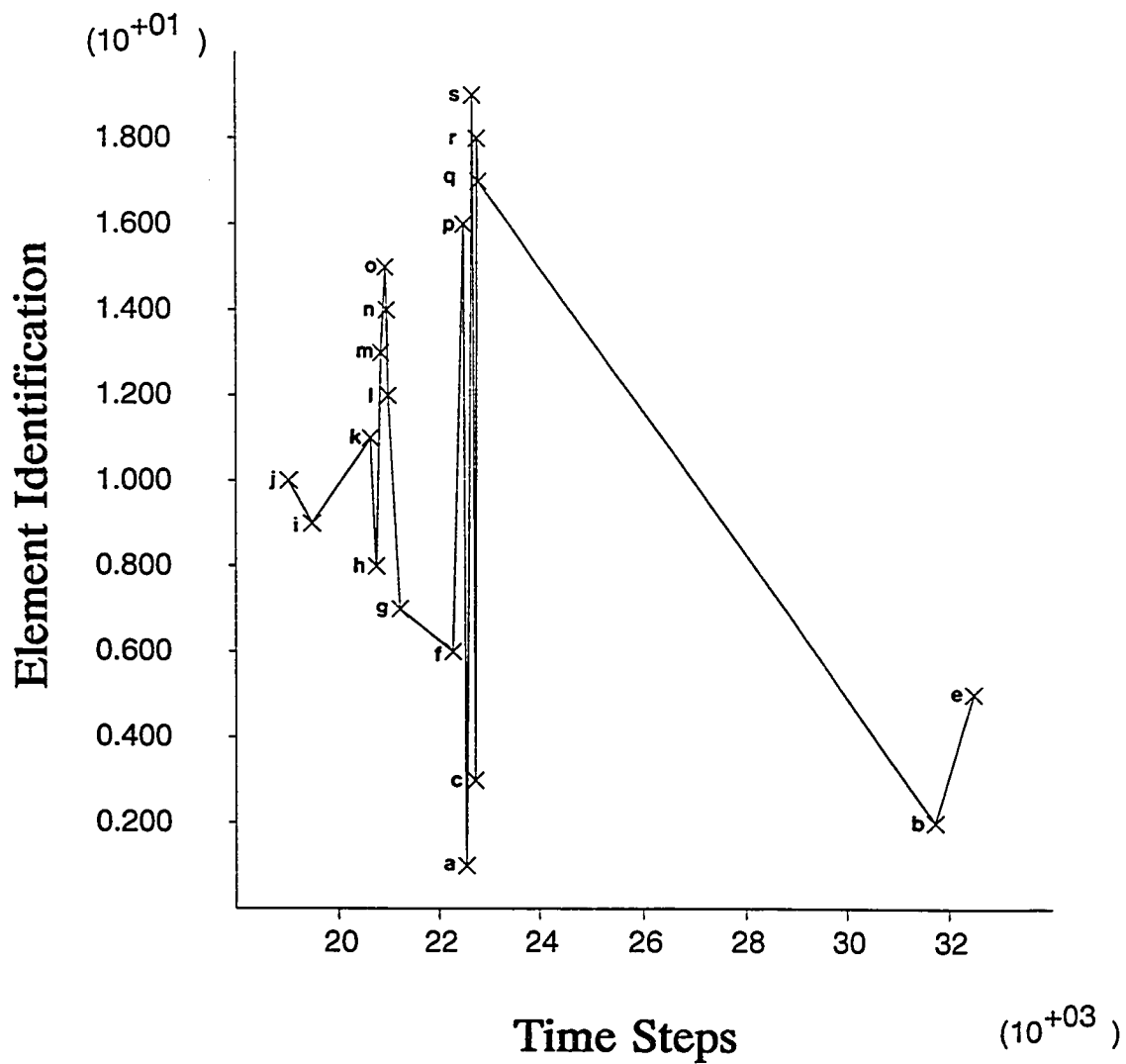


Fig. 6.60a Failure sequence of the elements along the failure surface, B-1 analysis

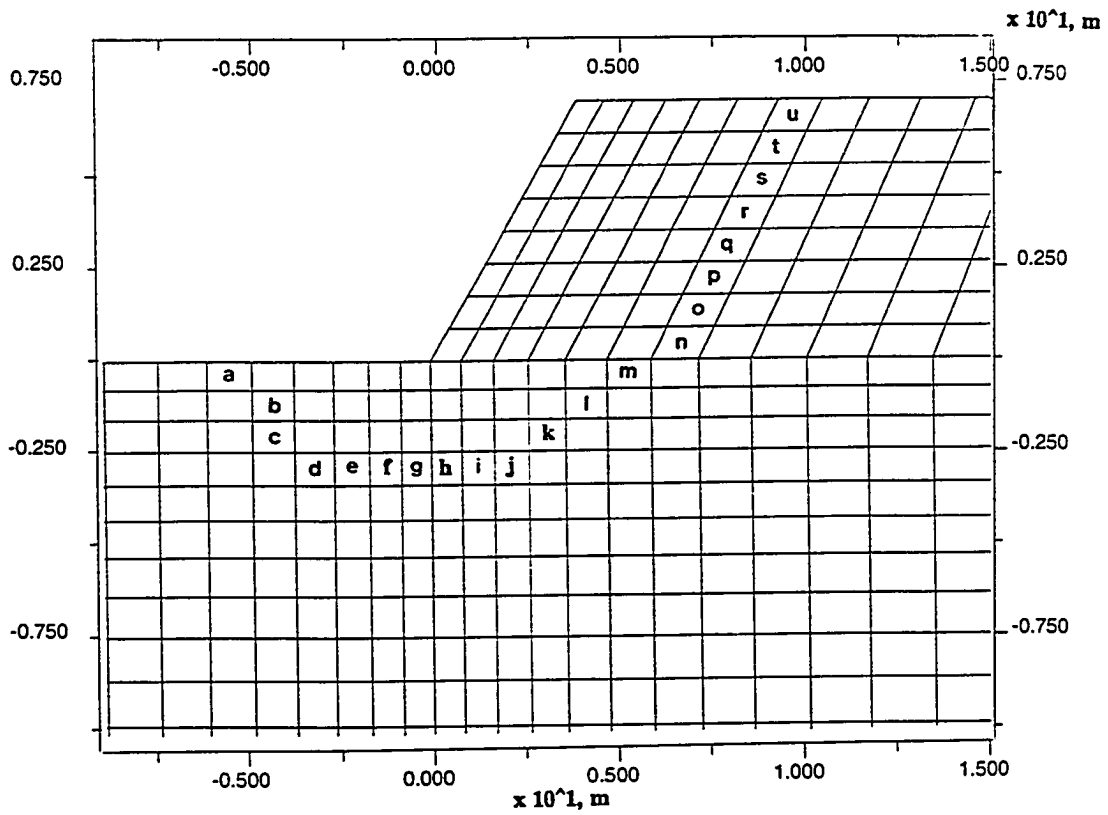


Fig. 6.60b Locations of the elements along the failure surface, B-1 analysis

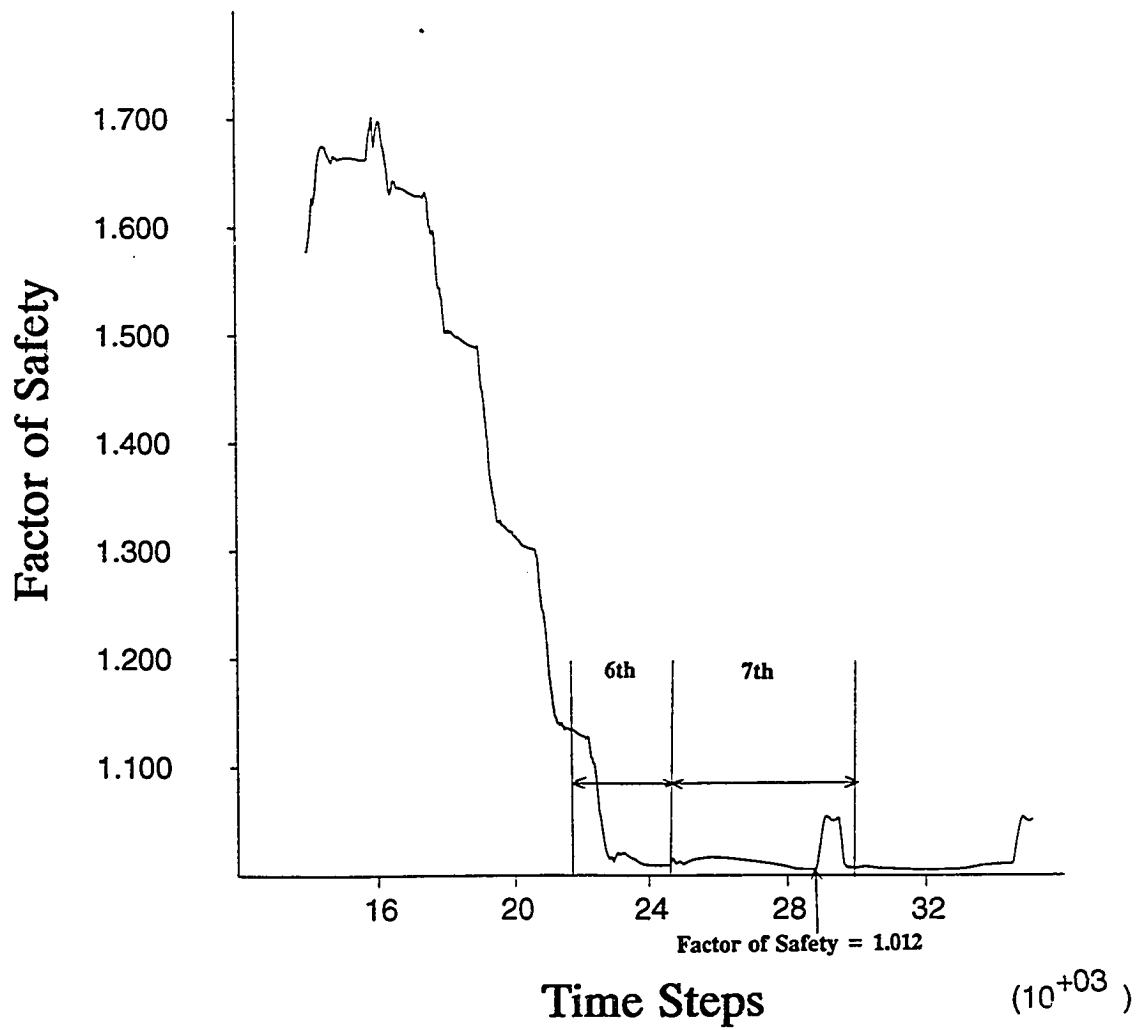


Fig. 6.61a Variation of factors of safety at the failure surface, B-1 analysis

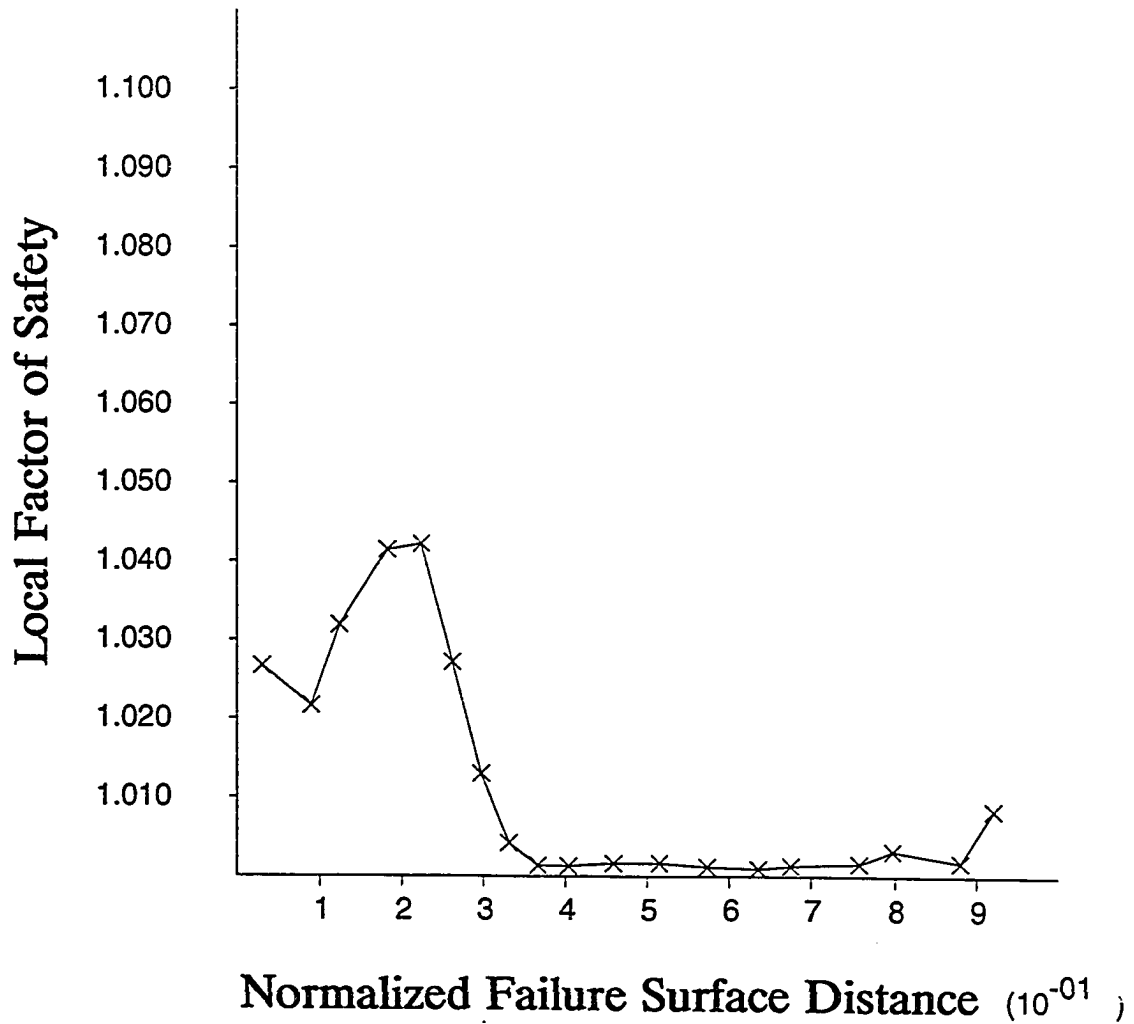


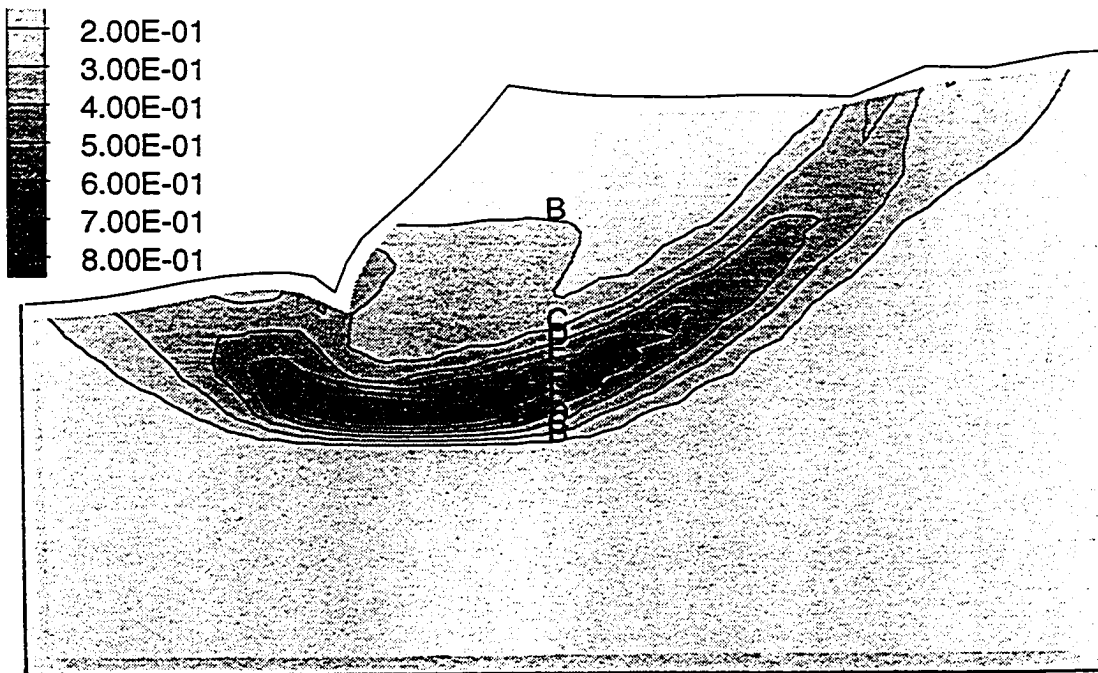
Fig. 6.61b Distribution of local factors of safety along the failure surface (7th layer excavation), B-1 analysis

them might have slightly less stress than strength due to readjustment of maximum shear stress by the Mohr-Coulomb failure envelop or temporary release of stress in the elements. This explains the factor of safety which is slightly greater than unity even at the failure state. The distribution of local factors of safety at the 7th layer excavation is shown in Fig. 6.61b.

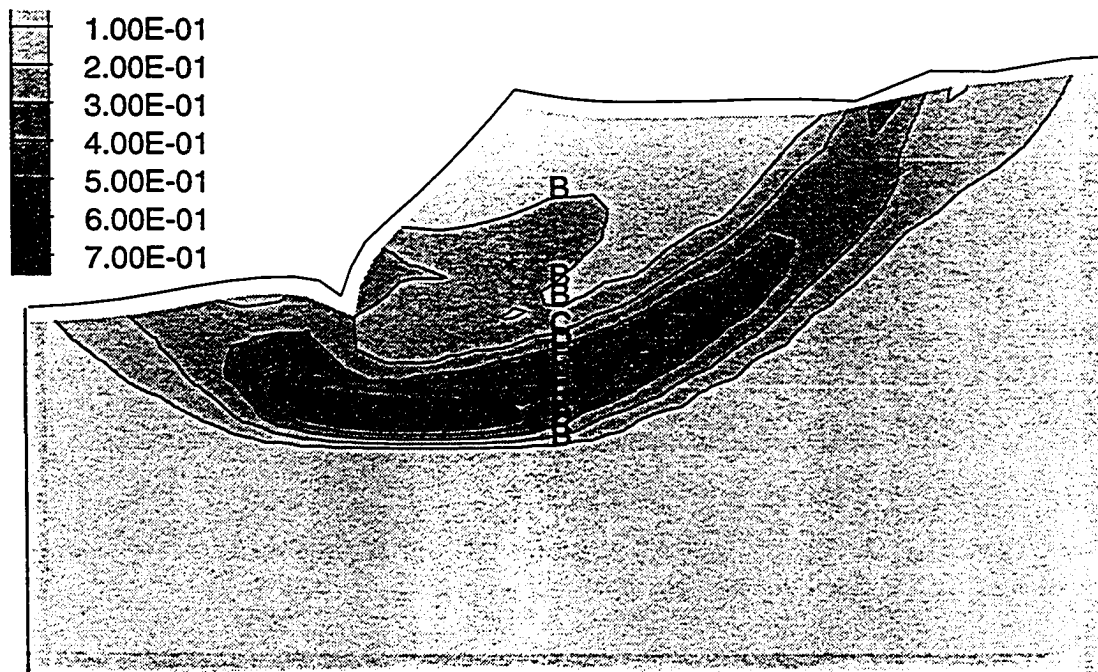
6.3.4 Anisotropic Strength with Straining Hardening and Softening Cases (C, D and E Analyses)

In order to simulate the extra brittle behavior of overconsolidated clay, the degree of strain softening in C and D analyses was increased up to 60%. In addition, extra series of analyses (E analyses) were carried out in which the stress-strain relations were defined such a way that all the elements reach peak strengths at small maximum shear strain levels (about 1.0%) with a constant degree of strain softening in the post peak region without regard to the i angle including the passive elements. The strength in the post peak region reaches residual level at the strain level of about 6.0%. The stress-strain relations of this type have often been assumed for highly overconsolidated clay so that those relations were bases of the postulates for progressive failure studies (Skempton, 1964; Peck, 1967; Bishop, 1967; Chandler and Skempton, 1974).

Figs. 6.62a, 6.62b and 6.62c show the maximum shear strain distributions at the final excavation stages in C-1-c, D-1-c and E-1-c analyses, respectively, as examples of those analyses. The maximum shear strain development patterns in

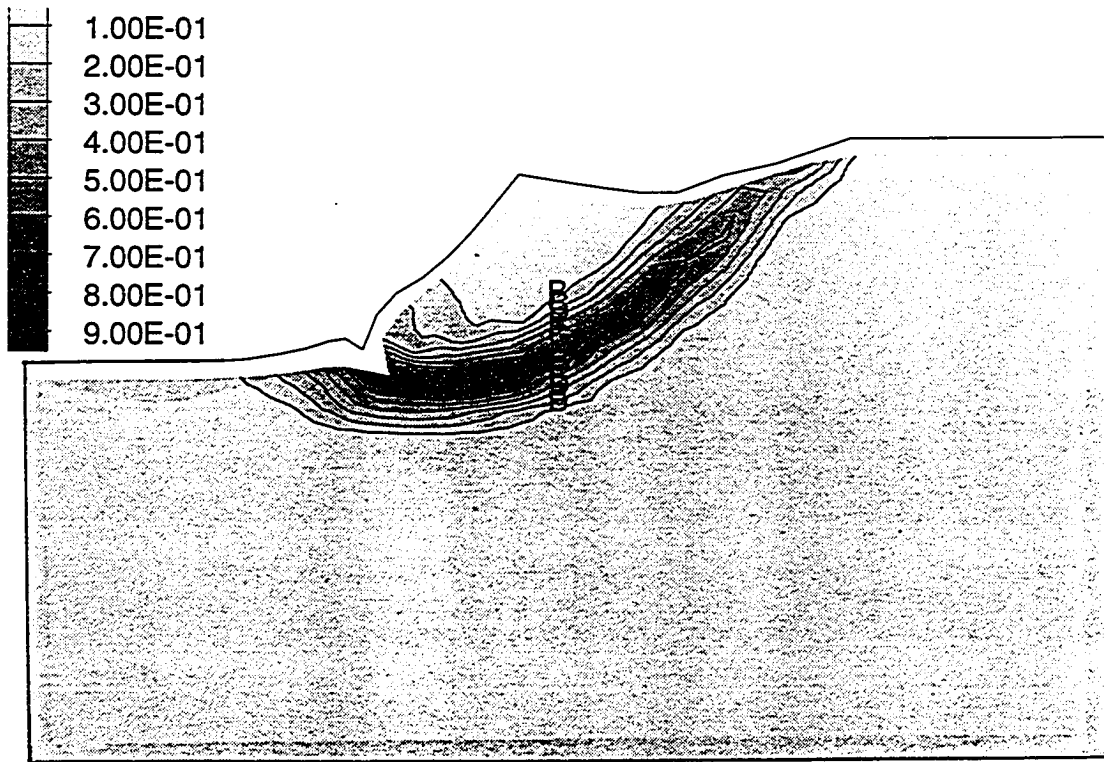


(a) 8th layer ($H_{\alpha} = 6.71$ m); Contour Interval = $1.0E-01$ (B: $1.00E-01$, F: $5.00E-01$)



(b) 8th layer ($H_{\alpha} = 6.71$ m); Contour Interval = $1.0E-01$ (B: $1.00E-01$, F: $5.00E-01$)

Fig. 6.62 Maximum shear strain distribution: (a) C-1-c analysis; (b) D-1-c analysis; and (c) E-1-c analysis



(c) 8th layer ($H_{\alpha} = 6.71$ m); Contour Interval = $1.0E-01$ (B: $1.00E-01$, I: $6.00E-01$)

Fig. 6.62 Maximum shear strain distribution: (a) C-1-c analysis; (b) D-1-c analysis; and (c) E-1-c analysis

C, D and E series analyses are very close to that in B analysis. The failure surfaces determined in the entire analyses in this section are presented together in Fig. 6.63. It is interesting to find that the failure obtained in E-1 analyses are rather close to a toe failure, while those in C-1-c and D-1-c are base failures. Note that the degree of strain softening for a given E analysis was constant for all stress paths so that its effect is much higher than those of C and D analyses (in C and D analyses, the degree of softening is greatest for $i=0^\circ$ element and is least for $i=45^\circ$ element). It should be recalled that whenever high degree of softening is used in the stress-strain relations, the failure surface was found to be much shallower than those of low degree of softening in the linearly increasing strength case of normally consolidated clay.

Fig. 6.64a shows the nodal displacements of the tip of the crest with increasing excavation heights in A, B and C series analyses. It is seen that the slope in B series analysis shows a drastic change in the magnitude of nodal displacement at the seventh layer excavation, reflecting the sudden global failure. On the other hand, the slopes in all C series analyses show rather smooth transition from stable state to failure state. It appears that the stage of failure is independent of degree of strain softening in C series analyses (i.e., all slopes fail at the seventh layer). Fig. 6.64b shows the nodal displacements in D-1 series of analyses along with those in A and B analyses. Similar displacement patterns to those of C analyses are observed. On the other hand, the nodal displacement patterns in E-1 series in Fig. 6.64c show somewhat different behavior than the

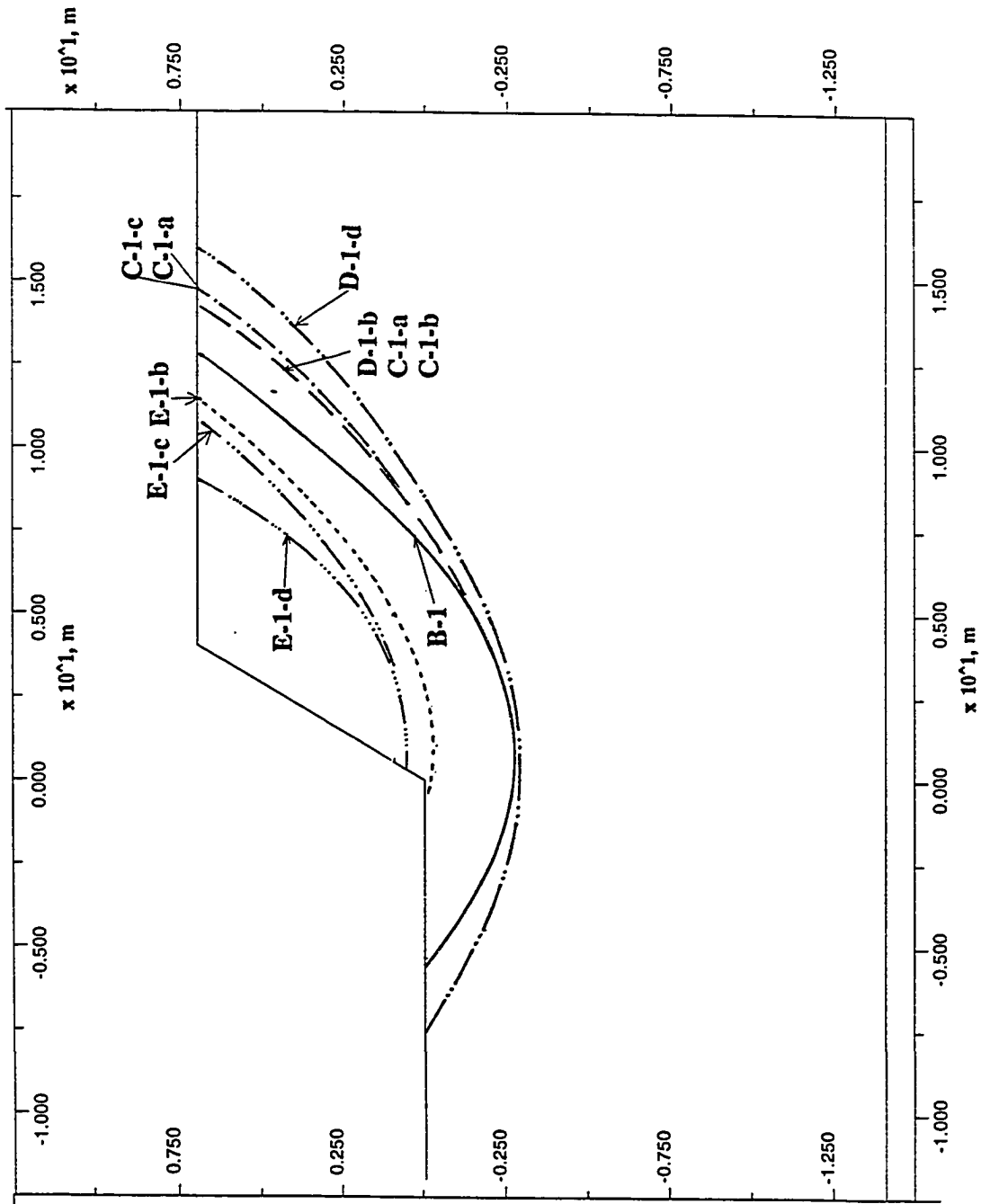


Fig. 6.63 Comparison of failure surfaces, C, D and E analyses

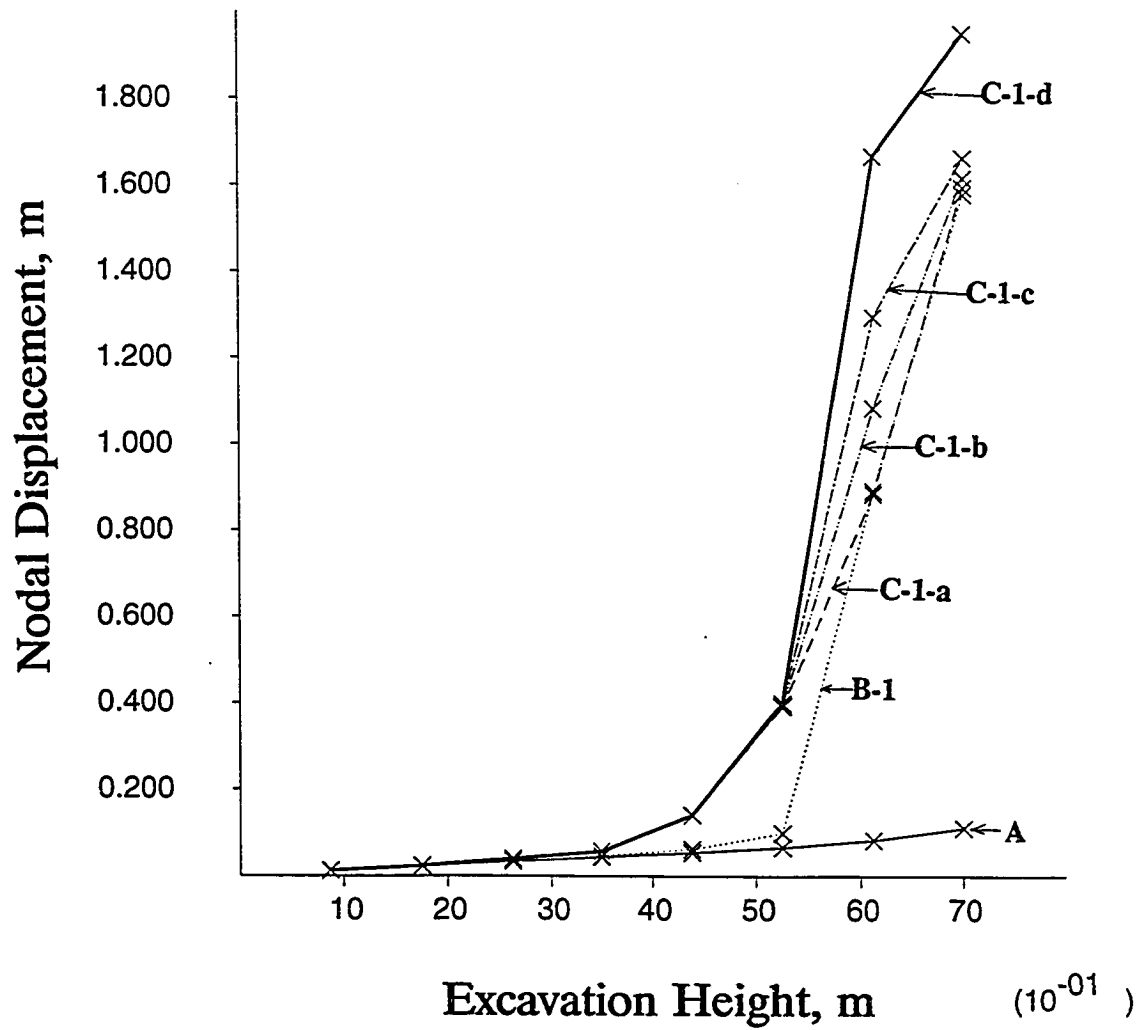


Fig. 6.64a Nodal displacements with increasing excavation heights, A, B-1 and C-1 series analyses

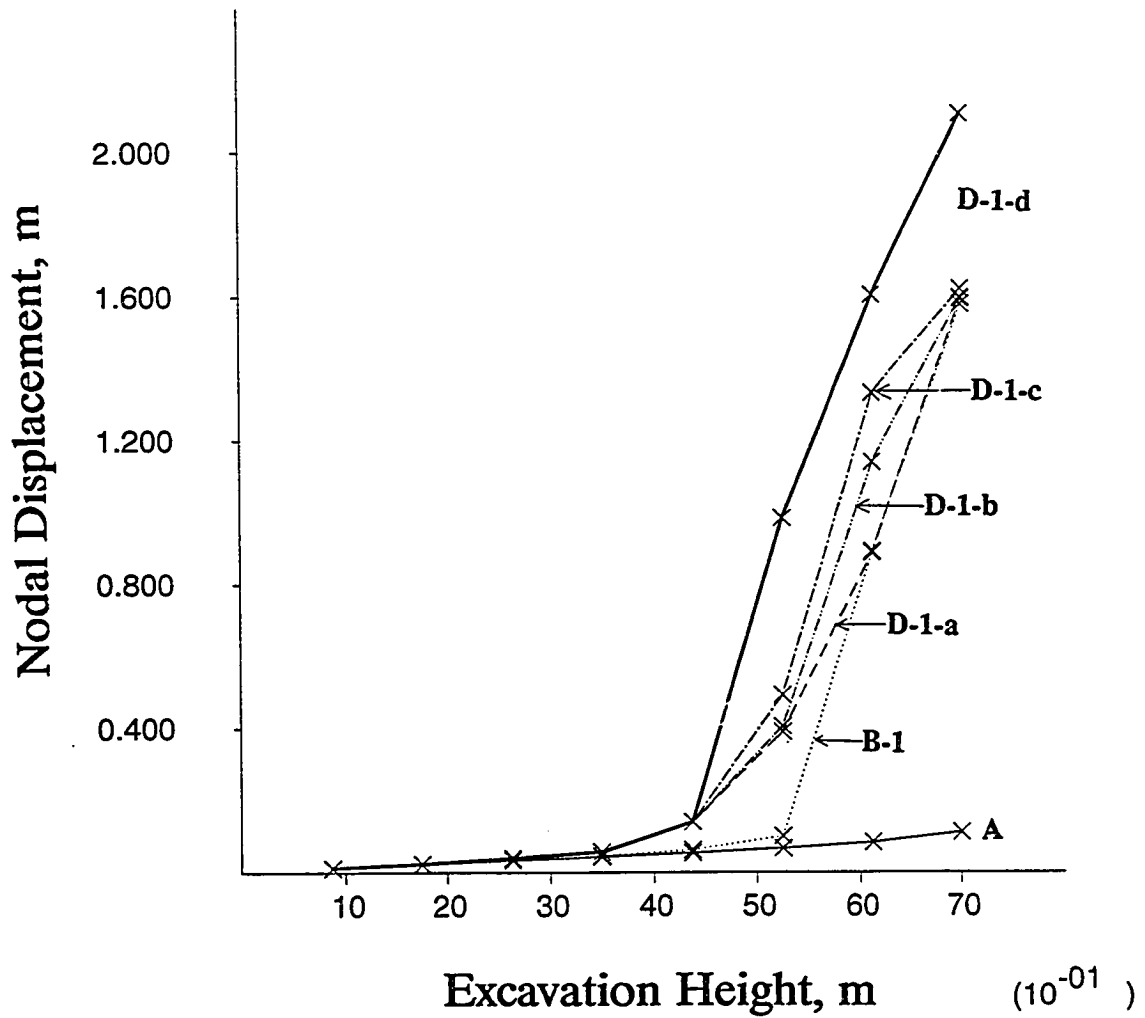


Fig. 6.64b Nodal displacements with increasing excavation heights, A, B-1 and D-1 series analyses

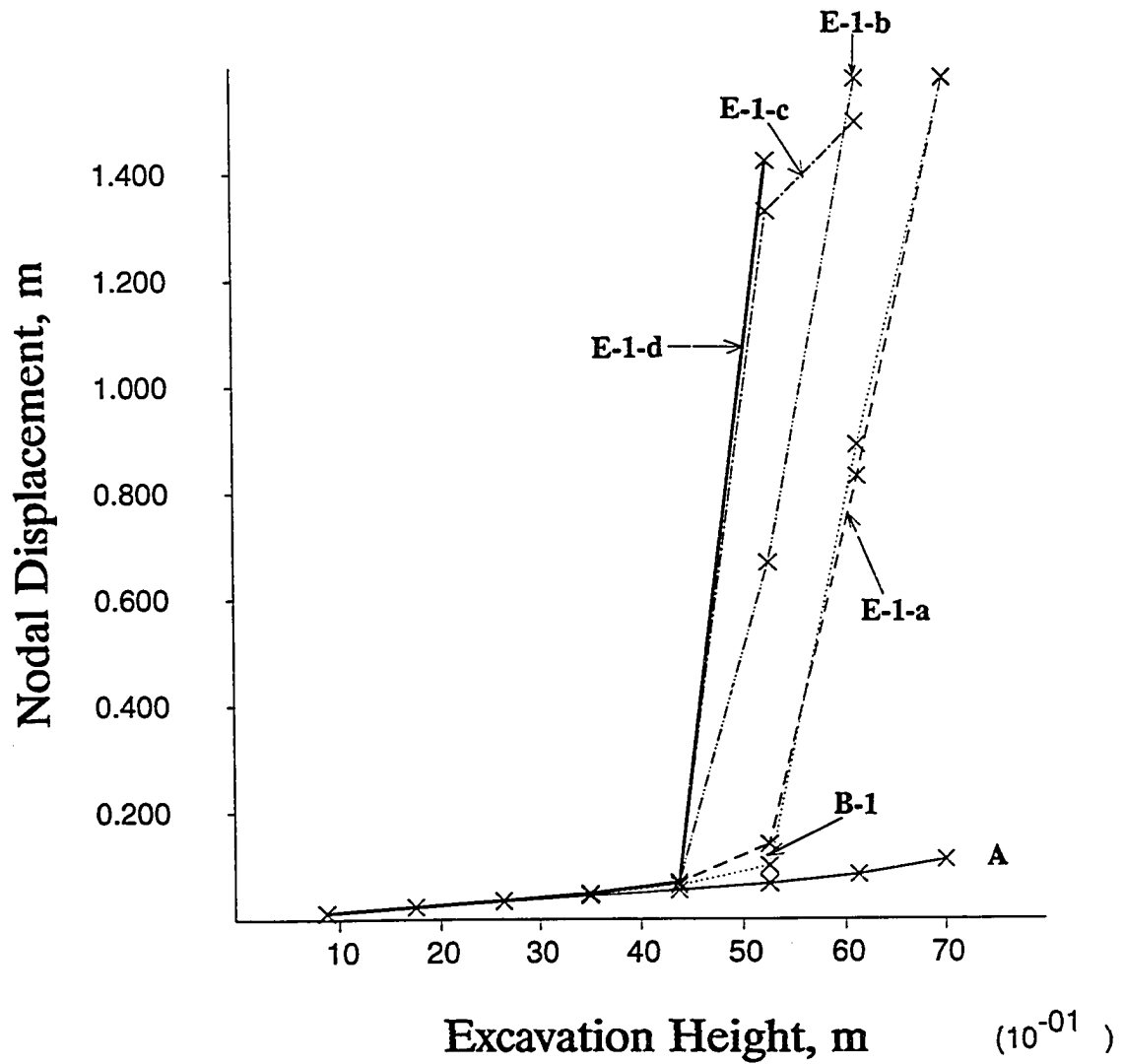


Fig. 6.64c Nodal displacements with increasing excavation heights, A, B-1 and E-1 series analyses

previous ones. It is seen that the slopes in E-1-b through E-1-d analyses fail at the 6th layer excavation, which is a layer earlier than the rest of slopes (B, C, D and E-1-a analyses). The brittle behavior in the nodal displacement pattern is a consequence of the stress-strain relations in which peak and residual strengths occur at small strain levels with the same degree of strain softening for all stress paths. Fig. 6.65a and 6.65b show the sequential pattern of peak strength mobilization of elements along the failure surface in C-1-c analysis. The relatively uniform patterns of the peak strength mobilization in E-1-c analyses as seen in Fig. 6.65c explains the brittle behavior of nodal displacement in comparison to C-1-c case.

Fig. 6.66a shows the relations between the time steps at which the peak strength of an element is mobilized ($\tau_{\max}/S_u=1.0$) and the corresponding element identification in C-1-c analysis. The elements along the failure surface are identified in Fig. 6.66b. It appears that the peak strength is first exercised by the element "q" which lies at a few elements below the crest. Then, the elements below the first-failed one are loaded to the peak strengths, resulting in complete yielding in the interior elements between element "r" to element "f" by the time steps of about 92000. Subsequently, elements in the crest and the toe are alternately subjected to the failure. The failure sequence observed here in C-1-c analysis is not the same as that appeared in B-1 analysis, but the similarity in the general trend can be found.

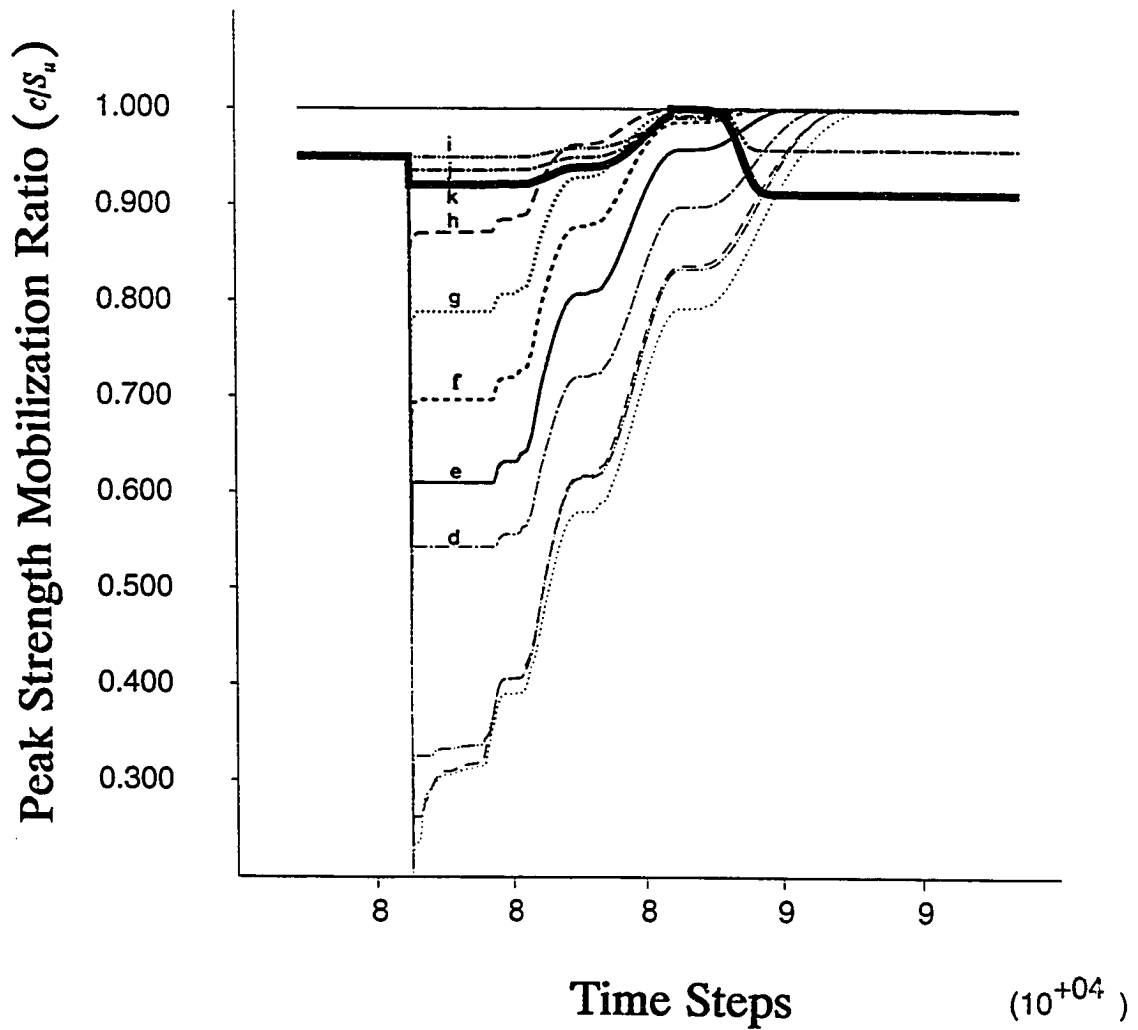


Fig. 6.65a Sequence of the peak strength mobilization with time steps, C-1-c analysis

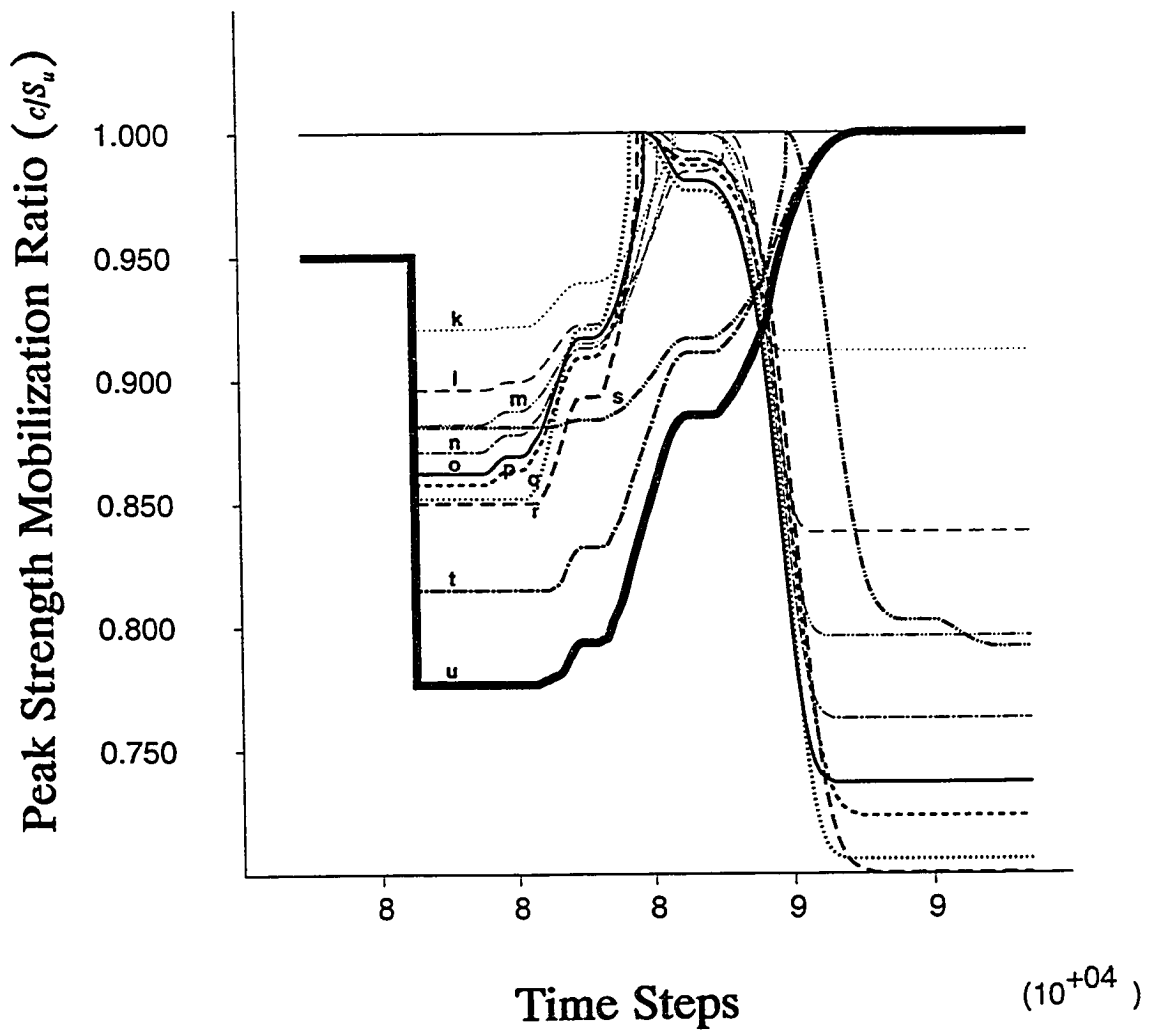


Fig. 6.65b Sequence of the peak strength mobilization with time steps, C-1-c analysis

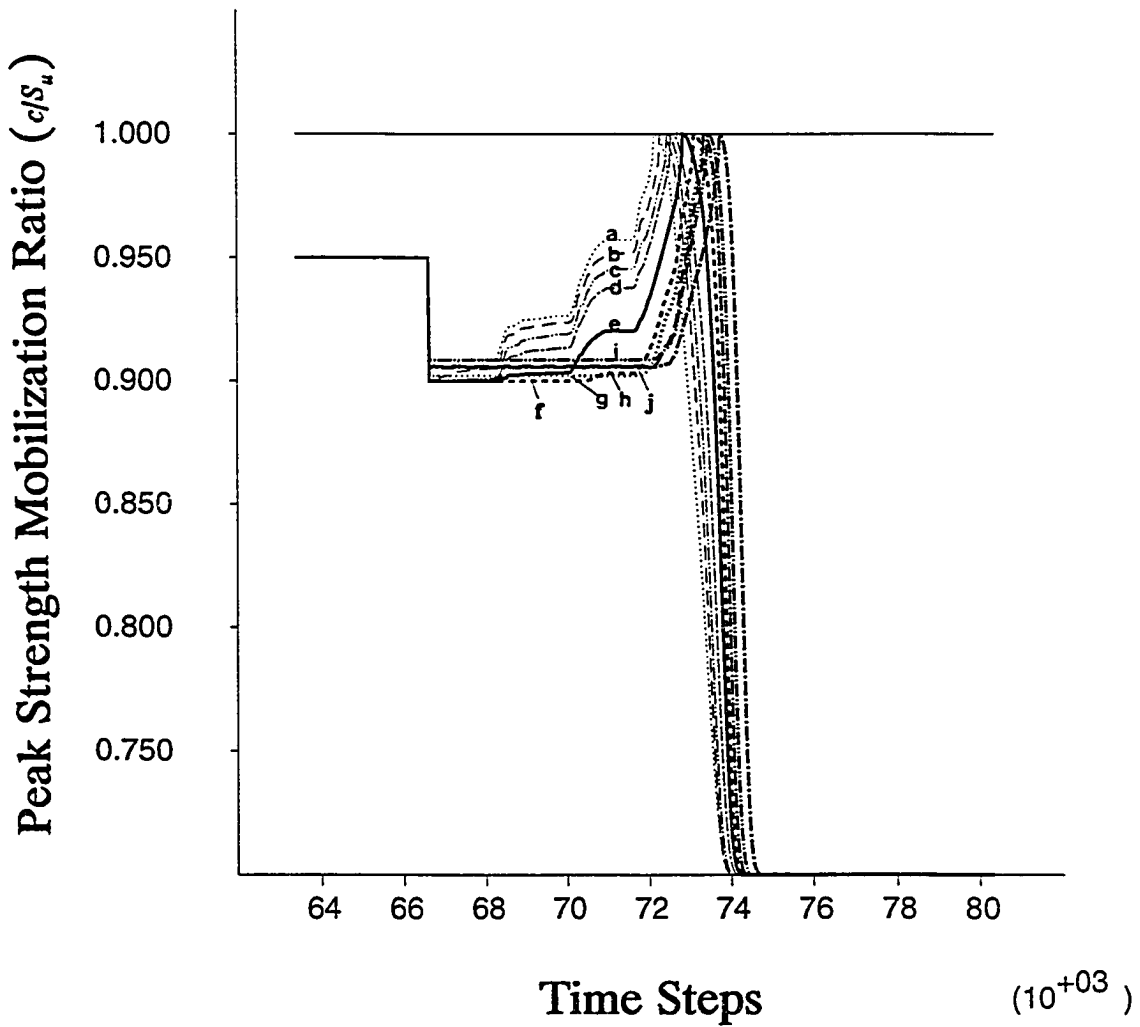


Fig. 6.65c Sequence of the peak strength mobilization with time steps, E-1-c analysis

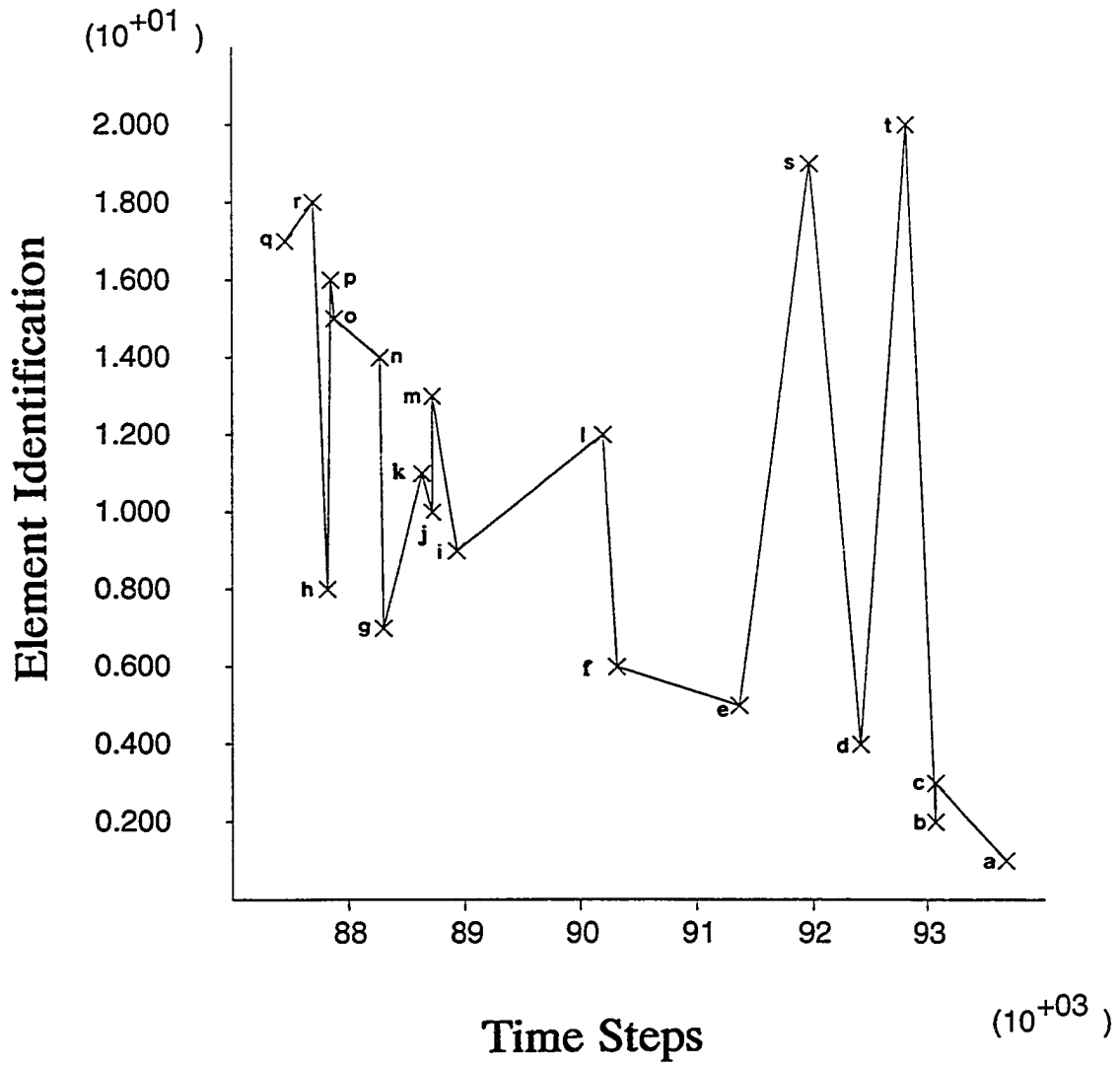


Fig. 6.66a Failure sequence of the elements along the failure surface, C-1-c analysis

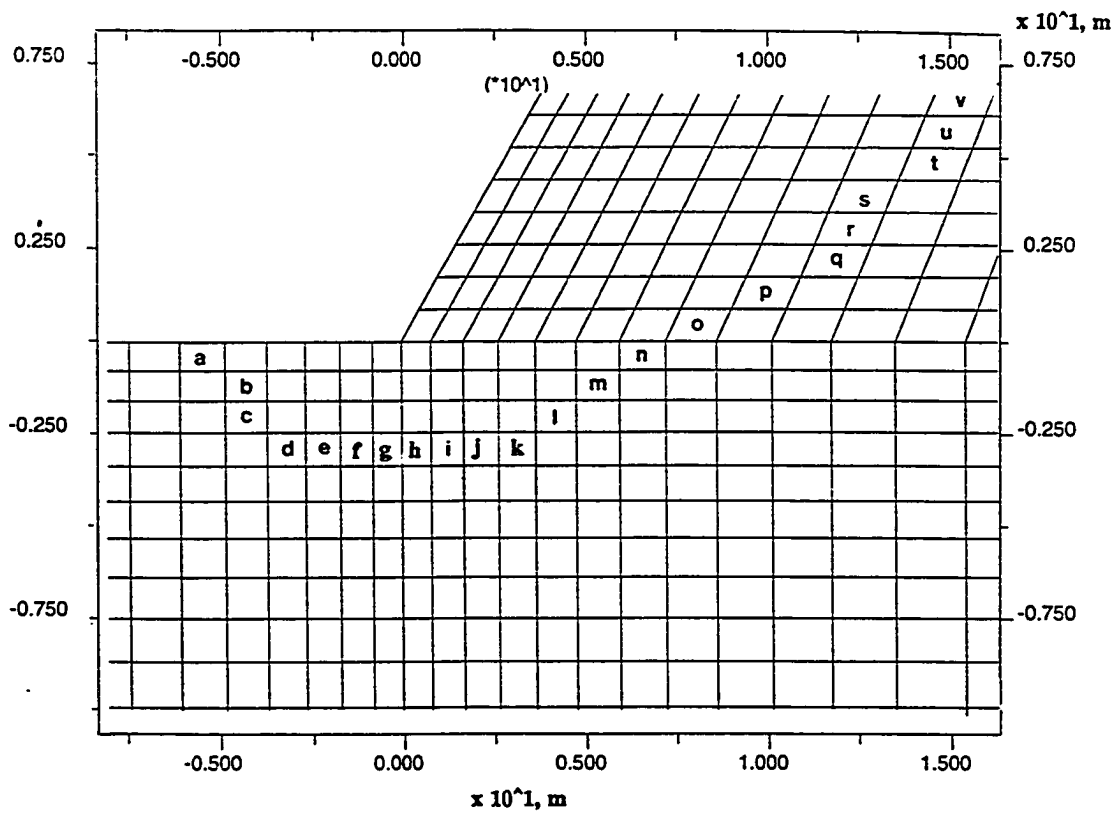


Fig. 6.66b Locations of the elements along the failure surface, C-1-c analysis

Figs. 6.67a, 6.67b and 6.67c show the variation in the mobilized strength ratio (curve "a") in C-1-c, D-1-c and E-1-c analyses, respectively. The mobilized strength ratio has already been defined as the ratio of the summation of strengths of the elements along the failure surface to the summation of the isotropic compression strengths of those elements at a given time. In the same figures, the variations in the ratios of summation of the maximum shear "stresses" of the

Table 6.16a Summary of the peak mobilized strength ratios (C analysis)

Case	C-1-a	C-1-b	C-1-c	C-1-d
R1	0.847	0.847	0.847	0.848
R2	0.847 (0.847)	0.818 (0.814)	0.812 (0.803)	0.806 (0.791)
OE ¹	18.0%	22.2%	23.2%	24.1%
OE ²	0.0%	3.55%	4.31%	5.21%

Table 6.16b Summary of the peak mobilized strength ratios (D and E analyses)

Case	D-1-b	D-1-c	D-1-d	E-1-b	E-1-c	E-1-d
R1	0.847	0.841	0.841	0.900	0.900	0.909
R2	0.805 (0.798)	0.786 (0.764)	0.776 (0.752)	0.879 (0.894)	0.869 (0.889)	0.870 (0.897)
OE ¹	24.2%	27.2%	28.9%	13.8%	15.1%	14.9%
OE ²	5.22%	7.00%	8.38%	2.39%	3.57%	4.48%

elements to the summation of the isotropic compression strengths, which was defined as "the mobilized stress ratio", are also presented (curve "b"). The drastic mobilized strength ratio drop in the residual state in E-1-c analysis is remarkable

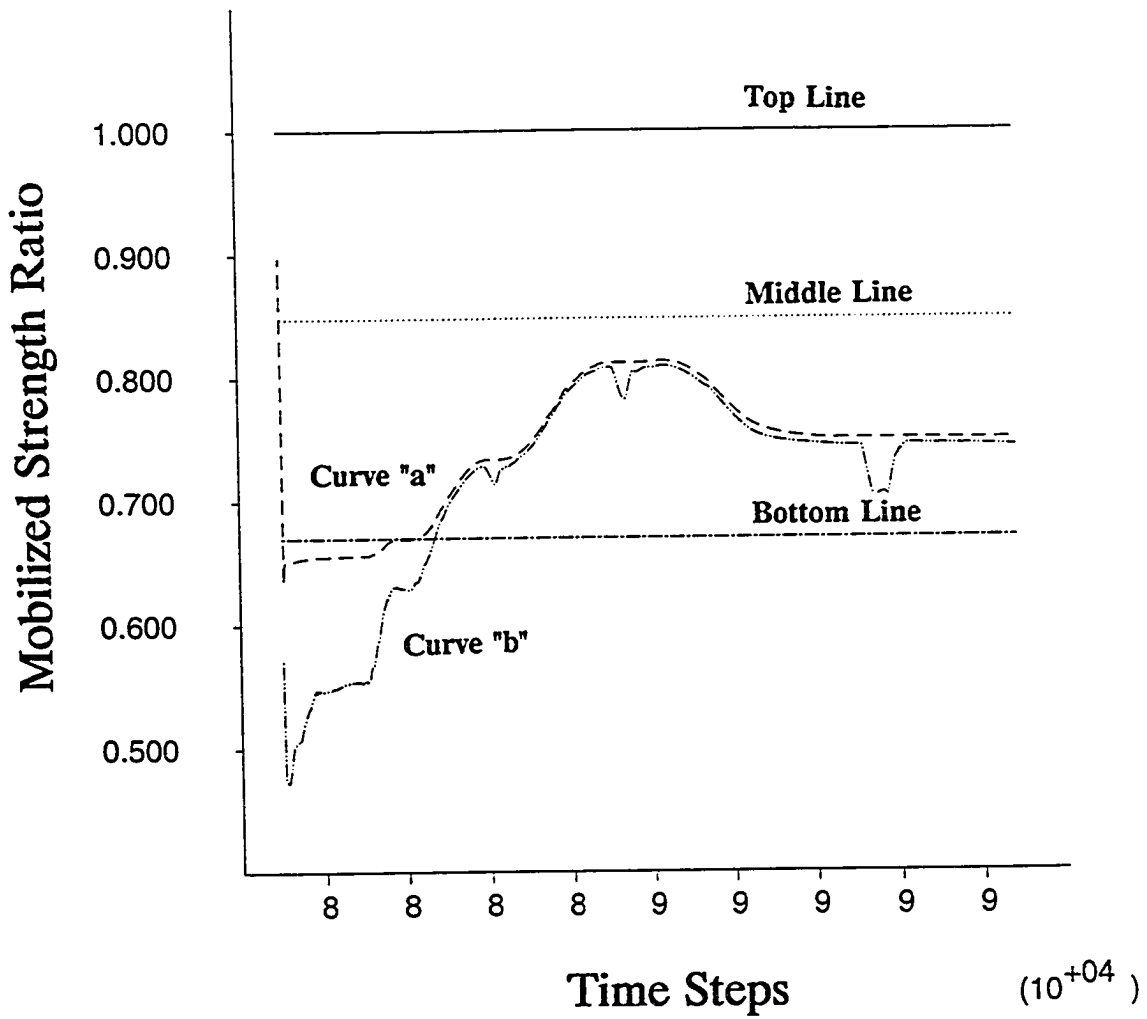


Fig. 6.67a Variation of the mobilized strength ratio with time steps, C-1-c analysis

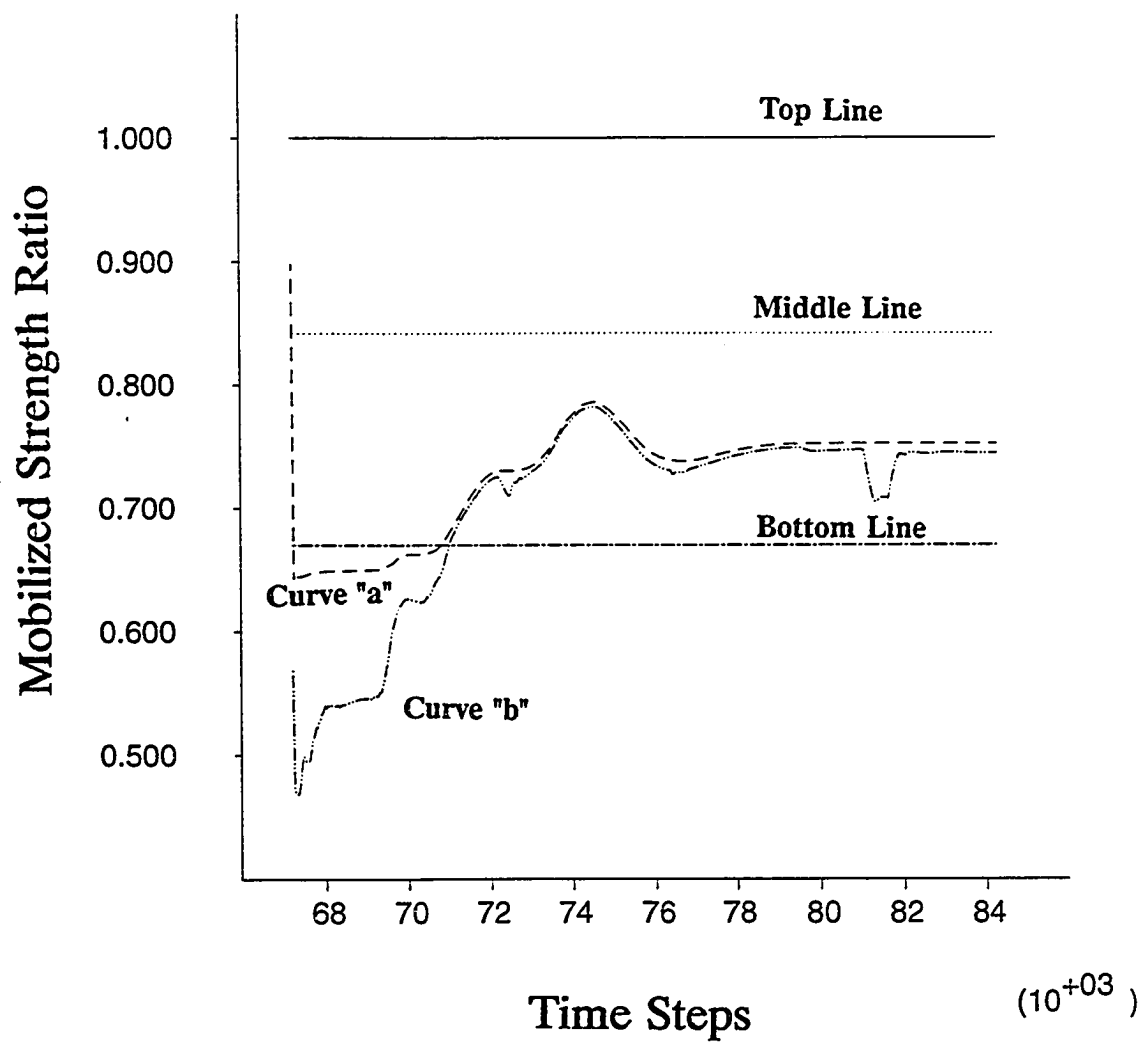


Fig. 6.67b Variation of the mobilized strength ratio with time steps, D-1-c analysis

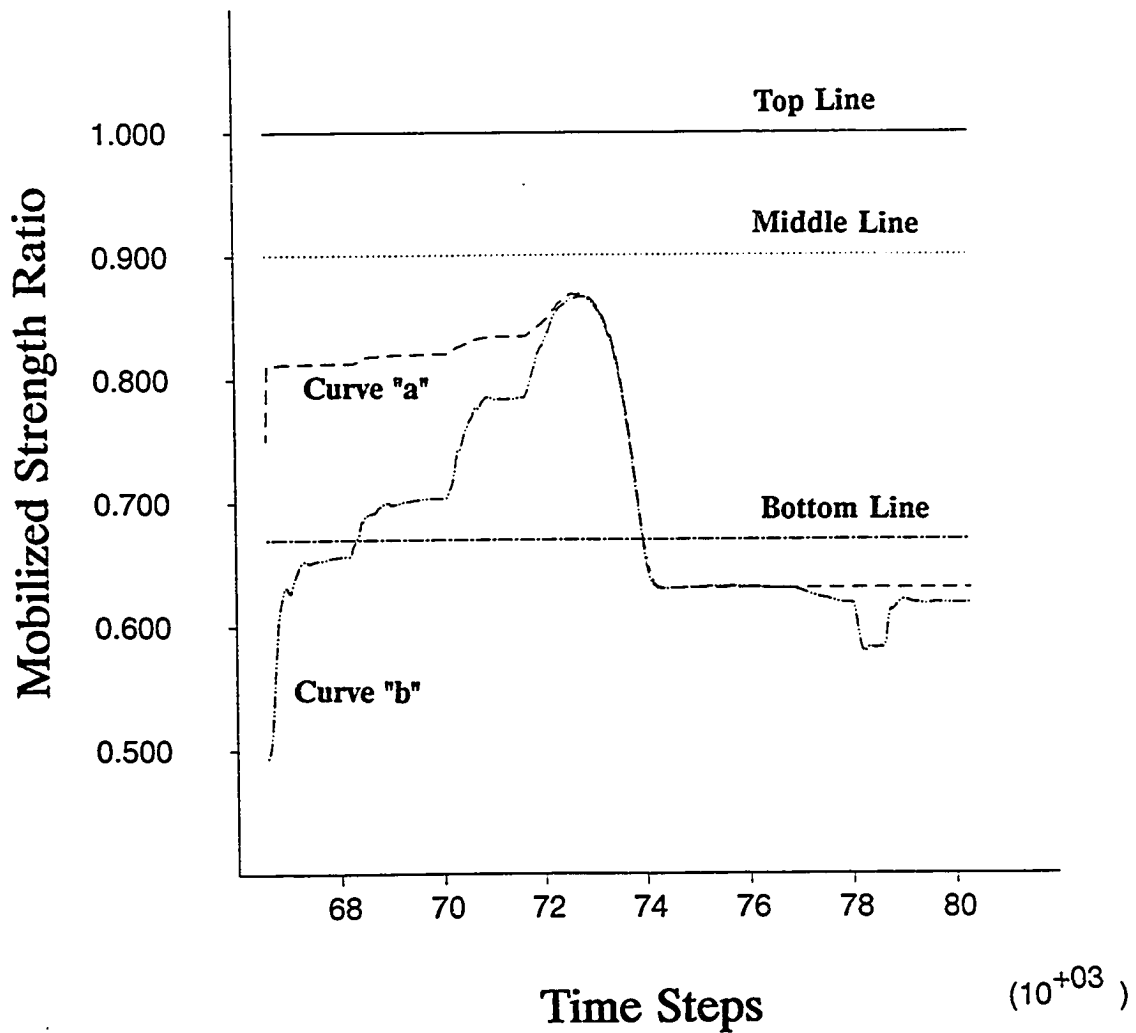


Fig. 6.67c Variation of the mobilized strength ratio with time steps, E-1-c analysis

(Fig. 6.67c). The peak mobilized strength ratios for the entire analyses are summarized in Tables 6.16a and 6.16b.

It can be seen in the tables that overestimate (OE^1) in the summation of strengths along the failure surface in A type analysis can be as large as 28.9% in D-1-d analysis. The overestimate (OE^2) in the mobilized strength which would be possible in B type analysis can be as large as 8.38% in D-1-d analysis. It is interesting to find that overestimates in E analyses are much less than those of C and D analyses. Considering the stress-strain relations in E analyses which are supposed to represent extra brittle behavior of soil, it is contradicting to our expectation. The reason for this contradiction is explained in the following. Figs. 6.68a, 6.68b and 6.68c show the plastic shear strain distributions along the failure surfaces at the peak mobilized strength ratios in C-1-c, D-1-c and E-1-c analyses, respectively. It is shown that the range of plastic shear strain distribution in E-1-c analysis is much narrower than those of the rest. When the plastic shear strain levels of the toe element (2.55%) and the crest element (0.82%) in Fig. 6.68c are used to obtain corresponding percentages of the peak strength mobilizations, they were 86.5% for the toe element in the softening stage and 97.1% for the crest element in the hardening stage as shown in Fig. 6.69. It is clear then that the plastic shear strain distribution in E-1-c analysis is relatively uniform enough for the entire elements to exercise near peak strengths when the mobilized strength ratio reaches the peak. This explains the reason for the relatively high peak mobilized strength ratios for E analyses in Table 6.16b.

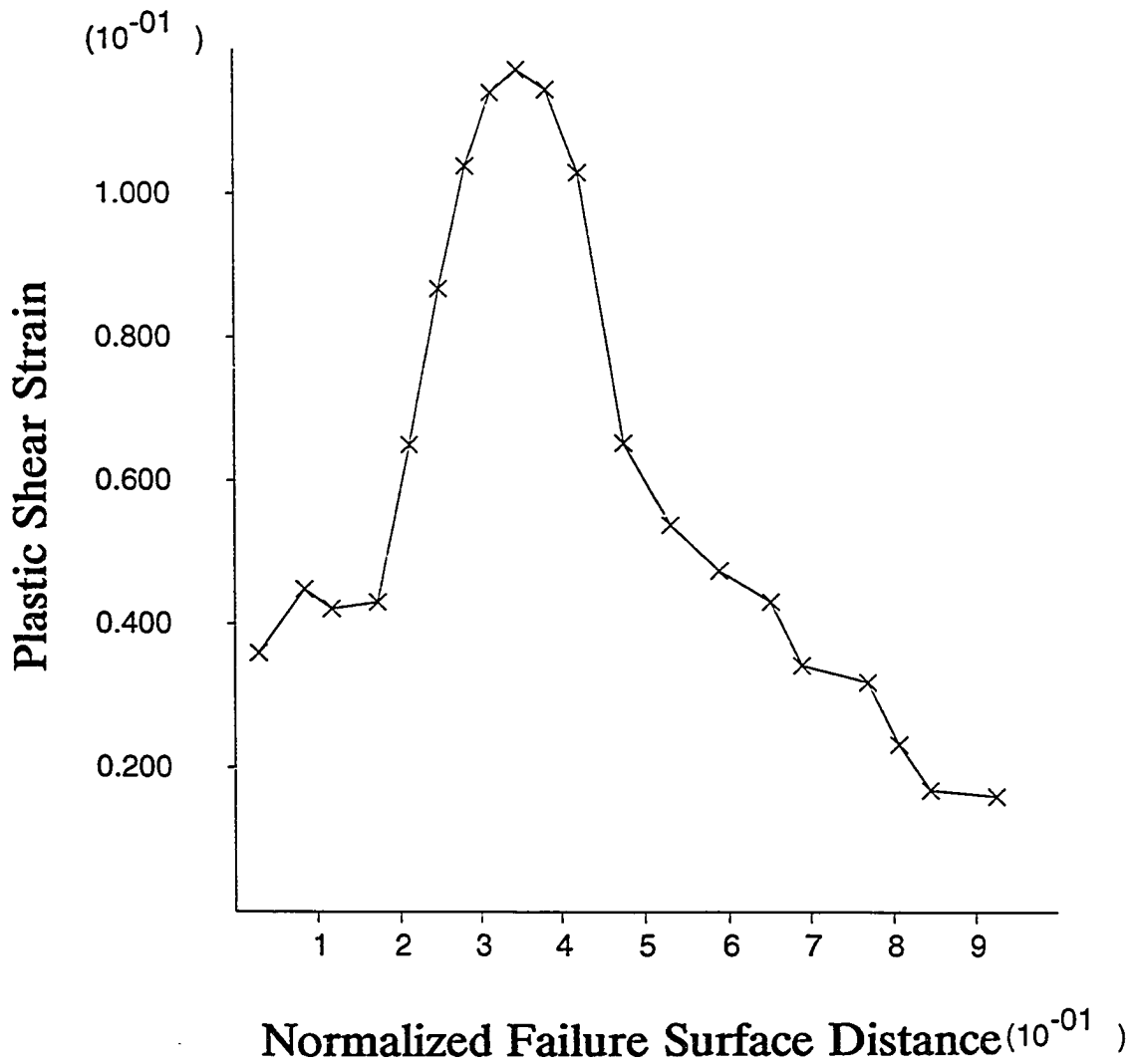


Fig. 6.68a Plastic shear strain distribution along the failure surface, C-1-c analysis

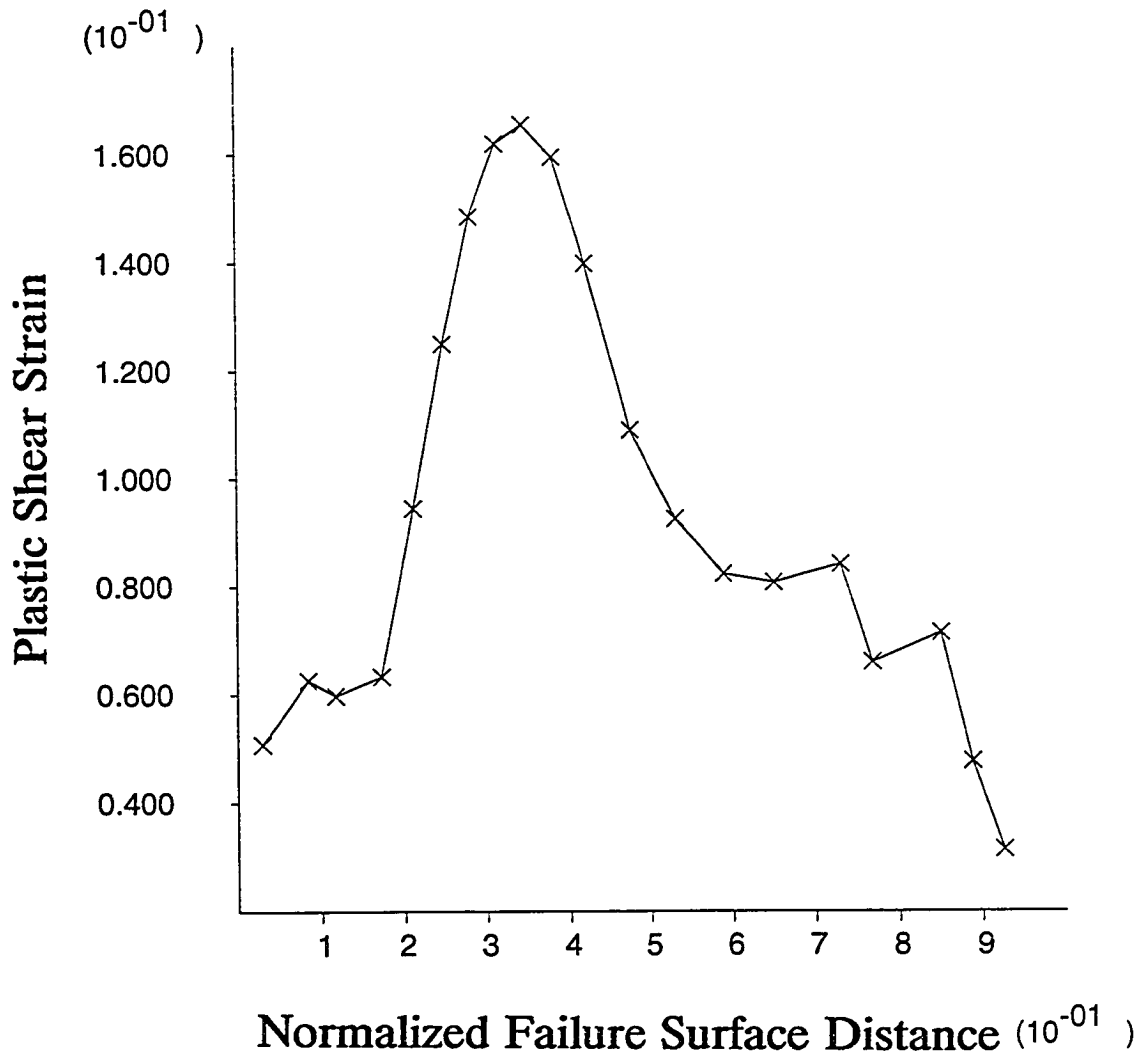


Fig. 6.68b Plastic shear strain distribution along the failure surface, D-1-c analysis

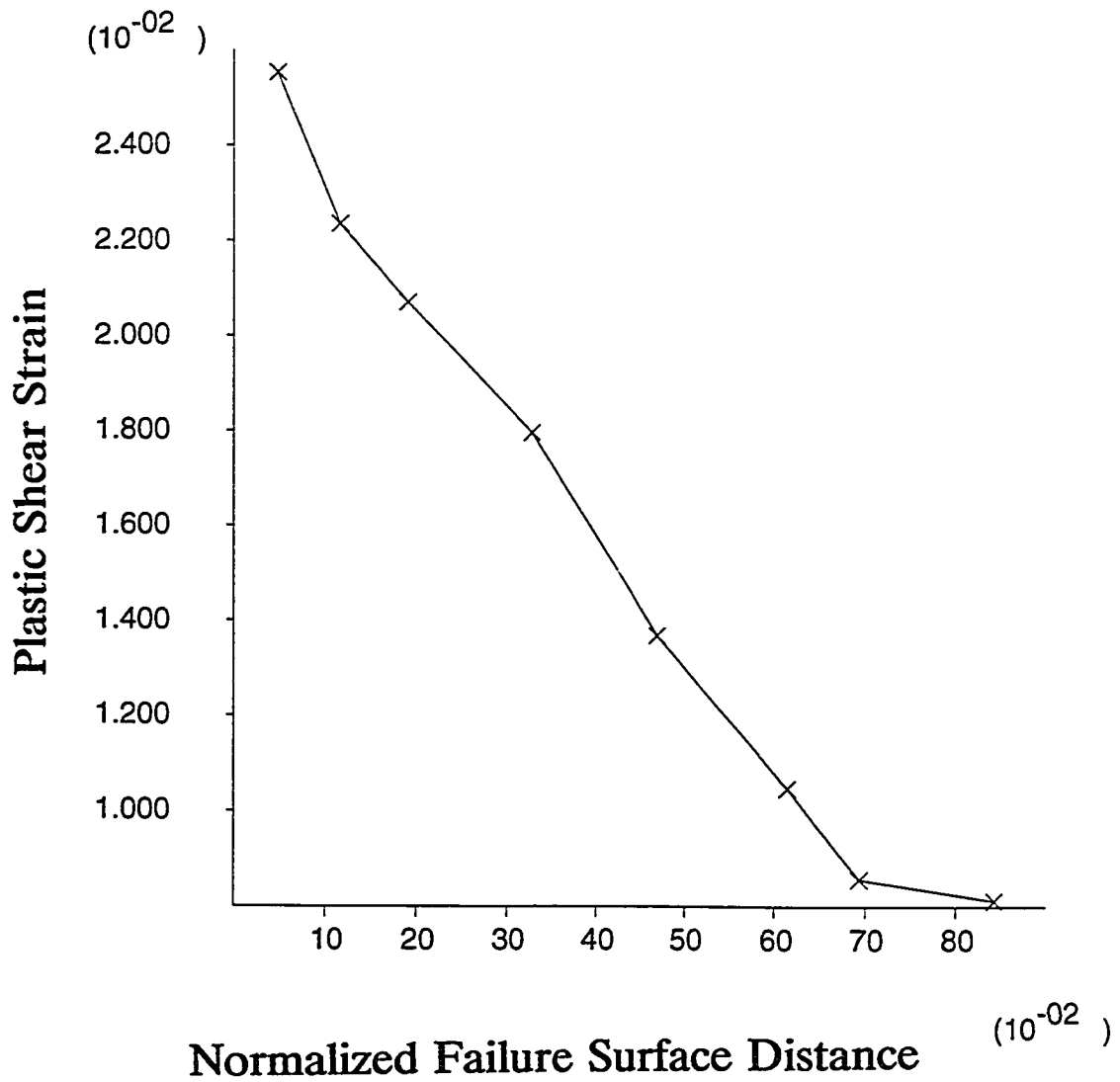


Fig. 6.68c Plastic shear strain distribution along the failure surface, E-1-c analysis

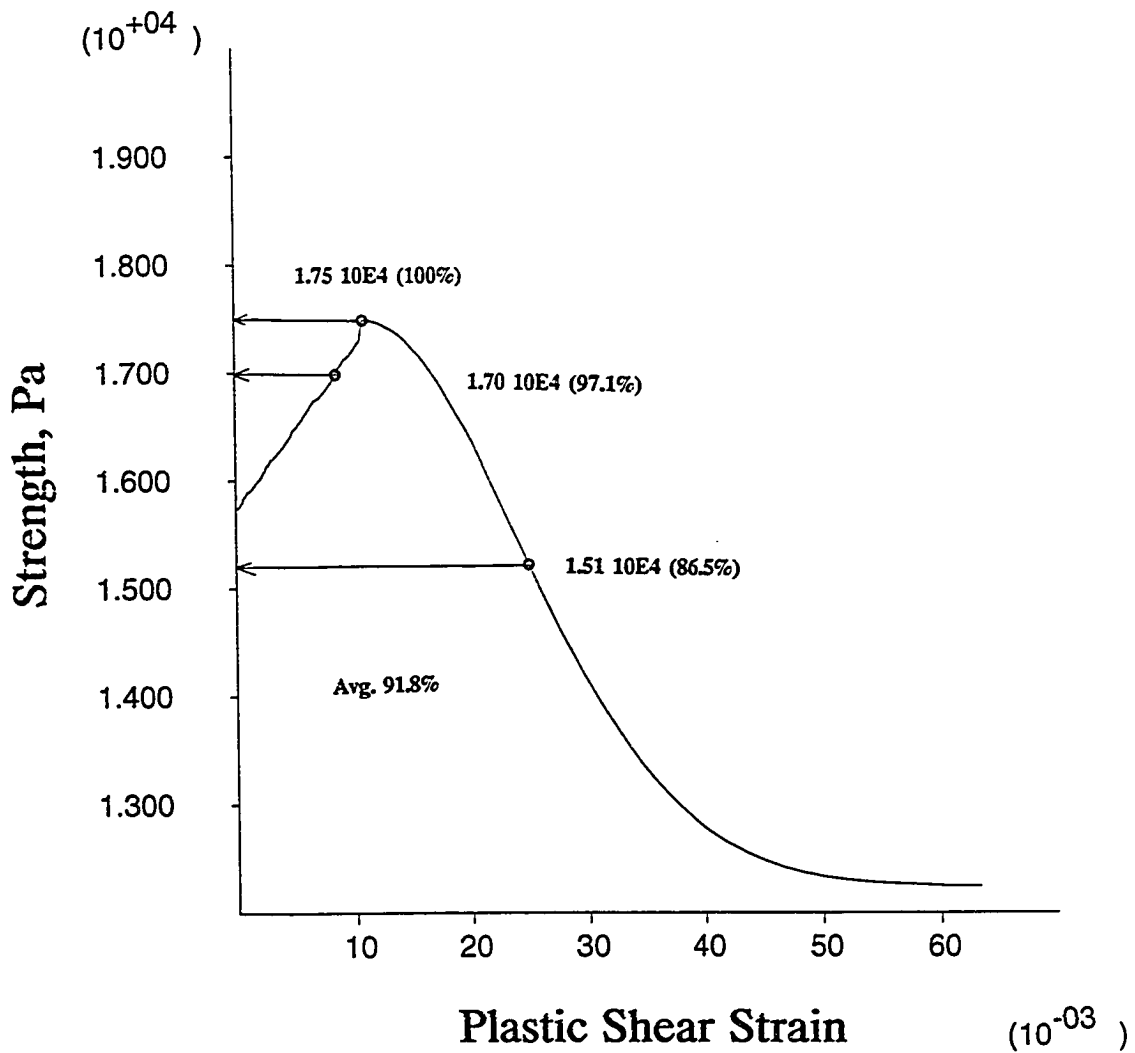


Fig. 6.69 Mobilized strengths for the toe and the crest elements at the peak mobilized strength ratio, E-1-c analysis

The stress-strain relations for the elements along the failure surface were used to apply the strain compatibility concept. The strengths at a given strain level were added and divided by the summation of the anisotropic peak strengths of those elements, which was defined as the strength ratio. The strength ratio reaches the peak at a certain strain level, which was defined as the peak strength ratio. Figs. 6.70a, 6.70b and 6.70c show the variations in the strength ratios for C,

Table 6.17 Summary of the peak strength ratios using strain compatibility technique.

C-1-b	C-1-c	C-1-d	D-1-b	D-1-c	D-1-d	E-1-b	E-1-c	E-1-d
0.961	0.948	0.933	0.942	0.909	0.894	0.993	0.987	0.987

D and E analyses, respectively. The peak strength ratios for the entire analyses are summarized in Table 6.17. When the peak strength ratios were converted to be comparable to those in Table 6.16 (see the numbers in parentheses in Table 6.16), it is found that the predictions of strength mobilization based on the assumption of uniform strain distribution (the strain compatibility concept) are constantly smaller than those of rigorous C and D analyses. On the other hand, they are slightly larger than those of E analyses. It is noted again that the reason for the higher predictions in E analyses is because the stress-strain relations are rather uniform so that the maximum shear stress reaches the peak at nearly constant strain levels (around 1.0%) for all stress paths.

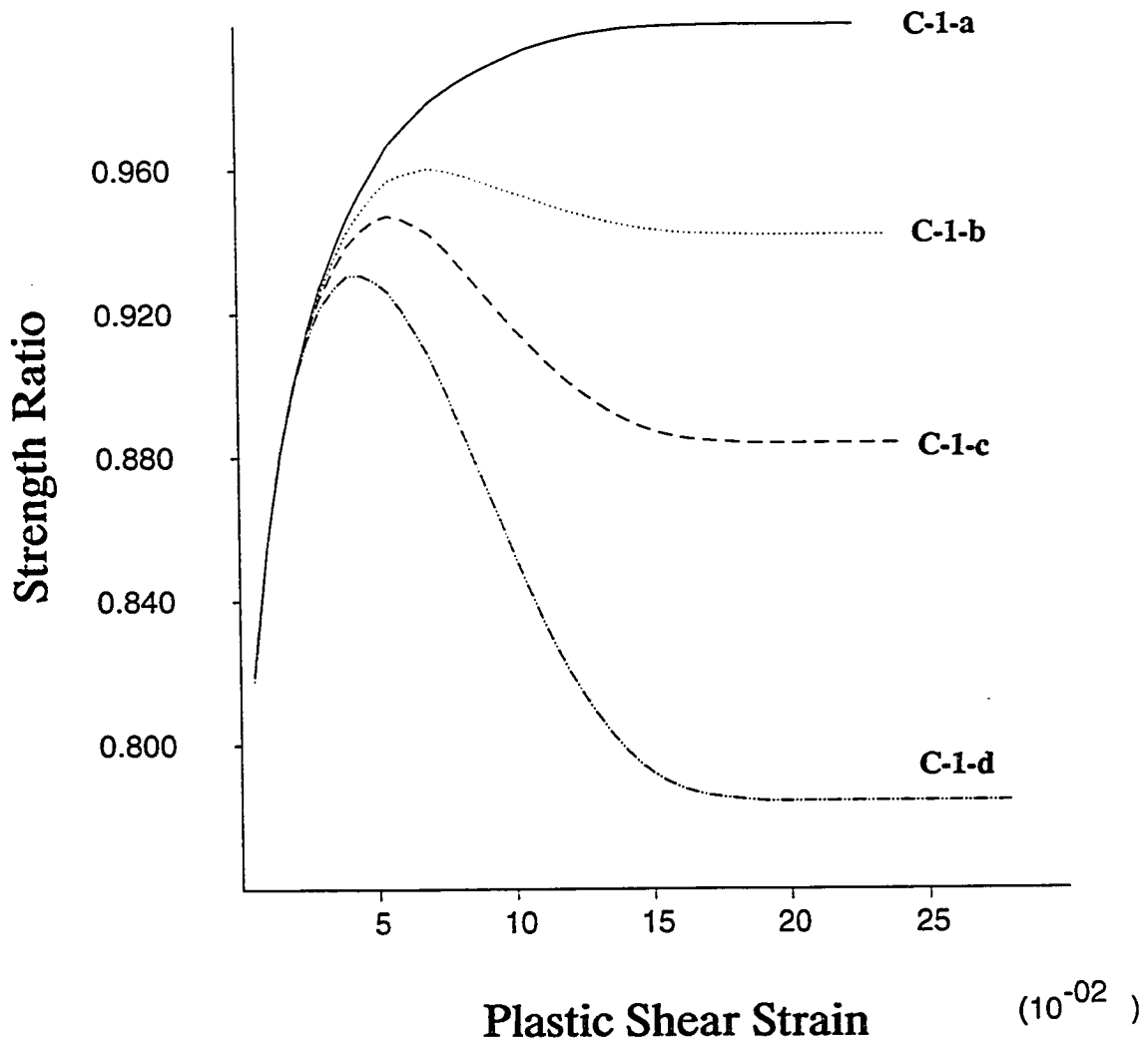


Fig. 6.70a Variation of strength ratios (strain compatibility concept), C-1 analyses

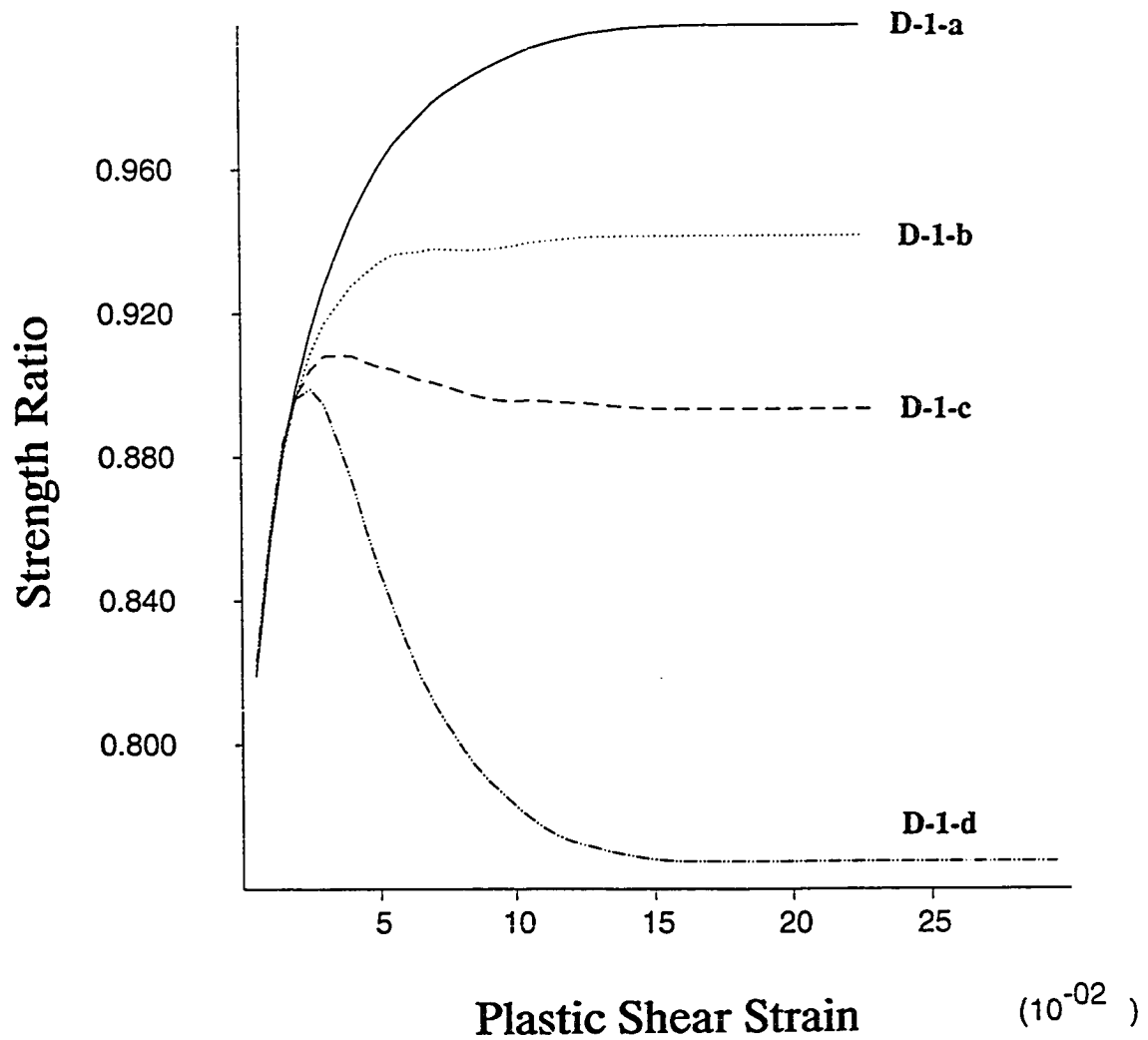


Fig. 6.70b Variation of strength ratios (strain compatibility concept), D-1 analyses

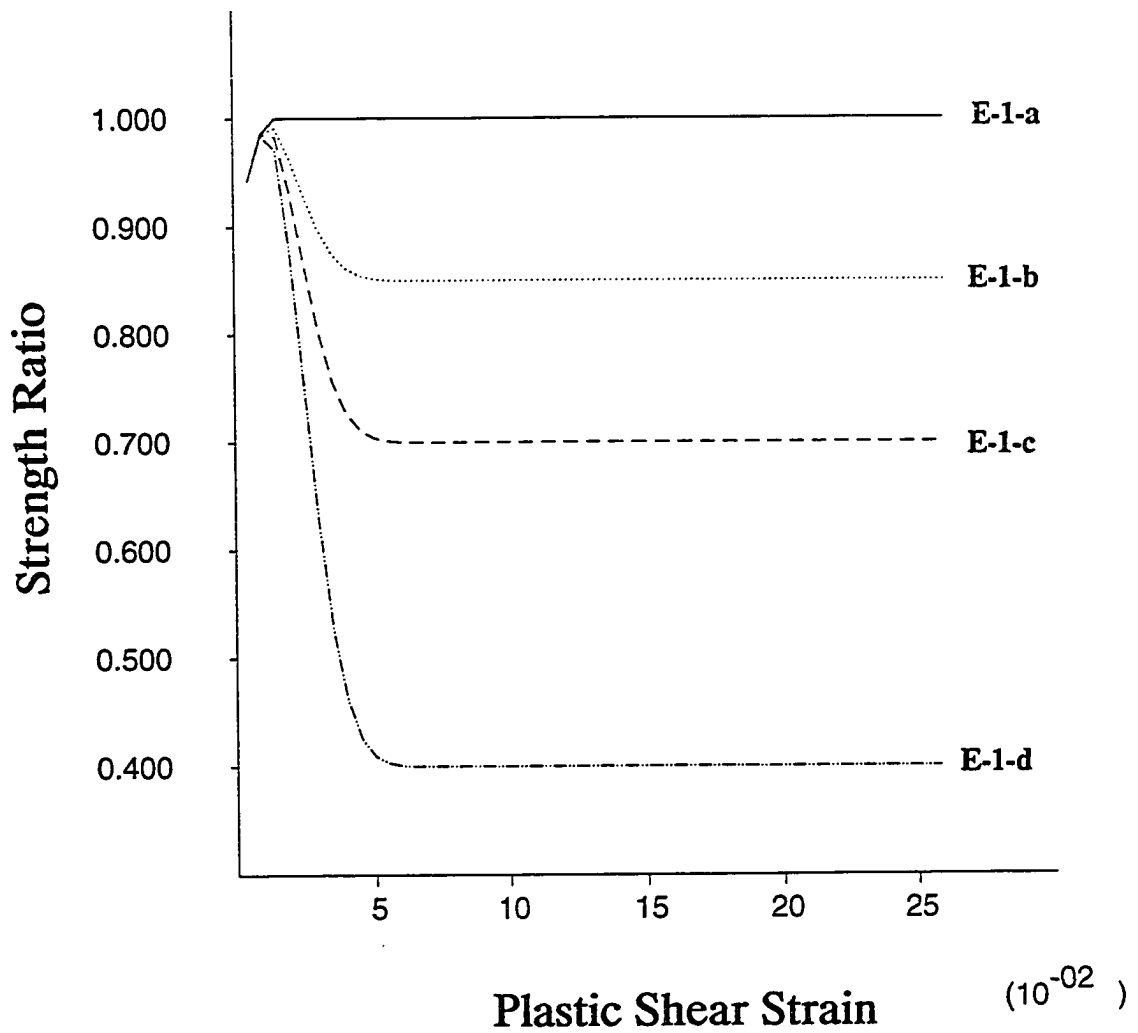


Fig. 6.70c Variation of strength ratios (strain compatibility concept), E-1 analyses

7. SUMMARY AND CONCLUSIONS

7.1 Summary

7.1.1 Homogeneous Strength Cases

It was observed in this study that the failure in the slope of a homogeneous strength profile propagates from the bottom of the failure surface toward the crest. Upon reaching the crest, the failure shifts toward the toe. This observation is slightly different from the generally assumed failure pattern in which the failure propagates from the bottom toward both the crest and the toe simultaneously. The failure surface predictions made by different series of analyses were very close to each other, which in turn closely match with the circular failure surface predicted by the Modified Bishop method. The i angles at the state of incipient failure were well distributed from about 90 degrees at the toe to about negative 5 degrees at the crest. This implies that strengths of elements with a wide range of stress paths are actually influencing the stability of slope. It was shown that in D-1-c analysis the overestimate in the peak value of the summation of the mobilized shear strengths due to neglecting both the progressive failure effect and anisotropic strength effect, by simply using isotropic strength parameters (used in A series analyses), is as large as 25.0%. On the other hand, in the same D-1-c analysis the overestimate due to neglecting only the progressive failure effect, by

using anisotropic strength parameter (used in B series analyses), is reduced to 9.13%. When the strain compatibility concept is applied to the stress-strain relations in C and D analyses, it resulted in slightly less peak strength predictions than those of C and D analyses.

7.1.2 Linearly Increasing Strength Cases

The failure surface predictions in B series analyses for both slopes (30° and 60°) were relatively close to those determined by the Modified Bishop method, while those in C and D analyses were much shallower than the latter. Particularly, it was found that the failure surface was much shallower (i.e., mid-slope failure) when a higher degree of strain softening (30%) was prescribed in the stress-strain relations. In spite of the high maximum shear strain concentration in the toe, it was explicitly shown that failures in all series analyses were initiated from an element a few elements below the crest and propagated toward the toe. The distribution of i angles in the 30 degree slope was much wider (-3.0° to 62.0°) than that of the 60 degree slope (-6.0° to 35.0°) so that a wider range of stress paths were involved in the failure for the 30 degree slope. However, the majority of the elements involved in the failure even in the 30 degree slope belonged to the active mode so that the slope stabilities in both slopes were mostly influenced by the active mode strengths.

The overestimates in the mobilized strength due to neglecting the progressive failure effect, which would be possible in B-3 and B-4 type analyses

were 9.96% in D-3-c and 6.62% in D-4-b, respectively. On the other hand, the overestimates due to neglecting both the progressive failure and anisotropic strength effects, which would be accompanied by A type analyses, were as large as 32.3% in C-3-c (30) and 17.0% in C-4-b (60). It was also found that the two types of overestimates increase as the anisotropic strength curve number increases. It is specifically shown that both the anisotropic strength and progressive failure effects are much greater for the 30 degree slope since the variation of stress paths involved in the failure is much wider. When the strain compatibility concept is applied to the stress-strain relations in C and D analyses, it resulted in slightly higher peak strength predictions than those of C and D analyses.

7.1.3 Overconsolidated Clay Cases

The most probable failure in A analysis based on the maximum shear strain distribution was of a toe type, which is in good agreement with that determined by the Modified Bishop method. However, when anisotropic strengths were implemented in B, C, D and E analyses, base failures occurred. The highly concentrated maximum shear strain at the toe is propagated toward the crest with excavation, but the peak strength was mobilized first at an element near the crest. The trend of shallow failure surfaces with a high degree of strain softening, which has been observed in normally consolidated clay, was also observed only in E series analyses. The α angles along the failure surface were found to be well

distributed in the range of 0° to about 90° . Particularly, i angles near the crest were found to be considerably greater than 0° due to high OCR.

It was shown that the overestimate in the mobilized strength due to neglecting the progressive failure effect, which would be possible in B-1 type analysis, is as large as 8.38% in D-1-d analysis. On the other hand, the overestimate due to neglecting both the progressive failure and anisotropic strength effects, which would be accompanied by A type analysis, was as large as 28.90% in D-1-d analysis. When the strain compatibility concept is applied to the stress-strain relations in C and D analyses, it resulted in slightly less peak strength predictions than those of C and D analyses.

In order to compare the stress path ranges involved along the failure surfaces, the i angle distributions at failures in the entire analyses performed in this study are plotted together as shown in Fig. 6.71. It is clearly shown that the slopes with base failure have relatively wider ranges of stress paths as compared to those of toe-failed slopes. When comparison is made between the toe-failed slopes of the normally consolidated clays, the stress path range in the 60 degree slope is much narrower than that of the 30 degree slope.

The peak strength ratios for the entire analyses performed in this study are summarized in Table 6.18.

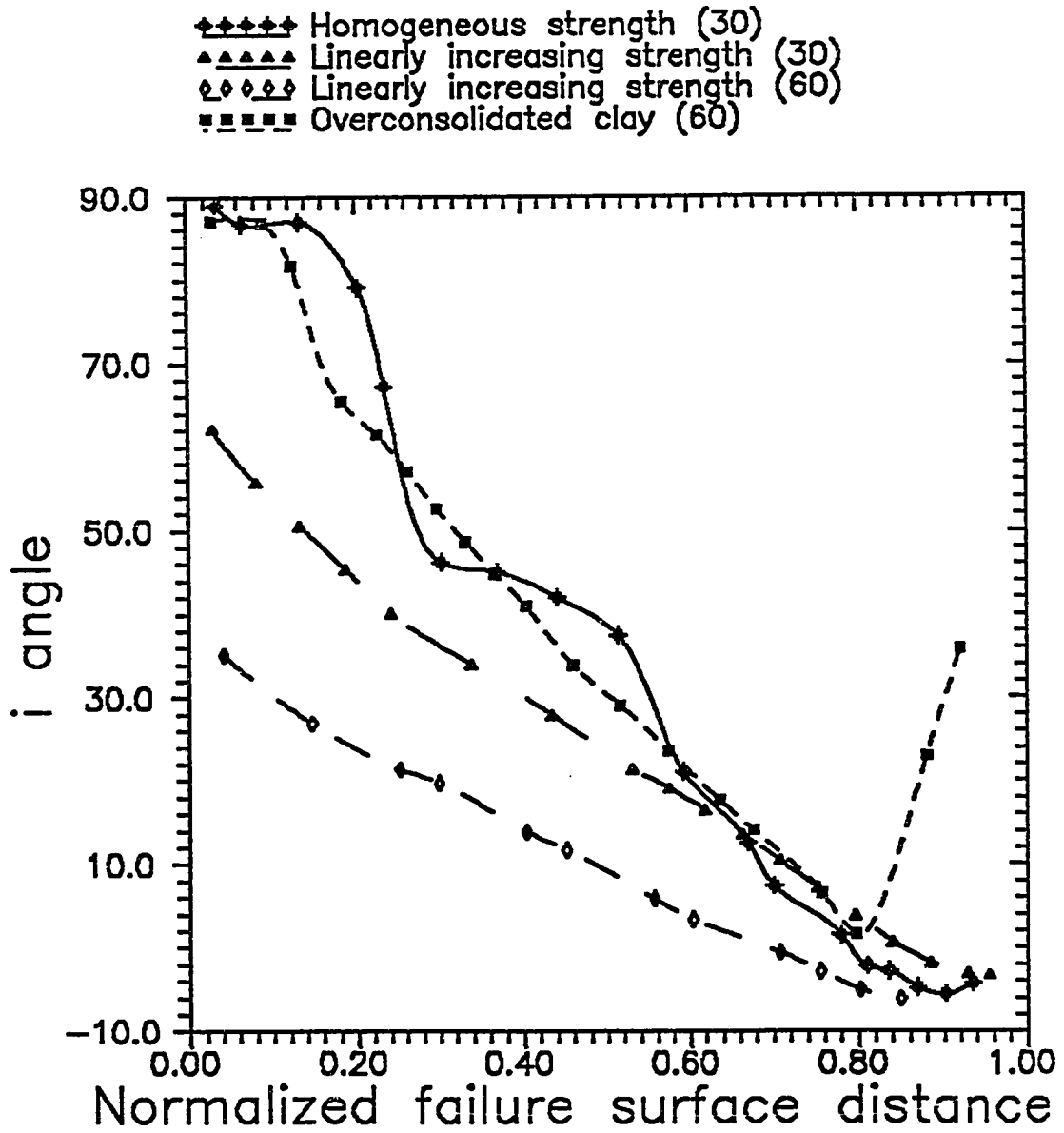


Fig. 6.71 Distributions of i angles along the failure surfaces

Table 6.18 Summary of the peak mobilized strength ratios from the entire cases

Material history	Normally consolidated clay			Overconsolidated clay (60 degree)
	Homogeneous (30 degree)	Linearly Increasing strength		
		30 degree	60 degree	
Case	D-1-c	C-3-c	C-4-b	C-1-d
OE ¹	25.0%	32.3%	17.0%	24.1%
Case	D-1-c	D-3-c	D-4-b	D-1-d
OE ²	9.13%	9.96%	6.62%	8.38%

7.2 Conclusions

This study has been focused on the evaluation of both anisotropic strength and progressive failure effects on the slope stability analysis. Based on the analyses results presented herein, the following conclusions can be made.

1. Based on the laboratory testing data collected in this study, it was found that strain softening is a common phenomenon even in normally consolidated clays. However, it is particularly pronounced in the mode of loading close to the K_0 -consolidated undrained compression and is negligible at the K_0 -consolidated undrained extension type of loading. Therefore, it is not appropriate to assume consistent stress-strain pattern and degree of strain softening for the entire stress paths.
2. The maximum overestimates in the mobilized strength which would be accompanied by the isotropic compression strength analysis (i.e., ignoring

both the anisotropic strength and progressive failure effects) may range from 16.3% up to 32.3% depending on the anisotropic strength variation and the range of stress paths involved in the slope failure.

3. The maximum overestimates in the mobilized strength, which would be resulted by anisotropic strength analysis (i.e., ignoring the progressive failure effect), may range from 6.62% up to 9.13% depending on the anisotropic strength variation and the range of stress paths involved in the slope failure.
4. Therefore, when the conventional limit equilibrium method is used with the isotropic compression strengths or anisotropic strengths, it is necessary to take into consideration the overestimate in the strength mobilization to reduce the factor of safety depending on the stress-strain relations of the elements along the failure surface.
5. As the inclination angle of slope increases beyond 60 degrees, especially in the normally consolidated clay with a linearly increasing strength profile, the range of stress paths, which would be involved in the toe failure, become narrow and the failure will be close to a simultaneous type. In such cases, rigorous slope stability analysis may be replaced by a simple isotropic strength analysis with the least overestimate in the strength mobilization, unless the soil is of highly anisotropy.
6. When the peak in summation of the undrained strengths along the failure surface takes place, the factor of safety in strict sense should be unity.

Since the peak occurs while the slope is experiencing a considerable amount of deformation, the design factor of safety in practice must be defined based on the allowable deformation of the slope in the slope analysis.

7. When a high degree of strain softening is prescribed in the stress-strain relations (except for homogeneous strength case), the deformation pattern of slope becomes much more brittle and the global failure tends to occur at an early excavation stage with less soil mass involved.
8. The non-uniformity of maximum shear strain distributions along the failure surface is high in the base failure case and moderate in the toe failure case particularly for the 60 degree slope.
9. In spite of the non-uniformity of maximum shear strain level along the failure surface, when the strain compatibility concept is applied to the stress-strain relations obtained in C and D analyses, it results in the similar peak strength values to those of C and D analyses. This can be explained by the fact that the stress-strain relations prescribed in the analyses are rather insensitive to the non-uniformity in the maximum shear strain distribution since the high degree of strain softening is limited to the elements with the stress paths close to $i=0^\circ$.

BIBLIOGRAPHY

- Abdel-Ghaffar, M.E.M (1990), "The Meaning and Practical Significance of the Cohesion Intercept in Soil Mechanics," Ph.D. Thesis, University of Illinois at Urbana-Champaign, Urbana, Ill.
- Adikari, G.S.N. and Parkin, A.K. (1981), "Effect of Stress-Strain Laws on Predictions of Rockfill Dam Performance," Proceedings of Symposium on Implementation of Computer Procedures and Stress-Strain Laws in Geotechnical Engineering, Chicago, Vol. 2, pp. 373-386.
- Alarcon-Guzman, A., Leonards, G.A., and Chameau, J.L. (1988), "Undrained Monotonic and Cyclic Strengths of Sands," Journal of Geotechnical Engineering Division, ASCE, Vol. 114, No. 10, pp. 1089-1109.
- Arthur, J.R.F., Chua, K.S., and Dunstan, T. (1977), "Induced Anisotropy in Sand," Geotechnique, No. 1
- Atkinson, J.H. and Richardson, D. (1987), "The Effect of Local Drainage in Shear Zones on the Undrained Strength of Overconsolidated Clay," Geotechnique, Vol. 37, No. 3, pp. 393-403.
- Barron, R.A. (1964), Discussion of "Stability Coefficients for Earth Slopes," by Bishop, A.W. and Morgenstern, N.R., Geotechnique, Vol. 14, No. 4, pp. 360-361.
- Biondi, P., Manfredini, F., Martinetti, S., Rickbackhi, R., and Riccioni, R. (1976), "Limit Load of a Foundation in a Strain Softening Soil," Proceedings of the 2nd International Conference on Numerical Methods in Geomechanics, ASCE, Blacksburge, VA, Vol. 1, pp. 580-589.
- Bishop, A.W. (1955), "The Use of the Slip Circle in the Stability Analysis of Slopes," Geotechnique, Vol. 5, No. 1, pp. 7-17.
- Bishop, A.W. (1966), "The Strength of Soils as Engineering Materials," Geotechnique, Vol. 16, No. 2, pp. 91-128.

- Bishop, A.W. (1967), "Progressive Failure - with Special Reference to the Mechanism Causing It," Proceedings of Geotechnical Conference, Oslo, Vol. 2, pp. 142-150.
- Bishop, A.W. (1971), "The Influence of Progressive Failure on the Choice of the Method of Stability Analysis," Geotechnique, Vol. 21, pp. 168-172.
- Bishop, A.W. and Bjerrum, L. (1960), "The Relevance of the Triaxial Test to the Solution of Stability Problems," Proceedings of Research Conference on Shear Strength of Cohesive Soils, ASCE, Boulder, Colorado, pp. 437-501.
- Bjerrum, L. (1967), "Progressive Failure in Slopes of Overconsolidated Plastic Clay and Clay Shales," Journal of the Soil Mechanics and Foundation, ASCE, Vol. 93, No. SM5, pp. 3-49.
- Bjerrum, L. (1973), "Problems of Soil Mechanics and Construction on Soft Clays: SOA Report," Proceedings of the 8th International Conference on Soil Mechanics and Foundation Engineering, Moscow, U.S.S.R., Vol. 3, pp. 111-159.
- Bjerrum, L. and Landva, A. (1966), "Direct Simple-Shear Tests on a Norwegian Quick Clay," Geotechnique, Vol. 16, pp. 1-20.
- Booker, J.R. and Davis, E.H. (1972), "A Note on a Plasticity Solution to the Stability of Slopes in Inhomogeneous Clays," Geotechnique, Vol. 22, No. 3, pp. 509-513.
- Boscardin, M.D., Selig, E.T., Lin, R.S., and Yang, G.Y. (1990), "Hyperbolic Parameters for Compacted Soils," Journal of Geotechnical Engineering, ASCE, Vol. 116, No. 1, pp. 88-104.
- Boughton, N.O. (1970), "Elastic Analysis for Behavior of Rockfill," Journal of Soil Mechanics and Foundation Division, ASCE, Vol. 96, No. 5, pp. 1715-1733.
- Bowels, J.E. (1982), Foundation Analysis and Design, 3rd Edition, McGraw-Hill Book Company, New York
- Burland, J.B. (1965), "The Yielding and Dilation of Clay," Geotechnique, Vol. 15, No. 2, pp. 211-214.
- Casagrande, A. and Carrillo, N. (1944), "Shear Failure of Anisotropic Materials," in Contribution to Soil Mechanics 1941-1953, Boston Society of Civil Engineers, Boston.

- Casagrande, A. and Wilson, S.D. (1960), "Testing Equipment, Techniques and Errors: Moderators' report, Session 2," Proceedings of Research Conference on Shear Strength of Cohesive Soils, ASCE, Boulder, Colorado, pp. 1123-1130.
- Castro, G. (1975), "Liquefaction and Cyclic Mobility of Saturated Sand," Journal of the Geotechnical Engineering Division, ASCE, Vol. 101, No. GT6, pp. 551-569.
- Cathie, D.N. and Dungar, R. (1978), "Evaluation of Finite Element Predictions for Constructional Behavior of a Rockfill Dam," Proceedings of Instn. Civil Engineers, Part II, Vol. 65, pp. 551-568.
- Chandler, R.J. (1984), "Recent European Experience of Landslides in Overconsolidated Clays and Soft Rocks," Proceedings of the 4th International Symposium on Landslides, University of Toronto Press, Toronto, Ontario, Canada, Vol. 1, pp. 61-81.
- Chandler, R. J. and Skempton, A.W. (1974), "The Design of Permanent Cutting Slopes in Stiff Fissured Clays," Geotechnique, Vol. 24, No. 4, 457-466.
- Chen, W.F. and Mizuno, E. (1990), Nonlinear Analysis in Soil Mechanics, Elsevier New York.
- Chen, W.F. and Scawthorn, C.R. (1970), "Limit Analysis and Limit Equilibrium Solutions in Soil Mechanics," Soils and Foundations, Japanese Society of Soil Mechanics and Foundation Engineering, Vol. 10, No. 3, pp. 13-49.
- Chowdhury, R.N. (1978), Slope Analysis, Developments in Geotechnical Engineering Vol. 22, Elsevier North-Holland Inc. New York.
- Christiansen, E.A. (1983), "The Denholm Landslide, Saskatchewan. Part 1: Geology", Canadian Geotechnical Journal, Vol. 20, pp. 197-207.
- Clough, R.W. and Woodward, R.J. (1967), "Analysis of Embankment Stresses and Deformations," Journal of Soil Mechanics and Foundation Division, ASCE, Vol. 93, No. 4, pp. 529-549.
- Collin, A. (1846), "Recherches Experimentales Sur Les Glissements Spontanes Des Terrains Argileux," Carrillan Coeury, Paris.
- Crooks, J.H.A., Been, K., Mickleborough, B.W., and Dean, J.P. (1986), "An Embankment Failure on Soft Fissured Clay," Canadian Geotechnical Journal, Vol 23, No. 1.

- Cundall, P.A. (1987), "Distinct Element Methods of Rock and Soil Structure," In Brown, E.T. (Ed.), Analytical and Computational Methods in Engineering Rock Mechanics, pp. 129-163.
- Cundall, P.A. (1989), "Numerical Experiments on Localization in Frictional Materials," Ingenieur-Archiv, Vol. 59, pp. 148-159.
- Dafalias, Y.F. and Popov, E.P. (1975), "A Model of Nonlinear Hardening Materials for Complex Loadings," Acta Mech., Vol. 21, pp. 173-192.
- Das, B.M. (1990), Principles of Geotechnical Engineering, 2nd Edition, PWS-KENT Publishing Company, Boston.
- Davis, E.H. (1968), "Theories of Plasticity and the Failure of Soil Masses," Soil Mechanics, Selected Topics, Lee, I.K. (Editor), American Elsevier, New York, N.Y., pp. 341-354.
- De Beer, E. (1969), "Experimental Data Concerning Clay Slopes," Proceedings of the 7th International Conference Soil Mechanics, Mexico, Vol. 2, pp. 517-525.
- De Jong, D.J.G. (1957), "Graphical Method for the Determination of Slip-Line Fields in Soil Mechanics," Ingenieur, 69(29), pp. 61-65 (in Dutch).
- Dembicki, E., Dravtchenko, J., and Sibille, E. (1964), "Sur Les Solutions Analytiques Approchees Des Problemes D'equilibre Limite Plan Pour Milieux Coherents et Pesants," Journal of Mechanics, Vol. 3, pp. 277-312.
- De Mello, V.F.B. (1977), "Reflections on Design Decisions of Practical Significance to Embankment Dams," Geotechnique, Vol. 27, pp. 279-355.
- Desai, C.S. and Siriwardane, H.J. (1984), Constitutive Laws for Engineering Materials with Emphasis on Geological Materials, Prentice-Hall, Inc., Englewood Cliffs, New Jersey.
- Desai, C.S., Phan, H.V., and Sture, S. (1981), "Procedure, Selection and Application of Plasticity Models for a Soil," International Journal of Numerical and Analytical Methods in Geomechanics, Vol. 5, pp. 295-311.
- Deschamps, R.J. (1993), "A Study of Slope Stability Analysis," Ph.D. Thesis, Purdue University.

- Deschamps, R.J. and Leonards, G.A. (1992) "A Study of Stability Analysis," Proceedings of a Specialty Conference, Geotechnical Special Publication No. 31, Stability and Performance of Slopes and Embankments-II, ASCE, New York, pp. 267-291.
- Drucker, D.C. (1953), "Limit Analysis of Two- and Three-Dimensional Soil Mechanics Problems," Journal of Mechanics and Physics of Solids, Vol. 1, pp. 217-226.
- Drucker, D.C. (1966), "Concepts of Path Independence and Material Stability for Soils," Kravtchenko, J. and Sirieys, P.M. (Editors), Proceedings of IUTAM Symposium, Grenoble., Springer, Berlin, pp. 23-43.
- Drucker, D.C. and Prager, W. (1952), "Soil Mechanics and Plastic Analysis or Limit Design," Quart. Applied Mathematics, Vol. 10, pp. 157-165.
- Duncan, J.M. (1992), "State of the Art: Static Stability and Deformation Analysis," Proceedings of a Specialty Conference, Geotechnical Special Publication No. 31, Stability and Performance of Slopes and Embankments-II, ASCE, New York, pp. 222-266.
- Duncan, J.M., Byrne, P.M., Wong, K.S., and Mabry, P. (1980), "Strength, Stress-Strain and Bulk Modulus Parameters for Finite Element Analysis of stresses and Movements in Soil Masses," University of California, Berkeley, CA, Report No. UCB/GT/80-01.
- Duncan, J.M. and Chang, C.Y. (1970), "Nonlinear Analysis of Stress and Strain in Soils," Journal of Soil Mechanics and Foundation Division, ASCE, Vol. 96, No. SM5, pp. 1629-1653.
- Duncan, J.M. and Dunlop, P. (1969), "Slopes in Stiff Fissured Clays and Shales," Journal of Soil Mechanics and Foundation Division, ASCE, Vol. 94, No. 2, pp. 467-492.
- Duncan, J.M. and Dunlop, P. (1969), "Behavior of Soils in Simple Shear Tests," Proceedings of the 7th International Conference in Soil Mechanics and Foundation Engineering, Vol. 1, pp. 101-109.
- Dunlop, P. and Duncan, J.M. (1970), "Development of Failure around Excavated Slopes," Journal of Soil Mechanics and Foundation Division, ASCE, Vol. 96, No. 2, pp. 471-494.

- Dunlop, P., Duncan, J.M., and Seed, H.B. (1968), "Finite Element Analyses of Slopes in Soil," Geotechnical Engineering Report No. TE-68-3, University of California, Berkeley
- Drucker, D.C., Gibson, R.E., and Henkel, D.J. (1957), "Soil Mechanics and Work-Hardening Theories of Plasticity," Transactions, ASCE, Vol. 122, pp. 338-346.
- Drucker, D.C., Greenberg, H.J., and Prager, W. (1952), "Extended Limit Design Theorems for Continuous Media," Quarter. Applied Mathematics, Vol. 9, pp. 381-346.
- Eisenstein, Z., Krishnayya, V.G., and Morgenstern, N.R. (1972), "An Analysis of the Cracking at Duncan Dam," Proceedings of Performance of Earth-Supported Structures, Lafayette, Indiana, Vol. I, pp. 765-777.
- Eisenstein, Z. and Simmons, J.V. (1975), "Three-Dimensional Analysis of Mica Dam," Proceedings of International Symposium on Criteria and Assumptions for Numerical Analysis of Dams, Swansea, U.K., pp. 1051-1070.
- Fang, H.Y. and Hirst, T.J. (1970), "Application of Plasticity Theory to Slope Stability Problems," Highway Research Record, 323, pp. 26-38.
- Fredlund, D.G. (1984), Discussion on Session VII(b), Proceedings of the 4th International Symposium on Landslides, Toronto, Ontario, Canada, 3, 135.
- Fredlund, D.G. and Krahn, J. (1977), "Comparison of Slope Stability Methods of Analysis," Canadian Geotechnical Journal, 14, pp. 429-439.
- Finno, R.J. and Rhee, Y. (1992), "Kinematically Unconstrained Compression of Soft Clay," Proceedings of a Specialty Conference, Geotechnical Special Publication No. 31, Stability and Performance of Slopes and Embankments-II, ASCE, New York, pp. 143-157.
- Gibson, R.E. and Morgenstern, N. (1962), "A Note on the Stability of Cuttings in Normally Consolidated Clays," Geotechnique, Vol. 12, pp 212-216.
- Graham, J. (1968), "Plane Strain Failure in Cohesionless Soils," Geotechnique, Vol. 18, pp. 301-316.
- Graham, J. (1986), "Slope Stability Analysis: Application in Plastic Clays," Proceedings of the 34th Annual Conference on Soil Mechanics and Foundation Engineering, Minnesota, pp. 13-48.

- Hansen, J.B. and Gibson, R.E. (1949), "Undrained Shear Strengths of Anisotropically Consolidated Clays," Geotechnique No. 3, pp. 189-204.
- Hardin, B.O. and Black, W.L. (1968), "Vibration Modulus of Normally Consolidated Clay," Proceedings of ASCE, Vol. 94, No. SM2, pp. 353-369.
- Harr, M.E. (1977), "Mechanics of Particular Media - A Probabilistic Approach," McGraw-Hill, New York, pp. 543.
- Hill, R. (1950), The Mathematical Theory of Plasticity, Oxford University Press, London, pp. 355.
- Hill, R. (1956), "On the Problem of Uniqueness in the Theory of a Rigid-Plastic Solid," Journal of Mechanics and Physics of Solids, Vol. 4.
- Hoeg, K. (1972), "Finite Element Analysis of Strain-Softening Clay," Journal of Soil Mechanics and Foundation Division, ASCE, Vol. 98, No. SM1, pp. 43-58.
- Hwang, C.T., Ho, M.K., and Wilson, N.E. (1969), "Finite Element Analysis of Soil Deformation," Proceedings of Symposium on Application of Finite Element Methods in Civil Engineering, Vanderbilt University, pp. 729-746.
- Ishibashi, I. and Choi, J.W. (1994), "Geotechnical Engineering Support for Craney Island Project - Phase II: Laboratory Determination of Soil Properties and Levee Stability Analysis," Geotechnical Engineering Report 94-1, Department of Civil and Environmental Engineering, Old Dominion University, Norfolk, Virginia.
- Itasca Consulting Group, Inc. (1993), FLAC: Fast Lagrangian Analysis of Continua, User Manual, Version 3.2, Minneapolis, Minnesota, U.S.A
- Jacobsen, M. (1967), "The Undrained Shear Strength of Preconsolidated Boulder Clay," Proceedings of Geotechnical Conference, Oslo, Vol. 1, pp. 119-122.
- Jamiolkowski, M., Ladd, C.C., Germaine, J.T. and Lancellotta, R. (1985), "New Developments in Field and Laboratory Testing of Soils," Proceedings of the 11th International Conference on Soil Mechanics and Foundation Engineering, Vol. 1, pp. 57-153.
- Janbu, N. (1954), "Application of Composite Slip Surfaces for Stability Analysis," Proceedings of European Conference on Stability of Earth Slopes, Stockholm, pp. 43-49.

- Janbu, N. (1957), "Earth Pressure and Bearing Capacity Calculations by Generalized Procedure of Slices," Proceedings of the 4th International Conference on SMFE, London, Vol. 2, 207-212.
- Jeyapalan, J.K., Duncan, J.M., and Seed, H.B. (1983), "Analysis of Flow Failures of Mine Tailings Dams," Journal of Geotechnical Engineering, ASCE, Vol. 109, No. 2, pp. 150-171.
- Kalteziotis, N.A. and Kyrou, K. (1985), "Undrained Bearing Capacity of Strain Softening Clay," Proceedings of the 11th International Conference on Soil Mechanics, San Francisco, Vol. 2, pp. 773-776.
- Kenny, T.C. (1963), "Stability of Cuts in Soft Soils," Journal of Soil Mechanics Division, ASCE, Vol. 89, No. SM5, pp. 17-37.
- Kenney, T.C. (1967), "Slide Behavior and Shear Resistance of a Quick Clay Determined from a Study of the Landslide at Selnes, Norway," Proceedings of Geotechnical Conference, Vol. 1, pp. 57-64.
- Koutsoftas, D. and Ladd, C. C. (March, 1985), "Design Strengths for an Offshore Clay," Journal of Geotechnical Engineering, ASCE, Vol. 111, No. 3, pp. 337-355.
- Kotter, F. (1903), "Die Bestimmung des Druckes an gekrummten Gleitflächen," eine Aufgabe aus der Lehre vom Erddruck., Monatsber., Akad., Wiss., Berlin, pp. 229-233.
- Krieg, R.D. (1975), "A Practical Two-Surface Plasticity Theory," Journal of Applied Mechanics, Vol. 42, pp. 641-646.
- Kulhawy, F.H. and Duncan, J.M. (1972), "Stresses and Movements in Oroville Dam," Journal of Soil Mechanics and Foundation Division, ASCE, Vol. 98, No. 7, pp. 653-665.
- Ladd, C.C. (1964), "Stress-Strain Modulus of Clay from Undrained Triaxial Tests," Proceedings of ASCE, Vol. 90, No. SM5.
- Ladd, C.C. (1965), "Stress-Strain Behavior of Anisotropically Consolidated Clays during Undrained Shear," Proceedings of the 6th International Conference on Soil Mechanics and Foundation Engineering, Vol. 1, pp. 282-286.
- Ladd, C.C. (1971), "Strength Parameters and Stress-Strain Behavior of Saturated Clays," Massachusetts Institute of Technology, Department of Civil Engineering, Research Report R71-23.

- Ladd, C.C. (1975), "Foundation Design of Embankments Constructed on Connecticut Valley Varved Clays," Research Report R75-7, Department of Civil Engineering, MIT, Cambridge, MA.
- Ladd, C.C. (1991), "Stability Evaluation during Staged Construction," Journal of Geotechnical Engineering, ASCE, Vol. 117, No. 4, pp. 540-615.
- Ladd, C.C., Foott, R., Ishihara, K., Schlosser, F., and Poulos, H.G. (1977), "Stress-Deformation and Strength Characteristics: SOA Report," Proceedings of the 9th International Conference on Soil Mechanics and Foundation Engineering, Vol. 2, pp. 421-494.
- Ladd, C.C. and Foott, R. (1974), "New Design Procedure for Stability of Soft Clays," Journal of Geotechnical Engineering Division, ASCE, Vol. 100, No. 7, pp. 763-786.
- Lade, P.V. (1977), "Elasto-Plastic Stress-Strain Theory for Cohesionless Soil with Curved Yield Surfaces," International Journal of Solids Structure, Vol. 13, pp. 1014-1035.
- Lade, P.V. (1982), "Localization Effects in Triaxial Tests on Sand," Proceedings of IUTAM Conference on Deformation and Failure of Granular Materials, Delft, pp. 461-471.
- Lade, P.V. and Duncan, J.M. (1973), "Cubical Triaxial Tests on Cohesionless Soil," Journal of Soil Mechanics and Foundation Division, ASCE, Vol. 99, No. SM10, pp. 793-812.
- Lade, P.V. and Duncan, J.M. (1975), "Elasto-Plastic Stress-Strain Theory for cohesionless Soil," Journal of Geotechnical Engineering Division, ASCE, Vol. 101, No. GT10, pp. 1037-1053.
- Lade, P.V. and Tsai, J. (1985), "Effects of Localization in Triaxial Tests on Clay," Proceedings of the 11th International Conference on Soil Mechanics and Foundation Engineering, Vol. 2, pp. 549-552.
- Lambe, T.W. (1964), "Methods of Estimating Settlement," Proceedings of ASCE Settlement Conference, Northwestern University.
- Lambe, T.W. and Whitman, R.V. (1969), "Soil Mechanics," Wiley, New York
- Larson, R. (1980), "Undrained Shear Strength in Stability Calculation of Embankment and Foundation of Soft Clays," Canadian Geotechnical Engineering Journal, Vol. 17, No. 4, pp. 591-602.

- Lee, K.L. and Seed, H.B. (1967), "Drained Strength Characteristics of Sands," Journal of the Soil Mechanics and Foundation Engineering Division, ASCE, Vol. 93, No. SM6, pp. 117-141.
- Leonards, G.A. (1962), "Engineering Properties of Soils," Foundation Engineering, Edited by Leonards, G.A., McGraw-Hill, New York.
- Leroueil, S., Tavenas, F., Brucy, f., LaRochelle, P., and Roy, M. (1979), "Behavior of Destructured Natural Clays," Journal of Geotechnical Engineering, ASCE, Vol. 105, No. GT6, pp. 759-778.
- Lo, K.Y. and Lee, C.F. (1972), Discussion, Journal of Soil Mechanics and Foundation Division, ASCE, Vol. 98, No. SM9, pp. 981-983.
- Lo, K.Y. and Lee, C.F. (1973), "Stress Analysis and Slope Stability in Strain-Softening Materials," Geotechnique, Vol. 23, No. 1, pp. 1-11.
- Mesri, G. and Abdel-Ghaffar, M.E.M. (1992), "Cohesion Intercept in Effective Stress-Stability Analysis," Journal of Geotechnical Engineering, Vol. 119, No. 8, pp. 1229-1249.
- Miki, H., Kutara, I., Minami, T., Nishimura, J., and Fukuda, N. (1988), "Experimental Studies on the Performance of a Polymer Grid Reinforced Embankment," Proceedings of International Geotechnical Symposium on Theory and Practice of Earth Reinforcement, Fukuoka, Japan, pp. 431-436.
- Mitchell, J.K. (1976), Fundamentals of Soil Behavior, John Wiley and Sons, Inc., New York.
- Morgenstern, N.R. and Price, V.E. (1965), "The Analysis of the Stability of General Slip Surfaces," Geotechnique, Vol. 15, No. 1, pp. 70-93.
- Mroz, Z, Norris, V.A., and Zienkiewicz, O.C. (1978), "An Anisotropic Hardening Model for Soils and Its Application to Cyclic Loading," International Journal of Numerical and Analytical Methods in Geomechanics, 2, pp. 203-221.
- Mroz, Z, Norris, V.A., and Zienkiewicz, O.C., (1979), "Application of an Anisotropic Hardening Model in the Analysis of Elasto-Plastic Deformation of Soils," Geotechnique, Vol. 29, No. 10, pp. 1-34.
- Novotortsev, V.I. (1958), "Application of the Theory of Plasticity to Problems of Determining the Bearing Capacity of Building Foundations," Izv., VNIG 22.

- Peck, R. B. (1967), "Stability of Natural Slopes," Journal of the Soil Mechanics and Foundations, ASCE, Vol. 93, No. SM4, pp. 403-415.
- Penman, A.D.M., Burland, J.B., and Charles, J.A. (1971), "Observed and Predicted Deformations in a Large Embankment Dam during Construction," Proceedings of Instn. Civil Engineers, 49, pp. 1-21.
- Potts, D.M., Dounias, G.T., and Vaughan, P.R. (1990), "Finite Element Analysis of Progressive Failure of Carsington Embankment," Geotechnique, Vol. 40, No. 1, pp. 79-101.
- Prandtl, L. (1920), "Uber die Harte plastischer Korper," Nachr. K. Ges. Wiss. Gott., Math.-Phys., Kl., pp. 74-85.
- Prevost, J.H. and Hoeg, K. (1975), "Effective Stress-Strain-strength Model for Soils," Journal of Geotechnical engineering Division, ASCE, Vol. 101, No. GT3, pp. 259-278.
- Reissner, H. (1924), "Zum Erddruckproblem," Proceedings of the 1st International Conference on Applied Mechanics, Delft, pp. 295-311.
- Richardson, A.M., Brand, E.W., and Menon, A. (1975), "In-Situ Determination of Anisotropy of a Soft Clay," Proceedings of Conference on In-Situ Measure of Soil Properties, ASCE, Vol. 1, pp. 336-349.
- Roscoe, K.H. and Burland, J.B. (1968), "On the Generalized Stress-Strain Behavior of 'Wet' Clay," Heyman, J. and Leckie, F.A. (Editors), Engineering Plasticity, Cambridge University Press, Cambridge, England, pp. 535-609.
- Roscoe, K.H. (1953), "An Apparatus for the Application of Simple Shear to Soil Samples," Proceedings of the 3rd International Conference on Soil Mechanics and Foundation Engineering, Vol. 1, pp. 186-191.
- Roscoe, K.H., Schofield, A.N., and thurairajah, A. (1963), "Yielding of Clays in State Wetter Than Critical," Geotechnique, Vol. 8, No. 1, pp. 22-53.
- Sambhandharaksa, S. (1977), "Stress-Strain-Strength Anisotropy of Varved Clays," Ph.D. Thesis, Massachusetts Institute of Technology, Massachusetts
- Sarma, S.K. (1973), "Stability Analysis of Embankments and slopes," Geotechnique, Vol. 23, pp. 423-433.

- Schofield, A.N. and Wroth, C.P. (1968), Critical State Soil Mechanics, McGraw-Hill, New York.
- Shibata, T., Tominaga, M., and Matsuoka, H. (1976), "FE Analysis of Soil Movements below a Test Embankment," Proceedings of Conference on Numerical Methods in Geomechanics, Blacksburg, Virginia, pp. 599-611.
- Skempton, A.W. (1957), "Discussion: the Planning and Design of the New Hong Kong Airport," Proceedings of Instn. Civil Engineers, London, Vol. 7, pp. 305-307.
- Skempton, A.W. (1964), "Long-Term Stability of Clay Slopes," Geotechnique, Vol. 14, No. 2, pp. 77-100.
- Skempton, A.W. (1977), "Slope Stability of Cuttings in Brown London Clay," Proceedings of the 9th International Conference on Soil Mechanics and Foundation Engineering, Tokyo, Japan, pp. 261-270.
- Smith, I.M., and Hobbs, R. (1976), "Biot Analysis of Consolidation Beneath Embankments," Geotechnique, Vol. 26, No. 1, pp. 149-171.
- Snitbhan, N., and Chen, W.F. (1976), "Finite Element Analysis of Large Deformations in Slopes," Proceedings of Conference on Numerical Methods in Geomechanics, Blacksburg, Virginia, pp. 744-756.
- Sokolovskii, V.V. (1965), Statics of Granular Media, Pergamon press, New York
- Spencer, A.J.M. (1962), "Perturbation Methods in Plasticity III, Plane-Strain of Ideal Soils and Plastic Solids with Body Forces," Journal of Mechanics and Physics of Solids, 10, pp. 165-177
- Spencer, E. (1967), "A Method of Analysis of the Stability of Embankments Assuming Parallel Interslice Forces," Geotechnique, Vol. 17, No. 1, pp. 11-26.
- Sture, S. and Ko, H.Y. (1976), "Stress Analysis of Strain-Softening Clay," Proceedings of the 2nd International Conference Numerical Methods in Geomechanics, ASCE, Blacksburg, VA, Vol. 1, pp. 580-589.
- Tavenas, F. and Leroueil, S. (1985), Discussion on Theme Lecture 2: "New Developments in Field and Laboratory Testing of Soils," by Jamiolkowski et al., Proceedings of the 11th International Conference on Soil Mechanics and Foundation Engineering, San Francisco, Vol. 5, pp. 2693-2694.

- Taylor, D.W. (1948), "Fundamentals of Soil Mechanics," Wiley, New York
- Terzaghi, K. and Peck, R.B. (1948), "Soil Mechanics in Engineering Practice," 2nd Edition, John Wiley and Sons, Inc, New York, U.S.A
- Thamm, B.R. (1979), "Numerical Analyses of Embankments over Soft Subsoils," Proceedings of the 3rd International Conference on Numerical Methods in Geotechnical Engineering, Aachen, pp. 725-731.
- Thomas, R.L., Pecquet, R.A., and Arman, A. (1976), "Numerical Analyses of Embankments over Soft Soils," Proceedings of Conference on Numerical Methods in Geomechanics, Blacksburg, Virginia, pp. 623-638.
- Thomson, S. and Kjartanson, B.H. (1985), "A Study of Delayed Failure in a Cut Slope in Stiff Clay," Canadian Geotechnical Journal, Vol. 22, pp. 286-297.
- Vermeer, P.A. and Borst, R.D. (1984), "Non-Associated Plasticity for Soils, concrete and Rock," HERON, Vol. 29, No. 3, pp. 1-62.
- Whitman, R.V. and Bailey, W.A. (1967), "Use of Computers for Slope Stability Analysis," Journal of the Soil Mechanics and Foundations Division, ASCE, Vol. 93, No. SM4, pp. 475-498.
- Wright, S.G., Kulhawy, F.H., and Duncan, J.M. (1973), "Accuracy of Equilibrium Slope Stability Analysis," Journal of the Soil Mechanics and Foundations Division, ASCE, Vol. 99, No. SM10, pp. 783-791.
- Wroth, C.P. and Simpson, B. (1972), "An Induced Failure at Trial Embankment: Part II Finite Element Computations," Proceedings of Performance on Earth and Earth-Supported Structures, Lafayette, Indiana, Vol. I, pp. 65-79.
- Yamada, Y., Yoshimura, N., and Sakurai, T. (1968), "Plastic Stress-Strain Matrix and Its Application for the Solution of Elastic-Plastic Problem by the Finite Element Method," International Journal of Mechanics and Science, 10, pp. 341-354.
- Yoshida, R.T. and Krahn, J. (1985), "Movement and Stability Analysis of the Beaver Creek Landslide," Saskatchewan, Canada, Canadian Geotechnical Journal, Vol. 22, pp. 277-285.

APPENDIX

Hardening and Softening Parameters

A simple example of a possible definition for a hardening parameter is the volumetric plastic strain:

$$\Delta e^{pv} = |\Delta e_1^{pv} + \Delta e_2^{pv} + \Delta e_3^{pv}| \dots\dots\dots A1$$

where $i=1,2,3$ and the superscript pv stands for the plastic volume. This particular choice is useful for a highly compressive material like clay (Schofield and Worth, 1968). In shear, Hill (1950) proposed a simple hardening parameter for the metal plasticity:

$$\Delta e^{ps} = \sqrt{2/3 \times (e_1^{ps} e_1^{ps} + e_2^{ps} e_2^{ps} + e_3^{ps} e_3^{ps})} \dots\dots\dots A2$$

where the superscript ps stands for the plastic shear. The factor $2/3$ is conveniently determined from the uniaxial test. In stressing a metal bar, we have:

$$e_2^{ps} = e_3^{ps} = -0.5 e_1^{ps} \dots\dots\dots A3$$

as metals show no plastic volume change. Then, the so-called hardening parameter Δe^{ps} simply coincides with the uniaxial plastic strain:

$$\Delta e^{ps} = \Delta |\epsilon_1^{ps}| \dots\dots\dots A4$$

When FLAC is used to model testing condition in axisymmetric mode (triaxial test), it is inappropriate to use the hardening constant, 2/3, as given by Hill (1950). It is because that the hardening constant is based on an isotropic yield surface in which all three components of the principal plastic strains are non-zero. Therefore, for the Mohr-Coulomb model, the constant was chosen such that the hardening parameter is identical to the axial plastic strain for a triaxial test as can be seen in Eq. E-24 in the FLAC manual.

It should be noted that in the axisymmetric test such as the triaxial compression test, the major principal stress is in the vertical direction, while the minor and intermediate stresses are in the horizontal direction. If the Mohr-Coulomb model is used to represent the testing condition, singularity is at the point at which $\sigma_x = \sigma_z$. If yielding occurs in x direction, then the flow rule tends to move the stress point toward z direction. If yielding occurs in z direction, then the opposite occurs. Hence, symmetry is maintained by the alternate yielding in x and z directions. This behavior is a consequence of the singularity in the Mohr-Coulomb yield surface.

VITA

Jong Woon Choi was born on February 11, 1960 in Pocheon, Kyung-Ki Do, Korea. He has an elder sister and a younger brother. He graduated from You-Shin high school in Su-Weon city, Kyung-Ki Do in 1978 and entered the bachelor's degree program of civil engineering at Dongguk University in Seoul, Korea. In the middle of the study in 1980, he joined the Navy of the Republic of Korea and returned to the college in 1983. He graduated from Dongguk University with a Bachelor of Engineering degree in 1985. After working for Korea Gas Corporation as a civil engineer for three years, he decided to study abroad in the United States of America. He pursued the study of civil engineering at Old Dominion University, Norfolk, Virginia, where he received his Master of Science degree in civil engineering in September, 1991. In the same university, he continued the study and earned his Doctor of Philosophy in civil engineering specializing in geotechnical engineering in May, 1996.